Crystallography Reports, Vol. 50, No. 2, 2005, pp. 167–176. Translated from Kristallografiya, Vol. 50, No. 2, 2005, pp. 199–208.

CRYSTAL CHEMISTRY

Systematic Studies of General Structural Characteristics of Organic Molecular Crystals and Prediction of Their Structures

L. N. Kuleshova*, D. W. M. Hofmann, and M. Yu. Antipin***

** Nesmeyanov Institute of Organoelement Compounds, Russian Academy of Sciences, ul. Vavilova 28, Moscow, 119991 Russia*

e-mail: lukul@xrlab.ineos.ac.ru

*** University of Frankfurt on Main, Marie Curie Str., Frankfurt on Main, D-60439 Germany*

Received December 5, 2003

Abstract—A strategy is developed for constructing noncentrosymmetric (polar) packings of crystals necessary for the manifestation of a number of important physical properties of crystals. The strategy is based on the analysis of the data obtained in the systematic studies of general structural characteristics of pairs of centro- and noncentrosymmetric polymorphic modifications of a number of organic molecular structures. An algorithm for prediction of such packings is designed on the basis of the potential function singled out by the method of automatic statistical search for information (Data Mining) in the Cambridge Structural Database. © *2005 Pleiades Publishing, Inc.*

INTRODUCTION

Crystal symmetry reflects the arrangement of molecules in crystals and determines many of the physical properties of solids including electrical, magnetic, linear and nonlinear optical properties, and electronic and ionic conductivity. Crystal engineering is a field of modern science dealing with the prediction and control of formation of crystal packings in order to create organic crystalline materials with the preset symmetry of the molecular environment that would ensure the manifestation of a desirable physical property. Since crystal formation depends not only on the thermodynamic but also on the kinetic factors (such as temperature, type of solvent, concentration, crystallization rate), a successful strategy for predicting packings should take into account the enthalpy of a possible packing and also the dynamic processes occurring in the solution. Although, in principle, it is possible to simulate molecular dynamics [1], the corresponding computations are very labor- and time-consuming. Therefore, the search for alternative ways of taking into account various kinetic factors is still an important problem in the experimental and theoretical construction of crystal symmetry. One of the possible approaches to a comparatively simple and fast (although not always explicit) method for taking into account the kinetic effects is analysis of a large bulk of structural information accumulated in various databases. Obviously, an experimentally determined crystal structure cannot provide information either on kinetics of nucleation or on kinetics of crystal growth, but it obviously demonstrates the final result of these processes. It is possible to assume that if a certain structural motif were encountered rather often it would reflect both the thermodynamic stability of the packing and the kinetic advantages of its formation. Therefore, the systematic study of the structures of typical supramolecular ensembles formed in crystals because of intermolecular bonds by the invocation of the information stored in the Cambridge Structural Database (CSD) acquires an ever-increasing importance for prediction of possible crystal structures [2, 3]. The attempts to study the types of supramolecular associates and their use in crystal engineering have repeatedly been made [4–12]. Thus, Gavezzotti and Filippini [13] suggested analysis of the CSD for better understanding of the possible ways of formation of various crystal packings. Earlier, we also undertook a systematic study of the crystal structures of the compounds which simultaneously formed centro- and noncentrosymmetric polymorphic modifications [14, 15]. The same chemical composition of the pairs of centro- and noncentrosymmetric polymorphic modifications allowed us to focus attention on the structural aspect and establish a number of the structural characteristics including common structural motifs of such modifications.

There have been numerous attempts to use the CSD data in the theoretical prediction of crystal packings [16, 17]. With this aim, Hofmann [18] used the method of automatic statistical search for information (Data Mining) in the CSD, managed to single out the real energy function, and made the minimum number of assumptions about the form of the functional. The force field of the potential function used by Hofmann allowed him to identify the "correct" structure in a list of predicted possible packings in 93% of the cases in

1063-7745/05/5002-0167$26.00 © 2005 Pleiades Publishing, Inc.

the sp. gr. $P1$ and 37% of the cases in the sp. gr. $P\bar{1}$. Since the accuracy of the parameterization of the Hofmann potential directly depends on the number and quality of the structural data analyzed, an ever-increasing number of precision structure determinations allows one to hope that the method of collecting structural information suggested by Hofmann would become an important instrument for solving numerous crystallographic problems and, in particular, for predicting crystal structures.

Below, we combine both above methods to design new materials with the structures with polar symmetries necessary for the manifestation of nonlinear optical activity and some magnetic properties.

BASIC STRUCTURAL CHARACTERISTICS OF PAIRS OF CENTRO- AND NONCENTROSYMMETRIC POLYMORPHIC MODIFICATIONS

Consider the most important structural characteristics established in the analysis of the structures of pairs of centro- and noncentrosymmetric polymorphic modifications [14, 15]. We selected the crystals described by the most widespread centrosymmetric $P\bar{1}$, $P2_1/c$, $Pbca$, chiral $P2_12_12_1$, $P2_1$, $P1$, and racemic noncentrosymmetric Pc, $Pna2_1$, $Pca2_1$ space groups. We analyzed the modifications with the same literal refcodes so that our sampling contained the compounds belonging to the groups of unresolved and rapidly inverted enantiomers.[1] The CSD (version 2000) has 128 such pairs.

When analyzing the structures of polymorphic modifications, we took into account the conditions of crystal formation, the molecule geometry, the type of a molecular associate formed in the crystal, and the unit-cell parameters.

All the structural information used in analysis was taken from the CSD, but, since the data on crystal formation are seldom indicated there, we also analyzed all the accessible original papers. The characteristics of the formation of centro- and noncentrosymmetric modifications were established by analyzing the most widespread pairs of polymorphs in the space groups $P2_1/c$ – $P2_12_12_1$ (41 pairs), $P2_1/c$ – $P2_1$ (17 pairs), $P2_1/c$ – $Pna2_1$ (16 pairs), and $P2_1/c$ – Pc (11 pairs).[2]

It turned out that in more than half of the centro- and noncentrosymmetric pairs considered, the polymorphs are formed in the same mother liquids and under the same kinetic conditions (concomitant polymorphism). Most of these pairs are formed by the compounds that may form rather strong intermolecular H bonds. It was also established that, in this case, both centro- and noncentrosymmetric modifications usually consist of the same supramolecular associates formed due to intermolecular hydrogen bonding.

The theoretical basis of the existence of concomitant polymorphism and the most typical examples of it were discussed in detail by Bernstein *et al.* [19]. Below, we analyze the structural characteristics of a large number of such modifications. We also compare the densities and thermodynamic stability of these modifications calculated with the use of the Hofmann potential function [17, 18] and the corresponding programs.

ENERGY CALCULATIONS AND DENSITY CORRELATIONS OF CENTRO- AND NONCENTROSYMMETRIC PACKINGS

Earlier, Gavezzotti and Filippini [13] compared the packing energies and some other thermodynamic properties of the pairs of centro- and noncentrosymmetric polymorphic modifications stable at room temperature found in the CSD, version 1991. However, they did not indicate the preferable type of packing because they were interested only in the absolute difference between these characteristics.[3] It was established that the differences between the packing energies (ΔE), packing densities (ΔD), and vibrational lattice entropies (ΔS) of two polymorphic modifications usually did not exceed several percent. Brock *et al.*, [20] took also into account the signs of these differences and performed comparative statistical analysis of crystal densities of the compounds crystallizing in both racemic and chiral space groups. They established that the character of the ΔD[4] distribution depends on the type of molecules forming a chiral–racemic pair of polymorphic modifications. Thus, they established that there is no noticeable difference between the packing densities of the racemic and chiral crystals for polymorphic modification of rapidly inverted enantiomers ($\Delta D_{av} = 0.20\%$). At the same time, on the average, the racemic crystals of the group of resolved enantiomers ($\Delta D_{av} = 0.92\%$) have denser packings than the chiral pairs.

Analysis of the differences in the densities of centro- and noncentrosymmetric polymorphic modifications in the crystals analyzed in [14, 15] is illustrated by the histograms in Fig. 1. Note that in our sampling the molecules of rapidly inverted enantiomers prevailed. We also show the normal distribution curves that describe these histograms. The average ΔD_{av} value for all the pairs of polymorphic modifications is –0.98%. (Characteristics of the normal distribution: the standard (root-mean-square) deviation $\sigma = 1.46$, the distribution amplitude $A_o = 15.89$, the correlation coefficients $K_{corr} = 0.858$). Thus, on the whole, the noncentrosymmetric structures in the modifications considered are denser than the noncentrosymmetric pairs.

[1] The modifications of resolved enantiomers (stereomers) often have different refcodes in the CSD.

[2] The structural characteristics of rare pairs of centro- and noncentrosymmetric polymorphic modifications will be considered in a separate publication.

[3] $\Delta P = [|(P_i - P_j)| \times 100]/P_i$.

[4] $\Delta D = [(D_{centro} - D_{noncentro}) \times 2 \times 100]/(D_{centro} + D_{noncentro})$.

We also made an attempt to see whether the type of an associate and the growth conditions influence the character of the ΔD distribution. With this aim, we divided all the ΔD values into two groups. The first one included the ΔD values of the polymorphs consisting of equivalent associates (mainly concomitant polymorphic modifications). The second group included the ΔD values of all the remaining polymorphic modifications synthesized under different conditions. It is seen from Figs. 1b and 1c that the distributions of the ΔD values for these two groups are different; in other words, the distribution of the ΔD values depends not only on the type of the molecules (as was indicated in [20]) but also on the method of preparation of the polymorphic modification. For the first group (Fig. 1b) (concomitant polymorphic modifications), the average ΔD_{av} value is –1.46% (σ = 0.84, A_o = 10.32, K_{cor} = 0.817); whence, it follows that the packings of concomitant polymorphic modifications are denser than the packings of their counterparts. In the second group (different crystallization conditions), ΔD_{av} = –0.31% (σ = 1.29, A_o = 9.17, K_{cor} = 0.852) (Fig. 1c) in full accordance with the results obtained in [20] for fast invertable enantiomers, where no noticeable difference between the densities of the packings of the racemic and chiral crystals was found either.

The distributions of the differences between energies are shown in Fig. 2.[5] The energies of the modifications were calculated using the FlexCryst program [18]. It is seen from Fig. 2 that the most energy advantageous modifications in our sampling are centrosymmetric ones. The average difference between energies is ΔE_{av} = 2.61% (characteristics of the distribution σ = 2.06, A_o = 4.20, K_{cor} = 0.59). These data are in good accordance with the results obtained by Gavezzotti and Filippini [13], who established that 80% of all the ΔE values lie within the range 1–3%. At the same time, the maximum in the ΔE distribution in [13] was located in the interval 0–1%.

In distinction from the ΔD distribution, the division of all the ΔE values into two groups in accordance with the associate type and the method of crystal synthesis (Figs. 2b, 2c) does not qualitatively influence the character of this distribution. The average ΔE_{av} value for the concomitant polymorphic modifications consisting of equivalent associates is 1.73% (σ = 0.55, A_o = 5.06, K_{cor} = 0.86, Fig. 2b) and for the pairs of modifications obtained under different conditions this value is 3.47% (very poor distribution parameters: σ = 22.2, A_o = 1.94, and K_{cor} = 0.49). The absence of any correlation in this case is explained by different crystal structures of the polymorphic modifications of this group. Thus, even if one takes into account a rather poor statistics of ΔE values, both concomitant modifications—centro- and noncentrosymmetric—obtained under different conditions are energetically favorable.

[5] $\Delta E = [(E_{centro} - E_{noncentro}) \times 2 \times 100]/(E_{centro} + E_{noncentro})$.

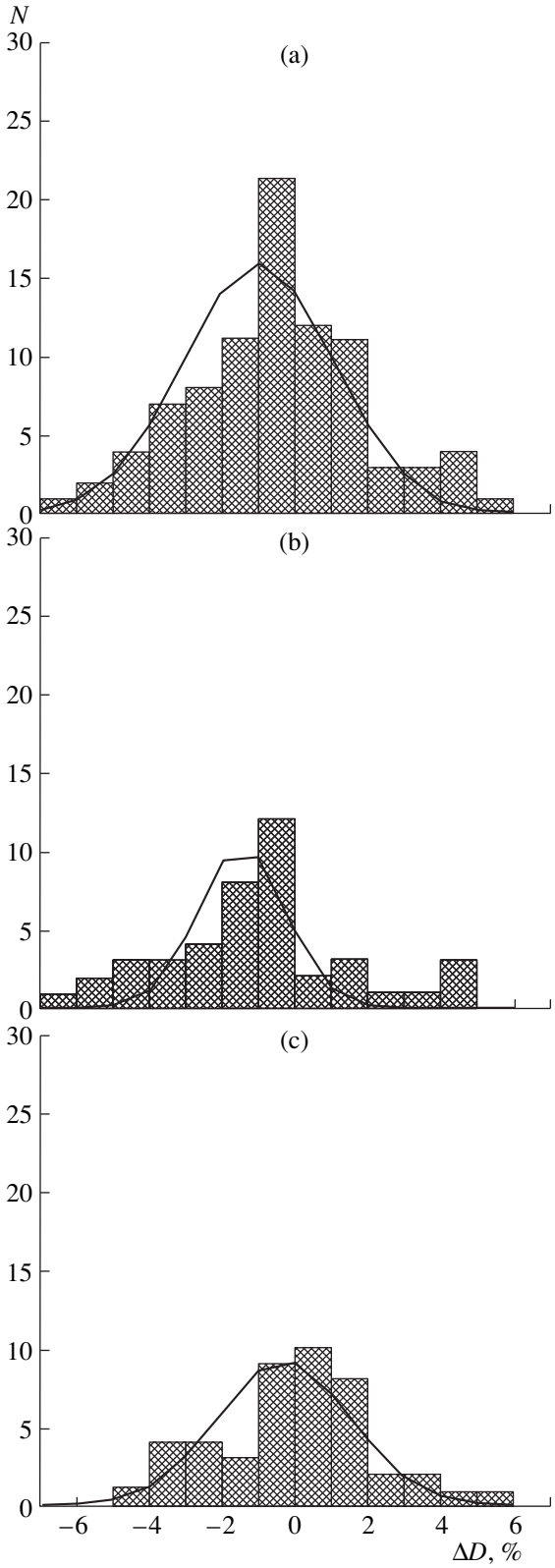

Fig. 1. Histograms of the ΔD distribution (and the corresponding normal distribution curves) for pairs of centro- and noncentrosymmetric polymorphic modifications: (a) general, (b) for the modifications constructed from equivalent supramolecular associates (concomitant polymorphic modifications), and (c) for modifications constructed from nonequivalent associates.

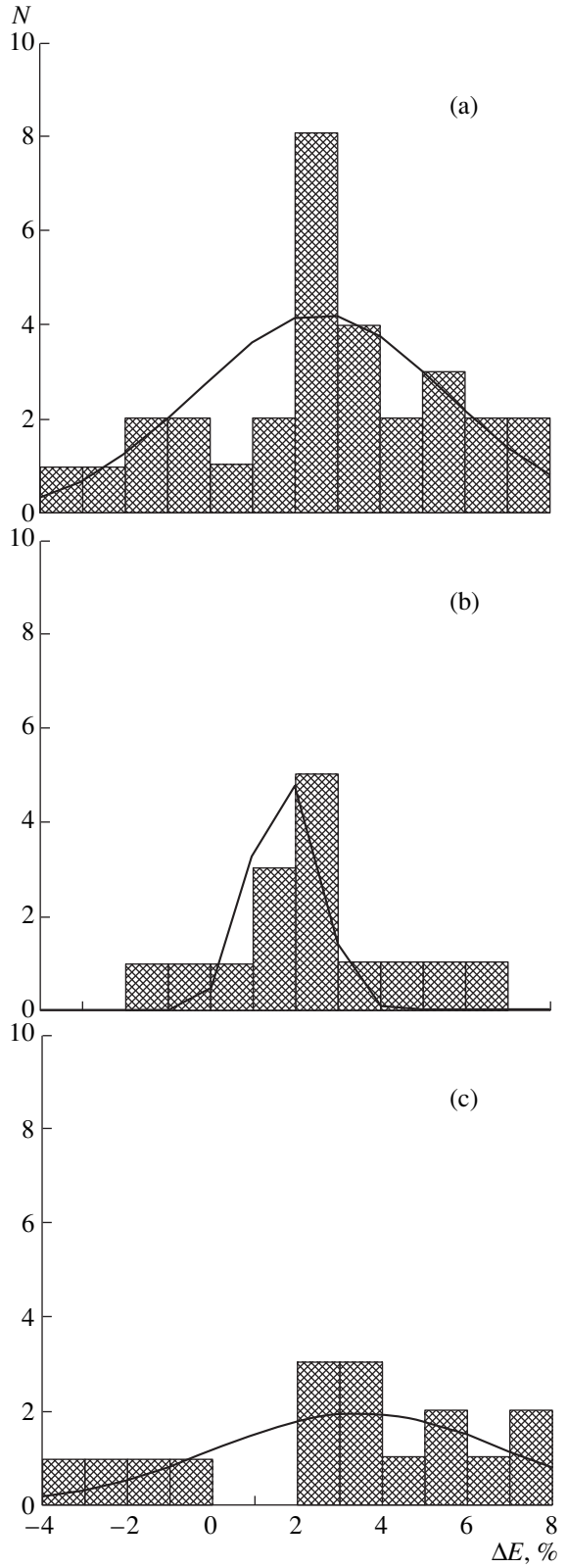

Fig. 2. Histograms of ΔE distributions (and the corresponding normal distribution curves) for pairs of centro- and noncentrosymmetric polymorphic modifications: (a) general, (b) for the modifications constructed from equivalent supramolecular associates (concomitant polymorphic modifications), and (c) for modifications constructed from nonequivalent associates.

Despite the existing difference between the densities, the centrosymmetric groups are more favorable. The point is that in denser packings (especially consisting of the equivalent supramolecular associates with hydrogen bonding) may have reduced intermolecular atom–atom contacts (in comparison with their equilibrium values). These reductions may give rise to stronger interatomic repulsion, which is reflected in a certain decrease in the total crystal energy. This may be illustrated by detailed analysis of atom–atom contacts in concomitant polymorphic modifications of *meta*-nitrophenol, MNPHOL [21, 22] ($P2_12_12_1$, $E_{noncentro}$ = –65.80 kJ/mol, ρ = 1.542 g/cm^3; $P2_1/n$, E_{centro} = –70.10 kJ/mol, ρ = 1.478 g/cm^3). In these crystals, the molecules linked by hydrogen bonds form equivalent molecular OH···O chains (Fig. 3). Table 1 lists the characteristics of the most representative contacts of the atoms participating in hydrogen bonding. As is seen from Table 1, a denser acentric structure described by the sp. gr. $P2_12_12_1$ has shorter contacts than the centrosymmetric crystal described by the sp. gr. $P2_1/n$. Considering the energy characteristics, we may state that, despite the unchanged character of the interatomic interactions (attraction of repulsion) in different modifications, the repulsive interaction is always much more pronounced in a denser structure. This reduces the total energy of the acentric structure in comparison with the energy of the centrosymmetric modification.

ROLE OF THE SYMMETRY OF MOLECULAR ASSOCIATE IN FORMATION OF CRYSTAL PACKING AND PREDICTION OF CRYSTAL STRUCTURE

When constructing a crystal with a preset symmetry, one has to bear in mind the conclusion drawn from the systematic study of pairs of centro- and noncentrosymmetric modifications: the symmetry of a molecular associate formed by sufficiently strong intermolecular hydrogen bonds plays an important role in the formation of the symmetry of a structure.

The two following cases are possible in the formation of centro- and noncentrosymmetric crystal packings (scheme 1):

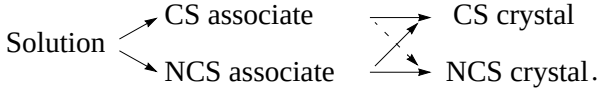

Scheme 1

If the molecules related by intermolecular hydrogen bonds form a noncentrosymmetric (NCS) associate, both noncentrosymmetric (NCS) or centrosymmetric (CS) crystal may be formed.[6] If the molecules related by intermolecular hydrogen bonds form a centrosym-

[6] It should be remembered that inversion in the molecules related to the group of unresolved enantiomers takes place without a considerable energy loss and, as a rule, proceeds due to rotations of the functional groupings by small angles with respect to one another.

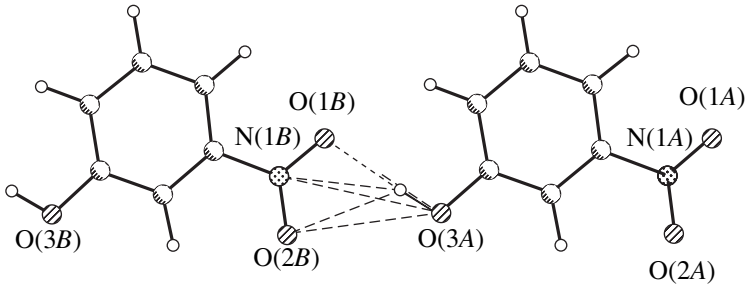

Fig. 3. Hydrogen bonding in polymorphic modifications of MNPHOL.

metric (CS) associate, a centrosymmetric (CS) crystal is usually formed. However, in some instances, a noncentrosymmetric (NCS) crystal structure with a pseudosymmetry and several molecules in the crystallographically independent part of the unit cell ($Z' > 1$) may be formed [23].

In both above cases, the crystal structure is formed not by individual molecules but by supramolecular associates which are more or less stable and still present in the mother liquor. Therefore, in terms of structure, the existence of polymorphic modifications, including concomitant ones, may be considered as the consequence of the multivariant superposition of the local equivalent supramolecular fragments (most often layers).

The results obtained were used to develop the strategy for constructing noncentrosymmetric crystal structures. This strategy reduces to the following. If molecules linked by intermolecular hydrogen bonds form a sufficiently stable noncentrosymmetric associate, the probability of the formation of a stable noncentrosymmetric structure under the appropriately selected crystallization conditions is rather high. In this case, the possibility of formation of a noncentrosymmetric associate may be confirmed either theoretically by computations (prediction of a crystal structure) or experimentally (presence of a noncentrosymmetric associate in a real but centrosymmetric crystal structure).

COMPUTATIONAL–THEORETICAL PREDICTION OF CRYSTAL STRUCTURE

At the first stage, it is very important to check whether the program and the statistical potential function suggested by Hofmann may generate real motifs of packings for compounds with strong intermolecular hydrogen bonds.

As a test, we tried to generate the crystal packing of a 3,4-dihydroxy-2-oxo-1-methyl-4-piperidine (TOMYEZ) crystal [24] in which the molecules form a branched system of intermolecular hydrogen bonds and rather strong double chains of centrosymmetric dimers (Fig. 4). The predicted optimum crystal structure turned out to be identical to the experimentally determined one and reproduced its unit-cell parameters, its system of hydrogen bonds, and the type of the supramolecular associate. Both the calculated and the experimentally determined crystal structures are shown in Fig. 5.

Another test example is a *meta*-nitrophenol (MNPHOL) crystal whose two well-known concomitant modifications have close unit-cell parameters and the same layered packings. The layers consist of infinite chains (hydrogen OH···H bonds) typical of monatomic alcohols (Figs. 6a, 6b) and connected via additional weaker CH···O interactions.

The predicted optimum MNPHOL structure is described by the orthorhombic sp. gr. *Pbca* with the *a* and *b* parameters close to the parameters of the well-known modifications and a double parameter *c*. The calculated packing and the real crystal structure have a layered nature. The layers are formed due to intermolecular hydrogen OH···O and CH···O bonds and have the topology (Fig. 6c) equivalent to the topology of the noncentrosymmetric orthorhombic polymorphic modification described by the sp. gr. $P2_12_12_1$. The unit-cell characteristics of the experimental and predicted packings are indicated in Table 2. The close unit-cell parameters of the experimentally determined and predicted structure and the equivalent topology of the supramolecular associates lead to the assumption that the predicted packing may be related to one of possible (but not implemented in practice) polymorphic modification of this compound and that the force field of the Hofmann potential function may reproduce the typical structural motifs even if they are formed by relatively weak hydrogen bonds.

CONSTRUCTION OF NONCENTROSYMMETRIC CRYSTAL STRUCTURE OF N'-(2-PHENYL-1H-INDOLE-3-ALDEHYDO-4-NITROPHENYLHYDROZONE)

An example of the successful use of the approach developed here is the construction of the packing of noncentrosymmetric N'-(2-phenyl-1H-indole-3-aldehydo-4-nitrophenylhydrozone) (**I**) crystals [25]. The donor–acceptor derivatives of hydrozones belong to the class of crystalline materials promising for nonlinear optics because they possess high values of molecular

Table 1. Lengths and energies of hydrogen bonds and reduced contacts in concomitant polymorphic modifications of MNPHOL

Contact	$D_{noncentro}$, Å $P2_12_12_1$	D_{centro}, Å $P2_1/n$	$E_{noncentro}$, kJ/mol $P2_12_12_1$	E_{centro}, kJ/mol $P2_1/n$	$E_{noncentro} - E_{centro}$
O(1*B*)···H	1.91	1.95	–0.16	–0.031	–0.129
O(1*B*)···O(3*A*)	2.89	2.94	0.859	0.459	0.400
O(2*B*)···H	2.53	2.65	0.799	0.629	0.170
O(2*B*)···O(3*A*)	3.25	3.32	–0.904	–0.975	0.071
N(1*B*)···H	2.53	2.62	1.291	0.875	0.416
N(1*B*)···O(3*A*)	3.46	3.52	–0.814	–0.784	–0.030
		Total energy	1.071	0.173	0.898

hyperpolarizabilities and may be readily synthesized by condensation of various donor derivatives of aromatic aldehydes and nitrophenylhydrazine. Crystals **I** are convenient objects for construction because they allow the comparatively easy control of formation of a crystal structure by varying the crystallization conditions [26–28]. Moreover, in crystals, hydrozone molecules usually form stable acentric supramolecular associates—planar chains—because of the hydrogen bonds of the central amino group to one of the oxygen atoms of the nitro group and the additional weak interaction between the CH group of the azomethine fragment with the same oxygen atom (the so-called Λ contacts). Molecules in **I** have additional groupings, the donors of hydrogen bonds, which, in principle, may change the scheme of formation of a supramolecular associate. However, our X-ray diffraction study of crystals **I** grown from dioxane [25] showed that their centrosymmetric packing described by the sp. gr. $P2_1/c$ is formed by noncentrosymmetric planar Λ chains characteristic of hydrozones (Fig. 7a). The geometric characteristics of a Λ contact are (N)H···O 2.01 Å and (C)H···O 2.54 Å.

An attempt of calculating the optimum packing of **I** using the Hofmann program [18] gave the desirable noncentrosymmetric crystal described by the sp. gr. *Cc* with a stable associate of another type (Fig. 7b) in which Λ chains are formed by the NH group of the indole fragment of the molecule and not by the NH group of the triadic grouping of hydrozone (the characteristics of an Λ contact: (N)H···O 2.14 Å and (C)H··O 2.31 Å). We also calculated molecular hyperpolariz-

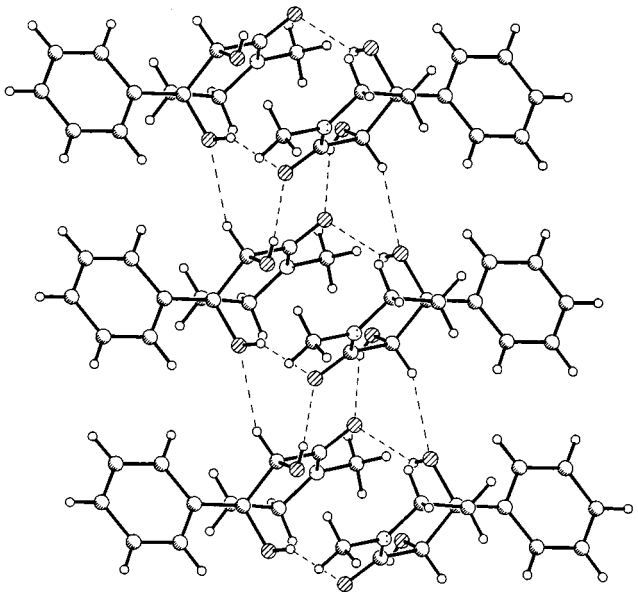

Fig. 4. Supramolecular associate formed due to H-bonds in the TOMYEZ structure.

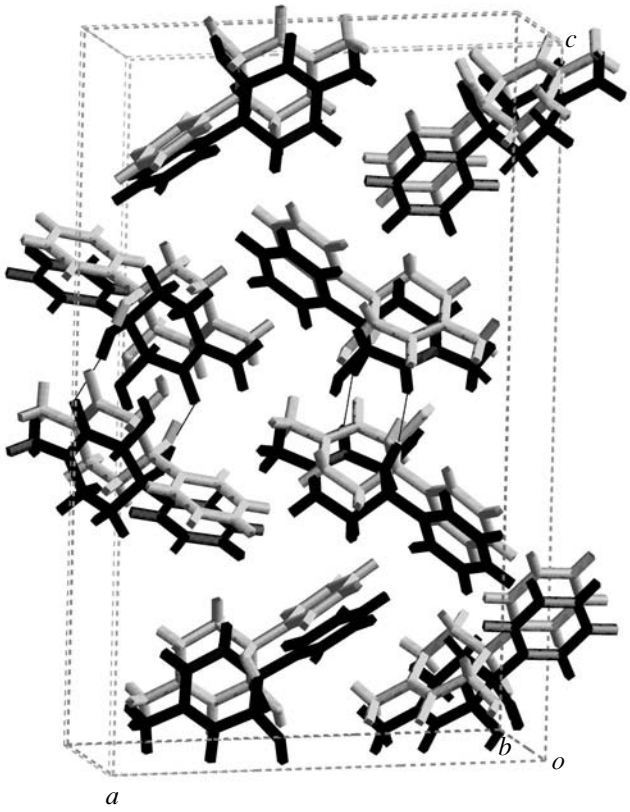

Fig. 5. Comparison of the experimentally determined and theoretically predicted TOMYEZ structures.

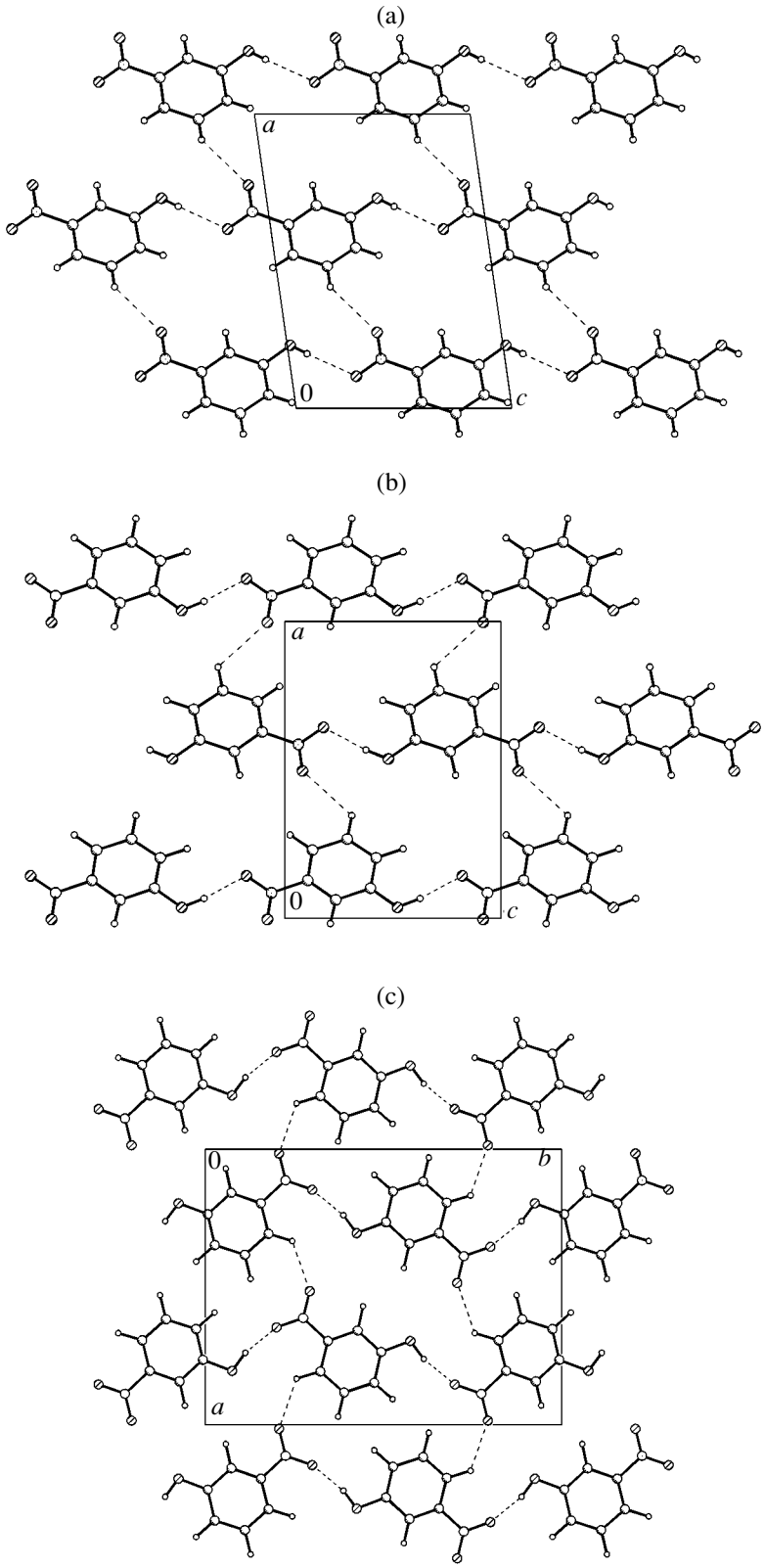

Fig. 6. Topology of supramolecular MNPHOL layers in (a) polymorphic modifications described by the sp. gr. $P2_1/c$, (b) polymorphic modifications described by the sp. gr. $P2_12_12_1$, and (c) predicted packing described by the sp. gr. *Pbca*.

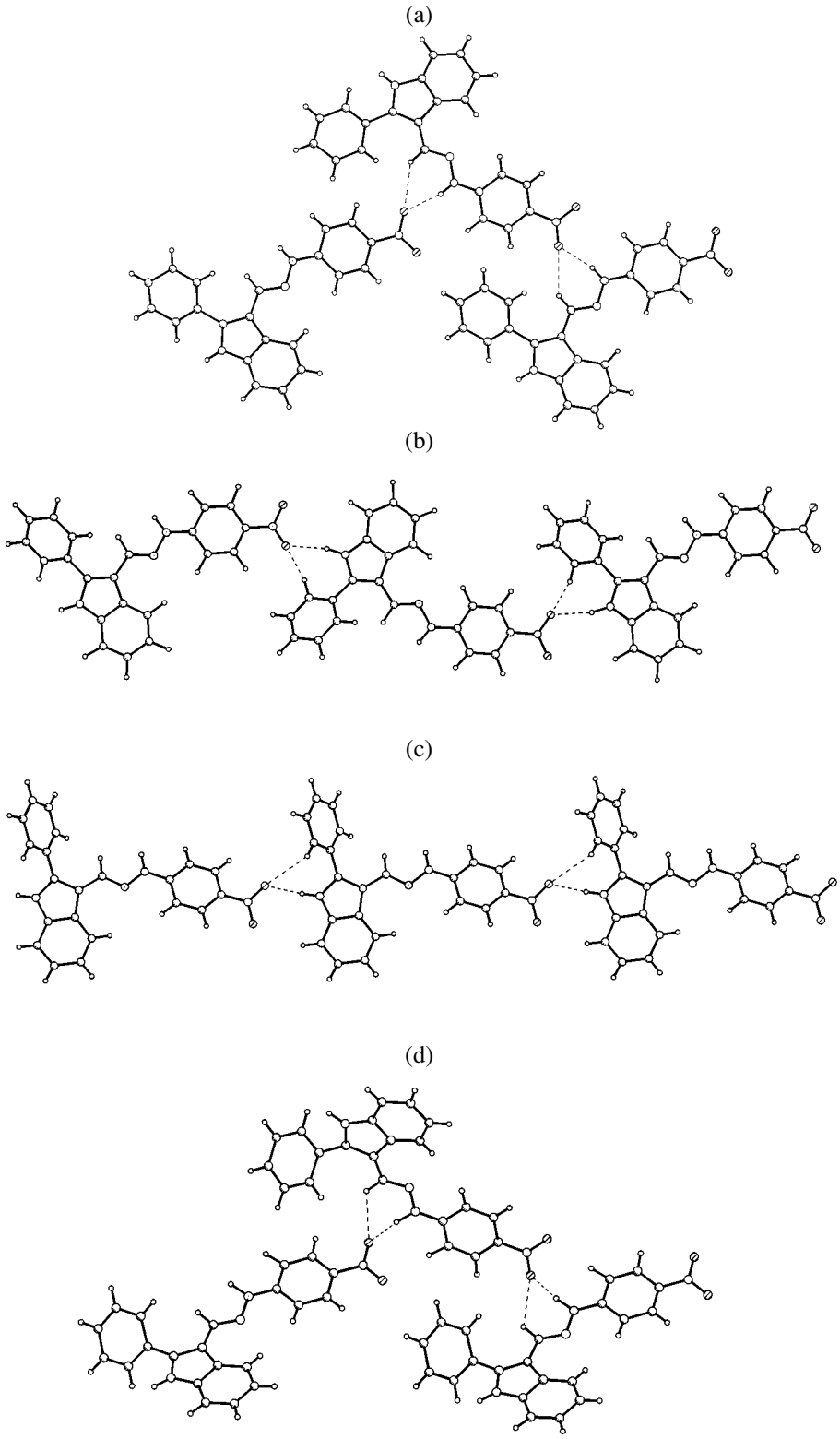

Fig. 7. Topology of the supramolecular chains in a N'-(2-phenyl-1H-indole-3-aldehydo-4-nitrophenylhydrozone) (**I**) crystal, sp. gr. $P2_1/c$. (a) Crystal grown from dioxane; (b) predicted packing, sp. gr. *Cc*; (c) crystal grown from pyridine, sp. gr. $P\bar{1}$; and (d) crystal grown from acetonitrile, sp. gr. $Pna2_1$.

Table 2. Unit-cell parameters of the polymorphic modifications of *meta*-nitrophenol and the predicted crystal structure

Sp. gr., *Z*	*a*, Å	*b*, Å	*c*, Å	α, deg	β, deg	γ, deg
$P2_1/c$, $Z = 4$	11.240	6.891	8.154	90	98.05	90
$P2_12_12_1$, $Z = 4$	11.136	6.649	8.091	90	90	90
Pbca, $Z = 8$	12.011	6.554	15.546	90	90	90

ability β and crystalline susceptibility *d* for the predicted noncentrosymmetric structure in accordance with [29]. The obtained characteristics of both molecular and crystalline nonlinearity were high ($\beta = 66.68 \times 10^{-51}$ cm^3/V^2, $d_{xxx} = 90.8$ pm/V and $d_{zzx} = 28.6$ pm/V). In the hope to obtain a real noncentrosymmetric crystal, we tried to grow other modifications of compound **I** by using various solvents. As a result, we obtained several new crystalline modifications;[7] however, only the crystals grown from pyridine and acetonitrile had the quality appropriate for X-ray diffraction analysis.

Crystals grown from pyridine were centrosymmetric, sp. gr. $P\bar{1}$. The structure of these real crystals consists of Λ chains of the same type as in the predicted noncentrosymmetric structure described by the sp. gr. *Cc* (Fig. 7c). Hydrogen bonding in this structure is formed with the participation of NH groups of indole fragments and oxygen atoms of nitro groups, (N)H···O 2.05 Å. However, because of the rotation of the phenyl group of the molecule, the CH···O contact stabilizing the planar structure of the Λ chain is considerably weakened, (C)H···O 2.97 Å.

The crystals grown from acetonitrile are noncentrosymmetric, sp. gr. $Pna2_1$, $Z = 4$. Like in crystals grown from dioxane, the supramolecular associate (Fig. 7d) is formed with the participation of the proton of the central amino group ((N)H···O 1.85 Å). However, as in the previous case, the contact between the CH group of the azomethine fragment and the oxygen atom of the nitro group is considerably weakened, (C)H···O 2.93 Å. As a result, the chain is not planar and the chain molecules are rotated with respect to one another so that the angle between the mean-square molecular planes of the chain amounts to 70.2°. Although molecular hyperpolarizability in the crystal is still rather high ($\beta = 65.7 \times 10^{-51}$ cm^3/V^2), the components of the susceptibility tensor ($d_{31} = -8.9$ pm/V, $d_{32} = 7.9$ pm/V, and $d_{33} = 23.2$ pm/V) are much lower than in the predicted optimum structure.

Thus, the developed construction strategy based on the establishment of common structural features, the rules of the formation of a desirable crystal structure, and the computational–theoretical prediction of optimum packings of promising compounds may become an important instrument for designing new materials with preset physical properties.

[7] The study of their structures by different methods including powder diffractometry and various computational methods are under way.

ACKNOWLEDGMENTS

This study was supported by the Russian Foundation for Basic Research, project no. 03-03-32716.

REFERENCES

1. A. Gavezzotti and G. Filippini, Chem. Commun. 287 (1998).
2. L. N. Kuleshova and M. Yu. Antipin, Usp. Khim. **68**, 3 (1999).
3. F. H. Allen and W. D. S. Motherwell, Acta Crystallogr., Sect. B: Struct. Sci. **58**, 407 (2002).
4. L. N. Kuleshova and P. M. Zorky, Acta Crystallogr., Sect. B: Struct. Crystallogr. Cryst. Chem. **36**, 2113 (1980).
5. Z. Berkovitch-Yellin and L. Leiserowitz, Acta Crystallogr., Sect. B: Struct. Sci. **40**, 159 (1984).
6. M. C. Etter, J. B. Bernstein, and J. M. McDonald, Acta Crystallogr., Sect. B: Struct. Sci. **46**, 256 (1990).
7. M. C. Etter, Acc. Chem. Res. **23**, 120 (1990).
8. J. Bernstein, R. Davis, L. Shimoni, and Chang Ning-Leh, Angew. Chem. Int. Ed. Engl. **34**, 1555 (1995).
9. G. R. Desiraju, Acc. Chem. Res. **29**, 441 (1996).
10. C. P. Brock and J. D. Dunitz, Chem. Mater. **6**, 1118 (1994).
11. G. R. Desiraju, Acc. Chem. Res. **35**, 565 (2002).
12. G. R. Desiraju, J. Mol. Struct. **656**, 5 (2003).
13. A. Gavezzotti and G. Filippini, J. Am. Chem. Soc. **117**, 12299 (1995).
14. L. N. Kuleshova and M. Yu. Antipin, Kristallografiya **47** (2), 303 (2002) [Crystallogr. Rep. **47**, 268 (2002)].
15. L. N. Kuleshova and M. Yu. Antipin, Kristallografiya **48** (2), 293 (2003) [Crystallogr. Rep. **48**, 259 (2003)].
16. A. Gavezzotti, Acc. Chem. Res. **27**, 309 (1994).
17. D. W. M. Hofmann and T. Lengauer, Acta Crystallogr., Sect. A: Found. Crystallogr. **53**, 225 (1997).
18. D. W. M. Hofmann and J. Apostolakis, J. Mol. Struct.: THEOCHEM **647**, 17 (2003).
19. J. Bernstein, R. J. Davey, and J.-O. Henk, Angew. Chem. Int. Ed. Engl. **38**, 3440 (1999).
20. C. P. Brock, W. B. Schwezer, and J. Dunitz, J. Am. Chem. Soc. **113**, 9811 (1991).
21. A. Coda, M. Fumagalli, F. Panderese, and L. Ungaretti, Acta Crystallogr., Sect. A: Cryst. Phys., Diffr., Theor. Gen. Crystallogr. **31**, 208 (1975).

22. F. Hamzaoui, F. Baert, and G. Wojcik, Acta Crystallogr., Sect. B: Struct. Sci. **52**, 159 (1996).

23. L. N. Kuleshova, M. Yu. Antipin, and I. V. Komkov, J. Mol. Struct.: THEOCHEM **647**, 41 (2003).

24. L. N. Kuleshova, V. N. Khrustalev, Yu. T. Struchkov, *et al.*, Kristallografiya **41** (4), 673 (1996) [Crystallogr. Rep. **41**, 636 (1996)].

25. L. N. Kuleshova, M. Yu. Antipin, V. N. Khrustalev, *et al.*, Kristallografiya **48** (4), 645 (2003) [Crystallogr. Rep. **48**, 594 (2003)].

26. C. Serbutoviez, C. Bossard, G. Knopfle, *et al.*, Chem. Mater. **7**, 1198 (1995).

27. I. Liakatas, M. S. Wong, V. Gramlich, *et al.*, Adv. Mater. **10** (10), 777 (1998).

28. F. Pan, C. Bossard, M. S. Wong, *et al.*, Chem. Mater. **9**, 1328 (1997).

29. *QCPE; MOPAC, Quantum Chemistry Program Exchange. Version 6* (1990).

Translated by L. Man

Crystallography Reports, Vol. 50, No. 2, 2005, pp. 177–184. Translated from Kristallografiya, Vol. 50, No. 2, 2005, pp. 209–216.

DIFFRACTION AND SCATTERING OF IONIZING RADIATIONS

Modern Possibilities for Calculating Some Properties of Molecules and Crystals from the Experimental Electron Density

A. I. Stash* and V. G. Tsirelson**

** Karpov Research Institute of Physical Chemistry, ul. Vorontsovo pole 10, Moscow, 103064 Russia*

*** Mendeleev University of Chemical Technology, Miusskaya pl. 9, Moscow, 125190 Russia*

e-mail: tsirel@muctr.edu.ru

Received October 16, 2003

Abstract—Methods for calculating some properties of molecules and crystals from the electron density reconstructed from a precise X-ray diffraction experiment using the multipole model are considered. These properties include, on the one hand, the characteristics of the electron density and the inner-crystal electrostatic field and, on the other hand, the local electronic energies (kinetic, potential, total), the exchange energy density, the electron-pair localization function, the localized-orbital locator, the effective crystal potential, and others. It is shown that the integration of these characteristics over pseudoatomic volumes bounded by the surfaces of the zero flux of the electron density gradient makes it possible to characterize directly from an experiment the properties of molecules and crystals in terms of the atomic contributions. The computer program WinXPRO2004, realizing these possibilities, is briefly described. © *2005 Pleiades Publishing, Inc.*

In recent years, precise X-ray diffraction experiment became an effective tool for studying the physical and chemical properties of solids that depend on the electron density distribution [1, 2]. The popularity of this method is due to the progress in the development of the experimental techniques and equipment [3–7] and improvement of the methods for processing experimental data and interpreting obtained results [1]. Reconstruction of the electron density from X-ray diffraction intensities (corrected for the absorption, thermal diffuse scattering, multiple scattering, and extinction) is generally performed using the structural multipole model [8–11]. The model (quasi-static) electron density is a function extrapolated to resolution of ~0.1 e $Å^{-3}$, which, despite the limited measurement accuracy and incomplete elimination of the effect of thermal averaging, is close to the quantum-mechanical electron density obtained from first principles. It is important that the model and quantum-mechanical electron densities are topologically similar (provided that the experimental data are sufficiently accurate and the diffraction and structural models used correspond to the physical reality) [12–15]. Therefore, the model electron density can be regarded as a homeomorphic image of the quantum-mechanical electron density, which is suitable for analysis in solid-state physics and chemistry.

In this paper, we report the results of the calculation of some properties of crystals based on the data on the experimental (model) electron density. Such calculations have not been reported previously.

Presently, the model electron density can be used to obtain, in good agreement with theory, the following characteristics of the electronic structure and properties of solids [16–18]:

the deformation, valence, and total electron densities;

the Laplacian of electron density [19];

the electrostatic potential [20–22];

the field of the electron density gradient [19] and/or the electrostatic potential field [23];

the dipole and quadrupole electric moments of molecules [24];

the electrostatic part of the intermolecular energy [1, 25];

the effective atomic charges corresponding to the electrostatic potential [26];

the electric field gradient at the positions of nuclei [1, 27];

the one-electron potential [28–33];

the local, kinetic, and potential electronic energies calculated within different approximations of the density-functional theory [34];

the critical points in the electron density, electrostatic potential, the Laplacian of the electron density, and the local energies;

the electron-pair localization function [35–37];

the localized-orbital locator [38];

the distribution of the exchange electron density in different approximations [17];

the local temperature and entropy of the electron gas [33, 39];

the exchange potential [17];

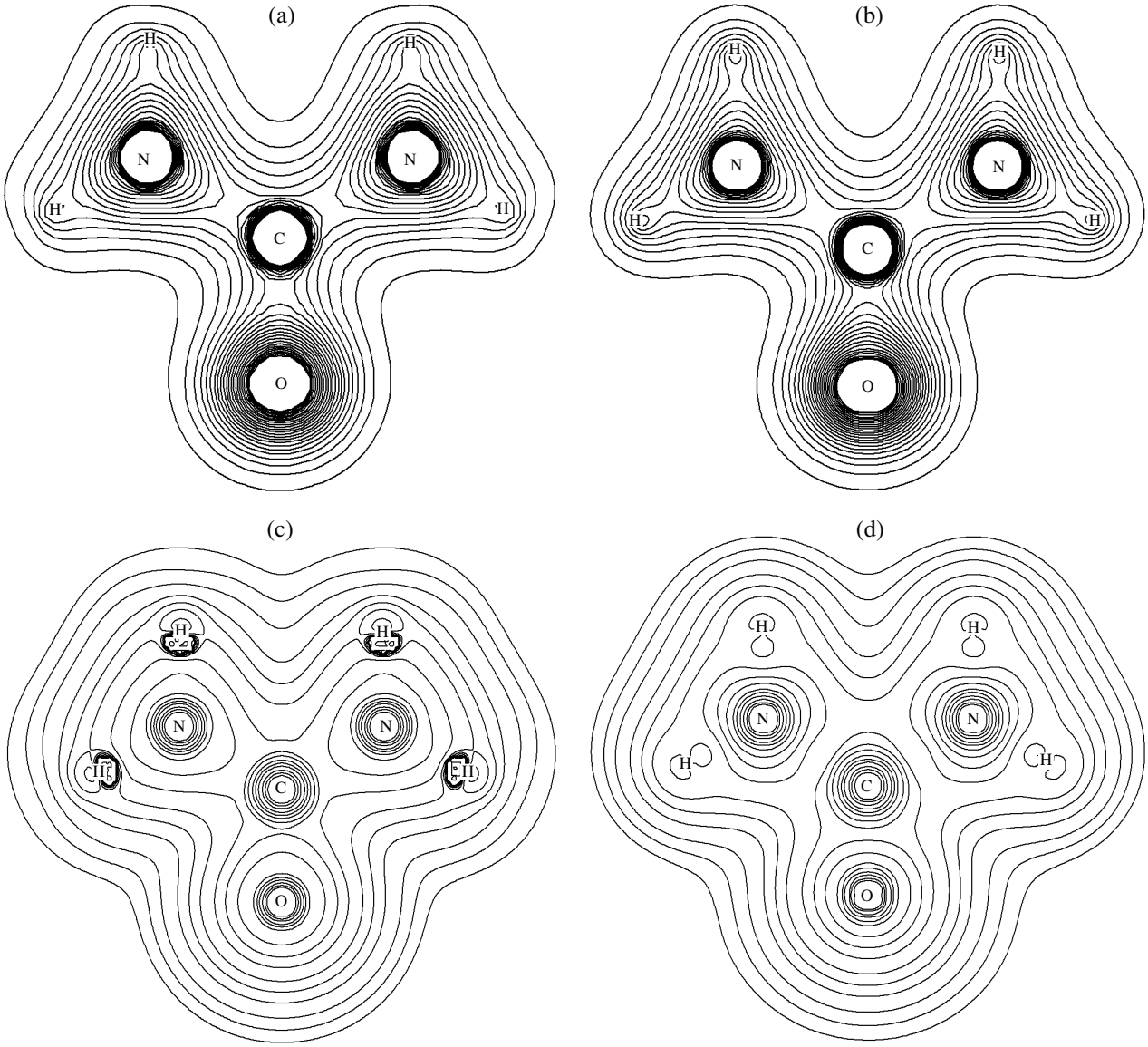

Fig. 1. Electron density distribution in a molecule of urea $CO(NH_2)_2$ (a) reconstructed from experimental X-ray diffraction data and (b) calculated by the *ab initio* Hartree–Fock method in the 6–311G** basis. Isolines are plotted with steps of 2×10^n, 4×10^n, and 8×10^n e Å^{-3} ($0 < n < 3$). The corresponding distributions of the kinetic energy density: (c) approximate distribution calculated from the experimental electron density according to (4) and (d) the Hartree–Fock distribution (isoline steps are 2×10^n, 4×10^n, and 8×10^n e Å^{-3} ($0 < n < 3$)). The experimental maps are constructed on the basis of the multipole parameters of one molecule. Small negative regions near the hydrogen nuclei (c) originate from the approximation scheme used (see [34] for more details).

the local Fermi momentum [17];

and any scalar field (electron density, electrostatic potential, local energies, and so on) integrated over a volume bounded by the surface of the zero flux of the electron density gradient.

Note that the local kinetic, potential, and exchange energies; the electron localization function; and the localized-orbital locator are calculated using the model electron density in the formulas of the density-functional theory [40]. In this case (the validity of which was demonstrated in [34]), theory and experiment are combined to the maximum extent.

The existence of corresponding software plays an important role in practical application of any new approach. There are programs [41–44] for calculating some of the properties listed above for the systems composed of atoms with $Z \le 36$. We have developed a new version of the WinXPRO program [45] which makes it possible to calculate all the above properties. The initial data for the calculation are the electron density parameters obtained within the Hansen–Coppens multipole model and the data on the crystal symmetry.

The WinXPRO program is a Windows application and has a graphical user interface which allows one to

easily create or automatically generate an input file using an output file and symmetry operations of the MOLLY [46] or XD [42] programs. The possibility of combining functions (for example, the effective crystal potential can be easily calculated as a sum of the electrostatic and exchange potentials) and the calculation of standard deviations of the electron density and its characteristics are provided. All characteristics can also be calculated for a promolecule or a procrystal. An atomic or a molecular cluster used in calculations is specified by choosing the distance from a specified atom (chosen point) or some space volume. The version of the WinXPRO2004 program used here makes it possible to perform calculations for a cluster of 350 independent atoms with $Z \le 76$.

The results of the calculations are given as both the numerical characteristics of the properties of molecules and crystals and their 1D, 2D, and 3D images, which can be visualized using the corresponding graphical programs (for more detailed information about the WinXPRO2003 program, see the Internet sites http://stash.chat.ru and http://xray.nifhi.ru/wxp).

Let us consider in more detail some new possibilities for calculating the properties of molecules and crystals within the above approach. We have chosen the characteristics that are especially important to establish the details of the chemical bond and the effect of structure on the physico-chemical properties of materials. As the objects of study, we chose a molecular crystal of urea, which is characterized by covalent and hydrogen bonds, and an $YBa_2Cu_3O_7$ crystal, in which bonds are predominantly ionic. The multipole parameters for these compounds were obtained in [47] (urea, measurement at 148 K) and [48] ($YBa_2Cu_3O_7$, synchrotron measurement [49] at room temperature).

The distribution of local kinetic energy in the one-electron theory is determined by the expressions [19]

$$k(\mathbf{r}) = -(1/2)\sum_i \lambda_i \nabla^2 \varphi_i(\mathbf{r}), \quad (1)$$

$$g(\mathbf{r}) = (1/2)\sum_i \lambda_i \nabla \varphi_i(\mathbf{r}) \nabla \varphi_i(\mathbf{r}), \quad (2)$$

which are related as follows:

$$k(\mathbf{r}) = g(\mathbf{r}) - \frac{1}{4}\nabla^2 \rho(\mathbf{r}) \quad (3)$$

(λ_i is the occupation number of the orbital $\varphi_i(\mathbf{r})$; from here on, the atomic system of units is used). The function $-\infty < k(\mathbf{r}) \le \infty$ is the quantum-mechanical (Schrödinger [19]) kinetic energy density. The function $g(\mathbf{r}) > 0$ is the quasi-classical kinetic energy density. Although it is impossible to unambiguously determine the kinetic energy density [50], expansion (2) gives the necessary condition for the nonnegativity of the electron distribution function over momenta and coordinates [50, 51].

Contributions to the electronic energy of the urea molecule (in au) calculated by integrating the local electronic energy density (6) over atomic volumes limited by the surfaces of the zero flux of the electron density gradient

C	O	N	H1	H2
–36.690	–75.193	–55.807	–0.215	–0.256
Total electronic energy of the molecule		–224.45 (crystal)	–224.046 (quantum-chemical calculation for one molecule)	

Using the result of Kirzhnits [52], which is well known in the density-functional theory [40], expression (2) can be approximated by the formula

$$g(\mathbf{r}) = \frac{3}{10}(3\pi^2)^{2/3}\rho^{5/3}(\mathbf{r}) + \frac{1}{72}\frac{|\nabla\rho(\mathbf{r})|^2}{\rho(\mathbf{r})} + \frac{1}{6}\nabla^2\rho(\mathbf{r}). \quad (4)$$

Thus, the density of the kinetic energy of electrons is approximately expressed in terms of the electron density and its first and second derivatives. The correct electron density cannot be obtained as a result of the minimization of the total energy within this approximation. However, in calculating $g(\mathbf{r})$, this approach makes it possible to use the experimental electron density, which is close to that calculated by the Hartree–Fock method (Figs. 1a, 1b). In this case, very good agreement with the Hartree–Fock kinetic energy density is obtained (Figs. 1a, 1b). Other examples concerning inorganic, organoelement, and organometallic systems were considered in [33, 39].

The distribution of the potential energy of electrons (the local potential energy density) is the field of the virial of the Ehrenfest force [19], which acts on an electron at a point $\mathbf{r}$ from nuclei and other electrons [53–55]. The Ehrenfest force governs the motion of electrons and, therefore, plays an important role in the quantum mechanics of molecules and crystals [54]. For each type of atomic interaction, the lines of maximum electron density connecting some nuclei (Bader bond paths) correspond to the lines of maximally negative potential energy density connecting the same nuclei (virial paths) [19]. The resulting pattern of the concentration/depletion of electrons in space accounts for the balance of forces providing the dynamical equilibrium structure of a molecule or a crystal. According to Bader [19], virial paths serve as a universal indicator to directly reveal chemically bound atoms and determine the molecular graph, which is invariant with respect to nuclear vibrations in a stable system. Thus, analysis of the potential energy distribution can be an efficient tool for detecting structure-forming interactions in molecules and crystals.

The local virial theorem [19]

$$2g(\mathbf{r}) + v(\mathbf{r}) = (1/4)\nabla^2\rho(\mathbf{r}) \quad (5)$$

makes it possible to determine the potential energy density from the experimental electron density by calculat-

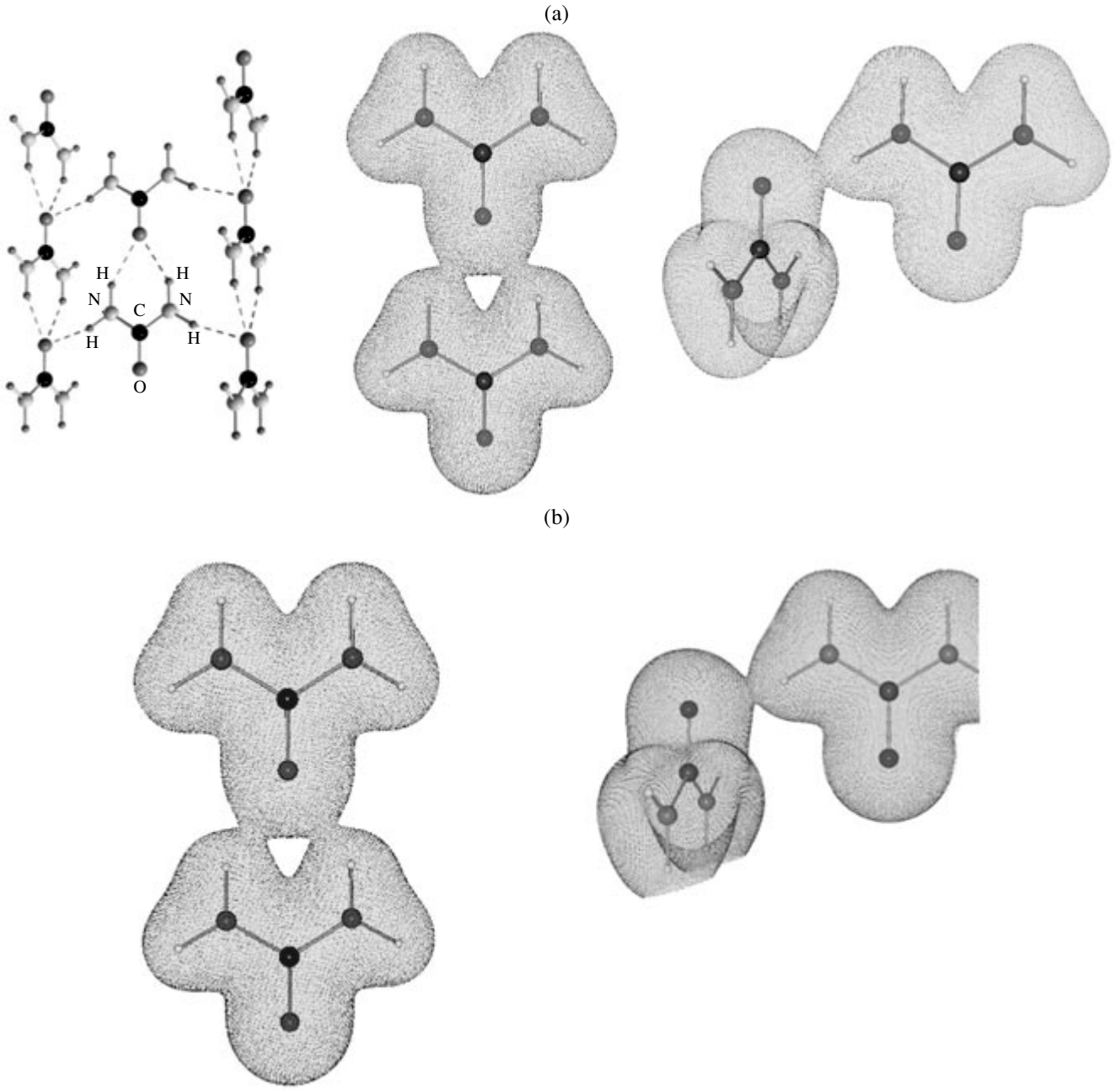

Fig. 2. Distributions of the (a) electron density and (b) potential energy density in pairs of neighboring molecules of urea $CO(NH_2)_2$ in a crystal reconstructed from the multipole parameters obtained in an X-ray diffraction experiment. Intermolecular contacts in bands of molecules and between bands are indicated. The geometric parameters are taken from the experiment. The surfaces corresponding to an electron density of 0.13 e $Å^{-3}$ and a potential energy density of –0.012 au are shown.

ing $g(\mathbf{r})$ from formula (4) and $\nabla^2\rho(\mathbf{r})$. Analysis of the local potential energy is highly effective in finding the physical reasons for the formation of the 3D structure of molecules and crystals [33, 34, 39]. For example, neighboring pairs of molecules in a urea crystal connected by electron density bridges are also connected by bridges of negative potential energy density (Fig. 2). Thus, electron density bridges are formed as a result of the energy redistribution upon the formation of a crystal from molecules and not from simple overlapping of atomic electron densities. This approach is especially effective in establishing the structural formula of molecules in nontrivial cases [55].

The density of the total electronic energy is

$$h(\mathbf{r}) = g(\mathbf{r}) + v(\mathbf{r}). \quad (6)$$

In principle, the electronic energy $h(\mathbf{r})$ clearly reveals the regions of electron concentration at covalent bonds

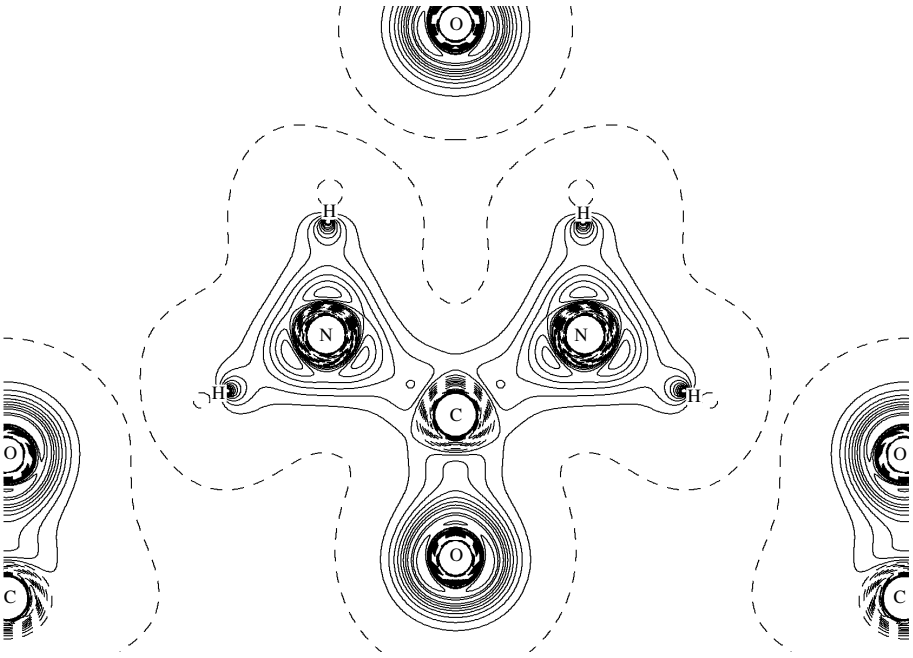

Fig. 3. Distribution of the electronic energy density (see expression (6)) in a $CO(NH_2)_2$ crystal calculated from the multipole model parameters (isoline step 0.2 au, positive lines correspond to negative values of the electronic energy density). It can be seen that the electronic energy density reveals core and valence regions in the urea molecule; the electron concentration at the covalent bonds C–O, C–N, and N–H; and unshared electron pairs of the oxygen atom. The regions of intermolecular hydrogen bonds O···H are characterized by positive values of the electronic energy density; the directionality of these bonds is very weakly expressed.

and unshared electron pairs, as well as the depletion of electrons in hydrogen bonds (Fig. 3). We will indicate here a new useful application of the analysis of electronic energy. It is known [19] that the regions around nuclei in a molecule or a crystal, separated by the surfaces of the zero flux of the electron density gradient,

$$\nabla\rho(\mathbf{r})\cdot\mathbf{n}(\mathbf{r}) = 0, \quad \nabla\mathbf{r}\in S_i(\mathbf{r}), \tag{7}$$

can be identified with bound atoms (pseudoatoms). An integral of any quantity $A(\mathbf{r})$ over the volume of such an atom Ω

$$\langle A\rangle = \int_{\Omega} A(\mathbf{r})dV \tag{8}$$

gives the average value of this quantity, and the sum of the atomic contributions is the total value of this quantity for the system under consideration. In particular, integrating the electronic energy distribution over atomic volumes and summing the contributions, one can calculate the energies of functional groups, bound molecules in the crystal, and the unit cell of a crystal. Figure 4 shows pseudoatoms bounded by the surfaces of the zero flux of the electron density gradient for a urea molecule in a crystal, and the atomic components of the electronic energy are listed in the table. Summation of the atomic contributions gives the electronic energy for a bound molecule. Its comparison with the quantum chemically calculated electronic energy for a free molecule shows that the result obtained correctly reflects the physically justified decrease in the energy in going from a free molecule to a crystal. In principle, this approach makes it possible to obtain the intermolecular interaction energy directly from an X-ray experiment. However, very accurate experimental data are required to do this.

Hunter [28, 29] considered the one-electron potential

$$P(\mathbf{r}) = \nabla^2\rho(\mathbf{r})/4\rho(\mathbf{r}) - |\nabla\rho(\mathbf{r})|^2/8[\rho(\mathbf{r})]^2, \tag{9}$$

which is a part of the effective potential in the Kohn–Sham equations [32, 56], and indicated that negative regions of $P(\mathbf{r})$ correspond to positive values of the local kinetic energy of electrons: an electron in these regions is referred to as classically allowed. In contrast, positive regions of $P(\mathbf{r})$ reveal classically forbidden potential barriers, where electrons demonstrate quantum behavior. It has been ascertained that the one-electron potential of free atoms reveals alternating minima and maxima related to fact that the atoms have a shell electronic structure. This structure manifests itself in the regions of concentration ($P(\mathbf{r}) < 0$) and depletion ($P(\mathbf{r}) > 0$) of electrons, which alternate with an increase in the distance from a nucleus [30, 31]. The second term in (9) is always negative, whereas the first term has the same sign as $\nabla^2\rho(\mathbf{r})$; hence, the classically allowed regions of $P(\mathbf{r})$ approximately correspond to the regions of the negative Laplacian of the electron density: the empirical characteristic of concentra-

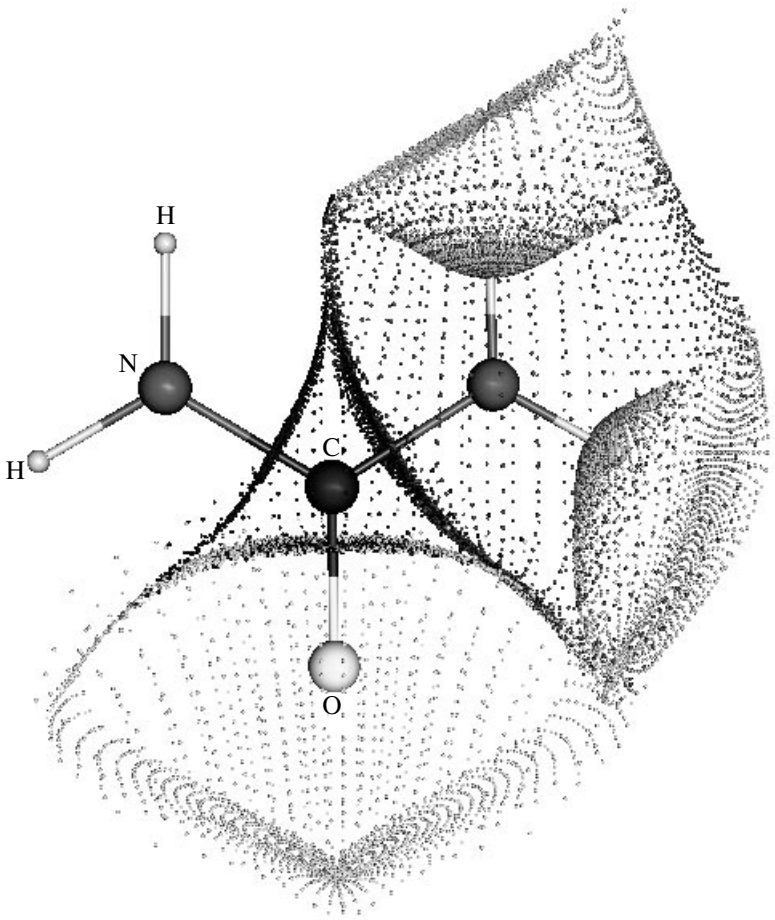

Fig. 4. Surfaces of the zero flux of the electron density gradient which separate atoms in a molecule of urea $CO(NH_2)_2$.

tion/depletion of electrons in the theory of the chemical bond developed by Bader [19]. Alternating negative minima and positive maxima of $P(\mathbf{r})$ are observed for all atoms, whereas the Laplacian of the electron density makes it impossible to distinguish the valence electron shells of some atoms, beginning with the fourth group of the periodic table [30, 31, 57]. The latter circumstance has important practical consequences. When analyzing a chemical bond, the regions of the valence shells of bound atoms, in which $\nabla^2\rho(\mathbf{r}) < 0$, are identified with the regions of concentration of valence electron pairs [19]. Since these regions do not manifest themselves in the Laplacian of the electron density for compounds with heavy atoms, the one-electron potential in fact may serve in this case as the only indicator of chemical bond features.

Let us illustrate the above considerations by the analysis of the function $P(\mathbf{r})$ along the interaction line between a Ba ion and one of the oxygen atoms in the Cu(2)–O plane of an $YBa_2Cu_3O_7$ crystal (Fig. 5). Free Ba and O atoms have, respectively, six and two pairs of minima and maxima of the one-electron potential $P(\mathbf{r})$. As a result of the interference of the valence orbitals of these atoms upon the formation of a crystal (a quantum effect), the external positive regions of the atomic functions $P(\mathbf{r})$ merge to form a unified classically forbidden region at the Ba–O line. This region contains a bond critical point (the point where $\nabla\rho(\mathbf{r}) = 0$ and the curvature of the electron density along the bond line is positive and both perpendicular curvatures are negative) located at a distance of 1.511 Å from the Ba ion (Fig. 5b). The manifestation of the concentrations of valence electrons in the Laplacian of the electron density is limited, and the Laplacian minimum in the region of interference of the valence Ba and O orbitals does not take negative values. As is known, a positive Laplacian of the electron density at the bond critical point is interpreted as the manifestation of interaction of a closed shell type [19]. The one-electron potential also demonstrates the depletion of electrons around the critical point. Simultaneously, the function $P(\mathbf{r})$ reveals a fine detail of interaction: the manifestation of the interference interaction between Ba and O ions in $YBa_2Cu_3O_7$. In other words, the one-electron potential shows the presence of a low electron concentration at the Ba–O bond, i.e., the covalent component of this bond.

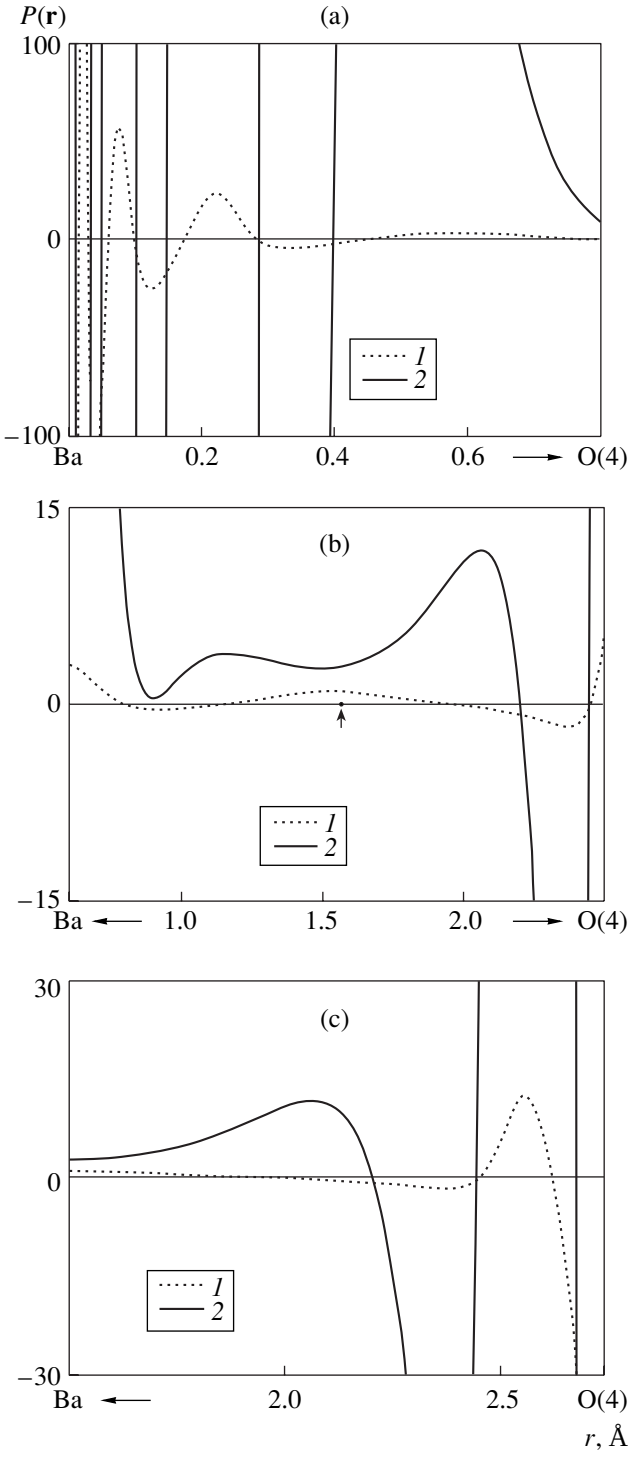

Fig. 5. Profiles of the one-electron potential (9) (dashed lines) and the Laplacian of the electron density (solid line) along the Ba–O(4) direction in the Cu(2)–O plane in a $YBa_2Cu_3O_7$ crystal. The arrow (b) indicates the position of the bond critical point.

According to (8), the integration of the electron density over atomic basins in $YBa_2Cu_3O_7$ (the volumes of barium and oxygen atoms are 23.50 and 12.03 Å^3, respectively) gives the following charges at the atoms: +1.48(2) and –0.86(2) e for Ba and O(4), respectively. These charges, differing from the formal ones (which one might expect in the case of a purely ionic bond), are in excellent agreement with the conclusions drawn on the basis of the analysis of the function $P(\mathbf{r})$.

ACKNOWLEDGMENTS

This study was supported by the program of the Ministry of Education of the Russian Federation for basic research in the field of natural and exact sciences, grant no. E02-5.0-161, and the Russian Foundation for Basic Research, project no. 04-03-33053.

REFERENCES

1. V. G. Tsirelson and R. P. Ozerov, *Electron Density and Bonding in Crystals* (Inst. of Physics, Bristol, 1996).
2. V. G. Tsirelson, *Chemical Bond and Thermal Motion of Atoms in Crystals* (VINITI, Moscow, 1993) [in Russian].
3. R. Boese, D. Blaeser, O. Heinemann, *et al.*, J. Phys. Chem. A **103**, 6209 (1999).
4. R. Bolotovsky, A. Darovsky, V. Kezerazhvili, *et al.*, J. Appl. Crystallogr. **28**, 86 (1995).
5. H. Graafsma, S. O. Svensson, and A. Kvick, J. Appl. Crystallogr. **30**, 957 (1997).
6. A. Martin and A. A. Pinkerton, Acta Crystallogr., Sect. B: Struct. Sci. **54**, 471 (1998).
7. Yu. V. Ivanov, E. A. Zhurova, V. V. Zhurov, *et al.*, Acta Crystallogr., Sect. B: Struct. Sci. A **55**, 923 (1999).
8. F. Hirshfeld, Acta Crystallogr., Sect. B: Struct. Crystallogr. Cryst. Chem. **27**, 769 (1971).
9. R. F. Stewart, Acta Crystallogr., Sect. A: Cryst. Phys., Diffr., Theor. Gen. Crystallogr. **32**, 567 (1976).
10. N. Hansen and P. Coppens, Acta Crystallogr., Sect. A: Cryst. Phys., Diffr., Theor. Gen. Crystallogr. **34**, 909 (1978).
11. E. V. Parini, V. G. Tsirelson, and R. P. Ozerov, Kristallografiya **30**, 857 (1985) [Sov. Phys. Crystallogr. **30**, 497 (1985)].
12. M. Kapphahn, V. G. Tsirelson, and R. P. Ozerov, Port. Phys. **19**, 213 (1988).
13. M. Kapphahn, V. G. Tsirelson, and R. P. Ozerov, Dokl. Akad. Nauk SSSR **303**, 404 (1989).
14. V. Tsirelson, Yu. Abramov, V. Zavodnik, *et al.*, Struct. Chem. **9**, 249 (1998).
15. V. G. Tsirelson, Can. J. Chem. **74**, 1171 (1996).
16. V. G. Tsirelson, in *Abstracts of II National Conference on Crystal Chemistry* (Chernogolovka, 2000), p. 34.
17. V. Tsirelson, in *Proceedings of Conference on Electron Density: Electron Density Measurement, Calculation, Application* (Wuerzburg Univ., Wuerzburg, 2002), p. 6.
18. V. Tsirelson, Acta Crystallogr., Sect. A: Found. Crystallogr. **58** (Suppl.), 2 (2002).
19. F. W. Bader, *Atoms in Molecules: a Quantum Theory* (Clarendon, Oxford, 1994; Mir, Moscow, 2001).
20. R. F. Stewart, Chem. Phys. Lett. **65**, 335 (1979).
21. A. A. Varnek, V. G. Tsirelson, and R. P. Ozerov, Dokl. Akad. Nauk SSSR **257**, 382 (1981).

22. Z. Su and P. Coppens, Acta Crystallogr., Sect. A: Found. Crystallogr. **48**, 188 (1992).
23. V. Tsirelson, Yu. Ivanov, E. A. Zhurova, *et al.*, Acta Crystallogr., Sect. B: Struct. Sci. **56**, 197 (2000).
24. M. Spackman, Chem. Rev. **92**, 1769 (1992).
25. K. Yu. Suponitsky, V. G. Tsirelson, and D. Feil, Acta Crystallogr., Sect. A: Found. Crystallogr. **55**, 821 (1999).
26. Z. Su, PhD Thesis (State Univ. of New York at Buffalo, 1993).
27. V. G. Tsirelson, V. A. Strel'tsov, E. F. Makarov, and R. P. Ozerov, Zh. Éksp. Teor. Fiz. **92**, 1894 (1987) [Sov. Phys. JETP **65**, 1065 (1987)].
28. G. Hunter, Int. J. Quantum Chem. **9**, 237 (1975).
29. G. Hunter, Int. J. Quantum Chem. **29**, 197 (1986).
30. M. Kohout, A. Savin, and H. Press, J. Chem. Phys. **95**, 1928 (1991).
31. M. Kohout, Int. J. Quantum Chem. **87**, 12 (2002).
32. M. Levy, J. P. Perdew, and V. Sahni, Phys. Rev. A **30**, 2745 (1984).
33. A. I. Stash and V. G. Tsirelson, in *Proceedings of 3rd European Charge Density Meeting and European Science Foundation Exploratory Workshop, ECDM-III* (Sandbjerg Estate, Denmark, 2003), p. O8.
34. V. Tsirelson, Acta Crystallogr., Sect. B: Struct. Sci. **58**, 632 (2001).
35. A. D. Becke and K. E. Edgecombe, J. Chem. Phys. **92**, 5397 (1990).
36. A. Savin, O. Jepsen, J. Flad, *et al.*, Angew. Chem. Int. Ed. Engl. **31**, 187 (1992).
37. V. Tsirelson and A. Stash, Chem. Phys. Lett. **351**, 142 (2002).
38. V. Tsirelson and A. Stash, Acta Crystallogr., Sect. B: Struct. Sci. **58**, 780 (2002).
39. V. G. Tsirelson, in *Proceedings of 3rd European Charge Density Meeting and European Science Foundation Exploratory Workshop, ECDM-III* (Sandbjerg Estate, Denmark, 2003), p. O7.
40. R. G. Parr and W. Yang, *Density-Functional Theory of Atoms and Molecules* (Oxford Univ. Press, New York, 1989).
41. N. E. Ghermani, N. Bouhmaida, and C. Lecomte, *ELECTROS: Computer Programs to Calculate Electrostatic Properties from the High-Resolution X-ray Diffraction Data* (Univ. Henri Poincare, Nancy I, France, 1992).
42. T. Koritsansky, S. T. Howard, Z. Su, *et al.*, *XD: Computer Program Package for Multipole Refinement and Analysis of Electron Densities from Diffraction Data* (Free Univ. of Berlin, Germany, 1995).
43. M. Souhassou and R. H. Blessing, J. Appl. Crystallogr. **32**, 210 (1999).
44. R. F. Stewart, M. A. Spackman, and C. Flensburg, *VALRAY98 Users Manual* (Carnegie Mellon Univ., Pittsburgh, USA and Univ. of Copenhagen, Denmark, 1998).
45. A. I. Stash and V. G. Tsirelson, J. Appl. Crystallogr. **35**, 371 (2002).
46. J. Protas, *MOLDOS96/MOLLY IBM PC-DOS—A Computer Program for Multipole Charge-Density Refinement* (Univ. Henri Poincare, Nancy I, France, 1995).
47. V. E. Zavodnik, A. I. Stash, V. G. Tsirelson, *et al.*, Acta Crystallogr., Sect. B: Struct. Sci. **55**, 45 (1999).
48. A. I. Stash, in *Proceedings of Japan–Russian Workshop on Accurate Charge Density Studies* (Nagoya, 2003), p. 147.
49. T. Lippmann, P. Blaha, N. H. Andersen, *et al.*, Acta Crystallogr., Sect. A: Found. Crystallogr. **59**, 437 (2003).
50. L. Cohen, J. Chem. Phys. **70**, 788 (1979).
51. P. W. Ayers, R. G. Parr, and A. Nagy, Int. J. Quantum Chem. **90**, 309 (2002).
52. D. A. Kirzhnits, Zh. Éksp. Teor. Fiz. **32**, 115 (1957) [Sov. Phys. JETP **5**, 64 (1957)].
53. R. W. F. Bader, Phys. Rev. B **49**, 13348 (1994).
54. R. W. F. Bader, J. Phys. Chem. A **102**, 7314 (1998).
55. E. A. Zhurova, V. G. Tsirelson, A. I. Stash, *et al.*, J. Am. Chem. Soc. **124**, 4574 (2002).
56. N. H. March, Phys. Lett. A **113A**, 66 (1985).
57. R. P. Sagar, A. C. T. Ku, and V. H. Smith, J. Chem. Phys. **88**, 4367 (1988).

Translated by Yu. Sin'kov

Crystallography Reports, Vol. 50, No. 2, 2005, pp. 185–190. Translated from Kristallografiya, Vol. 50, No. 2, 2005, pp. 217–222.

STRUCTURE OF INORGANIC COMPOUNDS

Crystal and Magnetic Structure of the $Sm_{0.45}Sr_{0.55}MnO_3$ Manganite Studied by Neutron Powder Diffraction

A. I. Kurbakov*, V. A. Trunov*, C. Martin, and A. Maignan****

** St. Petersburg Nuclear Physics Institute, Russian Academy of Sciences, Gatchina, Leningrad oblast, 188300 Russia*

e-mail:kurbakov@pnpi.spb.ru

*** Laboratoire CRISMAT, UMR 6508 ISMRA; Universite de Caen, Bd. du Marechal Juin, 14050 Caen, France*

Received February 9, 2004

Abstract—Neutron diffraction investigation of the $^{152}Sm_{0.45}Sr_{0.55}MnO_3$ manganite is performed. The diffraction data are compared with the magnetic and transport properties of this compound. The parameters of the crystal and magnetic structures are determined. Manganite belongs to the orthorhombic system (sp. gr. *Pnma*) and has a perovskite-like structure in the entire temperature range under study (1.5–260 K). The ground state of the $^{152}Sm_{0.45}Sr_{0.55}MnO_3$ manganite at low temperatures is a single-phase *A*-type antiferromagnetic insulator with $T_N \sim 180$ K. © *2005 Pleiades Publishing, Inc.*

INTRODUCTION

The discovery of the phenomenon of negative colossal magnetoresistance (CMR) in manganites with perovskite structure, i.e., the decrease in their resistivity in a magnetic field by several orders of magnitude, has stimulated numerous physical investigations in this field [1–3]. The main purpose of all these studies was the determination of the mechanisms responsible for the CMR. However, when carrying out a complex study of manganites, it turned out that these compounds are no less interesting from the point of view of manifestation of other fundamental properties of solids: metal–insulator transitions, first-order phase transitions, the formation of mixed ground magnetic states with phase separation (electronic, nanoscopic, microscopic, mesoscopic), the formation of charge and/or orbital ordering states, and strong cooperative Jahn–Teller effects. Since various physical properties of these compounds are related to a particular type of ordering of magnetic moments of Mn ions, neutron diffraction data are very important.

This work is a continuation of the systematic neutron diffraction investigation performed by us previously [4–8] on Sm–Sr manganites with the general formula $Sm_{1-x}Sr_xMnO_3$. These compounds are of much scientific interest because, owing to the large difference in the ionic radii of samarium and strontium, interactions between the electronic, phonon, and magnetic subsystems are pronounced in Sm–Sr manganites. The previous systematic investigation of ceramic samples of the Sm–Sr system by measuring the temperature and field dependences of the resistivity and magnetization [9, 10] demonstrated that the CMR effect manifests itself only in the range of hole doping at $0.3 \le x \le 0.52$ with a maximum at $x = 0.44$. Recently, these data were confirmed by a similar investigation on single crystals [11]. Some new results were obtained for concentrations $x \ge 0.5$, which, however, require confirmation and explanation.

In view of the above considerations, we believe that it is important to supplement the previously obtained neutron diffraction data on hole-doped $Sm_{1-x}Sr_xMnO_3$ manganites with the data on electron-doped Sm–Sr manganites having threshold values of x that correspond to a change in the sign of carriers near the region where the CMR effect exists. This is even more urgent because, presently, there are no experimental data on the ground magnetic states of such compounds in the literature. On the basis of these considerations, we choose the strontium content x to be 0.55.

EXPERIMENTAL

Preparation and certification of the sample. In order to suppress the very strong absorption of neutrons by the ^{149}Sm isotope present in natural samarium, the $Sm_{0.45}Sr_{0.55}MnO_3$ sample for neutron diffraction analysis was synthesized using the ^{152}Sm isotope.

The sample was prepared from a mixture of $^{152}Sm_2O_3$, $SrCO_3$, and MnO_2 in the corresponding ratio. The mixture was first heated in air for 12 h to carry out decarbonization; then ground; and, finally, pressed into pellets under a pressure of 1 t/cm^2. The synthesis was performed by heating the mixture at 1400°C for 12 h, after which the sample was slowly cooled at a rate of 5 K/min to 800°C and, finally, quenched to room temperature.

1063-7745/05/5002-0185$26.00 © 2005 Pleiades Publishing, Inc.

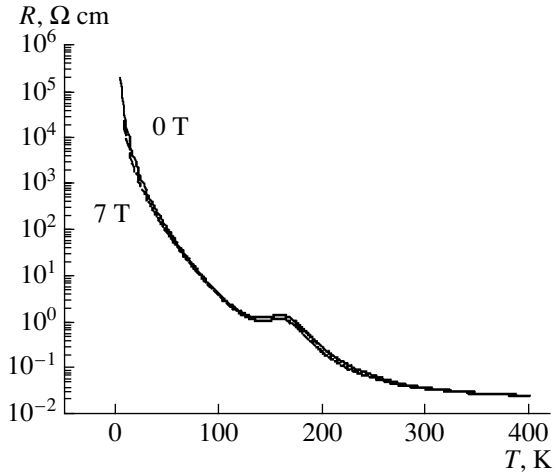

Fig. 1. Temperature dependences of the resistivity R of $^{152}Sm_{0.45}Sr_{0.55}MnO_3$ measured in a zero external magnetic field and in a field of 7 T.

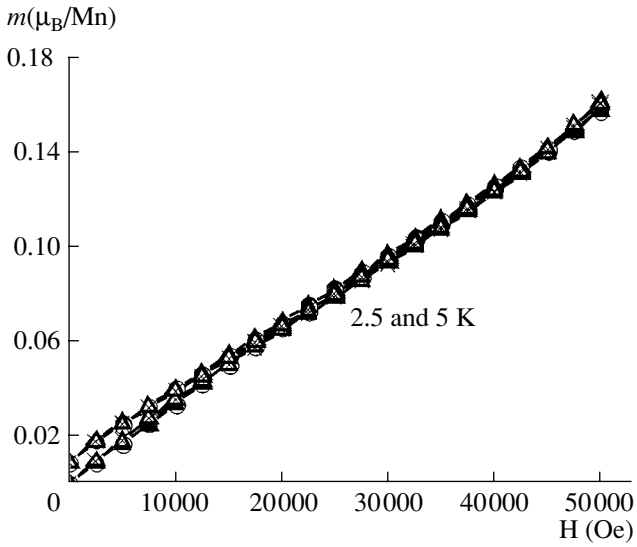

Fig. 2. Field dependences of the magnetization of $^{152}Sm_{0.45}Sr_{0.55}MnO_3$ at temperatures of 2.5 and 5.0 K (zero-field cooling). Different symbols denote different regimes of field cycling.

A large number of crystallites of the sample used for the neutron diffraction study were characterized by electron microscopy. For each crystallite, reciprocal-space reconstruction was performed at room temperature on a JEOL 200 CX electron microscope equipped with a sample holder that could be oriented obliquely. At low temperatures, the reconstruction was performed on a JEOL 2010 electron microscope. The cation composition was determined by energy-dispersive spectroscopic analysis using analyzers constructed on the basis of three electron microscopes. It was found that the distribution of cations is very uniform and the real composition is absolutely identical to the nominal one. The certification of the sample by X-ray diffraction analysis and iodometric titration confirmed that the compound under study is single-phase and has a homogeneous nominal composition.

Macroscopic measurements. The temperature dependence of the resistivity was measured upon cooling from 400 to 5 K in a zero magnetic field and in a field of 7 T by the conventional four-probe technique on columnar samples (obtained after cutting pellets) $2 \times 2 \times 10$ mm^3 in size. The magnetization was measured in magnetic fields from 0 to 5 T at $T = 2.5$ and 5 K after zero-field cooling of the sample.

Neutron powder diffraction. The diffraction measurements were performed on the Russian–French 7-section high-resolution neutron powder diffractometer G4.2 equipped with 70 counters [12] and installed on a cold neutron guide of the Orphee reactor (Leon Brillouin Laboratory, Saclay, France). Neutron diffraction patterns were measured in the superposition mode using monochromatic neutrons with a wavelength $\lambda = 2.3428$ Å in the angular range $3° \le 2\theta \le 174°$ upon heating at temperatures $T = 1.5$, 50, 100, 150, 177, and 260 K in a cryofurnace. During the measurements, the powdered sample was placed in a vanadium cylindrical container 8 mm in diameter.

RESULTS AND DISCUSSION

Macroscopic measurements. The temperature dependence of the resistivity of the $^{152}Sm_{0.45}Sr_{0.55}MnO_3$ sample (Fig. 1) demonstrates the absence of the metal–insulator transition, which is characteristic of all Sm–Sr manganites exhibiting the CMR effect. The sample remained an insulator in the entire temperature range under investigation, independent of the applied magnetic field (7 T). However, we should note that a small jump in the temperature dependence of the resistivity arises in the temperature range 130–170 K. A similar local maximum of the resistivity was observed previously in [11] for single crystals with $x = 0.5$–0.575.

The curves of the field dependence of magnetization (Fig. 2) confirm that ferromagnetic ordering is practically absent at low temperatures.

Neutron powder diffraction. The crystal structure of $Sm_{0.45}Sr_{0.55}MnO_3$ was determined by the Rietveld method using the FULLPROF program [13]. In the entire temperature range under study (1.5–260 K), the crystal structure of the sample is adequately described by the orthorhombic sp. gr. *Pnma*. Figure 3 shows as an example the refinement of the diffraction pattern measured at $T = 260$ K. Figure 4 shows all experimental diffraction patterns measured in the cryofurnace at temperatures $T = 1.5$, 50, 100, 150, 177, and 260 K.

The temperature dependences of the unit-cell parameters and volume are shown in Figs. 5a and 5b, respectively. As can be seen from Fig. 5a, the unit cell is characterized at all temperatures by the relation

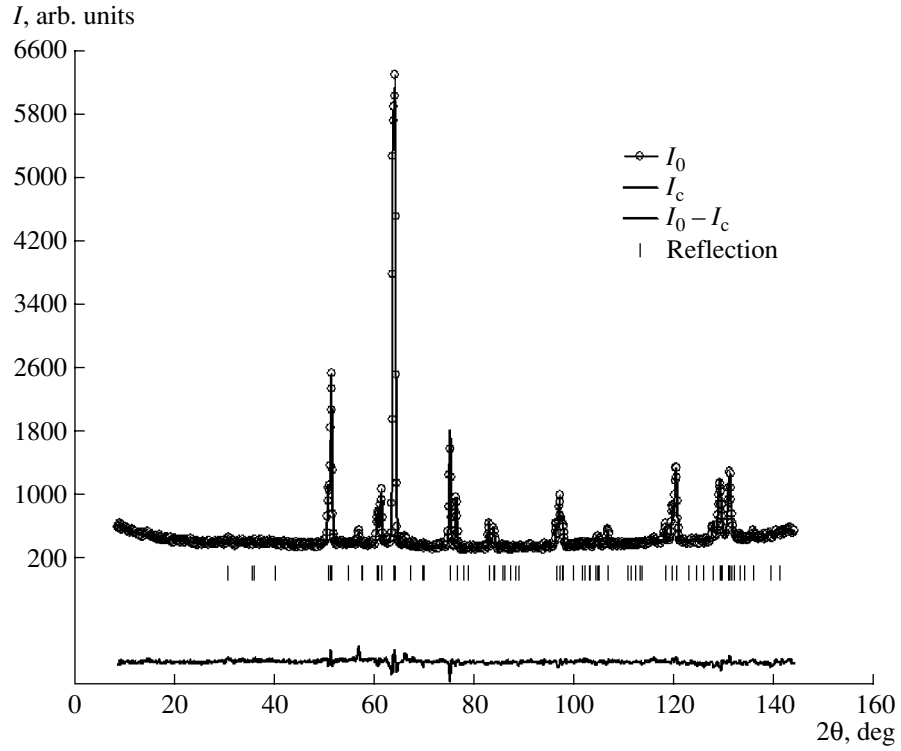

Fig. 3. Example of the refinement of the neutron diffraction pattern of the $^{152}Sm_{0.45}Sr_{0.55}MnO_3$ sample measured at T = 260 K: experimental (symbols) and Rietveld-refined (solid lines) neutron diffraction patterns. The positions of Bragg reflections are denoted by vertical bars. The difference (experiment minus calculation) curve is shown by a solid line at the bottom.

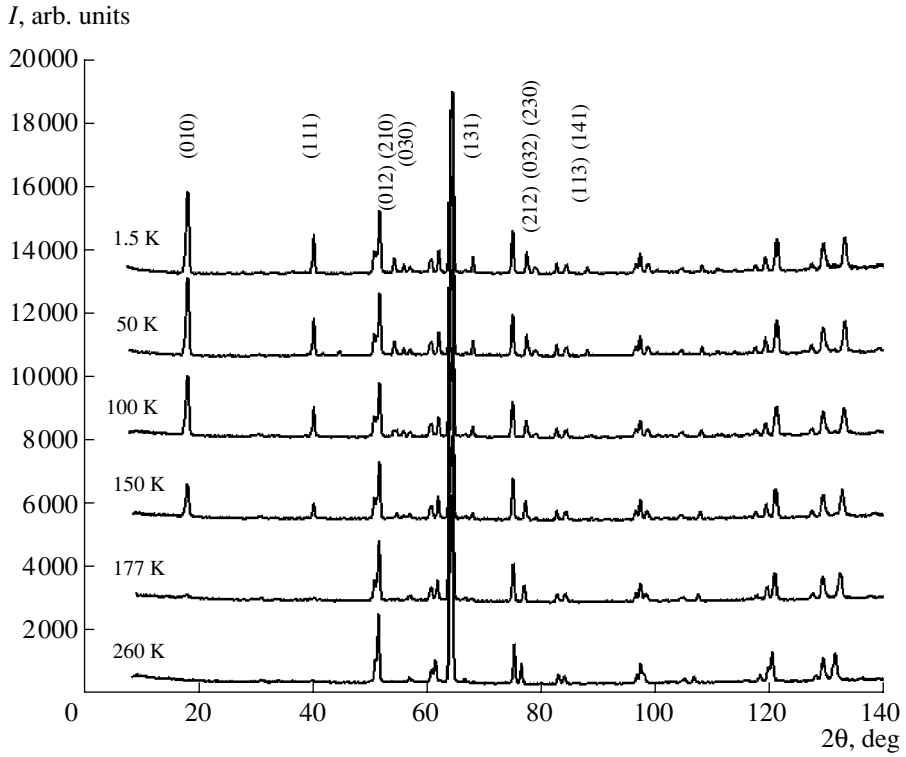

Fig. 4. Experimental powder neutron diffraction patterns of the $^{152}Sm_{0.45}Sr_{0.55}MnO_3$ sample measured at 1.5, 50, 100, 150, 177, and 260 K upon heating. The main antiferromagnetic reflections are indicated.

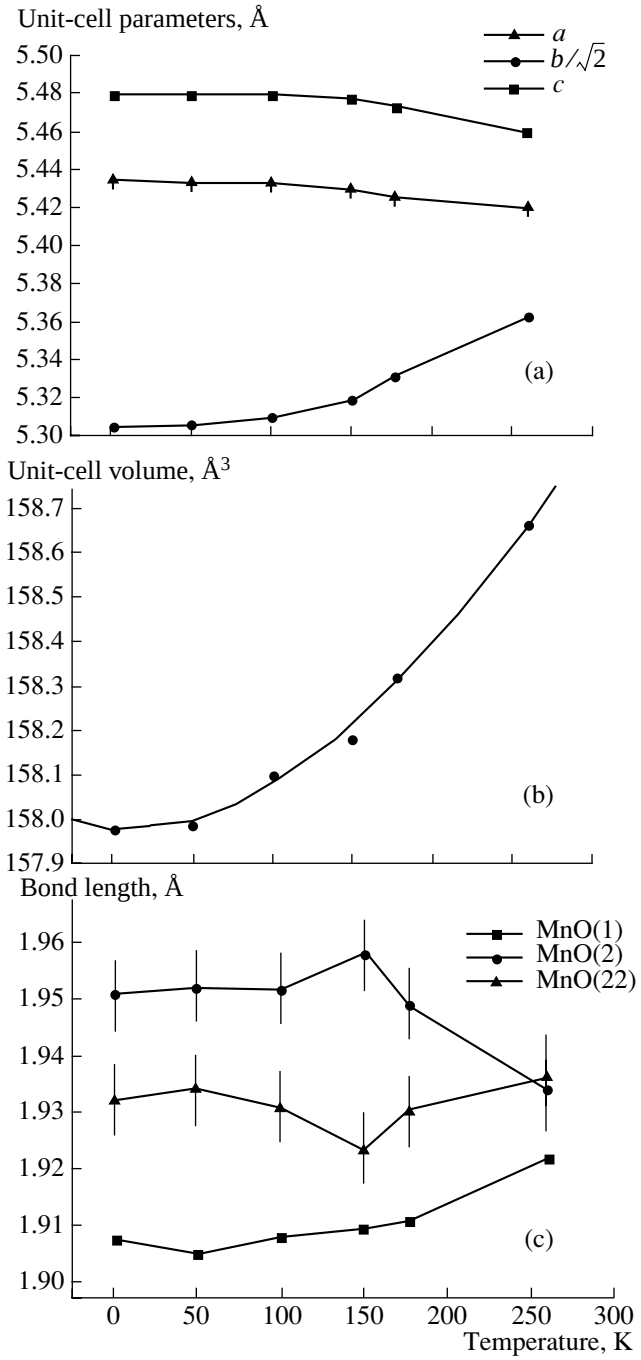

Fig. 5. Temperature dependences of the parameters of $^{152}Sm_{0.45}Sr_{0.55}MnO_3$: (a) the unit-cell parameters, (b) the unit-cell volume, and (c) the Mn–O bond lengths in MnO_6 octahedra (which demonstrate the presence of coherent Jahn–Teller distortions).

$b/\sqrt{2} < a < c$ and is typical of manganites, with tolerance factor $t < 0.94$ and distortion of the cubic perovskite lattice of the $a^-b^+a^-$ type [14]. The orthorhombic lattice distortion $\delta = (a - c)/(a + c)$ is fairly high ($\delta \sim 0.4\%$). At $T = 1.5$ K, MnO_6 octahedra are strongly compressed along the *b* axis. With an increase in temperature, the distortion of MnO_6 octahedra decreases and their symmetry tends to become cubic. The unit-cell parameters *a* and *c* decrease with a corresponding advanced increase in the parameter *b*. The unit-cell volume, due to the strong increase in *b*, demonstrates normal thermal expansion with increasing temperature.

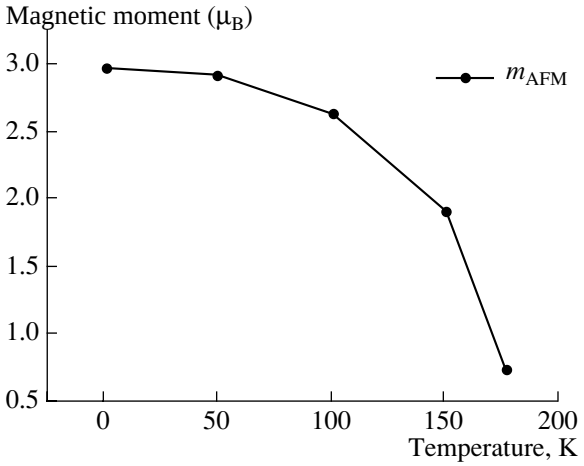

Fig. 6. Temperature dependence of the magnetic moment.

The neutron diffraction experiments carried out here yielded detailed data on the coherent Jahn–Teller distortions of MnO_6 octahedra (Fig. 6). At all temperatures, the apical Mn–O(1) bond length remains smaller than the equatorial Mn–O(2) and Mn–O(22) bond lengths; the equatorial bond lengths are almost equal at temperatures at which the $Sm_{0.45}Sr_{0.55}MnO_3$ sample under study is a paramagnet. In the temperature range in which the sample is an antiferromagnet, octahedra are distorted in the equatorial plane (maximally at temperatures close to the magnetic transition). This distortion decreases somewhat with a decrease in temperature. It should be noted that the distortion of MnO_6 octahedra in the equatorial plane is relatively small in comparison with similar distortions for the $Sm_{0.6}Sr_{0.4}MnO_3$ [5] and $Sm_{0.55}Sr_{0.45}MnO_3$ [7] compositions. The Mn–O–Mn bond angles are almost independent of temperature and equal to approximately 161° and 167° for the oxygen positions O(1) and O(2), respectively. The average value of the bond angle Mn–O–Mn at all temperatures is 164°. The values of the bond angles are similar to those obtained for the compounds with other Sr contents: 40, 45, and 50%. At the same time, the magnetic-ordering temperatures are quite different: 120 K for $Sm_{0.6}Sr_{0.4}MnO_3$, 122 K for $Sm_{0.55}Sr_{0.45}MnO_3$, 135 K for $Sm_{0.5}Sr_{0.5}MnO_3$, and 180 K for the compound under consideration: $Sm_{0.45}Sr_{0.55}MnO_3$.

The Rietveld analysis of the magnetic contribution to the neutron diffraction patterns at low temperatures was performed using the same FULLPROF program;

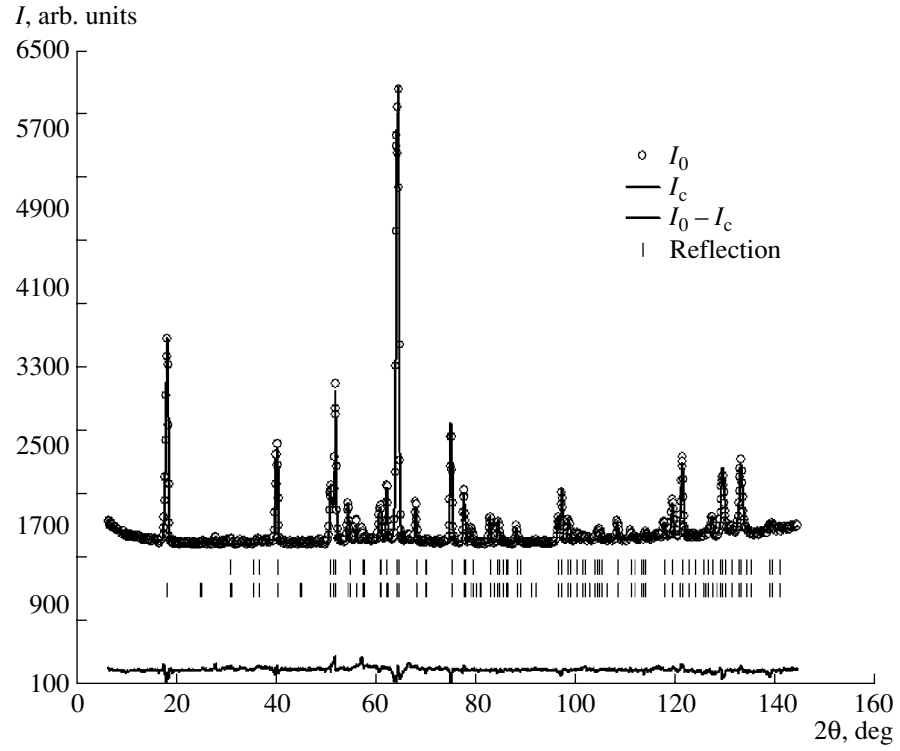

Fig. 7. An example of the refinement of a neutron diffraction pattern of $^{152}Sm_{0.45}Sr_{0.55}MnO_3$ measured at $T = 1.5$ K: experimental (symbols) and Rietveld-refined (solid lines) neutron diffraction patterns. The difference (experiment minus calculation) curve is shown by a solid line at the bottom. The positions of Bragg reflections are denoted by vertical bars; the upper row corresponds to the crystalline phase and the lower row corresponds to the *A*-type antiferromagnetic phase.

only a single-phase homogeneous model for the Mn sublattice based on the *Pnma* unit cell was considered.

The results of the analysis unambiguously indicate that the compound under investigation is homogeneous in the ground magnetic state and is an *A*-type antiferromagnet, which is sometimes referred to as a weak ferromagnet. In fact, we are dealing with the ferromagnetic ordering of the magnetic moments of Mn ions in a plane and the antiferromagnetic ordering between the planes, i.e., the two-dimensional ferromagnetic ordering. This antiferromagnetic phase is formed at $T_N \sim 180$ K (at $T = 177$ K, very weak antiferromagnetic (010) and (111) reflections are still observed in the measured neutron diffraction pattern). The value of the magnetic moment at low temperatures in the saturation regime is $m_{AFM} = 2.97(2)\ \mu_B$/Mn. The diffractometer resolution makes it possible to unambiguously determine that the antiferromagnetic moment is directed along the *a* axis. Figure 6 shows the temperature dependence of the antiferromagnetic moment. An example of the mathematical refinement of the pattern measured at $T = 1.5$ K is shown in Fig. 7.

It should be noted that no additional peaks, which could be related to the existence of long-range charge ordering, were observed in the neutron diffraction patterns.

CONCLUSIONS

Systematic investigation of the $^{152}Sm_{0.45}Sr_{0.55}MnO_3$ manganite with the threshold composition corresponding to the change in the sign of charge carriers near the range of Sr content $x = 0.30$–0.52 is performed. Here the CMR effects and the metal–insulator transition manifest themselves and the ground magnetic state is either homogeneous ferromagnetic (for $x = 0.45$) or mixed ferromagnetic and *A*-type antiferromagnetic with a dominating ferromagnetic phase ($x = 0.4$, 0.5). The results obtained confirmed that the $^{152}Sm_{0.45}Sr_{0.55}MnO_3$ compound belongs to perovskite-like structures with the sp. gr. *Pnma*. However, the ground magnetic state turned out to be purely antiferromagnetic without any impurity of the ferromagnetic phase and its magnetic structure is of the *A* type, just like it is in the antiferromagnetic phases in Sm–Sr hole-doped manganites exhibiting the CMR effect.

ACKNOWLEDGMENTS

This study was supported by the NIV program, project no. 40.012.1.1.1149.

REFERENCES

1. *Colossal Magnetoresistance. Charge Ordering and Related Properties of Manganese Oxides*, Ed. by C. N. R. Rao and B. Raveau (World Sci., Singapore, 1998).
2. *Colossal Magnetoresistive Oxides*, Ed. by Y. Tokura (Gordon and Breach, Amsterdam, 2000).
3. *Nanoscale Phase Separation and Colossal Magnetoresistace*, Ed. by E. Dagotto, G. Alvarez, S. L. Cooper, *et al.* (Springer Ser. Solid-State Sci., 2003), Vol. 136.
4. V. V. Runov, D. Yu. Chernyshev, A. I. Kurbakov, *et al.*, Zh. Éksp. Teor. Fiz. **118**, 1174 (2000) [JETP **91**, 1017 (2000)].
5. I. D. Luzyanin, V. A. Ryzhov, D. Yu. Chernyshov, *et al.*, Phys. Rev. B **64**, 094432 (2001).
6. J. M. De Teresa, M. R. Ibarra, P. Algarabel, *et al.*, Phys. Rev. B **65**, 100403(R) (2002).
7. A. V. Lazuta, V. A. Ryzhov, A. I. Kurbakov, *et al.*, J. Magn. Magn. Mater. **258–259**, 315 (2003).
8. A. M. Aliev, Sh. B. Abdulvagidov, A. B. Batdatlov, *et al.*, Fiz. Tverd. Tela (St. Petersburg) **45**, 124 (2003) [Phys. Solid State **45**, 130 (2003)].
9. F. Damay, N. Nguyen, A. Maignan, *et al.*, Solid State Commun. **98**, 997 (1996).
10. C. Martin, A. Maignan, M. Hervieu, and B. Raveau, Phys. Rev. B **60**, 12191 (1999).
11. V. Yu. Ivanov, A. A. Mukhin, V. D. Travkin, *et al.*, J. Magn. Magn. Mater. **258–259**, 535 (2003).
12. A. I. Kurbakov, V. A. Trounov, T. K. Baranova, *et al.*, Mater. Sci. Forum **321–324**, 308 (2000).
13. J. Rodriguez-Carvajal, Physica B (Amsterdam) **55**, 192 (1993).
14. P. M. Woodward, T. Vogt, D. E. Cox, *et al.*, Chem. Mater. **10**, 3652 (1998).

Translated by Yu. Sin'kov

Crystallography Reports, Vol. 50, No. 2, 2005, pp. 191–193. Translated from Kristallografiya, Vol. 50, No. 2, 2005, pp. 223–225.

STRUCTURE OF INORGANIC COMPOUNDS

Crystal Structure of a New Neodymium Hexamolybdotellurate, $Nd_2TeMo_6O_{24} \cdot 19H_2O$

I. A. Charushnikova*, A. M. Fedoseev*, A. B. Yusov*, and C. Den Auwer**

** Institute of Physical Chemistry, Russian Academy of Sciences, Leninskiĭ pr. 31, Moscow, 119991 Russia*

e-mail: chara@ipc.rssi.ru

*** CEA Marcoule, DRCP/SCPS/LCAM, Bagnols-sur-Céze, 30207 France*

Received October 8, 2003

Abstract—The crystal structure of a new compound, namely, $Nd_2TeMo_6O_{24} \cdot 19H_2O$, is determined using X-ray diffraction. The crystal has a chain structure and consists of $[Nd_2TeMo_6O_{24} \cdot 14H_2O]_n$ neutral chains aligned parallel to the [010] direction and crystallization water molecules. In a chain, each Nd atom links two heteropoly anions. The Nd^{3+} environment includes seven water molecules and two oxygen atoms of the two heteropoly anions adjacent in the chain. The polyhedron is a monocapped tetragonal antiprism. In the previously studied complex of similar composition, namely, $Nd_2TeMo_6O_{24} \cdot 18H_2O$, the Nd coordination polyhedron has the shape of a tricapped trigonal prism formed by six water molecules and three oxygen atoms of the two heteropoly anions adjacent in the chain. © *2005 Pleiades Publishing, Inc.*

INTRODUCTION

This paper continues our studies of *f*-element complexes with various heteropoly anions, in particular, those characterized by an Anderson structure [1], some of which exhibit luminescence properties [2–4].

Earlier [2], we described the crystal structure of $Nd_2TeMo_6O_{24} \cdot 18H_2O$ (**I**). This compound was synthesized by adding a 0.1 mol/l $Nd(NO_3)_3$ solution to a saturated (~0.02 mol/l) $TeMo_6O_{24}^{6-}$ solution. It was found that the reaction between diluted solutions (~0.002 mol/l $TeMo_6O_{24}^{6-}$, ~0.004 mol/l Nd^{3+}) yields crystals of a compound with a somewhat different formula, namely, $Nd_2TeMo_6O_{24} \cdot 19H_2O$ (**II**). After holding the solution for approximately 20 h, light lilac platelike crystals of **II** precipitated. The composition of **II** was determined using X-ray diffraction analysis.

EXPERIMENTAL

X-ray diffraction analysis was performed with a single-crystal fragment $0.18 \times 0.09 \times 0.07$ mm in size. The experimental data were collected on an Enraf–Nonius KappaCCD automated diffractometer (MoK_α radiation, graphite monochromator). The parameters of the triclinic unit cell were determined at 20°C from 10 images with $\Delta\varphi = 1°$ and were then refined using the complete set of reflections: a = 9.543(2) Å, b = 10.151(2) Å, c = 10.503(2) Å, α = 95.97(3)°, β = 104.48(3)°, γ = 112.92(3)°, space group $P\bar{1}$, Z = 1, and d_{calcd} = 3.227 g/cm^3. In the range $2° < \theta < 27.5°$, the intensities of 7168 reflections were measured, among which 3766 reflections [including 3354 reflections with $I > 2\sigma(I)$] were unique. The MULABS empirical absorption correction (PLATON [5]) was applied to the experimental set of intensities. The structure was solved by direct methods [6]. The positions of all the non-hydrogen atoms were refined using the full-matrix least-squares method [7] in the anisotropic approximation. The hydrogen atoms of the coordinated and crystallization water molecules were located from difference Fourier syntheses and refined with the constraint that the O–H bond lengths tend to be 0.85 Å and that the thermal parameters exceed the U_{eq} values of the oxygen atoms of the water molecules by a factor of 1.5. The final refinement of 298 parameters resulted in R_1 = 0.0414 and wR_2 = 0.0879 [for reflections with $I > 2\sigma(I)$]. The atomic coordinates in structure **II** have been deposited with the Inorganic Crystal Structure Database, Karlsruhe, Germany (ICSD no. 413 414).

RESULTS AND DISCUSSION

Crystal **II** (figure) has a chain structure and consists of $[Nd_2TeMo_6O_{24} \cdot 14H_2O]_n$ neutral chains aligned parallel to the [010] direction. In a chain, each Nd atom links two heteropoly anions. Crystallization water molecules are located between the chains.

The $TeMo_6O_{24}^{6-}$ heteropoly anions are located at the centers of inversion, and their structures are similar to those in $(NH_4)_6TeMo_6O_{24} \cdot Te(OH)_6 \cdot 7H_2O$ [8], $Nd_2TeMo_6O_{24} \cdot 18H_2O$ [2], and $(NH_4)_3[Tb(TeMo_6O_{24})(H_2O)_5] \cdot 5H_2O$ [3]. The coordination environment of the central Te atom is an almost

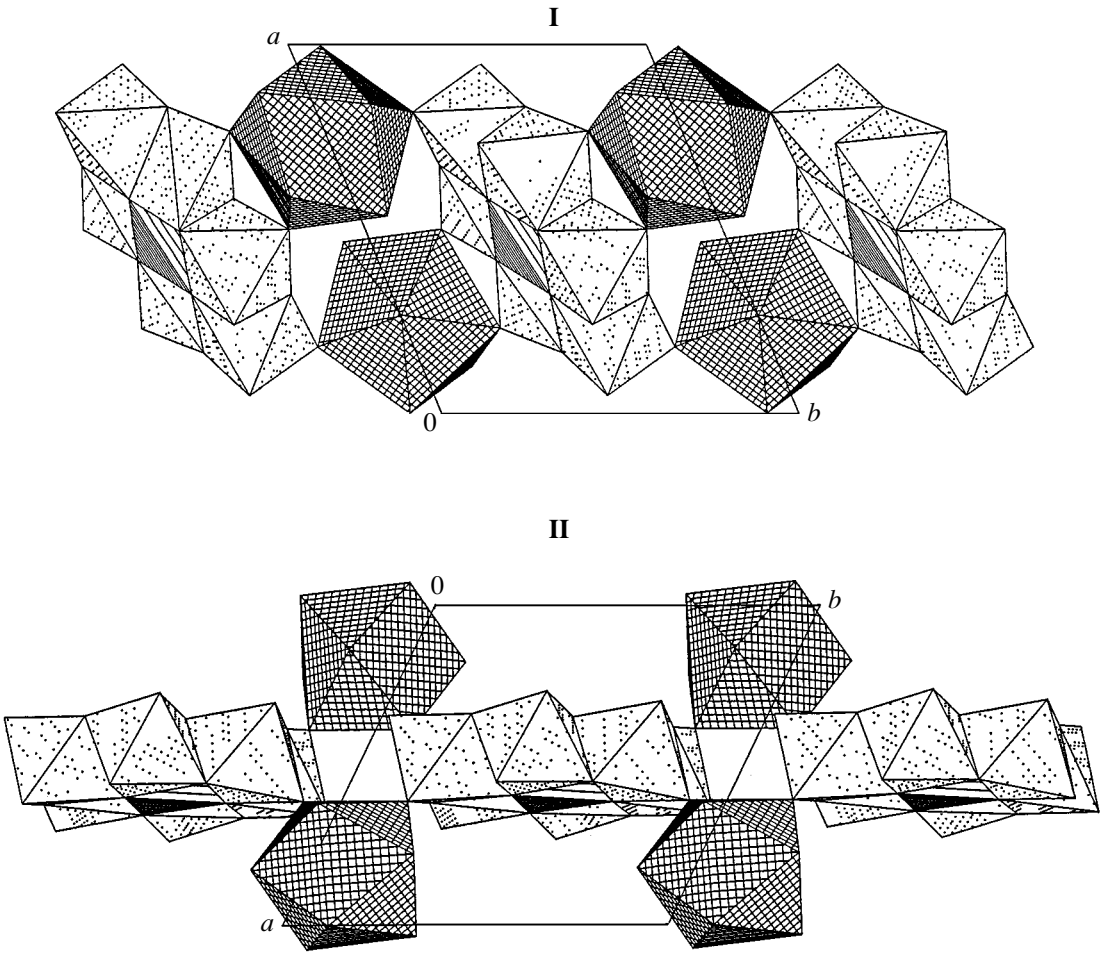

Chains of $[Nd_2TeMo_6O_{24} \cdot 12H_2O]_n$ in structure **I** and $[Nd_2TeMo_6O_{24} \cdot 14H_2O]_n$ in structure **II**.

undistorted oxygen octahedron, whereas the molybdenum octahedra are severely distorted.

The Nd^{3+} environment is formed by seven water molecules and two oxygen atoms of the two heteropoly anions adjacent in the chain. The coordination number of neodymium is nine, and the polyhedron is described as a monocapped tetragonal antiprism. The oxygen atoms of the heteropoly anions form a lateral edge of the antiprism. The Nd–O bond lengths in the coordination sphere of neodymium have close values, but the interatomic distance to the capping (apical) O(5*w*) atom is somewhat elongated. The mean length of the Nd–O bond involving the oxygen atoms located at the vertices of the tetragonal antiprism is equal to 2.494(4) Å, and the Nd–O(5*w*) bond length is 2.552(5) Å. The capped face is planar within 0.018 Å, and the lower face is planar within 0.046 Å. The dihedral angle between the upper and lower faces of the antiprism is 2°. The oxygen atoms in the environment of the central atom differ in nature, and the symmetry of the Nd coordination polyhedron is C_1.

The structure contains three independent molecules of crystallization water. One of these molecules is situated in the vicinity of the center of inversion; therefore, this site is half occupied. This corresponds to five crystallization water molecules per formula unit. The crystal packing is characterized by an extended system of hydrogen bonds. The oxygen atoms of the water molecules and heteropoly anions serve as acceptors of protons in these hydrogen bonds.

Compound **II** reported in this paper differs from the previously described compound **I**, which also has a chain-type structure [2]. In the structure of these compounds, the heteropoly anions are arranged in the chains in different fashions. In compound **I**, the axis perpendicular to the centered fragment of six MoO_6 octahedra are aligned parallel to the chain. In compound **II**, this axis is located at a right angle to the chain (figure). In **I**, the Nd environment consists of six water molecules and three terminal oxygen atoms of two $[Nd_2TeMo_6O_{24} \cdot 12H_2O]_n$ heteropoly anions that are adjacent in the chain. The Nd coordination polyhedron

is a distorted tricapped trigonal prism and also has a low symmetry (C_1).

CONCLUSIONS

Thus, the Nd^{3+} cation forms two complexes with the hexamolybdotellurate anion. The complexes are similar in composition but differ in structure. It can be assumed that different environments of the neodymium ions in compounds **I** and **II** will manifest themselves in the luminescence spectra. At present, we have investigated how the structure of rare-earth heteropoly complexes affect their luminescence properties. The results obtained will be published elsewhere.

ACKNOWLEDGMENTS

This study was supported by the Russian Foundation for Basic Research, project no. 03-03-32203.

REFERENCES

1. J. S. Anderson, Nature **140**, 850 (1937).
2. M. S. Grigor'ev, Yu. T. Struchkov, A. M. Fedoseev, *et al.*, Zh. Neorg. Khim. **37**, 2507 (1992).
3. A. M. Fedosseev, M. S. Grigoriev, N. A. Budantseva, *et al.*, J. Lumin. **87–89**, 1065 (2000).
4. A. B. Yusov, A. M. Fedosseev, G. B. Andreev, and I. B. Shirokova, Mendeleev Commun., No. 3, 86 (2001).
5. A. L. Spek, *PLATON: Multipurpose Crystallographic Tool* (Univ. of Utrecht, Netherlands, 1998).
6. G. M. Sheldrick, Acta Crystallogr., Sect. A: Found. Crystallogr. **46**, 467 (1990).
7. G. M. Sheldrick, *SHELXL97: Program for the Refinement of Crystal Structures* (Univ. of Göttingen, Germany, 1997).
8. H. T. Evans, J. Am. Chem. Soc. **90** (12), 3275 (1968).

Translated by I. Polyakova

Crystallography Reports, Vol. 50, No. 2, 2005, pp. 194–202. Translated from Kristallografiya, Vol. 50, No. 2, 2005, pp. 226–234.

STRUCTURE OF INORGANIC COMPOUNDS

Crystal Structure of Sakhaite from the Solongo Deposit in Connection with the Crystallochemical Interpretation of the Sakhaite–Harkerite Mineral Series

O. V. Yakubovich*, I. M. Still, P. G. Gavrilenko*, and V. S. Urusov***

** Moscow State University, Vorob'evy gory, Moscow, 119992 Russia*
e-mail: yakubol@geol.msu.ru
*** University of Chicago, Chicago, USA*
Received May 10, 2004

Abstract—The crystal structure of mineral sakhaite $Ca_{48}[Mg_{13.2}(Fe,Mn)_{2.8}](CO_3)_{16}\{Al[SiO_{3.75}(OH)_{0.25}]_4\}(BO_3)_{28}[(H_2O)_{3.3}(HCl)_{3.3}]$ from the Solongo deposit, Zabaykalye, is established (R 0.047) by X-ray diffraction analysis (Bruker Smart CCD diffractometer, $2\theta : \theta$ scan, λMoK_α radiation, graphite monochromator): a = 14.679(2) Å, sp. gr. $Fd3m$, Z = 1, ρ_{calcd} = 2.99 g/cm^3. It is shown that some part of BO_3 triangles in the structure of sakhaite from Solongo is replaced with five-member complexes $\{Al[SiO_3(O,OH)]_4\}$, established previously in the harkerite structure. Three schemes of isomorphism, which are characteristic of the sakhaite–harkerite mineral series, are selected and the general formula is proposed: $Ca_{48}(Mg,Fe,Mn)_{16}(CO_3)_{16}\{Al[SiO_3(O,OH)]_4\}_y(BO_3)_{32-y} \cdot n(H_2O,HCl)$ (Z = 1), y_{max} = 8, n_{max} = 16 – y. The structural relationship of sakhaite–harkerite minerals with borate–sulfates of the tychite family $Na_6(Mg,Fe,Mn)_2(BO_3)_4(SO_4)$ is revealed. The correlation between the number of harkerite fragments forming the mineral structure, the structural symmetry, and the degree of imperfection is ascertained. © *2005 Pleiades Publishing, Inc.*

INTRODUCTION

Ca,Mg–borate–carbonate sakhaite is a rock-forming mineral; it substitutes kotoite marbles and kurchatovite in the early stage of metasomatic calcic-skarn transformation of borate ores [1]. Sakhaite is the end member of the isomorphic sakhaite–harkerite series, in which individual phases differ by the content of SiO_2 and Al_2O_3: from tenths of a percent (sakhaite) to 20% (harkerite) [2]. It was proposed in [3] to consider sakhaite and harkerite as indicators of magnesian skarns since these minerals are characteristic of the least depths at which the metasomatic process can develop. These minerals were also found in greenschist-facies rocks in South Africa [4], in amphibolite-facies rocks in Sweden, and in granulite-facies rocks in North America [5]. On the basis of the estimation of the conditions of the formation of harkerite in granulite schists in the Adirondack Mountains (New York, the United States), it was concluded [5] that harkerite cannot be regarded as a typomorphic mineral fixing low pressures because it is also stable at moderate pressures (~8 kbar).

Sakhaite from magnesian skarns in Polar Yakutia was described as a new mineral by Ostrovskaya *et al.* [6]. On the basis of X-ray diffraction analysis, spectroscopic study, chemical analysis, and the experimental value of the density, the following crystallochemical formula was proposed: $Ca_{48}Mg_{16}(BO_3)_{28}(CO_3)_{16}Cl_4(OH)_8 \cdot 4(H_2O)$. Harkerite from Skye Island, Scotland, which was described for the first time in [7], was analyzed anew in [6] and its formula was reported: $Ca_{48}Mg_{16}Al_3(BO_3)_{15}(CO_3)_{18}(SiO_4)_{12}Cl_2(OH)_6 \cdot 3(H_2O)$. It was suggested in [6] that the main structural difference between these minerals is in partial substitution of triangular borate groups (sakhaite) with orthosilicate tetrahedra (harkerite).

The crystal structure of sakhaite was first determined for a synthetic material in the space group $F4_132$ [8]. The formula obtained $Ca_{48}Mg_{16}(BO_3)_{32}(CO_3)_{16} \cdot 2(H_2O) = 16[Ca_3Mg(BO_3)_2(CO_3) \cdot 0.125(H_2O)]$ differed from the formula of the mineral by the number of BO_3 groups (32 instead of 28) and the absence of Cl^- and $(OH)^-$ anions. In 1978, Yakubovich *et al.* reported the results of X-ray diffraction investigation of sakhaite from the Solongo deposit in Buryatia [9]. The systematic absence of reflections unambiguously indicated the sp. gr. $Fd3m$. However, the structural model in the sp. gr. $F4_132$ of the synthetic analog was preferred. The small size of the sakhaite single crystal ($r_{max} \approx 0.1$ mm) made it impossible to obtain, using the available technology of the 1980s, sufficiently representative experimental data for the detailed analysis of the crystal structure. Thus, the results obtained in [9] on the basis of 83 experimental reflections needed to be refined. In addition, statistical symmetry analysis performed by us

showed that the "axial" sp. gr. $F4_132$ is not characteristic of minerals; it has been recorded only for sakhaite (most likely, erroneously, taking into account the above facts). In this study, we report the results of repeated determination of the crystal structure of sakhaite from the Solongo deposit (Zabaykalye, Buryatia, East Siberia) and subsequent crystallochemical interpretation of the minerals of the sakhaite–harkerite series.

EXPERIMENT AND INTERPRETATION OF THE STRUCTURE

Sakhaite from the contact-metasomatic Solongo iron ore deposit, where it is coordinated with the rocks formed as a result of partial substitution of magnesian calciphyres by calcic skarns, was established and described by Malinko in [10] in the form of dense crystalline masses; more rarely, as individual octahedra of gray, brownish gray, or greenish brown color. This mineral has a greasy luster; it is optically isotropic and has the following parameters: the refractive index n = 1.648–1.650, and $\rho_{exp} = 2.91$ g/cm^3.

The composition of sakhaite from Solongo according to the chemical analysis data [10] is as follows: CaO, 50.88; MgO, 10.84; Al_2O_3, 1.42; SiO_2, 2.03; B_2O_3, 15.80; CO_2, 14.20; H_2O, 3.04; and Cl, 2.03; 100.24 wt % in total. It was also noted in [10] that the refractive index and the density of sakhaite from Solongo exceed the corresponding parameters of sakhaite from Yakutia, described for the first time by Ostrovskaya [6]. In addition, the high contents of silicon and aluminum and low content of boron in sakhaite from Solongo make this mineral closer to harkerite. According to [11], the silicon content in sakhaites from Solongo varies from 2 to 8 au per unit cell.

In this study, we performed X-ray analysis of the same single-crystal fragment from the sample supplied to us by Malinko that was investigated in [9]. A Bruker Smart three-circle diffractometer equipped with a highly sensitive CCD detector was used. The cubic symmetry of sakhaite from Solongo with the period $a \approx$ 14.7 Å, which corresponds to the pseudoperiod of harkerite, was confirmed. The measured reflection intensities are corrected for the Lorentz factor and the polarization effect.

All calculations were carried out using the SHELX program package [12, 13]. The atomic scattering curves and corrections for the anomalous dispersion [14] were used. The systematic absence of reflections unambiguously indicated the sp. gr. $Fd3m$, within which the structure was interpreted. The structural model found by direct methods was refined in the anisotropic approximation taking into account the absorption. The crystal data for sakhaite, the details of the X-ray diffraction study, and the refinement parameters are listed in Table 1. The coordinates of the basic atoms with thermal displacement parameters and the interatomic distances are given in Tables 2 and 3, respectively.

After the X-ray diffraction analysis, the composition of the polished sample of the same single-crystal fragment was investigated on an electron probe microanalyzer with a voltage of 15 kV, beam current of 10 nA, and beam diameter of 5 μm. As references, we used synthetic anorthite glass (Al, Si, Ca), natural olivine (Mn, Fe, Mg), and synthetic chlorine apatite (Cl). The obtained data on the elemental composition are listed in Table 4.

The main fragments forming the structure of the mineral studied are those that were established previously [8, 9]. These are large Ca polyhedra, octahedra predominantly occupied by Mg atoms, and CO_3 and BO_3 triangles. According to the X-ray spectroscopic data, the mineral contains Fe and Mn atoms. The most probable divalent forms of their cations have been fixed in most chemical analyses of sakhaites and harkerites [1, 2, 5]. Since Mn^{2+} ions can isomorphously substitute both Mg and Ca, we refined the degree of occupation of the 48-multiple position by Ca atoms. It was found that this position does not contain impurity defects and is completely occupied by calcium. Since the atomic scattering curves for Mn and Fe (neighbors in group IV of the periodic table) are similar to each other and the approximate ratio Fe : Mn in the sample under study is 3 : 1, we used the f curves for Mg and Fe in the refinement of the degree of occupation of the octahedral position. It is ascertained that the 16-multiple position is statistically occupied by Mg and Fe atoms in the ratio 13.2 : 2.8. Although Fe and Mn were not found in the composition of the sakhaite studied in [10], the data of the later chemical analyses of sakhaites from Solongo indicate the presence of these elements in all samples [11].

During the structure refinement, we also assumed that some part of BO_3 triangles are replaced by five-member complexes $\{Al[SiO_3(O,OH)]_4\}$ formed by an Al tetrahedron and four Si tetrahedra. Each Si tetrahedron shares one vertex with the Al tetrahedron (Fig. 1). Such complexes are characteristic of the harkerite structure [15, 16]. The unit cell of harkerite from Scotland [16] contains four $\{Al[SiO_3(O,OH)]_4\}$ groups, while the unit cell of harkerite from Yakutia [15] contains three such groups. The refinement of the occupations of the structural positions corresponding to the B, Si and Al atoms showed that in the case under consideration the unit cell contains 28 B, 4 Si, and 1 Al atoms. This indicates that in the structure of sakhaite from Solongo only one aluminosilicate group from five tetrahedra statistically substitutes four BO_3 triangles. It should be noted that, similar to the harkerite structure [15, 16], the Si atoms (upon statistical substitution) do not occupy the boron positions but are shifted along the threefold axis to the oxygen atoms O(3) which complete the tetrahedral configuration of the boron positions. The O(1) atoms which coordinate boron are also shifted in this case from their positions to the O(1') positions, remaining in the plane of symmetry m.

Table 1. Crystallographic data and the details of the X-ray data collection and refinement

Chemical formula	$Ca_3[Mg_{0.825}(Fe,Mn)_{0.175}](CO_3)\{Al[SiO_{3.75}(OH)_{0.25}]_4\}_{0.0625}(BO_3)_{1.75}[(H_2O)_{0.2}(HCl)_{0.2}]$
μ, mm^{-1}	2.56
Space group	*Fd*3*m*
Z	16
Unit cell parameter *a*, Å	14.679(2)
V, $Å^3$	3162.9(7)
ρ_{calcd}, g/cm^3	2.99
Diffractometer	Bruker Smart CCD
Radiation	MoK_α (graphite monochromator)
Temperature, K	293(2)
Range of collection: θ_{max}, deg	28.12
Total number of reflections	8795
Number of independent/collected with $I > 1.96\sigma(I)$ reflections	220/210
Refinement method	on F^2
Number of parameters in refinement	37
Absorption correction	Semiempirical, using equivalents
R_{int}, $\sigma(R_{int})$	0.051, 0.012
Reliability factors: *R* (for collected reflections)	0.047
wR_2 (for all independent reflections)	0.089
s	1.25
Residual electron density, $e/Å^3$	$\rho_{max} = 0.45$, $\rho_{min} = -0.57$

Table 2. Coordinates of the basic atoms and equivalent thermal displacement parameters

Atom	*G**	Position symmetry	*x*/*a*	*y*/*b*	*z*/*c*	U_{eq}, $Å^2$
Mg	0.0687(7)	$\bar{3}\,m$	0	0.5	0	0.0088(6)
Fe	0.0146(7)	$\bar{3}\,m$	0	0.5	0	0.0088(6)
Ca	0.25	*mm*	0.125	0.37706(9)	0.125	0.0249(3)
C	0.08333	$\bar{3}\,m$	0.25	0.25	0	0.062(4)
B	0.1462(9)	3*m*	−0.0351(4)	0.2851(4)	−0.0351(4)	0.012(1)
Si	0.0204(9)	3*m*	−0.0117(6)	0.2617(6)	−0.0117(6)	0.012(1)
Al	0.005(1)	$\bar{4}\,3m$	0.375	0.375	−0.125	0.06(2)
O(1)	0.44(1)	*m*	0.0059(2)	0.3603(3)	0.0059(2)	0.0222(9)
O(1')	0.06(1)	*m*	−0.005(2)	0.370(3)	−0.005(2)	0.0222(9)
O(2)	0.25	*m*	0.2296(4)	0.3330(5)	0.0204(4)	0.064(2)
O(3)	0.020(3)	3*m*	0.442(2)	0.308(2)	−0.058(2)	0.06(2)
O(4) (H_2O)	0.017(3)	3*m*	0.350(1)	0.400(1)	−0.150(1)	0.13(2)
Cl (HCl)	0.017(3)	3*m*	0.350(1)	0.400(1)	−0.150(1)	0.13(2)

* Ratio of the number of atoms in a given position to the multiplicity of the general position.

Table 3. Interatomic distances, Å

Mg(Fe,Mn) octahedron		B triangle	
M–O(1)	2.054(4) × 6	B–O(1)	1.395(5) × 3
O(1')	1.92(4) × 6	Si tetrahedron	
Ca eight-vertex polyhedron		Si–O(1')	1.59(4) × 3
Ca–O(2)	2.265(8) × 2	O(3)	1.77(6)
(or O(2)	2.718(2) × 4)	Si–O(av.)	1.63
O(1)	2.484(4) × 2	C triangle	
O(1)	2.587(1) × 4	C–O(2)	1.290(7) × 3
Ca–O(av)	2.537	Al tetrahedron	
O(1')	2.576(2) × 4	Al–O(3)	1.71(5) × 4
O(1')	2.70(4) × 2		
Ca–O(av)	2.59		

The O(2) atoms of carbonate groups are statistically (with a probability of 50%) located in the planes of symmetry *m*. In other words, CO_3 triangles can be interpreted as groups occupying two equiprobable positions around the threefold axis which passes through C atoms.

DESCRIPTION OF THE STRUCTURE

The B–O distances in BO_3 triangles, equal to 1.395(5) Å, are typical of B atoms in the threefold coordination. CO_3 triangles are systematically smaller, with C–O distances of 1.290(7) Å. Al atoms in the high-symmetry position $\bar{4}3m$ are tetrahedrally surrounded by oxygen atoms at a distance of 1.71(5) Å. Si atoms form strongly distorted tetrahedra with three shortened Si–O(1') distances of 1.59(4) Å and one extended Si–O(3) distance of 1.77(6) Å, corresponding to the bridge interaction between the vertices: Si–O(OH)–Al. The average Si–O distance of 1.63 Å is typical of Si in the tetrahedral coordination. The local valence balance for the O(3) atom, as well as the electroneutrality of the structure as a whole at a replacement of four BO_3 triangles by an $\{Al[SiO_3(O,OH)]_4\}$ tetrahedral pentagroup, is provided when 1/4 of the O(3) atoms are incorporated into OH groups. The presence of OH groups in the sakhaite structure correlates with both the X-ray diffraction data for harkerite from Scotland [16] and the features of the IR specta of the minerals of the sakhaite–harkerite series [6, 11].

The statistical character of substitution according to the scheme $4(BO_3) \longleftrightarrow \{Al[SiO_3(O,OH)]_4\}$ in sakhaite manifests itself in the change in the bond lengths in Mg(Fe,Mn) octahedra and Ca polyhedra. With a probability of 0.875, borate oxocomplexes are involved in the construction of the anion radical, while the octahedra are formed by O(1) atoms with Mg–O(1) distances of 2.054(4) Å. At the substitution of BO_3 triangles with island aluminosilicate groups, octahedra somewhat decrease in size: the Mg–O(1') distance becomes equal to 1.92(4) Å.

The reverse situation is observed for Ca eight-vertex polyhedra (or ten-vertex polyhedra: the possibility of twofold coordination of Ca is related to the statistical occupation of O(2) atoms of their positions). Indeed, the replacement of a borate anion by an aluminosilicate anion is accompanied by the increase in the Ca–O(1') distances up to 2.70(4) Å in comparison with the largest Ca–O(1) distances: 2.587(1) Å (Table 3).

The basis of the sakhaite structure is a framework formed by Ca eight-vertex (ten-vertex) polyhedra linked by shared edges and faces into columns extended in three directions along the coordinate axes (Fig. 2). Each Ca polyhedron belongs to two such columns. Each Mg octahedron, sharing six faces with Ca eight-vertex polyhedra, plays the role of the site in which three mutually perpendicular columns are linked. BO_3 and CO_3 triangles reinforce the framework, sharing

Table 4. X-ray microanalysis data for sakhaite

Wt %					Relative atomic numbers					
element	1*	2*	3*	synthetic sakhaite**	element	1*	2*	3*	synthetic sakhaite**	average
Fe	1.91	1.68	2.95			0.034	0.030	0.052		0.039
Mn	0.67	0.62	1.10			0.012	0.011	0.020		0.014
Mg	5.70	5.93	5.00	7.10		0.235	0.244	0.206	0.292	0.228
					Mg + Fe + Mn =	0.281	0.285	0.280	0.292	0.282
					Mg, %	84	86	73	100	81
Si	1.83	2.08	1.22			0.065	0.074	0.044		0.081
Al	0.71	0.72	0.61			0.026	0.027	0.023		0.025
Ca	33.5	34.3	33.6	35.3		0.837	0.858	0.840	0.883	0.845
Cl	2.81	2.80	3.37			0.079	0.079	0.095		0.084

* 1, 2, and 3 are measurement points on the sample.
** Synthetic sakhaite $Ca_3Mg(BO_3)_2(CO_3) \cdot nH_2O$.

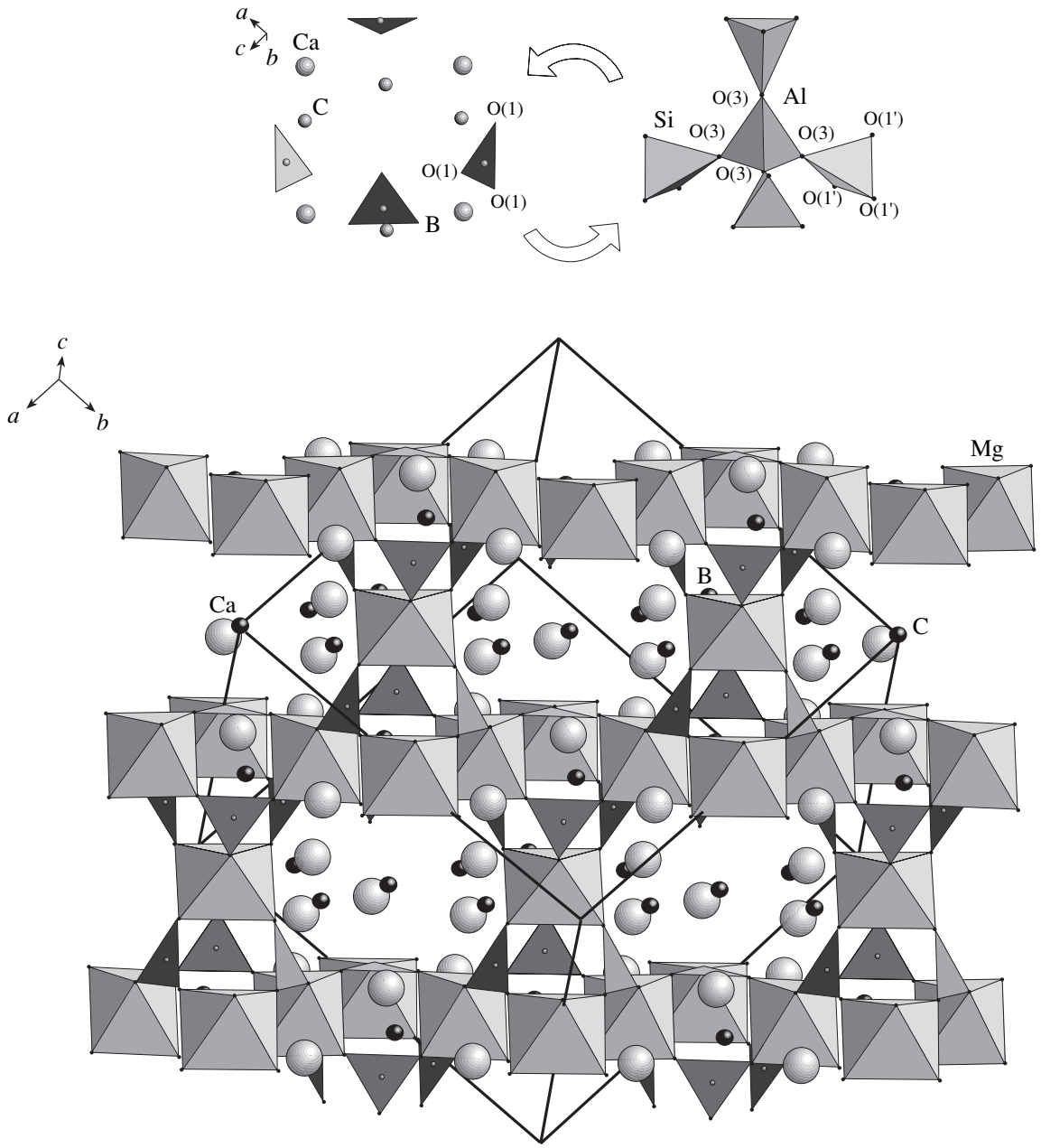

Fig. 1. Crystal structure of sakhaite in axonometry. The aluminosilicate pentagroup, which statistically substitutes four BO_3 triangles in the sakhaite unit cell, is shown at the top.

edges (BO_3) and vertices (CO_3) with Ca polyhedra. Cavities of two types, arranged similar to Na^+ and Cl^- ions in the rock salt structure [9], alternate with each other along the coordinate axes (Fig. 2). Small cavities, which are Archimedean cuboctahedra, are formed by four tetrahedrally arranged BO_3 triangles, four tetrahedrally arranged triangular faces of Mg octahedra (Fig. 3), and six rectangular (slightly distorted) faces of Ca polyhedra. Large cavities are formed mainly by Ca polyhedra, four tetrahedrally arranged BO_3 triangles, and four CO_3 triangles. Each CO_3 triangle belongs simultaneously to two large cavities separating neighboring cells in the framework, whereas BO_3 triangles separate cells of different type. When borate oxocomplexes are substituted by aluminosilicate ones, it is large cavities that serve as a reservoir for $\{Al[SiO_3(O,OH)]_4\}$ pentagroups (Fig. 1). Since only 1/8 of the cavities are statistically occupied by aluminosilicate five-member complexes, water molecules of zeolite type [O(4)] and HCl molecules are also incorporated into these cavities (Fig. 2). They equiprobably occupy the position with symmetry 3*m*, being statistically located at 20% of the points of the 32-multiple regular system. Thus, the unit-cell content of sakhaite

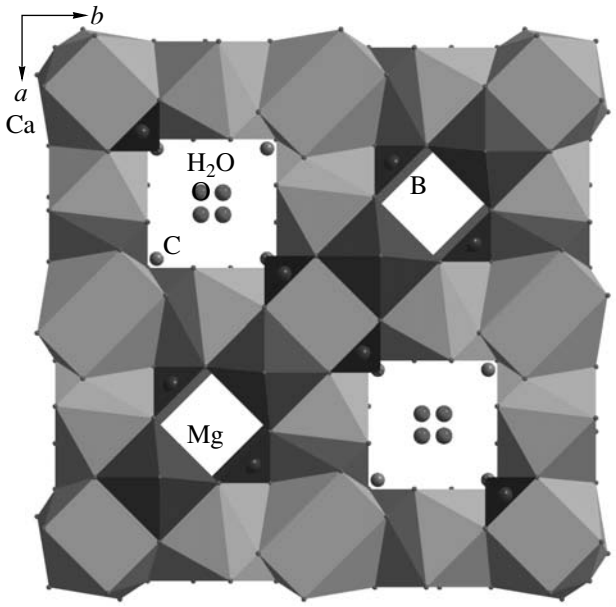

Fig. 2. Sakhaite crystal structure projected onto the *xy* plane.

from Solongo is described by the formula $Ca_{48}(Mg_{13}Fe_2Mn)(CO_3)_{16}\{Al[SiO_{3.75}(OH)_{0.25}]_4\}(BO_3)_{28} \cdot [(H_2O)_3(HCl)_3]$.

CRYSTALLOCHEMICAL FEATURES OF MINERALS OF THE SAKHAITE–HARKERITE ISOMORPHIC SERIES

The data obtained by us and the previous results [8, 15, 16] make it possible to distinguish three schemes of isomorphism that are typical of minerals of the sakhaite–harkerite series:

(i) The octahedra predominantly occupied by Mg^{2+} cations can also contain subordinate amounts of Fe and, more rarely, Mn atoms. Representatives of this mineral family with dominance of Fe (or Mn) over Mg are yet to be found.

(ii) The presence of Si and Al atoms in the mineral composition indicates the replacement of four borate triangular groups by equal-charge aluminosilicate oxocomplexes formed by one Al and four Si tetrahedra: $4(BO_3) \longleftrightarrow \{Al[SiO_3(O,OH)]_4\}$.

(iii) Neutral H_2O and HCl molecules can be statistically isomorphously incorporated into structural cavities. In this case, they are not involved in the coordination of cations, being molecules of zeolite type. Theoretically, they may also occupy positions in small cavities (as in synthetic sakhaite [8]) and large cavities [9, 15, 16]. The number of such molecules per unit cell must not exceed 16: the maximally possible number in the absence of aluminosilicate pentagroups.

Taking into account the above considerations, we propose the following general formula for minerals of the sakhaite–harkerite series (for $Z = 1$): $Ca_{48}(Mg,Fe,Mn)_{16}(CO_3)\{Al[SiO_3(O,OH)]_4\}_y(BO_3)_{32-y} \cdot n(H_2O,HCl)$, $y_{max} = 8$, $n_{max} = 16 - y$. At $y = 0$, the formula takes the form $Ca_{48}Mg_{16}(CO_3)_{16}(BO_3)_{32} \cdot n(H_2O) = 16[Ca_3Mg(CO_3)(BO_3)_2 \cdot nH_2O]$ which corresponds to the synthetic sakhaite composition [8]. The second end member of the series ($y = 8$) is a hypothetical carbonate aluminosilicate: $Ca_{48}(Mg,Fe,Mn)_{16}(CO_3)\{Al[SiO_3(O,OH)]_4\}_8 \cdot n(H_2O,HCl) = 16[Ca_3Mg(CO_3)\{Al[SiO_3(O,OH)]_4\}_{0.5} \cdot nH_2O]$. Natural or synthetic compounds of such composition are yet to be found. However, cubic borate–sulfates (sp. gr. $Fd\bar{3}$)—tychite $Na_{48}Mg_{16}(BO_3)_{32}(SO_4)_8 = 8[Na_6Mg_2(BO_3)_4(SO_4)]$ (a = 13.90 Å), ferrotychite $Na_6(Fe,Mg,Mn)_2(BO_3)_4(SO_4)$ (a = 13.96 Å) [17], and manganotychite $Na_6(Mn,Fe,Mg)_2(BO_3)_4(SO_4)$ (a = 14.00 Å), in whose unit cells eight SO_4 tetrahedra occupy the positions of AlO_4 tetrahedra of the hypothetical (harkerite) end member—are homeotypic with harkerite (Figs. 3, 4).

Table 5 contains the compositions of the mineral species of the series under consideration. These data show that, in comparison with the unit-cell contents of sakhaites and harkerites with known structures, the number of Mg atoms in chemical analyses is generally

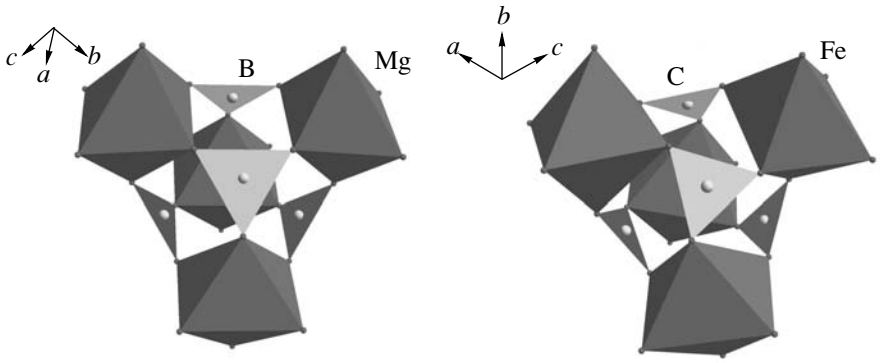

Fig. 3. Polyhedral environment of small cavities in the sakhaite crystal structure (left) in comparison with the environment of analogous cavities in the ferrotychite structure (right).

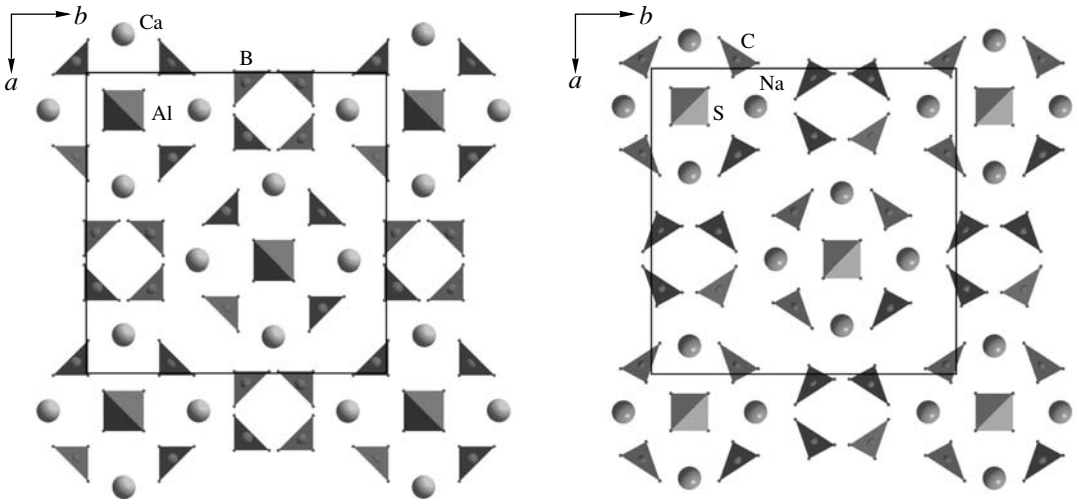

Fig. 4. Arrangement of tetrahedral ($[AlO_4]^{5-}$ and $[SO_4]^{2-}$) and triangular ($[BO_3]^{3-}$ and $[CO_3]^{2-}$) oxocomplexes in the sakhaite (left) and ferrotychite (right) crystal structures.

overestimated and the number of Ca atoms is underestimated. A similar situation occurs with the formula numbers of B and C atoms. As was noted in [5, 16], the systematic overestimation of the C content and corresponding deficit of B can be due to the contamination of the material studied by the wet chemistry method with calcite, which is always present in skarns. If we recalculate all analyses based on the numbers of atoms in defect-free structural positions Ca, 48; Mg + Fe + Mn, 16; and C, 16, we obtain the unit-cell contents that are in satisfactory agreement with the proposed general formula for the minerals of the sakhaite–harkerite series. As can be seen from Table 5, y takes different values from 0.1 to 4; i.e., specific mineral species are the members of a one isomorphic series and are derivative combinations of two minerals: harkerite $Ca_{6y}(Mg,Fe,Mn)_{2y}(CO_3)_{2y}\{Al[SiO_3(O,OH)]_4\}_y \cdot n(H_2O, HCl)$ and sakhaite $Ca_{48-6y}(Mg,Fe,Mn)_{16-2y}(CO_3)_{16-2y}(BO_3)_{32-4y} \cdot n(H_2O, HCl)$ (Fig. 5).

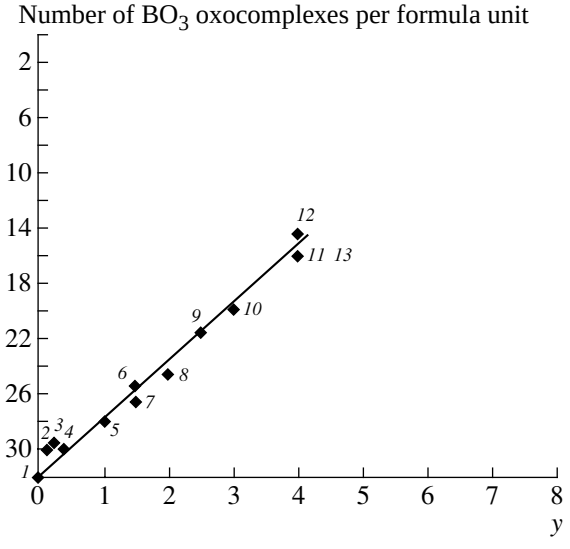

Fig. 5. Relation between the numbers of aluminosilicate groups and borate oxocomplexes in the sakhaite–harkerite mineral series. Numbers of points correspond to the numbers of samples from Table 5.

A gradual increase in the harkerite component up to $y = 1.5$ does not lead to a radical change in the structure: all minerals of the sakhaite edge of the isomorphic series are characterized by cubic symmetry and the absence of a pseudoperiod along the unit-cell axes [3, 4, 6, 10, 18]. X-ray powder patterns of the minerals containing two or more harkerite fragments per unit cell have a more complex, as compared with sakhaite, spectrum with lines shifted in the same direction and additional weak reflections. In addition, many lines are broad or split into doublets [3, 5, 6]. Such a character of the diffraction pattern indicates the presence of a pseudoperiod $a' = a/2$ and, possibly, rhombohedral symmetry. Rhombohedral symmetry was unambiguously established [7] for the harkerite from Scotland, in whose structure harkerite and sakhaite fragments ($y = 4$) are ordered in equal amounts along the threefold axis.

Apparently, the structural transformations from synthetic sakhaite (end member with ordered cubic structure, $y = 0$) to the harkerite from Scotland (intermediate member with ordered rhombohedral structure, $y = 4$) pass through the formation of imperfect cubic sakhaites with a relatively small (15 Å) cell (sakhaites from Yakutia, Buryatia, Kazakhstan, and Namibia) up to harkerite from the Tas Haiatah mountain ridge ($y = 2$), beginning with which the cubic unit-cell parameter doubles (harkerites from Yakutia, California, and New York). Further increase in the number of harkerite fragments ($y > 4$) should lead to the formation of new

Table 5. Compositions of the harkerite–sakhaite mineral species from skarns of different genesis*

Element	1	2		3		4		5				6		
	Synthetic sakhaite [8]	Moral'nyi River, Tas Haiatah, Yakutia [6]		Lou Lou River, Tas Haiatah, Yakutia [3]		Moral'nyi River, Tas Haiatah, Yakutia [3]		Solongo deposit, Zabaykalye, Buryatia [10]		Solongo deposit, our data		Sajak deposit, Pribalkhashie, Kazakhstan [20]		
	structure	chemical analysis	*N*****	chemical analysis	*N*	chemical analysis	*N*	chemical analysis	*N*	probe analysis	structure	probe analysis	chemical analysis	*N*
Si		0.2	0.2	0.9	0.9	1.4	1.4	1.8	1.8	3.5	4.0	5.6	6.3	5.6
Al		0.3	0.3	0.3	0.3	0.7	0.7	1.5	1.5	1.4	1.0	1.7	2.3	1.7
B	32.0	27.8	29.9	29.0	29.5	28.4	30.0	24.7	26.3	und.	28.0	und.	24.8	25.5
C	16.0	18.1	16.0	16.5	16	17.2	16.0	17.6	16.0	und.	16.0	und.	16.7**	16.0
Mn^{2+}				0.2	0.2	0.1	0.1			0.8		0.2	und.	0.2
Fe^{3+}		0.2	0.2	0.4	0.4	0.3	0.3			2.2	2.8	3.0	2.2	2.0
Fe^{2+}						0.5	0.5						1.0	1.0
Mg	16.0	16.3	15.8	16.7	15.4	17.0	15.1	14.6	16.0	13.0	13.2	15.3	12.9	12.8
Ca	48.0	47.3	47.8	46.7	48.0	46.3	48.2	49.4	48.0	48.0	48.0	48.7	50.0	48.7
Cl		4.1	4.1	4.8	4.8	4.8	4.8	3.1	3.1	4.8	3.3	5.5	4.1	4.8
H	4.0	15.0	15.0	7.5	7.5	8.5	8.5	18.4	18.4	und.	9.9	und.	3.2	3.2
*y****	0	0.1		0.25		0.4		1.0				1.5		
*n****	2.0	11.6		8.5		9.0		6.6				6.4		

Element	7		8		9		10	11			12		13	
	Kombat Mine, Namibia [4]		Lou Lou River, Tas Haiatah, Yakutia [3]		Crestmore quarry, Riverside County, California, the United States [5]		Yakutia [15]	Broadford, Skye, Scotland [7]			Adirondack Mountains, New York, the United States [5]		Albano, Italy [2]	
	chemical analysis	*N*	chemical analysis	*N*	chemical analysis	*N*	structure	chemical analysis	*N*	structure	chemical analysis	*N*	chemical analysis	*N*
Si	5.9	5.9	8.3	8.3	10.8	10.8	12.0	13.6	13.6	16.0	15.9	15.9	16.5	16.5
Al	1.5	1.5	3.7	3.7	2.7	2.7	3.0	3.2	3.2	4.0	3.4	3.4	3.6	3.6
B	26.2	26.6	19.5	24.6	16.4	21.6	20.0	12.9	16.5	16.0	10.1	14.5	11.8	15.9
C	16.4	16.0	21.1	16.0	21.2	16.0	16.0	19.6	16.0	16.0	20.4	16.0	20.1	16.0
Mn^{2+}			0.1	0.1									0.1	0.1
Fe^{3+}			0.7	0.7				0.6	0.6					
Fe^{2+}			0.7	0.7	0.4	0.4		0.4	0.4		0.6	0.6	1.5	1.5
Mg	16.6	16.0	14.5	14.5	15.8	15.6	16.0	16.0	15.0	16.0	16.2	15.4	16.1	14.4
Ca	47.4	48.0	47.5	47.5	47.7	47.9	48.0	47.6	48.6	48.0	47.2	48.0	46.3	48.0
Cl			3.5	3.5	4.0	4.0		2.2	2.2	2.0	2.1	2.1	0.1	0.1
H	30.5	30.5	14.0	14.0	4.0	4.0	8.0	5.2	5.2	4.0	4.0	4.0	8.2	8.2
*y****	1.5		2.0		2.5		3.0	4.0			4.0		4.0	
*n****	14.5		10.5		6.0		4.0	4.0			4.1		4.2	

und.—undetermined.

* The number of atoms in the unit cell is normalized to the basis Ca + Mg + Mn + Fe = 64.

** Was not determined; taken from the 100% sum.

*** The values correspond to the formula $Ca_{48}Mg_{16}(CO_3)_{16}\{Al[SiO_3(O,OH)]_4\}_y(BO_3)_{32-y} \cdot n(HCl,H_2O)$.

**** *N* is recalculated on the basis of the following contents: *C* = 16 (excess is added to the B content) and (Mg,Fe,Mn) = 16 (excess is added to the Ca content).

defects and structural disorder. One might expect a new ordered structure at $y = 8$, when only the harkerite component will form the second end member in the isomorphic mineral series under consideration. The existence of tychite (and its Fe and Mn analogs) in nature suggests that a harkerite can be found, in whose structure all borate oxocomplexes would be replaced with aluminosilicate ones.

However, the noted regularity is violated by harkerite from Albano, Italy [2]. Judging from the results of the chemical analysis and the X-ray diffraction data, this mineral is a disordered cubic species of harkerite from Skye, Scotland. While harkerite from Skye is genetically related to apomagnesian calcic skarns [11], harkerite from Albano is identified in metamorphized effusives in rock cavities [2]. The growth of crystals in cavities is indicative of fairly rapid cooling of the melt which may be the reason for the formation of disordered cubic polymorphs of minerals, whereas the slow growth of crystals in magnesian skarns at small depths is, apparently, the necessary basis for the formation of defect-free rhombohedral harkerite structure. The polymorphic character of the relationship between these mineral species was also suggested in [16].

ACKNOWLEDGMENTS

We are grateful to I.V. Pekov for his helpful participation in the discussion of the results.

This study was supported by the Russian Foundation for Basic Research, project no. 02-05-64845, and the program "Leading Scientific Schools," project no. NSh-1955.2003.5.

REFERENCES

1. S. M. Aleksandrov, Geokhimiya, No. 5, 492 (2003).
2. M. Barbieri, D. Cozzupoli, M. Federico, *et al.*, Lithos **10**, 133 (1977).
3. N. N. Pertsev, M. A. Bogomolov, and I. B. Nikitina, Tr. Mineral. Muzeya Akad. Nauk SSSR, No. 18, 105 (1968).
4. P. J. Dunn, D. R. Peacor, J. A. Nelen, *et al.*, Mineral. Mag. **54**, 105 (1990).
5. E. S. Grew, M. G. Yates, P. M. Adams, *et al.*, Can. Mineral. **37**, 277 (1990).
6. I. V. Ostrovskaya, N. N. Pertsev, and I. B. Nikitina, Zap. Vses. Mineral. O–va, No. 2, 193 (1966).
7. C. E. Tilley, Mineral. Mag. **29**, 621 (1951).
8. A. V. Chichagov, M. A. Simonov, and N. V. Belov, Dokl. Akad. Nauk SSSR **218** (3), 576 (1974) [Sov. Phys. Dokl. **19**, 559 (1975)].
9. O. V. Yakubovich, Yu. K. Egorov-Tismenko, M. A. Simonov, and N. V. Belov, Dokl. Akad. Nauk SSSR **239** (5), 1103 (1978) [Sov. Phys. Dokl. **23**, 225 (1978)].
10. S. V. Malinko and N. N. Kuznetsova, Zap. Vses. Mineral. O–va, No. 2, 164 (1973).
11. S. V. Malinko, N. V. Chukanov, and A. E. Lisitsyn, Zap. Vseros. Miner. O–va, No. 1, 96 (1999).
12. G. M. Sheldrick, *SHELXS97. Program for the Solution of Crystal Structures* (Univ. of Göttingen, Göttingen, 1997).
13. G. M. Sheldrick, *SHELXL97. Program for the Refinement of Crystal Structures from Diffraction Data* (Univ. of Göttingen, Göttingen, 1997).
14. *International Tables for Crystallography*, Ed. by T. Hahn, 8th ed. (Kluwer, Dordrecht, 1995).
15. M. P. Machin and G. Miehe, Neues Jahrb. Mineral., Monatsh., No. 5, 223 (1976).
16. G. Ginseppetti, F. Mazzi, and C. Tadini, Am. Mineral. **62**, 263 (1977).
17. Yu. A. Malinovskiĭ, S. V. Baturin, and N. V. Belov, Dokl. Akad. Nauk SSSR **249**, 1365 (1979) [Sov. Phys. Dokl. **24**, 951 (1979)].
18. A. D. Gorshenin, N. N. Pertsev, N. I. Organova, *et al.*, Dokl. Akad. Nauk SSSR **236** (5), 1203 (1977).

Translated by Yu. Sin'kov

Crystallography Reports, Vol. 50, No. 2, 2005, pp. 203–216. Translated from Kristallografiya, Vol. 50, No. 2, 2005, pp. 235–248.

STRUCTURE OF INORGANIC COMPOUNDS

Growth and Defect Crystal Structure of CdF_2 and Nonstoichiometric $Cd_{1-x}R_xF_{2+x}$ Phases (R = Rare Earth and In). Part 3. Crystal Structure of As-Grown $Cd_{0.90}R_{0.10}F_{2.10}$ (R = Sm–Lu, Y) Single Crystals

E. A. Sul'yanova*, A. P. Shcherbakov, V. N. Molchanov*, V. I. Simonov*, and B. P. Sobolev***

** Shubnikov Institute of Crystallography, Russian Academy of Sciences, Leninskiĭ pr. 59, Moscow, 119333 Russia*
e-mail: rahelen@ns.crys.ras.ru
*** Moscow State Academy of Fine Chemical Technology, Moscow, Russia*
Received November 15, 2004

Abstract—The structures of as-grown $Cd_{0.90}R_{0.10}F_{2.10}$ (R = Sm–Lu and Y) crystals are determined and related to the CaF_2 structure type. It is assumed that in all the crystals R^{3+} and Cd^{2+} ions form clusters with the tetrahedral configuration of the $[Cd_2R_2F_{26}]$ and $[CdR_3F_{26}]$ cations. The concentration of $[Cd_2R_2F_{26}]$ cations in crystals with R = Er–Lu and Y is considerably higher that in crystals with R = Sm–Ho. The tendency to a decrease in the coordination number of R^{3+} toward the end of the rare earth series manifests itself in the fact that the Yb^{3+} ions in $Cd_{0.90}Yb_{0.10}F_{2.10}$ occupy both tetrahedral (c.n. 10) and octahedral (c.n. 8) clusters. The Yb^{3+} ions in tetrahedral clusters are displaced from their basic positions by 0.15 Å along the ⟨100⟩ directions. In $Cd_{1-x}R_xF_{2+x}$ the relaxation of the anion sublattice of the fluorite matrix around clusters is much more pronounced than in the $Ca_{1-x}R_xF_{2+x}$ phases having similar geometry. © *2005 Pleiades Publishing, Inc.*

INTRODUCTION

This work continues the studies [1, 2] of synthesis, structures, and properties of CdF_2 crystals and nonstoichiometric fluorite phases of $Cd_{1-x}R_xF_{2+x}$ (R = RE and In). The structural part of these studies reduces to the establishment of the changes in the defect (cluster) structure of the phases with the fixed $Cd_{0.90}R_{0.10}F_{2.10}$ composition of as-grown crystals and the effect of subsequent annealing of these crystals across the RE series. The term *as-grown crystals* indicates crystals grown from melts and not subjected to any additional thermal treatment.

The prerequisite of the changes mentioned above is that the clusters of structural defects in all the fluorite phases with the composition $M_{1-x}R_xF_{2+x}$ (M = Ca, Sr, Ba, Cd, and Pb) also contain RE ions whose dimensions and electronic structure vary across the RE series. The result of such changes are the structural (morphotropic and polymorphic) transformations observed in homologous series of RE-containing compounds.

The most representative homologous series (17 compounds) with the simplest composition is the series of RE trifluorides. In the RF_3 series (R = La–Lu, Y, Sc), a decrease in the radius from that of La^{3+} to that of Lu^{3+} (effect of lanthanide contraction) and then to Sc^{3+} results in the change of the structure type in the following sequence: $LaF_3 \longrightarrow \beta\text{-}YF_3 \longrightarrow \alpha\text{-}UO_3 \longrightarrow ReO_3$. An increase of the temperature "spreads" the morphotropic change of the structure from one to several RF_3 groups. Two such groups may be called transitional groups. Each RF_3 forming a transitional group has two polymorphic modifications. One of these modifications is related to the structure of the previous morphotropic group, whereas the other is related to the structure of the subsequent morphotropic group. As a result, the RF_3 series consists of five morphotropic groups.

The first group includes RF_3 (LaF_3 to NdF_3) belonging to the tysonite structure type (LaF_3) in the whole temperature range from room temperature to the melting point. The second (transitional) group includes dimorphic RF_3 (R = Sm–Gd). These crystallized from melts in the tysonite structure type (LaF_3) but, when cooled, are transformed into the structure of orthorhombic $\beta\text{-}YF_3$. The compounds of the third group, TbF_3, DyF_3, and HoF_3, are crystallized from melt in the form of orthorhombic $\beta\text{-}YF_3$ and preserve this structure during cooling. The fourth (transitional) group consists of dimorphous RF_3 from ErF_3 to LuF_3. Their low-temperature phases preserve the $\beta\text{-}YF_3$ structure type, whereas the high-temperature modifications are isotypic to $\alpha\text{-}UO_3$. In accordance with the ionic radius, the Y^{3+} ion occupies the position intermediate between

Ho^{3+} and Er^{3+}; therefore, YF_3 is related to the fourth morphotropic group. The fifth group is formed by ScF_3 of the ReO_3 type.

An In^{3+} ion does not belong to the family of RE elements, but it is of interest as an ion with a radius intermediate between those of Lu^{3+} and Sc^{3+} and, thus, partly fills a considerable gap in the sizes of R^{3+} cations. Crystal–chemical analysis of the morphotropic and polymorphic transformations in RE fluorides was performed in [3].

The present publication describes the study of evolution of the defect structure of $Cd_{1-x}R_xF_{2+x}$ crystal–solid solutions in CdF_2 of RE trifluorides of the second (R = Sm, Gd), third (R = Dy, Ho), and fourth (R = Er–Lu and Y) morphotropic RF_3 groups. The basic structure of these groups belongs to the β-YF_3 (Fe_3C) structure type. This type is characterized by the change of the coordination number of a cation across the RE series with the preservation of the structure type [4]. To exclude the possible influence of the RF_3 concentration in the solid solution on the $Cd_{1-x}R_xF_{2+x}$ defect structure, we studied the isoconcentration series of the phases with 10 mol % RF_3.

The $M_{1-x}R_xF_{2+x}$ phases studied earlier were synthesized and studied by various research groups under various conditions by different experimental methods. This hinders the establishment of the regularities in the changes of the chemical composition of the defect structures in these $M_{1-x}R_xF_{2+x}$ phases across the RE series. Up to now, no structural study of the isoconcentration series of $M_{1-x}R_xF_{2+x}$ crystals with different RE components synthesized under the same conditions has been performed.

The data on the dependence of the defect structure of the $M_{1-x}R_xF_{2+x}$ phases on the synthesis conditions are rather scarce, unsystematic, and are obtained only for the CaF_2 phases. In [5], the influence of annealing on the symmetry of optical Gd^{3+} centers was studied by the NMR method. The structural data obtained in [6] show the stable defect structure of $Ca_{1-x}Gd_xF_{2+x}$ crystals in the temperature range from 500 to 900°C (powder neutron diffraction data). The results obtained in [6] were refuted by the study of the same crystals in [7]. In [8], it was shown that the $Ca_{0.68}Er_{0.32}F_{2.32}$ samples quenched from 1000°C and the $Ca_{0.68}Y_{0.32}F_{2.32}$ samples annealed at 700°C had different defect structures.

Earlier [1], we indicated optical inhomogeneity of as-grown $Cd_{1-x}R_xF_{2+x}$ crystals, which, in particular, reflects the appearance during cooling of thermal stresses in different parts of crystalline boules. This factor seems to be unimportant for the change of the defect structure. We decided to check the structure homogeneity of the $Cd_{1-x}R_xF_{2+x}$ phases by the X-ray diffraction method on $Cd_{0.90}Yb_{0.10}F_{2.10}$ samples obtained from various parts of one transverse cross section of a crystalline boule.

We also plan to continue our study of the influence of sample annealing on the structure of some $Cd_{1-x}R_xF_{2+x}$ crystals.

EXPERIMENTAL

The $Cd_{1-x}R_xF_{2+x}$ (R = Sm–Lu) crystals were grown from melt by the Bridgman method [1]. A $Cd_{1-x}Y_xF_{2+x}$ crystal was grown from melt in a graphite crucible placed into a C-1020 setup by the same method. The initial extra-pure grade reagent was preliminarily melted in a fluorinating atmosphere (products of Teflon pyrolysis). Crystal growth was performed in the same atmosphere at a velocity of crucible descend of 10 mm/h in a temperature gradient of about 33 K /cm. The crystal grown was first cooled at a rate of about 120 K/h for 4 h, and then the heater was switched off.

The as-grown $Cd_{1-x}R_xF_{2+x}$ (R = La–Lu) samples for diffraction experiments were cut off from the middle parts of crystalline boules. A $Cd_{1-x}Y_xF_{2+x}$ sample was cut off from the upper part of the crystal grown from the charge with 15% YF_3. The YF_3 concentration in the crystal fragment determined by atomic emission spectroscopy with inductively coupled plasma (ICP–AES) was equal to 11 ± 0.3 mol %. The content of LuF_3 in a $Cd_{1-x}Lu_xF_{2+x}$ sample determined by the same method was 11 ± 0.5 mol %. The $Cd_{1-x}R_xF_{2+x}$ (R = Lu, Y) structures were refined on the samples with $x = 0.11$ studied by ICP–AES.

Earlier, it was shown by ICP–AES on several samples [2] that the RF_3 concentration in the middle parts of the crystalline boules was close to their concentration in the charge (10 mol %). Therefore, in the refinement of the $Cd_{1-x}R_xF_{2+x}$ (R = Sm–Yb) structures of the samples not studied by the ICP–AES, the composition was assumed to be the same as in the charge containing 10% RF_3. Taking into account the close concentration of RF_3 in the crystals under study (within the accuracy of analysis), hereafter we use $Cd_{0.90}R_{0.10}F_{2.10}$ as the general composition. In the cases where chemical analysis was performed, the composition is given within an accuracy of 0.5 mol %.

To check the identity of the defect structures in different parts of a crystalline boule, we studied two $Cd_{1-x}Yb_xF_{2+x}$ samples cut from various parts of a disk with a diameter of 10 mm and a height of 3 mm. The disk is a transverse section normal to the growth axis in the middle part of the boule.

Some RE elements (Eu, Yb, Sm, and Tm indicated in the sequence of the decreasing propensity to reduction) in fluorides are in two reduction states, 2+ and 3+. The partial reduction of R^{3+} to R^{2+} may take place because of the melt's contact with the graphite crucible during crystal growth. We grew no $Cd_{0.90}Eu_{0.10}F_{2.10}$ crystals since, under the growth conditions in a graphite crucible, Eu^{3+} may be partly reduced to Eu^{2+}.

Table 1. Main characteristics of diffraction experiments on $Cd_{0.90}R_{0.10}F_{2.10}$ (R = Sm–Lu, Y) single crystals

R	Sm	Gd	Dy	Ho	Y
Diffractometer	CAD-4 Enraf Nonius				
Radiation	MoK_α, λ = 0.71069				
T, K	295				
Radius of spherical sample, μm	160(5)	170(5)	170(5)	150(5)	114(5)
Absorption coefficient, mm^{-1}	15.36	15.94	16.52	16.82	15.55
Interval of ω/2θ scanning, mm	0.80 + 0.35tan(θ)				
Maximum sinθ/λ, $Å^{-1}$		1.2		1.15	1.2
Total number of measured reflections	2390	1601	2487	1540	1448
Total number of crystallographically independent reflections	88	88	88	77	88
$R_{av}(I)$, %	1.70	2.31	2.00	1.56	3.21
Sp. gr.	$Fm3m$				
Lattice parameter, Å	5.451(5)	5.436(5)	5.429(5)	5.428(5)	5.452(5)
R	Er	Tm	Yb (sample 1)	Yb (sample 2)	Lu
Diffractometer	CAD-4 Enraf Nonius				
Radiation	MoK_α, λ = 0.71069				
T, K	295				
Radius of spherical sample, μm	156(5)	134(5)	170(5)	156(5)	142(5)
Absorption coefficient, mm^{-1}	17.13	17.44	17.76		18.60
Interval of ω/2θ scanning, mm	0.80 + 0.35tan(θ)				
Maximum sinθ/λ, $Å^{-1}$	1.2	1.1		1.2	
Total number of measured reflections	1426	1003	2391	3192	1725
Total number of crystallographically independent reflections	88	88	88	88	88
$R_{av}(I)$, %	2.31	1.85	2.86	2.26	1.86
Sp. gr.	$Fm3m$				
Lattice parameter, Å	5.426(5)	5.425(5)	5.422(5)		5.420(5)

Possible reduction of RE elements in the crystals grown was checked by taking the absorption spectra of $Cd_{0.90}Yb_{0.10}F_{2.10}$ and $Cd_{0.90}Sm_{0.10}F_{2.10}$ having the highest (after europium) propensity to reduction. The absorption spectra showed no lines corresponding to Yb^{2+} and Sm^{2+} absorption. The as-grown $Cd_{0.90}Yb_{0.10}F_{2.10}$ and $Cd_{0.90}Sm_{0.10}F_{2.10}$ crystals contain RE elements in the form R^{3+}.

The methods used in the diffraction experiments are described elsewhere [2]. The parameters of the diffraction experiment for $Cd_{1-x}R_xF_{2+x}$ (R = Sm–Lu, Y) are listed in Table 1.

REFINEMENT OF THE STRUCTURE OF AS-GROWN $Cd_{0.90}R_{0.10}F_{2.10}$ (R = Sm–Lu, Y) SINGLE CRYSTALS

Notation of fluoride-ion positions. Studying the structure of $Cd_{0.90}R_{0.10}F_{2.10}$ crystals, we had to consider the notation of fluoride-ion positions. In earlier studies of $Ca_{1-x}R_xF_{2+x}$ (R = La–Lu, Y) phases, the interstitial fluorine atoms were located in the positions 48*i* and 32*f* (sometimes, in both these positions) of the sp. gr. *Fm*3*m*. Characterizing the interstitial fluorine atoms by their displacements along the threefold axis from the basic fluorine position 8*c*, we have to consider the 32*f* position with a considerable displacement and high occupancy as an additional position. The position with smaller displacement and lower occupancy is considered as a relaxed position. The occupancy of the relaxed position in $Ca_{1-x}R_xF_{2+x}$ structure is comparable with the accuracy of the structure determination, which gives rise to some doubts about the existence of this position.

We determined three types of interstitial fluoride ions in the positions 32*f* of the sp. gr. *Fm*3*m* for all the $Cd_{1-x}R_xF_{2+x}$ phases studied in this work. The minimum and maximum displacements from these posi-

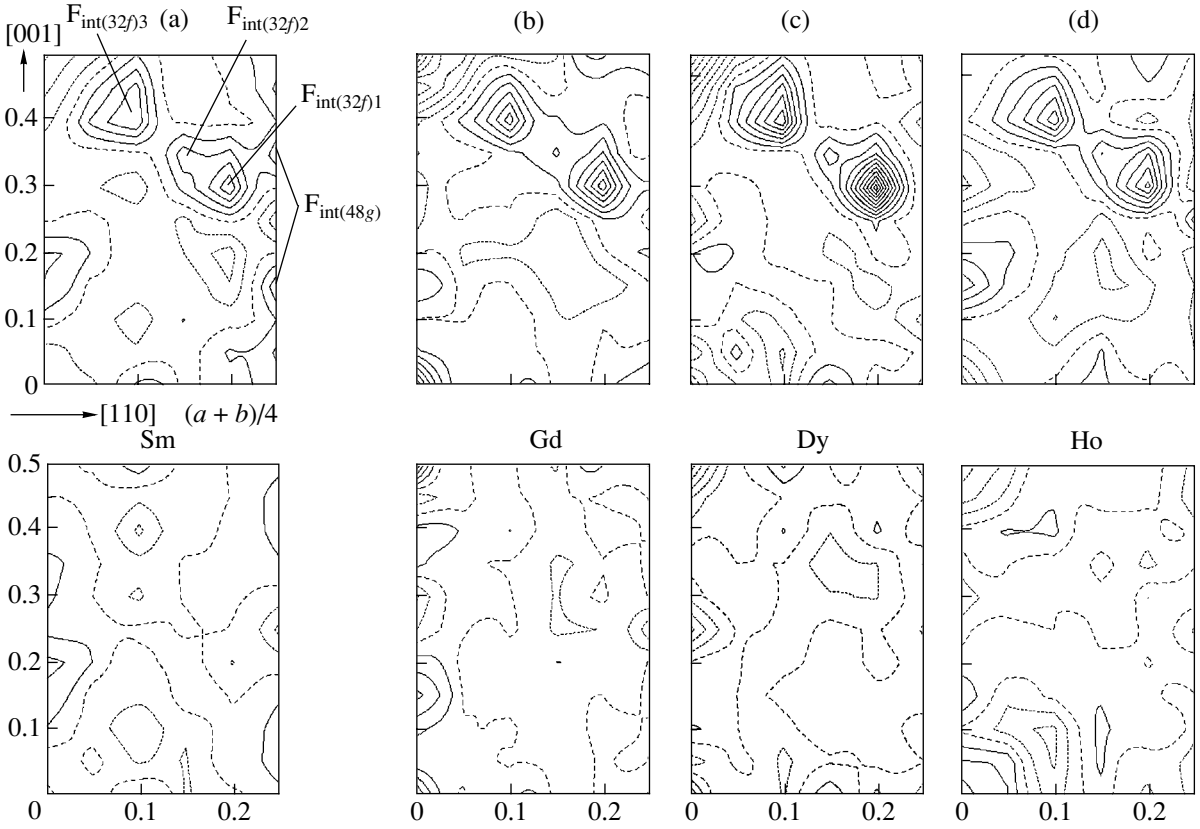

Fig. 1. The (110) difference and zeroth electron-density syntheses of $Cd_{0.90}R_{0.10}F_{2.10}$ (R = Sm–Ho) crystals. The (Cd^{2+}, R^{3+}) and $F_{(8c)}$ ions are subtracted. The isolines are spaced by 0.05 e/Å^3. Solid lines indicate positive electron density; small-scale dashed lines, negative electron density; and large-scale dashed lines, the zeroth level. The synthesis is constructed after the refinement of the occupancy with due regard for third-order anharmonicity of thermal vibrations of $F_{(8c)}$ ions and fourth-order anharmonicity of (Cd^{2+}, R^{3+}) ions.

tions approximately correspond to the displacements of fluorine atoms in the $Ca_{1-x}R_xF_{2+x}$ structure.

The $Cd_{1-x}R_xF_{2+x}$ structure also has the third 32*f* position occupied by interstitial fluorine atoms, with the displacement value being intermediate between the minimum and maximum displacements. The distribution of interstitial fluorine atoms in the position 32*f* into the additional and relaxed positions does not make sense for $Cd_{1-x}R_xF_{2+x}$ crystals. These positions do not differ qualitatively; they differ only quantitatively by their coordinates and occupancies. The electron-density syntheses of some $Cd_{1-x}R_xF_{2+x}$ crystals showed electron-density maxima in the 48*i* and 48*g* positions.

Thus, $Cd_{0.90}R_{0.10}F_{2.10}$ single crystals have five types of interstitial fluoride ions: one in the position 48*i* (*r*, *r*, 0.5), one in the position 48*g* (0.25, 0.25, *y*), and three in the position 32*f* (*w*, *w*, *w*). To make the structure description clearer, we suggested a new notation. According to this new notation, an interstitial fluoride anion is indicated as $F_{int(position)number}$, where "int" indicates that the anion is interstitial and the Wyckoff position is indicated in parentheses. If a crystal contains several F_{int} located in the same positions but with different coordinates, then the indicated position is followed by a number which indicates the corresponding position coordinate (in the sequence of its increase), i.e., the coordinate *r* for the position 48*i*, coordinate *y* for the position 48*g*, and coordinate *w* for the position 32*f*. If the position is occupied only by one type of F_{int} anion, the notation indicates only the position without its coordinates.

Then, the basic anionic position is indicated as $F_{(8c)}$, and the interstitial positions are indicated as $F_{int(32f)1}$, $F_{int(32f)2}$, $F_{int(32f)3}$, $F_{int(48i)}$, and $F_{int(48g)}$. This notation is somewhat cumbersome, but it uniquely indicates the anion position and allows one also to indicate new positions (if any) without a change of the notation. Also, this notation avoids the use of noninformative primes and terms.

Refinement of the structure of as-grown $Cd_{0.90}R_{0.10}F_{2.10}$ (R = Sm–Lu, Y) single crystals. The upper parts of Figs. 1 and 2 show the (110) sections of difference electron-density syntheses after the subtraction of (Cd, *R*) cations and the $F_{(8c)}$ fluoride ion. The

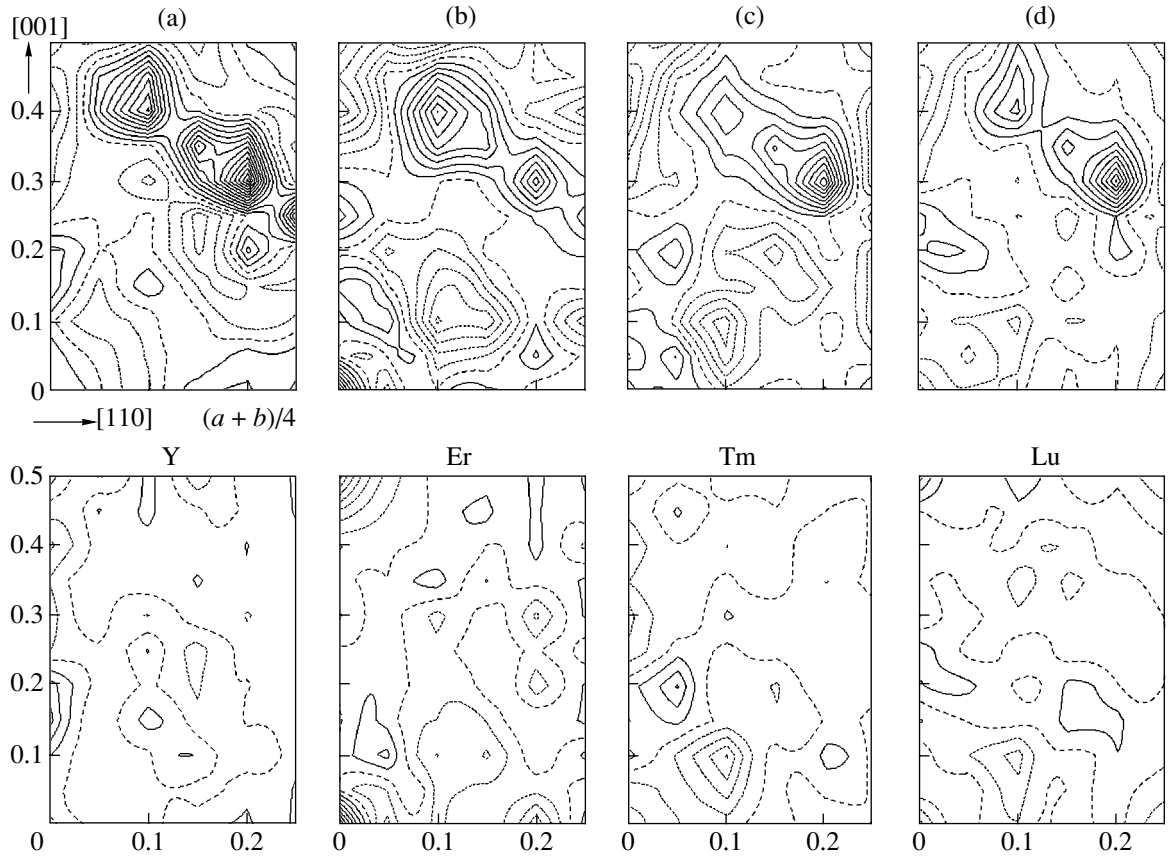

Fig. 2. The (110) difference and zeroth electron-density syntheses of $Cd_{0.90}R_{0.10}F_{2.10}$ (R = Y, Er, Tm, Lu) crystals. The isolines are spaced by 0.05 e/Å^3.

position occupancy for $F_{(8c)}$ was refined with due regard for the third-order anharmonicity of thermal vibrations. For $Cd_{0.90}R_{0.10}F_{2.10}$ (R = Sm–Ho, Y, Tm) crystals, fourth-order anharmonicity of (Cd, R) was also taken into account. The lower parts of Figs. 1 and 2 show the (110) sections of the zero electron-density synthesis.

Refinement of the $Cd_{0.90}R_{0.10}F_{2.10}$ (R = Sm–Tm, Lu, Y) structures. The difference syntheses of these crystals shown in Figs. 1a–1d and 2a–2d have three electron-density maxima corresponding to the 32*f* positions. These maxima were identified with the part of fluoride ions relaxed from the 8*c* position at the threefold axis ($F_{int(32f)1}$ and $F_{int(32f)2}$) and fluoride ions of the tetrahedral anionic grouping $F_{int(32f)3}$ [2].

The difference synthesis of a $Cd_{0.90}Sm_{0.10}F_{2.10}$ crystal shows a weak electron-density maximum in the position 48*g*, which was identified with the fluoride ion $F_{int(48g)}$ relaxed from the 8*c* position at the fourfold axis. Relaxation of the main fluoride ions along the fourfold axis in fluorite solid solutions of the composition $M_{1-x}R_xF_{2+x}$ was revealed for the first time. The difference electron-density syntheses of $Cd_{0.90}R_{0.10}F_{2.10}$ crystals with R = Er, Lu of the fourth morphotropic group are characterized by the absence of anharmonicity of thermal vibrations for cations.

Refinement of the structure of a $Cd_{0.90}Yb_{0.10}F_{2.10}$ single crystal. Figure 3 shows the (110) section of the difference (upper part) and zeroth (lower part) electron-density syntheses of samples 1 and 2 cut from a $Cd_{0.90}Yb_{0.10}F_{2.10}$ crystal.

Figure 3a shows the difference synthesis of $Cd_{0.90}Yb_{0.10}F_{2.10}$ crystals (sample 1) constructed after the refinement of the structure variant with both Cd and Yb cations being statistically located in the 4*a* (0, 0, 0) position. The synthesis contains the electron-density maximum in the position 24*e* (*x*, 0, 0), which cannot be removed by the allowance for the fourth-order anharmonicity of thermal vibrations of these cations. This maximum can indicate that Yb^{3+} cations are displaced from the 4*a* position along the fourfold axis to the 24*e* position. The difference synthesis shows only the "sole" of the Yb^{3+} cationic maximum in the position 24*e* not taken into account after the subtraction of the (Cd, R) cations in the position 4*a*. Therefore, the coordinate of the electron-density maximum in the position 24*e* on the difference synthesis does not correspond to the coordinate of the displaced Yb^{3+} ions. We refined

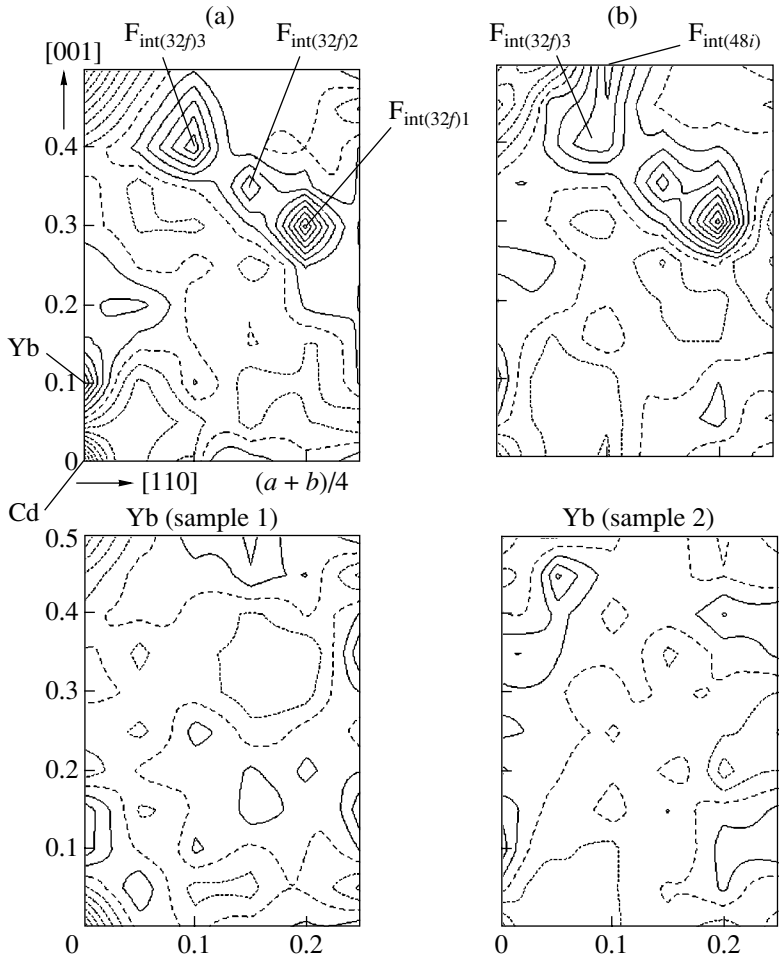

Fig. 3. The (110) section of difference and zeroth electron-density syntheses of $Cd_{0.90}Yb_{0.10}F_{2.10}$ crystals (samples 1 and 2).

the variant with all the Cd^{2+} ions being located in the 4*a* position and all the Yb^{3+} ions in the 24*e* position. This resulted in disappearance of the electron-density maximum in the 24*e* position from the difference synthesis. The subsequent refinement was performed with due regard of fluoride anions $F_{int(32f)1}$, $F_{int(32f)2}$, and $F_{int(32f)3}$ in the 32*f* position.

Figure 3b shows the difference synthesis of sample 2 cut from a $Cd_{0.90}Yb_{0.10}F_{2.10}$ crystal and constructed after the refinement of the variant with no Yb^{3+} displacement. This synthesis also shows the electron-density maximum in the 24*e* position, but it is much lower than in the analogous synthesis for sample 1. The syntheses of both samples 1 and 2 show electron-density maxima in the 32*f* position $F_{int(32f)1}$, $F_{int(32f)2}$, and $F_{int(32f)3}$.

The specific characteristic of the difference synthesis of sample 2 is an additional electron-density maximum in the 48*i* position at the twofold axis, which is denoted as $F_{int(48i)}$ in Fig. 3b. Fluoride ions in the 48*i* position indicate the formation in sample 2 of cuboctahedral anionic groupings which may form the core of octahedral cationic–anionic $[(Cd,R)_6F_{36}]$ clusters.

The difference synthesis of sample 1 cut from a $Cd_{0.90}Yb_{0.10}F_{2.10}$ crystal (Fig. 3a) indicates a larger number of Yb^{3+} cations displaced from the positions 4*a* to 24*e* than the synthesis of sample 2. Since all the F_{int} anions in sample 1 are located only in the 32*f* position, we assume that the Yb^{3+} displacement is a consequence of formation or the cause of formation of tetrahedral anionic groupings. The F_{int} anions in sample 2 occupy both 32*f* and 48*i* positions, which indicates the formation in this sample of both tetrahedral and cuboctahedral anionic groupings. The diffraction data did not allow us to perform the sufficiently reliable refinement of the occupancies of the F_{int} positions [2] and, thus, to determine the number of the tetrahedral and octahedral clusters in sample 2. Therefore, the refinement of the structure of sample 2 was performed without allowance for displacements of Yb^{3+} cations.

The total occupancy of the fluoride positions at the concluding stage of the structure refinement of the $Cd_{0.90}R_{0.10}F_{2.10}$ phases (*R* = Sm–Lu, Y) was fixed in accordance with the crystal composition at a level of 8.40 (8.44) anions per unit cell. The structure parame-

Table 2. Results of the final structural refinement of $Cd_{0.90}R_{0.10}F_{2.10}$ (R = Sm–Tm, Lu, Y) single crystals

R		Sm	Gd	Dy	Ho
x			0.10		
$(Cd_{1-x}R_x)$ (0, 0, 0)	$B_{11} \times 10^3$, Å^2	7.71(6)	7.14(2)	6.70(8)	7.53(4)
	$D_{1111} \times 10^8$, Å^2	1.6(5)	0	−1.3(5)	2.3(5)
	$D_{1122} \times 10^8$, Å^2	−0.6(2)	−0.57(9)	−0.8(2)	0
$F_{(8c)}$ (1/4, 1/4, 1/4)	Q, at./unit cell	6.88	6.73	6.74	6.53
	$B_{11} \times 10^2$, Å^2	1.19(2)	1.15(2)	1.14(2)	1.19(4)
	$C_{123} \times 10^6$, Å^2	2.2(5)	2.8(4)	2.8(4)	2.9(7)
$F_{int(48g)}$ (y, 1/4, 1/4)	Q, at./unit cell	0.31			
	y	0.17(2)			
	B_{iso}, Å^2	1.3(9)			
$F_{int(32f)1}$ (u, u, u)	Q, at./unit cell	0.39	0.75	0.85	0.90
	u	0.301(10)	0.300(7)	0.301(3)	0.300(9)
	B_{iso}, Å^2	1.5(8)	2.5(6)	1.6(2)	2.3(6)
$F_{int(32f)2}$ (v, v, v)	Q, at./unit cell	0.27	0.28	0.22	0.32
	v	0.340(14)	0.359(12)	0.349(5)	0.350(8)
	B_{iso}, Å^2	2.3(9)	2.4(9)	1.2(6)	2.8(9)
$F_{int(32f)3}$ (w, w, w)	Q, at./unit cell	0.55	0.64	0.59	0.65
	w	0.418(2)	0.418(4)	0.421(2)	0.411(6)
	B_{iso}, Å^2	1.7(3)	2.2(6)	1.6(2)	2.8(8)
Fraction of clusters $[Cd_2R_2F_{26}]$, %		9	50	29	54
Number of vacancies, vac/unit cell		0.01	0.08	0.01	0.09
Q, at./cluster	$F_{int(48g)}$	2.25	0	0	0
	$F_{int(32f)1}$	2.84	4.69	5.76	5.54
	$F_{int(32f)2}$	1.96	1.75	1.49	1.97
Number of independent structure factors		85	85	85	72
Number of parameters to be refined		19	15	16	15
R		0.24	0.32	0.23	0.29
R_w, %		0.26	0.36	0.29	0.33

R		Y	Er	Tm	Lu
x		0.11	0.10		0.11
$(Cd_{1-x}R_x)$ (0, 0, 0)	$B_{11} \times 10^8$, Å^2	9.5(2)		7.48(3)	
	$D_{1111} \times 10^8$, Å^2	9.3(6)		1.1(4)	
	$D_{1122} \times 10^4$, Å^2	2.5(5)		0	
	B_{iso}, Å^2		0.828(2)		0.864(2)
$F_{(8c)}$ (1/4, 1/4, 1/4)	Q, at./unit cell	6.34	6.53	6.58	6.11
	$B_{11} \times 10^2$, Å^2	1.67(4)	1.17(2)	1.24(3)	1.15(6)
	$C_{123} \times 10^6$, Å^2	6.0(9)	2.8(6)	3.0(6)	2.0(8)
$F_{int(48g)}$ (y, 1/4, 1/4)	Q, at./unit cell				
	y				
	B_{iso}, Å^2				
$F_{int(32f)1}$ (u, u, u)	Q, at./unit cell	0.94	0.82	0.84	1.16
	u	0.305(3)	0.299(3)	0.302(5)	0.289(8)
	B_{iso}, Å^2	1.1(2)	1.3(3)	1.7(3)	1.8(3)
$F_{int(32f)2}$ (v, v, v)	Q, at./unit cell	0.34	0.31	0.27	0.43
	v	0.343(4)	0.349(6)	0.350(8)	0.339(9)
	B_{iso}, Å^2	0.9(4)	1.6(7)	1.4(7)	2.1(7)
$F_{int(32f)3}$ (w, w, w)	Q, at./unit cell	0.82	0.74	0.71	0.74
	w	0.416(2)	0.422(3)	0.416(5)	0.419(4)
	B_{iso}, Å^2	1.8(3)	2.1(4)	2.8(6)	2.6(5)
Fraction of clusters $[Cd_2R_2F_{26}]$, %		85	84	78	62
Number of vacancies, vac/unit cell		0.18	0.16	0.13	0.12
Q, at./cluster	$F_{int(48g)}$	0	0	0	0
	$F_{int(32f)1}$	4.59	4.43	4.73	6.27
	$F_{int(32f)2}$	1.66	1.68	1.52	2.32
Number of independent structure factors		81	82	84	85
Number of parameters to be refined		15	14	15	14
R		0.36	0.33	0.31	0.31
R_w, %		0.39	0.36	0.37	0.34

Table 3. Results of the final refinement of the structure of $Cd_{0.90}Yb_{0.10}F_{2.10}$ single crystals

R		Yb (sample 1)	Yb (sample 2)
$Cd_{0.90}$ (0, 0, 0)	B_{iso}, Å^2	0.797(3)	0.850(2)
$Yb_{0.10}$ (*p*, 0, 0)	*p*	0.028	0
	B_{iso}, Å^2	1.3(1)	0.850(2)
$F_{(8c)}$ (1/4,1/4,1/4)	*Q*, at./unit cell	6.59	6.55
	$B_{11} \times 10^2$, Å^2	1.24(3)	1.20(3)
	$C_{123} \times 10^3$, Å^2	3.0(6)	2.8(6)
$F_{int(32f)1}$ (*u*, *u*, *u*)	*Q*, at./unit cell	0.65	0.69
	u	0.299(6)	0.298(6)
	B_{iso}, Å^2	1.5(5)	1.8(9)
$F_{int(32f)2}$ (*v*, *v*, *v*)	*Q*, at./unit cell	0.46	0.35
	v	0.344(11)	0.348(6)
	B_{iso}, Å^2	2.6(9)	1.5(6)
$F_{int(32f)3}$ (*w*, *w*, *w*)	*Q*, at./unit cell	0.70	0.31
	w	0.410(5)	0.409(7)
	B_{iso}, Å^2	2.6(7)	1.8(9)
$F_{int(48i)}$ (*r*, *r*, 0.5)	*Q*, at./unit cell		0.50
	r		0.400(6)
	B_{iso}, Å^2		1.7(6)
Fraction of clusters $[Cd_2R_2F_{26}]$, %		71	
Number of vacancies, vac/unit cell		0.13	0
Q, at./cluster	$F_{int(32f)1}$	3.71	
	$F_{int(32f)2}$	2.63	
Number of independent structure factors		81	85
Number of parameters to be refined		15	17
R		0.37	0.29
R_w, %		0.37	0.36

ters and reliability factors obtained after the refinement of as-grown $Cd_{0.90}R_{0.10}F_{2.10}$ (*R* = Sm–Tm, Lu, Y) crystals are listed in Table 2 those for $Cd_{0.90}Yb_{0.10}F_{2.10}$ crystals are listed in Table 3.

DISCUSSION OF RESULTS

Anionic composition of clusters. Fluoride ions in a CdF_2 crystal fully occupy the 8*c* position (anionic fluorite sublattice). During the formation of the heterovalent $Cd_{0.90}R_{0.10}F_{2.10}$ solid solution, the excessive charge of R^{3+} is compensated by the incorporation of fluoride ions (additional to the CdF_2 stoichiometry) into the fluorite structure. The total volume of large cubic voids of the structure with the center coordinates (1/2, 1/2,1/2) (which are called Goldschmidt voids) is too small for locating F^{1-} ions there. The difference syntheses of the $Cd_{0.90}R_{0.10}F_{2.10}$ phases show no electron-density maximum in the 4*b* position in the center of a cubic void. Additional F^{1-} ions in the CaF_2 structure may be located only after the rearrangement of the anionic motif of the structure.

F^{1-} ions in the CdF_2 structure form a simple cubic packing. In the $Cd_{0.90}R_{0.10}F_{2.10}$ structure, F_{int} ions may form groupings which fill the space with a higher density than the density of the main anionic motif of the fluorite structure. These may be both tetrahedral and cuboctahedral anionic groupings: the fragments of a cubic close packing.

Fluoride ions entering tetrahedral anionic groupings occupy the 32*f* position in $Cd_{0.90}R_{0.10}F_{2.10}$, whereas the fluoride ions entering cuboctahedral anionic groupings occupy the 48*i* position. Tetrahedral anionic groupings (see Fig. 3 in [2]) are formed instead of a void formed

due to removal of one fluoride ion, $F_{(8c)}$, whereas cuboctahedral anionic groupings are formed due to removal of eight $F_{(8c)}$ ions from their position (Fig. 4).

The first necessary condition for the formation of any grouping of fluoride ions in the fluorite structure is the existence of admissible F–F distances between the ions in these groupings. The second necessary condition is the formation of admissible distances with all the ions surrounding the formed groupings.

The electron density in the 48*i* position is seen only on the difference electron-density synthesis of a $Cd_{0.90}Yb_{0.10}F_{2.10}$ crystal (sample 2). The electron-density maximum has the coordinates (0.4, 0.4, 0.5). The distances between the maxima, 2.763(6) Å, are practically equal to the $F_{(8c)}$–$F_{(8c)}$ distances (2.7113(5) Å). Thus, we assume that all the interstitial anions in the 48*i* positions in the $Cd_{0.90}Yb_{0.10}F_{2.10}$ crystal (sample 2) are those from the cuboctahedral anionic groupings.

The electron density in the 32*f* position on difference electron-density syntheses is observed for all the crystals. However, since the $F_{int(32f)3}$–$F_{int(32f)3}$ distances in $Cd_{0.90}R_{0.10}F_{2.10}$ are approximately equal to the $F_{(8c)}$–$F_{(8c)}$ distance in the fluorite structure, tetrahedral anionic groupings may be formed only by fluoride ions with the maximum displacements from the main position, namely, by the $F_{int(32f)3}$ ions.

Relaxation of the anions sublattice. To avoid the inadmissibly short F–F distances with all the fluoride ions surrounding the formed grouping, the $F_{(8c)}$ ions are displaced from their positions (relax). Consider the relaxation observed in each of the $Cd_{0.90}R_{0.10}F_{2.10}$ crystals studied.

In tetrahedral anionic groupings formed in all the $Cd_{0.90}R_{0.10}F_{2.10}$ crystals, each $F_{int(32f)3}$ ion contacts six $F_{(8c)}$ anions, of which the three contacts with $F_{int(32f)3}$ are inadmissibly short. It is possible to assume that these $F_{(8c)}$ ions relax ($F_{(8c)} \longrightarrow F_{int(32f)1}$ relaxation). This relaxation provides leveling of the $F_{int(32f)3}$–$F_{int(32f)3}$ and $F_{int(32f)3}$–$F_{int(32f)1}$ distances.

However, the calculated number of $F_{int(32f)1}$ per tetrahedral anionic grouping in all the crystals is less than 6. The only exception is observed in $Cd_{0.90}Lu_{0.10}F_{2.10}$, where the number of $F_{int(32f)1}$ exceeds 6, and in $Cd_{0.90}Sm_{0.10}F_{2.10}$, where the number of $F_{int(32f)1}$ is almost twice as small as that in the remaining crystals.

In the $Cd_{0.90}Sm_{0.10}F_{2.10}$ crystal, interstitial fluorides are also located in the 48*g* position. The $F_{(8c)} \longrightarrow F_{int(48g)}$ relaxation provides leveling of the $F_{int(32f)3}$–$F_{int(32f)3}$ and $F_{int(32f)3}$–$F_{int(48g)}$ distances.

All the $Cd_{0.90}R_{0.10}F_{2.10}$ crystals contain $F_{int(32f)2}$ ions. Such relaxation provides leveling of the $F_{int(32f)3}$–$F_{(8c)}$ and $F_{int(32f)3}$–$F_{int(32f)2}$ distances. The $F_{(8c)} \longrightarrow F_{int(32f)2}$ relaxation yields inadmissibly short distances between $F_{int(32f)2}$ ions and the neighboring $F_{(8c)}$ ions. It is possible to assume that three $F_{(8c)}$ ions simultaneously relax to exclude the formation of inadmissibly short $F_{(8c)}$–$F_{int(32f)2}$ distances. This assumption is consistent with the calculated number of $F_{int(32f)2}$ per cluster ranging from 0 to 3 in $Cd_{0.90}R_{0.10}F_{2.10}$ compounds.

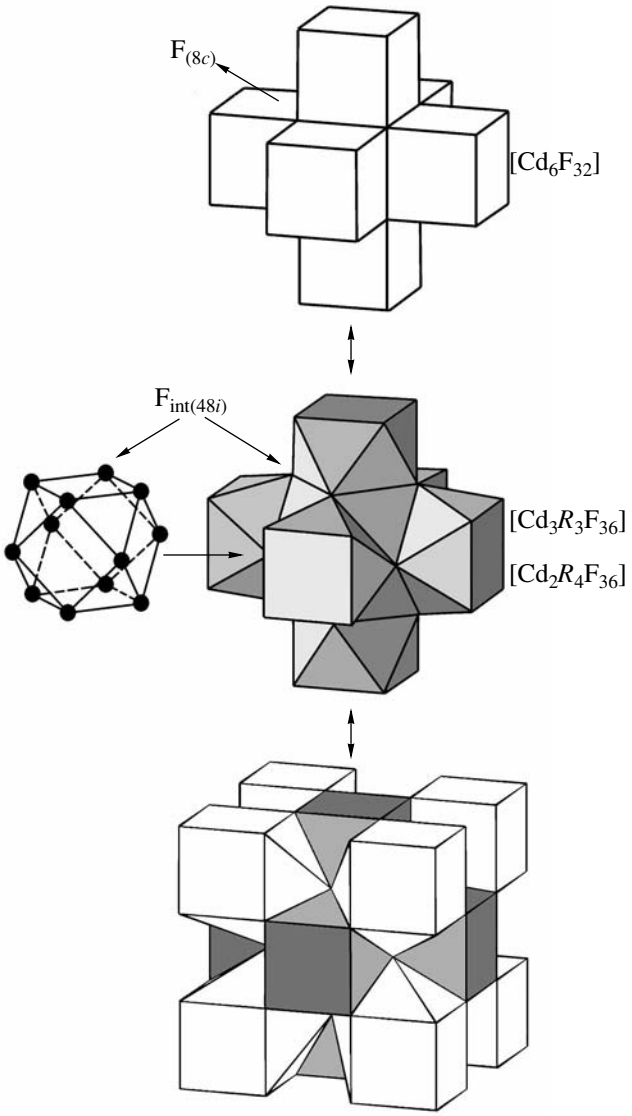

Fig. 4. Scheme of the formation of $[Cd_{6-n}R_nF_{24+12}]$ clusters (n = 3, 4) in the crystal structure of $Cd_{0.90}R_{0.10}F_{2.10}$ solid solutions.

It should be emphasized that the electron-density maximum of $F_{int(32f)2}$ on all the difference electron-density syntheses of all the crystals studied may be considered a result of anisotropy of thermal vibrations of $F_{int(32f)1}$ ions. The allowance for anisotropy for $F_{int(32f)1}$, results in disappearance of the $F_{int(32f)2}$ maximum. This may also be achieved by introducing into consideration one more $F_{int(32f)2}$ ion. To answer the question whether the electron density in the position denoted as $F_{int(32f)2}$

is caused by a fluoride ion, one has to perform the diffraction experiments at low temperatures.

Probably, the fluorine atoms surrounding a tetrahedral anionic grouping relax in different ways. It is also possible that the relaxation is caused by different cations, Cd^{2+} and R^{3+}, surrounding a tetrahedral anionic grouping. Then, it is possible to assume that RE elements in $Cd_{1-x}R_xF_{2+x}$ solid solutions may be located around either tetrahedral anionic or cuboctahedral anionic groupings, and vice versa, a tetrahedral anionic grouping (cuboctahedral anionic grouping) may be formed under the influence of RE groupings. In other words, the $Cd_{1-x}R_xF_{2+x}$ solid solutions may contain cationic–anionic clusters favorable in terms of the geometric factor.

Cationic composition of clusters. X-ray diffraction analysis does not give any information on the possible formation of RE groupings in $Cd_{0.90}R_{0.10}F_{2.10}$ crystals. However, since each R^{3+} cation contributes an excess positive charge to the fluorite structure, its interaction with an excess negative charge of the anionic groupings should result in a local charge compensation. This compensation was studied by spectroscopic methods mainly for $Ca_{1-x}R_xF_{2+x}$ crystals.

A modified model of tetrahedral clusters [9] in $Cd_{0.90}R_{0.10}F_{2.10}$ crystals was suggested in [2]. The modification concerned the cationic composition of the clusters. A tetrahedral anionic grouping introduces a local excess negative charge (–3). To compensate the excess negative charge of the anionic core, a tetrahedral cationic cluster should not contain more than three R^{3+} cations, and an octahedral cluster should not contain more than four R^{3+} cations. At a larger number of cations, the cluster would acquire a local positive charge, which would be compensated with interstitial fluorines in the positions different from $F_{int(32f)3}$ and $F_{int(48i)}$. None of the as-grown $Cd_{0.90}R_{0.10}F_{2.10}$ crystals showed the existence of such fluoride ions. The relaxed fluoride ions cannot compensate the charge difference since their existence in the structure excludes the presence of $F_{(8c)}$ in the nearest position and, thus, cannot ensure the charge compensation.

Thus, tetrahedral cationic clusters in $Cd_{0.90}R_{0.10}F_{2.10}$ crystals may contain only one or two Cd^{2+} ions. Consider the basis leading to the assumption that $[Cd_2R_2F_{26}]$ and $[CdR_3F_{26}]$ groupings are clusters of defects.

Earlier [10], we suggested inclusion into clusters of structural defects all those cations whose coordination with respect to fluorine differs from the ideal fluorite (undistorted cubic) structure. This was made for all the octahedral cationic groupings in $M_{1-x}R_xF_{2+x}$ (M = Ca, Sr, Ba). Now, apply a similar procedure to the $Cd_{0.90}R_{0.10}F_{2.10}$ crystals studied in the present work. A polyhedron of both R^{3+} and Cd^{2+} cations entering a tetrahedral cationic cluster presents itself as a cube one vertex of which is substituted by a triangle. The coordination number of each cation of such a grouping with respect to fluorine is ten. The coordination number of Cd^{2+} entering the cluster differs from the c.n. of Cd^{2+} cations of the fluorite CdF_2 matrix. In accordance with the assumption made in [10], such noncubic Cd^{2+} ions may be considered as a structural defect with respect to the fluorite matrix. The $[Cd_2R_2F_{26}]$ and $[CdR_3F_{26}]$ groupings with participation of such CdF_2 may be considered as tetrahedral cationic clusters.

The $[Cd_2R_2F_{26}]$ clusters have three sorts of $F_{(8c)}$ ions that should relax: one ion simultaneously contacting two R^{3+} cations (we consider only the cluster cations), one ion contacting two Cd^{2+} ions, and four anions contacting different cations. A $[CdR_3F_{26}]$ cluster has only two kinds of relaxing $F_{(8c)}$ anions: three anions contacting two R^{3+} cations and three anions contacting different kinds of cations.

Evolution of the defect (cluster) structure of as-grown $Cd_{0.90}R_{0.10}F_{2.10}$ phases with RE = Sm–Lu and Y. Figure 5 schematically illustrates the formation of tetrahedral cationic clusters containing two ($[Cd_2R_2F_{26}]$) or three ($[CdR_3F_{26}]$) R^{3+} cations in the $Cd_{1-x}R_xF_{2+x}$ phases with different RE elements. Small dark circles indicate $F_{(8c)}$ ions. The relaxed fluoride ions in the 32*f* position, $F_{int(32f)1}$ and $F_{int(32f)2}$, are indicated by large dark and light circles, respectively. The relaxed fluoride ions in the position 48*g*, $F_{int(48g)}$, are indicated by large hatched circles.

It is possible to assume that the $F_{(8c)}$ ions contacting only R^{3+} and the $F_{(8c)}$ ions contacting only Cd^{2+} relax in a different manner. The results obtained for the $Cd_{0.90}Tb_{0.10}F_{2.10}$ structure [2] allow us to answer the question in what way the $F_{(8c)}$ ions contacting different cations can relax. It is established that this crystal contains only relaxed $F_{int(32f)1}$ ions (about seven ions per cluster). This signifies that all six $F_{(8c)}$ ions which should relax do so in the same way. Since $Cd_{0.90}Tb_{0.10}F_{2.10}$ contains 96% of $[CdR_3F_{26}]$ not containing $F_{(8c)}$ contacting only Cd^{2+}, one may draw the conclusion that $F_{(8c)}$ ions contacting different cations relax in the same way as $F_{(8c)}$ contacting only the same R^{3+} cations.

The absence of relaxed $F_{int(32f)2}$ ions in $Cd_{0.90}Tb_{0.10}F_{2.10}$ allows us to assume that the presence of these ions depends on the number of the $[Cd_2R_2F_{26}]$ clusters formed. Since $Cd_{0.90}Tb_{0.10}F_{2.10}$ has only 4% of the $[Cd_2R_2F_{26}]$ clusters, it practically does not contain $F_{int(32f)2}$. In other words, the $F_{(8c)} \longrightarrow F_{int(32f)2}$ relaxation takes place only in the vicinity of Cd^{2+} cations entering the cluster.

Thus, the $F_{(8c)}$ ions contacting the same R^{3+} cations and the fluoride ions $F_{(8c)}$ containing different cations relax in the same way: $F_{(8c)} \longrightarrow F_{int(32f)1}$ relaxation. The

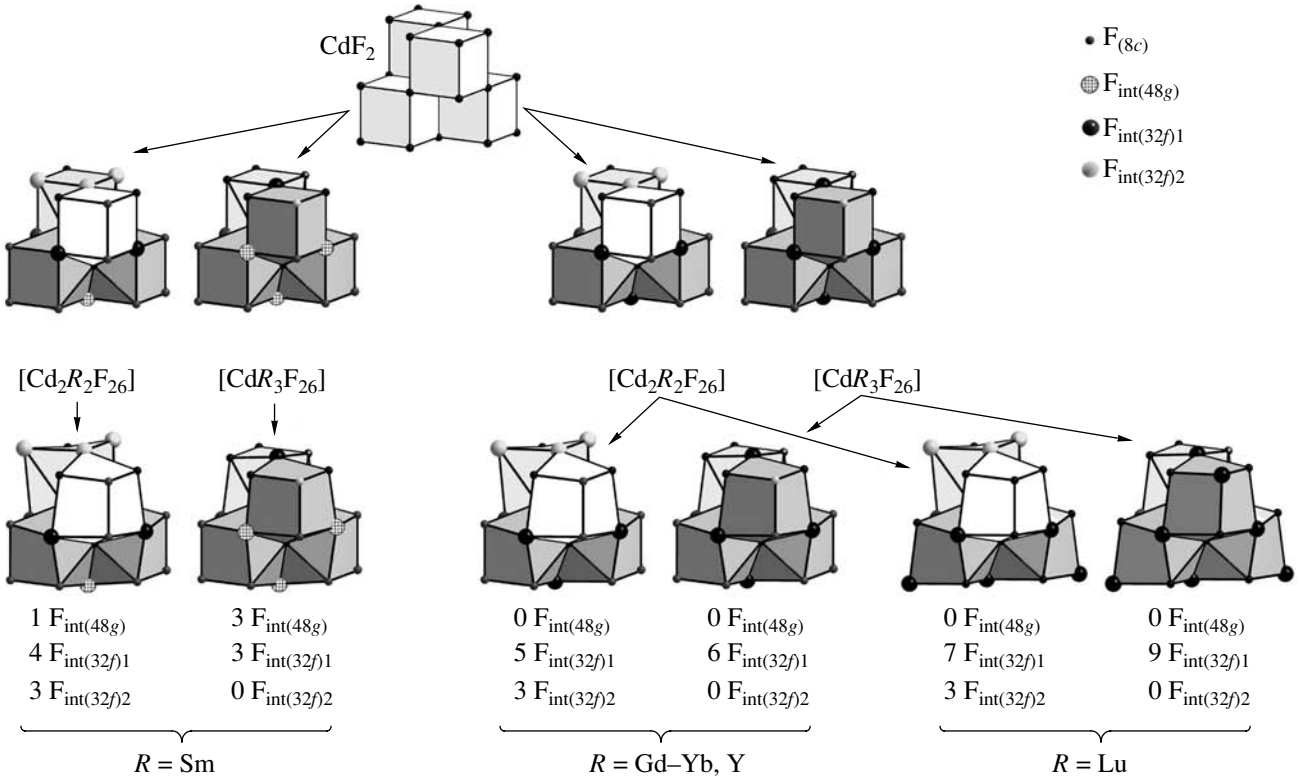

Fig. 5. Change in relaxation of the anionic sublattice of the fluorite matrix around the defect clusters in $Cd_{0.90}R_{0.10}F_{2.10}$ (R = Sm–Lu, Y) single crystals along the RE series.

fluoride ions $F_{(8c)}$ contacting the same Cd^{2+} cations, relax in different way: $F_{(8c)} \longrightarrow F_{int(32f)2}$ relaxation. Probably, $F_{(8c)}$ ions in $Cd_{0.90}Sm_{0.10}F_{2.10}$ contacting the same R^{3+} cations relax not along the threefold axis, as in all the other studied $Cd_{0.90}R_{0.10}F_{2.10}$ crystals, but along the fourfold axis to the position 48*g*.

A cluster in a $Cd_{0.90}Lu_{0.10}F_{2.10}$ crystal contains a larger number of $F_{int(32f)1}$ ions than clusters in other crystals. It is probable that the $F_{(8c)}$ ions occupying the vertices of Lu^{3+} polyhedra in this crystal also relax. This relaxation may arise because the Lu^{3+} cations tend to reduce a polyhedron's volume by decreasing the coordination number from 10 to 9 by removing one fluoride ion from a Lu^{3+} polyhedron. This leads to the assumption that the tetrahedral cationic configuration of clusters for R^{3+} ions at the end of the RE series becomes geometrically less advantageous than the octahedral one.

The structural data obtained for as-grown $Cd_{0.90}R_{0.10}F_{2.10}$ (R = Sm–Lu, Y) crystals indicate that the $[Cd_2R_2F_{26}]$ and $[CdR_3F_{26}]$ clusters may exist simultaneously. At the same time, it was noticed the ratio of the numbers of these clusters varies along the RE series. The estimation of the varying ratio of two types of cationic clusters (their cationic composition) according to the scheme suggested in [2] showed that the average content of $[Cd_2R_2F_{26}]$ clusters in $Cd_{0.90}R_{0.10}F_{2.10}$ (R = Er–Lu, *Y*) is considerably higher than in the analogous phases with R = Sm–Ho. The average content of the clusters in the transition from one RE group to another varies in a jumpwise manner. Such a character of the variation of the properties of RE-containing compounds is usually explained by the so-called effect of secondary periodicity in the RE series. We come back to this effect in defect structures of the isoconcentration series of the $Cd_{0.90}R_{0.10}F_{2.10}$ phases after the consideration of crystals with RE elements of the cerium subgroup (R = La–Nd).

Vacancies in the anionic sublattice of $Cd_{0.90}R_{0.10}F_{2.10}$ phases. If the number of cations in a tetrahedral (octahedral) cluster is less then three (four), the local negative charge of a cluster is compensated with the vacancies of the main anionic motif in the vicinity of the cluster.

The total occupancy of the positions of the basic and relaxed fluoride ions in all the crystals studied is much less than eight ions per unit cell. This signifies that the main anionic motif has some vacancies. The total number of the vacancies includes both anionic vacancies in the main fluorite motif and the voids inside clusters of tetrahedral (cuboctahedral) anionic groupings, which, strictly speaking, are not vacancies. There is one such void per each tetrahedral cluster and eight voids per

each octahedral cluster. Thus, the number of vacancies in the anionic $Cd_{1-x}R_xF_{2+x}$ sublattice is calculated as q (vacancies) = $8 - q(F_{(8c)}) - q(F_{int(32f)1}) - q(F_{int(32f)2}) - q(F_{int(48g)}) - q(F_{int(32f)3})/4 - 2/3 \times q(F_{int(48i)})$. The numbers of vacancies calculated according to such a scheme for all the $Cd_{0.90}R_{0.10}F_{2.10}$ crystals are listed in Tables 2 and 3.

The number of vacancies in the anionic sublattice of $Cd_{0.90}R_{0.10}F_{2.10}$ phases with R = Er–Lu, Y is considerably higher than for phases with R = Sm–Ho. Anionic vacancies participate in ionic transport and provide superionic conductivity with respect to fluoride ions in fluorite $Cd_{1-x}R_xF_{2+x}$ phases. Thus, one may expect that the conductivity of $Cd_{0.90}R_{0.10}F_{2.10}$ with R = Er–Lu, Y would be higher than the conductivity of the analogous phases with R = Sm–Ho. The results obtained in the study of ionic transport in $Cd_{0.90}R_{0.10}F_{2.10}$ crystals will be published later.

Variation of a defect structure within one crystalline boule. The study of two samples cut from different portions of a transverse section of the crystalline boule of an as-grown $Cd_{0.90}Yb_{0.10}F_{2.10}$ single crystal showed that they differ considerably. Sample 1 of the $Cd_{0.90}Yb_{0.10}F_{2.10}$ composition has only tetrahedral clusters, with all the Yb^{3+} ions being displaced by 0.15 Å from their positions along the fourfold axis. Sample 2 also contains octahedral clusters, with cations being practically not displaced. It is possible to assume that the Yb^{3+} ions are displaced only if they form a tetrahedral cationic cluster with large coordination numbers (10) of R^{3+} cations. A cation in such a polyhedron is not necessarily located in the center. In octahedral clusters with lower coordination numbers (8) of R^{3+} cations, no displacements of Yb^{3+} cations are observed.

The electron-density maxima in the 32*f* and 48*i* positions on the syntheses of sample 2 of $Cd_{0.90}Yb_{0.10}F_{2.10}$ cannot be uniquely interpreted as additional fluoride ions incorporated simultaneously into both positions. The point is that the maximum corresponding to the position 32*f* may also be interpreted as the overlap of the maxima due to fluoride ions in the 48*i* position.

Consider these possibilities proceeding from the obtained coordinates of F_{int} ions. The electron-density maximum in the position 48*i* of sample 2 of the composition $Cd_{0.90}Yb_{0.10}F_{2.10}$ has the coordinates (0.4, 0.4, 0.5). The three corresponding electron-density maxima with the coordinates (0.4, 0.4, 0.5), (0.4, 0.5, 0.4), and (0.5, 0.4, 0.4) are located in the plane $x + y + z - 1.3 = 0$, so that the maximum of their overlap should have the coordinates (0.433, 0.433, 0.433). It is seen from the synthesis in Fig. 3b, that the electron-density maximum of the anion $F_{int(32f)3}$ has the coordinates (0.409, 0.409, 0.409) and only the "sole" of this maximum includes the point (0.433, 0.433, 0.433). Thus, the electron density due to $F_{int(48i)}$ may only insignificantly contribute to the electron density due to $F_{int(32f)3}$. The zero synthesis (lower part of Fig. 3b) calculated with due regard for all the F_{int} ions shows the electron-density maximum in the position 32*f* with the coordinates (0.440, 0.440, 0.440), which may be interpreted as the overlap of the maxima in the 48*i* position. The above estimates lead to the assumption that sample 2 of a $Cd_{0.90}Yb_{0.10}F_{2.10}$ crystal contains additional fluoride ions simultaneously in the positions 48*i* and 32*f*. Earlier, a similar model was suggested for some crystals of the $Ca_{1-x}R_xF_{2+x}$ family.

Thus, the type of a defect structure may change even within a rather limited volume of a crystalline boule having no pronounced composition fluctuations. It is possible to assume that these structural changes are associated with insignificant noncontrollable variations of the thermal conditions in crystal growth.

The as-grown $Cd_{0.90}R_{0.10}F_{2.10}$ crystals are in a nonequilibrium state. Annealing of these crystals may result in their equilibrium state, which, in turn, may give rise to formation by RE cations of the fourth morphotropic group (R = Er–Lu, Y) of a more size-advantageous octahedral cationic configuration. The results of the study of annealed single crystals will be published later.

Comparison of the defect structure of as-grown $Cd_{0.90}R_{0.10}F_{2.10}$ fluorite phases with the structure of as-grown $Ca_{1-x}R_xF_{2+x}$ phases. Of all the fluorite crystalline MF_2 matrices underlying the formation of nonstoichiometric $M_{1-x}R_xF_{2+x}$ phases, the unit-cell parameter of the CdF_2 (a = 5.462 Å) [11] is the closest to the unit-cell parameter of CaF_2 (a = 5.393(3) Å) [2]. Therefore, it is reasonable to compare the data on the defect structures of these two families of nonstoichiometric phases: $Cd_{0.90}R_{0.10}F_{2.10}$ and $Ca_{1-x}R_xF_{2+x}$.

The as-grown $Cd_{0.90}R_{0.10}F_{2.10}$ crystals studied in this work differ from the $Ca_{1-x}R_xF_{2+x}$ crystals studied earlier by a considerably more pronounced relaxation of the anionic sublattice. In the $Ca_{1-x}R_xF_{2+x}$ phases, $F_{(8c)} \longrightarrow F_{int(32f)1}$ relaxation is rather weak, whereas $F_{(8c)} \longrightarrow F_{int(48g)}$ and $F_{(8c)} \longrightarrow F_{int(32f)2}$ relaxation does not take place at all. Probably, the more pronounced relaxation in $Cd_{1-x}R_xF_{2+x}$ crystal in comparison with relaxation in $Ca_{1-x}R_xF_{2+x}$ crystals is explained by more pronounced covalence of bonds in the former crystals.

In the first approximation, the geometric limit for formation of tetrahedral cationic clusters is determined by the ratio of the ionic radii of the matrix cations M^{2+} and an impurity component R^{3+}. The ionic radius of Cd^{2+} is practically equal to the radius of Ca^{2+} (in the system of ionic radii given in [12] for c.n. = 8, they are equal to 1.10 and 1.12 Å, respectively). In the $Ca_{1-x}R_xF_{2+x}$ crystals, an octahedral cluster is formed in the $Ca_{1-x}Dy_xF_{2+x}$ solid solution. Proceeding only from the geometric factor, we could expect the formation of an octahedral cationic cluster already in the

$Cd_{1-x}Dy_xF_{2+x}$ solid solution. The structural study of as-grown $Cd_{0.90}R_{0.10}F_{2.10}$ (R = Sm–Lu, Y) crystals shows that, although octahedral clusters were observed in the $Cd_{0.90}Yb_{0.10}F_{2.10}$ solid solution, they did not play the part of a prevalent type of defects. In an as-grown $Cd_{0.90}Lu_{0.10}F_{2.10}$ crystal with Lu^{3+} cations (following the ytterbium cation), only tetrahedral cationic groupings were observed.

CONCLUSIONS

It is shown by X-ray diffraction analysis that as-grown $Cd_{0.90}R_{0.10}F_{2.10}$ (R = Sm–Lu, Y) crystals belong to the CaF_2 structure type.

It is established that $Cd_{0.90}R_{0.10}F_{2.10}$ crystals have five types of interstitial fluoride ions (F_{int}): three in the 32*f* position (*w*, *w*, *w*), $F_{int(32f)1}$, $F_{int(32f)2}$, and $F_{int(32f)3}$, with the *w* coordinate ranging within 0.289 to 0.422; one $F_{int(48i)}$ in the position 48*i*; and one $F_{int(48g)}$ in the position 48*g*. The F_{int} ions in the position 32*f* were observed in all the crystals studied.

In a $Cd_{0.90}Sm_{0.10}F_{2.10}$ crystal, we observed for the first time in the family of fluorite $M_{1-x}R_xF_{2+x}$ phases the fluoride ions $F_{int(48g)}$ in the position 48*g*, i.e., the displacements from the position 8*c* along the fourfold symmetry axis.

In $Cd_{0.90}Yb_{0.10}F_{2.10}$ crystals, we revealed $F_{int(48i)}$ in the position 48*i* with the displacements along the twofold symmetry axis with respect to the position 8*c*.

The main grouping of the anionic defects (F_{int}) in $Cd_{0.90}R_{0.10}F_{2.10}$ (R = Sm–Lu, Y) crystals is a tetrahedral anionic grouping formed by $F_{int(32f)3}$ with the maximum displacement with respect to the main anionic position 8*c*.

In the as-grown $Cd_{0.90}Yb_{0.10}F_{2.10}$ crystals (to the end of the RE series), tetrahedral anionic groupings are formed along with cuboctahedral anionic groupings typical of the structures of most $M_{1-x}R_xF_{2+x}$ phases studied earlier.

Fluoride ions interact differently with cations. The ions from the main position $F_{(8c)}$, which form contacts with the same R^{3+} and different (Cd^{2+}, R^{3+}) cations, relax in the same way: $F_{(8c)} \longrightarrow F_{int(32f)1}$ relaxation. This relaxation levels $F_{int(32f)3}$ –$F_{int(32f)3}$ and $F_{int(32f)3}$ – $F_{int(32f)1}$ distances. The $F_{(8c)}$ ions contacting the same Cd^{2+} cations relax in different ways: $F_{(8c)} \longrightarrow F_{int(32f)2}$ relaxation leveling the $F_{int(32f)3}$–$F_{(8c)}$ and $F_{int(32f)3}$–$F_{int(32f)2}$ distances.

In a $Cd_{0.90}Lu_{0.10}F_{2.10}$ crystal, the presence of a large number of $F_{int(32f)1}$ ions is associated with relaxation of fluoride ions not contacting $F_{int(32f)3}$. This relaxation takes place because c.n. = 10 is not typical of small Lu^{3+} ions. As a result, these ions decrease the polyhedron volume by reducing the coordination number to nine. This process manifests itself in the general tendency to reduce the coordinating ability of RE ions across the series because a decrease in their size due to lanthanide contraction.

The variations in the anionic motif of the $Cd_{0.90}R_{0.10}F_{2.10}$ phases may be explained by formation of tetrahedral cationic–anionic $[CdR_3F_{26}]$ and $[Cd_2R_2F_{26}]$ clusters with tetrahedral anionic groupings playing the part of a cluster core. Both clusters may be formed in crystals simultaneously. In crystals with R = Er—Lu, Y, the $[Cd_2R_2F_{26}]$ content is much higher than in the phases with R = Sm–Ho.

In all the $Cd_{0.90}R_{0.10}F_{2.10}$ phases, the main anionic motif has vacancies in the position 8*c*. The concentration of such vacancies in the $Cd_{0.90}R_{0.10}F_{2.10}$ crystals with R = Er–Lu and Y is considerably higher than in phases with R = Sm–Ho. Anionic vacancies give rise to superionic conductivity with respect to fluoride ions.

We observed for the first time the parts of a crystalline boule of the $Cd_{0.90}Yb_{0.10}F_{2.10}$ composition having different defect structures. One part had the $Cd_{0.90}R_{0.10}F_{2.10}$ structure with tetrahedral cationic–anionic clusters but differs from such crystals by the displacement (0.15 Å) of Yb^{3+} ions to the 24*e* position along the fourfold symmetry axis. Differentiation of cations in the structure of $Cd_{0.90}R_{0.10}F_{2.10}$ solid solutions was observed in the fluorite $M_{1-x}R_xF_{2+x}$ phases for the first time. In the other type of the defect $Cd_{0.90}Yb_{0.10}F_{2.10}$ structure, the tetrahedral and octahedral cationic clusters simultaneously formed in the structure show no displacements of Yb^{3+} ions.

On the whole, the anionic sublattices of the $Cd_{0.90}R_{0.10}F_{2.10}$ (R = Sm–Lu, Y) phases are characterized by more pronounced relaxation than the $Ca_{1-x}R_xF_{2+x}$ phases. This may be explained by a considerably larger fraction of covalence in chemical bonding in CdF_2 against the background of which the processes of the formation of structural defects proceed in different ways.

ACKNOWLEDGMENTS

The authors are grateful to A.A. Artyukhov for the determination of the chemical compositions of the samples and D.N. Karimov for recording absorption spectra of $Cd_{0.90}Sm_{0.10}F_{2.10}$ and $Cd_{0.90}Yb_{0.10}F_{2.10}$ crystals.

This study was supported by the International Scientific and Technical Center, project no. 2136; the Russian Foundation for Basic Research, project no. 04-02-16241; and the Presidential Foundation of the Russian Federation for Support of Scientific Schools, projects nos. NSh 1642.2003.5 and NSh 1954.2003.2.

REFERENCES

1. I. I. Buchinskaya, E. A. Ryzhova, M. O. Marychev, and B. P. Sobolev, Kristallografiya **49** (3), 544 (2004) [Crystallogr. Rep. **49**, 500 (2004)].

2. E. A. Ryzhova, V. N. Molchanov, A. A. Artyukhov, *et al.*, Kristallografiya **49** (4), 668 (2004) [Crystallogr. Rep. **49**, 591 (2004)].
3. B. P. Sobolev, *The Rare Earth Trifluorides*, Part 1: *The High Temperature Chemistry of Rare Earth Trifluorides* (Inst. d'Estudis Catalans, Barselona, 2000).
4. B. P. Sobolev and P. P. Fedorov, Kristallografiya **18** (3), 624 (1973) [Sov. Phys. Crystallogr. **18**, 392 (1973)].
5. E. Fridman and W. Low, J. Chem. Phys. **33** (4), 1275 (1960).
6. A. K. Cheetham, B. E. F. Fender, and M. J. Cooper, J. Phys. C: Solid State Phys. **4** (18), 3107 (1971).
7. M. Hofmann, S. Hull, and G. J. McIntyre, J. Phys.: Condens. Matter **9** (4), 845 (1997).
8. J. P. Laval, A. Mikou, and B. Frit, Solid State Ionics **28–30**, 1300 (1988).
9. L. A. Muradyan, B. A. Maksimov, and V. I. Simonov, Koord. Khim. **12** (10), 1398 (1986).
10. B. P. Sobolev, A. M. Golubev, and P. Herrero, Kristallografiya **48** (1), 148 (2003) [Crystallogr. Rep. **48**, 141 (2003)].
11. B. T. M. Willis, Acta Crystallogr. **18**, 75 (1965).
12. R. D. Shannon, Acta Crystallogr., Sect. A: Cryst. Phys., Diffr., Theor. Gen. Crystallogr. **32** (5), 751 (1976).

Translated by L. Man

Crystallography Reports, Vol. 50, No. 2, 2005, pp. 217–223. Translated from Kristallografiya, Vol. 50, No. 2, 2005, pp. 249–255.

STRUCTURE OF ORGANIC COMPOUNDS

Template Synthesis and Crystal Structure of an Asymmetric Square-Planar Complex: Pyridine-2,6-Dicarbaldehyde-Bis(*S*-Methylisothiosemicarbazonato)nickel(II) Iodide

J. I. Gradinaru*, S. T. Malinovskiĭ*, M. A. Popovici*, and M. Gdaniec**

** Institute of Chemistry, Academy of Sciences of Moldova, Academiei 3, Chisinau, MD-20-28 Moldova*
e-mail: stanis@mail.md, stanis@dnt.md

*** Faculty of Chemistry, Mickiewicz University, Grunwaldzka 6, Poznan, 60-780 Poland*

Received April 4, 2003

Abstract—The asymmetric complex [Ni(H*L*)]I (where H_2L is pyridine-2,6-dicarbaldehyde-bis(*S*-methylisothiosemicarbazone)) is synthesized by the [2 + 1] template condensation of *S*-methylisothiosemicarbazide hydroiodide with pyridine-2,6-dicarbaldehyde in the presence of nickel(II) acetate. The crystal structure of the [Ni(H*L*)]I complex (where H*L* is $C_{11}H_{14}N_7S_2$) is determined using X-ray diffraction. The square-planar coordination of the nickel(II) central atom is provided by four N donor atoms of the chelating ligand, namely, one N atom of the pyridine residue and three N atoms of the isothiosemicarbazide fragments. The deprotonated isothiosemicarbazide fragment in the imino form and the neutral ammonium isothiosemicarbazide fragment differ in the degree of deprotonation, the mode of coordination to the central atom (N^1N^3 and N^2, respectively), and the conformation (*E* and *Z*, respectively). The structural features of the ammonium isothiosemicarbazide fragment are associated with the formation of zwitterions. It is established that the crystal structure of the compound under investigation contains centrosymmetric dimers. These dimers participate in the formation of the second coordination sphere N_4S of the central atom. © *2005 Pleiades Publishing, Inc.*

INTRODUCTION

Since the mid-1960s, the template synthesis, which is one of the most efficient synthetic techniques for designing polydentate systems with different topologies, geometries, and properties, has been extensively used in the preparative chemistry of Schiff's bases of isothiosemicarbazide derivatives [1–4].

S-alkylated isothiosemicarbazides (N^1H_2–N^2=C^1(S*R*)–$N^3H_2 \cdot$ HI) (S*R*-*Thsc*) have been successfully used as a diamine synton in the template synthesis for the purpose of designing polydentate ligands with a different set of donor atoms: N_2O, N_2O_2, N_3O, and N_4 [2]. Isothiosemicarbazones (i.e., the products of condensation of terminal hydrazine amino groups of *S*-alkylated isothiosemicarbazides with carbonyl compounds) are potentially tautomeric systems and can exist in the amino form (*R*)–C=N^1–N^2=C^1(S*R*)–N^3H_2 or the imino form (*R*)–C=N^1–N^2H–C^1(S*R*)=N^3H. As a rule, the isothiosemicarbazide fragment is coordinated to the central atom only through the terminal nitrogen atom (N^1 is the hydrazine nitrogen, and N^3 is the thioamide nitrogen) [5] with the formation of an *E* configuration (the S atom is in the *trans* position with respect to the azomethine bond) [6]. By varying the synthesis conditions, the stoichiometry of *S*-alkylated isothiosemicarbazides and carbonyl compounds, and their nature, it has become possible to prepare a large number of mononuclear and binuclear (homonuclear, heteronuclear), chelate [mono(isothiosemicarbazones), bis(isothiosemicarbazones)], and macrocyclic (symmetric, asymmetric) complex compounds. Salicylal, acetylacetone, nitromalondialdehyde, 1,1,3,3-tetraethoxypropane, and anthranilaldehyde have been used as carbonyl compounds in syntheses of the aforementioned complexes. Aromatic dicarbonyl compounds containing additional donor atoms or functional groups in their composition have rarely been used in the synthesis of Schiff's bases with *S*-alkylated isothiosemicarbazides. It seems likely that this series of compounds is represented only by 2,6-diacetylpyridine, 2,6-diformyl-4-methylphenol, and 3-formylsalicylic acid, which can increase the denticity of the ligands: N_5 [7, 8], N_4O [9, 10], and N_2O_4 [11].

The structural features of the compounds synthesized can also be affected by the nature of the metal. For example, 2,6-diacetylpyridine-bis(*S*-methylisothiosemicarbazone) (H_2L*) prepared by the template synthesis on 3*d* metal matrices is characterized by various coordination and structural features and different coordination modes depending on the template used [7, 8]. X-ray diffraction investigations revealed that the Schiff's base H_2L* with the Mn(II) ion behaves like the neutral pentadentate ligand N_5 due to the coordination through the pyridine nitrogen and terminal isothiosemicarbazide nitrogen atoms [7]. On the other hand, the ligand with the nickel(II) ion is monodeprotonated and

participates in the coordination through four nitrogen atoms (one pyridine and three isothiosemicarbazide nitrogen atoms) in a tetradentate coordination mode (N_4). It should be noted that one isothiosemicarbazide fragment is involved in a typical N^1 and N^3 coordination, whereas the second fragment is attached only through the N^2 atom. This mode of coordination is rather unusual and has very rarely been observed in compounds based on alkylated isothiosemicarbazides [8] (see Scheme 1).

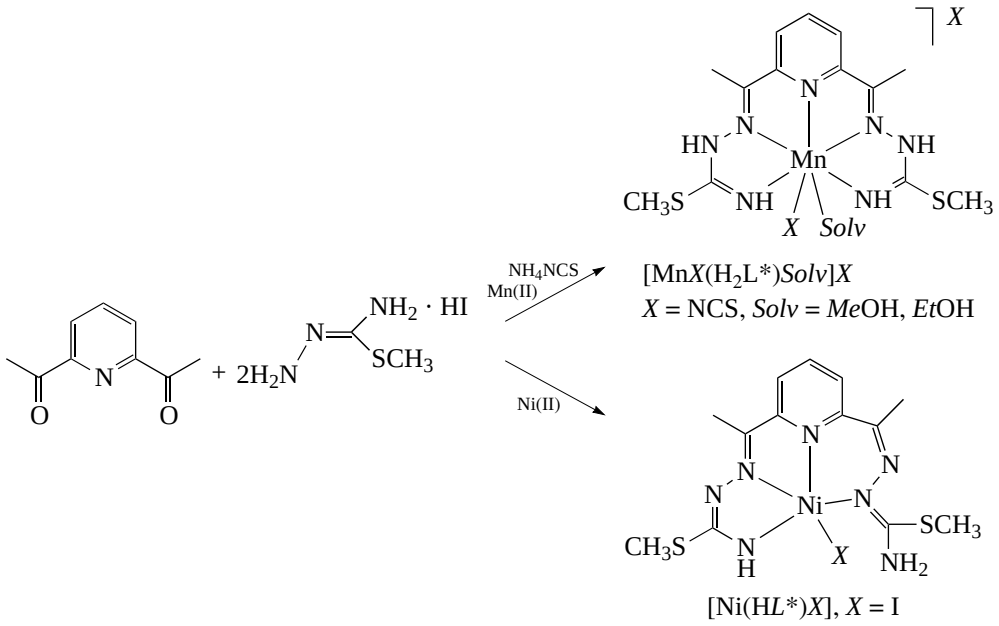

Scheme 1.

It is of interest to extend the class of aromatic functional dicarbonyl compounds used for template condensation of *S*-alkylated isothiosemicarbazides. Taking into account the higher reactivity of dialdehydes (as compared to ketones) in condensation with *S*-alkylated isothiosemicarbazides and the similarity of 2,6-diacetylpyridine to pyridine-2,6-dicarbaldehyde in both the geometry and the set of donor atoms (O, N), the latter compound seems to be promising for the use in the template synthesis on matrices containing nickel(II) ions.

The purpose of the present work is to investigate the crystal structure of pyridine-2,6-dicarbaldehyde-bis(*S*-methylisothiosemicarbazonato)nickel(II) iodide [Ni(H*L*)]I (**I**) (where H*L* is $C_{11}H_{14}N_7S_2$). This work is a continuation of systematic investigations into the template synthesis and structure analysis of 3*d* metal asymmetric coordination compounds based on alkylated isothiosemicarbazide and also into the influence of the nature of the dicarbonyl synton on the structure and conformation of the molecule as a whole.

EXPERIMENTAL

S-methylisothiosemicarbazide hydroiodide was prepared according to the procedure described earlier in [12]. The synthesis was performed with the use of commercial pyridine-2,6-dicarbaldehyde (Aldrich). Pyridine-2,6-dicarbaldehyde-bis(*S*-methylisothiosemicarbazonato)nickel(II) iodide [Ni(H*L*)]I (**I**) was synthesized according to Scheme 2.

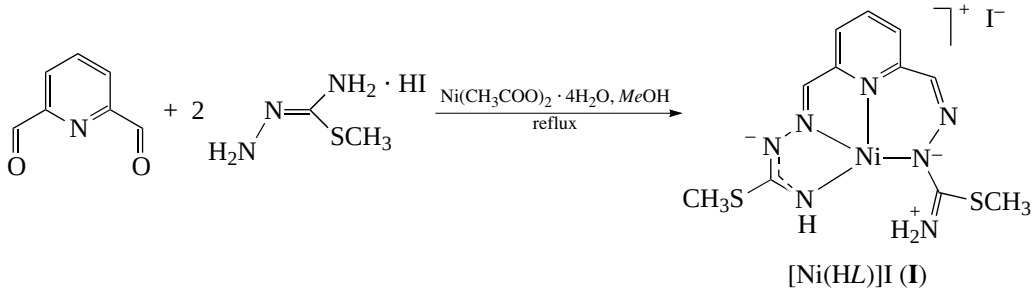

Scheme 2.

Pyridine-2,6-dicarbaldehyde (0.13 g, 1.0 mmol) was dissolved in methanol (15 ml). A solution of *S*-methylisothiosemicarbazide hydroiodide (0.47 g, 2.0 mmol) in methanol (15 ml) and a solution of $Ni(CH_3COO)_2 \cdot 4H_2O$ (0.25 g, 1.0 mmol) in methanol (20 ml) were sequentially added to the pyridine-2,6-dicarbaldehyde solution. The brown reaction mixture thus prepared was refluxed for 1 h. A finely crystalline greenish brown compound (0.19 g, 38.5%) precipitated upon cooling. Then, the compound was filtered off and washed with methanol and ether. MS *m*/*z*: 365.9 $[M\text{-I}]^+$ (I, 100%).

For $C_{11}H_{14}IN_7NiS_2$ anal. calcd. (%): C, 26.74; H, 2.88; N, 19.85; Ni, 11.88.

Found (%): C, 26.58; H, 2.97; N, 19.63; Ni, 11.64.

The experimental set of X-ray diffraction reflections was collected on a KM4CCD diffractometer (ω scan mode). The main crystal data, data collection, and refinement parameters are listed in Table 1. The structure was solved and refined with the SHELX97 program package [13]. The data on the crystal structure of compound **I** have been deposited with the Cambridge Structural Database (CCDC no. 213283).

The elemental analysis was performed by the micromethod at the Elemental Analysis Group of the Institute of Chemistry (Academy of Sciences of Moldova, Chisinau, Moldova). The electrospray ionization mass spectrum was recorded on a Finnigan LCQ mass spectrometer.

RESULTS AND DISCUSSION

The asymmetric nickel(II) complex [Ni(H*L*)]I was synthesized by the template condensation of *S*-methylisothiosemicarbazide hydroiodide with pyridine-2,6-dicarbaldehyde in the presence of nickel(II) acetate. The stoichiometric composition was determined from the data of the elemental analysis and mass spectrometry (*m*/*z* = 365.9 for $[M\text{-I}]^+$ (I, 100%), *m*/*z* = 318.1 for $[M\text{-I-SCH}_3]^+$ (I, 32%)). These results indicate that the [2 + 1] Schiff's base H_2L is successfully prepared from the initial compounds and that iodide ions are contained in the system under investigation. The diamagnetic properties of the synthesized compound and its brown color allow us to assume that complex **I** has a square-planar structure. Since 2,6-diacetylpyridine-bis(*S*-methylisothiosemicarbazone) with similar nature, geometry of donor atoms, and chemical prehistory can have different structural and coordination features, it is assumed that the newly synthesized Schiff's base H_2L can be coordinated in two modes, namely, the tetradentate mode and the pentadentate mode. In order to elucidate the specific features in the structure of the cationic complex and the formation of the crystal structure of compound **I**, we carried out X-ray diffraction analysis.

The crystal structure of compound **I** is composed of the asymmetric cationic complexes $[Ni(HL)]^+$ (where $HL^- = C_{11}H_{14}N_7S_2$) and the outer-sphere iodine anions (Fig. 1). The cationic complex contains two isothiosemicarbazide fragments. It is worth noting that the deprotonated residue is in the imino form and participates in a trivial coordination through the terminal atoms N^1 and N^3. On the other hand, the second isothiosemicarbazide residue, which can be treated as an ammonium form[1] of isothiosemicarbazide, is coordinated to the central atom in an unusual manner, namely, through the N^2 intermediate atom. It can be assumed that the ammonium modification of the isothiosemicarbazide fragment is most likely formed under the effect of the electrostatic field of the crystal lattice. The considerable contribution to the electrostatic field is made by iodide ions, which completely compensate for the charge of the $[Ni(HL)]^+$ cationic complexes. These cat-

Table 1. Crystal data, data collection, and refinement parameters for the structure of compound **I**

Compound	$C_{11}H_{14}IN_7NiS_2$
Molecular weight	612.27
Temperature, K	293(2)
Wavelength (λ)	0.71073
Crystal system, space group	Monoclinic, $P2_1/c$
a, Å	7.038(1)
b, Å	10.197(2)
c, Å	23.572(4)
β, deg	95.35(1)
V, Å^3	1684.1(6)
Z	4
ρ_{calcd}, g/cm^3	1.948
Crystal size, mm	$0.40 \times 0.10 \times 0.05$
μ, mm^{-1}	2.874
θ range, deg	3.47–26.37
Index ranges	$-8 \le h \le 6$, $-12 \le k \le 12$, $-29 \le l \le 28$
Number of reflections measured	9273
Number of unique reflections	3429 [R_{int} = 0.0998]
Number of parameter refined	211
GOOF	1.112
Final *R* factor [$I > 2\sigma(I)$]	R_1 = 0.0780, wR_2 = 0.1940
R factor for all reflections	R_1 = 0.0944, wR_2 = 0.2097

[1] The ammonium form is a modified imino form that implies the formation of N_2^-/N_3^+ zwitterions with transfer of a proton from the intermediate nitrogen atom N(2) to the terminal nitrogen atom N(3).

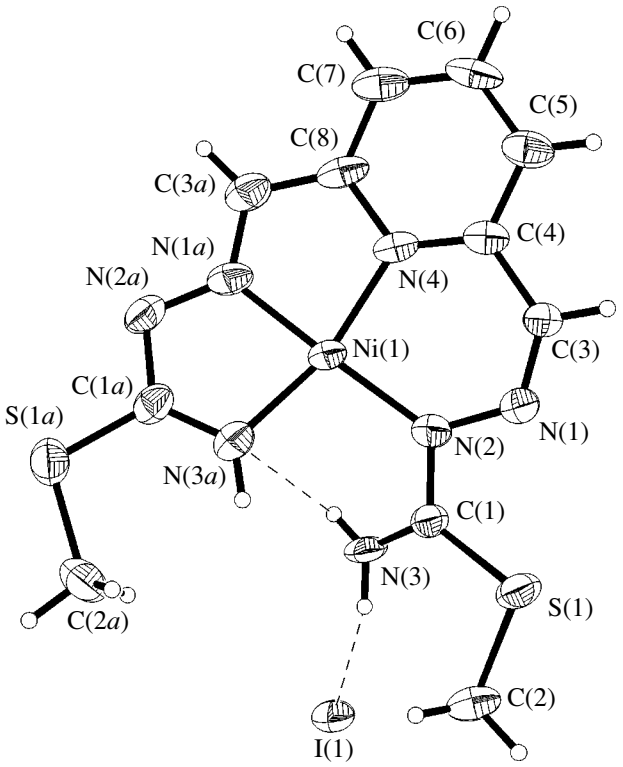

Fig. 1. Structure of the [Ni(H*L*)]I complex.

ionic complexes acquire positive charge due to the deprotonation of the N(2*a*) atom of the isothiosemicarbazide fragment in the imino form. A strong delocalization of the electron density is observed in the metallocycle of the deprotonated fragment. Therefore, it should be emphasized that the results obtained do not contradict the possible partial deprotonation of both the imino and ammonium isothiosemicarbazide fragments.

Apart from the complex [Ni(H*L**)I] (**II**) (where H*L**$^{-}$ = $C_{13}H_{18}N_7S_2$), which was described earlier by Leovac *et al.* [8], compound **I** is the second example of an unusual coordination of the ammonium form of the isothiosemicarbazide fragment to the central atom. Furthermore, apart from complexes **II** [8] and [Ni*L***$^{2-}$] (where *L***$^{2-}$ = $C_{16}H_{20}N_6OS_2$) [14], compound **I** is the third example of a new mode of coordination of the isothiosemicarbazide fragment (through the N^2 atom).

The square-planar coordination of the nickel(II) central atom is provided by three atoms, namely, the N(2), N(1*a*), and N(3*a*) atoms of two isothiosemicarbazide fragments, and the N(4) atom of the pyridine ring. The Ni(1)–N(1*a*) distance [1.839(6) Å] is somewhat shorter than the Ni(1)–N(3*a*) distance [1.874(6) Å] and agrees well with the previously revealed tendency for tetradentate bis(*S*-alkylthiosemicarbazones) according to which the bonding of the central atom to the terminal dihydrazine nitrogen atom is stronger than that to the thioamide nitrogen atom [4, 15].

The Ni(1)–N(2) bond [1.900(6) Å] in the ammonium isothiosemicarbazide fragment with the unusual coordination (through the intermediate hydrazine nitrogen atom) is the longest bond with the participation of the central atom and correlates well with the corresponding bond lengths in complexes **II** (1.893 Å) and [Ni*L***] (1.901 Å). The tendency toward an elongation of the Ni–N^2 distance is common for all three com-

Table 2. Selected interatomic distances (Å) and bond angles (deg) in the structures of compounds **I** and **II**

Atoms	**I**	**II**	Atoms	**I**	**II**
Ni(1)–N(1*a*)	1.839(6)	1.844(2)	N(2)–C(1)	1.368(9)	1.343(4)
Ni(1)–N(3*a*)	1.874(6)	1.890(3)	N(3)–C(1)	1.307(10)	1.308(4)
Ni(1)–N(4)	1.882(6)	1.879(2)	N(1*a*)–C(3*a*)	1.318(9)	1.300(4)
Ni(1)–N(2)	1.900(6)	1.893(2)	N(1*a*)–N(2*a*)	1.372(9)	1.359(4)
N(1)–C(3)	1.294(9)	1.286(4)	N(2*a*)–C(1*a*)	1.357(9)	1.339(4)
N(1)–N(2)	1.377(8)	1.379(3)	N(3*a*)–C(1*a*)	1.319(9)	1.315(4)
N(1*a*)–Ni(1)–N(3*a*)	81.2(3)	80.91(12)	N(1*a*)–Ni(1)–N(2)	174.5(3)	176.51(12)
N(1*a*)–Ni(1)–N(4)	84.5(3)	83.92(12)	N(3*a*)–Ni(1)–N(2)	101.4(3)	102.21(12)
N(3*a*)–Ni(1)–N(4)	163.5(3)	162.98(12)	N(4)–Ni(1)–N(2)	93.6(3)	93.21(12)

Table 3. System of hydrogen bonds in the structure of compound **I**

D–H	*d*(*D*–H)	*d*(H–*A*)	*DHA* angle	*d*(*D*···*A*)	*A*
N(3)–H(1)	0.749	2.388	123.3	2.868	N(3*a*)
N(3)–H(1)	0.749	2.473	149.3	3.140	N(2*a*)[#]
N(3)–H(2)	0.884	3.024	138.3	3.730	I(1)

[#] Symmetry code: $-x + 1, -y, -z + 1$.

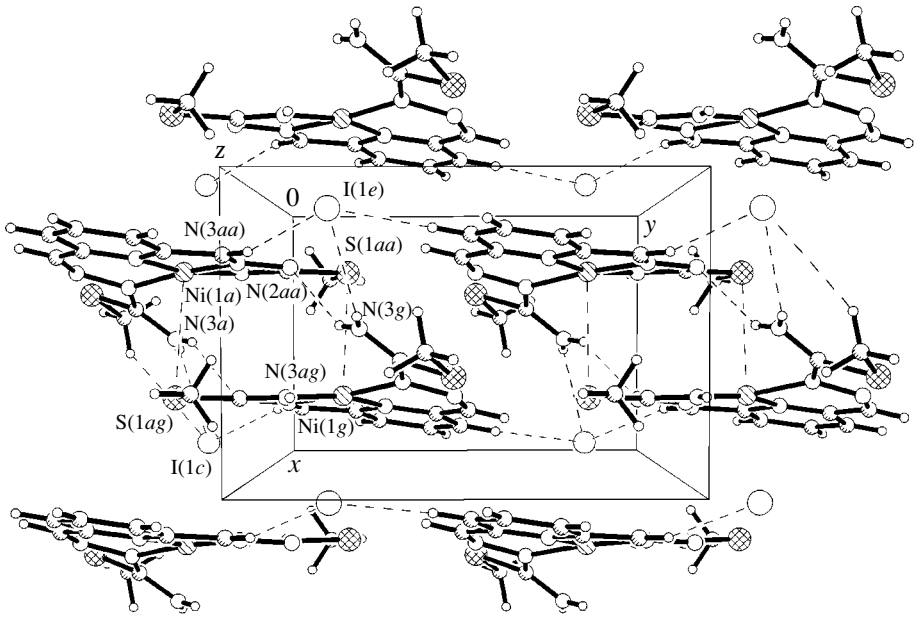

Fig. 2. A fragment of the crystal structure of the [Ni(H*L*)]I complex (projection along the [001] direction).

pounds (**I**, **II**, [Ni*L***]) and indicates that the electron-donating properties of the coordinated intermediate atom N^2 are weaker than those of the N^1 and N^3 atoms. Most probably, this can be associated with the acceptor effect exerted by the adjacent azomethine group $C^1{=}N^2$, which is not involved in the metallocycle. The nickel atom deviates by 0.022(3) Å from the root-mean-square plane formed by four nitrogen atoms. The Ni–N distances vary in the range from 1.839(6) to 1.900(6) Å. The chelate angles are equal to 81.2(3)° and 84.5(3)° in the five-membered metallocycles and 93.6(3)° in the six-membered metallocycle (Table 2).

Therefore, pyridine-2,6-dicarbaldehyde-bis(*S*-methylisothiosemicarbazone) is a monobasic tetradentate ligand N_4. The three metallocycles formed, namely, the two adjacent five-membered metallocycles NiNCCN and NiNCNN and the six-membered metallocycle NiNCCNN, have a nonplanar structure. The deviations of the atoms from the root-mean-square planes vary from –0.067(5) to 0.126(4) Å for the six-membered cycle and from –0.017(4) to 0.046(4) Å for the five-membered cycles. The dihedral angles which the plane passing through the Ni(1), N(2), N(1), C(3), and C(4) atoms makes with the plane through the Ni(1), N(4), C(8), C(3*a*), and N(1*a*) atoms and with the plane through the Ni(1), N(1*a*), N(2*a*), C(1*a*), and N(3*a*) atoms are equal to 6.8(2)° and 5.7(1)°, respectively.

The substantial difference between the structures of compound **I** and compound **II** described earlier in [8] lies in the fact that, in structure **I**, methyl substituents are absent in the 2,6 positions of the HL^- ligand and the iodide ion is not coordinated to the central atom. The latter circumstance is responsible for the difference not only in the coordination numbers of the nickel(II) central atoms in compounds **I** (the coordination number is four) and **II** (the coordination number is five) but also in the intermolecular interactions observed in these crystal structures. Note that, in the structure of compound **I**, there is a weak stabilizing intramolecular (S(6) [16]) hydrogen bond N(3)–H···N(3*a*) (2.868 Å) (Table 3). The formation of this bond makes it possible to distinguish one more pseudometallocycle. In this case, as in the [Ni*L***] complex [14], the molecule acquires a pseudomacrocyclic structure in which the 5,5,6,6-chelate metallocycles alternate with each other (Fig. 1).

The deprotonated isothiosemicarbazide fragment, which is coordinated in a bidentate mode through the terminal nitrogen atoms N(1*a*) (azomethine) and N(3*a*) (thioamide), forms a five-membered metallocycle in

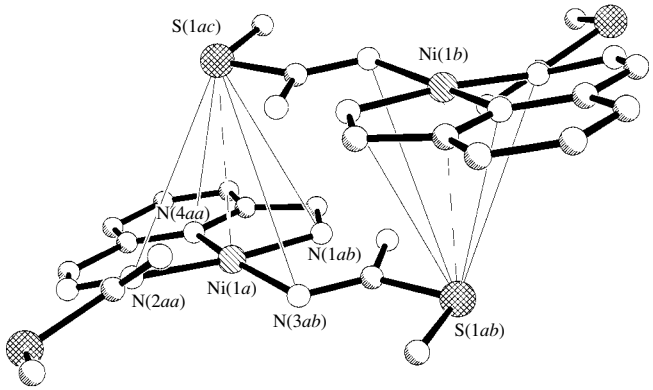

Fig. 3. Second coordination sphere of the nickel atom.

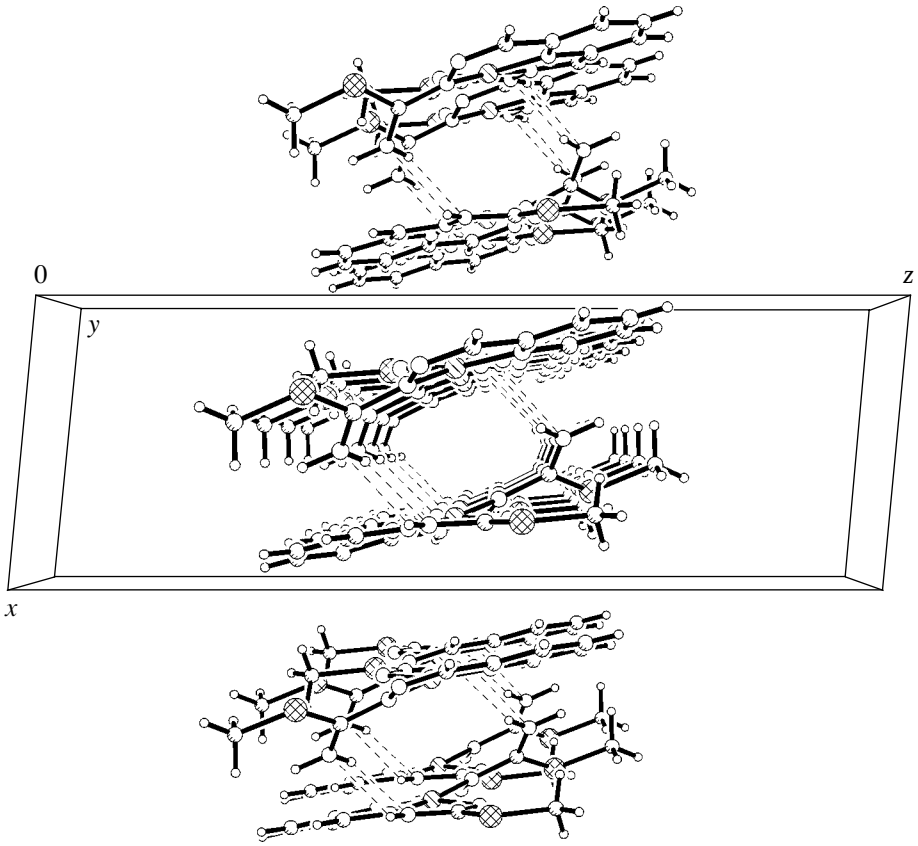

Fig. 4. A fragment of the crystal structure of the [Ni(H*L*)]I complex (projection perpendicular to the [010] direction).

the *E* configuration. The N(3*a*)–C(1*a*)–N(2*a*)–N(1*a*) torsion angle is equal to –4.1(5)°. The ammonium isothiosemicarbazide fragment is coordinated in a monodentate mode through the N(2) hydrazine nitrogen atom and resides in the *Z* configuration. The N(3)–C(1)–N(2)–N(1) torsion angle is equal to 158.7(7)°.

It should be noted that the hydrazine nitrogen atom N(2*a*) acquires electron-seeking properties owing to the participation in the formation of the intermolecular hydrogen bond N(3)–H···N(2*a*)$^{\#}$ (3.140 Å) (Table 3). In turn, these hydrogen bonds bring about the formation of centrosymmetric dimers in the crystal structure (Fig. 2). In contrast to compound **II** described in [8], the negatively charged iodine ion in compound **I** is not involved in the coordination of the central atom but forms a hydrogen bond with the N(3) atom of the anionic complex [N(3)–H···I(1), 3.730 Å]. The iodine ions are electrostatically bound to the carbon atoms of the adjacent dimers and join them together into double centrosymmetric layers that are aligned parallel to the (001) plane (Fig. 2). In the dimers, the nickel and sulfur atoms of the symmetrically related cationic complexes are also linked through a strong electrostatic interaction. This interaction is responsible for the formation of the second coordination sphere of the nickel atom in the form of a distorted square pyramid whose base contains four nitrogen atoms of the isothiosemicarbazide fragments and vertex is occupied by the sulfur atom (Fig. 3). In this case, the coordination polyhedron of the central atom can be described as N_4S, the Ni(1)–S(1)$^{\#}$ distance is equal to 3.553 Å, and the S–N$^{\#}$ distances vary from 3.605 to 4.536 Å. A fragment of the crystal structure in the projection perpendicular to the [010] direction is depicted in Fig. 4. The parameters of the hydrogen bonds formed in structure **I** are presented in Table 3.

CONCLUSIONS

Thus, the results obtained in this work demonstrated that the structure of the [Ni(H*L*)]I complex under investigation contains isothiosemicarbazide fragments of two types, namely, the deprotonated imine isothiosemicarbazide fragment and the neutral ammonium isothiosemicarbazide fragment. The potentially pentadentate ligand H_2L is coordinated in a tetradentate mode [N_4] and behaves like a monobasic Schiff's base (HL^-). The structural features of the ammonium isothiosemicarbazide fragment are associated with the formation of the N_2^-/N_3^+ zwitterions. The isothiosemicarbazide fragments differ in the degree of deprotonation, the confor-

mation, and the mode of their coordination to the central atom. The I^- anion completely compensates for the charge of the $[NiHL]^+$ cationic complex and does not participate in the coordination to the central atom. The crystal structure also contains centrosymmetric dimers. These dimers are responsible for the formation of the N_4S second coordination sphere of the central atom.

ACKNOWLEDGMENTS

We would like to thank Professor M.D. Revenko and Academician N.V. Gerbeleu for their interest expressed in discussions of the results obtained in this work and helpful remarks.

REFERENCES

1. N. V. Gerbeleu and F. K. Jovmir, Zh. Neorg. Khim. **27**, 547 (1982).
2. N. V. Gerbeleu, V. B. Arion, and J. Burges, *Template Synthesis of Macrocyclic Compounds* (Wiley–VCH, Weinheim, 1999).
3. V. Arion, M. Revenco, and J. Gradinaru, Rev. Inorg. Chem. **21**, 1 (2001).
4. J. Gradinaru, A. Forni, V. Druta, *et al.*, Inorg. Chim. Acta **338**, 169 (2002).
5. T. I. Malinovskiĭ, Yu. A. Simonov, and N. V. Gerbeleu, Probl. Kristallokhim. Nauk, No. 1, 39 (1985).
6. J. S. Casas, M. S. Garcia-Tasende, and J. Sordo, Coord. Chem. Rev. **209**, 197 (2000).
7. V. M. Leovac, E. Iverges, V. Cesljevic, *et al.*, J. Serb. Chem. Soc. **62**, 837 (1997).
8. V. M. Leovac, G. A. Bogdanovic, V. I. Cesljevic, *et al.*, Acta Crystallogr., Sect. C: Cryst. Struct. Commun. **56**, 936 (2000).
9. N. V. Gerbeleu, M. D. Revenko, F. K. Jovmir, *et al.*, Zh. Neorg. Khim. **31**, 2017 (1986).
10. F. K. Jovmir, Yu. A. Simonov, V. V. Zelentsov, *et al.*, Zh. Neorg. Khim. **33**, 2180 (1988).
11. F. K. Jovmir and N. V. Gerbeleu, Zh. Neorg. Khim. **29**, 2304 (1984).
12. E. Cattelain, Bull. Soc. Chim. **11**, 249 (1944).
13. G. M. Sheldrick, *SHELX97: Program for the Solution and Refinement of Crystal Structures* (Univ. of Göttingen, Germany, 1997).
14. J. Gradinaru, Yu. A. Simonov, V. B. Arion, *et al.*, Inorg. Chim. Acta **313**, 30 (2001).
15. A. A. Dvorkin, P. N. Bourosh, Yu. A. Simonov, *et al.*, Polyhedron **14**, 571 (1995).
16. R. Bernstein, E. Davis, L. Shimoni, and N. L. Chang, Angew. Chem. Int. Ed. Engl. **34**, 1555 (1995).

Translated by O. Borovik-Romanova

Crystallography Reports, Vol. 50, No. 2, 2005, pp. 224–229. Translated from Kristallografiya, Vol. 50, No. 2, 2005, pp. 256–261.

STRUCTURE OF ORGANIC COMPOUNDS

Synthesis and Structure of Oxovanadium(IV) Complexes [VO(*Acac*)$_2$] and [VO(*Sal* : *L*-alanine)(H$_2$O)]

E. V. Fedorova, V. B. Rybakov, V. M. Senyavin, A. V. Anisimov, and L. A. Aslanov

Moscow State University, Leninskie gory, Moscow, 119992 Russia

e-mail: anis@petrol.chem.msu.ru

Received June 24, 2003

Abstract—Bis(acetylacetonato)oxovanadium $C_{10}H_{14}O_5V$ (**I**) and (*S*)-[2-(*N*-salicylidene)aminopropionate]oxovanadium monohydrate $C_{10}H_9NO_5V$ (**II**) are synthesized. The crystal structures of compounds **I** and **II** are determined using single-crystal X-ray diffraction. Crystals of compound **I** are triclinic, $a = 7.4997(19)$ Å, $b = 8.2015(15)$ Å, $c = 11.339(3)$ Å, $\alpha = 91.37(2)°$, $\beta = 110.36(2)°$, $\gamma = 113.33(2)°$, $Z = 2$, and space group $P\bar{1}$. Crystals of compound **II** are monoclinic, $a = 8.5106(16)$ Å, $b = 7.373(2)$ Å, $c = 9.1941(16)$ Å, $\beta = 101.88(1)°$, $Z = 2$, and space group $P2_1$. The structures of compounds **I** and **II** are solved by direct methods and refined to $R_1 = 0.0382$ and 0.0386, respectively. The oxovanadium complexes synthesized are investigated by vibrational spectroscopy. © *2005 Pleiades Publishing, Inc.*

INTRODUCTION

Peroxovanadium complexes with optically active ligands are able, with a high stereoselectivity, to catalyze oxidation of organic compounds that belong to various classes [1]. Information on the crystal structure of these complexes can be used to control the oxidizing processes.

Bis(acetylacetonato)oxovanadium [VO(*Acac*)$_2$] is a good initial reactant for use in synthesizing oxovanadium complexes [2]. The replacement of an acetylacetonato ligand in this compound by bidentate and tridentate chiral ligands provides a way of producing optically active vanadium complexes, which have been extensively used in asymmetric catalysis. In this work, crystals of an optically active complex, namely, (*S*)-[2-(*N*-salicylidene)aminopropionate]oxovanadium monohydrate, were prepared for the first time. The structure of the compound synthesized was determined using X-ray diffraction analysis. Data on the structure of molecules in crystals of bis(acetylacetonato)oxovanadium $C_{10}H_{14}O_5V$ (**I**) and (*S*)-[2-(*N*-salicylidene)aminopropionate]oxovanadium monohydrate $C_{10}H_9NO_5V$ (**II**) discussed in this paper are not available in the Cambridge Structural Database (Version 11.02) [3].

EXPERIMENTAL

Synthesis of [VO(Acac)$_2$]

The oxovanadium complex [VO(*Acac*)$_2$] (**I**) was synthesized according to a modified procedure described in [4]. A mixture of V_2O_5 (20 g, 0.11 mol), distilled water (50 ml), concentrated sulfuric acid (30 ml), and ethanol (100 ml) was boiled with stirring for 30 min. The dark blue solution obtained was filtered, and freshly distilled acetylacetone (50 ml, 0.49 mol) was added to the filtrate. Then, a solution of sodium carbonate (80 g of Na_2CO_3 in 500 ml of water) in water (50 ml) was slowly added to the reaction mixture. The blue product was filtered off, washed with water, and dried in air. The yield was 50 g. Blue crystals were obtained by recrystallization from chloroform. The crystals were insoluble in water and soluble in CH_2Cl_2 and dimethyl sulfoxide. Complex **I** was formed according to Scheme 1:

$$V_2O_5 + 2H_2SO_4 + C_2H_5OH \longrightarrow 2VOSO_4 + CH_3CHO + 3H_2O,$$

$$VOSO_4 + 2C_5H_7O_2^- \longrightarrow VO(C_5H_7O_2)_2 + SO_4^{2-}.$$

Scheme 1.

Synthesis of [VO(Sal : L-alanine)(H$_2$O)]

Peroxovanadium complex **II** was synthesized according to a modified procedure described earlier by Theriot *et al.* [2]. The ligand in the complex is a bivalent tridentate Schiff's base, which was produced by the reaction of salicylal (*Sal*) with α-amino acid. *L*-alanine amino acid (0.1 mol) and sodium acetate (0.2 mol) were dissolved in distilled water (200 ml). In order to dissolve the amino acid completely, the solution was

1063-7745/05/5002-0224$26.00 © 2005 Pleiades Publishing, Inc.

Table 1. Crystal data, data collection, and refinement parameters for the structures of compounds **I** and **II**

Compound	$C_{10}H_{14}O_5V$ (**I**)	$C_{10}H_9NO_5V$ (**II**)
Molecular weight	265.15	274.12
Crystal system	Triclinic	Monoclinic
Space group	$P\bar{1}$	$P2_1$
a, Å	7.4997(19)	8.5106(16)
b, Å	8.2015(15)	7.373(2)
c, Å	11.339(3)	9.1941(16)
α, deg	91.37(2)	90
β, deg	110.36(2)	101.88(1)
γ, deg	113.33(2)	90
V, Å^3	589.7(2)	564.6(2)
Z	2	2
ρ_{calcd}, g/cm^3	1.493	1.613
$\mu(MoK_\alpha)$, cm^{-1}	0.843	0.887
Crystal size, mm	$0.3 \times 0.3 \times 0.3$	$0.3 \times 0.3 \times 0.3$
θ_{max}, deg	29.96	25.96
Number of reflections with $I \geq 2\sigma(I)$/Number of parameters	3383/158	1146/164
R_1/wR_2	0.0382/0.0942	0.0386/0.0823
$\Delta\rho_{max}/\Delta\rho_{min}$, e/Å^3	0.555/–0.330	0.359/–0.317

Table 2. Selected interatomic distances *d* (Å) in structure **I**

Bond	*d*
V(1)–O(1)	1.5859(15)
V(1)–O(21)	1.9644(13)
V(1)–O(12)	1.9665(13)
V(1)–O(22)	1.9678(14)
V(1)–O(11)	1.9727(13)
O(11)–C(11)	1.273(2)
O(12)–C(13)	1.280(2)
O(21)–C(21)	1.270(2)
O(22)–C(23)	1.274(2)

Table 3. Selected bond angles ω (deg) in structure **I**

Angle	ω
O(1)–V(1)–O(21)	105.01(7)
O(1)–V(1)–O(12)	104.75(7)
O(21)–V(1)–O(12)	150.23(6)
O(1)–V(1)–O(22)	107.16(8)
O(21)–V(1)–O(22)	87.57(6)
O(12)–V(1)–O(22)	83.90(6)
O(1)–V(1)–O(11)	107.23(8)
O(21)–V(1)–O(11)	83.94(6)
O(12)–V(1)–O(11)	87.17(6)
O(22)–V(1)–O(11)	145.61(6)
C(11)–O(11)–V(1)	128.78(11)
C(13)–O(12)–V(1)	128.10(12)
C(21)–O(21)–V(1)	128.96(11)
C(23)–O(22)–V(1)	129.13(11)

heated and filtered. A solution of salicylal(dehyde) (0.1 mol) in ethanol (250 ml) was added to the filtrate. A solution of vanadyl sulfate $VOSO_4 \cdot 2H_2O$ (0.085 mol) in water (80 ml) was slowly added to the above solution with continuous stirring. Thereafter, the solution acquired a dark brown color. In a matter of minutes, a heavy precipitate was formed. After stirring for 30 min, the substance was filtered off and washed with distilled water, 50% ethanol solution, and ethyl ether. The compound synthesized was dried in a vacuum desiccator at a temperature of 40°C. The yield of the product was approximately equal to 80% with respect to $VOSO_4 \cdot 2H_2O$. The final product was recrystallized from methanol. The blue crystals thus prepared were insoluble in water, acetone, ether, and benzene and soluble in methanol, pyridine, methylene chloride, and chloroform. The melting temperature of the crystals was estimated as $T_m \sim 250$°C.

X-ray Diffraction Analysis

The experimental intensities of diffraction reflections for the crystal structures of compounds **I** and **II** were collected on a CAD4 four-circle diffractometer

Table 4. Selected interatomic distances *d* (Å) in structure **II**

Bond	*d*
V(1)–O(5)	1.589(4)
V(1)–O(3)	1.925(4)
V(1)–O(2)	1.957(4)
V(1)–N(8)	2.021(5)
V(1)–O(4)	2.031(4)
O(1)–C(10)	1.214(7)
O(2)–C(10)	1.277(7)
O(3)–C(1)	1.323(7)

Table 5. Selected bond angles ω (deg) in structure **II**

Angle	ω
O(5)–V(1)–O(3)	107.99(19)
O(5)–V(1)–O(2)	109.20(19)
O(3)–V(1)–O(2)	142.70(19)
O(5)–V(1)–N(8)	106.3(2)
O(3)–V(1)–N(8)	87.2(2)
O(2)–V(1)–N(8)	79.85(18)
O(5)–V(1)–O(4)	108.0(2)
O(3)–V(1)–O(4)	87.48(17)
O(2)–V(1)–O(4)	83.82(17)
N(8)–V(1)–O(4)	145.22(19)
C(10)–O(2)–V(1)	119.9(3)
C(1)–O(3)–V(1)	126.0(4)
O(3)–C(1)–C(2)	119.0(6)
O(3)–C(1)–C(6)	122.7(5)
C(2)–C(1)–C(6)	118.3(5)
N(8)–C(7)–C(6)	125.4(6)
C(7)–N(8)–C(9)	120.0(5)
C(7)–N(8)–V(1)	126.0(5)
C(9)–N(8)–V(1)	113.9(3)
N(8)–C(9)–C(11)	110.2(5)
N(8)–C(9)–C(10)	107.0(4)
C(11)–C(9)–C(10)	109.3(4)
O(1)–C(10)–O(2)	123.2(5)
O(1)–C(10)–C(9)	120.5(5)
O(2)–C(10)–C(9)	116.3(5)

[5] (MoK_α radiation, graphite monochromator, ω scan mode) at room temperature. The unit cell parameters for crystals of compounds **I** and **II** were determined and refined using 25 reflections in the θ ranges 15°–16° and 15°–17°, respectively. The main crystal data, data collection, and refinement parameters for the structures of compounds **I** and **II** are summarized in Table 1.

The primary processing of the experimental data for crystals of compounds **I** and **II** was performed with the WinGX program package [6]. For both crystals, the North–Phillips–Mathews empirical correction for absorption [7] was introduced. All the subsequent calculations were carried out with the SHELX97 program package [8]. The crystal structures were determined by direct methods. The positional and thermal parameters for all the non-hydrogen atoms were refined in the anisotropic approximation. The hydrogen atoms of the methyl groups in molecules of compounds **I** and **II** and the hydrogen atoms of the phenyl ring in molecules of compound **II** were located from geometric considerations and refined as riding atoms together with the corresponding carbon atoms. In this refinement, the isotropic thermal parameters U_{iso} of the hydrogen atoms were kept greater than the equivalent isotropic thermal parameters U_{eq} of the carbon atoms bonded to the parent atoms by a factor of 1.5. The hydrogen atoms at the C(12) and C(22) atoms in molecule **I** and at the C(7) and C(9) atoms in molecule **II** were located from the electron-density difference syntheses and refined independently. The Flack parameter for compound **II** was equal to 0.14(5).

The selected interatomic distances and bond angles in the structures of compounds **I** and **II** are listed in Tables 2–5. The crystal data for both structures (CIF files) have been deposited with the Cambridge Structural Database (CCDC nos. 000000, 000001). The spatial arrangement of atoms in molecules of compounds **I** and **II** and their numbering are depicted in Figs. 1 and 2, which were drawn with the ORTEP-3 program package [9].

The IR spectra were recorded in the frequency range 400–4000 cm^{-1} on a Bruker 113v IR Fourier spectrometer with a resolution of 1–4 cm^{-1}. Samples were pressed in pellets with potassium bromide. The experimental IR spectrum of complex **I** is shown in Fig. 3.

The Raman spectra of bis(acetylacetonato)oxovanadium complex **I** were measured in the frequency range 100–4000 cm^{-1} on an Equinox 55 Fourier spectrometer with an FRA-106 (Bruker) attachment in a 180° geometry upon excitation with the 1064-nm line of an Nd–YAG laser at a power of approximately 50 mW. Attempts to record the Raman spectra of the [VO(*Acac*)$_2$] compound with the use of the 514.5- and 488.0-nm lines of an argon laser on a Coderg T-800 spectrometer were not successful because of the strong fluorescence and photodecomposition of the sample. The experimental Raman spectrum of complex **I** is depicted in Fig. 4.

RESULTS AND DISCUSSION

In the IR spectrum (Fig. 3), the intense bands observed at frequencies of 1558 (with a high-frequency shoulder) and 1377 cm^{-1} are assigned to the C–O stretching vibrations. In the latter case, judging from

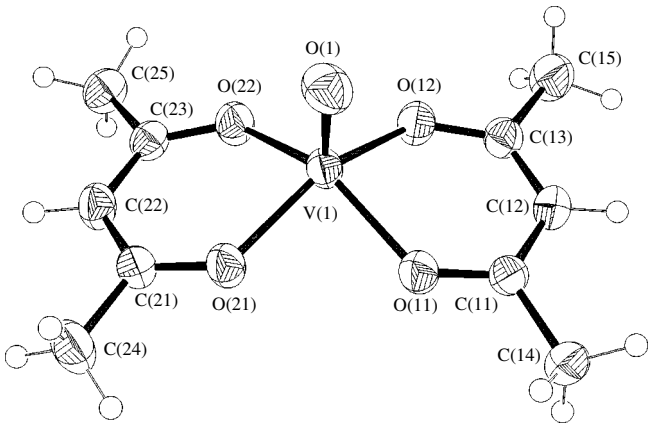

Fig. 1. Molecular structure and the atomic numbering for compound **I**. The ellipsoids of thermal vibrations are shown at the 50% probability level.

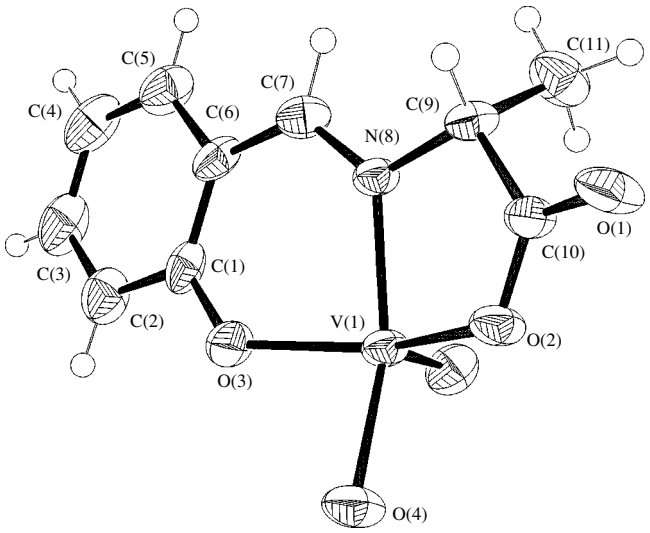

Fig. 2. Molecular structure and the atomic numbering for compound **II**. The ellipsoids of thermal vibrations are shown at the 50% probability level.

the calculated normal modes, the ν(CO) vibrations are strongly mixed with the C–C stretching vibrations, which also manifest themselves in the IR spectra at frequencies of 1535 and 1320–1270 cm^{-1}. In the ranges between 1535 and 1320–1270 cm^{-1}, the IR spectra exhibit bands associated with the bending vibrations of the CH_3 groups. In the range 1200–1000 cm^{-1}, the IR spectra contain bands attributed to the $\delta(H_3CC)$ vibrations mixed with the out-of-plane vibrations (distortions of the C–C–C angles), i.e., the vibrations associated with the deviations of the methyl groups from the planes of the ligand rings. The in-plane vibrations of the cyclic fragments manifest themselves at a frequency of 950 cm^{-1}. These vibrations involve simultaneous stretching of the C–C bonds and changes in the angles between these bonds. The vibrations of the C–C exo bonds are observed at slightly lower frequencies in the range characteristic of the ν(CC) vibrations. The frequency of the vibrations associated with the devia-

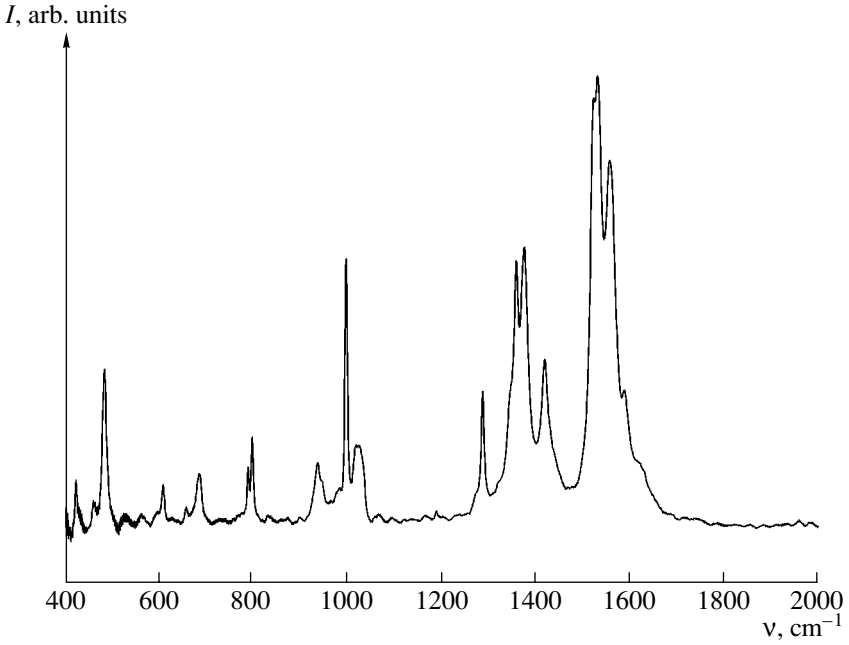

Fig. 3. IR spectrum of the [VO(*Acac*)$_2$] complex.

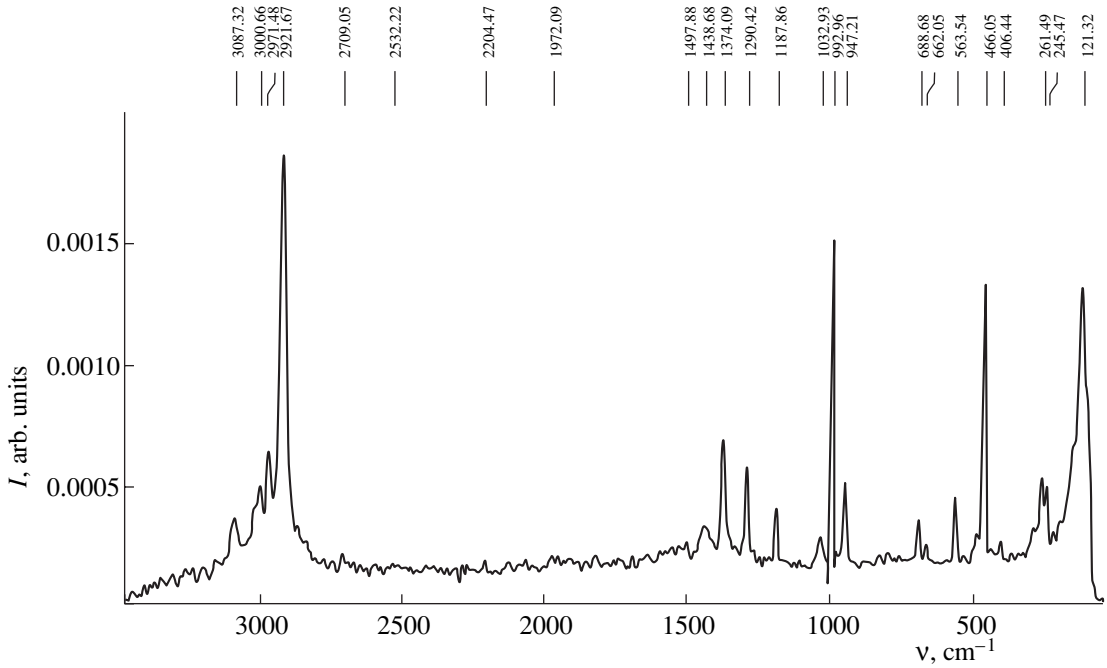

Fig. 4. Raman spectrum of the [VO(*Acac*)$_2$] complex.

tions of the C–H bonds from the ring planes is approximately equal to 800 cm^{-1}.

The Raman spectra (Fig. 4) contain an additional weak line at a frequency of 3086 cm^{-1}, which is assigned to the symmetric and antisymmetric C–H stretching vibrations. In the Raman spectrum, the most intense lines observed at frequencies of 993 and 466 cm^{-1} correspond to the stretching vibrations of the V=O bonds and the totally symmetric vibrations of the V–O bonds, respectively. The medium-intensity line at 610 cm^{-1} and an intense line at 486 cm^{-1} are associated with the two other (among the three remaining) $\nu_{as}(VO_4)$ vibrations.

In the IR spectra of complex **II**, the most intense bands correspond to the vibrations of crystallization water molecules (3450–3200 cm^{-1}) and the stretching vibrations of the V=O bonds (at 980 cm^{-1}). In the IR spectrum of this complex, the ligand vibrations are primarily responsible for the band at a frequency of 1625 cm^{-1}, which is associated with the stretching vibrations of the CH=N bonds.

The coordination polyhedron of the vanadium atom in complex **I** has the form of a tetragonal pyramid. Four oxygen atoms, namely, O(11), O(12), O(21), and O(22), which form the base of the pyramid and belong to two acetylacetonato ligands, and the O(1) oxo atom located at the vertex are coordinated to the vanadium atom (Fig. 1). The acetylacetonato ligand in this compound serves as a bidentate ligand. The V=O bond in complex **I** is nearly perpendicular to the plane formed by four oxygen atoms, namely, the O(11), O(12), O(21), and O(22) atoms of two acetylacetonato ligands. The vanadium atom slightly deviates toward the center of the polyhedron [0.5435(8) Å].

The coordination polyhedron of the vanadium atom in complex **II** is a distorted tetragonal pyramid (see Scheme 2).

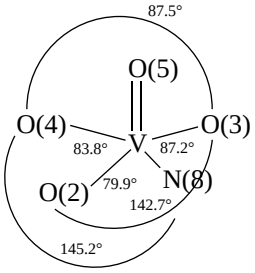

Scheme 2.

The vertex of the coordination pyramid is occupied by the O(5) oxygen atom. The base of the tetragonal pyramid is formed by two oxygen atoms, namely, O(3) and O(2), the N(8) nitrogen atom of the tridentate ligand, and the O(4) oxygen atom of the water molecule. The V(1)–O(5) bond length is equal to 1.589(4) Å, and the V(1)–O(4) bond length is 2.031(4) Å. The ligand in complex **II** is a bivalent tridentate Schiff's base.

The lengths of the V(1)–O(2) and V(1)–O(3) single bonds are almost identical and equal to 1.957(4) and 1.925(4) Å, respectively. The C(10)–O(1) bond length in the carboxyl group is 1.214(7) Å.

ACKNOWLEDGMENTS

We acknowledge the support of the Russian Foundation for Basic Research in the payment of the license for using the Cambridge Structural Database, project no. 02-07-90322.

REFERENCES

1. C. Chu, D. Hwang, S. Wang, and B. Uang, Chem. Commun. 980 (2001).
2. L. J. Theriot, G. O. Carlisle, and H. J. Hu, J. Inorg. Nucl. Chem. **31**, 2841 (1969).
3. F. H. Allen, Acta Crystallogr., Sect. B: Struct. Sci. **58**, 380 (2002).
4. *New Methods for Organic Synthesis: Practical Use of Transition Metals* (Khimiya, Moscow, 1989), p. 189 [in Russian].
5. *Enraf–Nonius CAD4 Software: Version 5.0* (Enraf–Nonius, Delft, The Netherlands, 1989).
6. L. J. Farrugia, *WinGX: X-ray Crystallographic Programs for Windows* (Univ. of Glasgow, UK, 2003).
7. A. C. T. North, D. C. Phillips, and F. S. Mathews, Acta Crystallogr., Sect. A: Cryst. Phys., Diffr., Theor. Gen. Crystallogr. **24**, 351 (1968).
8. G. M. Sheldrick, *SHELX97: Program for the Solution and Refinement of Crystal Structures* (Univ. of Göttingen, Germany, 1997).
9. L. J. Farrugia, *ORTEP-3 for Windows* (Univ. of Glasgow, UK, 2003).

Translated by O. Borovik-Romanova

Crystallography Reports, Vol. 50, No. 2, 2005, pp. 230–233. Translated from Kristallografiya, Vol. 50, No. 2, 2005, pp. 262–265.

STRUCTURE OF ORGANIC COMPOUNDS

Crystal and Molecular Structure of Barium Cyclohexane-1,2-Diamine-*N*,*N*,*N*',*N*'-Tetraacetatonickeloate Decahydrate Ba[Ni(*Cdta*)] · $10H_2O$

I. N. Polyakova*, V. S. Sergienko*, and A. L. Poznyak**

** Kurnakov Institute of General and Inorganic Chemistry, Russian Academy of Sciences, Leninskiĭ pr. 31, Moscow, 119991 Russia*

e-mail: sokol@igic.ras.ru

*** Institute of Molecular and Atomic Physics, Belarussian Academy of Sciences, pr. F. Skoriny 70, Minsk, 220072 Belarus*

Received December 22, 2003

Abstract—The X-ray diffraction study of Ba[Ni(*Cdta*)] · $10H_2O$ is performed ($R1 = 0.0441$ for 5136 observed reflections). The crystals are triclinic, $a = 8.833(2)$ Å, $b = 9.025(2)$ Å, $c = 16.922(3)$ Å, $\alpha = 80.56(3)°$, $\beta = 82.77(3)°$, $\gamma = 76.98(3)°$, $Z = 2$, and space group $P\bar{1}$. The crystal is built of the $[Ni(Cdta)]^{2-}$ anionic complexes, the $[Ba(H_2O)_6]^{2+}$ hydrated cations, and crystallization water molecules. The distorted octahedral coordination of the Ni atom includes two N and four O atoms of the $Cdta^{4-}$ ligand (mean Ni–N, Ni–O_G, and Ni–O_R are 2.080, 2.082, and 2.036 Å, respectively). The irregular nine-fold coordination of the Ba atom consists of six O atoms of water molecules and three O(*Cdta*) atoms from three anionic complexes (Ba–O, 2.715–3.090 Å). With consideration for the bonds with three Ba atoms, the $Cdta^{4-}$ ligand is octadentate (2N + 6O) and fulfills the pentadentate μ_4-bridging function. The structural units are linked through an extended network of hydrogen bonds.

INTRODUCTION

Cyclohexanediamine-*N*,*N*,*N*',*N*'-tetraacetic acid (H_4Cdta) is the nearest analogue of ethylenediaminetetraacetic acid (H_4Edta), which is a widely used and most completely studied aminocarboxylic acid. In the course of systematic structural studies of compounds of Group VIII transition metals with diamine aminocarboxylic acids, the crystal structure of Ba[Ni(*Cdta*)] · $10H_2O$ (**I**) was determined.

EXPERIMENTAL

Compound Ba[Ni(*Cdta*)] · $10H_2O$ was obtained by a reaction of NiH_2Cdta with $BaCO_3$ in an aqueous solution. Blue needle-like crystals suitable for the X-ray diffraction study were grown by slow evaporation of the solution.

Crystals $C_{14}H_{38}BaN_2NiO_{18}$ ($M = 718.51$) are triclinic, $a = 8.833(2)$ Å, $b = 9.025(2)$ Å, $c = 16.922(3)$ Å, $\alpha = 80.56(3)°$, $\beta = 82.77(3)°$, $\gamma = 76.98(3)°$, $V = 1290.9(5)$ Å^3, $Z = 2$, space group $P\bar{1}$, $d_{calcd} = 1.848$ g/cm^3, and $\mu(Mo) = 2.328$ mm^{-1}.

The set of reflections was obtained on a CAD4 automated diffractometer (λ-MoK_α ω scan mode, $2° < \theta < 28°$) from a single crystal $0.09 \times 0.12 \times 0.78$ mm in size. The structure was solved by the direct method. The H atoms were located from difference syntheses. The non-hydrogen atoms were refined in the anisotropic approximation, and the H atoms, except for five atoms of water molecules, were refined in the isotropic approximation. The H(2*w*1), H(2*w*2), H(2*w*3), H(2*w*4), and H(1*w*6) atoms were fixed in the positions found from a difference map with $U_{iso} = 0.08$ Å^2. The correction for absorption was performed by azimuthal scans [1].

The estimates of the refinement were as follows: $R1 = 0.0441$ and $wR2 = 0.1087$ for 5136 reflections with $I > 2\sigma(I)$; $R1 = 0.0519$ and $wR2 = 0.1140$ for the whole set of 5931 unique reflections; and $GOOF = 1.048$. The residual electron density on the zero map falls in the range $-3.144 < \Delta\rho < 2.216$ e Å^{-3}. All the significant peaks are located in the vicinity of the Ba or Ni atoms.

The calculations were performed with the SHELXS97 [2] and SHELXL97 [3] programs. Selected bond lengths are listed in Table 1. The crystallographic data for compound **I** have been deposited with the Cambridge Structural Database (CCDC no. 226912).

RESULTS AND DISCUSSION

The crystal structure of Ba[Ni(*Cdta*)] · $10H_2O$ is built of the $[Ni(Cdta)]^{2-}$ anionic complexes, the $[Ba(H_2O)_6]^{2+}$ hydrated cations, and crystallization water molecules.

The structure of the $[Ni(Cdta)]^{2-}$ anionic complex is shown in Fig. 1. The distorted octahedral environment of the Ni(1) atom consists of atoms N(1), N(2), O(1), O(3), O(5), and O(7) of the $Cdta^{4-}$ ligand. The hexadentate (relative to the Ni atom) $Cdta^{4-}$ ligand closes six five-membered metallocycles, namely, the Ni(1)N(1)C(9)C(10)N(2) (*E*) ethylenediamine ring and four glycine rings, two of which, Ni(1)N(1)C(1)C(2)O(1) (G_1) and Ni(1)N(2)C(5)C(6)O(5) (G_2), lie approximately in the plane of the *E* ring and two other rings, Ni(1)N(1)C(3)C(4)O(3) (R_1) and Ni(1)N(2)C(7)C(8)O(7) (R_2), are approximately perpendicular to this plane. The *R* rings are corrugated to a lesser degree than the *E* and *G* rings. The mean atomic deviations from the planes of rings *E*, G_1, G_2, R_1, and R_2 are 0.176, 0.185, 0.188, 0.074, and 0.059 Å, respectively. The $Cdta^{4-}$ ligand has an *EG*/*R* conformation [4], which is typical of the *Edta* and *Cdta* complexes: the methylene groups of the *E* and *G* rings lie on one side of the N(1)Ni(1)N(2) plane, and those of the *R* rings lie on the other side of this plane. The hexane ring C(9)–C(14) has a typical chair conformation: atoms C(10), C(11), C(13), and C(14) are coplanar within ±0.017 Å, and atoms C(9) and C(12) deviate from this plane by –0.590 and 0.708 Å, respectively.

The same structure of the $[Ni(Cdta)]^{2-}$ anionic complex was found earlier in compounds Cu[Ni(*Cdta*)] · $7H_2O$ (**II**) [5] and $Cu_3[Ni(Cdta)]_2(NO_3)_2 \cdot 15H_2O$ (**III**) [6], as well as in isostructural compounds *M*[Ni(*Cdta*)] · $6H_2O$ (M^{2+} = Mn, Ni), which are representatives of a large series whose structure was characterized by using the example of Zn[Cu(*Cdta*)] · $6H_2O$ [7].

In compound **I**, the mean Ni–N, Ni–O_G, and Ni–O_R bond lengths are 2.080, 2.082, and 2.036 Å, respectively. The differences in the Ni–O bond lengths do not correspond to the functions of the carbonyl groups. Thus, the shortest Ni–O bond is formed by the O(7)C(8)O(8) carboxyl group, which is additionally bound to two Ba atoms, and the longest bond is formed by the monodentate O(1)C(2)O(2) group. The mean lengths of coordination bonds in compound **II** are close to the corresponding values in **I** (2.082, 2.080, 2.036 Å), and the longest Ni–O bond is formed by the only bidentate carboxyl group. In compound **III**, the reverse relationship between the Ni–O bonds is observed; that is, the Ni–O_G bonds are shorter than the Ni–O_R bonds (mean, 2.039 and 2.113 Å, respectively), and the shortest Ni–O bond is formed by the only monodentate carboxyl group included in a *G* ring. Hence, the differences in the Ni–O_G and Ni–O_R bond lengths in the $[Ni(Cdta)]^{2-}$ complexes are not systematic. The same is true for the $[Ni(Edta)]^{2-}$ complexes. In distinction to the complexes with completely deprotonated ligands, acid nickel complexes are apparently characterized by the Ni–O_G > Ni–O_R relationship. In complexes $[Ni(H_2Cdta)(H_2O)] \cdot 4H_2O$ (**IV**) [8], $[Ni(H_2Edta)(H_2O)]$ (**V**) [9], $[Ni(HEdta)_2(H_2O)] \cdot 2H_2O$ (**VI**) [10], and $Li[Ni(HEdta)(H_2O)] \cdot H_2O$ (**VII**) [11], which were characterized structurally, one of the *G* arms is open and the remaining Ni–O_G bond is signifi-

Table 1. Selected bond lengths (*d*, Å) in structure **I**

Bond	*d*	Bond	*d*
Ni(1)–N(1)	2.080(3)	Ba(1)–O(3*w*)	2.820(3)
Ni(1)–N(2)	2.079(3)	Ba(1)–O(4*w*)	2.832(3)
Ni(1)–O(1)	2.091(3)	Ba(1)–O(5*w*)	2.777(3)
Ni(1)–O(3)	2.042(3)	C(2)–O(1)	1.253(5)
Ni(1)–O(5)	2.074(3)	C(2)–O(2)	1.240(5)
Ni(1)–O(7)	2.029(3)	C(4)–O(3)	1.276(5)
Ba(1)–O(6)$^{(i)}$	2.815(3)	C(4)–O(4)	1.240(5)
Ba(1)–O(8)	2.801(3)	C(6)–O(5)	1.278(4)
Ba(1)–O(8)$^{(ii)}$	2.823(3)	C(6)–O(6)	1.233(5)
Ba(1)–O(1*w*)	2.989(3)	C(8)–O(7)	1.269(4)
Ba(1)–O(1*w*)$^{(iii)}$	3.090(3)	C(8)–O(8)	1.245(4)
Ba(1)–O(2*w*)	2.715(3)		

Symmetry codes: (i) –1 + *x*, *y*, *z*; (ii) 1 – *x*, 1 – *y*, 1 – *z*; (iii) 1 – *x*, –*y*, 1 – z.

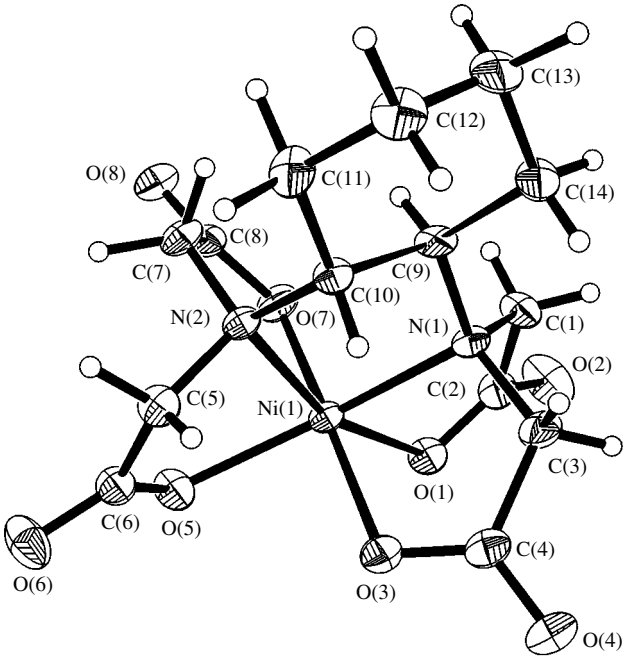

Fig. 1. Structure of the $[Ni(Cdta)]^{2-}$ anionic complex.

Table 2. Geometric characteristics of hydrogen bonds in structure **I**

X–H···*Y*	Symmetry code for atom *Y*	Distance, Å		*X*H*Y* angle, deg
		X···*Y*	H···*Y*	
O(1*w*)–H(1*w*1)···O(7)	1 –*x*, 1 – *y*, 1 – *z*	2.905(4)	2.09(6)	160(5)
O(1*w*)–H(2*w*1)*···O(8*w*)	1 – *x*, 1 – *y*, 1 – *z*	3.036(6)	2.24	151
O(2*w*)–H(1*w*2)···O(2)	*x*, –1 + *y*, *z*	2.744(5)	2.01(7)	176(8)
O(2*w*)–H(2*w*2)*···O(7*w*)	–1 + *x*, *y*, *z*	2.802(6)	1.91	156
O(3*w*)–H(1*w*3)···O(1)	*x*, –1 + *y*, *z*	2.705(4)	2.02(6)	175(7)
O(3*w*)–H(2*w*3)*···O(9*w*)	1 + *x*, –1 + *y*, *z*	2.741(5)	1.85	168
O(4*w*)–H(1*w*4)···O(3*w*)	1 – *x*, –*y*, 1 – *z*	2.782(4)	1.96(8)	164(8)
O(5*w*)–H(1*w*5)···O(6)	2 –*x*, 1 – *y*, 1 – *z*	2.773(5)	1.94(6)	168(5)
O(5*w*)–H(2*w*5)···O(9*w*)	1 – *x*, 1 – *y*, 1 – *z*	3.036(6)	2.03(10)	173(9)
O(6*w*)–H(1*w*6)*···O(4)	1 –*x*, 1 – *y*, 2 – *z*	2.797(5)	1.95	161
O(6*w*)–H(2*w*6)···O(10*w*)	1 – *x*, –*y*, 1 – *z*	2.856(7)	2.00(7)	155(6)
O(7*w*)–H(1*w*7)···O(3)	*x*, *y*, *z*	2.954(5)	2.12(7)	149(6)
O(7*w*)–H(2*w*7)···O(6*w*)	1 + *x*, *y*, *z*	2.768(6)	1.95(7)	165(7)
O(8*w*)–H(1*w*8)···O(3)	–1 +*x*, *y*, *z*	2.864(6)	1.99(10)	165(10)
O(8*w*)–H(2*w*8)···O(10*w*)	1 – *x*, 1 – *y*, 1 – *z*	2.987(7)	2.46(10)	143(10)
O(9*w*)–H(1*w*9)···O(8*w*)	*x*, *y*, *z*	2.698(7)	1.71(8)	154(7)
O(9*w*)–H(2*w*9)···O(4*w*)	*x*, 1 + *y*, *z*	2.765(5)	2.20(9)	144(10)
O(10*w*)–H(1*w*0)···O(2)	1 –*x*, 1 – *y*, 1 – *z*	2.717(6)	1.95(9)	166(9)
O(10*w*)–H(2*w*0)···O(4)	2 –*x*, 1 – *y*, 1 – *z*	2.915(6)	2.13(9)	166(8)

Note: The coordinates of the asterisked H atoms were fixed in the least-squares refinement.

cantly longer than the Ni–O_R bonds (Ni–O_G and mean Ni–O_R are 2.096 and 2.044 Å in **IV**, 2.159 and 2.035 Å in **V**, 2.128 and 2.022 Å in **VI**, 2.116 and 2.024 Å in **VII**).

In the $Cdta^{4-}$ ligand of compound **I**, the O(1)C(2)O(2) and O(3)C(4)O(4) carboxyl groups of the acetate arms bound to the N(1) atom are monodentate and form one bond each with the Ni atom. The

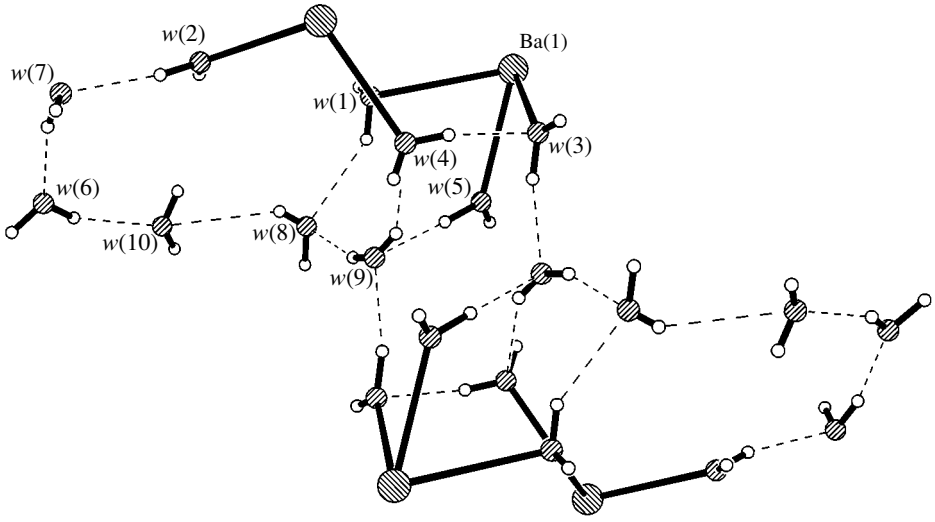

Fig. 2. A fragment of 20 water molecules included in the hydrogen-bond system.

O(5)C(6)O(6) and O(7)C(8)O(8) carboxyl groups of the acetate arms at the N(2) atom are bidentate and bound not only to the Ni atom but to one or two Ba atoms, respectively. The C–O bonds in the Ni metallocycles (1.253–1.278 Å) are, as usual, longer than the acyclic C–O bonds (1.233–1.245 Å). The coordination of the Ba atom by the O(6) and O(8) atoms does not result in the lengthening of the C(6)–O(6) and C(8)–O(8) bonds in relation to the actually terminal C(2)–O(2) and C(4)–O(4) bonds (mean, 1.239 and 1.240 Å, respectively). On the whole, with consideration for the bonds with three Ba atoms, the function of the $Cdta^{4-}$ ligand is described as an octadentate (2N + 6O) pentachelate μ_4-bridging one.

The Ba atom is surrounded by six O atoms of water molecules and three O atoms from three anionic complexes (Table 1). The *w*(1) water molecule coordinates two Ba atoms, and both Ba–O(1*w*) bonds [2.989(3) and 3.090(3) Å] are significantly longer than the remaining seven Ba–O bonds [2.715(3)–2.832(3) Å].

In structure **I**, layers of the $[Ni(Cdta)]^{2-}$ anionic complexes related by the *a* and *b* translations are distinguished. Neighboring layers that are related by the centers of inversion with the coordinate $z = 0$ are interlinked by hydrogen bonds involving the *w*(6), *w*(7), and *w*(10) crystallization water molecules. These double layers alternate along the *z* axis with the layers of hydrated Ba cations and the *w*(8) and *w*(9) crystallization water molecules. Ten independent water molecules in the structure form an extended system of hydrogen bonds, in which oxygen atoms of water molecules and the $Cdta^{4-}$ ligand serve as proton acceptors (Table 2). A remarkable fragment of the hydrogen-bond system is the centrosymmetric branched chain of twenty water molecules, which is connected by the "terminal" *w*(1), *w*(2), and *w*(5) molecules to the Ba atoms (Fig. 2). The totality of Ba–O and O–H···O hydrogen bonds links the $[Ni(Cdta)]^{2-}$ anionic complexes, $[Ba(H_2O)_6]^{2+}$ hydrated cations, and crystallization water molecules into a three-dimensional framework.

ACKNOWLEDGMENTS

We acknowledge the support of the Russian Foundation for Basic Research in the payment of the license for using the Cambridge Structural Database, project no. 02-07-90322.

REFERENCES

1. A. C. T. North, D. C. Phillips, and F. S. Mathews, Acta Crystallogr., Sect. A: Cryst. Phys., Diffr., Theor. Gen. Crystallogr. **24** (3), 351 (1968).
2. G. M. Sheldrick, *SHELXS97: Program for the Solution of Crystal Structures* (Univ. of Göttingen, Germany, 1997).
3. G. M. Sheldrick, *SHELXL97: Program for the Refinement of Crystal Structures* (Univ. of Göttingen, Germany, 1997).
4. M. A. Poraĭ-Koshits, A. I. Pozhidaev, and T. N. Polynova, Zh. Strukt. Khim. **15** (6), 1117 (1974).
5. A. Fuertes, C. Miravitlles, E. Escrivá, *et al.*, J. Chem. Soc. Dalton Trans., No. 8, 1847 (1987).
6. F. Sapiña, E. Escrivá, J. V. Folgado, *et al.*, Inorg. Chem. **31** (18), 3851 (1992).
7. A. Fuertes, C. Miravitlles, E. Molins, *et al.*, Acta Crystallogr., Sect. C: Cryst. Struct. Commun. **42** (4), 421 (1986).
8. T. V. Filippova, A. L. Poznyak, T. N. Polynova, and M. A. Poraĭ-Koshits, Koord. Khim. **22** (1), 54 (1996).
9. G. S. Smith and J. L. Hoard, J. Am. Chem. Soc. **81** (3), 556 (1959).
10. M. A. Poraĭ-Koshits, Ya. M. Nesterova, T. N. Polynova, and D. T. de Garcia Banus, Koord. Khim. **1** (5), 682 (1975).
11. T. N. Polynova, T. V. Filippova, and M. A. Poraĭ-Koshits, Koord. Khim. **12** (2), 273 (1986).

Translated by I. Polyakova

Crystallography Reports, Vol. 50, No. 2, 2005, pp. 234–253. Translated from Kristallografiya, Vol. 50, No. 2, 2005, pp. 266–286.

STRUCTURE OF ORGANIC COMPOUNDS

Structural Investigation of Model Compounds for an Acceptor Component of a New Type of Charge-Transfer Complexes Based on Viologen Analogues. Characteristic Features of the Molecular and Supramolecular Structures

L. G. Kuz'mina*, A. V. Churakov*, J. A. K. Howard, A. I. Vedernikov***, N. A. Lobova***, A. A. Botsmanova***, M. V. Alfimov***, and S. P. Gromov*****

** Kurnakov Institute of General and Inorganic Chemistry, Russian Academy of Sciences, Leninskiĭ pr. 31, Moscow, 119991 Russia*

e-mail: kuzmina@igic.ras.ru

*** Department of Chemistry, University of Durham, South Road, Durham DH1 3LE, UK*

**** Center of Photochemistry, Russian Academy of Sciences, ul. Novatorov 7a, Moscow, 119421 Russia*

Received January 10, 2004

Abstract—The crystal and molecular structures of six perchlorates (viologen analogues) are studied. These compounds serve as models of the acceptor component of new charge-transfer complexes containing bis(18-crown-6)stilbene as the donor. The polycyclic aromatic system of divalent cations is demonstrated to be virtually planar. In all cations, the side chains at the nitrogen atoms are oriented in opposite directions almost perpendicular to the plane of the cyclic system. This orientation of the spacers of these carbocations is indicative of their preorganization for the formation of 1 : 2 charge-transfer complexes. Analysis of the crystal packings provides evidence that two positive charges on the conjugated systems of the organic cations and the perchlorate anions play a destructive role in the formation of stacking motifs. An increase in the size of the conjugated system and the involvement of an aromatic solvent molecule as an additional building block in a supramolecular system are favorable for the formation of a stacking supramolecular architecture. © *2005 Pleiades Publishing, Inc.*

INTRODUCTION

New supramolecular systems based on bis(18-crown-6)stilbene and viologen analogues bearing two alkylammonium spacers have recently been investigated [1, 2]. These systems form brightly colored charge-transfer complexes (CTCs), contain a donor and an acceptor in a ratio of 1 : 1 or 2 : 1, and have the following compositions:

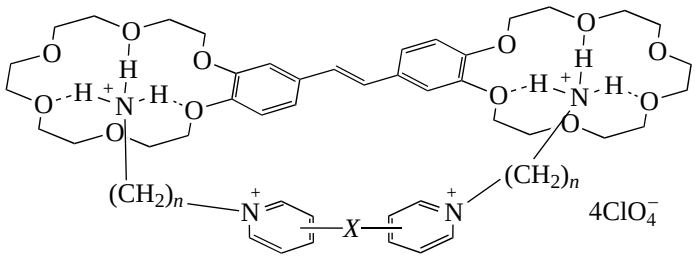

–*X*– = –CH=CH–, –CH_2CH_2–; *n* = 2, 3

1063-7745/05/5002-0234$26.00 © 2005 Pleiades Publishing, Inc.

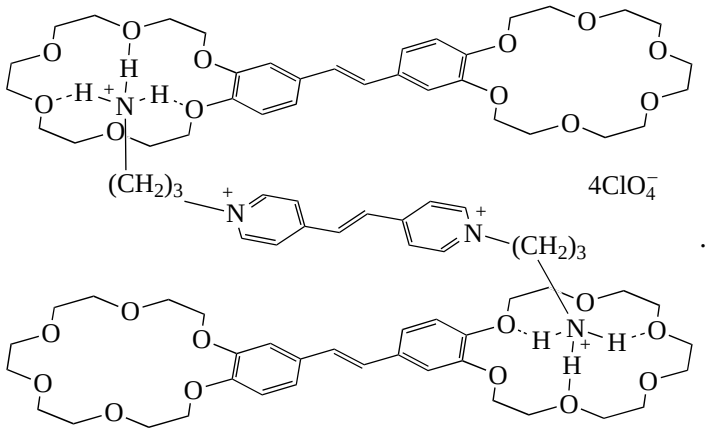

These CTCs are of interest as prospective photosensitive sensors. They respond to the presence of metal cations (which displace the ammonium groups from the crown ether fragments) in a solution by a change in the color and fluorescence emission. The formation of CTCs in acetonitrile solutions of such systems was studied by spectrophotometry, electrochemical methods, and ^{1}H-NMR and Raman spectroscopy [1–4]. The guest–host component (N–H···O hydrogen bonds) was found to make the major contribution to the stabilization of CTCs. The stacking and/or donor-acceptor components of interaction have an insignificant effect, which depends on the type of the bridging group between the pyridine fragments of the acceptor component of an CTC. This result may be due to the following: (1) the rings in the donor and/or acceptor components are noncoplanar; (2) in a supramolecular system of CTCs, the parallel offset mutual arrangement (which is typical of stacking interactions [5]) of the π-conjugated systems of the donor and acceptor is sterically hindered due to the presence of overly long or insufficiently flexible side chains (spacers); and (3) perchlorate anions present in the supramolecular system of CTCs are inserted between the donor and acceptor, thus exerting destructive effect on the stacking interactions and weakening donor–acceptor interactions.

However, π··π interactions (stacking and donor–acceptor components) are of importance, because only these interactions can hold the CTC components in the immediate vicinity of each other in the absence of terminal ammonium groups in viologen analogues. If CTCs contain smaller crown ether macrocycles, some metal cations can be coordinated simultaneously by two crown ether rings to form sandwich structures, which could give rise to more complicated structures of supramolecular systems characterized by a rather extended stacked architecture. This fact is of importance in studying the prospects of using such CTCs as photoconducting materials, because it is known that the conductivity of organic CTCs depends on the presence of stacks [6].

Our preliminary investigation of the stability of CTCs of model acceptor compounds **1**–**6**, which contain no ammonium groups in the side chains, with bis(18-crown-6)stilbene by ^{1}H-NMR spectroscopy demonstrated that the stability of the complexes in acetonitrile solutions increases in the series **3** < **2** < **4** < **1** < **5** ~ **6**. It should be noted that extended and conjugated acceptors show a certain tendency to form more stable supramolecular structures. Hence, it was of interest to study the crystal structures and the characteristic features of the supramolecular architecture of (1) model compounds for the acceptor components of these CTCs and (2) crown-containing stilbenes containing macroheterocycles of different sizes. In particular, it was of importance to study the degree of flattening of these macrocycles and electron density delocalization over the bonds in the chromophore fragments, examine the possibility of stack formation, and investigate the possible effect of perchlorate anions on the formation of a supramolecular structure by positively charged acceptor components.

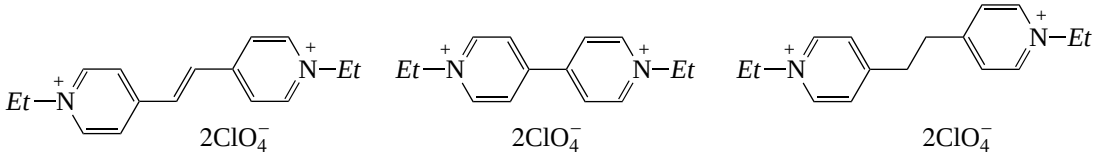

1 **2** **3**

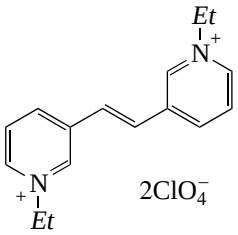

4

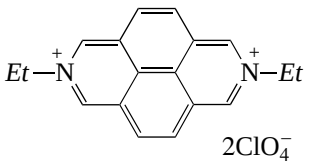

5

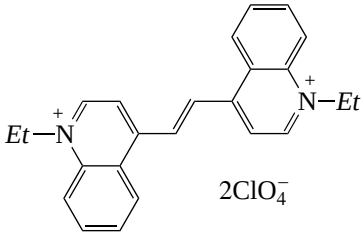

6

In this study, we performed structural investigation of model acceptors **1**–**6**. The results of the study of the structures of bis(crown)stilbenes will be published elsewhere.

EXPERIMENTAL

Synthesis. Compounds **1**–**6** were synthesized according to the following general procedure. A mixture of the corresponding heterocyclic base, such as 1,2-di(4-pyridyl)ethylene (Aldrich), 4,4'-dipyridyl (Chemapol), 1,2-di(4-pyridyl)ethane (Aldrich), 1,2-di(3-pyridyl)ethylene [7], 2,7-diazapyrene [8], or 1,2-di(4-quinolyl)ethylene [9], (0.3 mmol) and ethyl *p*-toluenesulfonate (0.24 g (1.2 mmol) for **1**–**4** or 1.20 g (6.0 mmol) for **5** and **6**) was fused at 140°C for 10 h (**1**, **3**, **4**) or 20 h (**2**, **5**, **6**). Then the reaction mixture was triturated with benzene (**1**, **2**, **4**, **6**), acetone (**3**), or anhydrous ethanol (**5**). The undissolved compound was filtered off, washed with benzene, dried, and dissolved by heating in ethanol (15 ml) in the presence of a minimal amount of distilled water. Then 0.20 ml (1.80 mmol) of a 70% $HClO_4$ solution was added. The reaction mixture was cooled to 5°C. The precipitate that formed was filtered off, washed with cold anhydrous ethanol and benzene, and dried. Then the reaction mixture was worked up once again using half amount of the 70% $HClO_4$ solution.

1-Ethyl-4-[(E)-2-(1-ethyl-4-pyridiniumyl)-1-ethenyl]pyridinium diperchlorate (1): yellowish powder, 88% yield, m.p. 297–298°C (with decomposition). ^{1}NMR spectrum (500.13 MHz, DMSO-d_6, 25°C, δ, ppm): 1.56 (t, 6 H, 2 CH_3, J = 7.3 Hz); 4.61 (q, 4 H, 2 CH_2, J = 7.3 Hz); 8.11 (s, 2 H, 2 CH=CH); 8.34 (d, 4 H, 2 H-3, 2 H-5, J = 6.7 Hz); 9.13 (d, 4 H, 2 H-2, 2 H-6, J = 6.7 Hz). According to the results of [3], m.p. = 295–296°C (with decomposition).

1-Ethyl-4-(1-ethyl-4-pyridiniumyl)pyridinium diperchlorate (2): white powder, 64% yield, m.p. 277–280°C. ^{1}NMR spectrum (500.13 MHz, D_2O, 60°C, δ, ppm): 1.64 (t, 6 H, 2 CH_3, J = 7.4 Hz); 4.71 (q, 4 H, 2 CH_2, J = 7.4 Hz); 8.47 (d, 4 H, 2 H-3, 2 H-5, J = 6.6 Hz); 9.06 (d, 4 H, 2 H-2, 2 H-6, J = 6.6 Hz). For $C_{14}H_{18}Cl_2N_2O_8$, anal calc (%): C, 40.69; H, 4.39; N, 6.78. Found (%): C, 40.54; H, 4.40; N, 6.72.

1-Ethyl-4-[2-(1-ethyl-4-pyridiniumyl)ethyl]pyridinium diperchlorate (3): white powder, 80% yield, m.p. 239–241°C (with decomposition). ^{1}NMR spectrum (500.13 MHz, DMSO-d_6, 50°C, δ, ppm): 1.54 (t, 6 H, 2 CH_3, J = 7.3 Hz); 3.34 (s, 4 H, CH_2CH_2); 4.59 (q, 4 H, 2 CH_2, J = 7.3 Hz); 8.06 (d, 4 H, 2 H-3, 2 H-5, J = 6.4 Hz); 8.99 (d, 4 H, 2 H-2, 2 H-6, J = 6.4 Hz). For $C_{16}H_{22}Cl_2N_2O_8$, anal calc (%): C, 43.55; H, 5.03; N, 6.35. Found (%): C, 43.59; H, 5.14; N, 6.38.

1-Ethyl-3-[(E)-2-(1-ethyl-3-pyridiniumyl)-1-ethenyl]pyridinium diperchlorate (4): white powder, 75% yield, m.p. 273–275°C. ^{1}NMR spectrum (500.13 MHz, DMSO-d_6, 30°C, δ, ppm): 1.61 (t, 6 H, 2 CH_3, J = 7.3 Hz); 4.68 (m, 4 H, 2 CH_2); 7.75 (s, 2 H, CH=CH); 8.23 (dd, 2 H, 2 H-5, J = 8.1 Hz; J = 6.1 Hz); 8.78 (d, 2 H, 2 H-4, J = 8.1 Hz); 9.07 (d, 2 H, 2 H-6, J = 6.1 Hz); 9.33 (s, 2 H, 2 H-2). For $C_{16}H_{20}Cl_2N_2O_8$, anal calc (%): C, 43.75; H, 4.59; N, 6.38. Found (%): C, 43.61; H, 4.55; N, 6.34.

2,7-Diethylbenzo[lmn][3,8]phenanthrolinium diperchlorate (5): pale-yellow powder, 72% yield, m.p. 345°C (with decomposition). ^{1}NMR spectrum (500.13 MHz, CD_3CN, 30°C, δ, ppm): 1.90 (t, 6 H, 2 CH_3, J = 7.3 Hz); 5.16 (q, 4 H, 2 CH_2, J = 7.3 Hz); 8.86 (s, 4 H, H-4, H-5, H-9, H-10); 9.92 (s, 4 H, H-1, H-3, H-6, H-8). For $C_{18}H_{18}Cl_2N_2O_8$, anal calc (%): C, 46.87; H, 3.93; N, 6.07. Found (%): C, 46.77; H, 3.94; N, 6.09.

1-Ethyl-4-[(E)-2-(1-ethyl-4-quinoliniumyl)-1-ethenyl]quinolinium diperchlorate (6): yellow powder, 79% yield, m.p. 295–297°C (with decomposition). ^{1}NMR spectrum (500.13 MHz, CD_3CN, 30°C, δ, ppm): 1.76 (t, 6 H, 2 CH_3, J = 7.3 Hz); 5.06 (q, 4 H, 2 CH_2, J = 7.3 Hz); 8.13 (m, 2 H, 2 H-7); 8.33 (m, 2 H, 2 H-6); 8.49 (d, 2 H, 2 H-3, J = 6.2 Hz); 8.50 (d, 2 H, 2 H-5, J = 7.5 Hz); 8.58 (s, 2 H, CH=CH); 8.79 (d, 2 H, 2 H-8, J = 8.2 Hz); 9.21 (d, 2 H, 2 H-2, J = 6.2 Hz). For $C_{24}H_{24}Cl_2N_2O_8 \cdot H_2O$, anal calc (%): C, 51.72; H, 4.70; N, 5.03. Found (%): C, 51.79; H, 4.34; N, 5.07.

X-ray diffraction study. Single crystals of salts **1**–**6** were prepared by slow saturation of their solutions in acetonitrile with benzene vapor at room temperature.

Single crystals were coated with a perfluorinated oil and mounted under a stream of cooled nitrogen on a Bruker SMART-CCD diffractometer (MoK_α radiation). X-ray diffraction data sets were collected using the ω-scan technique. The crystallographic parameters and

Table 1. Crystallographic parameters and details of X-ray diffraction study of compounds **1** and **2**

Compound	**1**	**2**
Molecular formula	$C_{16}H_{20}Cl_2N_2O_8$	$C_{14}H_{18}Cl_2N_2O_8$
Molecular weight, kg/kmol	439.24	413.20
Crystal system	Monoclinic	Monoclinic
Space group	$P2_1$	$P2_1/c$
a, Å	8.1781(2)	12.6135(4)
b, Å	11.6614(4)	14.2532(4)
c, Å	10.6492(3)	9.7307(3)
β, deg	107.295(1)	101.388(1)
V, Å^3	969.68(5)	1714.97(9)
Z	2	4
ρ_{calc}, g/cm^3	1.504	1.600
F(000)	456	856
$\mu(MoK_\alpha)$, mm^{-1}	0.382	0.426
Crystal dimensions, mm	0.40 × 0.30 × 0.20	0.10 × 0.10 × 0.10
T, K	120.0(2)	120.0(2)
Scanning mode/θ-scan range, deg	ω/2.00–27.50	ω/1.65–27.50
Ranges of reflection indices	$-10 \le h \le 10$, $-15 \le k \le 12$, $-13 \le l \le 13$	$-15 \le h \le 16$, $-18 \le k \le 18$, $-11 \le l \le 12$
Number of measured reflections	7038	11571
Number of independent reflections	3229 [$R(int)$ = 0.0548]	3946 [$R(int)$ = 0.0243]
Number of reflections with $I > 2\sigma(I)$	3229	3946
Number of refinement parameters	311	233
R factors based on reflections with $I > 2\sigma(I)$	R_1 = 0.0529, wR_2 = 0.1458	R_1 = 0.0678, wR_2 = 0.2011
R factors based on all reflections	R_1 = 0.0540, wR_2 = 0.1497	R_1 = 0.0831, wR_2 = 0.2165
Goodness-of-fit on F^2	1.058	1.108
Residual electron density, min/max, e/Å^3	–0.466/0.577	–1.033/1.182

characteristics of X-ray diffraction study are given in Tables 1–3. The X-ray diffraction data were processed using the Bruker SAINT software [10].

The structures were solved by direct methods and refined using the full-matrix least-squares method with anisotropic displacement parameters for non-hydrogen atoms against F^2. In all structures, the hydrogen atoms were located from difference Fourier syntheses. In the structures of salts **1**, **3**, and **6**, the hydrogen atoms were refined isotropically. In the structures of salts **2**, **4**, and **5**, the hydrogen atoms were refined using the riding model with isotropic displacement parameters, which were constrained to be 1.2 times greater than the corresponding parameters for the parent carbon or nitrogen atoms (1.5 times greater for the H atoms of the methyl groups).

The atomic coordinates and other X-ray diffraction data were deposited with the Cambridge Crystallographic Data Center (CCDC, 12 Union Road, Cambridge CB2 1EZ, UK; fax: (+44) 1223-336-033; e-mail: deposit@ccdc.cam.ac); the CCDC reference numbers are 238 948 (**1**), 238 949 (**2**), 238 950 (**3**), 238 951 (**4**), 238 952 (**5**), and 238 953 (**6**).

In salt **2** (containing the divalent cation and two perchlorate anions), both anions are disordered over a number of positions. The disorder can be described using the top model, in which one oxygen position is completely occupied, whereas other oxygen positions correspond to the rotation of the anions about the Cl–O bond involving the ordered O atom. All Fourier peaks present in the difference electron-density map were localized in the vicinity of the anions, which indicates that not all types of rotational disorder were taken into account in the final refined model of the structure of salt **2**. However, the subsequent refinement involving new electron-density peaks as oxygen atoms did not actually improve the results and gave low occupancies of the positions of new "rotamers." In the structure of salt **5**, one of the two anions is disordered. The other anion also includes a disordered component, whose content is vanishingly small. The presence of this component is evidenced by numerous peaks in the difference Fourier synthesis in the vicinity of the latter perchlorate anion.

Table 2. Crystallographic parameters and details of X-ray diffraction study of compounds **3** and **4**

Compound	**3**	**4**
Molecular formula	$C_{16}H_{22}Cl_2N_2O_8$	$C_{16}H_{20}Cl_2N_2O_8$
Molecular weight, kg/kmol	441.26	439.24
Crystal system	Monoclinic	Monoclinic
Space group	$P2_1/n$	$P2_1/c$
a, Å	6.5924(5)	24.688(3)
b, Å	10.8631(9)	7.3712(8)
c, Å	13.816(1)	16.372(2)
β, deg	102.128(2)	104.367(3)
V, Å^3	967.4(1)	2886.1(6)
Z	2	6
ρ_{calcd}, g/cm^3	1.515	1.516
$F(000)$	460	1368
$\mu(MoK_\alpha)$, mm^{-1}	0.383	0.385
Crystal dimensions, mm	0.24 × 0.18 × 0.08	0.28 × 0.24 × 0.08
T, K	100.0(2)	100.0(2)
Scanning mode/θ-scan range, deg	ω/3.02–28.00	ω/0.85–28.50
Ranges of reflection indices	$-8 \le h \le 8$, $-12 \le k \le 14$, $-18 \le l \le 17$	$-31 \le h \le 3$, $-9 \le k \le 9$, $-19 \le l \le 21$
Number of measured reflections	6284	17018
Number of independent reflections	2331 [$R(int) = 0.0205$]	7180 [$R(int) = 0.0254$]
Number of reflections with $I > 2\sigma(I)$	2331	7180
Number of refinement parameters	172	384
R factors based on reflections with $I > 2\sigma(I)$	$R_1 = 0.0298$, $wR_2 = 0.0854$	$R_1 = 0.0476$, $wR_2 = 0.1213$
R factors based on all reflections	$R_1 = 0.0323$, $wR_2 = 0.0868$	$R_1 = 0.1248$, $wR_2 = 0.1422$
Goodness-of-fit on F^2	1.067	1.058
Residual electron density, min/max, e/Å^3	–0.333/0.356	–0.461/0.353

Compound **5** forms a crystal solvate with benzene molecules, which fulfill the structure-forming function (see the discussion below).

All calculations were carried out using the SHELXTL-Plus software [11].

RESULTS AND DISCUSSION

Geometry of cations in salts 1–6. Salts **1**–**3** consist of a divalent organic cation and two ClO_4^- anions. The structures of the cations in these salts and the atomic numbering schemes are shown in Fig. 1. Selected geometric parameters of the cations of salts **1**–**3** are given in Tables 4–6, respectively.

In all these cations, both ethylene substituents at the nitrogen atoms are oriented in opposite directions approximately perpendicular to the mean plane of the π system.

The central fragment of the cation in salt **1** (Fig. 1) is approximately planar. The dihedral angle between the pyridine rings is 13.5°. The central ethylene bridge shows virtually no twisting: the C(2)–C(1)–C(11)–C(12) torsion angle is 178.2°. This geometry is favorable for the π conjugation over the entire fragment Py^1–CH=CH–Py^2. The distance between the centroids of the pyridine rings is 6.60 Å.

Both heterocycles are characterized by similar geometric distortions. Two opposite bonds, C(3)–C(4) and C(5)–C(6), in one ring and the C(13)–C(14) and C(15)–C(16) bonds in another ring are systematically shortened (1.369(5)–1.376(5) Å) as compared to the other C–C bonds in the rings (1.394(5)–1.415(4) Å). In the bridging ethylene group, the double bonds are essentially localized.

It should be noted that the endocyclic angles at the *ipso*-C(2) and -C(12) atoms are decreased to 117.4(3)° and 117.5(3)°, respectively, whereas the C–C–C angles at the carbon atoms of the ethylene bridge are increased to 124.3(3)° and 125.2(3)°. This is, apparently, due to the steric interactions between the atomic fragments in the planar molecular system.

The Cambridge Structural Database (CSD) (2003 release) [12] includes data on five structures with the divalent [*R*–*Py*–CH=CH–*Py*–*R*]$^{2+}$ cation (the refcodes

Table 3. Crystallographic parameters and details of X-ray diffraction study of compounds **5** and **6**

Compound	**5**	**6**
Molecular formula	$C_{21}H_{18}Cl_2N_2O_8$	$C_{24}H_{24}Cl_2N_2O_8$
Molecular weight, kg/kmol	497.27	539.35
Crystal system	Triclinic	Monoclinic
Space group	$P\bar{1}$	$P2_1/n$
a, Å	9.664(2)	13.0362(5)
b, Å	9.670(2)	6.8504(2)
c, Å	12.951(2)	14.5061(5)
α, deg	77.204(6)	90.0
β, deg	75.258(5)	115.552(2)
γ, deg	66.010(5)	90.0
V, Å^3	1059.8(3)	1168.74(7)
Z	2	2
ρ_{calcd}, g/cm^3	1.558	1.533
F(000)	512	560
$\mu(MoK_\alpha)$, mm^{-1}	0.360	0.333
Crystal dimensions, mm	$0.32 \times 0.20 \times 0.05$	$0.42 \times 0.36 \times 0.08$
T, K	100.0(2)	120(2)
Scanning mode/θ-scan range, deg	ω/1.64–27.00	ω/1.765–27.99
Ranges of reflection indices	$-12 \le h \le 11$, $-12 \le k \le 9$, $-10 \le l \le 16$	$-15 \le h \le 17$, $-8 \le k \le 8$, $-19 \le l \le 16$
Number of measured reflections	5477	6466
Number of independent reflections	4276 [*R*(*int*) = 0.0421]	2764 [*R*(*int*) = 0.0221]
Number of reflections with $I > 2\sigma(I)$	4276	2764
Number of refinement parameters	297	212
R factors based on reflections with $I > 2\sigma(I)$	$R_1 = 0.1162$, $wR_2 = 0.2921$	$R_1 = 0.0339$, $wR_2 = 0.0975$
R factors based on all reflections	$R_1 = 0.1361$, $wR_2 = 0.3034$	$R_1 = 0.0401$, $wR_2 = 0.1007$
Goodness-of-fit on F^2	1.125	1.033
Residual electron density, min/max, e/Å^3	−0.666/1.546	−0.498/0.347

AZSTBI, BPETCQ, EPECCQ, MPYRET, and WEMNUX). All these data were obtained with low accuracy. However, there is a clear tendency for systematic distortion of the geometry analogous to that observed in the structure of the cation of salt **1**. The average lengths of the shortened C–C bonds and all other C–C bonds in the rings are 1.364 and 1.390 Å, respectively. The average length of the C=C double bonds is 1.290 Å, and the average endocyclic C–C–C angle at the *ipso*-carbon atoms is 118°. In all the above-mentioned structures, the substituents at the nitrogen atoms are oriented in opposite directions from the mean plane of the conjugated system.

The cation in salt **2** consists of two pyridine rings directly bound to each other. The rings are twisted about the C(3)–C(13) bond by 15.8°. The cyclic systems in this cation display a *para*-quinoid structure analogous to that observed in the cation of salt **1** (see Table 5). The bond length between the pyridine rings (1.486(4) Å) has a standard value. The absence of a bridge between the rings leads to a decrease in the distance between the centroids of the rings to 4.28 Å. It should be noted that the endocyclic angles at the *ipso*-C(3) and -C(13) atoms in this cation also decrease to 117.8(3)°.

The CSD contains 126 entries for structures with the divalent dipyridilium cation $[R–Py–Py–R]^{2+}$ which are not involved in macrocyclic systems. Statistical analysis of their geometry confirmed the characteristic features revealed in this study. In actuality, the average length of the shortened (in accordance with the contribution of the *para*-quinoid structure) opposite C–C bonds in the rings is 1.371 Å. The average length of the other C–C bonds in the rings is 1.387 Å, the average bond length between the rings is 1.481 Å, and the average C–C–C angle at the key atoms of the conjugated system of the cation is 117.0°. In all these structures, the substituents at the nitrogen atoms are displaced in opposite directions from the mean plane of the viologen system.

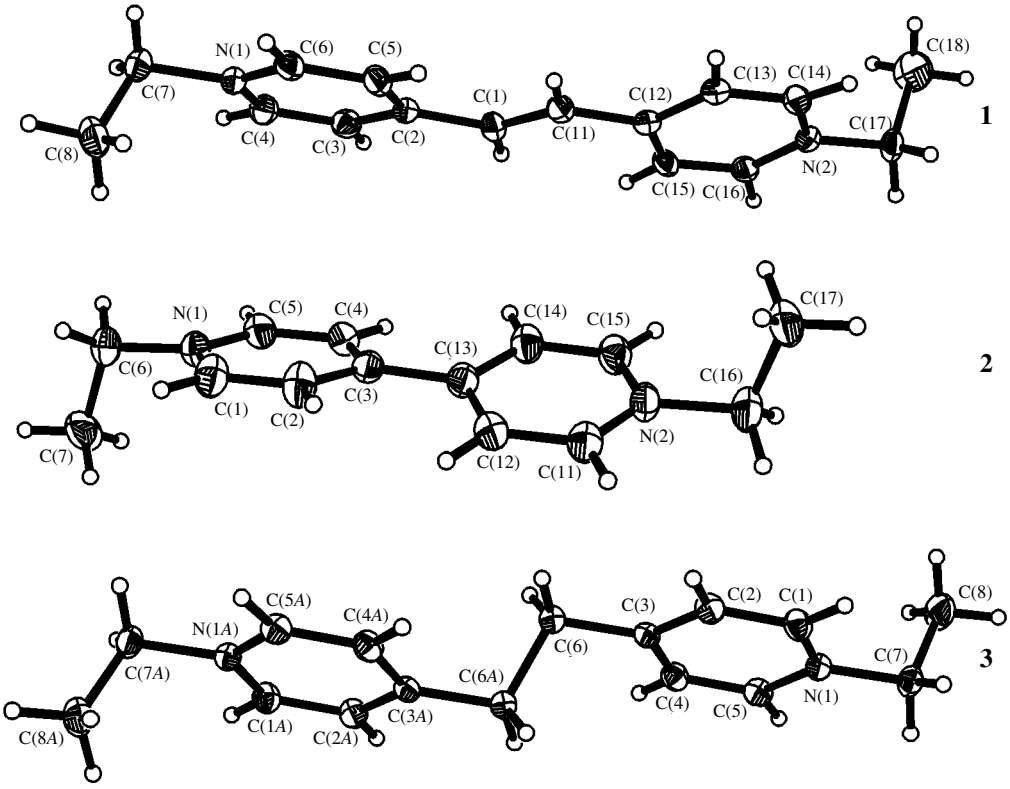

Fig. 1. Structures of the cations of salts **1**–**3**. Thermal ellipsoids are drawn at the 50% probability level.

In salt **3**, the divalent cation occupies a center of symmetry, due to which its pyridine rings are strictly parallel to each other. One crystallographically independent perchlorate anion is ordered.

The presence of the saturated $-CH_2CH_2-$ bridge between the pyridine rings precludes conjugation between them. Nevertheless, the geometric features of these rings are similar to those of the cations of salts **1** and **2**. Two opposite bonds, C(1)–C(2) and C(4)–C(5), are substantially shortened compared to the C(2)–C(3) and C(3)–C(4) bonds, and the endocyclic C(2)–C(3)–C(4) angle at the key atom decreases to 117.9(1)°.

Table 4. Selected interatomic distances (Å), bond angles (deg), and dihedral angles (deg) in the cation of salt **1**

N(1)–C(4)	1.360(4)	N(2)–C(14)	1.359(4)
N(1)–C(6)	1.353(4)	N(2)–C(16)	1.338(5)
N(1)–C(7)	1.486(5)	N(2)–C(17)	1.483(5)
C(1)–C(2)	1.465(5)	C(11)–C(12)	1.457(5)
C(2)–C(3)	1.394(5)	C(12)–C(13)	1.396(5)
C(2)–C(5)	1.410(4)	C(12)–C(15)	1.415(4)
C(3)–C(4)	1.371(5)	C(13)–C(14)	1.369(5)
C(5)–C(6)	1.371(5)	C(15)–C(16)	1.376(5)
C(1)–C(11)	1.345(4)	C(13)–C(12)–C(15)	117.5(3)
C(3)–C(2)–C(5)	117.4(3)	C(12)–C(11)–C(1)	125.2(3)
C(2)–C(1)–C(11)	124.3(3)		
Py^1/Py^2*	13.5	Py^1/N(1), C(7), C(8)	105.0
Py^2/N(2), C(17), C(18)	84.2		

* Py^1 and Py^2 denote the planes passing through the pyridine rings including the N(1) and N(2) atoms, respectively. Analogous notations are used also in Tables 5–9.

Table 5. Selected interatomic distances (Å), bond angles (deg), and dihedral angles (deg) in the cation of salt **2**

N(1)–C(1)	1.338(4)	N(2)–C(11)	1.339(4)
N(1)–C(5)	1.343(4)	N(2)–C(15)	1.351(4)
N(1)–C(6)	1.488(3)	N(2)–C(16)	1.492(4)
C(1)–C(2)	1.378(4)	C(11)–C(12)	1.378(4)
C(2)–C(3)	1.396(4)	C(12)–C(13)	1.381(4)
C(4)–C(5)	1.377(4)	C(14)–C(15)	1.378(4)
C(4)–C(3)	1.387(4)	C(14)–C(13)	1.399(4)
C(3)–C(13)	1.486(4)	C(12)–C(13)–C(14)	117.8(3)
C(4)–C(3)–C(2)	117.8(3)		
Py^1/Py^2	15.8	Py^1/N(1), C(6), C(7)	89.2
Py^2/N(2), C(16), C(17)	82.2		

Table 6. Selected interatomic distances (Å), bond angles (deg), and dihedral angles (deg) in the cation of salt **3**

N(1)–C(1)	1.345(2)	C(3)–C(4)	1.394(2)
N(1)–C(5)	1.348(2)	C(4)–C(5)	1.373(2)
N(1)–C(7)	1.487(2)	C(3)–C(6)	1.499(2)
C(1)–C(2)	1.378(2)	C(6)–C(6A)	1.544(2)
C(2)–C(3)	1.394(2)	C(2)–C(3)–C(4)	117.9(1)
Py^1/Py^2	0.0	Py^1/N(1), C(7), C(8)	94.4

These results provide evidence that the above-considered geometric parameters of the pyridine rings are determined by the character of the positive-charge delocalization in these rings. The $X^1\cdots X^2$ distance between the centroids of the rings (6.49 Å) is close to that found in the cation of salt **1**.

The CSD contains data on four structures with the divalent $[R–Py–CH_2–CH_2–Py–R]^{2+}$ cation. Two of these structures (the refcodes BPYETC and BUMYAJ10) were established with low accuracy. Hence we excluded these structures from consideration and used only more precise data on the remaining two structures (the refcodes EPETCR and MPETCQ). The structural features of these two compounds are analogous to those observed for the cation of salt **3**. The average length of the shortened C–C bonds in the rings characterized by a *para*-quinoid structure is 1.35 Å, the average lengths of the other C–C bonds in the rings is 1.39 Å, and the bond angle at the key C atom of the pyridine ring is 117°. In all four structures, the substituents at the nitrogen atoms are displaced in opposite directions from the mean plane of the chromophore system.

In the structure of salt **4**, the independent cations have nearly identical geometry. The structures of the cations and the atomic numbering scheme are shown in Fig. 2. Selected geometric parameters are listed in Table 7. The substituents at the nitrogen atoms of each cation are oriented in opposite directions with respect to the mean plane of the conjugated system and are located approximately perpendicular to this plane.

In the cation of salt **4**, the nitrogen atoms are in the *meta* positions with respect to the bridging ethylene group. In the cation located in a center of symmetry, the planes of the rings are strictly coplanar. In the cation located in a general position, the analogous planes are almost coplanar (the corresponding dihedral angle is 0.5°).

Although the accuracy of this investigation is substantially lower than the data on the above-mentioned three structures, it can be said with assurance that there are no systematic distortions of the C–C bond lengths in the pyridine rings. Nevertheless, the endocyclic angles at the C(4), C(14), and C(24) atoms involved in the bridging system are decreased, as in all the above-considered structures. In the ethenyl bridges of the cations, the double-bond lengths (1.333(7) and 1.328(4) Å) and the single-bond lengths (1.471(5), 1.469(4), and 1.467(4) Å) are virtually identical to those in the cation of salt **1**. It should be noted that data on the structures of analogous cations are lacking in the CSD.

Salt **5** crystallizes as a solvate with benzene. The cation : anion : solvate ratio is 2 : 4 : 1. The structure of the divalent cation is shown in Fig. 3. Selected geometric parameters are given in Table 8.

The geometry of the cation is substantially distorted toward a boat conformation. The dihedral angle between two formally pyridine rings is 11.4°. In this cation, the substituents at the nitrogen atoms are oriented in opposite directions virtually perpendicular to the mean plane of the cyclic system. There is a pronounced systematic alternation of the bond lengths in

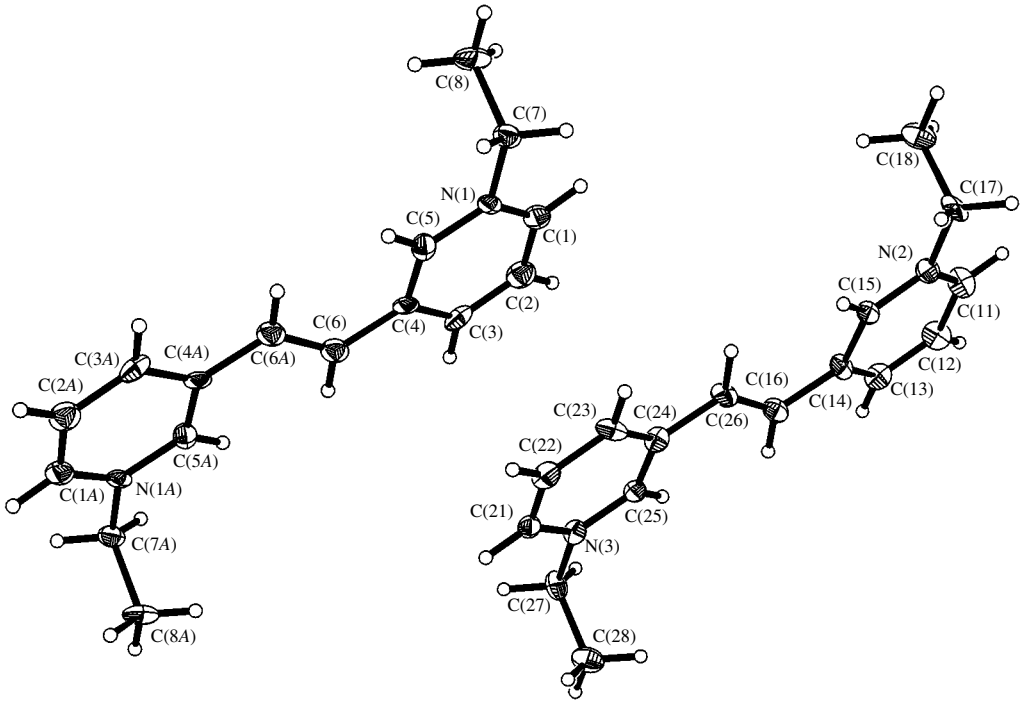

Fig. 2. Structures of two crystallographically independent cations of salt **4**. Thermal ellipsoids are drawn at the 50% probability level.

the cation, which corresponds to the following structural scheme:

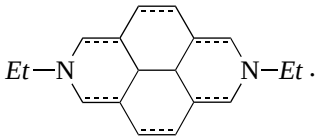

The lengths of the shortened C–C bonds vary from 1.364(8) to 1.401(8) Å, and the elongated bond lengths are in the range 1.403(8)–1.443(8) Å; the average bond lengths are 1.387 and 1.426 Å, respectively.

The CSD contains 12 entries for analogous cations which are not involved in macrocyclic systems (the ref-

Table 7. Selected interatomic distances (Å), bond angles (deg), and dihedral angles (deg) in the cation of salt **4**

N(1)–C(1)	1.344(4)	C(3)–C(4)	1.403(5)
N(1)–C(5)	1.354(4)	C(4)–C(5)	1.396(5)
N(1)–C(7)	1.492(5)	C(4)–C(6)	1.471(5)
C(1)–C(2)	1.395(6)	C(6)–C(6A)	1.333(7)
C(2)–C(3)	1.382(5)	C(16)–C(26)	1.328(4)
N(2)–C(11)	1.344(4)	N(3)–C(21)	1.370(4)
N(2)–C(15)	1.349(4)	N(3)–C(25)	1.344(4)
N(2)–C(17)	1.494(5)	N(3)–C(27)	1.494(5)
C(11)–C(12)	1.388(5)	C(21)–C(22)	1.358(6)
C(12)–C(13)	1.382(5)	C(22)–C(23)	1.398(5)
C(13)–C(14)	1.391(4)	C(23)–C(24)	1.405(4)
C(14)–C(15)	1.394(5)	C(24)–C(25)	1.398(5)
C(14)–C(16)	1.469(4)	C(24)–C(26)	1.467(4)
C(3)–C(4)–C(5)	116.7(3)	C(13)–C(14)–C(15)	117.6(3)
C(23)–C(24)–C(25)	118.5(3)	Py^1/N(1), C(7), C(8)	87.5
Py^2/N(2), C(17), C(18)	85.7	Py^3/N(3), C(27), C(28)	86.9
Py^1/Py^{1A}	0.0	Py^2/Py^3	0.5

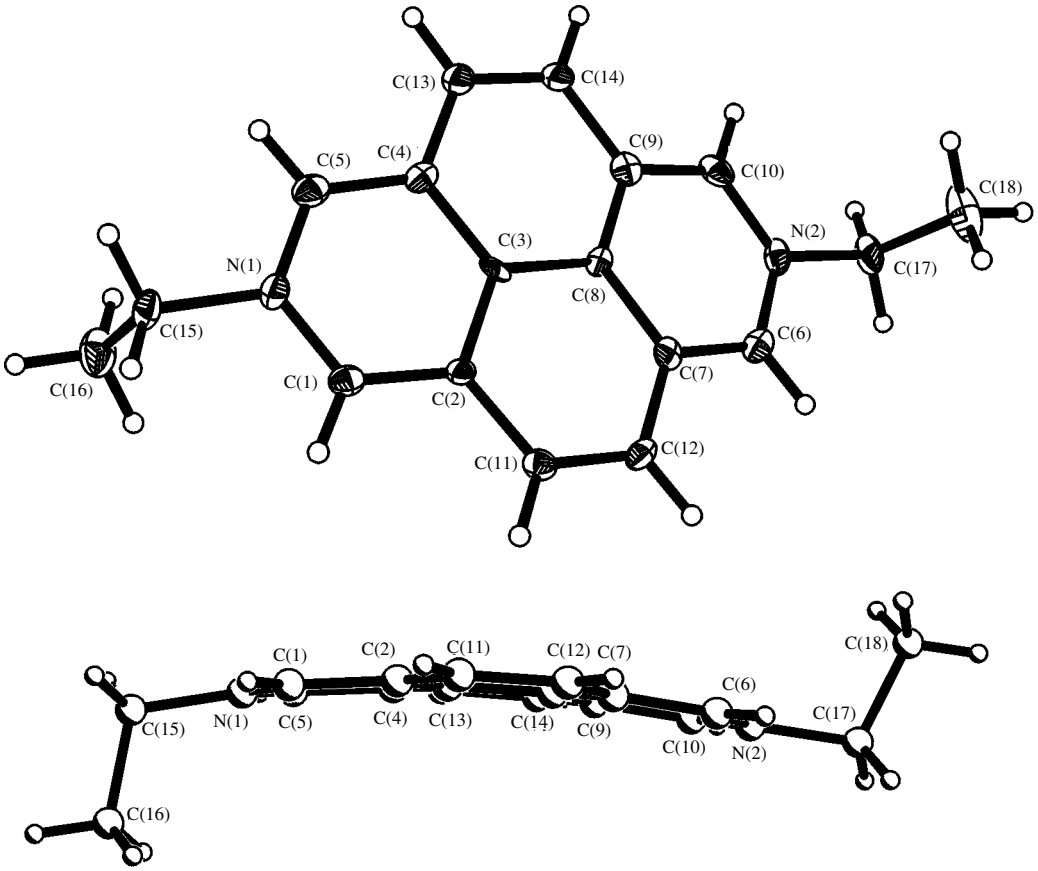

Fig. 3. Two projections of the structure of the cation of salt **5**. In the upper projection, thermal ellipsoids are drawn at the 50% probability level.

codes ECAXIP, ECAXOV, GOWKEK, GOYJIN, GOYKIO, GOYKOU, NEBQOA, TASHIE, TAXROZ, TAXROZ, and TAXROZ01; the final structure contains two independent formula units). In these structures, the average lengths of the C–C multiple bonds in the pyridine and benzene rings are 1.394 and 1.360 Å, respectively, and the average length of the elongated C–C bonds is 1.409 Å. Slight systematic differences between the geometric parameters of the conjugated system in the cation of salt **5** and those published in the literature are, apparently, related to stacking interactions between this conjugated system and the benzene solvate molecule which is located in the crystal between the planes of two adjacent cations. This fact is discussed in more detail in the next section.

The structure of the cation of salt **6** is shown in Fig. 4. Selected geometric parameters are given in Table 9.

The cation occupies a center of symmetry and is strictly planar. The double bond in the ethylene bridge in salt **6**, like those in **1** and **4**, is localized (C(10)–C(10*A*), 1.320(3) Å). In the pyridine rings, the character of alternation of the bond lengths differs from that observed in the other cations. The overall distribution of the bonds in the conjugated system is described by the following scheme:

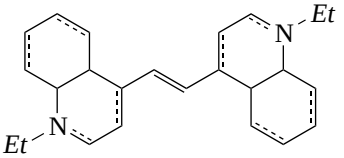

The length of the shortened C(2)–C(3) bond in the pyridine ring is 1.388(2) Å. The adjacent C(1)–C(2) and C(3)–C(4) bond lengths are 1.392(2) and 1.433(2) Å, respectively. The C(1)–N(1) bond (1.332(2) Å) is shorter than the C(9)–N(1) bond (1.386(2) Å). The C–C multiple-bond lengths in the benzene ring are 1.370(2) and 1.368(2) Å. Other bond lengths vary from 1.413(2) to 1.431(2) Å. The longest C(4)–C(9) bond is shared by two rings. The ethyl substituents are oriented in opposite directions virtually perpendicular to the conjugated system.

The distances between the centroids of the benzene rings in molecules **1**–**6** are 6.60, 4.28, 6.49, 6.63 (6.57), 4.19, and 6.64 Å, respectively. This distance in *trans*-stilbene (6.68 Å) is almost the same as those in the cations of salts **1**, **3**, **4**, and **6**. In the overwhelming major-

Table 8. Selected interatomic distances (Å), bond angles (deg), and dihedral angles (deg) in the cation of salt **5**

N(1)–C(1)	1.345(8)	N(2)–C(6)	1.354(8)
N(1)–C(5)	1.359(8)	N(2)–C(10)	1.352(8)
N(1)–C(15)	1.494(7)	N(2)–C(17)	1.499(7)
C(1)–C(2)	1.401(8)	C(6)–C(7)	1.389(8)
C(2)–C(3)	1.419(8)	C(7)–C(8)	1.413(8)
C(3)–C(4)	1.425(8)	C(8)–C(9)	1.403(8)
C(4)–C(5)	1.396(9)	C(9)–C(10)	1.392(8)
C(3)–C(8)	1.423(8)	C(11)–C(12)	1.364(8)
C(13)–C(14)	1.380(9)	C(2)–C(11)	1.437(8)
C(4)–C(13)	1.435(8)	C(7)–C(12)	1.433(8)
C(9)–C(14)	1.442(9)	C(7)–C(8)–C(9)	121.0(5)
C(2)–C(3)–C(4)	120.3(5)		
Py^1/Py^2	11.4	Py^1/N(1), C(15), C(16)	89.9
Py^2/N(2), C(17), C(18)	90.0		

Table 9. Selected interatomic distances (Å), bond angles (deg), and dihedral angles (deg) in the cation of salt **6**

N(1)–C(1)	1.332(2)	C(4)–C(9)	1.431(2)
N(1)–C(9)	1.386(2)	C(4)–C(5)	1.423(2)
N(1)–C(11)	1.497(2)	C(5)–C(6)	1.370(2)
C(1)–C(2)	1.392(2)	C(6)–C(7)	1.413(2)
C(2)–C(3)	1.388(2)	C(7)–C(8)	1.368(2)
C(3)–C(4)	1.433(2)	C(8)–C(9)	1.416(2)
C(3)–C(10)	1.472(2)	C(10)–C(10A)	1.320(3)
C(2)–C(3)–C(4)	118.1(1)	C(3)–C(10)–C(10A)	125.2(2)
Py^1/Py^2	0.0	Py^1/N(1), C(11), C(12)	84.3

ity of cases, stacking interactions between aromatic systems are known to lead to an offset superposition of the molecules [5, 13]. Hence, the equality of the $X^1\cdots X^2$ distances in donor–acceptor pairs is not as essential as the geometric factor for the occurrence of stacking interactions, and, vice versa, the inequality of these distances is not unfavorable for such interactions. In the former case, one would expect either a lateral offset of the superimposed planes of the molecules or a twist of the π systems of the donor and acceptor with respect to each other, whereas this does not necessarily occur in the latter case.

Crystal packings of compounds 1–6. A set of crystal packings formed by molecules of a particular class

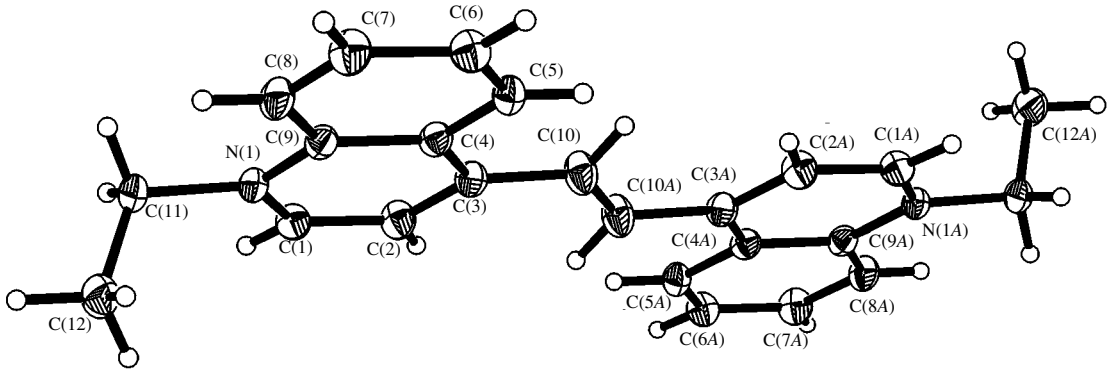

Fig. 4. Structure of the cation of salt **6**. Thermal ellipsoids are drawn at the 50% probability level.

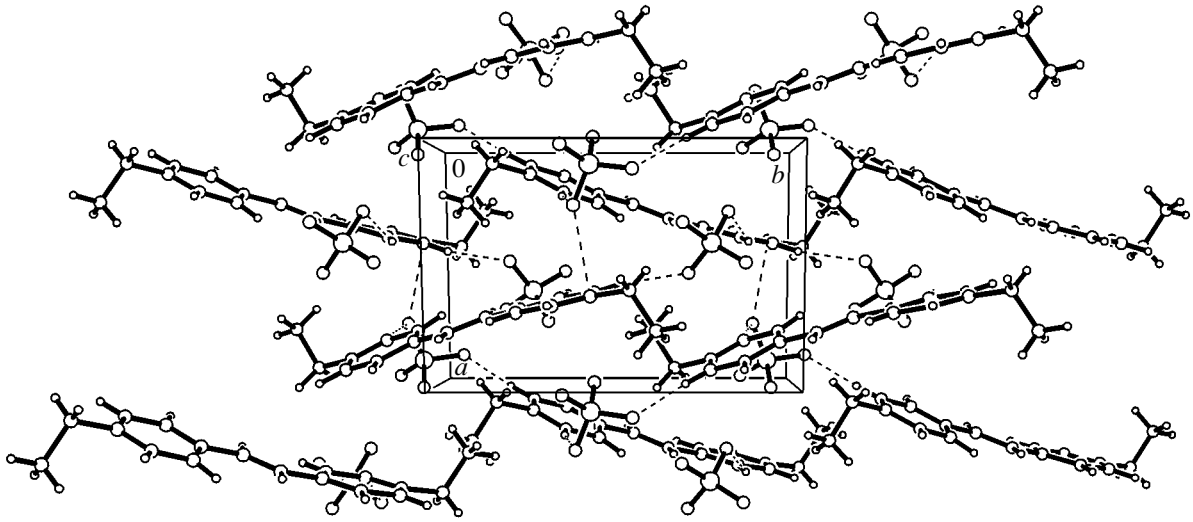

Fig. 5. Fragment of the crystal packing of salt **1**.

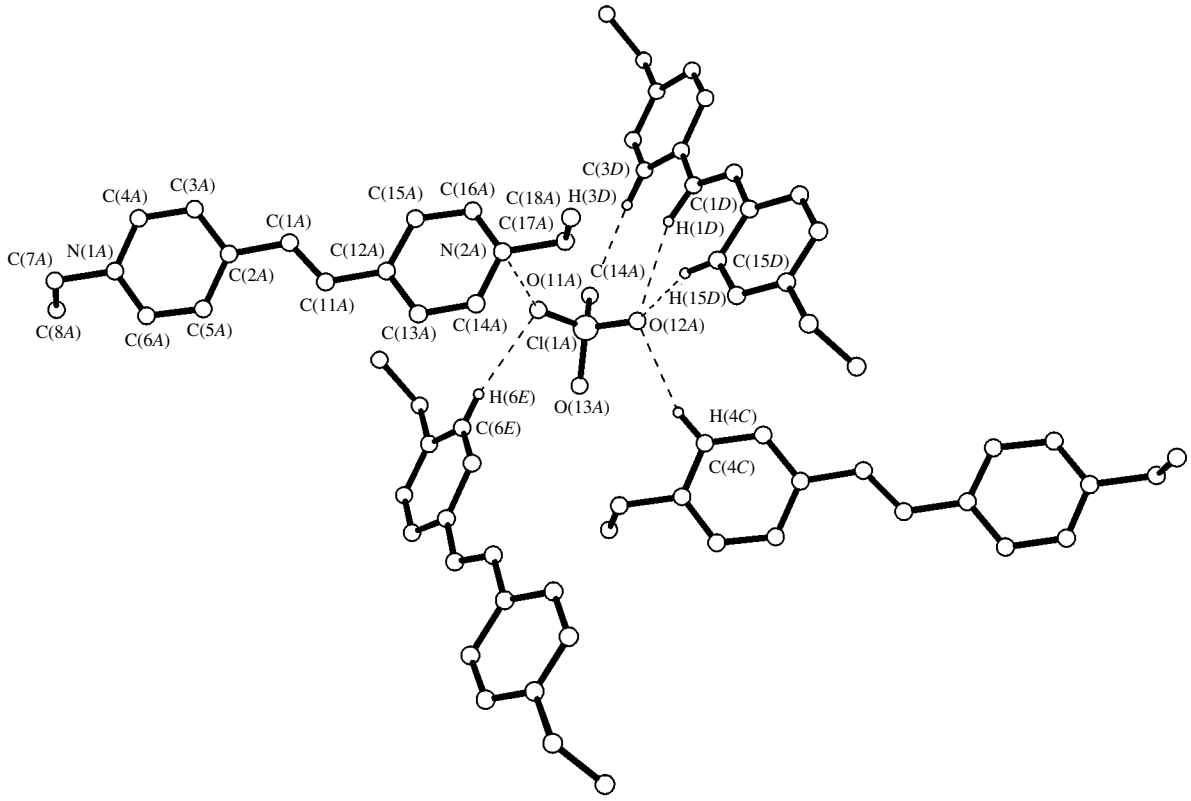

Fig. 6. Nearest environment of the perchlorate anion $Cl(1)O_4^-$ in the crystal of **1**.

of compounds gives an insight into the structures of supramolecular systems in a solution, although the latter are less well organized and less rigid compared to those in a crystal [14]. It is known that aromatic organic compounds having planar disklike structures can give rise to a moderate number of various packing motifs. Their classification was given in [15]. Elements of this classification are retained for conjugated organic systems of a more complicated shape. For example, both staircaselike [16] and stacking [17–19] architectures

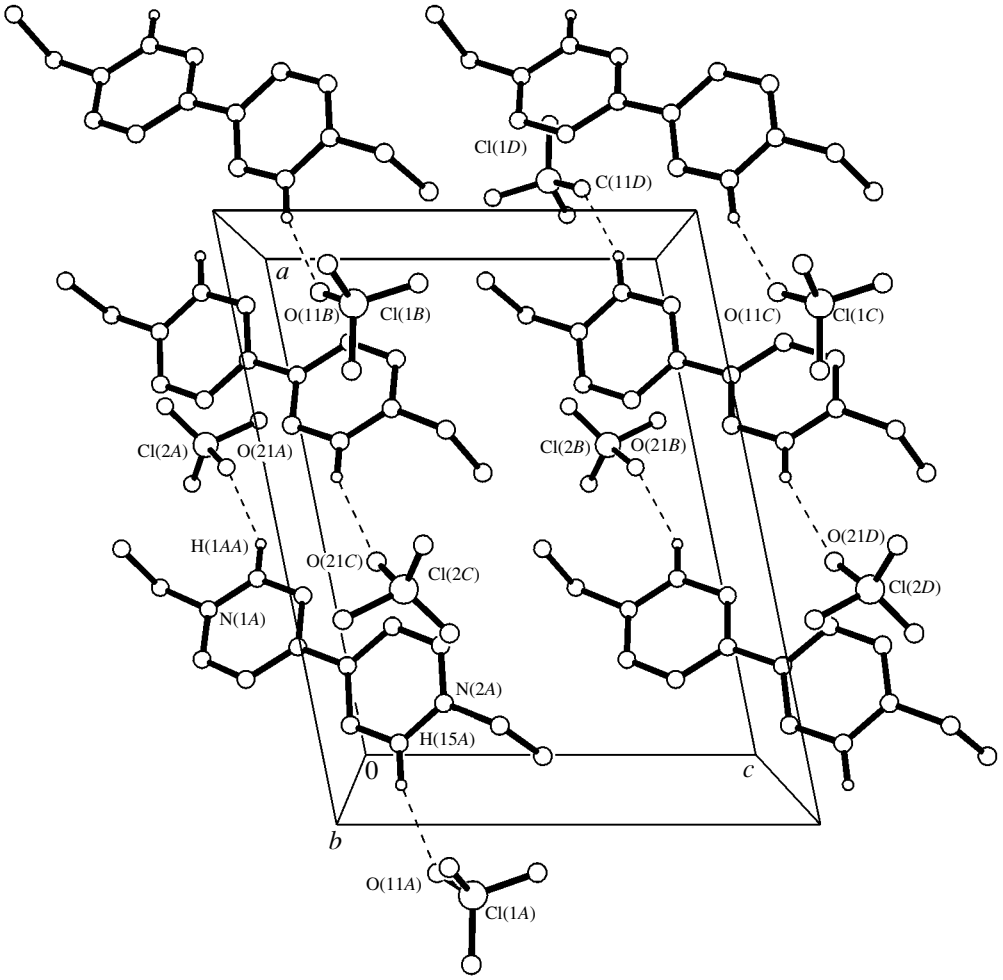

Fig. 7. Fragment of the crystal packing of salt **2**.

are observed for photochromic crown-containing dyes and substituted benzocrown ethers. In the case of the stacking architecture, stacking interactions are dominant, whereas C–H···π system interactions prevail in staircaselike structures [13, 20]. Interestingly, the stacking architecture is often observed even for conjugated organic cations of crown-containing dyes, in spite of the Coulomb repulsion between likely charged fragments.

"Staircases" can be packed in the following two fashions ((*a*), staircase-herringbone, (*b*), parallel-staircase):

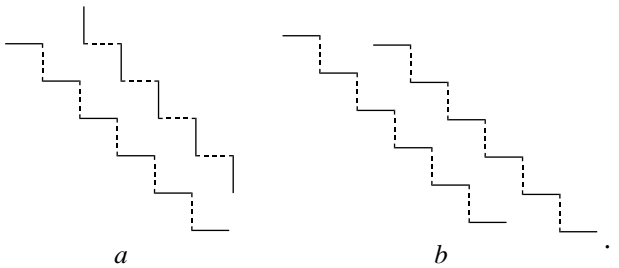

a *b*

In a solution, the transformation into a stacking structure in a "soft" supramolecule is equally probable for both these packings upon the corresponding cooperative shift of the molecules in their planes. When analyzing the crystal packings of compounds **1**–**6**, we were interested primarily in how the presence of two positive charges and additional structural elements (in the case under consideration, the presence of perchlorate anions) can affect the tendency of conjugated systems to form characteristic packings. In particular, we considered the possibility of preparing stacking structures in large supramolecules composed of the above-described CTCs. For CTCs containing the donor and acceptor components (*D* and *A*, respectively) in a ratio of 1 : 2, one can discuss the possibility of formation of stacking structures only between the donor components, because the acceptors are packed between the donors in the [*DAD*][*DAD*][*DAD*] fashion. For 1 : 1 CTCs, stacks can be arranged in supramolecules in the [*DA*][*DA*][*DA*] or [*AD*][*DA*][*AD*] fashion; other combinations are also possible. The possibility of the formation of stacks involving an additional element (for

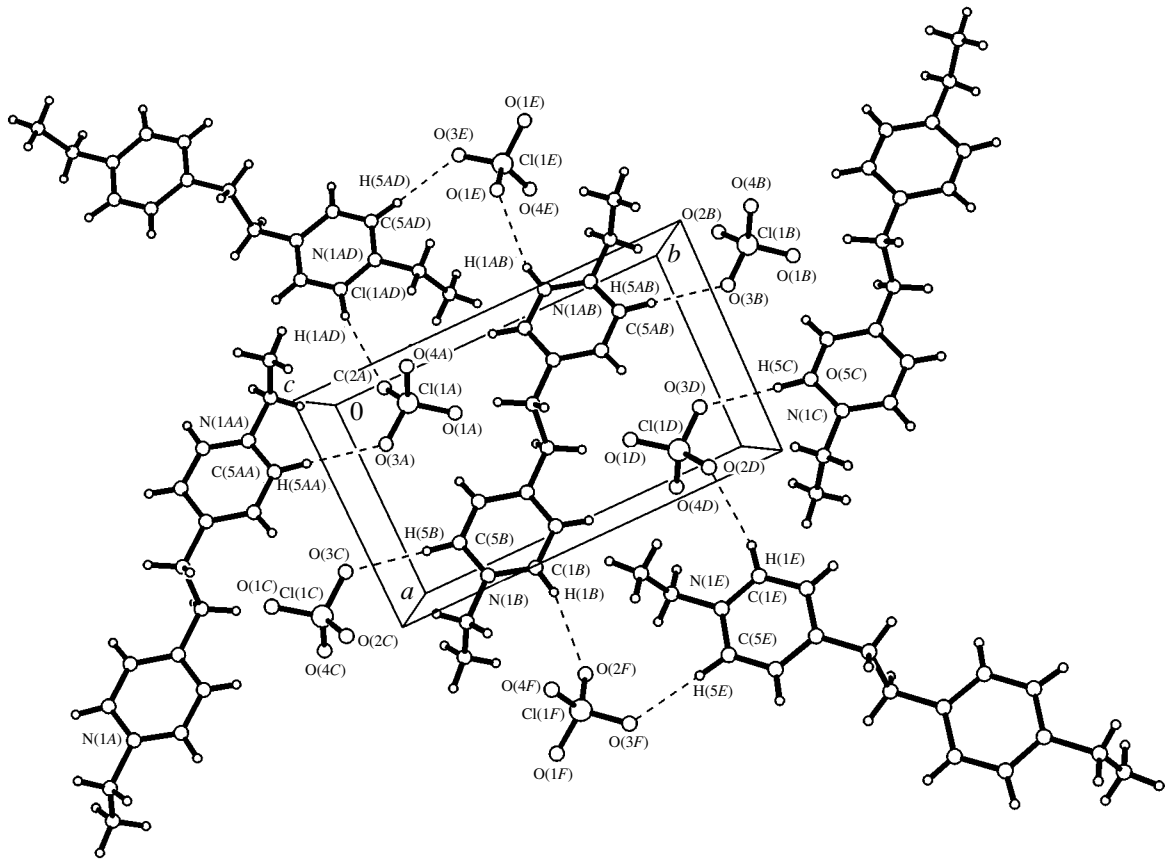

Fig. 8. One layer of the crystal packing of salt **3**.

example, aromatic solvent molecules) also cannot be excluded.

A fragment of the crystal packing of salt **1** is shown in Fig. 5. In the crystal structure, the aromatic fragments are packed neither in stacks nor in a staircase fashion because of the presence of perchlorate anions between the cations. It is possible that two positive charges in the cation give rise to a very strong Coulomb repulsion, which hinders the occurrence of a packing typical of conjugated systems. However, counterions can also have an effect. One type of anions (containing the Cl(2) atom) are located in the packing cavities and do not form secondary bonds with the adjacent atoms. On the contrary, the second perchlorate anion is involved in numerous secondary bonds, thus influencing the mutual arrangement of the cations in the structure. The environment of the latter perchlorate anion in the crystal packing is shown in Fig. 6.

The O(11*A*)···N(2*A*) contact (2.90 Å) corresponds to the sum of the van der Waals radii of these atoms. The O(11*A*)···N(2*A*)–C(14*A*), O(11*A*)···N(2*A*)–C(16*A*), and O(11*A*)···N(2*A*)–C(17*A*) angles at the nitrogen atom (85.4°, 93.5°, and 91.2°, respectively) indicate that the O(11) atom of the anion is, in fact, projected onto the nitrogen atom at which the positive charge of the cation is formally localized. It can be hypothesized that this arrangement is most favorable for the Coulomb interaction between the cation and anion, but it is also optimal for a weak n···π*-type orbital interaction. The O(11*A*)···H(6*E*) contact (2.44 Å), which is shortened compared to the sum of the van der Waalls radii (~2.6 Å), and the O(11*A*)···H(6*E*)–C(6*E*) angle (169°) are typical of hydrogen bonding. The O(12*A*) atom forms three short contacts: (O(12*A*)···H(1*D*), 2.48 Å; O(12*A*)···H(4*C*), 2.42 Å; and O(12*A*)···H(15*D*), 2.24 Å). The angles at the hydrogen atoms are 163°, 164°, and 158°, respectively, which are optimal for O···H–C hydrogen bonds. The O(14*A*) atom forms one hydrogen bond, O(14*A*)···H(3*D*)—C(3*D*), characterized by the parameters 2.42 Å and 175°.

Thus, the characteristic features of this crystal packing indicate that the ClO_4^- anions cannot only occupy the cavities in the packings whose motifs are determined by conjugated organic elements of the structure, but can also fulfill the structure-forming function. Apparently, this is responsible for the unusual supramolecular architecture of the conjugated organic systems in salt **1**.

A fragment of the crystal packing of salt **2** is shown in Fig. 7. Of two typical packing motifs (stacking and

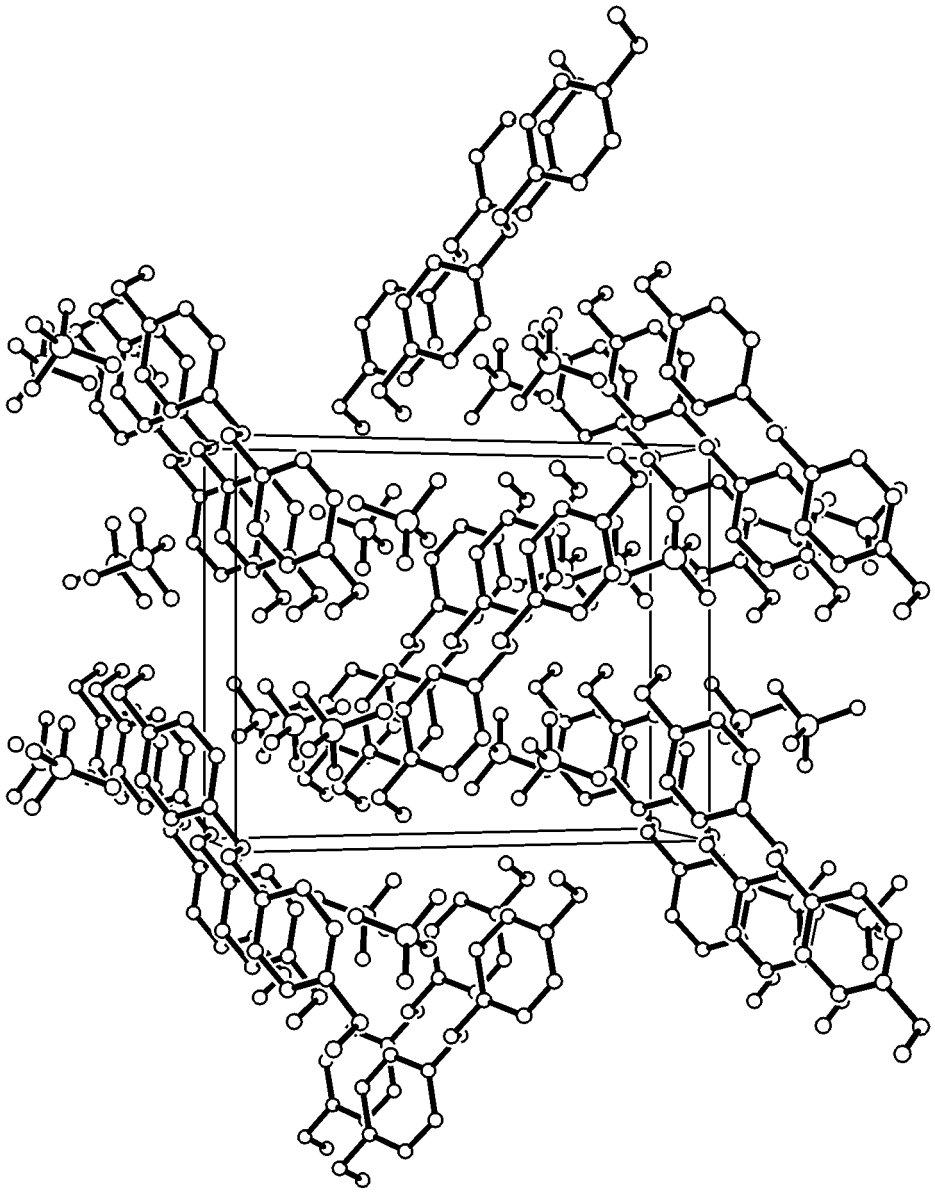

Fig. 9. Fragment of the crystal packing of salt **3**.

staircaselike), a staircase-herringbone packing of conjugated organic structural units is observed in the crystal of salt **2**. Both disordered perchlorate anions have only a slight effect on the type of this packing, each anion being involved in one hydrogen bond. It should be noted that it is these ordered oxygen atoms of the anions that are involved in the hydrogen bonding (see above).

The O(11*A*)···H(15*A*) and O(21*A*)···H(1*AA*) distances (2.41 and 2.37 Å, respectively) are comparable to those in the above-described structure. The angles at the hydrogen atoms are 156° and 157°, respectively. The formation of a larger number of secondary bonds between the anion and cation in the crystal of salt **1** compared to that observed in the crystal of salt **2** is, apparently, associated with higher electron-withdrawing ability of the cation of salt **1** in comparison with that of salt **2** owing to a more efficient mutual electron-withdrawing effect of the pyridine rings.

One layer of the crystal packing of salt **3** is shown in Fig. 8. This layer is composed of cations and anions linked to each other by hydrogen bonds. Each anion is involved in two hydrogen bonds, serving as a bridge between the adjacent cations. The O(2)···H(1) and O(3)···H(5) distances are 2.42 and 2.38 Å, respectively. The angles at these hydrogen atoms are 151° and 164°, respectively. A superposition of the layers gives rise to a typical staircase-herringbone motif (Fig. 9).

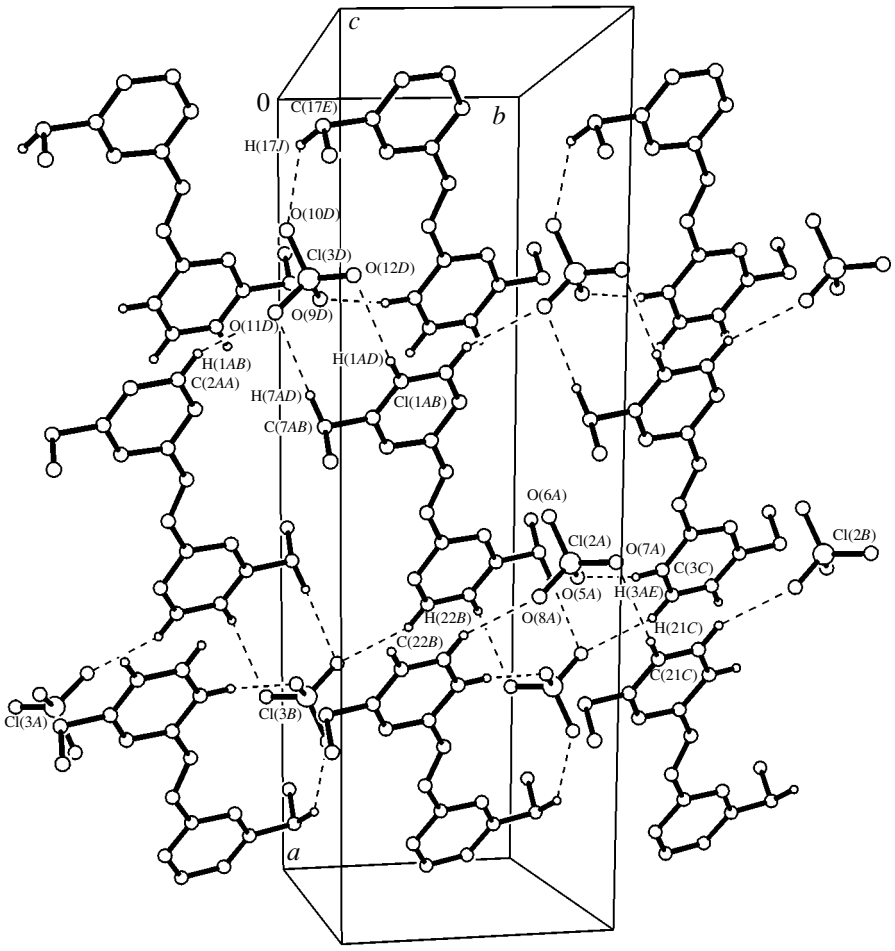

Fig. 10. Fragment of the crystal packing of salt **4** and the hydrogen bond network.

Therefore, although perchlorate anions in crystals of salt **3** fulfill the structure-forming function (within the layers), they have no effect on the character of superposition of the layers. Hence, the resulting crystal structure does not contradict the packing motif formed by the organic cations of salt **3**. This packing motif is typical of conjugated systems.

A fragment of the crystal packing of cations and anions of salt **4** is shown in Fig. 10. In this structure, cations are also packed in a staircase-herringbone fashion. Anions are located between the "staircases."

Three crystallographically different anions in this structure make different contributions to the stabilization of the crystal structure. The perchlorate anion $Cl(1)O_4^-$ occupies cavities in the crystal structure and is not involved in specific interactions. Two other anions form numerous hydrogen bonds with various C–H fragments of the adjacent molecules.

The $Cl(2)O_4^-$ anion forms three weak hydrogen bonds. The O(6) atom of this anion is not involved in the hydrogen bonding. The O(5) atom forms a weak hydrogen bond with the H(3)–C(3) fragment of the adjacent molecule (O···H, 2.55 Å; O···H–C, 159°). The O(7) atom is involved in the O(7)···H(21)–C(21) hydrogen bond with the parameters 2.52 Å and 140.9°. The O(8) atom forms the O(8)···H(22)–C(22) hydrogen bond (O···H, 2.43 Å; O···H–C, 139°). The perchlorate anion $Cl(3)O_4^-$ is involved in five weak hydrogen bonds. The O(11) atom of this anion forms the O(11)···H(7)–C(7) (O···H, 2.48 Å; O···H–C, 175°) and O(11)···H(2)–C(2) (O···H, 2.41 Å; O···H–C, 154°) hydrogen bonds with two adjacent molecules. The O(9), O(10), and O(12) atoms are involved in the weak interactions O(9)···H(23)–C(23), O(10)···H(17)–C(17), and O(12)···H(1)–C(1). The geometric parameters of these contacts are as follows: 2.55 Å and 159°; 2.50 Å and 141°; and 2.55 Å and 139°, respectively. All the above-mentioned contacts are rather long (comparable to the sum of the van der Waals radii) and are not quite optimal for hydrogen bonding. Hence, it is hardly probable that the packing requirements of the anions play a decisive role here. It is more likely that the anions are fitted to the packing motif determined by the cations.

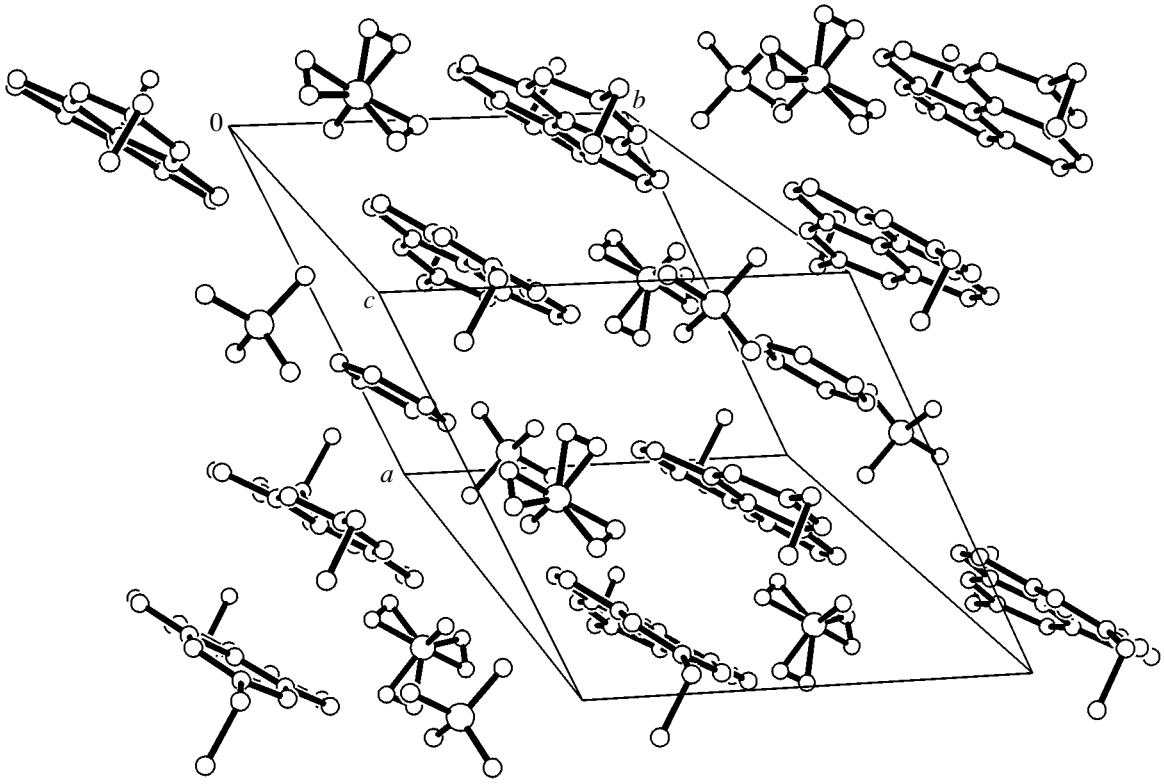

Fig. 11. Crystal packing of salt **5**. All hydrogen atoms are omitted for simplicity.

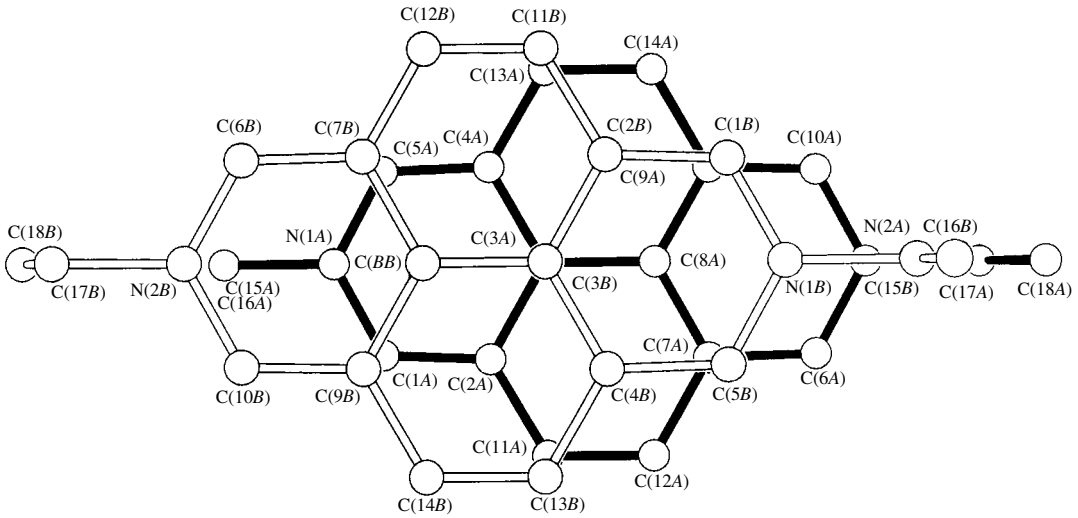

Fig. 12. Stacking pair of the cations projected onto the mean plane of one of the cations.

The crystal packing of salt **5** is shown in Fig. 11. It is characterized by a stacking structure. The stacks are formed with the participation of benzene solvate molecules, which occupy centers of symmetry in the crystal. Thus, the two cations between which a benzene molecule is located are related by the center of symmetry at (1/2 0 1/2). Each cation in the stack is surrounded on opposite sides by two cations which are related to the former cation by the centers of symmetry at (0 1/2 1/2). It should be noted that the concave sides of the cations (see above) face benzene molecules. This packing shows that the presence of two charges on the extended conjugated system of the cation does not hinder the pair stacking of the cations. However, the formation of the

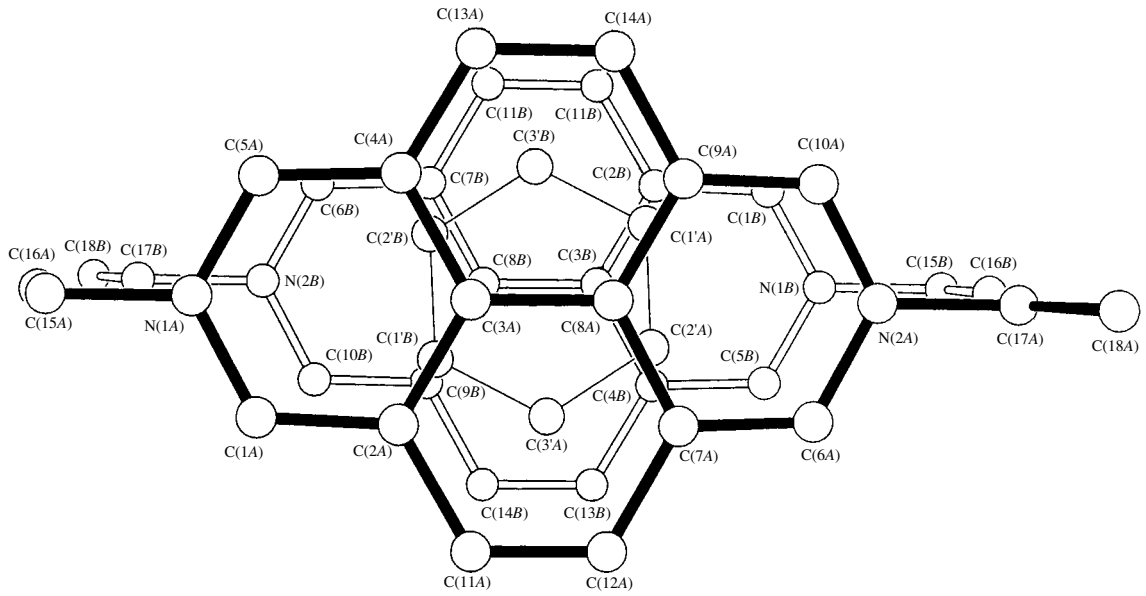

Fig. 13. Mutual arrangement of the structural units in a crystal of salt **5** in the cation–benzene–cation triad projected onto the plane of the benzene ring.

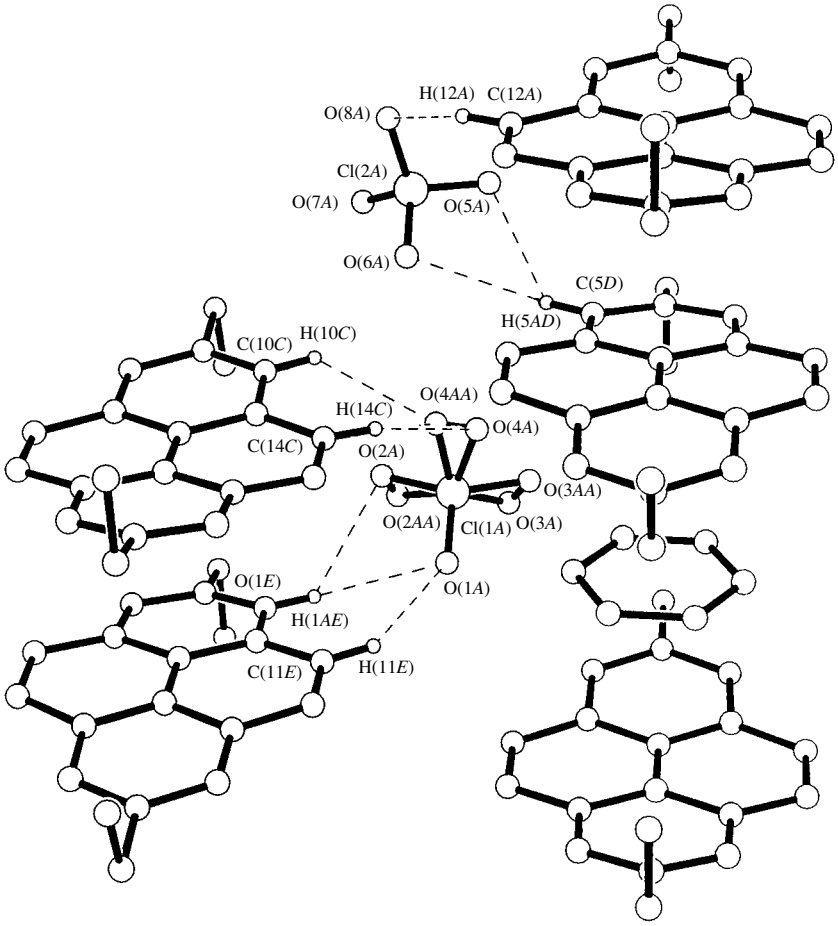

Fig. 14. Fragment of the crystal packing of salt **5** and the hydrogen-bond network. Only hydrogen atoms involved in hydrogen bonding are shown.

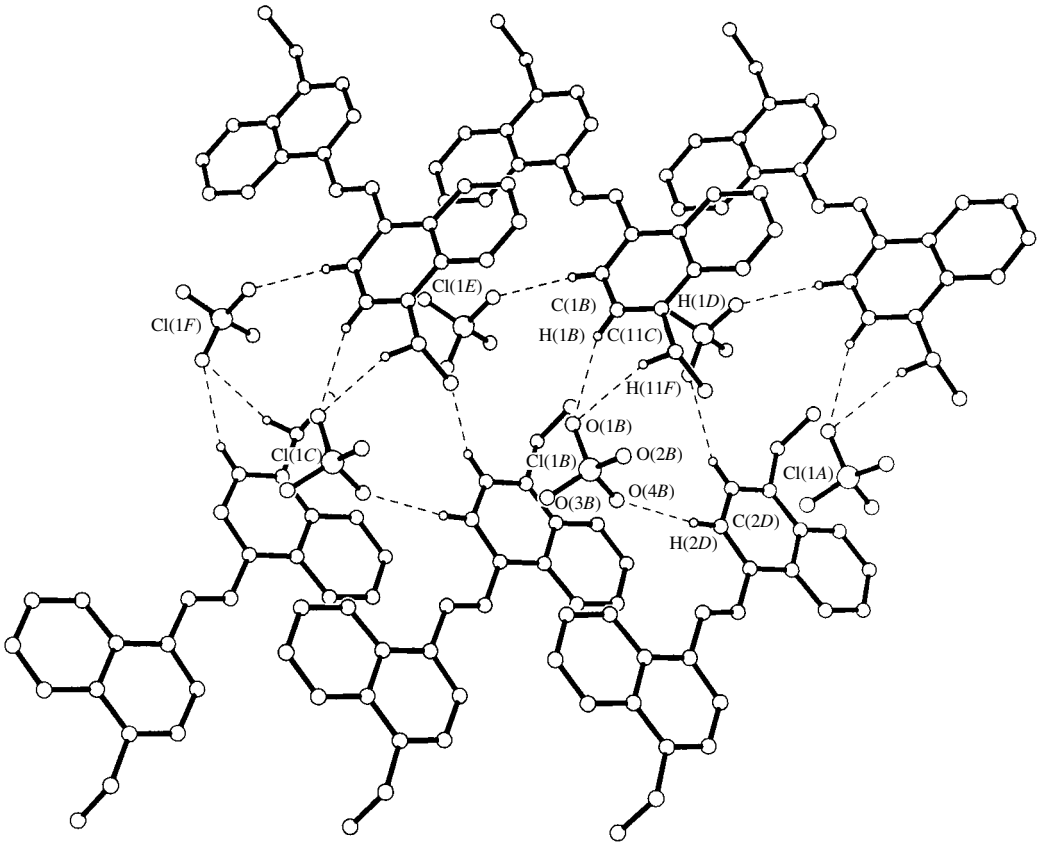

Fig. 15. Fragment of the crystal packing of salt **6**.

stack requires the presence of an aromatic solvent molecule as the third stabilizing element.

Two adjacent cations in the stack projected onto each other are shown in Fig. 12. The mean planes of these cations are strictly parallel, and the value of the interplanar distance (3.55 Å) is typical of stacking structures formed by neutral conjugated molecules (3.3–3.8 Å [5]). The mutual arrangement of the cations is offset, which is typical of systems with stacking interactions [5].

The mutual arrangement of the structural units in the cation–benzene–cation triad projected onto the plane of the benzene ring is shown in Fig. 13. Although the benzene molecule is not strictly parallel to the mean plane of the cation, the dihedral angle between these fragments is very small (0.8°). The average distance from the plane of the benzene ring to the mean plane passing through six atoms of the central fragment of each cation (3.42 Å) is rather short and undoubtedly corresponds to a stacking interaction.

In the crystal, perchlorate anions are located between stacks. Nevertheless, the anions form weak hydrogen bonds with the C–H fragments of the stacks. Figure 14 shows a fragment of the crystal packing involving two crystallographically independent anions which are located between the stacks.

All these hydrogen bonds are very weak, and their existence does not even preclude disorder of the $Cl(1)O_4^-$ anion. For the ordered perchlorate anion, the parameters of the O(8)···H(12)–C(12), O(5)···H(5)–C(5), and O(6)···H(5)–C(5) hydrogen bonds (the latter two bonds form a bifurcated hydrogen bond) are as follows: 2.42 Å and 154°, 2.52 Å and 135°, and 2.52 Å and 142°, respectively. For the disordered perchlorate anion, most weak interactions correspond to the sum of the van der Waals radii, the C–H···O angles varying from 131° to 156°.

A fragment of the crystal packing of salt **6** is shown in Fig. 15. In this structure, cations are packed in a herringbone-staircase fashion and anions are located between the staircases. The conjugated system of the cation in this structure, unlike that in the structure of salt **5**, is not sufficiently extended to form a pair stacking. It is not inconceivable that the molecules of this compound can also be packed in stacks upon crystallization from aromatic solvents.

In a crystal, perchlorate anions form a network of weak hydrogen bonds O(1)···H(1)–C(1), O(1)···H(11)–C(11), and O(4)···H(2)–C(2) with the following geometric parameters: 2.57 Å and 158°, 2.58 Å and 140°, 2.43 Å and 170°, respectively.

Qualitative consideration of the crystal packings of viologen analogues available in the CSD shows that almost all known types of supramolecular architectures were found in this study. The packing of these cations in stacks occurs rarely and only if either the coordination compounds $[M(d^8)X_4]^-$ (X is halogen) or carbanions, such as trisubstituted methanides (trinitromethanide or tricyanomethanide), serve as anions. These structures contain infinite stacks consisting of alternating cations and anions. When halogens (I^- or Cl^-), which are characterized by rather small sizes, are used as counterions, their influence on the supramolecular architecture is too strong, because these anions (especially I^-) tend to form extensive hydrogen-bond networks. In this case, the possible supramolecular architecture is much more difficult to predict. Structures of viologen analogues containing F^- as the counterion are lacking in the CSD.

CONCLUSIONS

On the basis of the comparative analysis of the geometric features of the cations in salts **1**–**6**, their crystal packings, and the related data available in the CSD, the following conclusions can be made:

In the crystalline state, the molecular cations of acceptors **1**–**6** have a nearly planar system of two pyridine rings. This is indicative of the possible occurrence of full stacking in CTCs containing these cations as acceptors.

In all cations, the substituents at the nitrogen atoms are oriented in opposite directions from the mean plane of the pyridine rings. Hence, the acceptor is preorganized for the formation of 2 : 1 rather than 1 : 1 CTCs.

The presence of perchlorate anions in the packing and the Coulomb repulsion between the cations are the main factors that hinder the stacked packing of the molecules and do not preclude the packing of molecules in a staircase fashion.

Perchlorate anions can play a destructive role against stacking interactions in the systems under consideration. In particular, anions can be inserted between a donor and an acceptor. Presumably, CTCs with such acceptor compounds can be synthesized with the use of other counterions which are less prone to hydrogen bonding.

The involvement of new elements (for example, aromatic solvents) in a supramolecular system can stabilize the stacked packing of this system.

ACKNOWLEDGMENTS

This study was supported by the Russian Foundation for Basic Research (project nos. 01-03-32474, 03-03-32178, and 03-03-32929), INTAS (grant no. 2001-0267), the Ministry of Science and Technology of the Russian Federation, and the Russian Academy of Sciences. L.G. Kuz'mina and A.V. Churakov acknowledge the support from the Royal Society and the Royal Society of Chemistry (Journals Grant for International Authors).

REFERENCES

1. E. N. Ushakov, S. P. Gromov, A. I. Vedernikov, *et al.*, J. Phys. Chem. A **106**, 2020 (2002).
2. K. P. Butin, A. A. Moiseeva, S. P. Gromov, *et al.*, J. Electroanal. Chem. **547**, 93 (2003).
3. S. P. Gromov, E. N. Ushakov, A. I. Vedernikov, *et al.*, Org. Lett. **1**, 1697 (1999).
4. I. S. Alaverdian, A. V. Feofanov, S. P. Gromov, *et al.*, J. Phys. Chem. A **107**, 9542 (2003).
5. C. Janiak, J. Chem. Soc. Dalton Trans. 3885 (2000).
6. F. Vögtle, *Supramolecular Chemistry. An Introduction* (Wiley, Chichester, 1991), p. 290.
7. P. Y. White and L. A. Summers, Aust. J. Chem. **30**, 1153 (1977).
8. S. Hünig, J. Gross, E. F. Lier, and H. Quast, Liebigs Ann. Chem. 339 (1973).
9. H. Andrews, S. Skidmore, and H. Suschitzky, J. Chem. Soc. 2370 (1962).
10. *SAINT. Version 6.02A* (Bruker AXS, Madison, WI, 2001).
11. *SHELXTL-Plus. Release 5.10* (Bruker AXS, Madison, WI, 1997).
12. F. H. Allen, Acta Crystallogr., Sect. B: Struct. Sci. **58**, 380 (2002).
13. K. Müller-Dethlerfs and P. Hobza, Chem. Rev. **100**, 143 (2000).
14. *Comprehensive Supramolecular Chemistry*, Ed. by J. L. Atwood (Pergamon, Oxford, 1996), Vol. 6, p. 1.
15. G. Desiraju, J. Chem. Soc. Chem. Commun. 1475 (1997).
16. Yu. V. Fedorov, O. A. Fedorova, E. N. Andryukhina, *et al.*, New J. Chem. **27**, 280 (2003).
17. S. P. Gromov, A. I. Vedernikov, E. N. Ushakov, *et al.*, Helv. Chim. Acta **85** (1), 60 (2002).
18. O. A. Fedorova, Yu. V. Fedorov, A. I. Vedernikov, *et al.*, New J. Chem. **26**, 543 (2002).
19. M. V. Alfimov, A. V. Churakov, Y. V. Fedorov, *et al.*, J. Chem. Soc. Perkin Trans. 2249 (1997).
20. H. Takahashi, S. Tsuboyama, Y. Umezawa, *et al.*, Tetrahedron **56**, 6185 (2000).

Translated by T. Safonova

Crystallography Reports, Vol. 50, No. 2, 2005, pp. 254–261. Translated from Kristallografiya, Vol. 50, No. 2, 2005, pp. 287–294.

LATTICE DYNAMICS AND PHASE TRANSITIONS

Neutron-Scattering Study of the Dynamics of Ammonium in Different Phases of Halides of $K_{1-x}(NH_4)_xHal$ Mixed Crystals

I. Natkaniec[1, 2], L. S. Smirnov[2, 3], and L. A. Shuvalov†[4]

[1] *Niewodniczanski Institute of Nuclear Physics, Polish Academy of Sciences, ul. Radzikowskiego 152, Krakow, 31-342 Poland*

[2] *Joint Institute for Nuclear Research, ul. Zholio-Kyuri 6, Dubna, Moscow oblast, 141980 Russia*

[3] *State Science Center of the Russian Federation, Institute of Theoretical and Experimental Physics, Bol'shaya Cheremushkinskaya ul. 25, Moscow, 117218 Russia*

e-mail: lsmirnov@nf.jinr.ru

[4] *Shubnikov Institute of Crystallography, Russian Academy of Sciences, Leninskiĭ pr. 59, Moscow, 119333 Russia*

Received August 7, 2003

Abstract—The effect of temperature and the concentration of ammonium on the lattice parameters and the amplitude-weighted phonon density of states in mixed salts of ammonium potassium halides is studied by neutron powder diffraction and incoherent inelastic neutron scattering. It is found that at 10 K incoherent inelastic neutron scattering spectra show four different excitation modes of ammonium: two resonant excitations below the cutoff energy of the phonon density of states of potassium halide and two localized excitations above the cutoff energy. The high-energy localized modes correspond to translational and librational vibrations of NH_4 ions in the crystal lattice. These modes are typical of ordered phases of ammonium halides. © *2005 Pleiades Publishing, Inc.*

INTRODUCTION

With decreasing temperature, ammonium halides undergo a series of structural phase transitions: α–β–δ in NH_4Cl, α–β–γ–δ in NH_4Br, and α–β–γ in NH_4I [1]. The α and β phases have cubic structures of the NaCl and CsCl types, respectively, with disordered arrangement of ammonium ions in the lattice. In the α phase, NH_4 tetrahedra are octahedrally surrounded by halide ions. It is generally accepted that NH_4 ions adapt themselves to the site symmetry C_{3v} in such a way that the bond formed by one of the hydrogen atoms is directed along the body diagonal of the cube ⟨111⟩, whereas the other hydrogen atoms of the ammonium ion are located at minimum distances from the nearest halogen atoms [2, 3]. The cubic symmetry of this phase is stabilized by fast reorientations of the NH_4 group between eight symmetrically equivalent positions. In the β phase, NH_4 groups are reoriented between two energetically equivalent orientations within the cubic environment formed by halide anions [4].

The anharmonic effects associated with the fast reorientation of ammonium ions at temperatures above ~100 K hinder the study of the harmonic lattice dynamics of disordered phases of pure ammonium halides. Preparation of solid solutions of ammonium potassium halides at room temperature was investigated in [5]. It was shown that $K_{1-x}(NH_4)_xI$ mixed crystals are formed throughout the concentration range of ammonium and $K_{1-x}(NH_4)_xBr$ and $K_{1-x}(NH_4)_xCl$ mixed crystals are formed in limited ranges of ammonium concentration. Further study of the *x*–*T* phase diagrams of mixed crystals of ammonium potassium halides in the concentration section at low temperatures showed that, with an increase in the ammonium concentration, those phases are reproduced that are observed with decreasing temperature from high to liquid helium temperature in pure ammonium halides [6–11]. This allows one to investigate the harmonic lattice dynamics of disordered phases and quantum-mechanical effects in the dynamics of NH_4 groups.

However, the *x*–*T* phase diagram of mixed crystals containing alkali metals, ammonium, and halogens becomes more complex at low temperatures owing to the formation of additional concentration ranges with structures that are absent in pure ammonium halides. The system of $K_{1-x}(NH_4)_xI$ mixed crystals has been investigated by different physical methods during last 15 years and has undergone a complex evolution predominantly in the average concentration range. The first observation (by dielectric spectroscopy) of the orientational glass state in $K_{1-x}(NH_4)_xI$ mixed crystals with concentrations $x = 0.14$ and 0.43 with "freezing" temperatures $T_g = 4.5$ and 18 K, respectively, was reported in [6]. Then, using X-ray diffraction and Raman and neutron scattering, the first *x*–*T* phase diagram of $K_{1-x}(NH_4)_xI$ mixed crystals was obtained in [7].

† Deceased.

It was shown in [7] that mixed crystals in the concentration range $0.82 < x < 0.92$ undergo $\alpha \Leftrightarrow \beta$ phase transitions with a large hysteresis; for compositions with $x < 0.72$, phase transitions are not observed; and the concentrations in the range from 0.72 to 0.82 are considered to be the critical concentrations x_c, below which (in the range $0.3 \le x < x_c$) the orientational glass phase is formed. In subsequent studies [8–10], the concentration dependence of the x–T phase diagram of $K_{1-x}(NH_4)_xI$ mixed crystals was studied in more detail. Using neutron single-crystal diffraction, Paasch *et al.* [9, 10] found in the concentration range $0.55 \le x \le 0.75$ a new phase (ε phase) with a crystal structure belonging to the space group $R3m$. The existence of the ε phase in $K_{1-x}(NH_4)_xI$ mixed crystals was confirmed in [11]. The concentration ranges of the orientational glass phase in $K_{1-x}(NH_4)_xI$ mixed crystals below $x = 0.55$ are different in [8, 9, 11] since these are divided into different subranges, for example, g_1, g_2, and g_3, with different boundaries [8, 9]. According to [11], the section of the x–T phase diagram at a temperature of 1 K depending on the lattice parameter a of $K_{1-x}(NH_4)_xI$ mixed crystals of the NaCl type at room temperature can be represented as follows:

$$\text{KI} \Leftrightarrow \alpha \text{ phase} \Leftrightarrow (7.115\ \text{Å}) \Leftrightarrow \text{OC} \Leftrightarrow (7.17\ \text{Å})$$
$$\Leftrightarrow \text{SRO} \Leftrightarrow (7.185\ \text{Å})$$
$$\Leftrightarrow \varepsilon \text{ phase} \Leftrightarrow (7.225\ \text{Å}) \Leftrightarrow \beta \text{ phase} \Leftrightarrow (7.255\ \text{Å})$$
$$\Leftrightarrow \gamma \text{ phase} \Leftrightarrow NH_4I.$$

Potassium halides lightly doped with ammonium were used to study the rotational tunneling transitions in NH_4 ions [12–15]. The results obtained demonstrated that the tunneling transitions in ammonium ions can be adequately described by the single-ion approximation [4, 12]. With an increase in the ammonium concentration, collective behavior arises due to the increasing role of ammonium–ammonium interactions [13, 14]. It has been suggested that the rotational tunnel excitations are suppressed by the formation of the orientational glass phase in $K_{1-x}(NH_4)_xI$ mixed crystals [13]. A temperature study demonstrated that there is a continuous transition from the quantum ($T < 5$ K) to classical ($T > 20$ K) nature of reorientational motion [12, 13]. The model of rotational tunneling states in the energy range up to 8 meV was proposed for NH_4-doped KBr crystals [15].

Investigation of $K_{1-x}(NH_4)_xI$ mixed crystals at 20 K in the concentration range $0.05 < x < 0.7$ by incoherent inelastic neutron scattering (IINS) revealed three pronounced inelastic features at 10, 21, and 31 meV [16]. Our neutron scattering studies of $K_{1-x}(NH_4)_xI$ mixed salts demonstrated an additional band at 2.5 meV [17, 18].

In this study, we examine the influence of the NH_4 concentration on the ammonium dynamics and the order–disorder phase transition in $K_{1-x}(NH_4)_xI$ mixed salts at 10 K. We also present the results obtained for the α phase of $K_{0.95}(NH_4)_{0.05}Br$ and $K_{0.95}(NH_4)_{0.05}Cl$ mixed salts.

EXPERIMENTAL RESULTS

Mixed crystals of ammonium potassium halides were prepared by evaporation of the corresponding stoichiometric aqueous solutions at a pressure of about 10 Pa at room temperature. Powder samples were dried for several hours at 50°C under normal pressure before the neutron scattering experiments. The neutron scattering spectra of the powder samples were measured on an IBR-2 high-flux pulsed reactor using the time-of-flight technique on an NERA high-resolution inverse-geometry spectrometer [19]. The neutron powder diffraction (NPD) and IINS spectra were measured simultaneously. The NPD spectra were recorded at four scattering angles (45°, 69°, 135°, and 144°). The IINS spectra were measured at 15 scattering angles in the range from 20° to 160°. The energy of incident neutrons was determined from the time of flight using a path length of 109.05 m between the neutron moderator and the sample. The energy of inelastically scattered neutrons was fixed at an average value of $E_0 = 4.53$ meV (which corresponds to the wavelength $\lambda_0 = 4.25$ Å) using a beryllium filter and pyrolytic-graphite analyzers. The full width at half maximum of the elastic peak of the NERA spectrometer was 0.6 meV.

NPD spectra make it possible to monitor the phase of the samples under study and investigate the concentration and temperature dependences of the lattice parameters. The dependence of the parameter a of the cubic lattice of the disordered α phase in the concentration range $0.05 < x < 0.60$ and the parameters a and c of the tetragonal lattice of the ordered γ phase for $x = 0.8$ and 1.0 in $K_{1-x}(NH_4)_xI$ mixed crystals at 10 K were determined from the NPD spectra and used to calculate the concentration dependence of the volume per formula unit [20].

In Fig. 1, the IINS spectra of $K_{0.95}(NH_4)_{0.05}Br$ measured at 290, 80, and 10 K are compared with the IINS spectrum of KBr measured at 80 K. The spectra, measured as a function of the incident-neutron wavelength, are summed over 15 scattering angles and normalized to the same number of incident neutrons and the same bromine concentration. The IINS spectrum measured at 290 K is indicative of a broad excitation-energy distribution of ammonium in the range from about 1 to 4.25 Å (the position of the elastic peak). Incoherent quasi-elastic neutron scattering (IQENS) observed on the wings of the elastic peak indicates the fast stochastic reorientation of NH_4 ions. The profile of the IQENS line is described by a Lorentzian whose position on the wavelength scale coincides with the position of the Gaussian describing the elastic peak intensity at the wavelength $\lambda_0 = 4.25$ Å. At the same time, while the width at half maximum of the Gaussian describes the

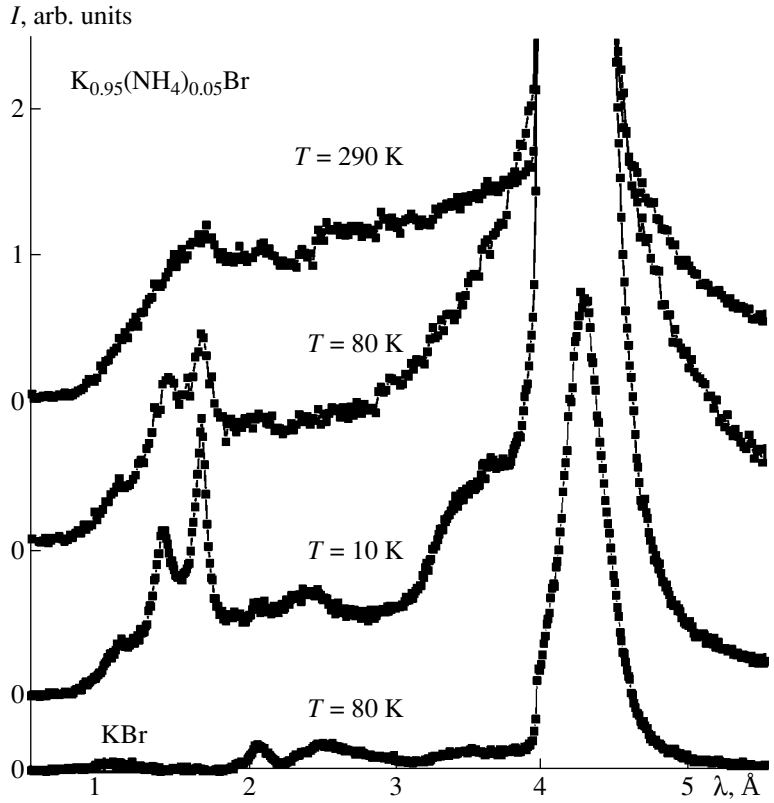

Fig. 1. Incoherent inelastic neutron scattering spectra of a $K_{0.95}(NH_4)_{0.05}Br$ mixed crystal at 10, 80, and 290 K and KBr at 80 K.

resolution function of the spectrometer, the width at half maximum of the Lorentzian is proportional to the frequency of reorientations of ammonium ions. However, with decreasing temperature, the linewidth of the Lorentzian describing the IQENS contribution is narrowed due to the decrease in the frequency of reorientations of ammonium ions, which is accompanied by the decrease in the contribution of the quasi-elastic scattering intensity at the wings of the elastic line. The spectrum measured at 80 K contains peaks corresponding to translational and librational excitations of ammonium (at wavelengths of about 1.65 and 1.45 Å, respectively) above the band of lattice vibrations of an KBr crystal, whose cutoff energy corresponds to the incident-neutron wavelength of about 2 Å. In the region of lattice vibrations of KBr, the IINS spectrum of a $K_{0.95}(NH_4)_{0.05}Br$ mixed crystal at 10 K shows two additional excitations at 2.4 and 3.5 Å.

The amplitude-weighted phonon densities of states $G(E)$ calculated from the IINS spectra in the approximation of one-phonon incoherent scattering [21] are shown in Fig. 2. Four pronounced bands, which correspond to vibrational excitations of ammonium ions in the disordered α phase of $K_{0.95}(NH_4)_{0.05}Br$, are clearly observed at 10 K. Two bands in the phonon spectrum of KBr are generally referred to as resonance modes. The modes corresponding to the band at 2.5 meV may be due to rotational tunneling excitations [4, 12–15], while the mode corresponding to the band at 9 meV is associated with librations of the ammonium ion around its dipole axis [16]. The modes at energies of 25 and 38.75 meV are related to localized translational and librational vibrations (perpendicular to the dipole axis) of ammonium ions, respectively. These two modes were observed for the ordered phase of NH_4Br with energies of 20 and 42.9 meV, respectively [22].

The temperature dependence of the amplitude-weighted phonon density of states $G(E)$ for a $K_{0.95}(NH_4)_{0.05}Cl$ mixed crystal is shown in Fig. 3. The $G(E)$ spectrum of $K_{0.95}(NH_4)_{0.05}Cl$ shows quite strong lattice vibrations of KCl due to a relatively high scattering cross-section of chlorine atoms. The low-energy resonance mode of ammonium with an energy of 2.5 meV has a high intensity at 10 K. The second resonance mode is lost against the high background of lattice vibrations of potassium chloride and is expected to appear at higher ammonium concentrations. The localized translational and librational modes are well defined with energies of 28.75 and 42.5 meV, respectively. The corresponding modes in the ordered phase of NH_4Cl were observed with energies of 22.5 and 49.4 meV, respectively [22].

We studied ammonium potassium iodide in wide concentration ($0.0 < x < 1.0$) and temperature (10–290 K) ranges [17, 18]. The results of our studies of the

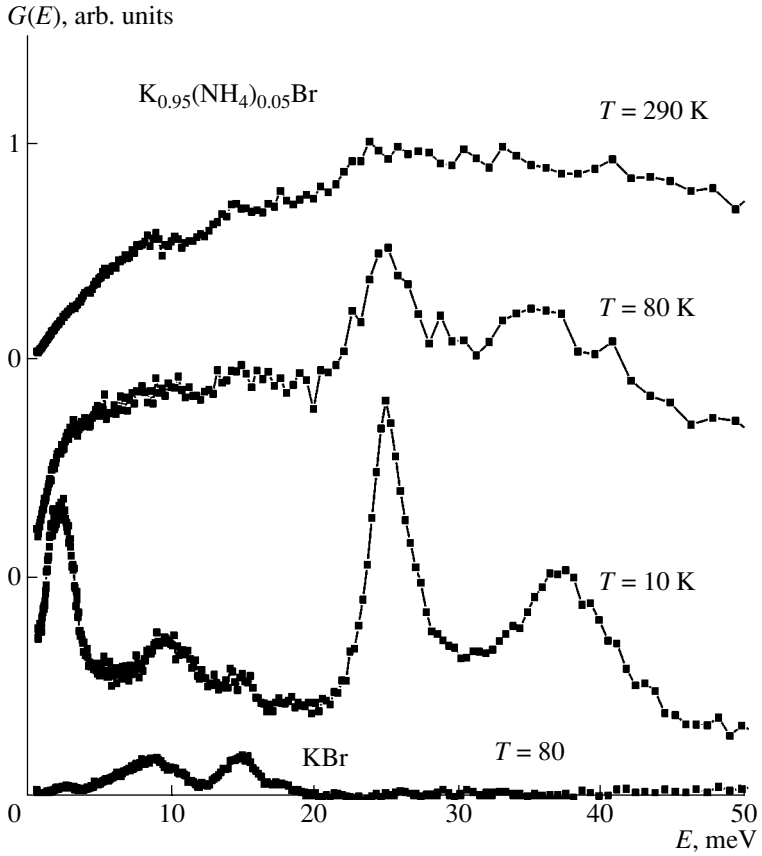

Fig. 2. Amplitude-weighted phonon density of states $G(E)$ for KBr at 80 K and a $K_{0.95}(NH_4)_{0.05}Br$ mixed crystal at 10, 80, and 290 K.

inelastic neutron scattering (INS) spectra of $K_{1-x}(NH_4)_xI$ solid solutions at 10 K are shown in Fig. 4. The $G(E)$ spectra of the disordered α phase in the concentration range $0.05 < x < 0.60$ clearly show four modes of ammonium with energies of 2.5, 8.75, 21.9, and 31.25 meV. The bandwidths of these modes are larger than the spectrometer resolution width. The $G(E)$ spectra of the γ phase demonstrate only localized modes of ammonium. Their bands with energies of 18.75 and 37.5 cm^{-1}, denoted as ν_5 and ν_6, correspond, respectively, to the translational and librational phonon modes of NH_4 groups in the crystal. The INS spectra of the ordered phases of ammonium halides, measured at low temperatures, also contain bands at higher energies, which correspond to the $\nu_5 + \nu_6$ combination band and excitations of higher harmonics, for example, $2\nu_6$. These bands are very weak in the $G(E)$ spectra of the disordered α phase. The mode ν_6 manifests itself as the most intense band in the $G(E)$ spectra of the γ phase, whose width is close to the resolution of the NERA spectrometer. The corresponding band in the spectrum of the α phase is broader and weaker and its energy decreases from 37.5 to 31.25 meV. This decrease in the energy of the librational mode at the order–disorder phase transition is consistent with the increase in the volume per formula unit [20]. The energy of translational phonons for the disordered α phase slightly decreases when the lattice expands due to the increase in the ammonium concentration (see Fig. 4). For these excitations, the $G(E)$ spectrum changes only slightly at the transition from the α to the γ phase. The excitation with an energy of 8.75 meV was attributed to librations of ammonium ions around the dipole axis under the assumption that tetrahedral ammonium ions adapt themselves to the octahedral environment formed by halogen atoms with the site symmetry C_{3v} [16]. The energy of this excitation slightly increases with an increase in the ammonium concentration in mixed salts (despite the lattice expansion).

It is likely that the broad resonance mode with an energy of 2.5 meV, which was observed in our studies of mixed ammonium potassium halides, corresponds to the tunneling transitions of ammonium tetrahedra in the octahedral field of halide ions. At low ammonium concentrations ($x < 0.01$) and low temperatures ($T < 5$ K), these transitions are observed as narrow peaks in the INS spectra [12–15]. These excitation peaks broaden as the concentration and temperature increase. In the case under consideration ($T = 10$ K and $0.05 < x < 0.6$), the low-energy excitations are convolved with the resolu-

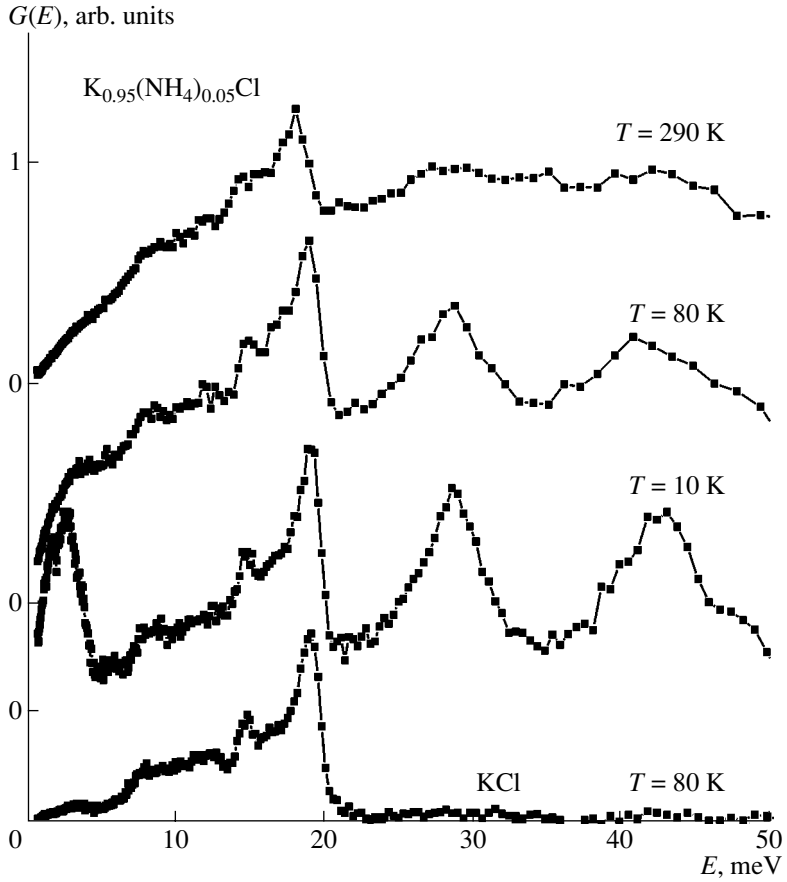

Fig. 3. Amplitude-weighted phonon density of states $G(E)$ for KCl at 80 K and a $K_{0.95}(NH_4)_{0.05}Cl$ mixed crystal at 10, 80, and 290 K.

tion function of the NERA spectrometer [19], which is similar to the Gaussian with a full width at half maximum of about 0.625 meV, if the transferred energy is 2.5 meV. Under these conditions, "tunneling transitions" are observed as a broad band at an energy of 2.5 meV, whose maximum and width slightly increase with an increase in the ammonium concentration. Our present study of a $K_{0.55}(NH_4)_{0.45}I$ sample demonstrates that the width of the band at 2.5 meV increases with an increase in temperature. At approximately 30–40 K, this band disappears, transforming into broad quasielastic wings [23].

DISCUSSION AND CONCLUSIONS

The amplitude-weighted phonon density of states $G(E)$ of ammonium in ammonium potassium halides with NaCl-type structure was measured in the entire energy range of lattice vibrations in the α phase. The ammonium dynamics in this phase is characterized by four pronounced bands, whose energies are shown in Fig. 5 as functions of the nitrogen–halogen distance. The energies of the translational (ν_5) and librational (ν_6) modes of ammonium in low-temperature ordered phases of ammonium halides with CsCl-type structure are also shown in Fig. 5 for comparison. The transition from the NaCl to CsCl type is related to the increase in the nitrogen–halogen distance (in the cubic-structure approximation, from $a/2$ to $(3a)^{1/2}/2$, where a is the halogen–halogen distance). This indicates that the translational modes ν_5 have higher energies in the α phase than in ordered phases of ammonium halides. The librational modes ν_6 of ammonium ions are influenced more by the geometry and the number of surrounding halogen atoms (which varies from six in the octahedral α phase to eight in the ordered cubic α phase or tetragonal β phase). The energies of the librational modes in the β and γ phases of ammonium halides exceed those in the α phase in spite of the large nitrogen–halogen distances.

The existence of two additional bands with lower excitation energies of ammonium in the α phase can be explained in terms of the so-called model of triple approximation, in which tetrahedral ammonium ions are adapted to the site symmetry C_{3v} in the octahedral environment of halide ions. Three rotational degrees of freedom of the ammonium tetrahedron, which are triply degenerate (F_1) within the site symmetry O_h in the cubic cell, are split into the modes E and A_2 within the

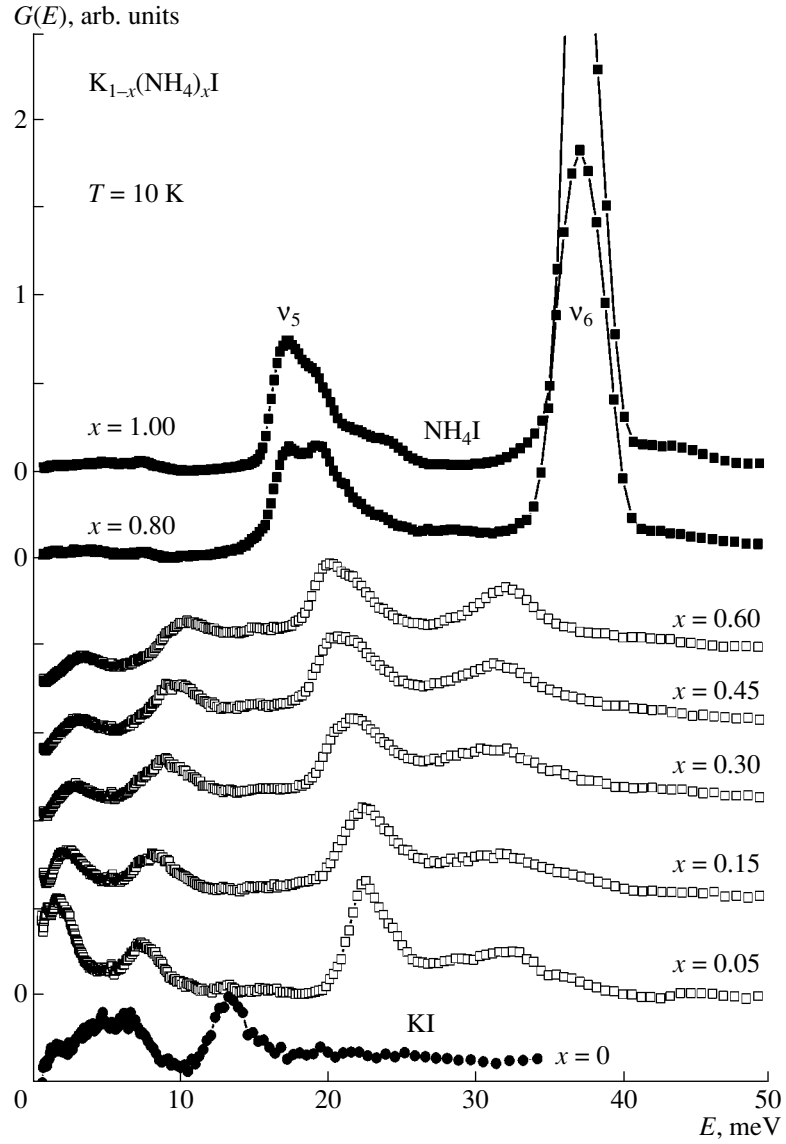

Fig. 4. Concentration dependences of the amplitude-weighted phonon density of states $G(E)$ for KI at 80 K (filled circles) and for the α phase (open squares) and the γ phase (filled squares) of $K_{1-x}(NH_4)_xI$ mixed crystals at 10 K.

site symmetry C_{3v}. The doubly degenerate mode ν_E relates the librations of ammonium ions around the axis perpendicular to the dipole moment directed along the C_{3v} symmetry axis [16]. The low energy of the ν_A mode suggests very low potential barriers for librations of ammonium ions around the C_{3v} symmetry axis and large splitting of the tunneling states [15]. The tunneling spectra are very sensitive to the ammonium concentration, and the lines below about 1.25 meV completely collapse into a quasi-elastic line at $x = 0.28$ [13]. The concentration dependence of higher frequency tunneling transitions has yet to be studied. In our spectra of the α phase of $K_{1-x}(NH_4)_xI$ mixed salts, the low-energy band at approximately 2.5 meV was observed at $T = 10$ K throughout the concentration range $0.05 < x < 0.6$ (see Fig. 4).

The concentration dependences of the average excitation energies of ammonium in $K_{1-x}(NH_4)_xI$ mixed salts are shown in Fig. 6. According to the present-day knowledge of the x–T phase diagram of $K_{1-x}(NH_4)_xI$ solid solutions, our samples of mixed ammonium potassium iodides with x of approximately 0.6 or 0.8 should correspond to the ε and β phases, respectively [9, 10]. The occurrence of the structural transition from the NaCl-type ε phase [10] to the CsCl-type β phase is confirmed by the NPD and INS spectra measured by us (see [20] and Fig. 4). A significant difference in the ammonium dynamics is observed only for these types of crystal lattices. The amplitude-weighted phonon density of states $G(E)$ for the α phase at 10 K is absolutely identical throughout the concentration range $0.05 < x < 0.6$. Local distortions, which violate the fcc

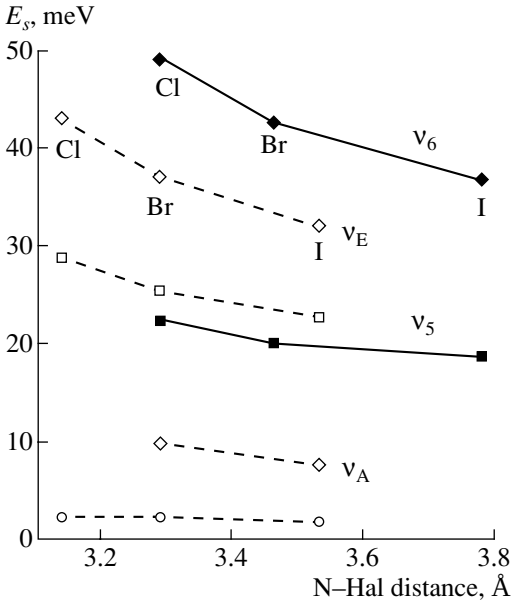

Fig. 5. Comparison of the average excitation energies E_s of ammonium in the disordered α phase of $K_{0.95}(NH_4)_{0.05}Hal$ mixed crystals (Hal = Br, Cl, or I) at 10 K (dashed lines) and in the ordered phases of ammonium halides at low temperatures (solid lines).

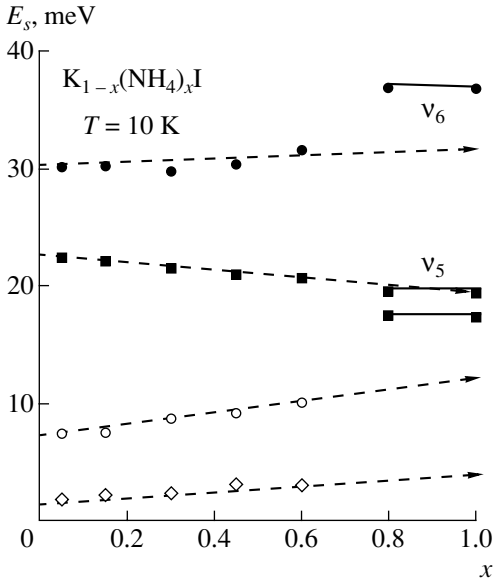

Fig. 6. Concentration dependences of the average excitation energies E_s of ammonium in the α phase (dashed lines) and the γ phase (solid lines) of $K_{1-x}(NH_4)_xI$ mixed salts at 10 K.

symmetry in glass phases, and the complex dipole order in the ε phase seem to be of less importance than the simple concentration dependence of the average excitation energies of ammonium. Hence, it appears to be reasonable to approximate the average energies of these excitations by a hypothetical α phase of ammonium iodide at low temperatures. It would be of interest to calculate the dynamics of lattice vibrations for the α phase with the antiferroelectric ordering of ammonium ions or for the ε phase with the complex dipole ordering and to compare these data with the experimental $G(E)$ spectra reported here. Calculations of the lattice dynamics for the ordered phase of ammonium chloride using the rigid-molecule model [24] adequately account for the experimental dispersion curves for ND_4Cl and the $G(E)$ spectra of NH_4Cl. The model of lattice dynamics used to study the dispersion curves for the α phase of ND_4Cl at 296 K [25] can account only for the translational band in the $G(E)$ spectra shown in Fig. 4.

It is unlikely that interactions in dipole glasses, which are similar to interactions in spin glasses, change the energies in the vibrational spectrum. However, these interactions can affect the width of certain bands in this spectrum [16]. The widths of the four bands corresponding to different excitations of ammonium in the α phase of ammonium potassium halides exceed the width of the resolution function. These bandwidths slightly increase with an increase in the ammonium concentration for the low-energy resonance modes and translational modes but decrease for the librational mode ν_E. However, it is difficult to perform their qualitative analysis because we measured the state density but did not estimate the width of the excitation band at well-determined transferred energy and momentum. The concentration dependences of the average excitation energies for ammonium in the α phase of $K_{1-x}(NH_4)_xI$ solid solutions are shown in Fig. 6. The average energies of the low-frequency resonance modes increase with an increase in the ammonium concentration in spite of the lattice expansion. This indicates that the direct ammonium–ammonium interaction affects the potential barrier that hinders the rotation around the C_{3v} dipole axis.

ACKNOWLEDGMENTS

We are grateful to A.I. Solov'ev for preparing samples of mixed salts and S.I. Bragin† for his help in measuring the neutron spectra.

This study was supported in part by the State Committee for Scientific Research of Poland (grant no. 2 PO3B 012 12), the Russian Foundation for Basic Research (project no. 02-02-17330), and the Leading Scientific School of L.A. Shuvalov (project no. NSh-1514.2003.2).

REFERENCES

1. G. N. Parsonage and L. A. K. Staveley, *Disorder in Crystals* (Clarendon Press, Oxford, 1978), Chap. 7.5.

† Deceased.

2. H. A. Levy and S. W. Peterson, J. Am. Chem. Soc. **75**, 1536 (1953).
3. R. S. Seymour and A. W. Pryor, Acta Crystallogr. **626**, 1487 (1970).
4. W. Press, *Single Particle Rotations in Molecular Crystals* (Springer, Berlin, 1981), Springer Tracts Mod. Phys., Vol. 92, Chap. 2.
5. R. J. Havighurst, E. Mack, Jr., and F. C. Blake, J. Am. Chem. Soc. **47**, 29 (1925).
6. I. Fehst, R. Böhmer, W. Ott, *et al.*, Phys. Rev. Lett. **64**, 3139 (1990).
7. J. F. Berret, C. Bostoen, and B. Hennion, Phys. Rev. B **46**, 13747 (1992).
8. M. Winterlich, R. Böhmer, and A. Loidl, Phys. Rev. Lett. **75**, 1783 (1995).
9. M. Paasch, M. Winterlich, R. Böhmer, *et al.*, Z. Phys. B: Condens. Matter **99**, 333 (1996).
10. M. Paasch, G. J. McIntyre, M. Reehuis, *et al.*, Z. Phys. B: Condens. Matter **99**, 339 (1996).
11. F. Güthoff, M. Ohl, M. Reehuis, and A. Loidl, Physica B (Amsterdam) **266**, 310 (1999).
12. A. Heidemann, J. Howard, K. J. Lushington, *et al.*, J. Phys. Soc. Jpn. **52**, 2401 (1983).
13. C. Bostoen, G. Coddens, and W. Wegener, J. Chem. Phys. **91**, 6337 (1989).
14. R. Mukhopadhyay, J. Tomkinson, and C. J. Carlile, Europhys. Lett. **17**, 201 (1992).
15. A. Inaba, H. Chihara, J. A. Morrison, *et al.*, J. Phys. Soc. Jpn. **59**, 522 (1990).
16. J. Tomkinson, B. A. Dasannacharya, P. S. Goyal, and R. Chakravarthy, J. Chem. Soc., Faraday Trans. **87**, 3431 (1991).
17. I. Natkaniec and L. S. Smirnov, Physica B (Amsterdam) **234–236**, 409 (1997).
18. I. Natkaniec, L. S. Smirnov, S. I. Bragin, and A. I. Solov'ev, Crystallogr. Rep. **45**, 211 (1998).
19. I. Natkaniec, S. I. Bragin, J. Brankowski, and J. Mayer, in *Proceedings of the ICANS XII Meeting, Abingdon, 1993*, Ed. by U. Steigenberger, T. Brome, G. Rees, and A. Soper (1994), RAL Report No. 94-025, Vol. 1, p. 89.
20. I. Natkaniec and L. S. Smirnov, Phase Transit. **76**, 873 (2003).
21. E. L. Bokhenkov, I. Natkaniec, and E. F. Sheka, Sov. Phys. JETP **43**, 536 (1976).
22. A. Bajorek, T. Matchekhina, and K. Parlinski, in *Proceedings of Symposium on Inelastic Scattering of Neutrons, Bombay, 1964* (IAEA, Vienna, 1965), Vol. 2, p. 355.
23. I. Natkaniec, L. S. Smirnov, and A. I. Solov'ev, in *Proceedings of National Conference on Materials Investigation by X-ray, SR, Neutrons and Electrons* (Dubna, 1997), JINR Report, Vol. 3, p. 25.
24. C. H. Kim, H. A. Rafizadeh, and S. Yip, J. Chem. Phys. **57**, 2291 (1972).
25. N. Vegelatos, J. M. Rowe, and J. J. Rush, Phys. Rev. B **12**, 4522 (1975).

Translated by Yu. Sin'kov

Crystallography Reports, Vol. 50, No. 2, 2005, pp. 262–269. Translated from Kristallografiya, Vol. 50, No. 2, 2005, pp. 295–302.

LATTICE DYNAMICS AND PHASE TRANSITIONS

Influence of Striction on Soliton Interaction in Crystals

S. A. Minyukov*, A. P. Levanyuk, and A. Cano****

** Shubnikov Institute of Crystallography, Russian Academy of Sciences, Leninskiĭ pr. 59, Moscow, 119333 Russia*

e-mail: minyukov@ns.crys.ras.ru

*** Universidad Autonoma de Madrid, Madrid, E-28049 Spain*

e-mail: levanyuk@uam.es

Received November 4, 2004

Abstract—Striction-mediated attraction of domain walls, solitons in incommensurate phases, and Abrikosov vortices in superconductors are considered. It is shown (a) that it is this type of attraction that can be responsible for a soliton-density jump in lock-in transitions and (b) that the strain-induced vortex interaction in superconductors with a high Ginzburg–Landau parameter is higher by one or two orders of magnitude than was assumed earlier. © *2005 Pleiades Publishing, Inc.*

INTRODUCTION

The influence of long-range elastic interactions on the properties of modulated phases, which are the regular structures of solitons, has long attracted attention in connection with the study of the properties of various systems such as dielectrics possessing structurally incommensurate phases [1] and second-order superconductors with Abrikosov-vortex lattices [2, 3]. Usually, this problem in incommensurate phases was studied with the aim to establish whether a lock-in transition is continuous or the soliton density at the transition point changes in a jumpwise manner. As a rule, the mechanisms that could give rise to a soliton-density jump were examined with no allowance for the striction effect. At the same time, in studies of vortex-lattice orientations in crystals, the striction-mediated interaction in superconductors was often considered as one of the main types of interactions. Such interaction was usually calculated based on a simplified model under the assumption that the elastic strains inducing vortex interactions are due only to vortex cores. However, it turned out that the interactions in these studies were considerably underestimated. Therefore, the present study is dedicated to the consideration of these problems.

At the beginning, the striction effect is considered on the simplest example of domain walls described by the one-dimensional distribution of a one-component order parameter. This example allows us to reveal the characteristic features of this interaction and to evaluate it for different types of domain walls. Then, following the concepts stated in [4, 5], we calculate the striction-mediated attraction of two-dimensional solitons in incommensurate phases and Abrikosov vortices in superconductors. Some computations are performed by a method somewhat different from the method used in the studies cited above, and some of the results obtained are considered in more detail.

A POLYDOMAIN CRYSTAL

Consider a polydomain structure described by a spatially inhomogeneous distribution of a one-component order parameter $\eta(x)$. The order parameter inside a domain wall is inhomogeneous and, at a certain point, goes to zero. Variation of the order parameter inside the wall should change the crystal strains in such a way that the temperature variation in a certain layer of a crystal undergoes no phase transitions. In this case, the relief at the site of the wall intersection by the surface should be distorted in conformity with relaxation of elastic stresses in the vicinity of the surface. It is natural that the strain and order-parameter distributions in the vicinity of the surfaces and in the crystal bulk are different. The strain distributions in the bulk can be calculated under the condition of zero bulk stresses. Then, in order to obtain the exact solution of the problem, one has to introduce some additional imaging forces having the zero average values at the surface. Since the problem is of a periodic nature, these forces should have a periodic distribution along the surfaces. As is well known [6], these forces give rise to additional strains decreasing in the crystal depth within a characteristic length of the order of the period of a surface-force distribution. Therefore, the contribution of the near-surface distortions to the energy of this regular structure is rather small because of the small ratio of the structure period to the crystal size. However, the distributions in the crystal bulk we are interested in are one-dimensional. It should be indicated that the solution of this elastic problem at the given one-dimensional distribution of the strain sources and arbitrary anisotropy was obtained in [7]. We are interested in the solution of a

more complicated problem in which the spatial distributions of strains and order parameter vary self-consistently.

Consider the case of an elastically isotropic medium and analyze the anisotropic case of an example of a more complicated domain-wall structure in an incommensurate phase. Represent the energy per volume unit of the system, f, in the form

$$f = \frac{1}{V}\int\left[\frac{1}{2}A\eta^2 + \frac{1}{4}B\eta^4 + \frac{1}{2}D\left(\frac{d\eta}{dx}\right)^2 + r\eta^2 u_{ll} + \mu\left(u_{ik} - \frac{1}{3}\delta_{ik}u_{ll}\right)^2 + \frac{K}{2}u_{ll}^2\right]dv, \quad (1)$$

where V is the sample volume, η is the order parameter varying along x, u_{ik} is the strain tensor, μ is the shear modulus, K is the bulk modulus, and $A = A_T(T - T_c) < 0$; i.e., the phase has a low symmetry.

For a homogeneous system, we have

$$\eta_e^2 = -\frac{A}{B'}, \quad u_{lle} = -\frac{r}{K}\eta_e^2, \quad f_{\text{hom}} = -\frac{1}{4}\frac{A^2}{B'}, \quad (2)$$

where $B' = B - 2r^2/K$.

Following [8], we start calculating the energy of a polydomain structure with the solution of the elastic problem. For one-dimensional strain distributions (along the x axis), the corresponding compatibility conditions have the form

$$\frac{d^2u_{zz}}{dx^2} = 0, \quad \frac{d^2u_{yy}}{dx^2} = 0, \quad \frac{d^2u_{yz}}{dx^2} = 0. \quad (3)$$

With due regard for the problem symmetry in the yz plane, only the following solutions of above equations are possible: $u_{zz} = u_{yy} = \tilde{u}$ and $u_{yz} = 0$, where $\tilde{u}$ is a constant.

The equations of the local elastic equilibrium have the form

$$\frac{d\sigma_{xx}}{dx} = 0, \quad \frac{d\sigma_{xy}}{dx} = 0, \quad \frac{d\sigma_{xz}}{dx} = 0, \quad (4)$$

where, in accordance with Eq. (1), elastic stresses have the form

$$\sigma_{ij} = \left(K - \frac{2}{3}\mu\right)u_{ll}\delta_{ij} + 2\mu u_{ij} + r\eta^2\delta_{ij}. \quad (5)$$

Moreover, in the absence of any external stresses, the σ_{ij} values averaged over the bulk should be equal to zero [9]:

$$\langle\sigma_{ij}\rangle = 0. \quad (6)$$

From Eqs. (4)–(6), we have

$$\sigma_{xx} = \left(K + \frac{4}{3}\mu\right)u_{xx} + \left(K - \frac{2}{3}\mu\right)(u_{yy} + u_{zz}) + r\eta^2 = 0, \quad (7)$$

$$\sigma_{xy} = 2\mu u_{xy} = 0, \quad \sigma_{xz} = 2\mu u_{xz} = 0. \quad (8)$$

As a result, the nonzero components of strain are

$$u_{xx} = -\left[\left(K - \frac{2}{3}\mu\right)2\tilde{u} + r\eta^2\right]\Big/\left(K + \frac{4}{3}\mu\right), \quad u_{zz} = u_{yy} = \tilde{u}. \quad (9)$$

Substituting these solutions into Eq. (1), we arrive at the free-energy density in the form

$$f = \frac{1}{2L}\int_{-L}^{L}\left[\left(\frac{A + 2r'\tilde{u}}{2}\right)\eta^2 + \frac{1}{4}B''\eta^4 + \frac{1}{2}D\left(\frac{d\eta}{dx}\right)^2 + \frac{K'}{2}\tilde{u}^2\right]dx, \quad (10)$$

where $2L$ is the sample dimension along the x axis, $r' = 4r\mu/(K + 4\mu/3)$, $K' = 12K\mu/(K + 4\mu/3)$, and $B'' = B - 2r^2/(K + 4\mu/3)$. Then, $\tilde{u}$ may be considered as a certain parameter which, similar to $\eta(x)$, may be determined by minimizing the free energy described by Eq. (10). Assuming that the distance l between the walls is much larger than the wall width, r_c, we may represent the solution for a polydomain structure (with the accuracy of exponentially small corrections) as a sum of the solutions $\sum_m \eta_1(x + ml)$ corresponding to isolated walls

$$\eta(x) = \sum_m \frac{(-A - 2r'\tilde{u})^{1/2}}{B''^{1/2}} \times \tanh\left(\frac{x - ml}{2^{1/2}D^{1/2}/(-A - 2r'\tilde{u})^{1/2}}\right). \quad (11)$$

Substituting Eq. (11) into Eq. (10), we obtain

$$f = -\frac{(A + 2r'\tilde{u})^2}{B''} + \frac{K'}{2}\tilde{u}^2 + \frac{2^{3/2}D^{1/2}(-A - 2r'\tilde{u})^{3/2}}{3B''}n, \quad (12)$$

where $n = l/(2L)$ is the wall concentration. If $n \ll 1$, then, minimizing Eq. (12) with respect to $\tilde{u}$, we obtain

$$f = -\frac{A^2}{4B'} + \frac{2^{3/2}D^{1/2}|A|^{3/2}B''^{1/2}}{3B'^{3/2}}n - \frac{16\mu r^2 D|A|B''^{1/2}}{3\tilde{K}KB'^2}n^2, \quad (13)$$

where $\tilde{K} = K + 4\mu/3$. The second term in the right-hand side of Eq. (13) corresponds to the sum of wall self-energies, whereas the third term corresponds to wall attraction.

Consider the interaction effect in more detail. It should be noted that Eq. (6) yields the ratio $\langle u_{ll}\rangle =$

$-r\langle\eta^2\rangle/K$, which, together with Eq. (9), gives rise to the equalities $u_{zz} = u_{yy} = \tilde{u} = -r\langle\eta^2\rangle/3K$. Then, Eqs. (7), (9), and (11) yield longitudinal stresses as

$$\sigma_{yy} = \sigma_{zz} = \frac{2\mu r(\eta^2 - \langle\eta^2\rangle)}{\tilde{K}} = \frac{2\mu r\eta_e^2}{K}\sum_m\left\{-\frac{1}{\cosh^2\dfrac{x-ml}{2r_c}} + \frac{r_c}{l}\right\}, \quad (14)$$

where $r_c = (DB')^{1/2}/(2|A|B'')^{1/2}$ is the correlation radius. It is seen from Eq. (14) that the walls give rise to longitudinal stresses not only in the regions of their localization but also in the whole crystal bulk, which results in the wall interaction.

INCOMMENSURATE PHASE

In the case of a multicomponent order parameter, striction corresponds to coupling between strain and the squared modulus of the order parameter. Moreover, the striction-mediated interaction strongly depends on the wall type. Thus, in the case of Bloch walls, the modulus of the order parameter, ρ, is constant in the region of wall localization; therefore, there is no wall interaction: the longitudinal stresses have zero values since $\rho^2 - \langle\rho^2\rangle \equiv 0$ (see Eq. (14)). For quasi-Bloch walls characteristic of incommensurate (IC) phases of type I (with the Lifshitz invariant in the free-energy expansion) with weak anisotropy in the space of order-parameter components, the local quantity $\rho^2 - \langle\rho^2\rangle$ has a very low nonzero value [1]. However, in this case, the wall width is of the order of a reciprocal wave vector (q_0) of the structure at the point of the transition "normal (*N*) phase–IC phase," whose typical value is of the order of $10^{-2}d_{at}^{-1}$ (where d_{at} is the interatomic distance). This signifies that, although the additional dilatation is rather small, it arises in extended regions because of a considerably increased wall interaction. It should be emphasized that the case of weak anisotropy has drawn great interest because the continuity of the lock-in transition in systems having no long-range interactions was rigorously proven [10]. This case is described in detail elsewhere [4]. Here, we only derive the basic relationships for the energy of soliton interaction in the vicinity of such a transition by a somewhat modified method.

In the simplest case, an IC phase is described by a one-dimensional modulation (along the *x* axis) of a certain two-component order parameter ($\eta_1 = \rho\cos\varphi$ and $\eta_2 = \rho\sin\varphi$, where ρ is the amplitude and φ is the phase of the order parameter). This order parameter describes lowering of the symmetry in the transition from the normal phase to the low-symmetric commensurate C phase. Then, free energy may be represented as

$$f = \frac{1}{V}\int\Big[\alpha\rho^2 + \beta\rho^4 + \gamma\rho^m\cos(m\varphi) - \sigma\rho^2\frac{\partial\varphi}{\partial x} + \delta\rho^2(\nabla\varphi)^2 + \delta(\nabla\rho)^2 + r_{ij}\rho^2u_{ij} + \frac{1}{2}\lambda_{ijkl}u_{ij}u_{kl}\Big]dv. \quad (15)$$

Here $\alpha = \alpha_T(T - \theta)$ and *m* is the anisotropy order ($m \geq 3$).

At the temperature $T_i > \theta$ determined by the conditions $\alpha_0 \equiv \alpha_T(T_i - \theta) = \sigma^2/4\delta$, the *N* phase undergoes a second-order transition to the IC phase, whose structure is described by a one-harmonic distribution of the order parameter ($\eta_1 = \rho\cos(q_0x)$, $\eta_2 = \rho\sin(q_0x)$) with the wave vector $q_0 \equiv \sigma/(2\delta)$. Because of anisotropy of the space of order-parameter components, the wave vector decreases with lowering of temperature, and the structure of the IC phase is transformed from a harmonic one into a domain-like one. Therefore, a lock-in (IC–C) transition undergone at a certain temperature may be considered as a transition leading to disappearance of domain walls.

As earlier, solving the elastic problem, we ignore near-surface distortions formed in a finite sample and consider, first, an elastically isotropic medium by setting that $\lambda_{ijkl} = [K - (2/3)\mu]\delta_{ij}\delta_{kl} + \mu(\delta_{ik}\delta_{jl} + \delta_{il}\delta_{jk})$ and $r_{ij} = r\delta_{ij}$. In this case, Eqs. (3)–(9) remain valid if we make the change $\eta \longrightarrow \rho$. Then, using the notation $u_{zz} = u_1$, we obtain instead of Eq. (10) the following equation:

$$f = \frac{1}{2L}\int\Big[\alpha(u_1)\rho^2 + \beta''\rho^4 + \gamma\rho^m\cos(m\varphi) - \sigma\rho^2\frac{\partial\varphi}{\partial x} + \delta\rho^2(\nabla\varphi)^2 + \delta(\nabla\rho)^2\Big]dx + \frac{K'u_1^2}{2}, \quad (16)$$

where $\alpha(u_1) = \alpha + r'u_1$, r' and K' have the same values as in Eq. (10), $\beta'' = \beta - r^2/(2\tilde{K})$, and $\tilde{K} = K + 4\mu/3$.

At a fixed value *u*, the distributions of the order parameter and free energy of the IC phase in the vicinity of the IC–C transition may be represented as the expansions in the anisotropy parameter $\varepsilon_m = -(m\pi^2/2^4)[\alpha_0/\alpha_c]$, where $\alpha_c = -2\beta''[\sigma^2/(2^5\gamma\delta)]^{2/(m-2)}$ [10]. In a lower approximation (approximation of a constant amplitude), the energy of the IC phase, being a function of the soliton density (*n*), has the form [1]

$$f = -\beta''\rho^4(u_1) + E(u_1)n + 4J(u_1)n\exp(-mp(u_1)/(2n) + \frac{K'}{2}u_1^2). \quad (17)$$

The coefficients in Eq. (17) are expressed in terms of the squared amplitude of the order parameter, $\rho^2(u_1) = -\alpha(u_1)/(2\beta'')$, and the wave number, $q_0 = \sigma/(2\delta)$, of the

IC structure at the point of the N–IC transition as follows:

$$p^2(u_1) = \frac{2\gamma}{\delta}\rho^{m-2}(u_1), \quad (18)$$

$$J(u_1) = \frac{4\sigma\rho^2(u_1)p(u_1)}{mq_0}, \quad (19)$$

$$E(u_1) = \frac{2\sigma\rho^2(u_1)}{mq_0}[2p(u_1) - \pi q_0]. \quad (20)$$

In this case, it follows from equations analogous to Eqs. (6)–(9) that $u_{zz} = u_{yy} = u_1 = -r\rho^2(u_1)/(3K)$. Substituting this relationship into Eq. (16), we see that, in the approximation of a constant amplitude, strains result only in the renormalization of the coefficient before ρ^4; i.e., $\beta \longrightarrow \beta' = \beta - r^2/(2K)$, and, therefore, $u_1 = r\alpha/(6K\beta') = u_c/3$ and $\rho^2(u_c) = -\alpha/(2\beta')$. Thus, in this approximation, solitons do not interact. In the next approximation with respect to the anisotropy parameter, two corrections appear: a spatially inhomogeneous correction to $\rho^2(u_c)$ denoted as $\rho_1^2(x)$ [1] and the corresponding correction to energy (17). Now, the equations of elastic equilibrium yield

$$u_{zz} - u_1 = u_{yy} - u_1 = \varepsilon_1,$$
$$u_{xx} - u_1 = -\left[\left(K - \frac{2}{3}\mu\right)2\varepsilon_1 + r\rho_1^2(x)\right]\Big/\left(K + \frac{4}{3}\mu\right), \quad (21)$$

where the additional strain $\varepsilon_1 = -r\langle\rho_1^2(x)\rangle/(3K)$ caused by appearance of solitons is proportional to the soliton density n. In the vicinity of the IC–C transition, $n \ll 1$; therefore, $\varepsilon_1 \ll u_c$. Then, we may expand Eq. (17) and minimize the result with respect to ε_1. As a result, we have $\varepsilon = -nr'E\beta''/K\beta'$ and the free energy of solitons has the form

$$\delta f \approx a_1 n - a_3 n^2 + a_2 n\exp(-N/n), \quad (22)$$

where $a_1 = E_1[\alpha(u_c) - \alpha_c]$; $a_3 = (r')^2E_1^2\beta'/(2K'\beta')$; $E_1 = (2 - m)\pi\sigma/(4m\beta'')$; $N = m\pi q_0/4$; and $a_2 = -4\pi\sigma\alpha_c/(m\beta'')$ is the energy of an isolated soliton, which goes to zero at the temperature determined by the condition $\alpha(u_c) = \alpha_c$. The term $-a_3n^2$ describes the soliton attraction and gives rise to a jump in the soliton density at the point of the IC–C transition.

Note that the main term of the soliton-energy expansion in an anisotropy parameter $\alpha - \tilde{\alpha}_c$ for the case $m = 4$ was calculated in [10]. In our notation, it has the form

$$\delta f = \frac{\pi^2\alpha_0(\alpha - \tilde{\alpha}_c)}{2\beta\ln\left|\dfrac{\alpha - \tilde{\alpha}_c}{4\alpha_c}\right|}. \quad (23)$$

The $\tilde{\alpha}_c$ value was calculated with a higher accuracy than α_c. Introducing the dependence of α on u into Eq. (23), we may, as earlier, calculate the value of soliton attraction. It turns out that the same (within the change $\alpha_c \longleftrightarrow \tilde{\alpha}_c$) result may also be obtained by minimizing Eq. (22) with respect to soliton density with a subsequent singling out of the main term of expansion in $\alpha - \alpha_c$ in the expression thus obtained.

Now, we show that the expression for free energy in the vicinity of the IC–C transition for anisotropic systems has the same form as Eq. (22) and that the coefficients in this expression may be obtained by the corresponding renormalization. We vary the initial expressions for free energy, Eqs. (15) and (16), with respect to the elastic degrees of freedom, and then compare the functionals thus obtained. Equation (15) should be varied separately for homogeneous strains ($\langle u_{ij}\rangle$) and inhomogeneous elastic displacements (u_i), which represent the independent degrees of freedom. It is convenient to pass to the following Fourier representation

$$u_{ij} = \langle u_{ij}\rangle + \frac{i}{2}\sum_{k\neq 0}[k_iu_j(\mathbf{k}) + k_ju_i(\mathbf{k})]\exp(i\mathbf{kr}), \quad (24)$$

where, in virtue of one-dimensionality of the problem under consideration, $\mathbf{k} = (k_x, 0, 0)$. For simplicity, we limit our consideration to often-encountered systems described by the symmetry class D_{2h}. Then, minimizing Eq. (15) with respect to the elastic degrees of freedom in the $\mathbf{k}$ space, we obtain from the last two terms

$$\delta f = -\frac{1}{2}r_{ij}r_{kl}\lambda^{-1}_{ijkl}f_0^2 - \frac{r_{33}^2}{2\lambda_{3333}}\sum_{k_x\neq 0} f_{k_x}f_{-k_x}, \quad (25)$$

where f_{k_x} is the Fourier component of the function $f = \rho^2$ and λ^{-1}_{ijkl} is the tensor reciprocal to the tensor λ_{ijkl}. Returning to the real space in Eq. (25), we obtain

$$\delta f = -\frac{1}{2}\left[r_{ij}r_{kl}\lambda^{-1}_{ijkl} - \frac{r_{33}^2}{\lambda_{3333}}\right]\langle\rho^2\rangle^2 - \frac{r_{33}^2}{2\lambda_{3333}}\langle\rho^4\rangle, \quad (26)$$

where $\langle\ldots\rangle$ indicates averaging over the bulk. Here, the last term is understood as the renormalization of the term $\beta\langle\rho^4\rangle$ in Eq. (15).

In turn, minimization of the elastic contribution in the isotropic case yields

$$\delta f = -\frac{2r^2\mu}{3K\tilde{K}}\langle\rho^2\rangle^2 - \frac{r^2}{2\tilde{K}}\langle\rho^4\rangle. \quad (27)$$

Comparing Eqs. (26) and (27), we see that the free-energy functionals which are determined by the distribution of the order parameter alone have the same form in both cases and differ only by their coefficients. It follows that, minimizing these functionals with respect to the order-parameter distribution, one arrives at the

same results for free energy within the accuracy of the following replacements:

$$\beta - r^2/(2\tilde{K}) \longrightarrow \beta - r_{33}^2/(2\lambda_{3333}),$$
$$4r^2\mu/(3K\tilde{K}) \longrightarrow r_{ij}r_{kl}\lambda_{ijkl}^{-1} - r_{33}^2/\lambda_{3333}. \quad (28)$$

When considering the IC–C transition in the systems characterized by weak anisotropy, one has also to take into account some other interactions [4]. For displacive phase transitions, the most important of which is described by the dependence of the Lifshitz invariant on strain. The estimates made in [4] show that if anisotropy is not too weak ($10^{-2} < \varepsilon_m < 1$) the striction contribution prevails in attraction. However, in ferroelectric systems of the order–disorder type, one more mechanism may play an important role: attraction due to thermal domain-wall bending.

As a result of attraction, an IC–C transformation should be a first-order transition. Expression (22) with the renormalized coefficients allows one to determine the basic transition characteristics: the transition temperature, the temperature of maximum supercooling, the soliton density at the transition point, the latent heat of transition, and the anomaly in heat capacity. It should be indicated that the anomalous part of heat capacity varies according to the Curie–Weiss law and diverges at the point of maximum supercooling.

In the cases of pronounced anisotropy or an IC phase of type II (the Lifshitz invariant is forbidden by the symmetry of the normal phase), the striction-mediated interaction of solitons may be evaluated using the first term on the right-hand side of Eq. (26). This interaction equals $n^2(r^2/\tilde{K})(\Delta\eta^2 r_c)^2$, where $\Delta\eta^2$ is the squared change in the amplitude of the order parameter in a wall of width r_c.

MIXED STATE IN A SUPERCONDUCTOR

The effect of striction-mediated attraction on the properties of vortices in second-order superconductors was first considered in connection with vortex pinning at defects. Much later, it was considered in connection with its influence on the orientation of vortex structures relative to the crystal lattice (see references in [3, 5]).

As in the studies of the thermodynamics of a vortex lattice, in general, when analyzing the above effects, one usually singles out two regions where the external magnetic field is either close or not too close to the upper critical field H_{c2}. To describe the two-dimensional spatial distributions of a complex order parameter $\Psi = \rho\exp(i\phi)$ in these regions, two qualitatively different approximations are used [11]. In the vicinity of H_{c2}, the basic periods of the vortex lattice are close to the correlation radius ξ and the distribution of the order-parameter modulus in the regions between vortices is inhomogeneous. In the fields not too close to H_{c2}, the distances between vortices considerably exceed ξ. In the conventionally used London approximation, it is assumed that the order-parameter modulus varies only in the cores of vortices with radii $r \sim \xi$. Since, in fact, the variation of the squared modulus of the order parameter caused by vortex appearance describes the distribution of the striction-mediated strain sources, it was assumed that, in the applicability range of the London approximation, the role of these strain sources is played by vortex cores. Following [5], consider the effects of a long-range elastic action in an approximation more accurate that the London approximation in the fields $H \ll H_{c2}$. In other words, we take into account the change in the order-parameter modulus not only in the vortex core but also in the surrounding noncore region limited by the penetration depth λ much larger than ξ in superconductors with a pronounced Ginzburg–Landau parameter ($\kappa = \lambda/\xi$).

We proceed from the Ginzburg–Landau free-energy expansion with allowance for its dependence on elastic strains:

$$f = \frac{1}{V}\int\left[\frac{H^2}{8\pi} + a|\Psi|^2 + \frac{b}{2}|\Psi|^4\right. \quad (29)$$
$$\left. + \frac{1}{4m}\left|\left(-i\hbar\nabla - \frac{2e}{c}\mathbf{A}\right)\Psi\right|^2 + r_{ij}|\Psi|^2 u_{ij} + \frac{1}{2}\lambda_{ijkl}u_{ij}u_{kl}\right]dv,$$

where Ψ is the order parameter corresponding to the transition to the superconducting state, **A** is the vector potential, and H is the magnetic field.

The equilibrium equations have the form

$$\left[a + b|\Psi|^2 + r_{ij}u_{ij} + \frac{1}{4m}\left(-i\hbar\nabla - \frac{2e}{c}\mathbf{A}\right)^2\right]\Psi = 0, \quad (30)$$

$$\nabla\mathbf{H} = \frac{4\pi e}{mc}\left[\frac{\hbar}{2i}(\Psi^*\nabla\Psi - \Psi\nabla\Psi^*) - \frac{2e}{c}|\Psi|^2\mathbf{A}\right], \quad (31)$$

$$\frac{\partial}{\partial x_j}(\lambda_{ijkl}u_{kl} + r_{ij}|\Psi|^2) = 0, \quad (32)$$

$$\lambda_{ijkl}\langle u_{kl}\rangle + r_{ij}\langle|\Psi|^2\rangle = 0, \quad (33)$$

where, as earlier, $\langle\ldots\rangle$ indicates averaging over the bulk.

Relationship (33) describes the result of free-energy variation over homogeneous strains and may be regarded as the necessary condition for absence of any homogeneous external stresses. As in the case of a regular soliton structure in an incommensurate phase considered above, we ignore the near-surface vortex-lattice distortions propagating into the crystal bulk for distances comparable with the period of this lattice.

From Eqs. (30) and (33), we obtain the spontaneous values in the homogeneous superconducting state:

$$|\Psi_s|^2 = -a/b^*, \quad (34)$$

$$u_{ij}^s = -r_{kl}\lambda_{ijkl}^{-1}|\Psi_s|^2 = ar_{kl}\lambda_{ijkl}^{-1}/b^*, \quad (35)$$

where $b^* = b - r_{ij}r_{kl}\lambda^{-1}_{ijkl}$.

To calculate the vortex interactions induced by elastic strains in an isotropic medium, consider the limit of an infinite shear modulus. In this limit, only homogeneous dilatation u exists, which considerably simplifies the solution of the elastic problem. Varying Eq. (29) with respect to the elastic degrees of freedom (homogeneous strains and two-dimensional inhomogeneous displacements) of an elastically isotropic medium with a finite and infinite shear moduli, one can show that all the data for the finite μ may be obtained from the corresponding relationships for the limiting case $\mu = \infty$ after the following renormalization: $b \longrightarrow b - r^2/\tilde{K}$ and $r^2/K \longrightarrow (r^2/K)[4\mu/(3\tilde{K})]$.

In the case $\mu = \infty$, the two last terms of the free-energy expansion (29) have the form $r^2|\Psi|^2u + Ku^2/2$. Strain u may be regarded as a variation parameter. Since this parameter modifies the coefficient before $|\Psi|^2$, we may introduce the notation $a(u) = a + ru_s + r\varepsilon$, where, in accordance with Eq. (35), $u_s = ra/b^*$, $b^* = (b - r^2/K)$, and ε is the vortex-induced strain. Then, using the results obtained in [11, 12], we may represent the free-energy density of the vortex lattice as a function of magnetic induction B ($B = n\Phi_0$, where Φ_0 is the flux quantum and n is the vortex density) in the form

$$f_{VL} = \begin{cases} \dfrac{BH_{c1}}{4\pi} + Ku_s\varepsilon + \dfrac{K\varepsilon^2}{2}, & H \approx H_{c1} \\ \dfrac{1}{8\pi}\left[B^2 + BH_{c1}\dfrac{\ln(\nu d/\xi)^2}{\ln\kappa}\right] + Ku_s\varepsilon + \dfrac{K\varepsilon^2}{2}, & \\ H_{c1} \ll H \ll H_{c2}, & \end{cases} \quad (36)$$

where H_{c1} is the lower critical field. For a triangular lattice (considered for the sake of definiteness), we have $\beta_A = \langle\Psi^4\rangle_V/\langle\Psi^2\rangle_V = 1.16$ and $2\ln\nu = 2(\gamma - 1) + \ln[3^{1/2}/(8\pi)]$, where $\gamma = 0.577\ldots$ (Euler constant) [12]. The magnetic induction is $B = 2\Phi_0/(3^{1/2}d^2)$, where d is the distance between the vortices. It should be indicated that, in the first of relationships (36), we ignored the contribution due to vortex interactions at short distances.

In our case, H_{c1} in relationships (36) depends on u:

$$\begin{aligned} H_{c1}(u) &= \frac{\ln\kappa}{2^{1/2}\kappa}2a(u)\sqrt{\pi/b} \\ &= \frac{\ln\kappa}{2^{1/2}\kappa}(2a\sqrt{\pi/b^*} + 2r\sqrt{\pi/b}\varepsilon). \end{aligned} \quad (37)$$

Moreover, d/ξ also depends on u; i.e., $(d/\xi)^2 = d^2 4m|\Psi_s|^2 b\hbar^{-2}(1 + r\varepsilon/a)$. Minimizing expression (36) with respect to ε, we obtain

$$f_{VL} = \begin{cases} \dfrac{1}{8\pi}\left(2BH^0_{c1} - \dfrac{\ln^2\kappa\Delta K}{2\kappa^2 K}B^2\right), & H \approx H_{c1} \\ \dfrac{1}{8\pi}\left[B^2 + BH^0_{c1}\dfrac{\ln(\nu d/\xi)^2}{\ln\kappa} - \dfrac{\ln^2(\nu d/\xi)^2\Delta K}{4\kappa^2 K}B^2\right], & \\ H_{c1} \ll H \ll H_{c2}. & \end{cases} \quad (38)$$

Here $\Delta K/K$ is a relative jump of the bulk modulus in the transition from the normal to a superconducting phase (usually $\Delta K/K \ll 1$). The terms proportional to B^2 in Eqs. (38) correspond to the contributions of the noncore regions to the elastic vortex attraction.

When calculating the contributions due to vortex cores, the latter are usually considered as normal-phase cylinders with radii ξ [2, 3]. However, the corresponding contribution and the ratio of this contribution to the noncore contribution may be determined more exactly. With this aim one has to determine the strength of a dilatation source created by an isolated vortex. This strength is determined by the change in the volume due to vortex formation. The latter quantity is equal to the pressure derivative of the vortex energy $(\Phi_0/4\pi\lambda)^2(\ln\kappa + 0.08)$ [11], where Φ_0 is a flux quantum; λ depends on pressure; and the terms containing $\ln\kappa$ correspond to the noncore region, whereas the remaining terms correspond to the core region. Then, in the vicinity of H_{c1}, the ratio of the core to the noncore contributions to the vortex interactions equals $(0.08/\ln\kappa)^2$. If $H_{c1} \ll H \ll H_{c2}$ (the distance between vortices becomes less than the penetration depth ($1 \ll d/\xi \ll \kappa$)), the contribution of noncore regions decreases because of their overlap (see Eq. (38)), although it remains to be much larger than the core contribution.

Consider the vortex interactions in a finite medium with elastic anisotropy. As usual [11], we first simplify the free-energy expression. Integrating the terms with $\nabla\Psi$ in Eq. (29) by parts with the boundary condition $\mathbf{n}\left(-i\hbar\nabla - \dfrac{2e}{c}\mathbf{A}\right)\Psi|_\Sigma = 0$ (where $\mathbf{n}$ is the normal to the surface Σ) and using Eq. (30), we obtain

$$f = \frac{1}{V}\int\left[\frac{H^2}{8\pi} - \frac{b}{2}|\Psi|^4 + \frac{1}{2}\lambda_{ijkl}u_{ij}u_{kl}\right]dv. \quad (39)$$

Equation (39) is the extension of the well-known Abrikosov equation for free energy [11] to a deformable medium.

At $H \ll H_{c2}$, it is convenient to single out the vortex contribution by writing $|\Psi|^2 = |\Psi_s|^2 - h$ and $u_{ij} = u^s_{ij} + u^v_{ij}$, where the quantities $|\Psi_s|^2$ and u^s_{ij} are determined by Eqs. (34) and (35), respectively. For vortices parallel

to the z axis, Eqs. (32) and (33) for u_{ij} yield

$$u_{ij}^{v} = r_{kl}\lambda_{ijkl}^{-1}\langle h\rangle + \frac{1}{2}\sum_{q\neq 0}[q_i S_k(\mathbf{q})G_{kj}(\mathbf{q}) + q_j S_k(\mathbf{q})G_{ki}(\mathbf{q})]h(\mathbf{q})e^{i\mathbf{qr}}, \quad (40)$$

where $S_k(\mathbf{q}) = r_{ij}q_j$, $G_{ki}(\mathbf{q}) = \lambda_{ijkl}q_j q_l$, and $\mathbf{q} = (q_x, q_y, 0)$ is a two-dimensional wave vector.

Taking into account the smallness of the coefficients r_{ij} in the calculations of h, one may limit oneself to the first approximation with respect to r_{ij}. Then, $h \cong h_0 + h_1$, where h_0 is the solution of Eq. (30) at $r_{ij} = 0$, and $h_1 = r_{ij}u_{ij}^{v}/b$ is the first correction to this solution, which, in the approximation under consideration, arises only in the noncore regions. Equation (40) also yields $r_{ij}u_{ij}^{v}(q) = b'(q)h(q) \cong b'(q)h_0(q)$, where

$$b'(\mathbf{q}) = \begin{cases} r_{ij}r_{kl}\lambda_{ijkl}^{-1}, & (\mathbf{q} = 0) \\ S_i(\mathbf{q})S_j(\mathbf{q})G_{ij}(\mathbf{q}), & (\mathbf{q} \neq 0). \end{cases} \quad (41)$$

The function $b'(q)$ at $\mathbf{q} \neq 0$ depends only on the orientation of the vector $\mathbf{q}$. As a result, one the following obtains [5] for the free energy described by Eq. (29):

$$f \cong f_s + b^*|\Psi_s|^2\zeta\langle h_0\rangle + \left\langle\frac{H^2}{8\pi}\right\rangle - \frac{b}{2}\langle h_0^2\rangle - \frac{1}{2}\sum_{\mathbf{q}} b'(\mathbf{q})h_0(\mathbf{q})h_0(-\mathbf{q}), \quad (42)$$

where $f_s = -b^*|\Psi_s|^4/2$ and $\zeta = 1 + b'(0)/b$. The latter term corresponds to the contribution of elastic strains to the energy of the vortex lattice, and the term containing $q = 0$ corresponds to the contribution of homogeneous strains. Since the elastic constants enter this term in the invariant combination (see Eq. (41) for $b'(0)$), this term is independent of the vortex orientation with respect to the crystal lattice. Such a dependence may arise only due to the terms with $\mathbf{q} \neq 0$.

In the vicinity of H_{c1}, the expression for the energy of vortex interactions may be simplified if one takes into account that these vortices form a regular lattice. With this aim, we represent $h_0(\mathbf{c})$ as a sum over the coordinates of the vortex centers, $h_0(\mathbf{c}) = \sum_i h_{01}(\mathbf{c} - \mathbf{c}_i)$. Then, $h_0(\mathbf{q}) = S^{-1}\sum_i \int h_{01}(\mathbf{c} - \mathbf{c}_i)e^{-i\mathbf{q}\rho} = S^{-1}\sum_i h_{01}(\mathbf{q})e^{-iq\rho_i}$ (where S is the area of the sample section in the x, y plane). Substituting this expression into Eq. (42), we may single out the interaction energy by subtracting the terms containing the factors $e^{-iq\rho_i}e^{-iq\rho_j}$ at $i = j$. Then, taking into account that $S^{-1}\sum_i \exp(-i\mathbf{q}\rho_i) = n\delta_{q,Q}$ (where n is the vortex density and $\mathbf{Q}$ are the reciprocal-lattice vectors), we obtain $h_0(\mathbf{q}) = nh_{01}(\mathbf{q})\delta_{q,\mathbf{Q}}$. The direct calculation shows that, with an increase in q, the noncore contribution to $h_{01}(q)$ dramatically decreases only if $q \sim \xi^{-1}$. Therefore $h_{01}(Q)$ may be approximated by its value at small wave vectors. As a result, we obtain for the energy of vortex interaction

$$f^{\text{int}} \cong -\frac{n^2}{2}h_{01}^2(0)\left[b'(0) + \sum_{Q\neq 0} b'(\mathbf{Q})\right] + \frac{n}{2S}\sum_{q\neq 0} b'(\mathbf{q}) \cong -\frac{n^2}{2}h_{01}^2(0)\left([b'(0) - \langle b'(\mathbf{Q})\rangle_\varphi] + \sum_{\mathbf{Q}\neq 0}[b'(\mathbf{Q}) - \langle b'(\mathbf{Q})\rangle_\varphi]\right), \quad (43)$$

where $\langle b'(\mathbf{Q})\rangle_\varphi = (2\pi)^{-1}\int_0^{2\pi} b'(\mathbf{Q})d\varphi$ is the $\mathbf{Q}$ value averaged over the orientations (it should be remembered that $b'(\mathbf{Q})$ is independent of the modulus of the vector $\mathbf{Q}$). We also used here the relationship $S^{-1}\sum_{q\neq 0} b'(\mathbf{q}) \approx \int b'(\mathbf{q})d\mathbf{q} = \int_0^{Q_{\max}} 2\pi q\langle b'(\mathbf{q})\rangle_\varphi dq \cong n\sum_Q \langle b'(\mathbf{Q})\rangle_\varphi$. An important conclusion following from the expressions (43) is that the vortex energy (bulk part) is independent of the sample shape. This follows from the fact that the spectrum of the wave vectors in Eq. (43) has no terms with small wave vectors of the order of the reciprocal of the sample size. The opposite conclusion about the dependence of the interaction on a sample shape drawn in [3] was based on the analysis of only a part of the elastic interactions, i.e., of the sum of pair interactions, each of which was calculated for an infinite medium.

The first term in parentheses in Eq. (43) corresponds to the interactions associated with the finite sample dimensions, i.e., with the action of imaging forces, whereas the second term has a nonzero value only in the presence of elastic anisotropy. In the isotropic case $b'(0) = r^2/K$ and $b'(\mathbf{Q} \neq 0) = r^2/(K + 4\mu/3)$. Since in the limit $\mu = \infty$ Eq. (43) should coincide with the first of Eqs. (38), we have

$$h_{01}(0) = 2\pi|\Psi_s|^2\xi^2\ln\kappa, \quad (44)$$

where it was taken into account that $nH_c\xi^2 = B/(2^{3/2}\pi\kappa)$ and $H_c = 2^{1/2}\kappa H_{c1}/\ln\kappa$. Equations (43) and (44) allow one to calculate the energy of the vortex interactions in a crystal of finite dimensions. However, since the function $b'(\mathbf{Q})$ depends on vector orientations in a rather complicated way, the final result may be obtained only numerically and only for crystals of certain symmetries. Evaluating each of two terms in parentheses on the right-hand side of Eq. (43) as $b\Delta K/K$ and taking into account Eq. (44), we obtain the vortex interaction in the

vicinity of H_{c1} as $f^{int} \approx -10^{-2}((\ln\kappa)/\kappa)^2(\Delta K/K)B^2$, i.e., the value exceeding the core contribution by a factor of $\sim 10^2 \ln^2(\kappa)$.

If $H_{c1} \ll H \ll H_{c2}$, the computations are more complicated because one also has to take into account the dependence of h_{01} on $\mathbf{q}$ in Eq. (42) with $h_0(\mathbf{q}) = S^{-1}\sum_i h_{01}(\mathbf{q})e^{-i\mathbf{q}\rho_i}$. A similar calculation shows that in this case $h_{01}(0) = 2^{1/2}\pi|\Psi_s|^2\xi^2\ln\kappa$. However, now $Q > 1/\lambda$ and $h_{01}(Q) \approx h_{01}(0)\ln(\xi^{-1}Q^{-1})$. By using the same method, it is possible to obtain from Eq. (42), the relationship for calculating the energy of the vortex interaction for fields $H_{c1} \ll H \ll H_{c2}$ having a more general form than Eq. (43). At the same time, the result obtained for the isotropic case allows us to conclude that, in this field as well, the main contribution to the strain-induced vortex interaction in superconductors with high κ values comes from the change of the order parameter in noncore regions.

Thus, the results obtained show that in fields $H \ll H_{c2}$ the main contribution to the strain-induced vortex interaction in superconductors with high κ values comes from the change in the order parameter in noncore regions. The noncore contribution may exceed the core contribution by one or even two orders of magnitude. This conclusion is very important for studying the orientations of the vortex structures in crystals. For example, in the cases where the previous estimates showed that the difference between the elastic energies at various orientations of the vortex lattice is less than the differences of the corresponding London energies, the refinement of the elastic-interaction value may change the conclusion about the prevalence of one or another orientation.

Concluding the article, we would like to indicate that the method considered above, which is based on analysis of the case of an isotropic medium with an infinite shear modulus, considerably simplifies the calculation of the contribution of long-range elastic interaction to the energy of any one-dimensionally periodic structure in a finite medium with arbitrary anisotropy. Moreover, this method is also effective in the calculations of the striction contributions to the energy of two- and three-dimensional regular structures in an isotropic medium, e.g., for branching domains or systems of quantum dots. This statement is based on the facts that, as in the one-dimensional case, one may ignore here the near-surface distortions of such structures and that the elastic contribution to the free energy in an isotropic medium is independent of the orientation of the wave vectors of the structure with respect to the crystal lattice.

REFERENCES

1. *Incommensurate Phases in Dielectrics*, Ed. by R. Blinc and A. P. Levanyuk (North-Holland, Amsterdam, 1986), Vol. 1.
2. H. Ullmaier, R. Zeller, and P. H. Dederichs, Phys. Lett. A **44**, 331 (1973).
3. V. G. Kogan, N. I. Bulaevskii, P. Miranovic, and L. Dobrosavljevic-Grujic, Phys. Rev. B **51**, 15344 (1995).
4. A. P. Levanyuk, S. A. Minyukov, and A. Cano, Phys. Rev. B **66**, 014111 (2002).
5. A. Cano, A. P. Levanyuk, and S. A. Minyukov, Phys. Rev. B **68**, 144515 (2003).
6. W. Nowacki, *Teoria Sprezystosci* (PWN, Warszawa, 1970; Mir, Moscow, 1975).
7. S. S. Orlov and V. L. Indenbom, Kristallografiya **14** (5), 780 (1969) [Sov. Phys. Crystallogr. **14**, 675 (1970)].
8. V. A. Zhirnov, Zh. Éksp. Teor. Fiz. **35** (4), 1175 (1958) [Sov. Phys. JETP **8**, 822 (1959)].
9. L. D. Landau and E. M. Lifshitz, *Course of Theoretical Physics*, Vol. 7: *Theory of Elasticity*, 4th ed. (Nauka, Moscow, 1987; Pergamon, New York, 1986).
10. V. A. Golovko, Izv. Akad. Nauk SSSR, Ser. Fiz. **48** (12), 2463 (1984).
11. A. A. Abrikosov, *Fundamentals of the Theory of Metals* (Nauka, Moscow, 1987; North-Holland, Amsterdam, 1988).
12. A. L. Fetter and P. Hohenberg, in *Superconductivity*, Ed. by R. D. Parks (Marcel Dekker, New York, 1983), Vol. 2, p. 817.

Translated by L. Man

Crystallography Reports, Vol. 50, No. 2, 2005, pp. 270–277. Translated from Kristallografiya, Vol. 50, No. 2, 2005, pp. 303–311.

LATTICE DYNAMICS AND PHASE TRANSITIONS

Low-Frequency Phonon Dynamics, Spin-Lattice Relaxation, and Sound Attenuation in Crystals with Incommensurate Phases

S. A. Minyukov* and A. P. Levanyuk**

** Shubnikov Institute of Crystallography, Russian Academy of Sciences, Leninskiĭ pr. 59, Moscow, 119333 Russia*

e-mail: minyukov@ns.crys.ras.ru

*** Universidad Autonoma de Madrid, Madrid, E-28049 Spain*

e-mail: levanyuk@uam.es

Received November 4, 2004

Abstract—Specific features of the low-frequency response of a phason and an amplitudon in the region of small wave vectors are considered in incommensurate displacive-type phases at high and low temperatures. The corresponding anomalies of spin-lattice relaxation (SLR) rate and attenuation of the longitudinal sound in the vicinity of the normal phase transformation into an incommensurate phase are analyzed. It is shown that the divergence of the amplitudon response at small wave vectors and low frequencies induced by the interaction with phasons clearly manifests itself only at low temperatures T and that the pronounced amplitudon contribution proportional to T^3 to the SLR rate is associated with this divergence. The phason-response divergence at low temperatures leads to the frequency-independent contribution proportional to T to the SLR rate. © *2005 Pleiades Publishing, Inc.*

INTRODUCTION

As is well known (see, e.g., [1, 2]), the characteristic properties of incommensurate (IC) phases are determined by fluctuations corresponding to the phason branch of vibrations. The phason branch appears in the excitation spectrum of the IC phase of a crystal because of degeneracy typical of incommensurate phases: the system energy is independent of the phase of a certain order parameter. As a result, the phason spectrum has no gap and the corresponding fluctuations diverge at small wave vectors and low frequencies. However, this does not signify that the phase fluctuations are critical over the whole region of the IC phase existence because their interactions remain finite. This allows one to develop for IC phases a perturbation theory with respect to anharmonic interactions which would allow one to calculate any physical quantity. In this case, the influence of the diverging phase fluctuations may be studied within lower orders of the perturbation theory. Thus, the divergence of the amplitude fluctuations related to phase fluctuations arises only in the second order of the interaction between these fluctuations.

Below, we consider the typical features of low-frequency dynamics of the order parameter and its manifestation in the anomalies of spin-lattice relaxation and attenuation of the longitudinal sound in the vicinity of the transition of the normal N phase to the IC phase in displacive-type systems. Such anomalies in structural incommensurate phases were repeatedly studied experimentally [1–3]. However, in most of the cases, the experimental data obtained were interpreted under some simplifying assumptions. Therefore, it seems useful to consider the basic results obtained in this field within a consistent perturbation theory [4–7].

LOW-FREQUENCY PHONON DYNAMICS

The anomalies observed in the kinetic properties of crystals in the vicinity of phase transitions are determined by spectral densities of fluctuations of the order parameter, which, in turn, may be calculated from the corresponding dynamic susceptibilities. Therefore, the most important problem reduces to calculation of these susceptibilities from the motion equations of the order parameter.

First, we should like to remind the reader about the main experimental data on the dynamics of a one-component order parameter η in displacive-type systems in the vicinity of the points of second-order phase transitions [8]. In this case, the motion equation is of the oscillatory type,

$$m\ddot{\eta} + \gamma\dot{\eta} + \left(\frac{\partial^2 f_\eta}{\partial \eta^2}\right)_{\eta_e}(\eta - \eta_e) - \Delta D\eta = 0, \qquad (1)$$

where $f_\eta = A\eta^2/2 + B\eta^4/4$ with $A = A_T(T - T_c)$ and $A_T \sim d^{-5}$, $B \sim T_{at}d^{-7}$, and $D \sim T_{at}d^{-3}$ (where T_c is the transition temperature, $T_{at} \sim 10^4$–10^5 is the atomic temperature, and d is of the order of an interatomic distance). In a symmetric phase ($\eta_e = 0$), the viscosity coefficient γ (or the analogous quantity $\Gamma \equiv \gamma/m$) depends on the ratio of the soft-mode dispersion ($(D/m)^{1/2}$) and the velocity of

sound (v). If dispersion is weak ($(D/m)^{1/2} < v$), the soft-mode attenuation is determined by the interaction of the soft and acoustic modes and the corresponding contribution is estimated as

$$\Gamma_a \approx \Omega_D(T/T_{\text{at}}), \tag{2}$$

where Ω_D is the Debye frequency. The quantity Γ_a only slightly depends on both temperature and frequency. For a soft mode with pronounced dispersion ($(D/m)^{1/2} > v$), the temperature dependences of Γ at high and low frequencies are substantially different. The major contribution in the high-frequency region comes from the interaction with acoustic modes, so estimate (1) remains valid. At the same time, attenuation at low frequencies depends only on soft-mode intrinsic anharmonicity (η^4) and has a pronounced temperature anomaly

$$\Gamma_c \approx \Omega_D\left(\frac{T}{T_{\text{at}}}\right)^2\left(\frac{T_{\text{at}}}{T-T_c}\right)^{1/2} \sim \xi\Gamma_a, \tag{3}$$

where $\xi \sim (T_c/T_{\text{at}})^{1/2}(T_c/|T-T_c|)^{1/2} < 1$ is the parameter of the perturbation theory.

In a low-symmetric phase, third-order anharmonicity appears, which results in an additional contribution ($\delta\Gamma_c$) to low-frequency attenuation. The quantity $\delta\Gamma_c$ has a pronounced spatial dispersion at the wave vectors (q) of the order of $\gamma/(mD)^{1/2}$, whose magnitudes are much less than the reciprocal correlation radius, ($r_c^{-1} = (2|A|/D)^{1/2}$). In the limit $q \longrightarrow 0$, this contribution exceeds Γ_a in the whole applicability range of the Landau theory and is equal to

$$\delta\Gamma(q \longrightarrow 0) \approx \Omega_D(T_c - T)^{1/2}/(T_{\text{at}})^{1/2} \approx \omega_0, \tag{4}$$

where $\omega_0 = (2|A|/m)^{1/2}$ is the soft-mode frequency. At the same time, this attenuation at $q \approx r_c^{-1}$ may be estimated as

$$\delta\Gamma(q \approx r_c^{-1}) \approx (TB)/(Dcm), \tag{5}$$

which is much less than $\delta\Gamma(0)$ and is of the same order of magnitude as Γ_a [5].

In degenerate phases, third-order anharmonicity also plays a more important role. Thus, one of the major manifestations of this anharmonicity, e.g., in Heisenberg magnetics, is the divergence of the longitudinal fluctuations of the magnetic moment at $q \longrightarrow 0$ [9]. Similar divergence in structural IC systems was discussed in [10]. The dynamic susceptibilities for Heisenberg magnetics were calculated elsewhere [11]. However, the kinetics of the order parameter in degenerate structural systems has a number of distinctive features associated mainly with pronounced phason attenuation at $q \longrightarrow 0$. The corresponding characteristics of dynamic susceptibilities were studied in [4].

The main characteristic features of the kinetics of the order parameter in incommensurate phases may be illustrated by the simplest example of an IC phase with a one-dimensional harmonic distribution of a certain order parameter,

$$\eta(x) = \eta_1\cos(k_0x) + \eta_2\sin(k_0x). \tag{6}$$

It is convenient to introduce an order parameter with the components η_1 and η_2. Then, the expansion of the free-energy density has the form

$$\frac{A}{2}(\eta_1^2 + \eta_2^2) + \frac{B_1}{4}(\eta_1^2 + \eta_2^2)^2 + \frac{D}{2}[(\nabla\eta_1)^2 + (\nabla\eta_2)^2], \tag{7}$$

where $A = A_T(T - T_i)$, T_i is the temperature of the N–IC transition, and all the coefficients are of the same order of magnitude as in Eq. (1). Naturally, if one passes to the polar coordinates $\eta_1 = \rho\cos\varphi$ and $\eta_2 = \rho\sin\varphi$ in Eq. (7), one arrives at the expression independent of the phase φ. The absence of invariants anisotropic in the η_1, η_2 space of reflects that the phase formed is incommensurate; i.e., its period is incommensurate with respect to the lattice periods. Expression (7) may also be considered as an expansion in the components of the order parameter which describes lowering of the symmetry in the N–IC transition. These components are linear combinations of the normal system coordinates whose frequency goes to zero at the point of the N–IC transition at the wave vectors ($\pm k_0$, 0, 0). In this case, the use of expansion (7) signifies not only neglect of higher harmonics of the space distribution of the order parameter in the IC phase but also neglect of a slight change in the modulation period with the temperature variation. However, in the vicinity of the N–IC transition, such simplifications are quite justified.

It is possible to assume that, in the IC phase, $\eta_{e1} \neq 0$ and $\eta_{e2} = 0$, where η_{e1} has to be calculated in each order of the thermodynamic perturbation theory. However, we limit our consideration to the zeroth approximation by setting $\eta_{e1} = (-A/B)^{1/2}$, which does not considerably influence the results thus obtained which are considered below. Then, in the harmonic approximation, the quantity $\eta_1'(\mathbf{r}, t) = \eta_1(\mathbf{r}, t) - \eta_{e1}$ (hereafter, we omit the prime in the fluctuation notation) corresponds to an amplitudon and $\eta_2(\mathbf{r}, t)$ corresponds to phason fluctuations. It should be emphasized that, e.g., in the case of a two-component Heisenberg magnetic, the free-energy expansion may also be represented in form (7) if η_1 and η_2 are understood as longitudinal and transverse components of the magnetic moment, respectively. Similar to this case, the use of polar coordinates as components of the order parameter would complicate analysis of nonlinear effects associated with the phase (φ) fluctuations of the order parameter.

In accordance with expression (7), the equations of motion for $\eta_1(\mathbf{r}, t)$ and $\eta_2(\mathbf{r}, t)$ have the form

$$\begin{aligned} m\ddot{\eta}_1 + \gamma\dot{\eta}_1 + 2B_1\eta_{e1}^2\eta_1 + 3B_1\eta_{e1}\eta_1^2 \\ + B_1\eta_1\eta_2^2 + B_1\eta_1^3 - D\Delta\eta_2 = 0, \end{aligned} \tag{8}$$

$$m\ddot{\eta}_2 + \gamma\dot{\eta}_2 + 2B_1\eta_{e1}\eta_1\eta_2 + B_1\eta_1^2\eta_2 + B_1\eta_2^3 - D\Delta\eta_2 = 0, \quad (9)$$

where the coefficient γ is determined by the interaction of the order parameter with the hard and acoustic modes and, at high frequencies, may be estimated from Eq. (2). Passing to the Fourier representation, we may write Eqs. (8) and (9) in the form

$$(-m\Omega^2 - i\Omega\gamma + 2B_1\eta_{e1}^2 + Dq^2)\eta_1(\mathbf{k}, \omega) = -3B_1\eta_{e1}\sum_{\mathbf{k}}\int_{-\infty}^{+\infty}\eta_1(\mathbf{k}, \omega)\eta_1(\mathbf{q}-\mathbf{k}, \Omega-\omega)\frac{d\omega}{2\pi} - B_1\eta_{e1}\sum_{\mathbf{k}}\int_{-\infty}^{+\infty}\eta_2(\mathbf{k}, \omega)\eta_2(\mathbf{q}-\mathbf{k}, \Omega-\omega)\frac{d\omega}{2\pi}, \quad (10)$$

$$(-m\Omega^2 - i\Omega\gamma + Dq^2)\eta_2(\mathbf{k}, \omega) = -2B_1\eta_{e1}\sum_{\mathbf{k}}\int_{-\infty}^{+\infty}\eta_2(\mathbf{k}, \omega)\eta_1(\mathbf{q}-\mathbf{k}, \Omega-\omega)\frac{d\omega}{2\pi}, \quad (11)$$

where $\mathbf{q}$ and $\mathbf{k}$ are the wave vectors, Ω and ω are the frequencies, and the fourth-order anharmonicities are ignored. The most obvious manifestation of such anharmonicities in terms of the problems considered here is an additional contribution to attenuation estimated in the same way as in the case of a one-component order parameter.

The inverse response functions of a phason and an amplitudon in the zero approximation are determined by relationships

$$\chi_{01}^{-1}(\mathbf{q}, \Omega) = -m\Omega^2 - i\Omega\gamma + 2B_1\eta_{e1}^2 + Dq^2, \quad (12)$$

$$\chi_{02}^{-1}(\mathbf{q}, \Omega) = -m\Omega^2 - i\Omega\gamma + Dq^2. \quad (13)$$

Consider the fluctuation correction to the reciprocal phason susceptibility, $(\Sigma_2(\mathbf{q}, \Omega))$. Using Eq. (11), we obtain, in the second order of the perturbation theory,

$$\Sigma_2(\mathbf{q}, \Omega) = -4B_1^2\eta_e^2\sum_{\mathbf{k}}\int_{-\infty}^{+\infty}\frac{\langle|\eta_1(\mathbf{q}-\mathbf{k}, \Omega-\omega)|^2\rangle}{m(-\omega^2 + \omega_{02}^2(\mathbf{k}) - i\omega\Gamma)}\frac{d\omega}{2\pi} - 4B_1^2\eta_e^2\sum_{\mathbf{k}}\int_{-\infty}^{+\infty}\frac{\langle|\eta_2(\mathbf{q}-\mathbf{k}, \Omega-\omega)|^2\rangle}{m(-\omega^2 + \omega_{01}^2(\mathbf{k}) - i\omega\Gamma)}\frac{d\omega}{2\pi}, \quad (14)$$

where $\langle\ldots\rangle$ indicates averaging over fluctuations and

$$\langle|\eta_i(\mathbf{q}, \Omega)|^2\rangle = [2T/(\Omega V)]\mathrm{Im}\chi_{0t}(\mathbf{q}, \Omega). \quad (15)$$

It follows from Eq. (14) that estimate (5) may be used to renormalize attenuation ($\Omega^{-1}m^{-1}\mathrm{Im}\Sigma_2(q = 0, \Omega) \equiv \delta\Gamma_2$). In this case, $\delta\Gamma_2$ has no considerable dispersion in the region of small wave vectors. When calculating the amplitudon response function, the interaction $B_1\eta_{1e}\eta_1\eta_2^2$ gives rise to contributions diverging at $q \longrightarrow 0$. Similar divergences also arise in the next orders of the perturbation theory. However, this problem may be avoided if one formulates the perturbation theory in the direct response functions (and not reciprocal ones, as was done in derivation of Eq. (14)). Then, the motion equations (10) and (11) yield the amplitudon susceptibility in the form

$$\chi_1(\mathbf{q}, \Omega) = \frac{1}{-m\Omega^2 - i\Omega\gamma + 2B_1\eta_{e1}^2 + Dq^2} - \frac{\Sigma_1(\mathbf{q}, \Omega)}{(-m\Omega^2 - i\Omega\gamma + 2B_1\eta_{e1}^2 + Dq^2)^2}, \quad (16)$$

where $\Sigma_1(\mathbf{q}, \Omega)$ is determined by the following equality:

$$\Sigma_1(\mathbf{q}, \Omega) = -36(B_1\eta_{e1})^2 \times \sum_{\mathbf{k}}\int_{-\infty}^{+\infty}\frac{\langle|\eta_1(\mathbf{q}-\mathbf{k}, \Omega-\omega)|^2\rangle}{m(-\omega^2 + \omega_{01}^2(\mathbf{k}) - i\omega\Gamma)}\frac{d\omega}{2\pi} - 4(B_1\eta_{e1})^2\sum_{\mathbf{k}}\int_{-\infty}^{+\infty}\frac{\langle|\eta_2(\mathbf{q}-\mathbf{k}, \Omega-\omega)|^2\rangle}{m(-\omega^2 + \omega_{02}^2(\mathbf{k}) - i\omega\Gamma)}\frac{d\omega}{2\pi}, \quad (17)$$

with $\omega_{01}^2(\mathbf{k}) = (2B_1\eta_{e1}^2 + Dk^2)/m$ and $\omega_{02}^2(\mathbf{k}) = (Dk^2)/m$. Now, divergence of the second term on the right-hand side of Eq. (17) is real. It reflects the divergence of the longitudinal susceptibility at $q \longrightarrow 0$ and $\Omega \longrightarrow 0$, because the remaining terms of the perturbation series do not diverge within the applicability range of the Landau theory. This statement is a classical version of the well-known statement made in [11] for a Heisenberg magnetic. In terms of the perturbation theory, the absence of divergence in higher orders of the perturbation theory signifies their mutual compensation, which is characteristic of degenerate phases.

Denoting the second term in Eq. (17) by $-4(B_1\eta_{1e})^2\Pi_2(\mathbf{q}, \Omega)$ and taking into account renormalization of phason damping described above, we have

$$\Pi_2(\mathbf{q}, \Omega) = \frac{T}{8\pi^4 m^2}\iint\frac{\Gamma_2 d\mathbf{k}d\omega}{\{[(\omega-\Omega)^2 - c^2(\mathbf{k}-\mathbf{q})]^2 + (\omega-\Omega)^2\Gamma_2^2\}(-\omega^2 + c^2k^2 - i\omega\Gamma_2)}, \quad (18)$$

where $c = \sqrt{D/m}$. To single out the main divergence in Eq. (18), we may assume that $m = 0$. Then, according to [4], we have

$$\Pi_2(\mathbf{q}, \Omega) = \frac{T}{8\pi D^{3/2}}\left(\frac{1}{[D(2q/\pi)^2] + |\Omega|\gamma_2]^{1/2}} + \frac{i\gamma_2\Omega}{(Dq^2 + |\Omega|\gamma_2)^{3/2}}\right). \quad (19)$$

At $m \neq 0$, the additional divergence of the imaginary part $\mathrm{Im}\Pi_2(\mathbf{q}, \Omega) = -\Omega\Pi_2''(\mathbf{q}, \Omega)$ is the most important. We find from Eq. (18) that

$$\delta\Pi_2''(\mathbf{q}, \Omega) = \frac{T}{16\pi D^2 q}\frac{1}{\Gamma_2} \quad (20)$$

at $q \ll \Gamma_2/c$ and that

$$\delta\Pi_2''(\mathbf{q}, \Omega) = \frac{T}{8\pi D^2 q}\frac{1}{cq} \quad (21)$$

in the opposite case where $q \gg \Gamma_2/c$. We see that at low frequencies ($\Omega \ll \Gamma_2$) it is possible to ignore the quantity $\delta\Pi_2''(\mathbf{q}, \Omega)$ in comparison with the imaginary part of Eq. (19) if $q \ll \Gamma_2/c$, whereas if $q \gg \Gamma_2/c$, this quantity makes the main contribution. In this case, relationships (16), (17), and (21) show that estimate (5) remains valid for the damping constant of an amplitudon at $q \approx r_c^{-1}$. Thus, the specific softness of the phase fluctuation influences the low-frequency amplitudon susceptibility only at $q < 0$, whereas in the main region of the **q** space, this influence results in the same change of attenuation as in the case of a one-component order parameter.

Now, consider the specific features of the dynamics of an order parameter in IC phases at low temperatures. Low-temperature phonon losses were analyzed in a number of works (see [12]). As earlier, we consider here the low-frequency attenuation coefficients ($\Omega \longrightarrow 0$), i.e., the loss fraction proportional to Ω. These losses are caused by the association processes in which a phonon under consideration is scattered by a thermal phonon (with the energy of the order of T) and, thus, gives rise to two new phonons (in the general case, the contributions of processes accompanied by appearance of only one phonon are proportional to higher powers of Ω and, therefore, may be neglected). No doubt, only low-energetic acoustic phonons and phonons of the phason branch may play the role of thermal phonons at low temperatures. By virtue of the laws of energy conservation, only phonons of the same branches with the energies either of the order of T or lower than T may be created. Therefore, only phason–phason and phason–acoustic phonon interactions are important. Because of a large value of phason attenuation in this case, the interaction inside the phason branch should be more important than the interaction between a phason and acoustic vibrations.

Phason attenuation at low temperatures was calculated in [5, 13]. It was shown that one has to take into account in an effective Hamiltonian not only the $B_1\eta_2^4/4$ interaction but also the interaction between a phason and an amplitudon $B_1\eta_{e1}\eta_1\eta_2^2$. Each of the corresponding anharmonicities gives rise to certain contributions to reciprocal susceptibility which diverges at small wave vectors and frequencies; however, these divergences are mutually compensated in each order of the perturbation theory. The result of this compensation may be described with the aid of a specially introduced effective four-phonon interaction in the phason branch. The value of this interaction is squared with respect to the wave vectors (k_i) and frequencies (ω_i) at $k_i \longrightarrow 0$ and $\omega_i \longrightarrow 0$. The phason damping constant at low temperatures is represented as

$$\Gamma_2(q \approx 0, \Omega \approx 0) \approx 10^{-2}\omega_T\frac{T^2}{|A|^2}k_T^2\frac{B^2}{D^2} \approx (10^{-1}-10^{-2})\Omega_D\left(\frac{T}{T_D}\right)^5, \quad (22)$$

where $k_T \approx d^{-1}(T/T_D)$ and $\omega_T \approx \Omega_D(T/T_D)$ are the wave vector and the frequency of a thermal phonon, respectively. It was also assumed that $T_c \approx T_D$. Equation (22) shows that at low temperatures and frequencies the constant of phason damping considerably exceeds that of "ordinary" optical phonons, e.g., damping of polar modes in a centrosymmetric crystal determining dielectric losses. In the latter case, damping of the optical modes is caused by their interactions with $P_i u_{jk} u_{lm} \nabla u_{pq}$-type acoustic modes. These interactions are proportional to k^4 and result in damping in the second-order of the perturbation theory, $\sim T^9$ [12]. The exception is a hexagonal crystal with random degeneracy in the acoustic waves along certain directions in which $P_i u_{jk} \nabla u_{lm}$-type interactions result in damping proportional to T^5. It was indicated above that the effective interaction in the phason branch is proportional to k^2 (ω^2) and that the main contribution at low temperatures comes from the association processes with the participation of thermal phonons. Then, phason attenuation is described as $T^9/(k_T^2)^2 \sim T^5$, which corresponds to the result described by Eq. (22). It should also be indicated that the $\eta_2^2 u_{ll}$-type interaction is unimportant for estimating $\Gamma_2(q \approx 0, \Omega \approx 0)$ at the conventional difference between the sound and phason velocities.

The amplitudon response function at low temperatures has the form [5]

$$\chi_1(\mathbf{q}, \Omega) = \frac{1}{m[\omega_{01}^2(\mathbf{q}) - \Omega^2 - i\Gamma_1\Omega]} + \frac{2T(B\eta_{e1})^2}{m^4[\omega_{01}^2(\mathbf{q}) - \Omega^2 - i\Gamma_1\Omega]^2}\Phi(\mathbf{q}, \Omega), \quad (23)$$

where the first term corresponds to the zeroth approximation in intrinsic anharmonicity of the order parameter and the second term corresponds to the interaction between an amplitudon and phason. For simplicity, we first assume that $\Gamma_1 = 0$ in Eq. (23). If $\Omega \longrightarrow 0$, the function $\Phi(q, \Omega)$ diverges at small wave vectors. This divergence is weaker that the divergence of $\chi_1(q, \Omega)$ at high temperatures [5]. If $T \longrightarrow 0$, $\mathrm{Re}\Phi(q, \Omega \longrightarrow 0)$ diverges as $\ln q$. For the imaginary part $\Phi(q, \Omega)$ we have

$$\mathrm{Im}\,\Phi(q, \Omega \longrightarrow 0)|_{q < k_T} \cong \frac{\Omega}{4\pi^2 q^2 c^5}. \quad (24)$$

Now, consider the corrections due to finiteness of Γ_1. It is more difficult to calculate Γ_1 than the phason attenuation, because, generally speaking, the amplitudon vibrations are accompanied by a change of temperature. This is explained by the fact that an amplitudon is a fully symmetric vibration, which makes our problem somewhat similar to the determination of the attenuation of longitudinal sound. However, planning the further calculation of spin-lattice relaxation rate at the Larmor-frequency $\Omega_0 \geq 10^8$ s^{-1} at temperatures of the order of several Kelvins (see below), one has to take into account that such frequencies turn out to exceed the reciprocal lifetime of thermal phonons responsible for the phason and acoustic branches. Indeed, the lifetime of thermal acoustic phonons is estimated as [12]

$$\tau_N^{-1} \approx \frac{T^5}{\rho\hbar^4 v^5}, \quad (25)$$

where ρ is the density. For the reciprocal lifetime of thermal phasons, τ_{ph}^{-1}, which, along with the acoustic thermal phonons, determines the value of Γ_1, the estimate (22) remains valid; i.e., $\tau_{\mathrm{ph}}^{-1} \approx \Gamma_2(q \approx 0, \Omega \approx 0)$. At $T \cong 1$ K, the estimates τ_N^{-1} and τ_{ph}^{-1} yield 10^2–10^3 s^{-1}, and at $T \cong 10$ K, we have 10^7–10^8 s^{-1}. Thus, $\Omega_0 > \tau_N^{-1}$, τ_{ph}^{-1}. At such frequencies, the temperature concept becomes inadequate because the thermalization time of thermal phonons becomes less than the period of the low-frequency vibrations considered here. Therefore, both sound and amplitudon attenuation are determined by the Landau–Rumer multiphonon mechanism.

In the calculations by Eq. (23), we took into account the direct interaction between an amplitudon and phason. Now, when calculating Γ_1, we have to take into account only some additional interactions resulting in scattering of phonons of the amplitudon branch. The most effective processes here are the four-quantum processes corresponding to the $\eta_{e1}\eta_1 u_{ii}^3$- and $\eta_{e1}\eta_1\eta_2^2 u_{ii}$-type interactions (in the symmetric phase, $(\eta_1^2 + \eta_2^2)u_{ii}^3$ and $(\eta_1^2 + \eta_2^2)^2 u_{ii}$ interactions). The $\eta_{e1}\eta_1 u_{ii}^2$ -type interactions squared with respect to strains give the contribution small with respect to the parameter $(\hbar\Omega_0/T)^n$ $(n \geq 1)$ because of the constraints imposed by the laws of conservation [12]. The calculations made in [5] showed that $\Gamma_1(\Omega_0)$ is proportional to T^7, which may readily be seen from the comparison of this attenuation with phason attenuation. Thus, the interaction $\eta_{e1}\eta_1 u_{ii}^3$ is proportional to k^3, whereas the damping constant Γ_1 is squared with respect to this interaction; hence, $\Gamma_1 \sim k_T^2\Gamma_2 \sim T^7$. The contribution to Γ_1 caused by the interaction containing the squared amplitude of the order parameter $\eta_{e1}\eta_1((\eta_{e1} + \eta_1)^2 + \eta_2^2)u_{ii}$ has the same temperature dependence but with a larger multiplier. Nevertheless, the quantity Γ_1 has such a low value that the corresponding corrections to $\chi_1(\mathbf{q}, \Omega)$ may be ignored.

SPIN-LATTICE RELAXATION

To reveal the specific features of the anomalies of the spin-lattice relaxation rate in IC phases, we consider the simplest case, where a perturbed part of the Hamiltonian may be represented as a product of the operator **A** acting on spin variables and the function $F(t)$ is dependent on the lattice variables. The SLR rate is expressed as

$$T_1^{-1} = gJ(\Omega_0), \quad (26)$$

where Ω_0 is the Larmor frequency,

$$J(\omega) = \int_{-\infty}^{+\infty} \langle F(t)F(t+\tau)\rangle e^{i\omega t} d\tau. \quad (27)$$

Now, we single out from F its dependence on the order parameter

$$F = F_0 + a_1\eta_1 + a_2\eta_1^2 + b_1\eta_2 + b_2\eta_2^2 + \ldots \quad (28)$$

and consider only direct processes since the contributions from all the other processes (in particular, Raman processes) to the SLR rate in the vicinity of the points of structural phase transitions in the displacive-type systems are usually less significant [4, 5]. Then, we may limit ourselves in the expression for $J(\Omega_0)$ to the

terms squared with respect to the order parameter,

$$J(\Omega_0) = a_1^2\sum_{\mathbf{q}}\langle|\eta_1(\mathbf{q},\Omega_0)|^2\rangle + b_1^2\sum_{\mathbf{q}}\langle|\eta_2(\mathbf{q},\Omega_0)|^2\rangle. \quad (29)$$

The dynamic correlation functions in Eq. (29) may be calculated on the basis of the fluctuation–dissipation theorem for the dynamic susceptibilities (response functions $\chi_i(\mathbf{q}, \Omega_0)$) defined above.

Equations (13), (14), and (29) yield the following phason contribution ($J_{1\text{ph}}$) to the SLR rate:

$$J_{\text{ph}}(\Omega_0) = b_1^2\frac{T\gamma_2^{1/2}}{2^{3/2}\pi D^{3/2}}\frac{1}{\Omega_0^{1/2}}, \quad (30)$$

which coincides with the well-known result obtained in [14] with the only difference that the coefficient γ_2 is estimated by Eq. (5).

Now consider the contribution of amplitude fluctuations to the SLR rate. Excluding the effect caused by susceptibility divergence at small q, which will be considered later, we may calculate this contribution by redefining the response function (12) in the zeroth approximation. With this aim, we used instead of γ the damping constant Γ_1/m, which, in accordance with the first terms on the right-hand side of Eq. (17), is estimated at $q \approx r_c^{-1}$ from Eq. (5). Then the quantity $\int \text{Im}\,\chi_{01}(q, \Omega)dq$ determines the corresponding amplitudon contribution to the SLR rate. This contribution equals

$$J_{\text{am}}(\Omega_0) \approx a_1^2\frac{mT\Gamma_1}{2^{5/2}\pi^2 D^{3/2}}\frac{1}{|A|^{1/2}} \approx a_1^2\frac{d^2}{\Omega_D}\left(\frac{T_c}{T_{\text{at}}}\right)^{3/2}\left(\frac{T_c}{T_c - T}\right)^{1/2}. \quad (31)$$

It should be noted that the SLR rate in a symmetric phase is strongly dependent on the soft-mode dispersion [4]. At a weak dispersion, the low-frequency damping of the doubly degenerate soft mode is of the order of $\Omega_D T/T_{\text{at}}$ and estimate (31) is valid. At a strong dispersion, the damping constant is of the same order as in Eq. (3); therefore, the SLR rate is considerably lower but has a more pronounced temperature dependence, $(T - T_i)^{-1}$.

To calculate the contribution caused by divergence χ_1 at small q, it is sufficient to compare the quantities $\int \text{Im}\,\chi_{01}(\mathbf{q}, \Omega)d\mathbf{q}$ and $\int \text{Im}\,\delta\chi_{01}(\mathbf{q}, \Omega)d\mathbf{q}$ in which the second integral is calculated in the region $q < \Gamma_2/c$ and

$$\delta\chi_{01}(\mathbf{q},\Omega) = \frac{i\Omega 4(B\eta_{e1})^2\Pi_2''(\mathbf{q},\Omega)}{(2B_1\eta_{e1}^2 + Dq^2 - i\Omega\gamma_1)^2}. \quad (32)$$

The $\Pi_2''(\mathbf{q}, \Omega)$ is determined by relationship (19). Calculating the ratio of the above two integrals, we obtain

$$\delta J_{\text{am}} \cong \frac{1}{2^{3/2}\pi^2}\frac{\Gamma_2}{\Gamma_1}\xi\ln\frac{\Gamma_2}{\Omega_0}J_{\text{am}}, \quad (33)$$

where $\xi = BT_c/(|A|D^{3/2})$ is the parameter of the perturbation theory. Thus, the correction for diverging longitudinal fluctuations is logarithmically dependent on the Larmor frequency but includes the parameter ξ which is not small only at the boundary of the applicability range of the perturbation theory.

It is natural to expect that the specific features of the lattice dynamics in an IC phase would manifest themselves at low temperatures as well. Nonconducting molecular crystals with low-temperature IC phases were intensely studied in this temperature range [15–17] and the respective measurements were made up to the temperature 1 K. Hereafter, we consider a low-temperature range a region in which the condition $\hbar\Omega_0 \ll T \ll T_D$ is fulfilled. Since the Larmor frequencies are of the order of 10^8 s^{-1}, this condition is also true for $T \sim 1$ K. Furthermore, the effect of a phonon bottle neck is neglected because the SLR time at $T \sim 1$ K is usually of the order of several seconds, whereas the phason lifetime (closely related to the effects we are interested in) is much shorter (see Eq. (22)).

Since it follows from Eq. (22) that phason damping is very weak ($\Gamma_2 \equiv \gamma_2/2m < \Omega_0$), when calculating the response function, one has also to take into account the inertia term. It follows from the condition $\hbar\Omega_0 \ll T$ that the correlation function at the Larmor frequency may be written in the classical limit of Eq. (15). Then, the phason contribution to the SLR rate is [5]

$$J_{1\text{ph}}(\Omega_0) = b_1^2\sum_{\mathbf{q}}\frac{2\gamma_2 T}{V[(-m\Omega^2 + Dq^2)^2 + (\Omega\gamma_2)^2]} = b_1^2\frac{T}{2^{3/2}\pi D^{3/2}}\frac{1}{\Omega_0} \quad (34)$$

$$\times[((m\Omega_0^2)^2 + (\gamma_2\Omega_0)^2)^{1/2} + m\Omega_0^2]^{1/2} \approx b_1^2\frac{Tm^{1/2}}{2\pi D^{3/2}}.$$

In other words, the SLR rate is independent of Ω_0. It should be emphasized that the contribution of direct phason processes described by Eq. (34) to the SLR rate considerably exceeds the contribution of acoustic phonons forming the background at low temperatures. This contribution also includes a small factor $(\Omega_0/\Omega_D)^2$ which arises because a spin Hamiltonian depends on

the strain-tensor component, i.e., on the derivatives of displacements.

The characteristic temperature T_b separating the high-temperature region ($J_{ph}(\Omega_0) \sim \Omega_0^{-1/2}$) and the low-temperature region ($J_{ph}(\Omega_0) = \text{const}$) may be evaluated from the condition $\Gamma_2(T_b) \approx \Omega_0$, which, in accordance with Eq. (22) yields

$$T_b \approx T\left(\frac{\Omega_0}{10^{-2}\Omega_D}\right)^{1/5}. \quad (35)$$

It follows from expression (35) that T_b may be lower by an order of magnitude than T_D and, therefore, it is quite possible to observe both "modes" of the SLR rate.

The estimate of the amplitudon contribution is obtained from Eqs. (23), (24), and (29) as

$$J_{am} \approx a_1^2 \frac{mT^3}{8\pi^3\hbar D^3 \eta_{1e}^2(T \approx 0)}, \quad (36)$$

where $\eta_{1e}^2(T \approx 0) \approx T_i/T_{at}$. The value of this contribution is less than J_{ph} from Eq. (34) but considerably higher than the phason contribution in Raman processes [5]. As follows from Eq. (23), the correction to Eq. (36) due to finiteness of Γ_1 ($\Gamma_1 \sim T^7$) is proportional, at least, to T^8; i.e., it is negligible at low temperatures. Thus, unlike the case of a high temperature, the divergence of $\chi_1(\mathbf{q}, \Omega)$ due to the interaction of an amplitudon with a phason determines the major contribution ($\sim T^3$) of an amplitudon to the SLR rate.

SOUND ATTENUATION

Ultrasonic properties of a medium are described by a complex frequency-dependent elastic modulus $\lambda(\Omega) = \lambda'(\Omega) - i\lambda''(\Omega)$ corresponding to the limit of small wave vectors. The real part $\lambda'(\Omega)$ determines the sound velocity, whereas its imaginary part determines sound attenuation. In the low-frequency limit, $\lambda''(\Omega)$ is a thermodynamic quantity whose temperature anomaly may be calculated within the framework of the thermodynamic theory of perturbations. This quantity also determines quite well the sound velocity at ultrasonic frequencies because the corresponding frequency dispersion in this region is usually quite small. Attenuation is a kinetic effect and to calculate it one has to invoke the dynamic theory of perturbations.

We consider the specific features of longitudinal-sound attenuation in an IC phase in an example of elastically isotropic medium. In this case, some additional terms corresponding to elastic energy should be added to the expansion of the free-energy density described by Eq. (7),

$$r(\eta_1^2 + \eta_2^2)u_{ii} + \frac{K}{2}u_{ii}^2 + \mu\left(u_{ik} - \frac{1}{3}u_{ii}\delta_{ik}\right)^2, \quad (37)$$

where K is the bulk modulus and μ is the shear modulus. The complex elasticity modulus may be determined from the corresponding motion equations of the order parameter and longitudinal deformation by using the standard perturbation theory.

For an IC phase, similar to the case of a low-symmetric phase in the case of a one-component order parameter, the effect of fluctuations on longitudinal-sound attenuation depends not only on the dynamics of the order parameter but also on the dynamics of the acoustic subsystem [6]. Therefore, the anomaly of the sound attenuation cannot be described by an arbitrary elementary function of temperature even in lower orders of the perturbation theory. Relatively simple expressions can be obtained only in two limiting cases of the zeroth ($\rho = 0$) or infinite ($\rho = \infty$) inertia of acoustic fluctuations. We consider here the first limiting case. The elastic modulus of an IC phase for a displacive system in the limit $\rho = 0$ may be represented as [6, 7]

$$\lambda(\Omega) \cong \lambda - \frac{4r^2\langle\eta_1\rangle^2}{2B\eta_{e1}^2 - i\Omega\gamma_1} - 16r^2\left(\frac{B''}{B}\right)^2\Pi_1(0, \Omega) + 4r^2\frac{(\Omega\gamma)^2}{(2B_1\eta_{e1}^2 - i\Omega\gamma_1)^2}\Pi_2(0, \Omega), \quad (38)$$

where $B'' = B_1 - 2r^2/(K + 4\mu/3)$ and γ_1 is the low-frequency amplitudon attenuation. The second term on the right-hand side of Eq. (38) corresponds to the Landau–Khalatnikov mechanism and is calculated in the mean-field approximation. The third term corresponds to the contribution of amplitudon fluctuations and, for displacive systems, we obtain

$$\Pi_1(0, \Omega) = \sum_{k,\omega}\frac{\langle|\eta_1(k, \omega - \Omega)|^2\rangle}{2B_1\eta_{e1}^2 + Dk^2 - i\omega\gamma - m\omega^2} \cong \frac{T_c}{16\pi D^{3/2}(2|A|)^{1/2}}\left(1 + \frac{i\Omega\Gamma}{2(\Omega^2 + \Gamma^2)}\right), \quad (39)$$

where $\Gamma = \gamma/m$ is the amplitudon damping constant at the amplitudon mode frequency. Evaluating γ_1 in the first term using Eqs. (2) or (3), one may readily see that, in the applicability range of the perturbation theory, the corresponding attenuation $\gamma_1 r^2/(B\eta_{e1}^2)$ is considerably less than the contribution corresponding to the amplitude fluctuations being proportional to $\mathrm{Im}\Pi_1(0, \Omega)$.

Since an amplitudon in the harmonic approximation is analogous to the soft mode in the nonsymmetric phase, its contribution to sound attenuation has the same form as in the case of a one-component order parameter. Thus, the third term in Eq. (38) contains the fluctuation corrections to r and also the fluctuation contribution to low-frequency amplitudon attenuation evaluated by Eq. (4). Similar corrections considerably (by a factor of $4(B'')^2/B^2$ for $\rho = 0$) increase the contribution

of amplitude fluctuations to sound attenuation in the incommensurate phase. This was usually ignored in the interpretation of the experimental data [3]. It should also be noted that in order–disorder transitions the fluctuation correction to sound attenuation is considerably lower than the value of $\Omega\gamma r^2/(B\eta_{e1}^2)$; however, it may have an arbitrary sign [6].

The last term in (38) corresponds to the phason contribution, and $\Pi_2(0, \Omega)$ in this contribution is determined by the Eq. (18) at $q = 0$. To reveal the major divergence in Eq. (18), one has to assume, as earlier, that $m = 0$. Then

$$\Pi_2(0,\Omega) = \sum_{\mathbf{k},\omega} \frac{\langle|\eta_2(\mathbf{k}, \omega-\Omega)|^2\rangle}{Dk^2 - i\omega\gamma_2} = \frac{T}{8\pi D^{3/2}} \frac{(1 + i\,\mathrm{sgn}(\Omega))}{\sqrt{\Omega\gamma_2}}. \quad (40)$$

It is seen from Eqs. (38) and (40) that the phason contribution to the sound attenuation is negative and proportional to $\Omega^{3/2}$. It is natural that the total coefficient of sound attenuation is positive because of the amplitudon contribution.

To explain the nonanalytical frequency dependence of the phason contribution to sound attenuation, we compare it with the contribution corresponding to fluctuations of the elastic displacements. Although the fluctuations of the displacement vector diverge if the wave vectors and frequencies are small, they do not give rise to nonanalytical contribution to the attenuation, because their own attenuation is proportional to k^2. (It is because of this that the attenuation of fluctuations corresponding to the acoustic branch was neglected in Eq. (38).) Thus, one may state that it is the finite attenuation of diverging phase fluctuations that gives rise to the nonanalytical contribution to sound attenuation in an IC phase.

For displacive-type systems at frequencies $\Omega < \Omega_r = 2|A|/(m\Gamma)$, the ratio of phason and amplitudon contributions is proportional to $(\Omega/\Omega_r)^{1/2}(\Gamma^2 m/|A|)$. Since, in the applicability range of the perturbation theory, $\Gamma^2 m/|A| \ll 1$, the phason contribution at frequencies $\Omega < \Omega_r$ is infinitesimal. At the frequencies $\Omega > \Omega_r$, both contributions become comparable; however, in the study of displacive-type systems, this region is of no interest because Ω_r in such regions considerably exceeds the amplitudon frequency.

It should be noted that, in fact, the last term in Eq. (38) corresponds to the sum of the contributions, each of which diverges at $\Omega \longrightarrow 0$ [7]. However, these divergences are compensated both in the approximation considered above and in higher approximations of the perturbation theory. This compensation arises because a phason is not directly related to longitudinal strains and influences these strains via amplitudon fluctuations.

In conclusion, we would like to emphasize that, in all the above cases, we considered ideal crystals. Of course, defects in real crystals lead to pinning of the order-parameter phase [1] and, as a result, the phason spectrum at small wave vectors acquires a gap. However, the experimental results show that in some occasions (e.g., in extremely pure crystals) this gap is rather small even in comparison with the Larmor frequencies [17, 18]. In such cases, the results obtained above may underlie the interpretation of the corresponding experiments.

REFERENCES

1. *Incommensurate Phases in Dielectrics*, Ed. by R. Blinc and A. P. Levanyuk (North-Holland, Amsterdam, 1986), Vol. 1.
2. V. A. Golovko and A. P. Levanyuk, in *Light Scattering Near Phase Transitions*, Ed. by H. Z. Cummins and A. P. Levanyuk (North-Holland, Amsterdam, 1983; Nauka, Moscow, 1990).
3. H. Z. Cummins, Phys. Rep. **185**, 211 (1990).
4. A. P. Levanyuk, S. A. Minyukov, J. Etrillard, and B. Toudic, Phys. Rev. B **56**, 13785 (1997).
5. A. P. Levanyuk, S. A. Minyukov, J. Etrillard, and B. Toudic, Phys. Rev. B **56**, 8734 (1997).
6. A. P. Levanyuk, S. A. Minyukov, and M. Vallade, J. Phys. I **2**, 1949 (1992).
7. N. I. Lebedev, A. P. Levanyuk, S. A. Minyukov, and M. Vallade, J. Phys. I **2**, 2293 (1992).
8. V. G. Vaks, *Introduction to the Microscopic Theory of Ferroelectrics* (Nauka, Moscow, 1973) [in Russian].
9. A. Z. Patashinskiĭ and V. L. Pokrovskiĭ, *Fluctuation Theory of Phase Transitions*, 2nd ed. (Nauka, Moscow, 1982; Pergamon, Oxford, 1979).
10. A. D. Bruce and R. A. Cowley, J. Phys. C: Solid State Phys. **11**, 3609 (1978).
11. V. G. Vaks, A. I. Larkin, and S. A. Pikin, Zh. Éksp. Teor. Fiz. **53**, 1089 (1967) [Sov. Phys. JETP **26**, 647 (1968)].
12. V. L. Gurevich, *Kinetics of Photon Systems* (Nauka, Moscow, 1980) [in Russian].
13. S. Takada, K. Y. M. Wong, and T. Holstein, Phys. Rev. B **32**, 4639 (1985).
14. S. Zumer and R. Blinc, J. Phys. C **14**, 465 (1981).
15. A. Taye, D. Michel, and J. Petersson, Phys. Rev. B **66**, 174102 (2002).
16. R. Blinc, T. Apih, J. Dolinsek, *et al.*, Phys. Rev. B **51**, 1354 (1995).
17. R. E. Souza, M. Engelsberg, and D. J. Puisol, Phys. Rev. Lett. **66**, 1505 (1991).
18. P. Mischo, F. Decker, U. Hacker, *et al.*, Phys. Rev. Lett. **78**, 2152 (1997).

Translated by L. Man

Crystallography Reports, Vol. 50, No. 2, 2005, pp. 278–283. Translated from Kristallografiya, Vol. 50, No. 2, 2005, pp. 312–318.

PHYSICAL PROPERTIES OF CRYSTALS

Magnetostimulated Changes of Microhardness in Potassium Acid Phthalate Crystals

M. V. Koldaeva, T. N. Turskaya, and E. V. Darinskaya

Shubnikov Institute of Crystallography, Russian Academy of Sciences, Leninskiĭ pr. 59, Moscow, 119333 Russia

e-mail: mkoldaeva@ns.crys.ras.ru

Received April 7, 2004

Abstract—A decrease in microhardness along the (010) cleavage in potassium acid phthalate single crystals by 15–18% after the application of a permanent magnetic field is revealed for the first time.[1] It is shown that the effect revealed is of the volume character. The role of interlayer water in the processes stimulated by a magnetic field is studied. Interlayer water does not cause the observed changes; it only plays the part of an indicator of these changes in potassium acid phthalate crystals in a magnetic field. It is established that microhardness in the (100) plane of the crystal in an applied a magnetic field first increases by 12–15% and then remains constant in time within the accuracy of the experiment. The possibility of varying the crystal structure of potassium acid phthalate crystals by applying magnetic fields inducing rearrangement in the system of hydrogen bonds or in the defect structure is discussed. © *2005 Pleiades Publishing, Inc.*

The influence of weak magnetic fields on the mechanical properties of nonmagnetic crystals (magnetoplastic effect) is observed in both micro- [1] and macroplasticity [2–9] and is studied by scientists who use plastic physics methods.

The studies started in 1987 [1] showed that the magnetoplastic effect is explained by the action of a magnetic field on spin-dependent electron transitions either in a system dislocation–paramagnetic center [10, 11] or in magnetosensitive complexes of point defects [12, 13]. The electron transitions stimulated by magnetic fields may change the local energy of the dislocation interaction with a point defect, which results in plasticization (or hardening [14]) of a number of diamagnetic alkali halide, semiconductor, and metal crystals [10, 11]. As was shown earlier, similar processes may also change the rates of chemical reactions in magnetic fields [15, 16]. Up to now, the study of the magnetoplastic effect has been performed mainly on isotropic crystals. Interest has arisen in the study of the influence of a magnetic field on the properties of nonmagnetic anisotropic crystals with complicated structures widely used in technology.

We studied a potassium acid phthalate (KAP) crystal of the composition $C_8H_5O_4K$ with ionic, covalent, and hydrogen bonds [17, 18]. An orthorhombic crystal is described by the point symmetry group *mm*2. The crystal properties are explained by the presence of the polar ⟨001⟩ axis and a large distance between the (010) cleavages (~13 Å). Figure 1 shows the structural formula of KAP crystals possessing piezoelectric properties [19] that are widely used as analyzers in the long-wavelength range of the X-ray spectrum and as monochromators in various high-resolution X-ray instruments [20]. In the temperature range from 300 to 2 K, KAP crystals are diamagnetic along all the three main crystallographic directions.[2]

SAMPLE PREPARATION AND PROCESSING OF RESULTS

The experimental methods used in our study were selected in accordance with the studies of mechanical properties of KAP crystals [21–23] and, in particular, of their microhardness [23]. Motion of dislocations was not studied in any cited works. In [21, 22], considerable anisotropy of crystal deformation was observed: depending on the mutual orientation of the compression and polar (*z*) axes, crystals demonstrated brittle fracture, kink bands, or plastic deformation. To detect the influence of a magnetic field on the crystals we used a fast technically simple method of microindentation.

The KAP crystals used in our experiments were grown from aqueous solution by the method of decreasing temperature [19] at the Institute of Crystallography of the Russian Academy of Sciences. The samples were cut from crystalline boules by a wet thread. The faces were mechanically polished against a smooth wet silk. Microhardness was measured in the (010) and (100)

[1] Most of the results obtained in this study were first presented at the First Russian Conference of Young Scientists on Physical Material Science in Kaluga, October 4–7, 2001 (M.V. Koldaeva, *Collected Abstracts* (Kaluga, Manuskript, 2001), pp. 39–40).

[2] Magnetic susceptibility of KAP crystals was measured by Yu.G. Shvedenkov at the International Tomography Center, Siberian Division, Russian Academy of Sciences, Novosibirsk.

1063-7745/05/5002-0278$26.00 © 2005 Pleiades Publishing, Inc.

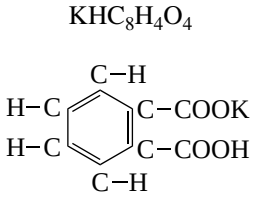

Fig. 1. Structural formula of a potassium acid phthalate (KAP) crystal.

faces. To measure microhardness in the (010) plane, we cleaved thin $3 \times 0.3 \times 7$ mm large plates along the cleavage. The $3 \times 3 \times 7$ mm samples for measurements in the (100) face were additionally polished prior to the experiment first mechanically and then by chemical polishing to remove a thin (about 0.15 mm) surface layer. Indentation was made with a Vickers pyramid under a load of 0.2 N, the impression diagonal was measured with the aid of a standard attachment to a Neophot-21 microscope.

Figure 2 (courtesy of N.L. Sizova from the Institute of Crystallography) shows typical impressions in the (010) cleavage (Fig. 2a) and in the perpendicular (100) plane (Fig. 2b) with the singled-out polar direction *z* and the diagonal *d*. Figure 2a shows that the impression in the (010) cleavage gives rise to cracking characteristic of brittle crystals [24]. Nevertheless the impression has an obvious faceting which allows one to make measurements. To measure microhardness in the (100) plane, the crystal was oriented in such a way that the angle formed by *d* and *z* was about 45°. The impression was almost a square shape; no cracks were recorded (Fig. 2b).

To avoid any confusion associated with the uniqueness of each measured surface and possible dependence of the results obtained on atmospheric conditions, each experimental point was measured on 3–5 thin plates sawed from two different bulky samples cut from the same growth pyramid. The microhardness of these plates was the same. Figure 3 shows a typical histogram of the diagonal *d* of the impression measured on face (010) of different samples. It is seen that the histogram is characterized by a normal Gaussian distribution. Thus, physically, averaging along the impression diagonals *d* measured under the same conditions on different cleavages is quite justified. The statistical errors δd were calculated using 50–100 measurements by the Microsoft Excel program and ranged within 2–4%. Microhardness *H* (in GPa) was calculated by the conventional formula for a Vickers pyramid [24] as

$$H = 1.854 \times 10^5 P/d_{st}^2,$$

where d_{st} is the statistical average of the impression diagonals measured in microns and *P* is the load applied to an indenter in grams. The measurement error δH was calculated as

$$\delta H = 2H(\delta d/d_{st}),$$

where δd is the statistical error of diagonal averaging over the sampling.

EXPERIMENTAL RESULTS AND DISCUSSION

In the first run of experiments, the samples in the shape of thin 3×7 mm plates with a thickness of ~0.3 mm were cleaved along the cleavage plane of one of the growth pyramids. One of two as-cleaved mirror-smooth surfaces was placed for 5 min into a 0.9 T magnetic field (**B** ∥ **z**), whereas the other sample served as a reference. Then microhardness of the surfaces of both samples was measured for 7–10 days as a function of time passed since cleavage. The results of these experiments are shown in Fig. 4a. After keeping the sample for five minutes in a 0.9 T magnetic field, microhardness decreased by 15–18% (curve *2*) in comparison with the microhardness of the mirror-smooth cleavage of the reference sample (curve *1*). This difference decreased with time and disappeared after 7–8 days. It was also interesting to consider microhardness as a function of time passed since the sample preparation. Therefore, we studied the surface of the reference sample (Fig. 4a, curve *1*). The removal of interlayer water from an as-cleaved surface was studied in [25]. Inter-

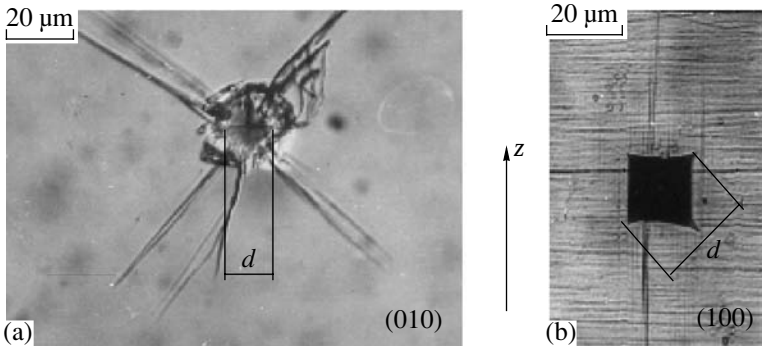

Fig. 2. Typical impression of an indenter with the single-out *z* direction and the diagonal *d* (a) in the (010) and (b) (100) planes.

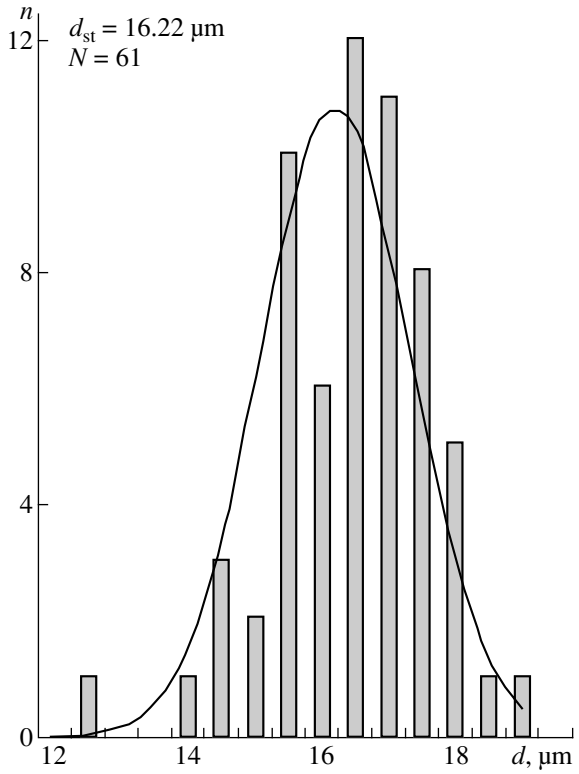

Fig. 3. Histogram of diagonals d of indenter impressions for four samples; the solid curve is the normal distribution of d calculated from the average d_{st} value and dispersion over the histogram.

layer water is always present in potassium acid phthalate crystals but it is not a structure-forming element. Possibly softening of the cleavage with time is explained by such processes.

To clarify the role of interlayer water in magnetostimulated processes, we had to diminish the amount of interlayer water in the bulk of potassium acid phthalate crystals. With this aim, we annealed the crystals for six hour at 220°C and then slowly cooled the crystals in an argon flow. With an increase of the temperature, water located in interplanar space leaves the crystal but is absorbed again during subsequent cooling [25]. To prevent water absorption, the furnace was constantly blown with a flow of argon both during annealing and cooling. The magnetostimulated changes of microhardness in annealed crystals were studied according the same scheme as in unannealed crystals.

The microhardness curve of the as-cleaved surfaces of annealed reference samples (Fig. 4b, curve *1*) is considerably lower than microhardness curve of unannealed samples (Fig. 4a, curve *1*). However, in this case as well, microhardness of annealed samples treated in a magnetic field (curve *2*) decreased by 15–18% in comparison with microhardness of the annealed reference samples.

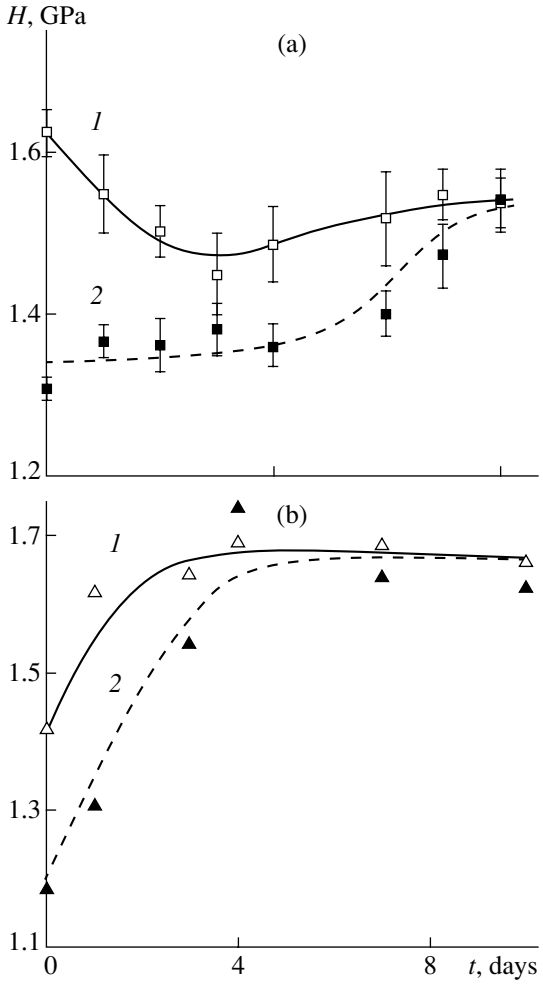

Fig. 4. Microhardness of the (010) face of a potassium acid phthalate crystal as a function of time passed since the preparation of mirror-smooth cleavages: (*1*) reference sample, (*2*) sample treated for 5 min in a 0.9 T magnetic field, (a) unannealed and (b) annealed crystals. In all the cases **B** || **z**.

Comparing the kinetics of surface aging (which manifests itself in the changes of microhardness with time) in unannealed and annealed samples (curves *1* in Figs. 4a, 4b, curves *1*), we assumed that surface aging of potassium acid phthalate crystals is associated with loss of water after preparation of cleavage and the interaction of its surface with atmosphere. After the treatment in a magnetic field, surface aging of unannealed crystals proceeds much slower than in the samples not kept in a magnetic field (Fig. 4a). At the same time, the initial slope of the $H(t)$ curves of the annealed crystals containing much less interlayer water did not change after treatment in a magnetic field (Fig. 4b). Thus, interlayer water is only an indicator of the changes taking place in potassium acid phthalate crystals in a magnetic crystal, and it cannot give rise to these changes.

To establish whether it is only a surface effect or the magnetic field that gives rise to the changes in the crystal bulk, we broke a bulky sample into two parts. Like

in the first run of experiments, one part of the crystal was kept for five min in a 0.9 T magnetic field (**B** || **z**), whereas the other part served as the reference sample. In this case, before every measurement a new cleavage was made, which allowed us to follow the possible changes in the bulk of the crystal subjected to the action of a magnetic field. To improve statistics, three bulk samples were used in these experiments.

Within the accuracy of the experiment, no temporal changes were observed in the reference part of the crystal (Fig. 5a, curve *1*). Microhardness of cleavages of the crystal part subjected to the action of a magnetic field (Fig. 5a, point *2*) decreased after keeping the crystal in a magnetic field at the same value as in the experiments of the first run. The influence of the magnetic field in the crystal bulk decreases with time. However, these changes have no component due to surface aging. Thus, the properties of potassium acid phthalate crystals kept in a magnetic field change not only at the surface but also in the crystal bulk.

Figure 5b shows the kinetics of microhardness changes after the application of the magnetic field. The $\Delta H(t)$ dependence corresponds to the difference in microhardness values (Figs. 4a, 4b, 5a; points *1* and *2*). It should be indicated that the ΔH value reflects the influence of the magnetic field on crystal microhardness. It is seen that the changes in microhardness in all the above experiments (Fig. 5b) in annealed and unannealed crystals vary with time almost in the same way and completely disappear after 6–7 days. Thus, this effect does not depend on the preliminary treatment of the sample. It should be remembered that, on the contrary, the magnetoplastic effect associated with the influence of a magnetic field on the state of the system of point defects in a crystal strongly depends on the preliminary thermal treatment of crystals. This is well seen in an example of alkali halide crystals [13]. Possibly, the structure of KAP crystals itself is changed under the action of a magnetic field.

As was mentioned above, potassium acid phthalate crystals are anisotropic; therefore, possible structural changes may be different at different faces. Therefore, in the next run of experiments, we performed indentation of the (100) face. To remove the defect layers formed due to sawing and to obtain smooth surfaces, we treated the crystals by the method considered above directly before the experiment. Then we broke each sample into two parts and, as in all the experiments performed, placed one part. into a 0.9 T magnetic field (**B** || **z**) for 5 min, whereas the other part served as a reference sample. It turned out that microhardness in the (100) plane treated in a permanent magnetic field increased by 12–15% (within the experimental accuracy) and then remained constant with time (Fig. 6, curve *2*). Microhardness of the reference (100) surface increased after aging for four–five days by 12–15% (Fig. 6, curve *1*). Thus, the effect of magnetostimulated changes in microhardness of KAP crystals of the same

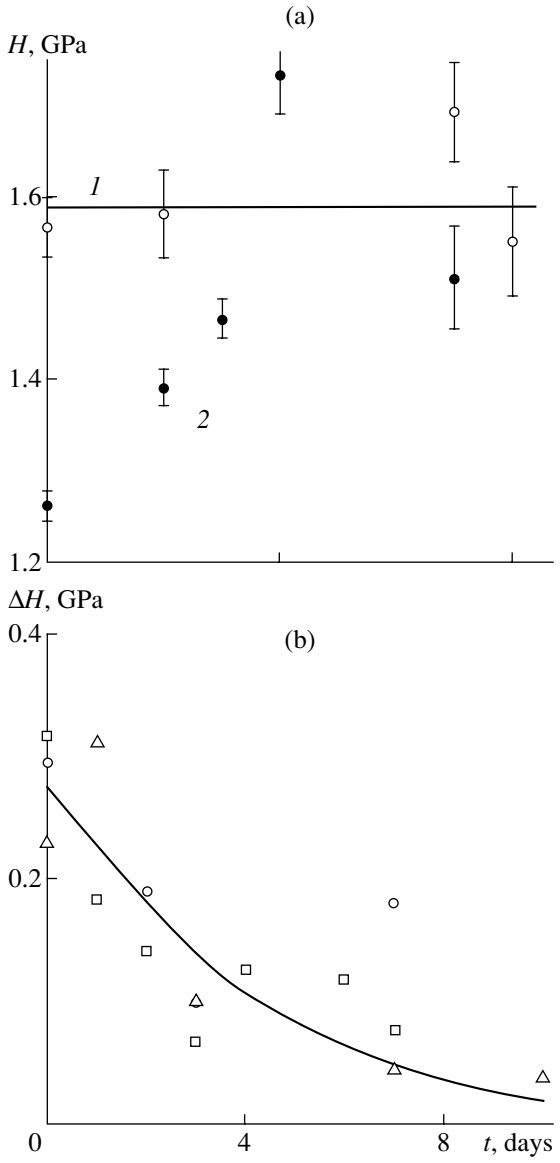

Fig. 5. (a) Microhardness and (b) differences in microhardness of the reference and magnetically treated samples in the (010) face of a potassium acid phthalate crystal as functions of time passed after 5-min treatment of samples in a 0.9 T magnetic field (**B** || **z**); (a) each measurement was made (*1*) on an as-cleaved face of the reference sample and (*2*) on a sample treated in a magnetic field; (b) on unannealed samples (□), annealed samples (△), and on cleavages prepared from a bulky sample directly prior to each measurement (○).

orientation in a magnetic field has opposite signs on the perpendicular faces (Figs. 4a and 6). It should also be noted that the magnetic field blocked aging of both (010) and (100) surfaces of unannealed crystals.

Figure 7 shows a fragment of the model of a potassium acid phthalate crystal constructed on the basis of data from [18]. It is seen that the perpendicular faces of the crystal have different structures and face-forming elements. However, Figs. 4a and 6 show that aging of

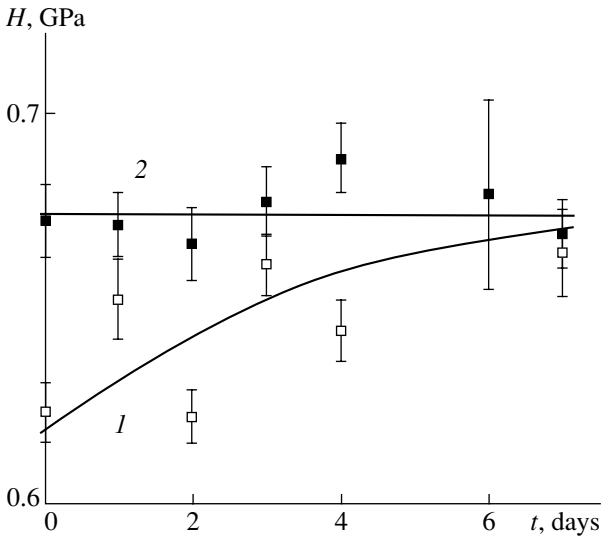

Fig. 6. Microhardness of the (100) face of a potassium acid phthalate crystal as a function of time passed after sample preparation: (*1*) for the reference sample, (*2*) for a sample treated for 5 min in a 0.9 T magnetic field.

the (010) and (100) faces of unannealed crystals is blocked by a constant magnetic field.

The effects observed in potassium acid phthalate crystals may hardly be explained by magnetostimulated changes in the local energy of interactions in the system dislocation–paramagnetic impurity center. First, the character of deformation described above shows that the main role is played by the displacements of the layers with respect to one another that are parallel to cleavage planes and not to generation and motion of dislocations as in alkali halide crystals. Second, unlike alkali halide crystals, in potassium acid phthalate crystals, the relative value of the effect does not depend on thermal treatment of crystals. Third, the change of microhardness after the equivalent action of a magnetic field has opposite signs at the perpendicular faces of the crystal. This may readily be understood if one assumes that the crystal structure has changed. Then, because of anisotropy, a different reaction of the magnetically treated perpendicular faces to the indenter may have different signs. These changes may also hinder the removal of the interlayer water from the crystal, i.e., influence the kinetic of surface aging. Of course, the above experimental data are still insufficient for reliable consideration of structural changes in potassium acid phthalate crystals; however, it seems reasonable to analyze their structure.

The layers of K^+ ions are located in the parallel (010) planes at different heights, whereas cations form corrugated layers separated by double layers of anions. The hydrophobic parts (benzene rings) inside the layers "look" at one another and are linked by van der Waals interactions. Hydrophylic groups are attached to cationic layers and form the chains along the *z* axis linked by intermolecular hydrogen bonds [18]. A fragment of such a chain is shown in the left-hand part of Fig. 7. Hydrogen bonds are depicted by dashed lines. It is possible to assume that, initially, some structural elements

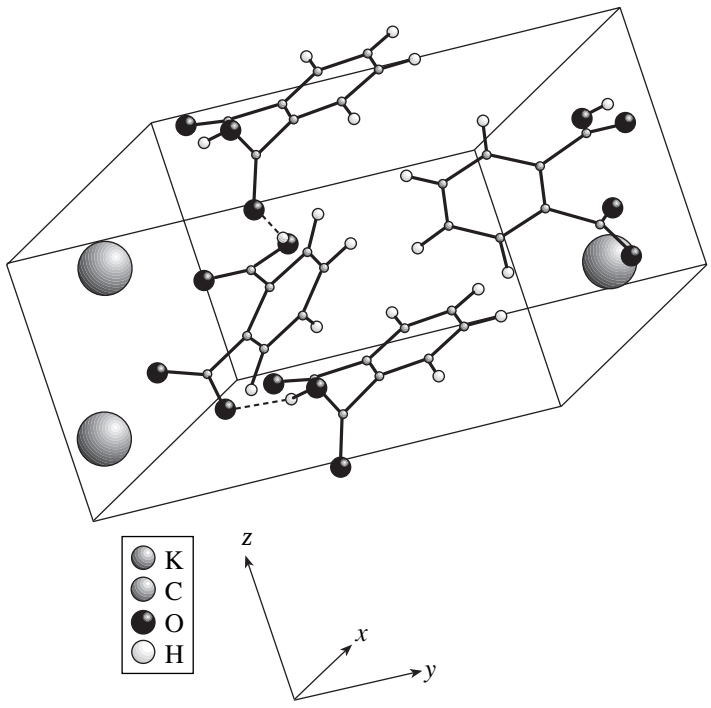

Fig. 7. Structural model of a potassium acid phthalate crystal and the unit cell and a chain of anions (solid line) linked by hydrogen bonds (dashed line).

in a potassium acid phthalate crystal are in the metastable state but then relax. It seems that, in a magnetic field, the conditions are created which stimulated their transition to an energetically more advantageous state. At this stage of the study, it is difficult to say in what way a magnetic field affects a KAP crystal and how it changes its structure. A structural element whose configurational changes may be of a fluctuating nature may be a hydrogen bond, since the fluctuation may transform an O–H···O bond into an O···H–O bond [26], and a magnetic field creates the conditions for such a transformation. Of course, we should not exclude possible transformation of some defect complexes related to structural elements under the action of a magnetic field.

The suggested interpretation of experimentally observed magnetostimulated change of microhardness in KAP crystals should be considered only as a working hypothesis. The verification of this hypothesis and the search for the explanations of such a pronounced effect of a magnetic field on microhardness of potassium acid phthalate crystals require further studies with invocation of spectroscopic and X-ray diffraction methods.

ACKNOWLEDGMENTS

This study was supported by the Russian Foundation for Basic research, project no. 03-02-17021.

We are also grateful to V.I. Alshits, A.I. Baranov, V.L. Berdinskiĭ, R.M. Zakalyukin, O.V. Klyavin, N.K. Moroz, E.A. Petrzhik, O.F. Pozdnyakov, N.L. Sizova, and N.G. Furmanova for fruitful discussions; R.B. Morgunov for the methodical help in crystal annealing; and Yu.G. Shvedenkova for measuring magnetic susceptibility.

REFERENCES

1. V. I. Alshits, E. V. Darinskaya, T. M. Perekalina, and A. A. Urusovskaya, Fiz. Tverd. Tela (Leningrad) **29** (2), 467 (1987) [Sov. Phys. Solid State **29**, 265 (1987)].
2. Yu. I. Golovin and R. B. Morgunov, Pis'ma Zh. Éksp. Teor. Fiz. **61** (7), 583 (1995) [JETP Lett. **61**, 596 (1995)].
3. B. I. Smirnov, N. N. Peschanskaya, and V. I. Nikolaev, Fiz. Tverd. Tela (St. Petersburg) **43** (12), 2154 (2001) [Phys. Solid State **43**, 2250 (2001)].
4. V. I. Alshits, N. N. Bekkauér, A. E. Smirnov, and A. A. Urusovskaya, Zh. Éksp. Teor. Fiz. **115** (3), 951 (1999) [JETP **88**, 523 (1999)].
5. N. A. Tyapunina, V. L. Krasnikov, and É. P. Belozerova, Izv. Ross. Akad. Nauk, Ser. Fiz. **64** (9), 1776 (2000).
6. O. I. Datsko, Fiz. Tverd. Tela (St. Petersburg) **44** (2), 289 (2002) [Phys. Solid State **44**, 300 (2002)].
7. A. E. Smirnov and A. A. Urusovskaya, Fiz. Tverd. Tela (Leningrad) **29** (3), 852 (1987) [Sov. Phys. Solid State **29**, 485 (1987)].
8. Yu. I. Golovin, R. B. Morgunov, D. V. Lopatin, and A. A. Baskakov, Phys. Status Solidi A **160**, R3 (1997).
9. A. A. Skvortsov, A. M. Orlov, and L. I. Gonchar, Zh. Éksp. Teor. Fiz. **120** (1), 134 (2001) [JETP **93**, 117 (2001)].
10. V. I. Alshits, E. V. Darinskaya, and E. A. Petrzhik, Mater. Sci. Eng. A **164**, 322 (1993).
11. V. I. Al'shits, E. V. Darinskaya, M. V. Koldaeva, and E. A. Petrzhik, Kristallografiya **48** (5), 826 (2003) [Crystallogr. Rep. **48**, 768 (2003)].
12. R. B. Morgunov and A. A. Baskakov, Fiz. Tverd. Tela (St. Petersburg) **43** (9), 1632 (2001) [Phys. Solid State **43**, 1700 (2001)].
13. Yu. I. Golovin and R. B. Morgunov, Zh. Éksp. Teor. Fiz. **115** (2), 605 (1999) [JETP **88**, 332 (1999)].
14. E. V. Darinskaya and M. V. Koldaeva, Pis'ma Zh. Éksp. Teor. Fiz. **70** (3), 226 (1999) [JETP Lett. **70**, 228 (1999)].
15. A. L. Buchachenko, R. Z. Sagdeev, and K. M. Salikhov, *Magnetic and Spin Effects in Chemical Reactions* (Nauka, Novosibirsk, 1978) [in Russian].
16. Ya. B. Zel'dovich, A. L. Buchachenko, and E. L. Frankevich, Usp. Fiz. Nauk **155** (1), 3 (1988) [Sov. Phys. Usp. **31**, 385 (1988)].
17. Y. Okaya, Acta Crystallogr. **19**, 879 (1965).
18. T. A. Eremina, N. G. Furmanova, L. F. Malakhova, *et al.*, Kristallografiya **38** (4), 236 (1993) [Crystallogr. Rep. **38**, 554 (1993)].
19. L. M. Belyaev, G. S. Belikova, A. B. Gil'varg, and I. M. Sil'vestrova, Kristallografiya **14** (4), 645 (1969) [Sov. Phys. Crystallogr. **14**, 544 (1969)].
20. G. S. Belikova, T. M. Okhrimenko, T. N. Turskaya, *et al.*, in *Apparatus and Methods of X-ray Analysis* (Mashinostroenie, Leningrad, 1983), Vol. 31, p. 171 [in Russian].
21. V. I. Vladimirov, A. A. Birkovskiĭ, V. R. Regel', *et al.*, Fiz. Tverd. Tela (Leningrad) **31** (10), 125 (1989) [Sov. Phys. Solid State **31**, 1722 (1989)].
22. V. R. Regel', V. I. Vladimirov, N. L. Sizova, *et al.*, Kristallografiya **34** (6), 1490 (1989) [Sov. Phys. Crystallogr. **34**, 892 (1989)].
23. N. L. Sizova, L. A. Lutfullaeva, V. R. Regel', *et al.*, Kristallografiya **37** (4), 1047 (1992) [Sov. Phys. Crystallogr. **37**, 558 (1992)].
24. Yu. S. Boyarskaya, *Crystal Deformation at Their Testing on Microstrength* (Shtiintsa, Chisinau, 1972) [in Russian].
25. O. F. Pozdnyakov, B. P. Redkov, A. S. Smirnov, *et al.*, Kristallografiya **33** (4), 994 (1988) [Sov. Phys. Crystallogr. **33**, 588 (1988)].
26. G. C. Pimentel and A. L. McClellan, *The Hydrogen Bond* (Freeman, San Francisco, 1960; Mir, Moscow, 1964).

Translated by L. Man

Crystallography Reports, Vol. 50, No. 2, 2005, pp. 284–290. Translated from Kristallografiya, Vol. 50, No. 2, 2005, pp. 319–325.

PHYSICAL PROPERTIES OF CRYSTALS

Luminescence of Crystals of Divalent Tungstates

A. A. Blistanov*, B. I. Zadneprovskiĭ, M. A. Ivanov***, V. V. Kochurikhin***, V. S. Petrakov*, and I. O. Yakimova***

** Moscow Institute of Steel and Alloys, Leninskiĭ pr. 4, Moscow, 117936 Russia*

e-mail: crystalXXI@misis.ru

*** All-Russia Research Institute for Synthesis of Mineral Raw Materials, ul. Institutskaya 1, Aleksandrov, Vladimir oblast, 601600 Russia*

**** Institute of General Physics, Russian Academy of Sciences, ul. Vavilova 38, Moscow, 119991 Russia*

Received March 23, 2004

Abstract—Crystals of divalent tungstates are characterized by two main luminescence spectral ranges: a short-wavelength (blue) luminescence band in the range 390–420 nm and a group (often two groups) of longer wavelength (green) bands in the range 480–520 nm. For crystals of calcium, strontium, barium, cadmium, magnesium, zinc, and lead tungstates, it is shown that the wavelength corresponding to the maximum of the blue luminescence band (λ_{max}) correlates with the melting temperature (T_m) of these compounds. The position of the blue luminescence band is the same (in the range 510–530 nm) for crystals with different divalent cations. Annealing in vacuum and electron irradiation decrease the intensity of both blue and green luminescence bands but do not change the ratio of their maximum intensities. This circumstance suggests that vacancies serve as luminescence quenchers to a greater extent rather than facilitate the formation of emission centers responsible for a particular luminescence band. © *2005 Pleiades Publishing, Inc.*

INTRODUCTION

The high density of crystals of calcium, cadmium, and zinc tungstates (and especially lead tungstate), along with their high quantum yield, makes it possible to use them as phosphors and scintillators to detect both high-energy particles and low-energy radiation (medical tomography). Recently, particular attention has been given to $PbWO_4$ crystals, which are characterized by very short luminescence lifetimes (~10 ns) [1]. Despite a large number of studies devoted to tungstates, many questions concerning the mechanisms of formation and relaxation of excited states in these crystals are yet to be answered.

The crystals under consideration are characterized by two main luminescence spectral ranges: short-wavelength (blue) luminescence in the range from 390 to 420 nm and long-wavelength (green) luminescence in the range 480–520 nm [2, 3]. This fact indicates the existence of at least two types of luminescence centers. Earlier models of the centers (by the example of $CaWO_4$) relate the luminescence to complexes $(WO_4)^{2-}$ that are distorted by closely located defects [4] or complexes containing W^{5+} ions [5].

When analyzing the possibility of controlling the optical properties of crystals, the main problem is to determine the type of luminescence centers. In particular, the role of the matrix ions and structural defects in the formation of optical centers remains unclear for tungstates. Estimation of the number of blue luminescence centers [6] indicated a low probability of the presence of defects with a required concentration and made it possible to suggest that the blue luminescence should be assigned to a regular crystal. The blue-green luminescence of wolframite-related representatives of tungstates is interpreted in terms of radiative transitions in octahedral complexes $(WO_6)^{6-}$ [7], and the presence of two luminescence bands is attributed to the existence of two types of internal centers of a different structure [8]. It has been noted previously [6, 9] that divalent cations Me^{2+} (except for lead cations) do not affect the formation of luminescence spectra of scheelites.

These questions have been most fully studied by the example of lead tungstate $PbWO_4$. According to the existing concepts, the blue luminescence band of $PbWO_4$ is due to the $6p6s \longrightarrow 6s^2$ transitions in Pb^{2+} ions [10, 11] or intracenter transitions in isolated groups $(WO_4)^{2-}$ [12, 13]. In the latter case, the green luminescence is attributed to the charge transfer from the ground orbitals of lead ions to the empty orbitals of the *d* type in $(WO_4)^{2-}$ groups. By taking into account the polarization of the green radiation (the blue radiation is not polarized), it was suggested [14] that green luminescence is due to the presence of WO_3 groups containing an oxygen vacancy $[(WO_4)^{2-}\text{-}V_o]$ or *F* centers $[(WO_4)^{2-}\text{-}F]$ and $[(WO_4)^{2-}\text{-}F^+]$. The fact that green luminescence is very sensitive to the crystal history (oxidizing or reducing action on a crystal during its growth or annealing) confirms the suggestion that defects are involved in the formation of green lumines-

cence centers. According to this scheme, the excitation of a Pb^{2+} ion is transferred to $[(WO_4)^{2-}\text{-}V_o]$ or $[(WO_4)^{2-}\text{-}F]$ groups. Raspite-like distortions of the scheelite lattice of $PbWO_4$ [15] and inclusions of the oxygen-deficient $Pb_7W_8O_{32-x}$ phase were also considered as possible green luminescence centers [16].

In view of the fact that some fraction of lead cations are in a higher oxidation state, it was suggested [17] that centers of absorption at 425 nm, which are characteristic of $PbWO_4$, and green luminescence centers are formed involving Pb^{3+} cations stabilized by excess interstitial oxygen.

Despite the difference between the models, it is generally suggested that excitation centers are formed on the basis of Pb^{2+} (or Pb^{3+}) cations with subsequent energy transfer to tungsten–oxygen complexes, in which luminescence occurs (in regular WO_4 groups in the blue spectral range and in their various distorted modifications in the green range). The appearance of photoconductivity, accompanying the green luminescence in $CaWO_4$ [18] and $PbWO_4$ [20], indicates that energy can be transferred to luminescence centers involving charge transfer processes.

Thus, refinement of the concepts about the features of luminescence of tungstates remains an urgent problem in view of the synthesis and practical application of these promising phosphors and scintillators.

The purpose of this study is to verify the effect of divalent cations on the luminescence of crystals with scheelite structure by comparing the luminescence spectra of crystals of lead tungstates and group (II) cations and to analyze the effect of structural defects due to vacuum annealing and electron irradiation on the luminescence spectra of tungstate crystals.

EXPERIMENTAL RESULTS

Crystals of all tungstates, except for the $MgWO_4$, were grown by the Czochralski method. The $MgWO_4$ crystal was grown by the flux method.

$PbWO_4$ crystals of two types were used:

(i) uncolored crystals grown at the Bogoroditsk Plant of Techno-Chemical Products (BPTCP), and

(ii) crystals with a yellowish color grown at the All-Russia Research Institute for Synthesis of Mineral Raw Materials (ARRISMRM).

Transmission spectra of the crystals were measured on a SPECORD system and luminescence spectra were recorded using a DMR-3 monochromator and X-ray excitation (CuK_α radiation). The luminescence intensity was measured in the photon-counting mode. The thermally stimulated luminescence was measured in the temperature range from 100 to 300 K.

The crystals were subjected to reducing annealing in vacuum at 800°C and 6-MeV electron irradiation in an accelerator.

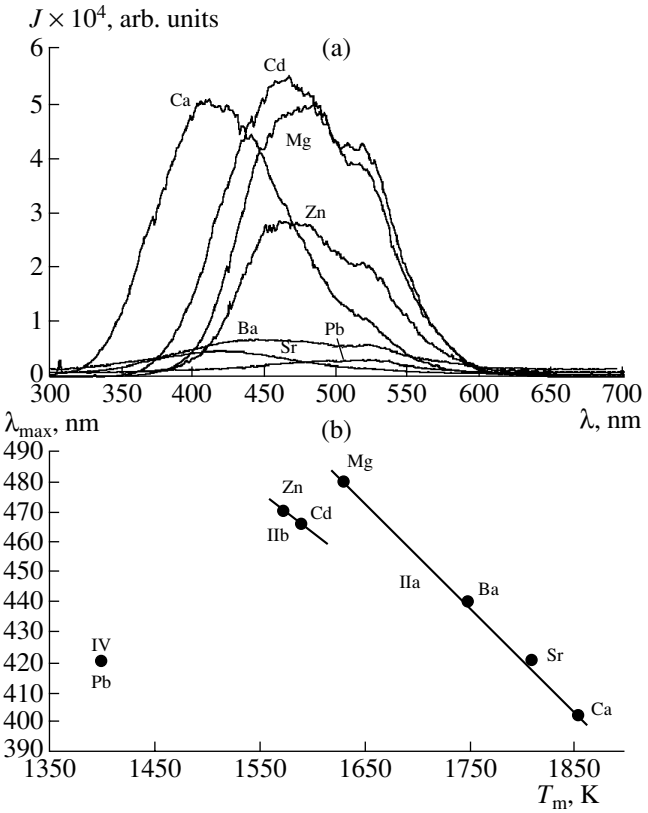

Fig. 1. (a) Luminescence spectra $J(\lambda)$ of tungstates $Me^{2+}(WO_4)^{2-}$ with different divalent metal cations (Ca, Cd, Mg, Zn, Ba, Sr, Pb). (b) Dependence of the luminescence peak position (λ_{max}) on the melting temperature T_m of a crystal. Cations and their subgroups are indicated near corresponding points and lines.

Figure 1a shows the luminescence spectra $J(\lambda)$ of crystals of calcium, strontium, barium, cadmium, magnesium, zinc, and lead tungstates (in what follows, the values of J are given in arbitrary units). The spectra were obtained under the same excitation and measurement conditions. The luminescence spectra of all crystals contain two broad bands. One of them (green) has maximum λ_{max} in the range 520–530 nm, whose position is independent of the type of divalent cations. The position of the other (blue) band significantly depends on the cation type and is shifted from the blue-green (λ_{max} = 480 nm) spectral range for $ZnWO_4$ to the blue (λ_{max} = 420 nm) range for $CaWO_4$. The wavelength at which the blue luminescence band is peaked correlates with the melting temperature (T_m) and, therefore, with the crystal lattice energy (Fig. 1b). This correlation gives a linear dependence $\lambda_{max}(T_m)$ for the crystals with cations belonging to one subgroup (IIa). The blue luminescence peaks for the crystals with cations belonging to the IIb subgroup are somewhat shifted to shorter waves as compared with the dependence $\lambda_{max}(T_m)$ for the subgroup (IIa). The blue luminescence peaks for $PbWO_4$ crystals are even more shifted to shorter wave-

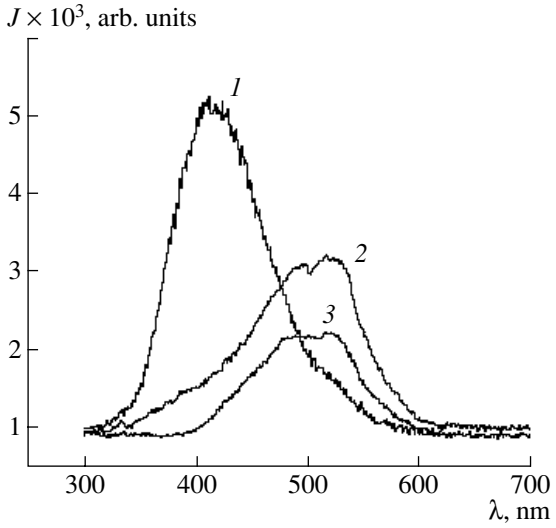

Fig. 2. Luminescence spectra of crystals of lead tungstates and molybdates: (*1*) uncolored $PbWO_4$ grown in a nitrogen atmosphere, (*2*) colored (yellow) $PbWO_4$, and (*3*) colored (yellow) $PbMoO_4$.

lengths, which is in agreement with the general behavior since the Pb^{2+} ion belongs to group (IV). Obviously, the dependence $\lambda_{max}(T_m)$ manifests itself within cations of the same subgroup and sharply changes in going to a neighboring group (subgroup).

The effect of hexavalent cations on the luminescence spectra can be seen from the comparison of the luminescence spectra of $PbWO_4$, $PbMoO_4$, $CaWO_4$, and $CaMoO_4$ crystals (Figs. 2, 3). The luminescence spectra of uncolored $PbWO_4$ crystals grown in a nitrogen atmosphere (BPTCP) (curve *1*) are characterized by a strong blue band at 420 nm and a very weak green band at 510 nm. The luminescence spectra of colored (yellow) $PbWO_4$ crystals grown in air (ARRISMRM) (curve *2*) and $PbMoO_4$ crystals (curve *3*) show a wide band with two maxima at 465 and 520 nm (Fig. 2). The luminescence spectrum of a $PbWO_4$ crystal (curve *2*) contains an additional band in the blue spectral region.

The $CaWO_4$ crystal (uncolored) shows strong luminescence in the blue spectral range and very weak luminescence in the green range (Fig. 3, curve *1*). $CaMoO_4$ crystals, colored (as-grown) and uncolored (annealed in air at 800°C), have similar luminescence spectra, which can be resolved into two bands in the green range (Fig. 3, curves *2*, *3*). It should be noted that the absorption edge in the spectra of $CaMoO_4$ crystals is shifted to longer wavelengths in comparison with the spectra of $CaWO_4$ crystals (Fig. 4).

The effect of annealing and electron irradiation was studied mainly for the crystals of lead and calcium tungstates and molybdates. Vacuum annealing of $PbWO_4$, $CaWO_4$, and $CaMoO_4$ crystals (Figs. 5–7, respectively) led to the reduction of their luminescence intensity. $CaWO_4$ crystals annealed in vacuum had a violet color and their spectra contained an absorption band in the range 450–650 nm (Fig. 8).

Electron irradiation decreased the luminescence intensity for all as-grown crystals (Fig. 9). However, for the crystals previously annealed in vacuum, the effect of electron irradiation on the luminescence intensity was ambiguous. Low-dose electron irradiation of the $CaMoO_4$ and $CaWO_4$ crystals annealed in vacuum (colored) increased their luminescence. However, with a further increase in the irradiation dose, the luminescence intensity decreased (Figs. 10, 11).

The existing models of optical centers suggest a different contribution of intrinsic point defects to the formation of blue and green luminescence centers; thus, oxygen vacancies may play a key role in the formation of green luminescence centers. Since vacuum anneal-

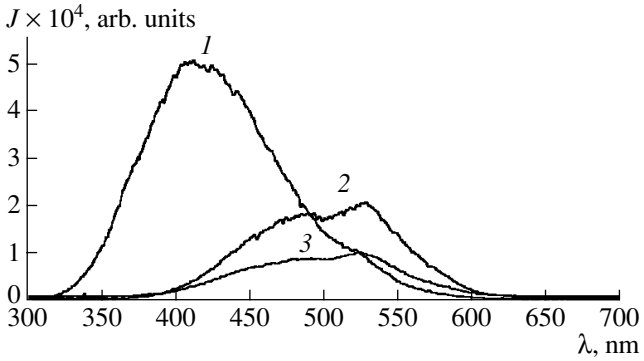

Fig. 3. Luminescence spectra of crystals of calcium tungstates and molybdates: (*1*) uncolored $CaWO_4$, (*2*) uncolored $CaMoO_4$, and (*3*) colored (blue) $CaMoO_4$.

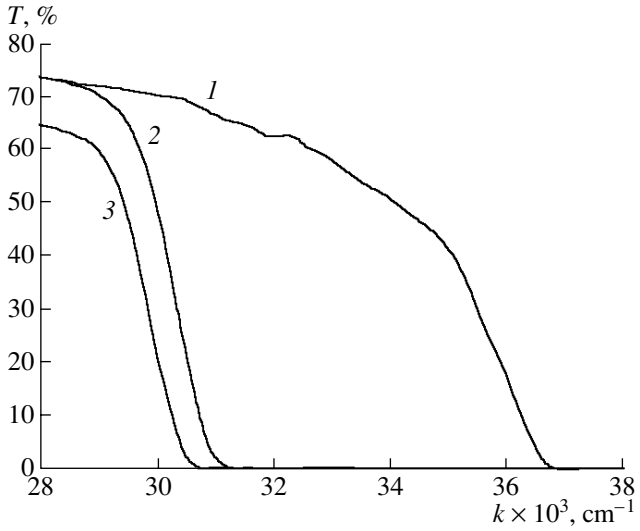

Fig. 4. Transmission spectra $T(k)$ (in %, k is the wave number) of crystals of (*1*) uncolored $CaWO_4$, (*2*) uncolored $CaMoO_4$, and (*3*) colored (blue) $CaMoO_4$.

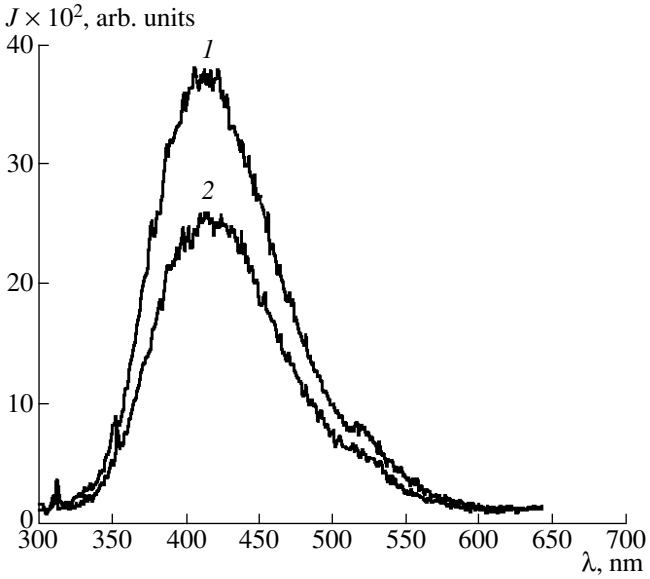

Fig. 5. Luminescence spectra of $PbWO_4$ crystals: (*1*) initial uncolored crystal (before annealing) and (*2*) crystal annealed at 800°C for 4 h.

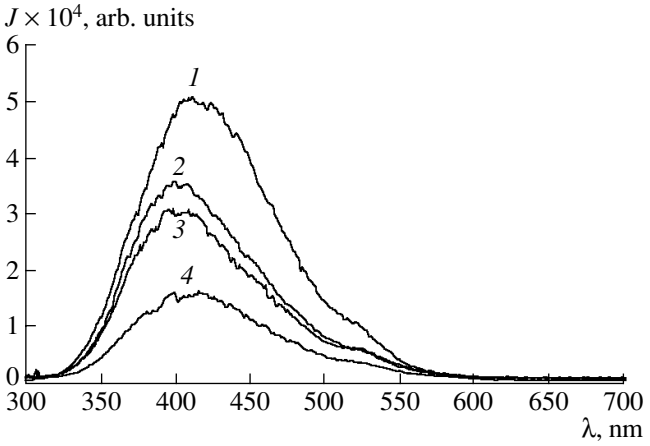

Fig. 6. Luminescence spectra of $CaWO_4$ crystals: (*1*) initial crystal (before annealing); (*2*) annealing at 800°C for 4 h, (*3*) additional annealing at 800°C for 4 h, and (*4*) additional annealing at 800°C for 4 h.

ing and electron irradiation lead to an increase in the oxygen vacancy concentration, one might expect that such treatments of scheelite crystals would lead to an increase in the intensity of green luminescence with respect to the blue luminescence. As can be seen in Figs. 6–11, the ratio of the intensities of the maxima of the green and blue luminescence bands of the crystals under study almost does not change under the action of both annealing and electron irradiation. To verify this observation, the luminescence spectra of all crystals studied were resolved into Gaussian curves corresponding to the blue and green components by the ORIGIN program. Figure 12 shows an example of such resolution for $PbWO_4$ crystals. As can be seen, neither vacuum annealing (Fig. 12b) nor electron irradiation (Fig. 12c) increase the intensity of the green luminescence with respect to the blue luminescence in comparison with the initial crystal (Fig. 12a). The ratio of the intensities of the blue (J_{max} for 3.0 eV) and green (J_{max} for 2.3 eV) luminescence bands in the spectrum of the initial crystal is equal to 16. For the crystals annealed in vacuum and the crystals irradiated with electrons, this ratio is 15.6 and 16, respectively. The same effect was observed for $CaWO_4$ crystals. Therefore, the ratio of the intensities of the blue and green luminescence bands, at least in these crystals, is independent of the concentration of intrinsic point defects formed during annealing and electron irradiation.

DISCUSSION

The dependence of the position of the blue luminescence band on the divalent cation type and the crystal binding energy indicates that not only the excitation of this band but also the luminescence of tungstates is determined by the properties of divalent cations. This circumstance suggests that the blue luminescence of tungstates is determined by the relaxation of excited Me^{2+}–O^{2-} bonds. The fact that the green luminescence is independent of the divalent cation type indicates that the latter may be related to the $(Me^{6+}O_4^{2-})^{2-}$ groups.

Generally, crystals of tungstates contain molybdenum as an impurity. It can be seen in Figs. 2 and 3 that the blue luminescence of molybdates is suppressed in comparison with tungstates. The W^{6+} and Mo^{6+} ions

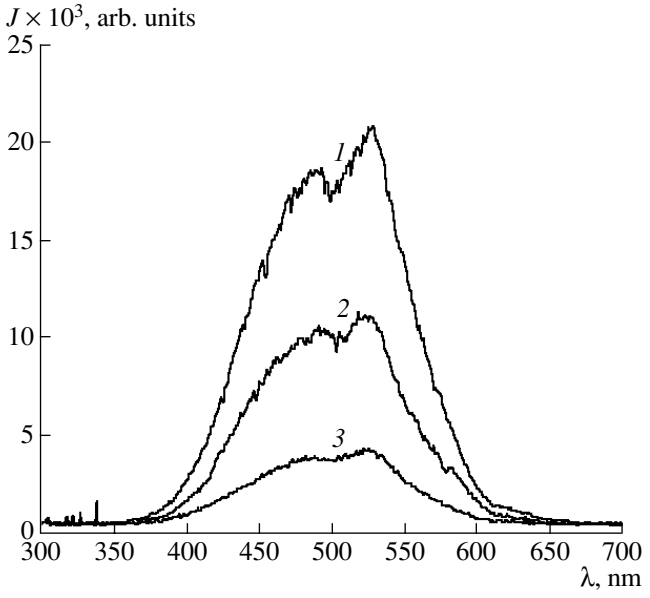

Fig. 7. Luminescence spectra of $CaMoO_4$ crystals: (*1*) initial crystal (before annealing); (*2*) annealing at 800°C for 4 h, and (*3*) additional annealing at 800°C for 4 h.

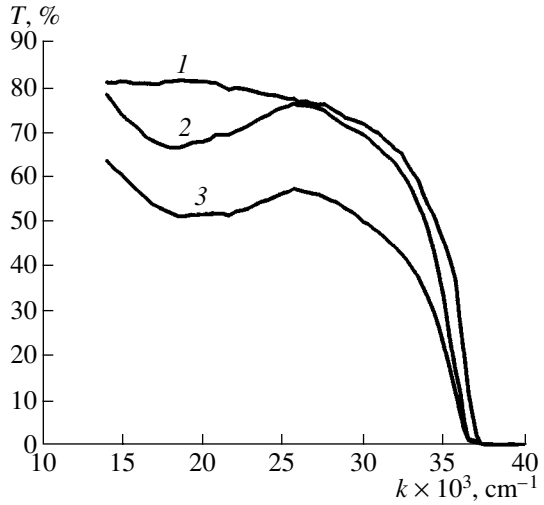

Fig. 8. Transmission spectra $T(k)$ (in %, k is the wave number) of $CaWO_4$ crystals: (*1*) initial uncolored crystal, (*2*) after vacuum annealing at 800°C for 4 h, and (*3*) after additional vacuum annealing at 800°C for 4 h.

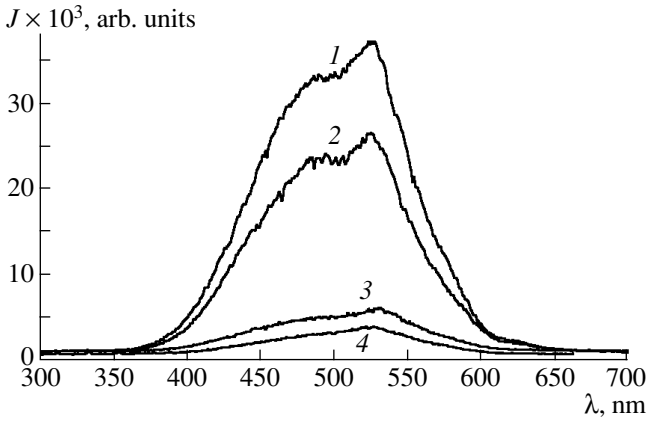

Fig. 9. Luminescence spectra of an uncolored $CaMoO_4$ crystal (*1*) in the initial state and after electron irradiation with the dose D = (*2*) 4×10^{15}, (*3*) 12×10^{15}, and (*4*) 70×10^{15} cm^{-2}.

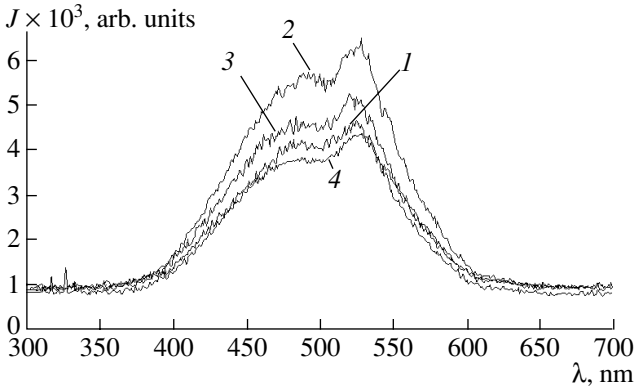

Fig. 10. Luminescence spectra of a $CaMoO_4$ crystal annealed in vacuum at 800°C for 4 h (colored) before (*1*) and after electron irradiation with the dose D = (*2*) 4×10^{15}, (*3*) 8×10^{15}, and (*4*) 12×10^{15} cm^{-2}.

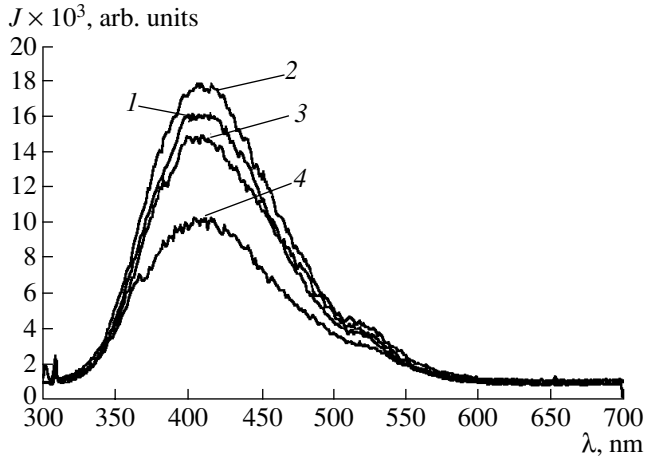

Fig. 11. Luminescence spectra of a $CaWO_4$ crystal annealed in vacuum (colored) (*1*) after annealing at 800°C for 8 h and after electron irradiation with the dose D = (*2*) 4×10^{15}, (*3*) 8×10^{15}, and (*4*) 12×10^{15} cm^{-2}.

have the same charge and the same ionic radii (0.042 and 0.065 nm in the tetrahedral and octahedral coordinations, respectively). The difference between these ions is that the covalence of the Mo–O bond exceeds that of the W–O bond owing to the smaller screening of the nucleus of the Mo^{6+} ion. This circumstance leads to a higher polarizability of the $[MoO]^{2-}$ ion as compared with the $[WO]^{2-}$ ion (in particular, due to this fact the melting temperatures of molybdates are lower than those of corresponding tungstates). Therefore, the substitution of W^{6+} ions in the scheelite lattice by Mo^{6+} ions leads to the formation of $[MoO]^{2-}$ octahedra, in which O^{2-} ions are more easily ionized. As a result, the absorption edge is shifted to longer wavelengths. Apparently, the same properties of the Mo^{6+} ion lead to the decrease in the blue luminescence intensity when tungsten is replaced with molybdenum and the shift of the main luminescence band of molybdates to the green range in comparison with tungstates.

The question of the role of point defects in the formation of green luminescence centers remains open. Since the vacuum annealing and the electron irradiation (which lead to the increase in the oxygen vacancy concentration) do not enhance the green luminescence with respect to that of blue, we can suggest that oxygen vacancies are not involved in the formation of green luminescence centers. Thus, the green luminescence should be related directly to the relaxation of excited Me^{6+}–O^{2-} bonds in $[MeO_4]$ groups. There are no reasons to doubt that the green luminescence involves charge transfer. It is possible that this process occurs

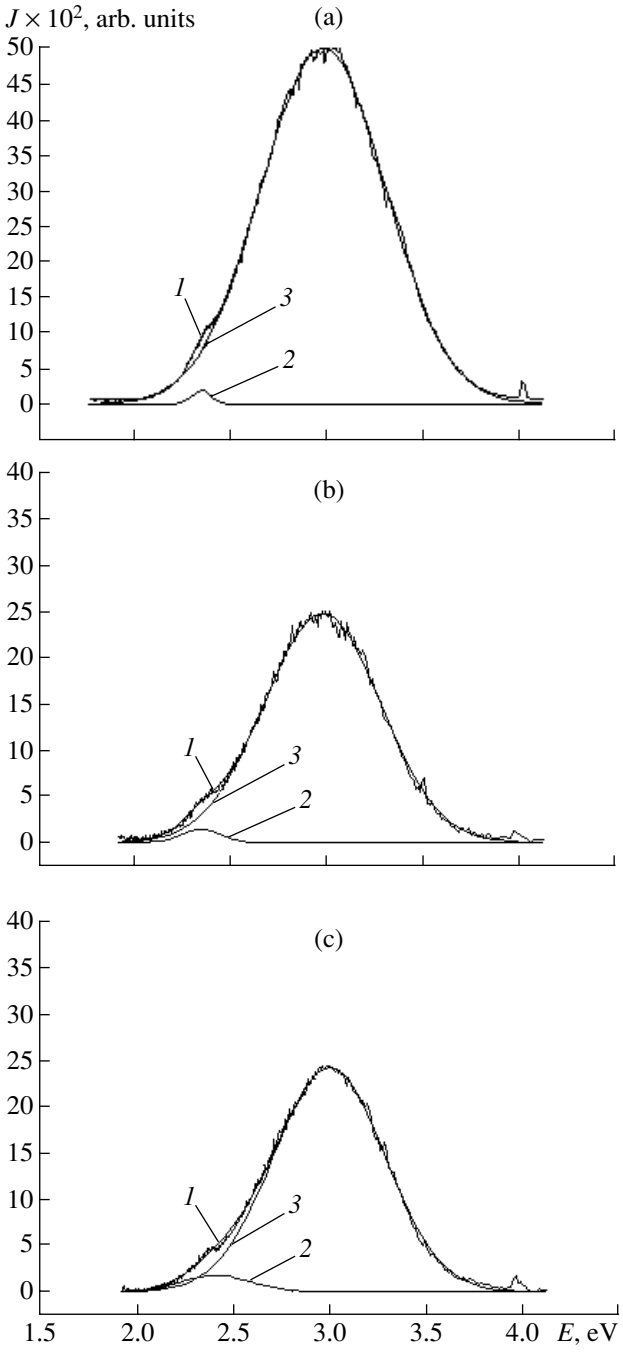

Fig. 12. Luminescence spectrum of a $PbWO_4$ crystal (*1*) resolved into Gaussian curves (*2*, *3*); the sample (a) in the initial state, (b) after annealing in vacuum at 800°C, and (c) after electron irradiation with the dose $D = 4 \times 10^{15}$ cm^{-2}.

according to the following scheme: excitation of a Me^{2+} ion, transfer of the excited charge to a $[MeO_4]$ group, radiative relaxation of excited Me^{6+}–O^{2-} bonds.

In all cases, the increase in the vacancy concentration due to the annealing reduces the luminescence of light (uncolored) crystals. Electron irradiation of the crystals that were preliminary colored by vacuum annealing also reduces their luminescence but only at significant (>10^{14} cm^{-2}) doses. Thus, the oxygen vacancies arising as a result of these treatments serve as luminescence quenchers. The luminescence quenching due to the annealing can be explained by the fact that the lattice distortions caused by increasing vacancy concentration facilitate the expansion of the phonon spectrum and increase the probability of nonradiative recombination due to the electron–phonon interaction.

It is more difficult to explain the enhancement of luminescence and the color decay caused by the low-dose electron irradiation of previously colored crystals. The treatments leading to the increase in the oxygen vacancy concentration are reducing ones. We can suggest that, in the crystals previously colored (restored) by vacuum annealing, the increase in the concentration of point defects due to the low-dose irradiation is small in comparison with the concentration of existing defects. Therefore, the effect of luminescence quenching caused by the irradiation is also small. In this case, the irradiation, causing ionization, may have an oxidizing effect and, thus, increase the luminescence intensity.

CONCLUSIONS

The position of the maximum of the blue luminescence band of divalent tungstates is determined by the divalent ion type.

The shift of the intrinsic absorption edge to longer wavelengths in the spectra of molybdate crystals is accompanied by the shift of the luminescence peaks to the green spectral range in comparison with the luminescence spectra of tungstates.

The ratio of the intensities of the blue and green luminescence is not affected by electron irradiation and vacuum annealing; i.e., this ratio is independent of a change in the concentration of point defects.

An increase in the concentration of point defects under the action of electron irradiation and vacuum annealing leads to luminescence quenching.

Low-dose electron irradiation of $CaWO_4$ and $PbWO_4$ crystals, previously colored by vacuum annealing, enhances the luminescence, which can be related to the reconstruction of luminescence centers rather than the increase in the defect concentration.

ACKNOWLEDGMENTS

We are grateful to V.V. Antipov, S.Z. Shmurak, L.I. Ivlev, V.A. Nefedov, and L.I. Potkin for supplying crystals for the experiments.

REFERENCES

1. P. Lecoq, L. Dafinei, E. Auffray, *et al.*, Nucl. Instrum. Methods Phys. Res. A **365**, 291 (1995).

2. F. A. Kroger, *Some Aspects of Luminescence of Solids* (Elsevier, Amsterdam, 1948).
3. G. A. Blasse, Philips Res. Rep. **24**, 273 (1969).
4. V. G. Krongauz, in *Luminescent Materials and High-Purity Substances* (VNII Lyuminofor, Stavropol, 1974), No. 11, p. 12 [in Russian].
5. A. M. Gurevich, V. B. Gutan, and A. A. Mikhalev, in *Luminescent Materials and High-Purity Substances* (Kharkov, 1975), No. 12, p. 30 [in Russian].
6. E. G. Reut, Izv. Akad. Nauk SSSR, Ser. Fiz. **49** (10), 2032 (1985).
7. A. E. Ovechkin, V. D. Ryzhikov, G. Tamulaitis, and A. Zukauskas, Phys. Status Solidi A **103**, 285 (1987).
8. M. Springis, V. Tale, I. Tale, *et al.*, in *Proceedings of International Conference on Inorganic Scintillators and Their Application, SCINT'95* (Delft, Netherlands, 1995), p. 303.
9. M. I. Tombak and A. M. Gurevich, Zh. Prikl. Spektrosk. **4** (6), 564 (1966).
10. W. van Loo, Phys. Status Solidi A **27**, 565 (1975).
11. W. van Loo, Phys. Status Solidi A **28**, 227 (1975).
12. J. A. Groenink and G. Blasse, J. Solid State Chem. **39** (1), 9 (1980).
13. A. Fyodorov, M. V. Korshik, O. Missevitch, *et al.*, Radiat. Meas. **26** (1), 107 (1996).
14. A. Fyodorov, V. Korzhik, O. Missevitch, *et al.*, LAPP-EXP-94 (1994), p. 25.
15. D. I. Alov, N. V. Klassen, N. N. Kolesnikov, and S. Z. Shmurak, in *Proceedings of International Conference on Inorganic Scintillators and Their Application, SCINT'95* (Delft, Netherlands, 1995), p. 267.
16. A. Annenkov, E. Auffray, M. Korzhik, *et al.*, CMS Note 1998/041 (CERN, 1998), p. 13.
17. B. I. Zadneprovskiĭ, V. A. Nefedov, A. A. Smirnov, and I. S. Bykov, Neorg. Mater. **35** (3), 370 (1999).
18. M. I. Tombak and A. M. Gurevich, Zh. Prikl. Spektrosk. **4** (6), 564 (1966).
19. E. G. Reut, Fiz. Tverd. Tela (Leningrad) **23** (8), 2514 (1981) [Sov. Phys. Solid State **23**, 1476 (1981)].

Translated by Yu. Sin'kov

Crystallography Reports, Vol. 50, No. 2, 2005, pp. 291–296. Translated from Kristallografiya, Vol. 50, No. 2, 2005, pp. 326–331.

PHYSICAL PROPERTIES OF CRYSTALS

Monotonic and Jumpwise Deformation of Bulk Amorphous $Zr_{46.8}Ti_8Cu_{7.5}Ni_{10}Be_{27.5}$ Alloy in Nanoindentation

Yu. I. Golovin*, V. I. Ivolgin*, A. I. Tyurin*, S. V. Potapov*, V. Z. Bengus, and E. D. Tabachnikova****

** Tambov State University, Tambov, 392622 Russia*

e-mail: golovin@tsu.tmb.ru

*** Institute of Low Temperatures, National Academy of Sciences of Ukraine, Kharkov, Ukraine*

Received June 19, 2003

Abstract—The study is aimed at the establishment of regions of stable (monotonic) and unstable (jumpwise) plastic flow in bulk amorphous $Zr_{46.8}Ti_8Cu_{7.5}Ni_{10}Be_{27.5}$ alloy under the conditions of local deformation. The characteristics of the jumpwise plastic flow in bulk amorphous $Zr_{46.8}Ti_8Cu_{7.5}Ni_{10}Be_{27.5}$ alloy are studied by the method of continuous nanoindentation (depth-sensing testing) in the range of strain rates $\dot{\varepsilon}$ from 10^{-2} to 10^4 s^{-1}. The boundaries between the regions of homogeneous and localized plastic strain are established and the fractions of monotonic and jumpwise plastic strain under the indenter are determined. © *2005 Pleiades Publishing, Inc.*

INTRODUCTION

Despite the fact that, unlike elastic deformation, plastic deformation is always inhomogeneous at the atomic level and manifests itself in a number of strain jumps $\Delta\varepsilon_i$ (i is the number of the strain jump) (Fig. 1a), in physics of plasticity, one usually distinguishes the homogeneous and localized flow modes [1–7]. The conventional boundary between these modes is determined mainly by the test temperature T, strain rate $\dot{\varepsilon}$, sample history and its characteristic dimensions, and the state of its surface [2, 5, 8–14]. To a great extent, the position of this boundary also depends on the characteristics of the testing machine and, in particular, its rigidity, inertia, sensitivity to the variations in the deforming force, and sample dimensions. The equipment traditionally used in deformation experiments (Instron testing machines) allows one to record not all the possible flow instabilities (Fig. 1b) but only relatively pronounced jumps of macroscopic strain characterized by a low frequency arising due to collectivized behavior of a large number of elementary carriers of plastic deformation. As a result, the statistics of the recorded jumps

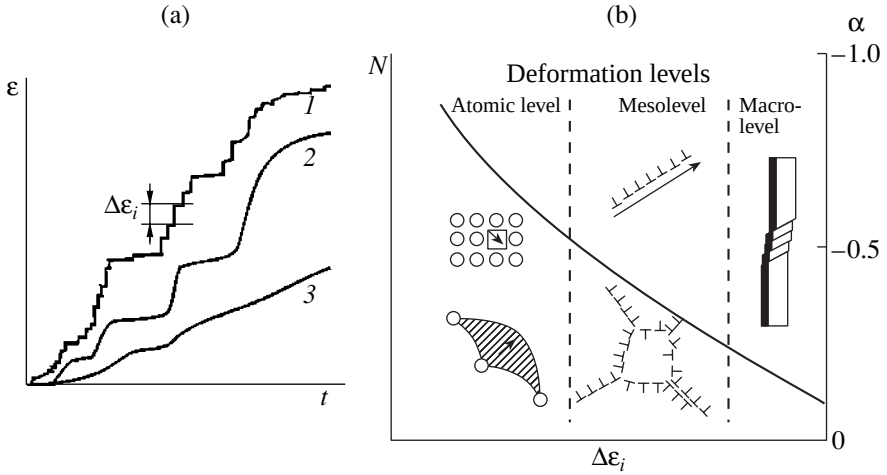

Fig. 1. Jumpwise plastic deformation. (a) (*1*) Temporal curve of the true deformation kinetics at the atomic level ("devil staircase" of i–x jumps $\Delta\varepsilon_i$; (*2*, *3*) reaction of the testing machine at the (*2*) moderate and (*3*) low time and space resolution. (b) Number N and fraction of jumps $\alpha = \dfrac{\sum_i \Delta\varepsilon_i}{\varepsilon_\Sigma}$ in the total strain ε_Σ as functions $\Delta\varepsilon_i$ of their amplitude A and characteristic times τ at different hierarchical levels of the structure.

1063-7745/05/5002-0291$26.00

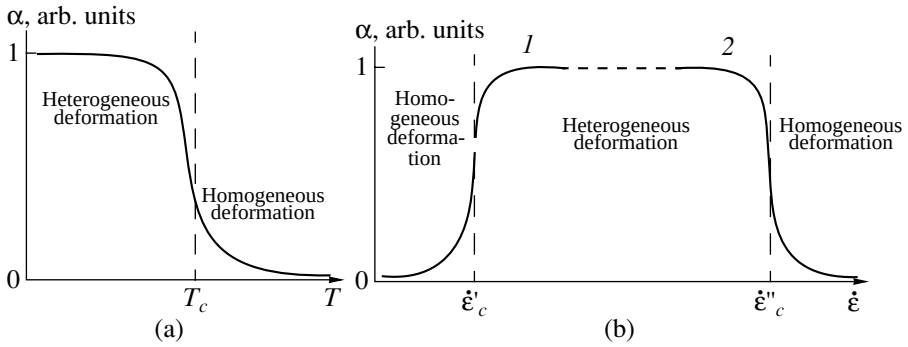

Fig. 2. (a) Schematic of the transition from heterogeneous to homogeneous deformation as a function of temperature fraction of jumps $\alpha = \frac{\sum_i \Delta\varepsilon_i}{\varepsilon_\Sigma}$ in the total deformation ε_Σ, $T_c \sim 0.7T_g$, where T_g is the vitrification temperature. (b) The same as function of the strain rate $\alpha = \frac{\sum_i \Delta\varepsilon_i}{\varepsilon_\Sigma}$ in macrotests. The transition from homogeneous to heterogeneous deformation is characterized by $\dot{\varepsilon}'_c$, whereas the transition from heterogeneous to homogeneous deformation is characterized by $\dot{\varepsilon}''_c$.

is poor and distorted, and their apparent role in the total accumulated strain is considerably underestimated.

To study the dynamics and correlation of the deformation jumps at a lower hierarchical level (in particular, mesoscopic one), it is necessary to considerably increase the space–time resolution of the apparatus and reduce sample volume. This would allow one to perform subsequent analysis of instabilities in plastic flow in terms of the theory of self-organization in nonequilibrium dissipative media such as plastically deformable solids, because these measures would increase the number of the recorded jumps and establish would make the correlation relations between these jumps more obvious.

With this aim we used the method of continuous nanoindentation (depth-sensing testing) in our study which allowed us to record the deforming force P as a function of the depth of indenter penetration h (analogue of the $\sigma = f(\varepsilon)$ diagram in uniaxial deformation) and also time development of $P(t)$ and $h(t)$ for submicron regions. The limiting resolution of modern commercial nanoindentometers in terms of the penetration depth attains a value of 0.1 nm; in terms of time, a value of 10^{-2} s; and in terms of deforming force, several micronewtons, i.e., the values higher by several orders of magnitude in traditional testing machines. This allows one not only to study smaller and faster jumps but also to increase the range of strain rates in the region of high $\dot{\varepsilon}$ values (up to 10^4–10^6 s^{-1}) and to perform the whole experiment on one sample. All this, in addition to the above advantages, allows one to reveal the boundaries of the scale and velocity invariance of the manifestation of steady and unsteady flow modes and to study the nanoscale region of sample dimensions.

The first studies of strain jumps by the nanoindentation method appeared several years ago [15–17]. They were directed mainly at the study of the specific features of unsteady flow in fcc metals and polycrystalline aluminum–magnesium alloys studied earlier in detail by the macrodeformation methods [18, 19]. The related information for amorphous alloys is scarce and, as far as we know, is discussed only in a few publication [20–23], where multiple strain nanojumps were observed in local deformation of bulk amorphous palladium- and zirconium-based alloys by the nanoindentation method. It is well known from the macroscopic experiments that, at the moderate strain rates ($10^{-5} \le \dot{\varepsilon} \le 10^{-3}$ s^{-1}) in the temperature range $T_c \le 0.65$–$0.7T_g$ (here T_g is the vitrification temperature), the flow is localized, whereas at higher temperatures, the flow is homogeneous. Such a transition is characterized by a decrease in the relative fraction of jumps $\alpha = \frac{\sum_i \Delta\varepsilon_i}{\varepsilon_\Sigma}$ in the total strain ε_Σ at higher temperatures (Fig. 2a). It is assumed that this transition takes place due to leveling of the strain and directional structure-relaxation rates [4, 5, 12, 13]. Obviously, at room temperature, this transition from homogeneous to localized flow corresponds to a very low critical deformation rate $\dot{\varepsilon}'_c$, which cannot be attained under conventional conditions of active deformation. On the other hand, it is shown that, at higher strain rates strain $\dot{\varepsilon}''_c$ s^{-1}, a reverse transition from the jumplike mode to monotonic flow may take place; the nature of this monotonic flow is not discussed here. It was shown [24] that such a transition really takes place in a number of amorphous alloys if $\dot{\varepsilon}''_c$ attains a value of the order of ~0.1 s^{-1}. Both these transitions may be schematically illustrated by constructing the functional dependence $\alpha = f(\dot{\varepsilon})$ (Fig. 2b).

Our goal was to reveal the regions of steady (monotonic) and unsteady (jumpwise) plastic flow in bulk amorphous $Zr_{46.8}Ti_8Cu_{7.5}Ni_{10}Be_{27.5}$ alloy under the conditions of local deformation at different deformation rates and at different indentation depths. We also made an attempt to determine the corresponding parameters and clarify the role of jumps in the total mass transport of the material from the deformed region under the indenter.

EXPERIMENTAL

Bulk samples of the amorphous $Zr_{46.8}Ti_8Cu_{7.5}Ni_{10}Be_{27.5}$ alloy were obtained by the method of melt quenching. Prior to measurements, the sample surface was polished with diamond pastes. The studies were performed on a specially designed and constructed computer-controlled nanotester [24, 25], the depth of indentations produced by a Berkovich diamond pyramid ranged from 1 to 10 nm (depending on the limiting deforming force and the loading rate). The time resolution (periodicity of discrete readings) was up to 50 μs, which considerably (by several orders of magnitude) exceeded the possibilities provided by foreign apparatuses and allowed us to resolve the jumps without integration at their duration at the front ≥100 μs.

Loading was performed by of a triangular force pulse with an amplitude up to 80 mN and the duration from 20 ms to 500 s. The $P(t)$ and $h(t)$ or $P(h)$ dependences were recorded simultaneously (Fig. 3). Later, the recorded data were used to determine more than ten parameters characterizing mechanical properties of the material in the subsurface layer. Under the above testing conditions, the maximum indentation depth in the alloy ranged within 800–900 nm. We observed no cracks with in an optical microscope. Altogether we recorded 1000 files of data on individual loading cycles; i.e., we collected a data set sufficient for quantitative and statistical processing of the jumps.

RESULTS AND DISCUSSION

The first analysis of the data obtained showed that strain jumps may arise in the course of increasing the deforming force and in the course of unloading but not in the whole range of loading parameter variations. The number of jumps recorded in one indentation cycle at the given amplitude of the deforming force $P = 80$ mN is about 5–7 jumps and was practically independent of $\dot{\varepsilon}$ in the range 0.02–20 s^{-1} (Fig. 4), where $\dot{\varepsilon} = (dh/dt)/h$ is the rate of the sample deformation averaged over the whole locally deformed volume. Unlike the jumps observed in deformation of polycrystalline aluminum–magnesium alloys [15–17, 26, 27], there was no obvious regularity in the moments of jump appearance, whereas the amplitude Δh varied from 1 to 20 nm and was not associated with h or $\dot{\varepsilon}$. Despite the extremely high time resolution of the apparatus used, we failed to measure duration τ of most of the jumps. In other words, the jumps were observed for time less than the discretization time $\tau_d = 50$ μs. With due regard for the average jump amplitude $\Delta h_m \sim 10$ nm, this allowed us to estimate the velocity of the indentation surface motion during a jump from below as $\langle \upsilon \rangle = \Delta h_m/\Delta t_m = 20$ cm/s. Since we never observed jumps with $\tau > \tau_d$ (we

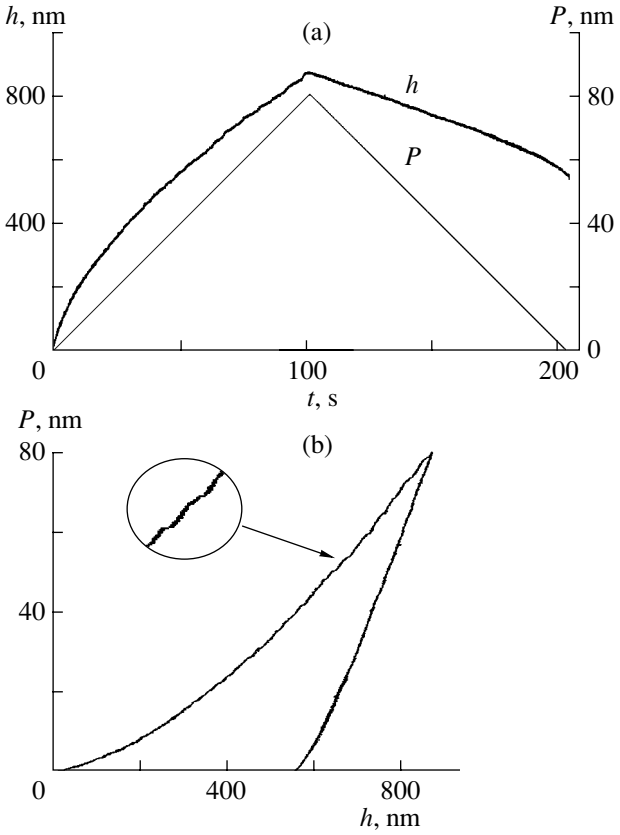

Fig. 3. Typical kinetic dependences of the force $P(t)$ and the depth $h(t)$ of the indenter penetration (a) in dynamic indentation and (b) the corresponding $P(h)$ diagram. The inset shows the fragments of the $P(h)$ diagram.

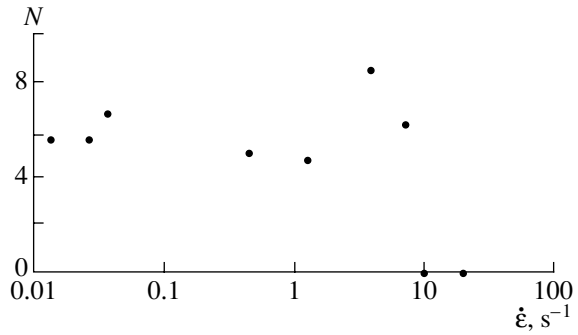

Fig. 4. Dependence of the number N of jumps of unstable plastic flow on strain rate $\dot{\varepsilon}$ at the constant amplitude of the acting force $P_{max} = 56$ mN.

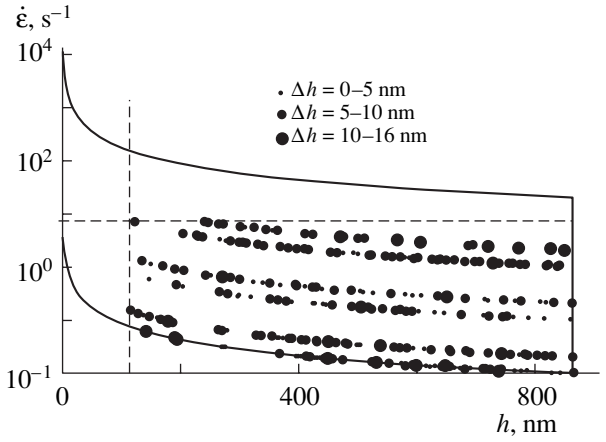

Fig. 5. Region of jump formation on the $P(h)$ diagram at various rates of dynamic nanoindentation by a symmetric triangular loading pulse (points on the diagram). The region determined by the possibilities provided by the setup is shown by solid lines; h is the indentation depth; $\dot{\varepsilon}$ is the strain rate.

processed several hundred jumps), we assumed that the real velocity considerably exceeded our estimate.

For more convenient consideration and comparison of our results with the data obtained by other authors, we classified our data (approximately 600 jumps) according to their amplitudes and constructed the respective curves in the h–$\dot{\varepsilon}$ coordinates (Fig. 5). It is seen from Fig. 5 that, at low $\dot{\varepsilon}$ and high h values, the experimental points are close to the boundaries of the region studied in the phase space shown by a solid line. In other words, we failed to determine the minimum $\dot{\varepsilon}$ values and the maximum h values at which the jumpwise deformation would have disappeared. On the contrary, the clear boundary between the jumpwise and monotonic flow modes is observed from the side of high $\dot{\varepsilon}$ values (dashed line in Fig. 5). In the range $0 < h < 130$ nm, no characteristic jumps in the $\dot{\varepsilon}$ range studied were observed and the critical depth of the appearance of the first jump, $h_c = 130$ nm, was independent of the $\dot{\varepsilon}$ value. There exists a certain critical level of the strain rate, $\dot{\varepsilon}_c \sim 7 \pm 1$ s^{-1}, after the attainment of which no jumps are observed at all. This level is almost independent of h. At $h \geq 130$ nm, neither the number nor the amplitude of the jumps noticeably change (Fig. 6); therefore, it is possible to assume that their characteristics start to be determined by the characteristics of the material state in the zone under the indenter. At the same time, the role played by the jumps in the total mass transport from the zone under the indenter becomes less important with an increase in h in the range $0 < h < 100$ nm (Fig. 7).

The data on the number and the amplitude of the jumps Δh allows one to evaluate their role in the mass transport of the material from the zone under the indenter during the indentation formation. Figure 8 shows the dependence of the volume fraction of the material $\gamma = \sum_i \Delta V_i / V_{\max}$ transported as a result of the jumpwise deformation from μ (where $\Delta V_i = kh^2 \Delta h_i$ is the volume of the material displaced as a result of the ith deformation jump with the amplitude Δh_i, $V_{\max}$ is the volume of the indentation thus formed, $\mu = dP/dt$ is the loading rate, and k is the coefficient taking into account the indenter shape; for a Berkovich indenter, $k = 23.969$). It is seen that γ varies from 0 to 10–15% depending on h and $\dot{\varepsilon}$.

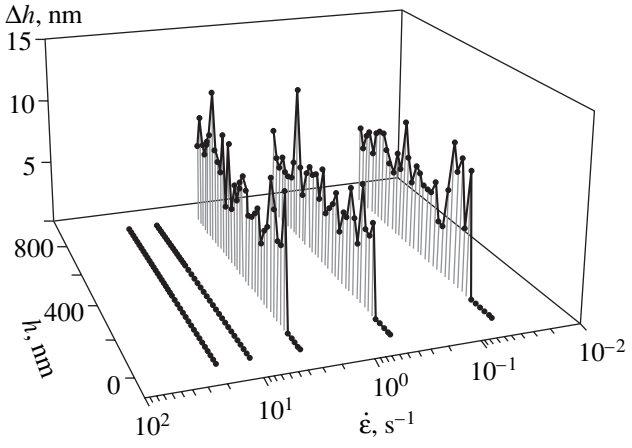

Fig. 6. Dependence of the averaged jump amplitude Δh_i on the strain rate $\dot{\varepsilon}$ and the indentation depth h.

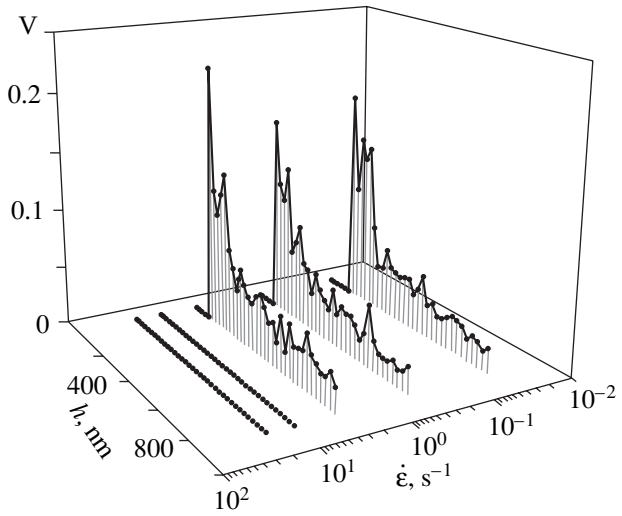

Fig. 7. Dependence of the volume fraction of the material $\beta = \Delta V_i / V_i$ displaced by the individual deformation jump Δh_i during the formation of indentation. ΔV_i is the volume of material displaced by the ith jump Δh_i; V_i is the indentation volume formed by the moment of the completion of the ith jump.

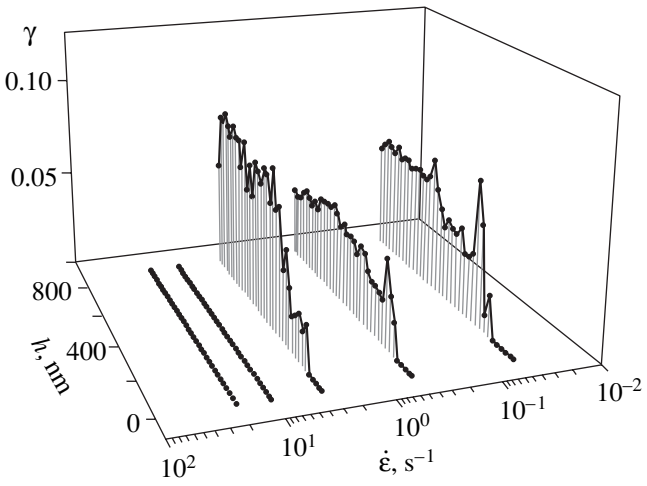

Fig. 8. Volume fraction $\gamma = \sum_i \Delta V_i / V_{max} = f(\mu)$ displaced as a result of jumpwise deformation as a function of the strain rate. $\sum_i \Delta V_i$ is the total volume of the material displaced as a result of the jumpwise deformation; ΔV_i is the volume of the material displaced as a result of the ith deformation jump Δh_i; $\mu = dP/dt$ is the loading rate, and V_{max} is the volume of the indentation formed.

The recent phenomenological theories explain the limited range of $\dot{\varepsilon}$ in which the jumpwise mode of plastic deformation is observed with the invocation of the *N*-like function of the flow stress dependent on $\dot{\varepsilon}$ [28]. The nature of the segment with a negative differential slope is different depending on the material and the type of the process analyzed. It may be associated with different mechanisms such as local heating and deformation aging in plastic flow, a nonmonotonic velocity dependence of the critical intensity coefficient on $\dot{\varepsilon}$ during crack formation, a hysteresis in pressure-induced polymorphous phase transformations, etc. In the situation considered here, all these mechanisms are unlikely or even impossible. The estimates made by a number of scientists (see, e.g., [29, 30] show that short heating in the localized shear band in glass at room temperature does not exceed several dozens of degrees even in the adiabatic mode. Moreover, it cannot decrease with an increase in $\dot{\varepsilon}$. The thorough electron microscopy study of the surface of the indentation and the region around it showed that the strain jumps in the amorphous palladium-based alloy under nanoindentation are caused by localized plastic flow and not by fracture [23]. Thus, the formation of cracks, if any, cannot give rise to the transitions observed.

In [29], the formation of nanocrystals was observed in the regions of localized shear. These nanocrystals were formed during low-rate nanoindentation of amorphous palladium-based alloy at room temperature. The formation and growth of such nanocrystals at a low temperature require a long time. In [29], the total loading time τ was about 10 s. With a decrease in τ (increase in $\dot{\varepsilon}$ at all the stages of indenter loading), the nucleation and growth of a new phase may require a long time and, thus, this mechanism of unsteady flow becomes blocked. As a result, the fraction of jumpwise strain in the total volume of the indentation formed decreases with a decrease in τ up to its complete disappearance at a certain critical strain rate (Fig. 5).

Thus, the upper limit of the existence of the jumpwise mode of deformation (with respect to $\dot{\varepsilon}$) may be determined by the crystallization kinetics of an amorphous metal alloy during its nanoindentation.

CONCLUSIONS

The jumpwise modes of plastic flow during continuous local deformation are revealed in the amorphous $Zr_{46.8}Ti_8Cu_{7.5}Ni_{10}Be_{27.5}$ alloy. The main characteristics of the strain jumps are determined including their amplitude, their number, their fraction in the mass transport from the zone under the indenter, and the region of jump formation on the $P(h)$ diagram. The boundaries of the region of the jumpwise flow mode are established during nanoindentation in the h–$\dot{\varepsilon}$ phase space.

ACKNOWLEDGMENTS

This study was supported by the Russian Foundation for Basic Research, project no. 01-02-16573, and the Ministry of Education of the Russian Federation, project no. E02-3.4-263.

REFERENCES

1. A. S. Bakai, Mater. Sci. Forum **123–125**, 145 (1993).
2. A. M. Gleĭzer and B. V. Molotilov, *Structure and Mechanical Properties of Amorphous Alloys* (Metallurgiya, Moscow, 1992) [in Russian].
3. L. A. Davis and S. Kavesh, J. Mater. Sci. **10**, 435 (1975).
4. V. A. Khonik, K. Kitagawa, V. A. Mikhailov, and A. Yu. Vinogradov, J. Appl. Phys. **83** (11), 5724 (1998).
5. V. A. Khonik, Phys. Status Solidi A **177**, 173 (2000).
6. *Amorphous Metal Alloys*, Ed. by F. E. Lyuborskiĭ (Metallurgiya, Moscow, 1987) [in Russian].
7. Yu. A. Osip'yan, Vestn. Akad. Nauk SSSR, No. 9, 3 (1987).
8. C. A. Pampillo, J. Mater. Sci. **10** (7), 1194 (1975).
9. T. Masumoto and R. Maddin, Mater. Sci. Eng. **19** (1), 1 (1975).
10. T. Masumoto and T. Murata, Mater. Sci. Eng. **25**, 71 (1976).
11. H. Kimura and T. Masumoto, Acta Metall. **28**, 1663 (1980).
12. A. Yu. Vinogradov, V. A. Mikhaĭlov, and V. A. Khonik, Fiz. Tverd. Tela (St. Petersburg) **39** (12), 885 (1997) [Phys. Solid State **39**, 787 (1997)].

13. A. Yu. Vinogradov, K. Kitagava, and V. A. Khonik, Fiz. Tverd. Tela (St. Petersburg) **41** (12), 2167 (1999) [Phys. Solid State **41**, 1989 (1999)].
14. V. Z. Bengus, E. D. Tabachnikova, V. V. Gaĭko, *et al.*, Metallofizika (Kiev) **8** (6), 3 (1986).
15. G. Berces, N. Q. Chinh, A. Juhasz, and J. Lendvai, Acta Mater. **46** (6), 2029 (1998).
16. G. Berces, N. Q. Chinh, A. Juhasz, and J. Lendvai, J. Mater. Res. **13** (6), 1411 (1998).
17. N. Q. Chinh, Gy. Horvath, Zs. Kovacs, and J. Lendvai, Mater. Sci. Eng. **324**, 219 (2002).
18. M. A. Lebedkin and L. R. Dunin-Barkovskiĭ, Zh. Éksp. Teor. Fiz. **113** (5), 1816 (1998) [JETP **86**, 993 (1998)].
19. M. Lebyodkin, Y. Brechet, Y. Estrin, and L. Kubin, Acta Mater. **44**, 4531 (1996).
20. Yu. I. Golovin, V. I. Ivolgin, V. A. Khonik, *et al.*, Scr. Mater. **45**, 947 (2001).
21. C. A. Schuh and T. G. Nieh, Acta Mater. **51**, 87 (2003).
22. Yu. I. Golovin, V. I. Ivolgin, A. I. Tyurin, and V. A. Khonik, Fiz. Tverd. Tela (St. Petersburg) **45** (7), 1209 (2003) [Phys. Solid State **45**, 1267 (2003)].
23. R. Vaidyanathan, M. Dao, G. Ravichandran, and S. Surech, Acta Mater. **49**, 3781 (2001).
24. H. Kimura and T. Masumoto, in *Amorphous Metal Alloys*, Ed. by F. E. Lyuborskiĭ (Metallurgiya, Moscow, 1987), p. 183.
25. Yu. I. Golovin, V. I. Ivolgin, V. V. Korenkov, and A. I. Tyurin, Zh. Tekh. Fiz. **70** (5), 82 (2000) [Tech. Phys. **45**, 605 (2000)].
26. Yu. I. Golovin, V. I. Ivolgin, V. V. Korenkov, *et al.*, Kondens. Sredy Mezhfaz. Granitsy **3** (2), 122 (2001).
27. Yu. I. Golovin, V. I. Ivolgin, and M. A. Lebedkin, Fiz. Tverd. Tela (St. Petersburg) **44** (7), 1254 (2002) [Phys. Solid State **44**, 1310 (2002)].
28. M. Lebyodkin, Y. Brechet, Y. Estrin, and L. Kubin, Acta Mater. **44** (11), 4531 (1996).
29. J.-J. Kim, Y. Choi, S. Suresh, and A. S. Argon, Science **295**, 654 (2002).
30. W. J. Wright, R. B. Schwarz, and W. D. Nix, Mater. Sci. Eng. A **319–321**, 229 (2001).

Translated by L. Man

Crystallography Reports, Vol. 50, No. 2, 2005, pp. 297–307. Translated from Kristallografiya, Vol. 50, No. 2, 2005, pp. 332–343.

PHYSICAL PROPERTIES OF CRYSTALS

Anomalous Crystal Optics of Heterogeneous Crystals

Yu. O. Punin and A. G. Shtukenberg

St. Petersburg State University, Universitetskaya nab. 7/9, St. Petersburg, 199164 Russia

e-mail: sasha@as3607.spb.edu

Received November 24, 2003

Abstract—Various approaches to analysis of the characteristics of optically heterogeneous crystals (with the characteristic thicknesses of layering lamellae exceeding the light wavelength) are considered in the example of layered two-component heterogeneous structures. In the simplest cases, the quantitative information on the layering structure may be obtained from analysis of numerical characteristics such as the moments of the appearance of visible isogyres or the positions of isotropic compensation points. In more complicated cases, it may be reasonable to use the program specially written by the authors for constructing conoscopic figures of heterogeneous crystals. Finally, the heterogeneity of complex crystals may be characterized proceeding from the qualitative estimate of the degree of distortion of their conoscopic figures. © *2005 Pleiades Publishing, Inc.*

INTRODUCTION

Natural and synthetic crystals have a large number of diverse heterogeneous structures which, morphologically, seem to be single crystals but, in fact, are not single crystals. These crystals are more or less regular formations or combinations of various phases. The components of these formations may have different dimensions (from several angstroms to several centimeters), different compositions, and different structures. These include such formations as several polytypic modifications, syntactic accretions, polysynthetic twins, exsolution microstructures, etc. The phases of such formations may have different dimensionalities, but the most widespread and interesting in terms of crystal optics are two-dimensional (layered) heterogeneous structures built by alternating plates of different thicknesses having different compositions, structures, or orientations. Such heterogeneous crystals are the objects of the present study.

The nature of such "composites" may readily be established by X-ray diffraction and electron microscopy studies. However, these methods are too intricate for use on a mass scale. Moreover, in many instances the X-ray diffraction methods are insufficiently sensitive to a low content of one of the phases. Also, the optical properties of such objects may vary considerably. Therefore, when studying "single crystals," researchers often encounter various distortions of the optical indicatrix caused by crystal heterogeneity.

Considering the optical properties of heterogeneous crystals, one has to distinguish between two types of such crystals. If the layering scale or the size of a phase inclusion is less than the light wavelength, it is impossible to distinguish the object considered from a single crystal both in terms of morphology and in terms of crystal optics. The composite structure of such *optically homogeneous* systems is indicated by their anomalous optical properties, which manifest themselves in pronounced variations of the shape and orientation of the optical indicatrix both within single crystals and in different crystals of an ensemble. The variations of the optical characteristics are not related (at least, directly) to the variations of the chemical composition. If the layer thickness exceeds the light wavelength, a crystal is *optically heterogeneous*, which is seen from the absence of extinction in orthoscopy and distortions of its conoscopic figures. These two types of systems often behave quite differently and should be considered separately. Optically homogeneous systems have been studied rather well. There are several methods for constructing the resulting optical indicatrix of layered crystals. For a number of simple cases, the inverse problem is also solved; i.e., it is possible to calculate the layering parameters from the known optical properties of the crystal [1–4]. The behavior of optically heterogeneous systems has been studied to a much lesser degree. Therefore, we undertook this study to better understand the behavior of the these systems.

If the layer thickness exceeds the visible-light wavelength, each of the components acts on polarized light as an independent crystal. Therefore, it is impossible to construct the total indicatrix for such a system as a whole. In fact, this is the manifestation of the optical heterogeneity of such a heterogeneous crystal. If the system components are oriented arbitrarily, then, in the general case of orthoscopy, no system extinction takes place; thus, the orthoscopic method is inapplicable. The situation with the conoscopic method is quite different. A conoscopic figure is formed by light waves propagating in the crystal along different directions. Along some of these directions, the directions of vibrations in different components may coincide; i.e., extinction becomes possible. Thus, in principle, one may calculate the mutual orientations of the components. Further on, the

1063-7745/05/5002-0297$26.00 © 2005 Pleiades Publishing, Inc.

intensity of light transmitted along the given system direction is determined not only by the component orientations but also by the component thicknesses; i.e., it is also possible to determine the fraction of each component in a heterogeneous crystal. This problem is very complicated, so we consider it only for the simplest case of a two-component system with the particular misorientation of the optical indicatrices of the components.

Consider a crystal consisting of two components characterized by indicatrices having different shapes and misoriented by an arbitrary angle ψ with respect to the common indicatrix axis (normal to the layering plane) which is either n_g or n_p (the case of misorientation around n_m is not considered). It should also be noted that, in this case, each component may represent an optically homogeneous but structurally heterogeneous system. This situation is often encountered in *OD* crystals (heterogeneity at several scale levels) [5, 6]. In particular, this model is applicable to heterogeneous crystals of micas and some other polytypic compounds.

The optical heterogeneity of a system manifests itself in distortions of the conoscopic figures of these crystals. The distorted interference patterns differ from normal undistorted ones by deformation of interference bands and unusual behavior of isogyres.

The distorted conoscopic patterns of natural micas [7, 8], synthetic phlogopite [9, 10], and potassium ferrocyanide [11] were repeatedly observed and described. These patterns were interpreted qualitatively correctly as a result of the superposition of differently oriented lamellae and the optical indicatrices. However, as far as we know, no attempts to quantitatively interpret the anomalous conoscopy were undertaken. Not claiming an exhaustive analysis of this complex phenomenon, we consider below the main characteristics of distorted conoscopic figures.

BEHAVIOR OF ISOGYRES

The main characteristics of the isogyre behavior in optically heterogeneous crystals were discussed in detail elsewhere [3]; therefore, we consider here only the most important aspects of isogyre behavior.

An isogyre is the geometric locus of points in the visual field of a conoscope with the equivalent directions of the light-wave vibrations [12], whereas a visible isogyre is the geometric locus of the points with the vibration directions coinciding with the vibration directions in polarizers. For most of the light waves propagating in a heterogeneous crystal at different angles, the directions of vibrations in its two components do not coincide. Therefore, in the general case, the isogyres are invisible in the visual field of a conoscope. When the microscope stage is rotated, the isogyres of the two components start moving in the visual field with different velocities and along different directions. Therefore, at a certain moment, both isogyres will be located at the same site of the visual field (Fig. 1A); in other words, the directions of vibrations at the merging points of both components coincide with the directions of vibrations in polarizers. It is at this moment that the isogyres become visible (and darkness appears at the coincidence points). At the smallest stage deviation from this position, the visible isogyres disappear. It is clear that, within the complete stage rotation, this situation should be repeated four times. The distance ρ^* from the wire-cross center to a visible isogyre characterizes the "effective" angle between the optic axes in the crystal (Fig. 1A (c)). The expression for ρ^* as a function of the angle between the optic axes of the components and their misorientation is given in [3] as well as the expression for the angle η^* of the stage rotation from the extinction position of one of the components prior to the appearance of a visible isogyre. It is clear that the thickness (volume fraction) ratio of the components does not affect these characteristics.

In some particular cases, the coincidence (and appearance) of isogyres takes place in the extinction position, i.e., at $\psi = 0°$ or 90° (the planes of the optic axes of the components are either parallel or perpendicular to one another), or if one of the components is uniaxial. The complete rotation of the stage four times gives rise to cross appearance in the absence of visible isogyres in other positions. In orthoscopy, this system shows complete extinction; i.e., it is undistinguishable from a single crystal! It is this situation that is characteristic of heterogeneous potassium ferrocyanide crystals [13].

A somewhat more complicated situation is observed if the components are rotated by a certain angle ψ about a direction forming a certain small (several degrees) angle α with acute or obtuse bisectors. This situation takes place in fluorphlogopite and some lepidolites. In this case, the rotation of the microscope stage results in the nonsimultaneous appearance of two visible isogyre branches in opposite quadrants. This may readily be seen if one separates the points of emergence of the acute bisectors of the components (point *O* in Fig. 1A (c)) to separate by the angle 2α (points *O*' and *O*" in Fig. 1B (a); for simplicity, the bisectors are rotated along the diagonal of the visual field). It is clear that in this case isogyres become invisible. The isogyres of the components will overlap if one rotates the stage from this position in any direction. Then, the isogyre branches coincide either in quadrant I or in quadrant III. The calculations show that the angle of rotation of the stage between the moment of appearance of two branches of the visible isogyre $\Delta\eta^*$ at the given α increases with a decrease in the angle between the optic axes of the components and with an increase in the effective angle between the optic axes of the crystal. The experiments on fluorphlogopite show that $\Delta\eta^*$ varies from 0° to 20° [6]. Of course, the value $\Delta\eta^*$ depends only on the optical characteristics and component misorientation and does not depend of the component fractions. The wide range of value $\Delta\eta^*$ in fluorphlogopite

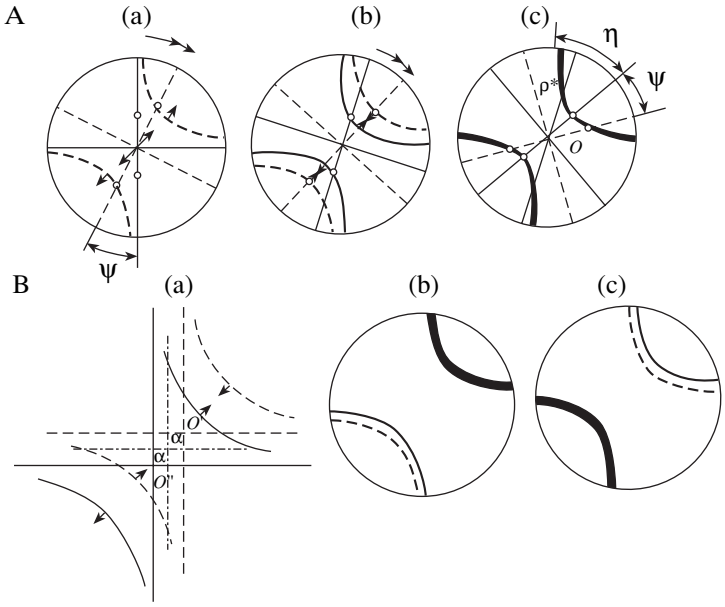

Fig. 1. Scheme of appearance of isogyres (broad black hyperbolas in Figs. 1A (c) and 1B (b) and 1B (c)) during the rotation of the microscope stage. (A) Simultaneous appearance of the isogyre branches: (b, c) successive rotations from (a) the extinction position of one of the components in the direction of a double arrow. Solid and dashed lines are the optic elements of different components misoriented by the angle ψ; half-bold lines show the direction of the isogyre motion. (B) Alternating appearance of two isogyre branches: (a) directions of the motion of isogyre branches of different components (solid and dashed crosses are the asymptotic curves of the corresponding isogyres; the dot-and-dash line indicates the position of the cross wires); (b, c) conoscopic figures formed at different positions of the stage. For the remaining notation see the text.

is explained by the fact that the components of an optically heterogeneous crystal are not pure polytypes but are optically homogeneous stacks with a layering scale less than the light wavelength.

BEHAVIOR OF INTERFERENCE BANDS

Unlike optically homogeneous systems, the shape of interference bands cannot be described by the Cassinian ovals and does not remain constant during stage rotation, which is quite unusual in conventional conoscopy. Anomalous conoscopic figures of even one compound are very diverse (see figures in [8]). Nevertheless, it is possible to indicate a number of common characteristics of distortion of interference bands. These are:

deformation of Cassinian ovals, including their extension and contraction, skewness and local curvature;

disrupture and relative displacement of interference bands along the common isogyre of the system. The segments of the interference bands may be closed and form distorted rings or may roll into spirals;

the appearance of two symmetric dark spots: compensation (isotropic) points. Unlike the first two characteristics continuously varying during rotation of the stage, the compensation points do not change their positions in the reference system of the crystal. These positions depend on the optical properties of the components, their misorientation, and their volume fractions during layering.

It is easy to quantitatively analyze the positions of the compensation points characterized by the constant polar distance $\tilde{\rho}$. Let us consider what factors affect this distance. It has already been indicated that vibration directions of two components are different at all the points of the viewing field of the conoscope except for the points lying along the coinciding isogyres. The emergence points of the optic axes of both components lie at the common isogyre (Fig. 2). At the points of isogyre branches lying between the emergency points of the optic axes, the vibration directions of two fast or two slow waves are mutually perpendicular. At the external segments of the isogyre branches these directions are parallel. Thus, two conclusions may be drawn. First, the points of the common isogyre (and only these points in the viewing field of the conoscope) preserve their color during the rotation of the microscope stage. Second, the path differences between two optic axes of the components, which are attained by light in each of the components, are subtracted. Therefore, there should exist an isotropic compensation point at which the intensity of the transmitted light equals zero. The positions of the compensation points may be determined from the well-known expressions for birefringence at the arbitrary indicatrix section (see, e.g., [14, 15]) and

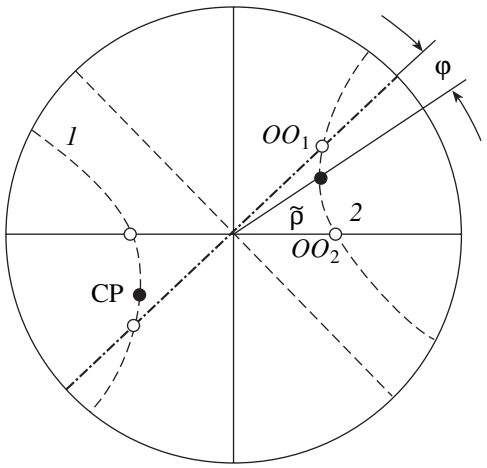

Fig. 2. Scheme of the position of the compensation point (CP). OO_1 and OO_2 are the emergence points of the optic axes of components 1 and 2, respectively. Numbers *1* and *2* indicate the positions of the common isogyres.

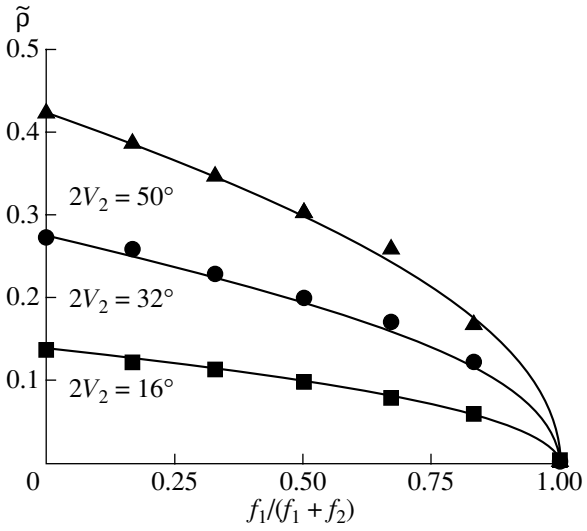

Fig. 3. Polar distance for the compensation points calculated for the case of intergrowth of the uniaxial ($2V_1 = 0$) and biaxial components (angle $2V_2$ is indicated in figure) with the same main birefringence values as a function of the volume–fraction ratio $f_1/(f_1 + f_2)$ of the components. The lines show the calculation by Eq. (2); the points are determined from the data of computer simulation.

under the condition of the zero total path difference. For a polar distance between the compensation point and the emergence point of the common axes of the component indicatrices lying in the unit circle $\tilde{\rho} = \sin\theta$ (where θ is the angle between the normal to the section plane and the given direction of the light-wave propagation), we arrive at the following equation, which depends either on the thickness ratio h_2/h_1 or the volume-fraction ratio f_2/f_1 of these components:

$$\frac{(n_g - n_p)_2^2 h_2^2}{(n_g - n_p)_1^2 h_1^2} = \frac{\rho_1^2[\rho_1^2\tilde{\rho}^2(\tilde{\rho}^2 + \rho_1^{-2} - \cos^2\varphi)^2 - 4\sin^2\varphi]}{\rho_2^2[\rho_2^2\tilde{\rho}^2(\tilde{\rho}^2 + \rho_2^{-2} - \cos^2(\varphi + \psi))^2 - 4\sin^2(\varphi + \psi)]}. \quad (1)$$

Here $\rho_i = \sin V_i$, $2V_i$ and $n_g - n_p$ are the angle formed by the optic axes and birefringence of the *i*th component, respectively; and φ is the angle for which the microscope stage should be rotated from the position of extinction of the first component in order to bring the compensation point to the ocular cross wire. In some particular cases, Eq. (1) may considerably be simplified. Thus, if layers are formed by two biaxial components with the rotation angle $\psi = 90°$ or if a uniaxial component ($2V_1 = 0°$) alternates with a biaxial component, we have $\varphi = 0°$ (i.e., the isotropic point lies in the plane of the optic axes of one of the components). Then, expression (1) takes the form

$$\frac{(n_g - n_p)_2^2 h_2^2}{(n_g - n_p)_1^2 h_1^2} = \frac{\rho_1^2 + \tilde{\rho}^2 - \rho_1^2\tilde{\rho}^2}{\rho_2^2 - \tilde{\rho}^2}. \quad (2)$$

In this case, the dependence of the compensation-point position on the thickness ratio of the components or their angles $2V$ (Fig. 3) becomes rather simple.

An equation of type (1) may also be obtained for any other point of the common isogyre if one determines the path difference at this point with the aid of a quartz wedge or a compensator. This may be necessary if no data on the compound under study are known a priori and one has to determine the optical properties of the following components from the anomalous interference figure: $2V_i$ and $(n_g - n_p)_i$; the angle of their misorientation ψ; and the thickness or volume fraction ratio, h_2/h_1 or f_2/f_1. In some instances, some data on the compound are known a priori, e.g., characteristics of its components or the misorientation angle. Then, the number of parameters of the heterogeneous crystal that should be measured is reduced somewhat.

SIMULATION OF DISTORTED CONOSCOPIC FIGURES

It is possible to calculate distorted conoscopic figures using the known optical properties and misorientation angles of the components. In principle, this calculation may be performed for any number of the components and for any optical characteristic of each of the system components. However, we limit our consideration to two-component systems only. The relative intensity I/I_0 of light transmitted through a crystalline plate located between two crossed polarizers may be

calculated by the well-known formula [14, 16]

$$I/I_0 = \sin^2 2\eta \sin^2(\delta/2). \quad (3)$$

In Eq. (3), the angle η corresponds to the angle between the direction of vibrations in one of the polarizers and the direction of vibrations in the crystal and the phase difference $\delta = 2\pi h_l(n'_g - n'_p)/\lambda$ is determined by the difference in the refractive indices in the given section $(n'_g - n'_p)$, the light path in the crystal h_l, and the light wavelength λ. For a plane-parallel plate, the light path in a crystal is $h_l = h/\cos\theta$, where h is the plate thickness and θ is the angle between the plate normal and the direction of the light incidence. The above formula allows one to calculate the intensity of the transmitted light at any point with the polar coordinates χ and $\rho = \sin\theta$ in the viewing field of the conoscope; in other words, it allows one to calculate the conoscopic figure. When calculating conoscopic figures, one has to introduce the correction for light refraction at the crystal/medium (usually air) interface $\rho_o/\rho = n_c/n$, where $\rho_o = \sin\theta_o$ is the observed polar coordinate of the point, and n_c/n is the ratio of the refractive index of the crystal in the direction normal to the layer plane to the refractive index of the medium. One may calculate η and δ at the given point (χ, ρ) either by the equations following from the Fresnel theorem [16, 17] or, as we have done in this work, by the direct transformation of the permittivity tensor. The behavior of isogyres in the conoscopic figure thus obtained is described by varying the first multiplier in the right-hand side of Eq. (3), i.e., by the misorientation of the directions of vibrations of the waves in the crystal and polarizers. The shape of the interference bands reflects the change in the path difference; i.e., it is determined by the second multiplier in the right-hand side of Eq. (3). Fast and accurate simulation of conoscopic figures of crystals became possible only with the advent of powerful computers and, as far as we know, the first program for such calculations was written only in 1980 [18]. Today, the calculation of conoscopic figures is not a difficult problem any more and is performed, e.g., for simulating the conoscopic figures of optically active crystals [19].

For optically heterogeneous two-component systems with $i = 1, 2$ and the volume fractions $f_i = h_i/(h_1 + h_2)$, it is possible to calculate η_i and δ_i at the given point (χ, ρ) for each component and then to use the following well-known expression for the intensity of light transmitted through two superimposed plates located between two crossed polarizers [14, 20]:

$$\begin{aligned} I/I_0 = &-\sin 2\eta_1 \cos 2\eta_2 \sin 2(\eta_2 - \eta_1)\sin^2(\delta_1/2) \\ &+ \cos 2\eta_1 \sin 2\eta_2 \sin 2(\eta_2 - \eta_1)\sin^2(\delta_2/2) \\ &+ \sin 2\eta_1 \sin 2\eta_2 \cos^2(\eta_2 - \eta_1)\sin^2([\delta_1 + \delta_2]/2) \\ &- \sin 2\eta_1 \sin 2\eta_2 \sin^2(\eta_2 - \eta_1)\sin^2([\delta_2 - \delta_1]/2). \end{aligned} \quad (4)$$

One can readily see that if the components having the same optical characteristics are not misoriented with respect to one another and if $\eta_1 = \eta_2$, then Eq. (4) is transformed into Eq. (3).

SOME EXAMPLES OF CALCULATIONS OF DISTORTED CONOSCOPIC FIGURES

As we have already indicated, conoscopic figures of heterogeneous crystals are highly diverse. Therefore, it is hardly possible to consider all the variants of these figures. Thus, we discuss here only some particular cases of their widespread variants. It should also be noted that the characteristics of distorted conoscopic figures, such as the positions of the compensation points or the moments of appearance of visible isogyres on the calculated figures, agree well with the values calculated by the analytical formulas of type (1) (Fig. 3). Moreover, in all the cases, the comparison of the model calculations with the experimental observations shows that the calculation made at one wavelength reflects quite well the specific features of the conoscopic figures obtained at the wavelengths of white light.

Layering of Uniaxial and Biaxial Lamellae

This is the simplest case. Consider a layered heterostructure consisting of uniaxial ($n_g - n_m = 1.588$, $n_p = 1.552$, the optic axis is normal to the layer plane, the volume fraction of the component is f_1) and biaxial ($n_g = 1.588$, $n_m = 1.552$, $2V = 48°$, the acute bisector n_p is normal to the layering plane, the volume fraction of the component is f_2) components. The conoscopic figures differ depending on the ratio of volume fractions (thicknesses) of the components. If, in the crystal, one of the components prevails, the conoscopic figure contains more details characteristic of this component and the figure distortions are not especially noticeable. The most pronounced distortion takes place if the volume fractions of the components are equal (or, more exactly, if the path differences of these components are the same; in our example this corresponds to the equal thicknesses of the components). Figure 4 shows the distorted conoscopic figures of such a crystal at different positions of the biaxial component with respect to the crossed polarizers η and different ratios of the volume fractions f_i (or thicknesses $h_i = f_i(h_1 + h_2)$) of the components. Proceeding from the symmetry considerations, the complete picture of the conoscopic figure requires the consideration of only one-eighth of the total rotation of the microscope stage. The total thickness of the heterostructure $h_1 + h_2$ was taken to be equal to 0.3 mm.

The analysis of the figures shows that, in this case, the dark cross in the visual field appears four times during the complete stage rotation. The crystal orientation at this moment corresponds to the extinction position of the biaxial component. The compensation points are

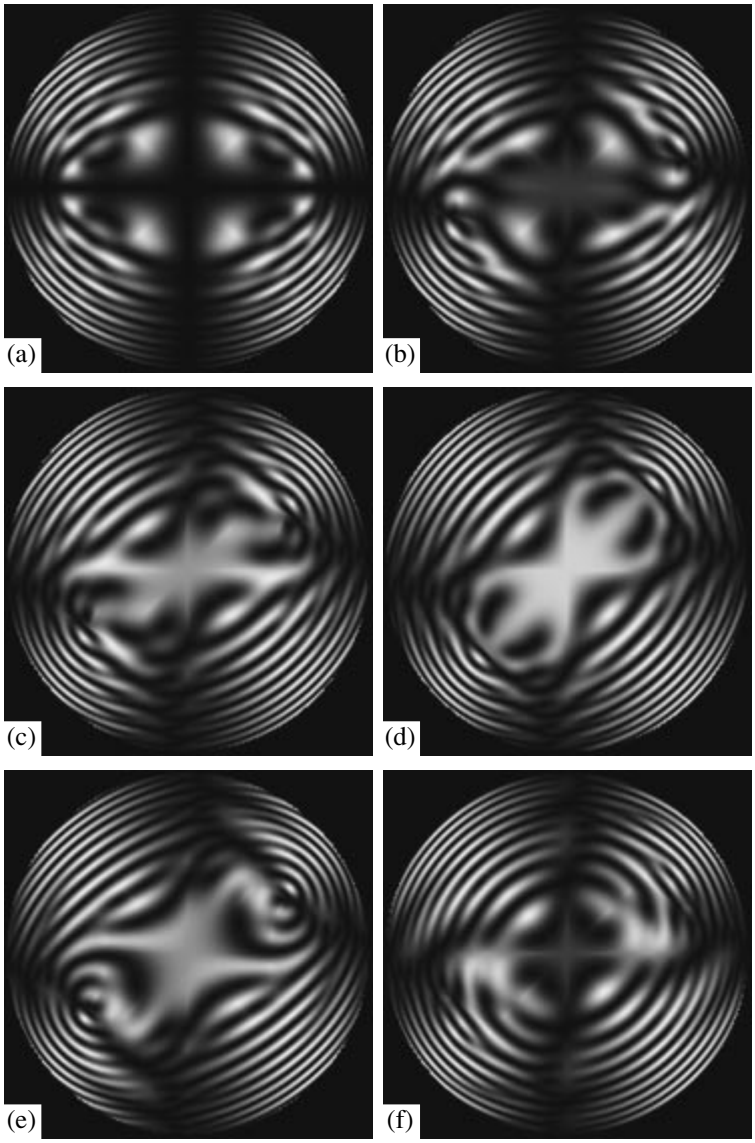

Fig. 4. Calculated conoscopic figures of a heterostructure consisting of uniaxial ($2V_1 = 0°$) and biaxial ($2V_2 = 48°$) components in monochromatic light with the wavelength 565 nm. The visual field $\arcsin(\rho_{max}) = 40°$; the volume-fraction ratio of the components $f_1/f_2 = 1$. Four successive figures (a–d) correspond to the rotation of the microscope stage from the position of extinction of the biaxial component in the counterclockwise direction by an angle η equal to 0°, 15°, 30°, and 45°; (e, f) the same for $\eta = 30°$ and $f_1/f_2 = 1/3$ and 3, respectively (cf with Fig. 4c).

located on one of the cross arms. These points are surrounded with the parts of the interference bands adjacent to the interference bands of the next order. When rotating the stage from this position, we observed the intensity redistribution at the cross arms such that there was no extinction in the central part of the viewing field and, only at the viewing-field periphery, where the directions of component vibrations were close, was the extinction preserved. The shape of the interference bands continuously vary during stage rotation. The figure looses its two symmetry planes. The asymmetric junction of the segments of the interference bands of various orders provides the formation of a helicoidal shape. During rotation by 45°, the conoscopic figure acquires its two symmetry planes located along the diagonals with respect to the wire cross. In the quadrants to which the points of the emergence of optic axes of the second component moved, the compensation point and isolated segments of the interference bands are located on the diagonals. In two other quadrants, the segments of the interference rings are also located along the diagonals. On the whole, the variation of the thickness ratio of the components affects neither the structure of the conoscopic figures nor their symmetry. However, if one type of lamella dominates, it is this type that makes the major contribution to the resulting

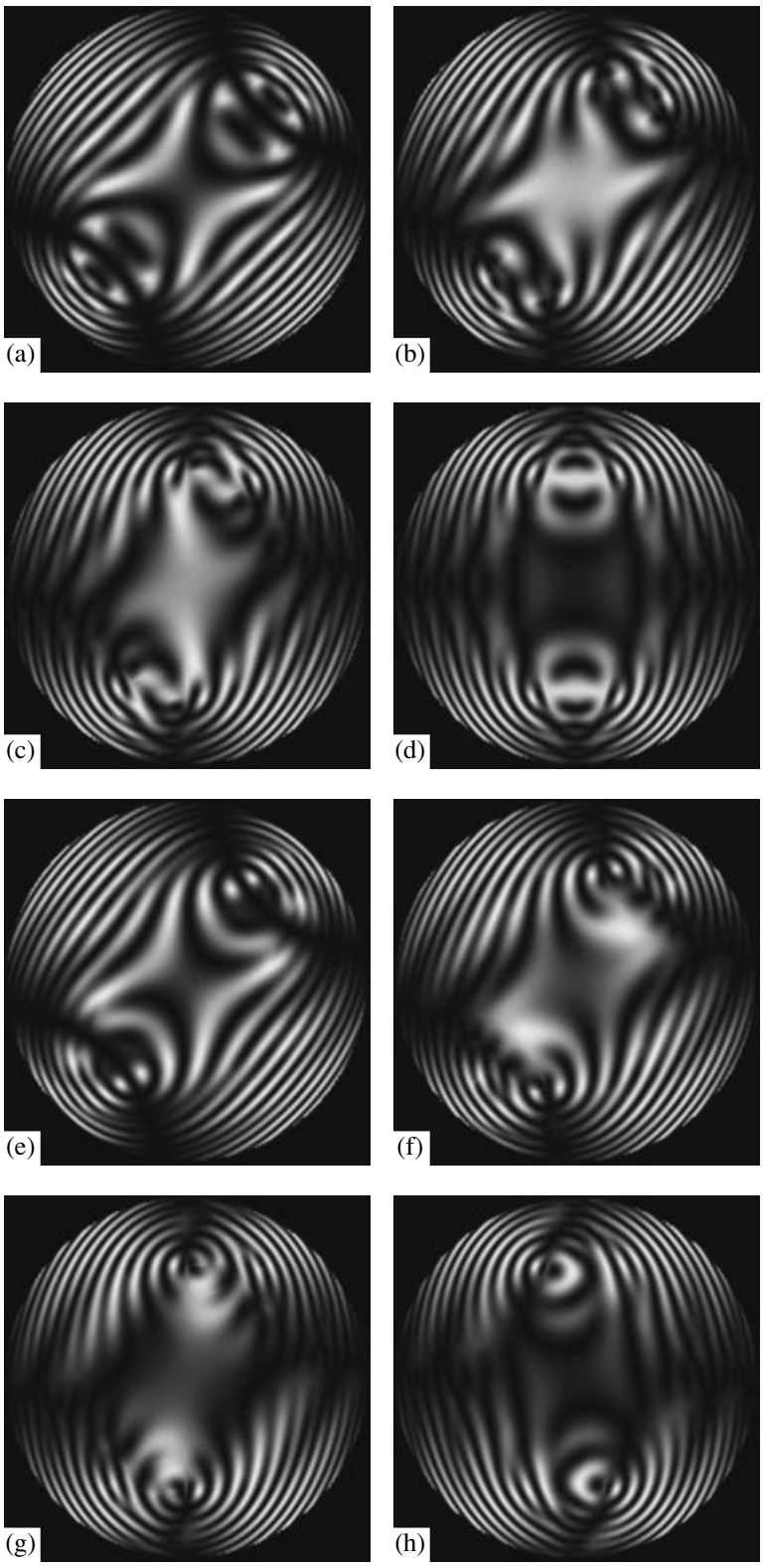

Fig. 5. Calculated conoscopic figures of a heterostructure consisting of two equivalent biaxial components ($2V_2 = 48°$) in monochromatic light with the wavelength 565 nm. The viewing field $\arcsin(\rho_{max}) = 40°$; the volume-fraction ratio of the components $f_1/f_2 = 1$. Four successive figures (a–d) correspond to the rotation of the microscope stage from the position of extinction of the first component by an angle η equal to 30°, 45°, 60°, and 75°. The four remaining figures (e–h) correspond to the case $f_1/f_2 = 1/3$ and $\eta = 30°$, 45°, 60°, and 75°, respectively (cf with Figs. 5a–5d). The rotation angle of the components $\psi = 30°$.

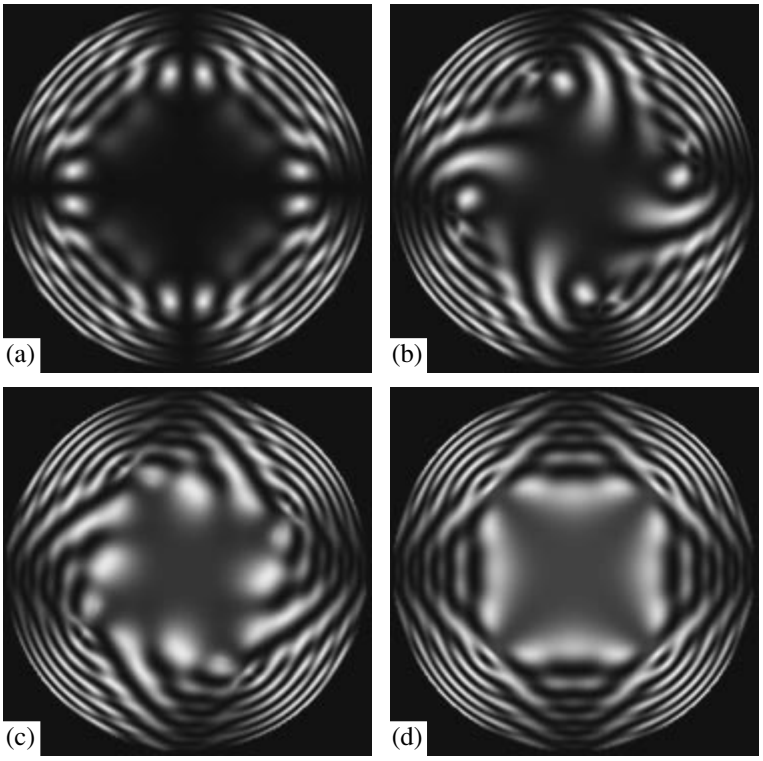

Fig. 6. Calculated conoscopic figures of the heterostructure consisting of two equivalent biaxial components ($2V_2 = 48°$). (a–d) The volume–fraction ratio of the components $f_1/f_2 = 1$; the rotation angle of the components $\psi = 90°$; and the angle η is 0°, 15°, 30°, and 45°, respectively. For the remaining notation, see Fig. 5.

conoscopic figure, and the corresponding standard conoscopic figure is clearly seen against the background of the more complicated total pattern (Figs. 4e and 4f).

Layering of Two Types of Equivalent Biaxial Lamellae Rotated by Angle ψ Relative to Acute Bisector

In this case, the conoscopic figures are more diverse since, in addition to the rotation of the heterogeneous system with respect to crossed polarizers and the ratio of the volume fractions of the components, one may also vary the misorientation angle ψ between the components. Consider the same heterogeneous system as in the previous section with only one difference: the uniaxial component is substituted by the biaxial one with the crystallographic and optical characteristics of the second component. The model calculations were performed at three misorientation angles $\psi = 30°$, 60°, and 90° (Fig. 5).

The optical distortions are the most pronounced at equal volume fractions of the components. The optical picture acquires two symmetry planes in the two following cases. (1) The position of the crossed polarizers coincides with the bisectors of the angles formed by the planes of the optic axes of the components (Fig. 5d). In this variant, the compensation points lie on one of the cross wires (vertical in Fig. 5d) and are symmetrically surrounded with the pieces of the lemniscates of the first and the second components. Along the second wire, a broad extinction region not touching the center of the viewing field is located where the directions of the component vibrations are considerably misoriented. (2) Bisectors of the angles formed by the planes of the optic axes of the components coincide with the diagonal directions in the position of the crossed polarizers (Fig. 5a). In this case, the hyperbolic branches of a visible isogyre appear at the vertices where the compensation points are located. The interference bands closest to these points are disrupted, displaced along the isogyre branches, and closed at the interference bands of the next order.

If the volume fractions of the crystal components are not equal, the conoscopic figures lose the symmetry 2*mm* in the positions considered above. The interference bands are skewed with respect to the cross wires (position 1) or the diagonal (position 2), and the compensation points are displaced along the common isogyre toward the direction of the emergence of the optic axis of a "thicker" component. In the other positions, highly complicated figures having no symmetry planes are observed irrespective of the thickness ratio of the components. These figures are characterized by the considerable change of the intensity along the interference bands and the asymmetric closure of the fragments of the interference bands of different orders. This

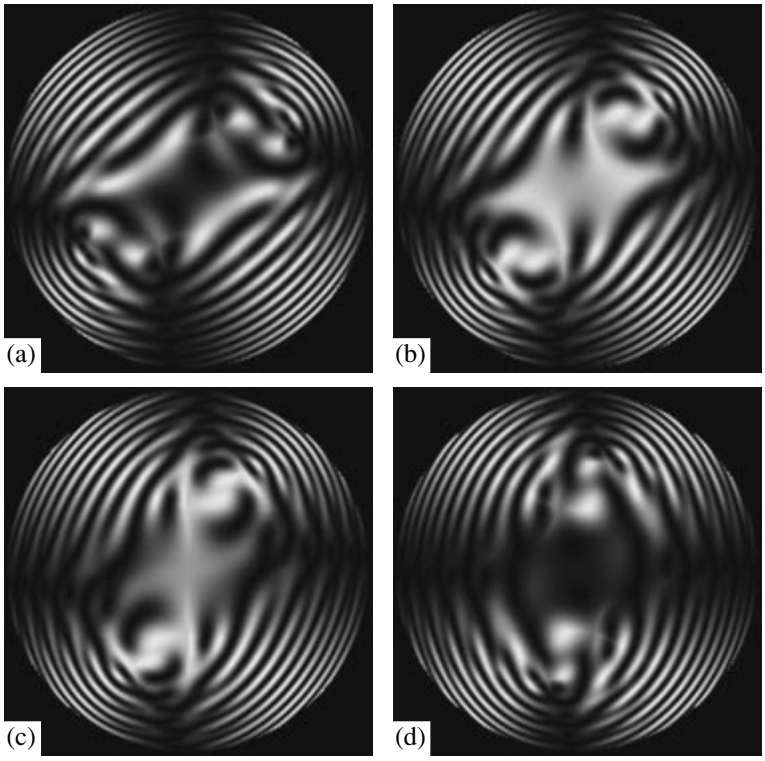

Fig. 7. Calculated conoscopic figures of the heterostructure consisting of two biaxial components with different angles of the optic axes ($2V_1 = 48°$, $2V_2 = 26°$). The volume–fraction ratio of the components $f_1/f_2 = 1$, and the angle of the component rotation $\psi = 30°$. The angle η equals 30°, 45°, 60°, and 75° for (a–d), respectively. For the remaining notation, see Fig. 5.

results in the formation of twisting bands. Similar to the case of a heterostructure consisting of uniaxial and biaxial crystals, in the case of the domination of one type of lamella, it is this type of lamella that makes the major contribution to the resulting figure clearly seen against the background of the more complicated total figure (Figs. 5e–5c). The conoscopic figure becomes close to the normal one also with a decrease in the misorientation angle ψ and its tendency to zero.

Another very interesting particular case is observed if the components are misoriented by the angle $\psi = 90°$. This is characteristic, e.g., of *OD* potassium ferrocyanide crystals. The conoscopic figure in the case of crystal with equally thick components acquires a fourfold symmetry axis irrespective of the position of the microscope stage (Fig. 6). It should be indicated that orthoscopy of this system shows normal extinction (see above), but the shape of the conoscopic figure allows direct diagnostics of the optical heterogeneity of the crystal. The isochromic curves have the characteristic square shape in the direct and diagonal positions of the plane of the optic axes of the crystal relative to the wire cross and have the helical form at all the other positions. If the component thicknesses are not equal, no fourfold symmetry is observed.

Layering of Two Types of Lamellae with Different Angles between Optic Axes

In this case, the conoscopic figures are asymmetric irrespective of the thickness ratio of the components and the rotation angle of the microscope stage (Fig. 7). However, in this case, the appearance of visible isogyres at certain crystal positions with respect to the cross wires and the presence of isotropic compensation points can be seen clearly. This situation differs from the situation for the other interference bands that do not change their positions in the reference system of the crystal during the rotation of the microscope stage. It should also be indicated that even in the case of equal thicknesses of the components the emergence points of the optic axes may be seen against the background of the conoscopic figure. This is also true for the crystals with the components having the same optical properties. However, the effect is more pronounced if the angles of the optic axes are different (Fig. 7).

DISTORTED CONOSCOPY AS A CHARACTERISTIC OF CRYSTAL HETEROGENEITY

Thus, proceeding from the positions of isogyres and compensation points, one may calculate the main characteristics of macrolayering. However, these calculations are very time- and labor-consuming and, thus, may hardly be used in practice. It is also possible to

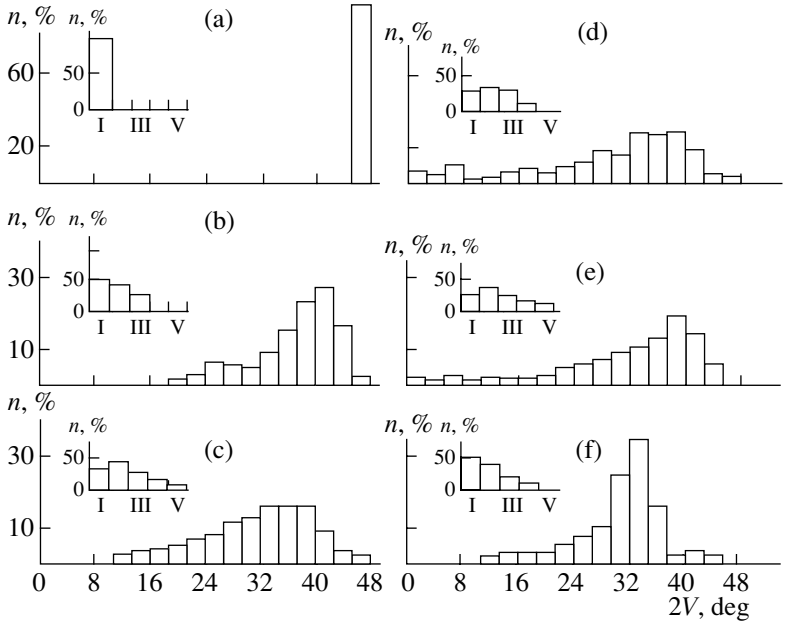

Fig. 8. Effect of the chemical composition on the variation of the angle 2*V* and degree of distortion of conoscopic figures (I–V) of lithium–aluminum micas. LiO_2 content, %: (a) up to 0.7, (b) 0.7–1.2, (c–e) 1.2–4.0, (f) 4.0–5.8.

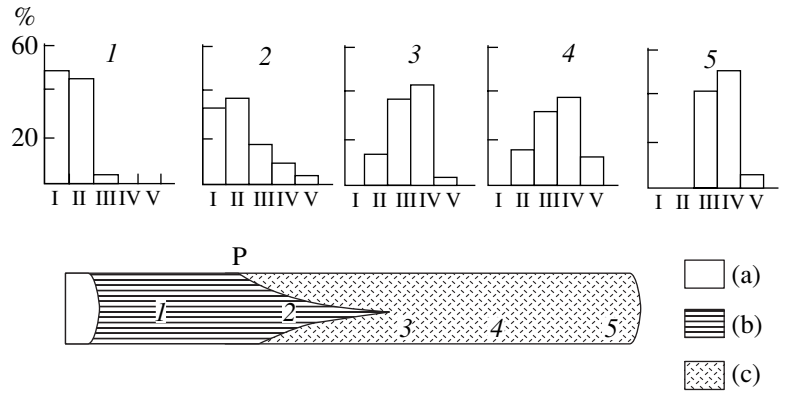

Fig. 9. Distribution of fluorphlogopite crystals over the degree of conoscopy distortion in zones 1–5 of the ingot. (a) Seed, (b) single crystal, (c) polycrystal. P is the position of the furnace at the moment of its switching off (thermal shock). The degree of crystal heterogeneity dramatically increases in the transition from zone *1* to zone *3* and then increases more smoothly to zones *4* and *5*, which is explained by the thermal shock and subsequent accumulation of impurities in the ingot during directional crystallization. The degree of distortion of conoscopic figures changes in accordance with this scheme.

compare the observed conoscopic figures with the simulated ones. In this case, thorough preliminary work is necessary for the subsequent calculation of the sets of standard figures for each concrete system. This corresponds to different variants of layering. It should also be remembered that the above consideration is valid only for two-component systems and only for a particular (although widespread) case of component misorientation. As opposed to the optically homogeneous systems, the general case of macrolayering requires further development. Nevertheless, the anomalous conoscopy may successfully be used for qualitative estimation of the degree of layering heterogeneity. With a decrease in the thickness of any one or both components, the intensity of the light transmitted through the system along the given direction tends to the intensity given by Eq. (3), where η and δ determine either a thicker plate (in the first case) or the resulting optically homogeneous system (in the second case). The distortion of the shape of interference bands becomes weaker and the compensation points are displaced to the emergence point of the optic axes of a thicker component (in the first case) or are transformed into the emergence points of the optic axes of the homogeneous system (in the second case), in full accordance with results of the computer simulation (Figs. 4 and 5). The total degree of distortion of the conoscopic figure decreases in comparison with the standard one. Thus, the degree of distortion of the conoscopic figure is the characteristic of the degree of the optical and, therefore, structural heterogeneity of the crystal.

Today it is impossible to suggest any rigorous quantitative estimates of the degree of conoscopy distortion; however, it is possible to estimate this distortion qualitatively, e.g., on a five-point scale. The advantage of this method is its simplicity and high efficiency, which are necessary in the statistical study of a large number of samples. Comparison of the histograms of crystal distribution in accordance with the degree of distortion of their conoscopic figures for various objects (samples, some regions of deposits and deposits themselves, etc.) gives the possibility of creating the picture of the variation of structural heterogeneity depending on the conditions of crystal formation. Thus, such histograms were constructed for lithium–aluminum micas from rare-earth metal pegmatites depending on the mica compositions (Fig. 8) [4, 21, 22]. The sequence given in Figs. 8a–8f corresponds to the sequence of the change of the morphological–chemical types of the micas from selvages to the axis of the pegmatitic vein (some links of the chain may be absent in some concrete deposits). Another example is illustrated by Fig. 9, showing the change of heterogeneity along the ingot length of fluorphlogopite crystals, which is associated with the change of the crystallization rate caused by a thermal shock during the incident in the furnace and the subsequent accumulation of the impurities in the course of directional crystallization [3]. Thus, the usefulness of the qualitative estimation of the distortion of conoscopic figures for the study of the nature and genesis of heterogeneous crystals is obvious.

CONCLUSIONS

The study of optically heterogeneous crystals consisting of layered lamellae of two types showed that, in many instances, the characteristics of layering such as the thickness ratio of the lamellae, their mutual orientation, and their optical characteristics may be obtained by analyzing their distorted conoscopic figures.

A special program was written for calculation such conoscopic figures. The use of this program allows one to considerably simplify analysis of anomalous conoscopy of composite crystals and to simulate their possible optical distortions. The experimental studies of polytypic accretions of natural and synthesis micas and potassium ferrocyanide show that the optical picture is often determined not only by the characteristics of pure layering polytypes but also by the optically homogeneous (but structurally heterogeneous) stacks of such polytypes possessing their own optical indicatrix. In this case, the qualitative estimation of the degree of conoscopic figure distortion on the point scale turns out to be useful.

ACKNOWLEDGMENTS

This study was supported by the Russian Foundation for Basic Research, project no. 02-05-65279.

REFERENCES

1. A. S. Marfunin, Dokl. Akad. Nauk SSSR **127** (5), 869 (1959).
2. J. Hauser and H. R. Wenk, Z. Kristallogr. B **143**, 188 (1976).
3. Yu. O. Punin, Zap. Vses. Mineral. O–va, Part 118 (1), 76 (1989).
4. E. N. Kotel'nikova, Yu. O. Punin, and V. A. Frank-Kamenetskiĭ, *Methods of Diffraction Studies of Crystalline Materials* (Nauka, Novosibirsk, 1989), p. 107 [in Russian].
5. K. Dornberger-Shiff, Kristallografiya **27**, 126 (1982) [Sov. Phys. Crystallogr. **27**, 73 (1982)].
6. Yu. O. Punin, E. N. Kotel'nikova, and V. A. Frank-Kamenetskiĭ, *Crystallography and Crystal Chemistry* (Leningr. Gos. Univ., Leningrad, 1985), No. 5, p. 78 [in Russian].
7. P. Groth, *Physikalische Krystallographie und Einleitung in die Krystallographische Kenntniss der Wichtigsten Substanzen* (Engelmann, Leipzig, 1895; K. L. Rikker, St. Petersburg, 1897).
8. V. I. Sokolov, *E.S. Fedorov Universal Stage* (Akad. Nauk SSSR, Moscow, 1953), p. 394 [in Russian].
9. F. D. Bloss, G. V. Gibbs, and D. Cumings, J. Geol. **71**, 537 (1963).
10. G. G. Shmelev and A. A. Bobr-Sergeev, *Yearbook-69 of Siberian Institute of Geochemistry* (Irkutsk, 1970), p. 251 [in Russian].
11. M. Toyoda, N. Niizeki, and S. Waku, J. Phys. Soc. Jpn. **15**, 1831 (1960).
12. V. B. Tatarskiĭ, *Crystal Optics and the Immersion Method of Study of Minerals* (Nedra, Moscow, 1965) [in Russian].
13. Yu. O. Punin, E. N. Kotel'nikova, V. Yu. Zhogoleva, and G. P. Isaeva, *Crystallography and Crystal Chemistry* (Leningr. Gos. Univ., Leningrad, 1982), No. 4, p. 6 [in Russian].
14. F. Pockels, *Lehrbuch der Kristalloptik* (Leipzig, Berlin, 1906).
15. L. A. Shuvalov, A. A. Urusovskaya, I. S. Zheludev, *et al.*, in *Modern Crystallography*, Vol. 4: *Physical Properties of Crystals*, Ed. by B. K. Vaĭnshteĭn, A. A. Chernov, and L. A. Shuvalov (Nauka, Moscow, 1981; Springer, Berlin, 1988).
16. A. V. Shubnikov, *Optical Crystallography* (Akad. Nauk SSSR, Moscow, 1950) [in Russian].
17. A. N. Zavaritskiĭ, *E.S. Fedorov Universal Stage* (Akad. Nauk SSSR, Moscow, 1953), p. 456 [in Russian].
18. C. M. Bethke and R. W. Birnite, Am. Mineral. **65**, 1294 (1980).
19. K. A. Rudoĭ, B. V. Nabatov, V. I. Stroganov, *et al.*, Kristallografiya **48**, 334 (2003) [Crystallogr. Rep. **48**, 300 (2003)].
20. N. H. Hartshorne and A. Stuart, *Crystals and Polarising Microscope* (Edward Arnold, London, 1970).
21. P. B. Sokolov, Yu. O. Punin, E. N. Kotel'nikova, *et al.*, Mineral. J. **9** (1), 55 (1987).
22. Yu. O. Punin, E. N. Kotel'nikova, P. B. Sokolov, *et al.*, Zap. Vses. Mineral. O–va, Part 118 (5), 1 (1989).

Translated by L. Man

Crystallography Reports, Vol. 50, No. 2, 2005, pp. 308–315. Translated from Kristallografiya, Vol. 50, No. 2, 2005, pp. 344–351.

LIQUID CRYSTALS

Molecular Aspects of the Main Phase Transition in Lipid Systems as a Weak First-Order Phase Transition: 1. Model of Thermodynamic Behavior of Lipid Membranes

S. A. Pikin*, D. P. Kharakoz, L. I. Tiktopulo***, and E. S. Pikina******

** Shubnikov Institute of Crystallography, Russian Academy of Sciences, Leninskiĭ pr. 59, Moscow, 119333 Russia*

e-mail: pikin@ns.crys.ras.ru

*** Institute of Theoretical and Experimental Biophysics, Russian Academy of Sciences, Pushchino, Moscow oblast, 142292 Russia*

**** Institute of Proteins, Russian Academy of Sciences, Moscow oblast, Russia*

***** Institute for Problems of Oil and Gas, Russian Academy of Sciences, Moscow, Russia*

Received October 20, 2004

Abstract—The possibility to describe the principal phase transition in lipid systems as a weak orientational first-order phase transition with characteristics close to those of a second-order phase transition characterized by pretransition phenomena and rather strong fluctuations has been considered. A first order transition is explained by interactions between fluctuations of molecule orientations and density fluctuations at a low shear modulus. The jumpwise behavior of enthalpy, volume, heat capacity, compressibility, sound velocity and absorption, and the order parameter are analyzed. It is shown that because of molecular van der Waals interactions the shear modulus should give rise to more pronounced jumps of the above quantities with an increase in molecule lengths. © *2005 Pleiades Publishing, Inc.*

INTRODUCTION

Recently, the physical nature of the phase transition "melting–chain ordering" and its relation to interlayer interactions in lipid systems have been intensively studied [1–4]. These problems are of the fundamental importance both from physical and biological standpoints. Each bilayer in a membrane is a quasi-two-dimensional system, which undergoes the so-called main phase transition (chain ordering), and is similar to a first-order liquid–solid phase transition characterized by the jumps of the first derivatives of free energy with respect to temperature [1, 5]. At the same time, in the vicinity of the transition temperature T_M, the lipid systems demonstrate the behavior characteristic of second-order phase transitions, i.e., an increase in the density fluctuations in the bilayer plane, a jump in the flexural rigidity, and an anomalous increase in a distance between bilayers in the film (swelling) [6–8]. The cause of anomalous swelling and its relation to the nature of the main transition are the subjects of permanent discussions. There are two alternative approaches to the explanation of this phenomenon. The first is based on the assumption that lipid bilayers are in the state close to critical [7, 8]. The second is based on the concept that the main phase transition is a weak first-order transition and has nothing in common with any critical state [6]. This approach yields the consistent quantitative explanation of such properties of a system of packed lipid molecules as density fluctuations, compressibility, and flexural rigidity. The concept of a weak first-order transition turned out to be rather fruitful in description of phase transformations in many solids [9, 10]. There also exist some approaches to the description of phase transitions in smectic liquid crystals with two- and three-dimensional structures which take into account far- and short-range orientational and positional ordering [11, 12].

Below, we consider the possibility of describing the above main phase transition in lipid systems as a weak orientational first-order phase transition whose characteristics are close to those of a second-order phase transition characterized by pretransition phenomena and pronounced fluctuations. A first order transition in this case is explained by interactions between the molecule and density fluctuations at a low shear modulus. It was assumed [9, 10] that a shear modulus μ has the same finite value both in the low- and high-temperature phases. Only the case of a logarithmic temperature behavior of heat capacity was considered. In the present study, when studying dipalmitoyl-phosphatidylcholine (DPPC) and dimyristoyl-phospatidylcholine (DMPC), we considered the case of the zero μ value in the high-temperature phase (of the type of smectic *A* with the point symmetry group $D_{\infty h}$) and the case of a finite μ value in the low-temperature phase with the correlation of tilted molecules in the smectic plane (either of a smectic *C* or a smectic *G* with the point group C_{2h} or C_i). Moreover, the μ value may be a function of temper-

1063-7745/05/5002-0308$26.00 © 2005 Pleiades Publishing, Inc.

ature and the temperature dependences of the thermodynamic quantities are described by power laws. We consider the thermodynamics of a weak phase transition in this situation for multilayer and one-layer membranes.

GENERAL APPROACH TO THE DESCRIPTION OF WEAK FIRST-ORDER PHASE TRANSITION

Earlier [9], it was shown that, in the general case, the compressibility and interactions between molecules with different characteristics (electric and magnetic moments, director orientations, spins, etc.) due to phonon exchange results in the change of the character of a phase transition undergone by such a material and a first-order phase transition takes place in such a material in these cases where, in the absence of the above acoustic effects, a second-order phase transition would have taken place. At the nonzero shear modulus, the interaction via phonon exchange cannot fully compensate the compressibility effect giving rise to a first-order phase transition. When the shear modulus acquires the zero value, the above compensation takes place, which results in a second-order phase transition with the corresponding fluctuation effects.

Order parameter in a main phase transition. The order parameter in the phase transition under consideration is of great interest but is still unclear. Unfortunately, no accurate crystallographic data have been obtained on the low-temperature phase of lipid membranes. One may only state that the membrane consists of tilted molecules and that there is a certain correlation in molecular positions. In this study, we assumed that the main characteristic of this order parameter is the average molecule tilt (deviation θ from the normal *z* to a smectic monolayer (in fact, to a lipid bilayer) or to the membrane *xy* plane along a certain direction). Above the temperature of this transition T_M (or T_c, as is usually considered in the theory of phase transitions), no such average deviation of molecules exist. The formation of a certain three-dimensional crystal lattice below T_M would be characterized by the appearance of a low shear modulus as a result of the above positional correlations of lipid molecules.

It is possible to imagine a zigzag molecule shape, which is sometimes used as a model in physics of liquid crystals (Fig. 1). In this case, the thickness of a smectic monolayer is less than the double length *l* of a molecule and is equal to the absolute value of the projection l_z. Then, the system of two-dimensional rotators (ξ_1, ξ_2) of the unit length having the tensor nature $\xi_1 = \frac{l_z l_x}{\sqrt{(l_x^2 + l_y^2)l_z^2}}$, $\xi_2 = \frac{l_z l_y}{\sqrt{(l_x^2 + l_y^2)l_z^2}}$ undergoes the phase transition to the gel state (low-temperature phase). In other words, a fixed azimuthal angle in the *xy* plane (measured, e.g., from the *x* axis) and a small deviation angle θ from the normal to this plane, $\theta \approx \langle l_x \rangle / l_z \approx \langle l_x \rangle / l$

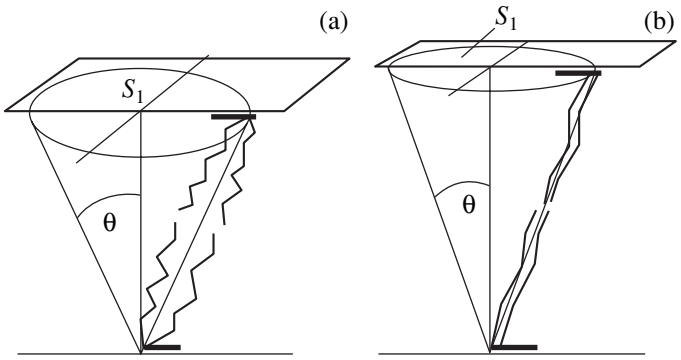

Fig. 1. Molecular model of a smectic monolayer (lipid bilayer) which takes into account orientational fluctuations and conformational changes. (a) Pronounced orientational disorder and pronounced conformational changes far from the transition temperature; (b) an increase in the bilayer thickness in the vicinity of T_M due to considerable orientational correlations and weak conformational changes.

are formed if the azimuth angle equals zero. In the smectic *A*–smectic *C* transitions in liquid crystals, the thickness l_z of the smectic layer either remains constant at the constant length of the molecules or decreases with lowering of temperature because of an increase in the tilt θ of the molecules. In first-order phase transitions below T_M in lipid systems, the average value of the order parameter $\langle \xi_1, \xi_2 \rangle$ should change in a jumpwise manner and increase with an increase in the molecular-chain length, $\theta(T_M) \sim (T_M - T)^\beta \sim \mu^{\beta/\alpha} \sim l^{2\beta/\alpha}$.

It should be noted that it was observed experimentally that the lipid membranes considered here become thicker as they approach the point T_M from the side of high temperatures (swelling effect) [6–8]. This phenomenon may be associated with a certain ordering mechanism of molecules which experience both conformational changes and fluctuation effects in the vicinity of T_M (Fig. 1). Another reason may be thickening of water interlayers between the smectic layers in a membrane. Experimentally, it is possible to separate such effects and to separately study the role of each of these factors. These phenomena will be considered in the second part of this work.

Model of a first-order phase transition in a lipid system. It was assumed [9] that the character of the transition is similar to that in a molecular system with the Hamiltonian H_0 in the case where the effective interactions do not lead to singularities at small phonon momenta **k**. The interactions via phonon exchange have no place if $\mathbf{k} = 0$ but have a nonvanishing limit at $\mathbf{k} \longrightarrow 0$. It is possible to single out the tensor of uniform deformation

$$\frac{\partial u_\alpha(\mathbf{r})}{\partial r_\beta} = u_{\alpha\beta} + \frac{1}{N}\sum_{k \neq 0} i k_\beta u_\alpha(\mathbf{k}) \exp(i\mathbf{kr}), \qquad (1)$$

where N is the number of molecular cells in the unit volume. To avoid the above singularity and calculate the free energy $F = -T\ln\Sigma\exp(H/T)$, we have to add to the Hamiltonian H the term $-(1/2)\nu H_0^2$, which describes the interaction with the zero transferred momentum. The parameter ν is selected in a way that the total interaction has no singularity in the Hamiltonian $\tilde{H} = H - (1/2)\nu H_0^2$ at small $\mathbf{k}$. As a result, the quantity H is written in the form

$$H = \tilde{H} + \xi H_0 + \frac{1}{2}\nu H_0^2 + \frac{1}{2}K_0 u_{\alpha\alpha}^2, \qquad (2)$$

where $\xi = qu_{\alpha\alpha}$, $\nu = q^2/(K_0 + (4/3)\mu)N$, $u_{\alpha\alpha}$ is the change of the volume, q is the striction coefficient, and K_0 is the volume elasticity modulus. The Hamiltonian H_0 leads to the following expression with a singularity

$$F(\nu = 0) = -T_0 f\left(\frac{T - T_0}{T_0} - g\xi\right) + \frac{1}{2}K_0 u_{\alpha\alpha}^2; \qquad (3)$$

e.g., $f(x) \propto |x|^{2-\alpha}$, since the second term in Eq. (2) does not change the character of the singularity but leads to the change of the transition temperature T_0.

To determine F for $\nu \neq 0$, it is possible to use the well-known method suggested in [9]. The function F satisfies the statistical accuracy with the equation

$$2\frac{\partial F}{\partial \nu} = \left(\frac{\partial F}{\partial \xi}\right)^2 \qquad (4)$$

at the initial condition (3). The solution of this equation in the parametric form is written as

$$F = -\frac{1}{2\nu g^2}\left(\frac{T - T_0}{T_0} - g\xi - x\right)^2 - T_0 f(x), \quad \frac{\partial F}{\partial x} = 0. \qquad (5)$$

Substituting the quantities ν and ξ into Eq. (5) and expressing $u_{\alpha\alpha}$ in terms of pressure P with the aid of the equation $P = -\partial F/\partial u_{\alpha\alpha}$, we arrive at the thermodynamic potential Φ.

It was assumed [9, 10] that the shear modulus μ has the same finite value in high- and low-temperature phases. Moreover, only the logarithmic behavior of the function $f''(x)$, i.e., heat capacity, was considered. Now, we consider the case where the shear modulus of DPPC and DMPC has the zero value in the high-temperature phase (of smectic *A* type) but has a nonzero finite value in the low-temperature phase with tilted correlated molecules in the smectic plane. Moreover, μ may be a function of x; e.g., $\mu = \mu(x) \propto |x|^\varepsilon$ at $x \leq 0$ in accordance with the singular behavior of the function $f(x)$. Below, we assume that the exponents α and ε have low positive values and that $\varepsilon < \alpha$. As a result of the above procedure for negative x values, we find from Eq. (5) that

$$\Phi = \Phi_0 - \frac{P^2}{2K_0} + T_0\left[-f(x) + \frac{1}{2\lambda(x)}\left(\frac{T - T_0 - cP}{T_0} - x\right)^2\right], \qquad (6)$$

$$\frac{\partial \Phi}{\partial x} = 0,$$

where

$$\lambda(x) = \frac{4\mu(x)K_0 c^2}{T_0(3K_0 + 4\mu(x))}, \qquad (7)$$

the constant c is the derivative of the critical temperature $T_0 + cP$ with respect to pressure P, and Φ_0 is the nonsingular part of the potential. At $x > 0$, we have

$$x = \frac{T - T_0 - cP}{T_0}, \qquad (8)$$

$$\Phi = \Phi_0 - \frac{P^2}{2K_0} - T_0 f\left(\frac{T - T_0 - cP}{T_0}\right). \qquad (9)$$

POWER DEPENDENCES OF THERMODYNAMIC CHARACTERISTICS

Consider in more detail the case, where, in the absence of acoustic motion, the function $f(x)$, heat capacity $C \propto f''(x)$, susceptibility χ, and correlation radius r_c vary with the temperature according to the power laws

$$f(x) = \frac{A}{(2-\alpha)(1-\alpha)}|x|^{2-\alpha}, \qquad (10)$$

$$f''(x) = A|x|^{-\alpha}, \quad \chi \propto |x|^{-\gamma}, \quad r_c \propto |x|^{-\eta}.$$

It should be remembered that, if $\mu = \text{const}$ and $\lambda = \text{const}$ in both phases, Eq. (6) shows that the quantity $\tau \equiv (T - T_0 - cP)/T_0$ is not a monotonic function of x (Fig. 2a). Therefore, Φ depends on τ not in the way illustrated by Fig. 2b, because x, being a function of T, is not unique and x and Φ have two branches (a singularity point corresponding to the values $x = \tau = 0$ lies in the region of absolute instability, $x^- \leq x \leq x^+$). The temperature of a first-order phase transition is found as the point of intersection of the two branches of Φ.

If the curve which describes the behavior of the shear modulus μ is not symmetric, we arrive at the dependence $\lambda = \Lambda|x|^\varepsilon$ for negative x and $\lambda = 0$ for positive x. In this situation, Eqs. (6)–(10) yield the following results at low ε values:

$$\tau \propto \left(\frac{A\lambda}{\varepsilon}\right)|x|^{1+\varepsilon/2-\alpha/2} \quad \text{at} \quad x < 0, \ |x| \ll (A\lambda\varepsilon)^{1/\alpha-\varepsilon};$$

$$\tau \propto A\lambda|x|^{1+\varepsilon-\alpha} \quad \text{at} \quad x < 0, \ 1 \gg |x| \gg (A\lambda\varepsilon)^{1/\alpha-\varepsilon};$$

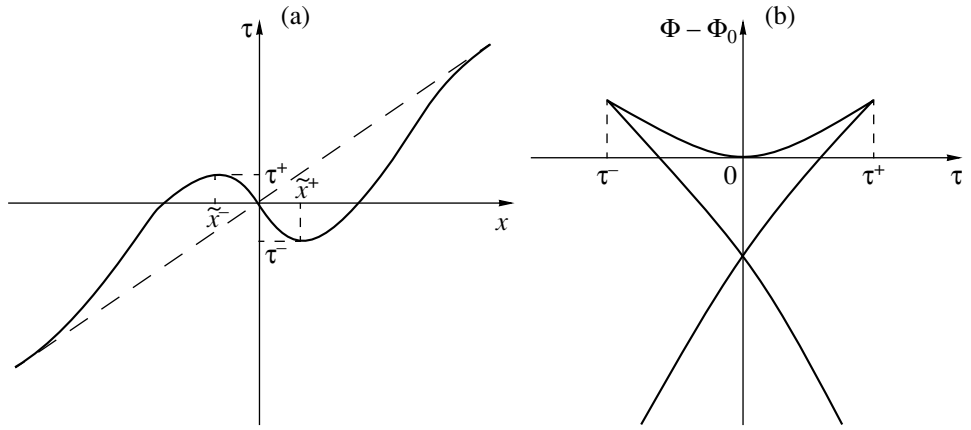

Fig. 2. Qualitative (a) $\tau(x)$ and (b) $\Phi(\tau)$ dependences at the same values of the shear modulus above and below T_c.

$$\tau = 0 \quad \text{at} \quad x = x^- \approx -\left(\frac{A\lambda}{1-\alpha} + \frac{\varepsilon}{2}\right)^{1/\alpha-\varepsilon};$$

$$\tau = \tau^+ \approx \frac{\alpha}{1-\alpha}(A\lambda)^{1/\alpha-\varepsilon}$$

$$\text{at} \quad x = \tilde{x}^- \approx -(A\lambda)^{1/\alpha-\varepsilon}; \tag{11}$$

$$\tau = x \quad \text{at} \quad x > 0;$$

$$x_c^- \approx \left[\frac{A\lambda(2-\alpha)}{2(1-\alpha)}\right]^{1/\alpha-\varepsilon};$$

$$x_c^+ = \tau_c \approx \frac{\alpha}{2}\left(1-\frac{\alpha}{2}\right)^{1/\alpha-\varepsilon-1}\left(\frac{A\lambda}{1-\alpha}\right)^{1/\alpha-\varepsilon}.$$

Expressions (11) show that low ε values do not qualitatively change the above results and yield the effective index $\alpha - \varepsilon$. Only the dependence $\tau(x)$ at very low values $|x|$ is changed at finite ε, but $\tau(x) \propto A\lambda|x|^{1-\alpha}$ at $\varepsilon = 0$ in the region of absolute instability. Therefore, in what follows, we consider the case where $\varepsilon = 0$, i.e., the constant parameters μ and λ at $x < 0$. It is also assumed that the quantities $A\lambda$ and α are much less than unity. Qualitatively, the $\tau(x)$ and $\Phi(\tau)$ dependences in the "nonsymmetric" situation under consideration are illustrated by Fig. 3.

Under the above assumptions, differentiation of the potential Φ with respect to temperature and pressure yields the following expressions for entropy S, the change in the volume ΔV, heat capacity C_P, and hydrostatic compressibility $1/K$:

$$S = S_0 + f'(x) \quad \text{at} \quad x < 0,$$

$$S = S_0 + f'(\tau) \quad \text{at} \quad x > 0;$$

$$\Delta V = -\frac{P}{K_0} + cf'(x) \quad \text{at} \quad x < 0,$$

$$\Delta V = -\frac{P}{K_0} + cf'(\tau) \quad \text{at} \quad x > 0;$$

$$C_P = C_P^0 + \frac{1}{T_0}\frac{f''(x)}{1-\lambda f''(x)} \quad \text{at} \quad x < 0, \tag{12}$$

$$C_P = C_P^0 + \frac{1}{T_0}f''(\tau) \quad \text{at} \quad x > 0;$$

$$\frac{1}{K} = \frac{1}{K_0} + \left(\frac{1}{K_0} + \frac{3}{4\mu}\right)\frac{\lambda f''(x)}{1-\lambda f''(x)} \quad \text{at} \quad x < 0,$$

$$\frac{1}{K} = \frac{1}{K_0} + \frac{c^2}{T_0}f''(\tau) \quad \text{at} \quad x > 0.$$

The temperature of a first-order phase transition T_c is determined as

$$T_c \approx T_0 + cP + T_0\frac{\alpha}{2}(A\lambda)^{1/\alpha}. \tag{13}$$

Thus, the coefficient c is equal to the derivative of the transition temperature with respect to pressure. The maximum temperature hysteresis (Fig. 2b) is

$$\delta T = T_0\tau^+ \approx T_0\alpha(A\lambda)^{1/\alpha}. \tag{14}$$

The jumps of entropy and volume in a first-order phase transition are

$$\delta S = f'(x_c^-) - f'(\tau_c) \approx A(A\lambda)^{1/\alpha}, \tag{15}$$

$$\delta V = c[f'(x_c^-) - f'(\tau_c)] \approx cA(A\lambda)^{1/\alpha}. \tag{16}$$

It is seen from Eqs. (11)–(14) that the δT, δS, and δV values are low because of the smallness of the quantities $A\lambda$ and α, but the hysteresis δT contains an additional factor small in comparison with δS and δV. An increase in the shear modulus μ and, thus, in the parameter λ results in an increase in the above jumps; i.e., it becomes more obvious that we are dealing here with a first-order phase transition. At the transition point $T =$

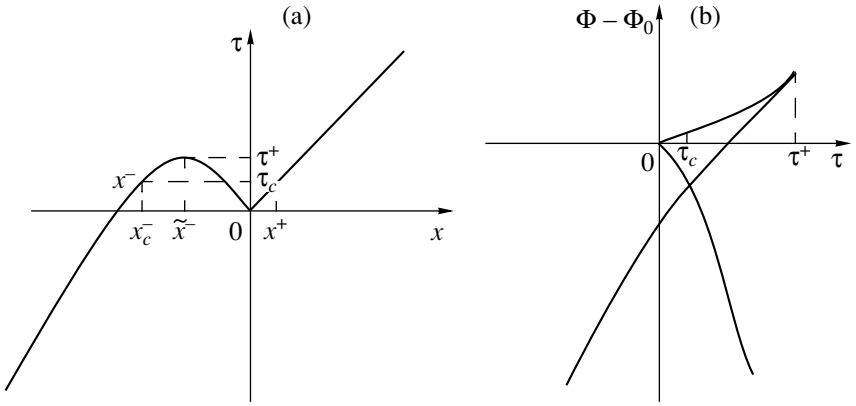

Fig. 3. Qualitative (a) $\tau(x)$ and (b) $\Phi(\tau)$ dependences at the zero value of the shear modulus above T_c and the finite value of the modulus μ below T_c.

T_c, the quantities C_P and $1/K$ have high but finite values,

$$C_P \approx C_P^0 + \left(\frac{2}{\alpha}\right)^{\alpha} \frac{1}{\lambda T_0} \quad \text{at} \quad T \longrightarrow T_c + 0,$$
$$C_P \approx C_P^0 + \frac{2}{\alpha\lambda T_0} \quad \text{at} \quad T \longrightarrow T_c - 0; \tag{17}$$

$$\frac{1}{K} = \frac{1}{K_0} + \left(\frac{2}{\alpha}\right)^{\alpha}\left(\frac{1}{K_0} + \frac{3}{4\mu}\right) \quad \text{at} \quad T \longrightarrow T_c + 0,$$
$$\frac{1}{K} = \frac{1}{K_0} + \frac{2}{\alpha}\left(\frac{1}{K_0} + \frac{3}{4\mu}\right) \quad \text{at} \quad T \longrightarrow T_c - 0. \tag{18}$$

The results obtained are valid for an elastically isotropic model of a solid. However, it was shown in [11, 12] that these conclusions are also valid for smectic liquid crystals possessing elastic anisotropy. In such liquid crystals, elastic isotropy exists in the smectic plane and the role of the parameter μ may be played by the shear modulus in this plane.

Earlier [9] it was noticed that in many instances heat capacity in the presence of acoustic phonons behaves in the following way. In the region not too close to the transition point, heat capacity is described by the phenomenological Landau theory and undergoes a jump at the transition temperature. With an approach to the transition temperature, an important role is played by the correlation corrections proportional to $|T - T_c|^{-1/2}$, whereas in the direct proximity of the temperature of a second-order phase transition, heat capacity acquires very high values and obeys a power or logarithmic law.

The function $f''(x)$ may be calculated in the first approximations of the self-consistent field for molecular systems with a sufficiently large radius of intermolecular interactions. For Ising-type systems with short-range interactions between the nearest neighbors, the function $f''(x)$ has the form $-A\ln|x|$ and the Landau approximation becomes invalid. For multilayer vesicles considered here, it is possible to assume the existence of sufficiently long-range intermolecular (van der Waals) interactions and, thus, the existence of a temperature region in which the noticeable correlation corrections would be proportional to $|T - T_c|^{-1/2}$, which corresponds to a three-dimensional case. In a one-layer membrane corresponding to a two-dimensional case, these correlation corrections should be proportional to $(T - T_c)^{-1}$.

In general, it is possible to expect [9] that a first-order phase transition takes place if the following inequality is fulfilled:

$$\frac{\mu}{T_c}\left(\frac{\partial T_c}{\partial P}\right)^2 \Delta C_P \geq 1, \tag{19}$$

where ΔC_P is the anomalous part of heat capacity. If the left-hand side of the above inequality still exceeds unity in the phenomenological region, where ΔC_P is the jump of heat capacity, a first-order phase transition may be described by the simple Landau approximation (approximation of a self-consistent field); in this case, no fluctuation phenomena are observed. This is true, e.g., for systems with high values of the derivative $\partial T_c/\partial P$ and shear modulus μ. Since $\mu \sim l^2$, then, because of van der Waals interactions of lipid molecules with long chains (l is the molecule length), the fluctuations become weaker.[1] For substances with low values of these parameters, a first-order phase transition may be accompanied by noticeable fluctuation phenomena (pretransition behavior). However, in both cases, the change of transition enthalpy $\Delta H = T\delta S$ (see Eq. (15)) is proportional to $\lambda^{1/\alpha} \sim l^{2/\alpha}$; i.e., it is strongly dependent on the molecule length l (dramatic increase in ΔH with an increase in l), which was confirmed experimentally [13, 14]. In a similar way, the temperature hysteresis δT should increase as $l^{2/\alpha}$; therefore, the jump of the orien-

[1] This rough estimate corresponds to the assumption that all the atoms of a molecule interact with all the atoms of another molecule in the same way. In fact, this dependence may be weaker because such atoms interact differently since they are located at different interatomic distances.

tational order parameter in the $\theta_c \propto |x_c^-|^\beta$ transition should increase as $l^{2\beta/\alpha}$.

COMPARISON OF RESULTS WITH WELL-KNOWN EXPERIMENTAL DATA

Thermodynamics of nucleation of a solid phase in liquid lipid films. Consider well-known experimental data [6] on the thermodynamics of the main phase transition in multilayer and one-layer lipid films. The character of the temperature dependences of the specific heat capacity C_P, enthalpy $\Delta H = T\Delta S$, and volume ΔV in the vicinity of the transition temperature reminds the characteristics of a first-order phase transition (Fig. 4): the function $C_P(T)$ has a sharp maximum in the temperature range with the width of about 1 K in the vicinity of the temperature $T_c = 41.2$°C. One also sees the characteristic region of fluctuations (from 0.1 K to several degrees above T_c); the functions $\Delta H(T)$ and $\Delta V(T)$ rapidly change in a narrow temperature interval (about 0.1 K in the vicinity of T_c, with this change being better seen than for a second-order phase transition, and the change in $\Delta V(T)$ being more steep than the change in $\Delta H(T)$). Thus, it is possible to conclude that specific enthalpy and volume in this transition would have jumps $T\delta S \sim 4 \times 10^4$ J/mol, $\sim 4 \times 10^3$ N/cm^2, and $\delta V \sim 40$ cm^3/mol ~ 0.04 at the molecular weight of the order of 10^3. These data also lead to the conclusion that the temperature hysteresis δT may be of the order of 0.1 K. This low hysteresis was not observed in the experiments under consideration because the transition interval did not exceed 1 K owing to effects induced by impurities and structural defects smoothening the thermodynamic functions. The ratio of the quantities given by Eqs. (15) and (16) allowed us to estimate the coefficient as $c \sim 3 \times 10^{-3}$ K cm^2/N ~ 0.03 K/bar, which agrees with the measured value. Correspondingly, expressions (14)–(16) allow us to obtain the following estimates $A\lambda \sim 2 \times 10^{-2}$, $A \sim 4 \times 10^5$ J/(K mol), $\sim 4 \times 10^4$ N/(K cm^2), and $\lambda \sim 5 \times 10^{-7}$ K cm^2/N at $\alpha \approx 1/2$. The use of expression $\lambda \approx (\mu/T)c^2$ allowed us to estimate the shear modulus μ (in gel) as $\mu \sim 10$ N/cm^2, a value much lower than the typical value $K \sim 10^3$–10^4 N/cm^2.

Analysis of heat capacities in the fluctuation region above T_c shows that the change of ΔC_P in this temperature range is about 5 kJ/(K mol) [6]. The use of expressions (10) and (12) for the description of such a change in one-layer membranes (two-dimensional case) leads to the conclusion that the index α may be close to unity; i.e., the correlation corrections are proportional to the power dependence $|\tau|^{-1}$ and, thus, considerably differ from the logarithmic dependence $-\ln|\tau|$ and the dependence $|T - T_c|^{-1/2}$ (Fig. 5). Similar analysis of the situation in multilayer membranes (three-dimensional case) lead to the conclusion that the best approximation here is the proportionality of the correlation correction to the dependence $|T - T_c|^{-1/2}$, in other words, the index α in this case may be close to the value 1/2 (Fig. 6).

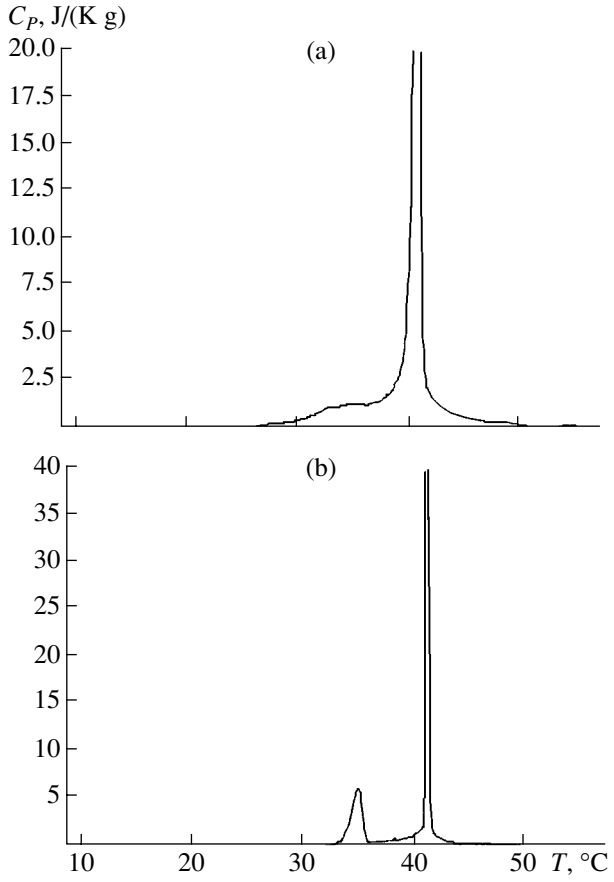

Fig. 4. Experimental temperature dependence of heat capacity C_P in (a) one-layer and (b) multilayer lipid membranes [6].

A similar qualitative conclusion may also be drawn from the experimental data for functions $\Delta H(T)$ and $\Delta V(T)$ in the same temperature range. It should be indicated that the quantity $\lambda\Delta C_P$ only slightly differs from unity in this temperature range, which confirms the possibility of calculating the function $f''(x)$ as the first correlation correction. Thus, the fluctuation phenomena in the thermodynamics of the multi- and one-layer DPPC vesicles are interpreted within the first approximations of the theory of a self-consistent field.

Experiments on ultrasound propagation and absorption. The experimental data on specific ultrasound absorption I and the sound velocity U as a function of temperature in lipid systems were obtained in [6]. Since $U = \sqrt{K/\rho}$, where ρ is the material density, expressions (6) and (12) show that the sound velocity above the temperature T_c is approximately equal to

$$U \approx \sqrt{K_0/\rho}\left(1 - \frac{c^2}{2T_c}A\tau^{-\alpha}\right), \qquad (20)$$

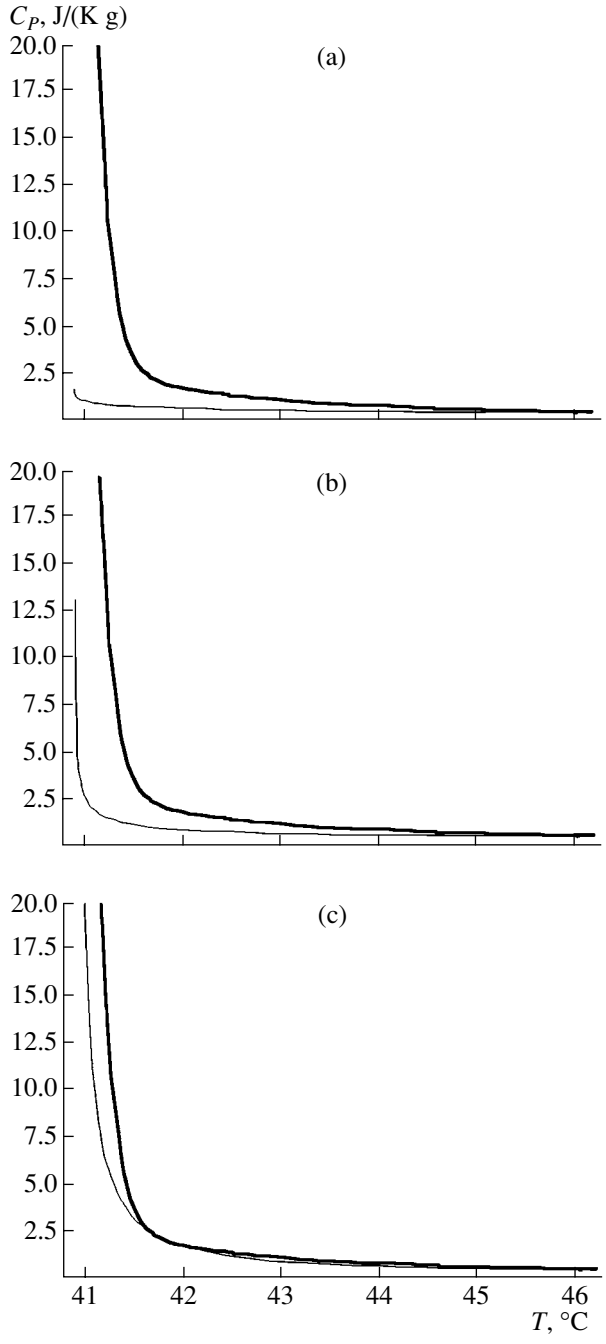

Fig. 5. Comparison of the correlation corrections proportional to the (a) $-\ln|\tau|$, (b) $|T - T_c|^{-1/2}$, and (c) $|\tau|^{-1}$ dependences and the experimental C_P data for a one-layer dipalmitoyl-phosphatidylcholine (DPPC) membrane. The details of the experiment will be considered in a separate article.

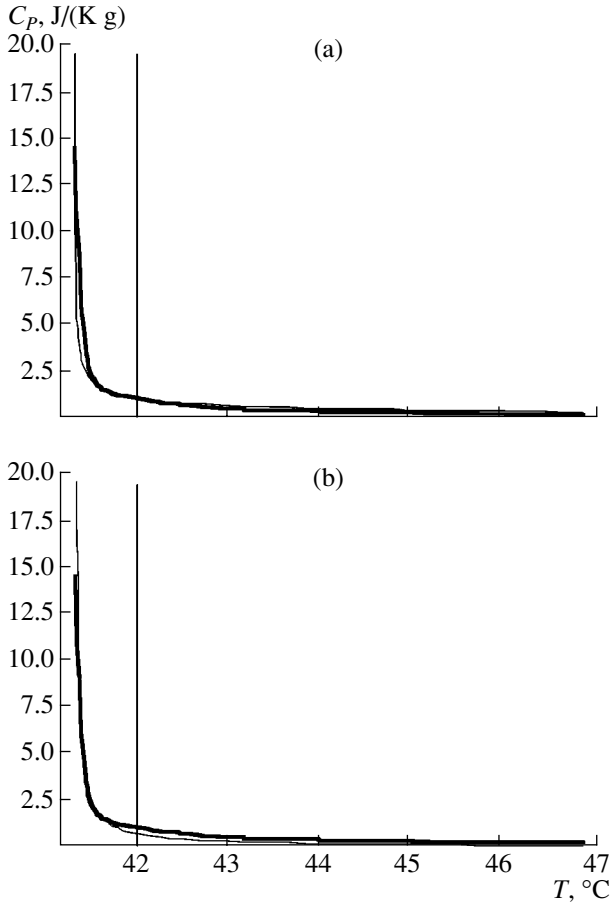

Fig. 6. Comparison of the correlation corrections proportional to the (a) $|T - T_c|^{-1/2}$ and (b) $|\tau|^{-1}$ dependences with the experimental C_P data [6] in a multilayer dipalmitoylphosphatidylcholine (DPPC) membrane.

where the correlation corrections are assumed to be small (which is true at $\tau \geq A\lambda^{1/\alpha}$). Analysis of the experimental data in the region from several tenths of a degree to several degrees above T_c indicates once again that the correlation correction in a three-dimensional case is described by a power law with the index $\alpha \sim 1/2$. Below T_c, the ultrasound velocity can hardly be interpreted because of the effects induced by the shear modulus. Generally speaking, the sound velocities in smectics are characterized by angular dependences and these phenomena should take place in multilayer lipid vesicles. Moreover, ultrasonic waves are adiabatic rather than isothermal. We have already discussed the temperature behavior of the isothermal modulus K (see Eq. (12)); however, it was shown [9] that the adiabatic K_{ad} value is characterized by a weaker temperature dependence in the vicinity of T_c.

The measured ultrasound absorption $I(T)$ demonstrates a pronounced increase in the vicinity of T_c [6] and even in a interval exceeding the interval for sonic velocity. This effect was expected because of the relation of acoustic vibrations and the order parameter, e.g., with the average tilt angle of molecules. This is characteristic of all the order–disorder phase transitions [11, 12]. If the response (susceptibility χ in (10)) of the lipid systems considered may be described by the classical Landau theory (with the first correlation correc-

tions), the main contribution to such a response is described by the dependence $I(T) \sim |T - T_c|^{-1}$. Small correlation corrections to this contribution may be of the order of $|T - T_c|^{-3/2}$ with the corresponding small coefficient. The experimental data on ultrasonic absorption are described sufficiently well by the temperature dependence $I(T) \sim |T - T_c|^{-1}$. Strictly speaking, $I(T)$ at the finite frequencies cannot have an infinite value at the point T_c, and the maximum of the $I(T)$ function decreases with an increase in the ultrasonic frequency.

CONCLUSIONS

A model of a weak first-order phase transition in lipid systems has been suggested that takes into account the low hardness (low shear modulus) of the gel phase and the average tilt of lipid molecules: the most important order parameters of this phase. The power laws which describe the critical temperature behavior of all the thermodynamic quantities in a pure orientational second-order transition are considered. As a result, it becomes possible to analyze the jumpwise behavior of enthalpy, volume, heat capacity, compressibility, sound velocity and absorption, and the order parameter. Since, according to the model suggested, the molecule orientations play the main part in all the phenomena considered, the molecular parameters such as the molecule length pronouncedly influence their characteristics. Because of intermolecular van der Waals interactions, the shear modulus dependent on the molecular length should give rise to an increase in these jumps with an increase in the molecule length. These conclusions are in good qualitative agreement with the experimental data used in estimates of the main model parameters. In the second part of this study we will show that, because of the conformational changes in molecules and appearance of structural defects, the main phase transition in lipid membranes may become a second-order transition for rather short molecules and thin lipid layers.

ACKNOWLEDGMENTS

This study was supported by INTAS, project no. 01-0105. The authors are grateful to P. Laggner, G. Pubst, and E.I. Kats for fruitful discussions of the results.

REFERENCES

1. R. Biltonen, J. Chem. Thermodyn. **22**, 1 (1990).
2. J. Israelichvili and H. Wennerström, Nature **379**, 219 (1996).
3. J. E. Nagle and S. Tristram-Nagle, Biochim. Biophys. Acta **1469**, 159 (2000).
4. M. Bloom, E. Evans, and O. G. Mouritsen, Q. Rev. Biophys. **24**, 293 (1991).
5. M. Porsch, U. Rakusch, Ch. Mollay, and P. Laggner, J. Biol. Chem. **10**, 1761 (1983).
6. D. P. Kharakoz and E. A. Shlyapnikova, J. Phys. Chem. B **104**, 10368 (2000).
7. J. Lemmich, K. Mortensen, J. H. Ipsen, *et al.*, Phys. Rev. Lett. **75**, 3958 (1995).
8. J. F. Nagle, H. I. Petrache, N. Gouliaev, *et al.*, Phys. Rev. E **58**, 7769 (1998).
9. A. I. Larkin and S. A. Pikin, Zh. Éksp. Teor. Fiz. **56**, 1664 (1969) [Sov. Phys. JETP **29**, 891 (1969)].
10. S. A. Pikin, Zh. Éksp. Teor. Fiz. **58**, 1406 (1970) [Sov. Phys. JETP **31**, 753 (1970)].
11. S. A. Pikin, *Structural Transformations in Liquid Crystals* (Nauka, Moscow, 1981; Gordon and Breach, New York, 1991).
12. S. A. Pikin, Physica A (Amsterdam) **194**, 352 (1993).
13. R. Koynova and M. Caffrey, Biochim. Biophys. Acta **1376**, 91 (1998).
14. R. Koynova and M. Caffrey, Chem. Phys. Lipids **69**, 1 (1994).

Translated by L. Man

Crystallography Reports, Vol. 50, No. 2, 2005, pp. 316–319. Translated from Kristallografiya, Vol. 50, No. 2, 2005, pp. 352–355.

LIQUID CRYSTALS

Specific Features of Electromechanical Conversion in Various Liquid Crystalline Phases

E. V. Popova, A. P. Fedoryako, L. A. Kutulya, and V. P. Seminozhenko

Institute for Single Crystals, National Academy of Sciences of Ukraine, pr. Lenina 60, Kharkov, 61001 Ukraine

e-mail: popova@isc.kharkov.com

Received September 4, 2003

Abstract—Electromechanical effect in various liquid crystalline phases—nematic, smectic *A*, and smectic *C*—is studied. It is shown that a liquid crystal (LC) sample in the nematic phase does not differ from an electromechanical converter containing an isotropic dielectric and exhibits no features characteristic of LCs at electromechanical conversion. A phenomenon similar to the piezoelectric effect may occur in ferroelectric LCs due to their biaxiality. *© 2005 Pleiades Publishing, Inc.*

INTRODUCTION

Some studies dealing with electromechanical conversion in nematic liquid crystals (NLCs) have been published recently. An ac electric field was applied to an NLC with a planar alignment and positive dielectric anisotropy and the sound generated in the LC sample was recorded [1]. Generally, the sound generation is attributed to director reorientation. However, no theory of this phenomenon has been proposed. Electromechanical conversion in ferroelectric liquid crystals (FLCs) was described in detail in [2–4]. Eber, Bata, and Jakli proposed a theory of linear electromechanical effect in FLCs [2, 5]. They showed that cross effects between the dielectric relaxation and viscous flow are possible in the Sm*C** phase owing to its chirality and biaxiality. Under the action of a field applied to a sample of such an LC, a flow displacing the cell plates is generated in it. The field-induced flow in a sample with a planar alignment is described by the equation

$$\rho\frac{\partial v}{\partial t} = -\frac{\partial}{\partial x}\left[-\mu(x)\frac{\partial v}{\partial t} - \gamma(x)\frac{\partial E}{\partial t}\right], \qquad (1)$$

where ρ is the LC density, v is the flow velocity, $\mu(x)$ is the effective viscosity coefficient, and $\gamma(x)$ is the effective electromechanical-coupling coefficient.

$$\left.\begin{aligned}\mu(x) &= \mu_{11} + \mu_5\sin^2\varphi(x)\cos^2\varphi(x)\\ \gamma(x) &= [\gamma_5 - (\gamma_2 - 2\gamma_5)\cos^2\varphi(x)]\end{aligned}\right\}, \qquad (2)$$

where $\varphi(x)$ is the azimuthal tilt angle of the director, μ_{11} and μ_5 are the viscosity coefficients, and γ_5 and γ_2 are the electromechanical-coupling coefficients. The coefficients $\mu(x)$ and $\gamma(x)$ depend on the director field configuration along the normal to the sample plates.

According to the theory, LC phase biaxiality is required for the occurrence of the electromechanical effect. Therefore, the flows arising in a uniaxial NLC cannot result in the displacement of the cell plates. To reveal specific features of the electromechanical conversion in various LC phases, we studied the parameters of acoustic vibrations in LC samples at different temperatures.

EXPERIMENTAL

Experiments were performed with three mixtures. Each consisted of an achiral smectic *C* (host) and a chiral dopant (CD).

Mixture I (achiral smectic I, CD content is 10.24 wt %). The phase sequence and transition temperatures are $I \longrightarrow 120.5 \longrightarrow N^* \longrightarrow 106 \longrightarrow$ Sm*A** $\longrightarrow 66 \longrightarrow$ Sm*C** $\longrightarrow$ Cr. Spontaneous polarization is 13.5 nC/cm^2 at t = 46°C.

Mixture II (achiral smectic II, CD content is 9.93 wt %). The phase sequence and transition temperatures are $I \longrightarrow 83 \longrightarrow N^* \longrightarrow 72 \longrightarrow$ Sm*C** $\longrightarrow$ Cr. Spontaneous polarization is 12 nC/cm^2 at t = 46°C.

Mixture III (achiral smectic I, CD content is 17.61 wt %). The phase sequence and transition temperatures are $I \longrightarrow 106 \longrightarrow N^* \longrightarrow 99 \longrightarrow$ Sm*A** $\longrightarrow$ 41.5 $\longrightarrow$ Sm*C** $\longrightarrow$ Cr. Spontaneous polarization is

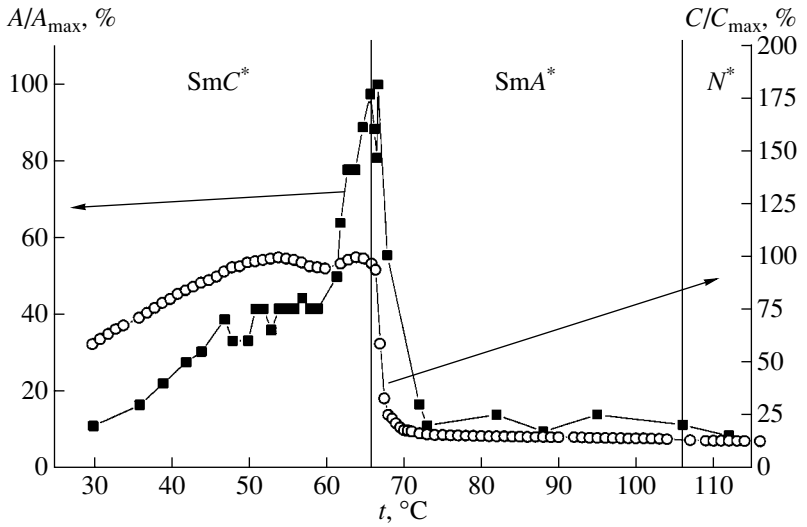

Fig. 1. Temperature dependences of the sound intensity (■) and the sample capacitance (○) for mixture I (cooling).

23.3 nC/cm^2 at t = 21°C.

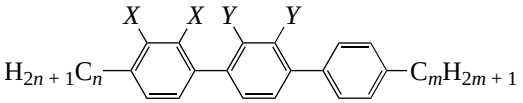

Achiral smectic I

n = 5, m = 7, X = F, Y = H – 25%
n = 5, m = 7, X = H, Y = F – 50%
n = 7, m = 5, X = F, Y = H – 25%

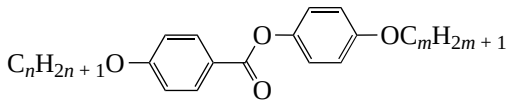

Achiral smectic II

m = 6, n = 8

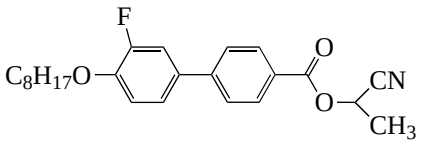

Chiral dopant

A FLC was placed in a cell consisting of two plane-parallel glasses coated with transparent ITO electrodes. The area of the cell plates was no less than 6.6 cm^2. The cell thickness, set by spacers, was 7 μm. Special boundary conditions were chosen to obtain planar alignment of the cell.

A sinusoidal voltage generated by the audio board of a personal computer was fed to the LC cell via an amplifier. The radiated sound was recorded by a microphone, fed to the audio board of another personal computer, and processed. To obtain a "sounding" texture, the sample in the SmC* phase was subjected to a shear strain until a sound was generated. First, the mechanical-resonance frequency (determined by the mass of a movable plate and the viscoelastic properties of the LC) was found from the amplitude-frequency characteristic of the FLC sample. Further studies were carried out at the resonant frequency. Along with the sound intensity, we also measured the cell capacitance.

RESULTS AND DISCUSSION

As can be seen from Figs. 1 and 2, in the temperature ranges of the nematic and smectic A phases, the sound intensity changes little, as well as the capacitance. According to the theory of electrostatic converters containing an isotropic dielectric [6], the amplitude of the cell-plate displacement is proportional the converter capacitance, which is actually the case in nematic and smectic A phases. Apparently, the specificity of these phases does not manifest itself in electromechanical conversion. In the nematic phase, the electromechanical conversion in our experiments was accompanied by the director reorientation. However, in going from the nematic to smectic A phase, no director reorientation was observed, whereas the radiated-sound intensity did not change. Therefore, the electromechanical conversion in these phases is not due to the director reorientation. Near the smectic A–smectic C* phase transition, the intensity of the radiated sound rises steeply within the temperature range in which the electroclinic effect manifests itself. Since the character of the temperature dependence of the capacitance differs strongly from the temperature dependence of the sound intensity, the electromechanical conversion in this temperature range seems to be peculiar to liquid crystals. As was noted previously [2, 4, 5, 7], the electromechanical conversion is due to the electroclinic effect. However, there is no direct confirmation of this statement. In other temperature ranges of mesophase existence, the dependences of the sound intensity and the capacitance have a similar character. Resemblance of these dependences was also found for mixture II (Fig. 2), in which no electroclinic effect was observed.

A great number of harmonics were found in the spectrum of the radiated sound. Thus, the electromechanical response of a FLC to an external field is nonlinear. To reveal the sound generation mechanisms that

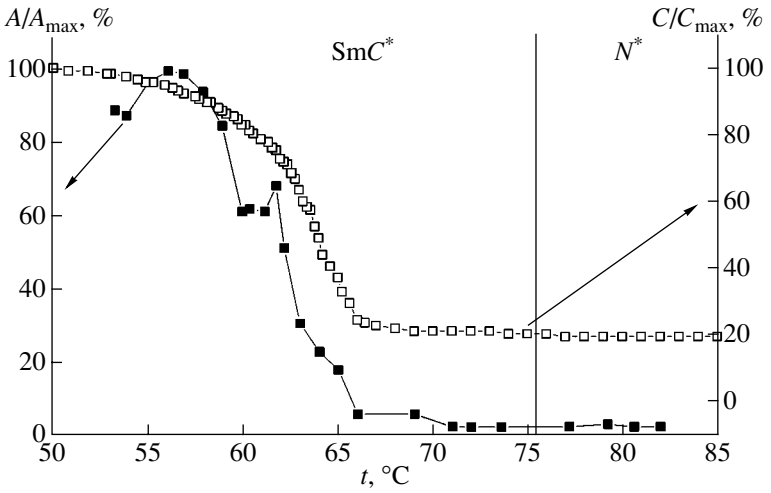

Fig. 2. Temperature dependences of the sound intensity (■) and the sample capacitance (□) for mixture II (cooling); the vertical line corresponds to the phase transition temperature.

are peculiar to the mesophase, we studied the field dependences of the first and second harmonics of the radiated sound.

It is easy to show that the sound generated in the converters with isotropic dielectrics is the second harmonic with respect to the excited frequency. The amplitude of the second harmonic must depend quadratically on the field voltage. The experiment completely confirmed this mechanism of sound generation in the smectic *C** phase. As can be seen from Fig. 3, the amplitude of the second harmonic depends quadratically on the field voltage. At low voltages, the amplitude of the first harmonic, which is related to the director reorientation, is larger than that of the second harmonic; i.e., the mechanism peculiar to LCs is dominant. The contribution of the second harmonic increases with an increase in voltage. When the amplitudes of the first and second harmonics become equal, a further increase in the voltage suppresses the first harmonic. It is likely that the linear response of an FLC is accompanied not only by the shear strain but also by a variation in the sample thickness. If the change in the sample thickness related to the linear and nonlinear responses is in antiphase, this may result in the suppression of one of the mechanisms of electromechanical conversion. The mechanism of the phenomenon observed has not been studied yet; however, one must take it into consideration when studying the nature of the electromechanical response of LCs. The experiments must be performed in the voltage range in which the first harmonic of the sound dominates. The sensitivity of our experimental setup was not sufficient to investigate the field dependence of the sound harmonics in the nematic and smectic *A* phases. High voltages were used to excite sound in these phases. In this case, we only observed the second harmonic. However, it is possible that the first harmonic was suppressed by the voltage, as in the smectic *C* phase. Therefore, the issue remains open on whether mechanisms of the electromechanical response that are peculiar to the nematic and smectic *A* phases exist.

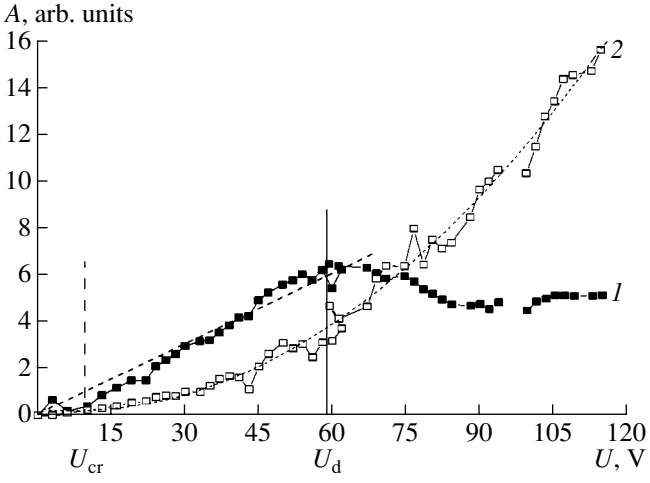

Fig. 3. Dependences of the amplitude of the (*1*) first and (*2*) second harmonics of the radiated sound on the electric field voltage (the frequency of the fed sound is 1500 Hz) for mixture III at $t = 20°C$; U_{cr} is the helix unwinding voltage; and U_d is the voltage at which the first harmonic amplitude is maximum.

CONCLUSIONS

Nonlinear properties of a FLC sample were found in the study of its electromechanical response. It was shown experimentally that the electroclinic effect is the main reason for the sound generation in the Sm*C**-phase near the phase transition. The observed square dependence of the amplitude of the second harmonic of the sound on the field strength is due to the interaction

between the electrically charged cell plates rather than the specificity of the mesomorphic state. An effect of the suppression of the first harmonic was revealed, which should be taken into account in study of the mechanisms of the electromechanical effect.

ACKNOWLEDGMENTS

We are grateful to V.V. Vashchenko and M.V. Kozitskaya for the synthesis of liquid crystals and chiral dopants.

REFERENCES

1. Y. J. Kim and J. S. Patel, Appl. Phys. Lett. **75**, 1985 (1999).
2. A. Jakli, N. Eber, and L. Bata, Liq. Cryst. **5**, 1121 (1989).
3. A. Jakli and L. Bata, Liq. Cryst. **7**, 105 (1990).
4. A. P. Fedoryako, M. N. Pivnenko, E. V. Popova, and V. P. Seminozhenko, Funct. Mater. **4**, 375 (1997).
5. A. Jakli, L. Bata, A. Buka, and N. Eber, Ferroelectrics **59**, 145 (1984).
6. M. S. Veksler, *Measuring Instruments with Electrostatic Mechanisms* (Énergiya, Moscow, 1974) [in Russian].
7. M. M. Pivnenko, O. P. Fedoryako, and V. P. Seminozhenko, Ukr. Fiz. Zh. **42**, 1314 (1997).

Translated by A. Zolot'ko

Crystallography Reports, Vol. 50, No. 2, 2005, pp. 320–326. Translated from Kristallografiya, Vol. 50, No. 2, 2005, pp. 356–362.

SURFACE, THIN FILMS

Study of Structural Properties of $In_xGa_{1-x}As/In_yAl_{1-y}As$ Heterosystems on InP Substrates

R. M. Imamov*, V. G. Mokerov, É. M. Pashaev*, I. A. Subbotin*, and Yu. V. Fedorov****

** Shubnikov Institute of Crystallography, Russian Academy of Sciences, Leninskiĭ pr. 59, Moscow, 119333 Russia*

e-mail: pashaev@ns.crys.ras.ru

*** Institute of High-Frequency Semiconductor Electronics, Russian Academy of Sciences, Moscow, Russia*

Received October 29, 2004

Abstract—The structural properties of $In_xGa_{1-x}As/In_yAl_{1-y}As$ samples on InP substrates are studied as functions of growth conditions by the method of high-resolution diffractometry. The results obtained and the photoluminescence spectroscopy data are used to optimize the technology of preparation of high-quality heterostructures with sharp interfaces. The parameters of the two-dimensional electron gas of such heterostructures measured at 77 and 300 K are comparable with the best world standards in this field, so these heterostructures may be used to manufacture transistors and integral amplifiers operating at the frequency 40 GHz and even higher. © *2005 Pleiades Publishing, Inc.*

INTRODUCTION

The $In_xGa_{1-x}As/In_yAl_{1-y}As$ heterostructures on InP substrates possess important physical properties and are still the objects of detailed scientific studies. This is explained by enormous advantages provided by the use of high-electron-mobility (HEM) structures on InP substrates in devices which require anomalous high-frequency or low-noise parameters. The pseudomorphous HEM structures on GaAs substrates contain only about 20–30% of In, whereas the channel of HEM structures on InP substrates admits the use of up to 70% In and even higher.

An increase in the indium content in a heterostructure allows one not only to increase the mobility and concentration of the electron gas in the channel but also to considerably increase the drift velocity of electrons. As a result, InP-based HEM devices are the most rapid of all the devices known at present. The main technological lines of InP-based HEM devices with 65% In in the channel provide the attainment of frequencies f_t = 300 GHz and f_{max} = 450 GHz. These samples allow one to attain considerably higher amplification than pseudomorphous GaAs-based HEM devices and also better noise parameters in the whole frequency range. It has become clear that HEM structures on InP devices yield the best amplifying parameters with respect to power at frequencies exceeding 60 GHz.

At present, there exist devices with the output power of 200 mW at 40% power-added efficiency (PAE) and 1000 mW at 25% PAE [1, 2]. Even at higher frequencies (94 GHz), the output power of HEM structures on InP substrates reaches 450 mW at 20% PAE. These fast elements were also used for construction of the fastest monolithic coplanar amplifiers operating at frequencies 215 GHz with the amplification coefficient 15 dB [2].

The present study is dedicated to design and optimization of a Russian technology of preparation of $In_xGa_{1-x}As/In_yAl_{1-y}As$ heterostructures on InP substrates by the method of molecular beam epitaxy (MBE). To determine the principal parameters of heterostructures, we performed the complex studies of the samples by the methods of high-resolution double-crystal X-ray diffractometry and photoluminescence spectroscopy.

SAMPLE PREPARATION

The samples were grown by the MBE method on a RIBER-32P setup (France). To obtain the (100) oriented InP substrates, we cut the (111) oriented InP ingots at an angle of 45°. The substrates with the necessary degree of structural perfection were selected with the aid of X-ray diffractometry diagnostics. As is well known, the half-width of the rocking curve of a perfect InP crystal equals W = 9.5", whereas the percentage of reflection is P_R = 54%. The samples were grown on InP substrates with the best structural parameters (W = 10.2" and P_R = 49%).

The absence of oxides on the surface of InP substrates for epitaxial growth of heterostructures was checked by the electron diffraction method. Heating of the substrates in the temperature range 350–400°C resulted in the appearance of bright reflection from the crystal structure on the electron diffraction patterns. This seems to result from partial removal of indium oxides from the substrate surface. The electron diffrac-

Table 1. Growth parameters of the heterostructure layers

Chemical element	T, °C	Flow pressure, 10^{-8} torr	Growth rate of In-containing compounds on InP substrate, nm/s	Fraction of In in $In_xGa_{1-x}As$ and $In_yAl_{1-y}As$
Ga	852	11.5	0.06357	$(1 - x) = 0.47$
In	757	21.5	0.0713	$x = 0.53$, $y = 0.52$
Al	1070	6.43	0.06307	$(1 - y) = 0.48$

Table 2. Growth and electrophysical parameters of test HEM structures

Sample	Pressure of As flow, 10^{-6} torr	Annealing temperature, °C	Growth temperature, °C	Channel "thickness," d_c, nm	Hall parameters of structures			
					300°K		77°K	
					concentration N_e, 10^{12} cm^{-2}	mobility μ_e, cm^2/V s	concentration N_e, 10^{12} cm^{-2}	mobility μ_e, cm^2/V s
A	6	470	400	40	3.74	5430	3.28	10630
B	15	540	490	40	3.28	10640	3.2	38000
Ref. [3]	–	–	500	40	3.3	10657	3.3	39000

tion patterns did not change either during sample cooling or its heating over the large temperature range.

The source temperatures were selected in such a way that the steady-state flows of Ga, Al, and In corresponded to the selected composition of solid-solution. The growth parameters of the grown layers are listed in Table 1.

RESULTS OF MEASUREMENTS AND DISCUSSION

The MBE modes of growth $In_{0.53}Ga_{0.47}As/In_{0.52}Al_{0.48}As$ layers on InP substrates were selected using conventional HEM structures and then selectively doped for measurements of the electrophysical parameters of the two-dimensional gas (Fig. 1). These structures consist of rather thick layers of $In_{0.53}Ga_{0.47}As$ channels with two-dimensional electron gas whose parameters allow one to evaluate the quality of the structures grown (~36 nm) and a buffer $In_{0.52}Al_{0.48}As$ layer (500 nm). X-ray diffraction measurements and the study of the photoluminescence spectra were performed after the completion of the growth process. The X-ray diffractometric data and photoluminescence spectra obtained allowed us to extract the information on the layer composition. Moreover, analysis of the rocking curves allowed us to estimate structural perfection of layers grown and interlayer boundaries (interfaces) [4, 5].

We prepared a series of similar structures which differed by the conditions of the primary annealing and growth temperature of an epitaxial layer, the thickness of the $In_{0.53}Ga_{0.47}As$ channel, and different As flows. Growth of each sample was followed by measurement of its electrophysical parameters by the Hall method (rapid control). The results of these measurements allowed us to refine the growth conditions and structural parameters.

The procedure of oxide removal from InP surfaces was tested on the first samples. An electron diffraction experiment showed that at ~560°C the 2×4 surface is rearranged into the 4×2 surface. At the "thickness" of

Undoped 5-nm-thick $In_{0.53}Ga_{0.47}As$ protective layer
Undoped 23-nm-thick $In_{0.52}Al_{0.48}As$ barrier layer
δ-Si: $N_{Si} = 7 \times 10^{12}$ cm^{-2} donor layer
Undoped $In_{0.52}Al_{0.48}As$ 4-nm-thick spacer layer
Undoped 40 nm $In_{0.53}Ga_{0.47}As$ channel
Undoped 500-nm-thick $In_{0.52}Al_{0.48}As$ buffer layer
Semi-insulating InP (100) substrate

Fig. 1. Schematic of an epitaxial HEM structure.

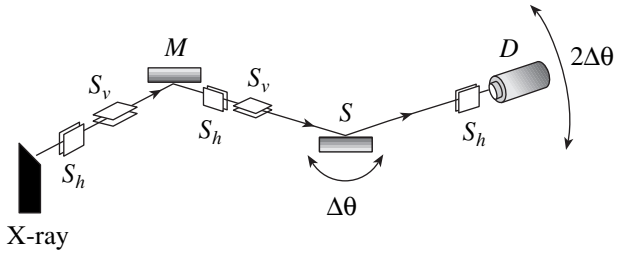

Fig. 2. Schematic of a double-crystal X-ray spectrometer. *S*—sample, *M*—crystal–monochromator, $S_{h,\,v}$—horizontal and vertical slits, *D*—detector of X-ray radiation.

the $In_{0.53}Ga_{0.47}As$ channel exceeding 20 nm, intense reflections appeared on the electron diffraction pattern which indicated the development of a certain surface relief.

To reveal the factors giving rise to mismatching of the heterostructure layers, we grew a number of samples. We consider here the results obtained from one of the intermediate samples *A* and also from the sample *B* possessing the best electrophysical parameters. The growth temperature of all the layers in the sample *A* decreased to 410°C, with the flows of all the elements being preserved. Comparing this result with the data obtained for previous samples, we established that the parameters of sample *A* were much better (the data on the samples *A* and *B* are listed in Table 2). We drew the conclusion that the main cause of the composition change of the $In_xGa_{1-x}As$ channel is the reevaporation of deposited In atoms, which becomes less intense with a decrease in the growth temperature. As is seen from Table 2, the best electrophysical parameters were obtained for sample *B*.

X-ray diffraction study of samples *A* and *B* were performed on a double-crystal X-ray spectrometer using $CuK_{\alpha 1}$ radiation in the θ–2θ mode over a large (about 6000 angular seconds) range (Fig. 2). The monochromator was a perfect Ge(400) single crystal. The diffuse background was suppressed using the slits $S_{h,v}$. The coherent and diffuse components of scattering were separated with the aid of a narrow horizontal slit S_h (the window in front of the detector had an aperture of 330 angular seconds). The use of the slit considerably limited the diffuse component incident from the crystal under study onto the detector. The rocking curves were recorded in the step-by-step mode at a step of four angular seconds, whereas the central part of the curve was recorded at a step of 1 angular second. The intensity was measured in the statistical mode (up to 1000 counts) at each point of the rocking curve. The minimum recording time was 2 s; the recording maximum time was 100 s. The accuracy of the X-ray intensities (even at the rocking-curve tails) was higher than 5%.

To estimate the surface inhomogeneity caused by the fluctuations of the growth parameters of heterostructure, we performed X-ray diffraction measurements of several regions of a relatively narrow angular range (Fig. 3). The measurements showed the scatter in the *y* values for the $In_yAl_{1-y}As$ solid solution of the order of 2.5 and 0.5% along two mutually perpendicular directions. Photoluminescence studies yielded values *y* along the surface, which almost exactly coincided with the values *y* obtained by X-ray diffraction data.

Now let us consider X-ray diffraction data obtained for samples *A* and *B* (Fig. 4). The rocking curves of these samples obtained in the wide angular range dramatically differ. The rocking curve of sample *B* is characterized by a large number of oscillations with differ-

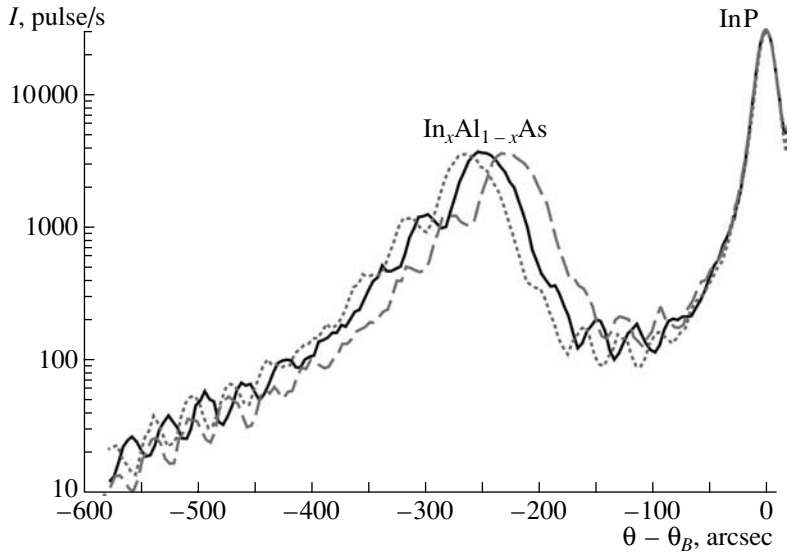

Fig. 3. Fragment of the rocking curve from sample *B*. The solid line passes through the sample center, and the dashed lines pass 2 mm above and below the sample center. The difference in the *x* values along this direction at the sample surface equals 0.5%.

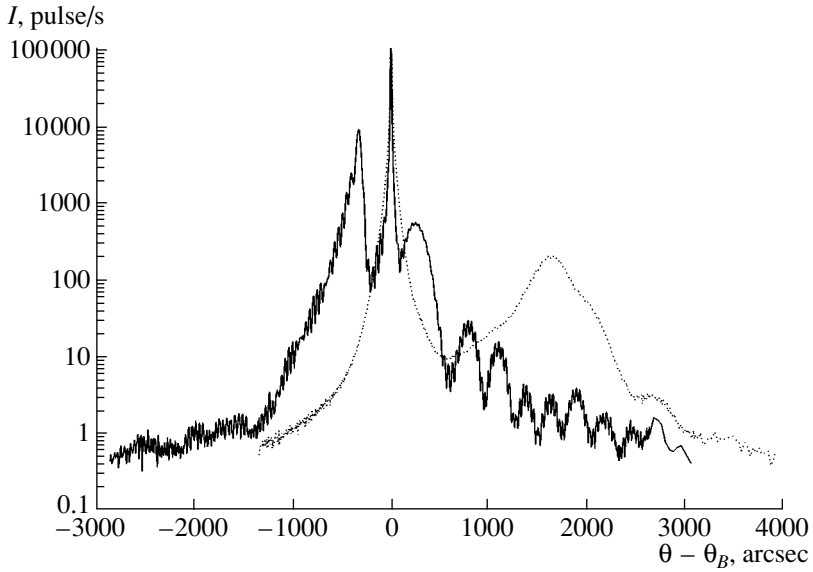

Fig. 4. Rocking curves of the *A* (dashed line) and *B* (solid line) samples. Solid line of the 400 reflection.

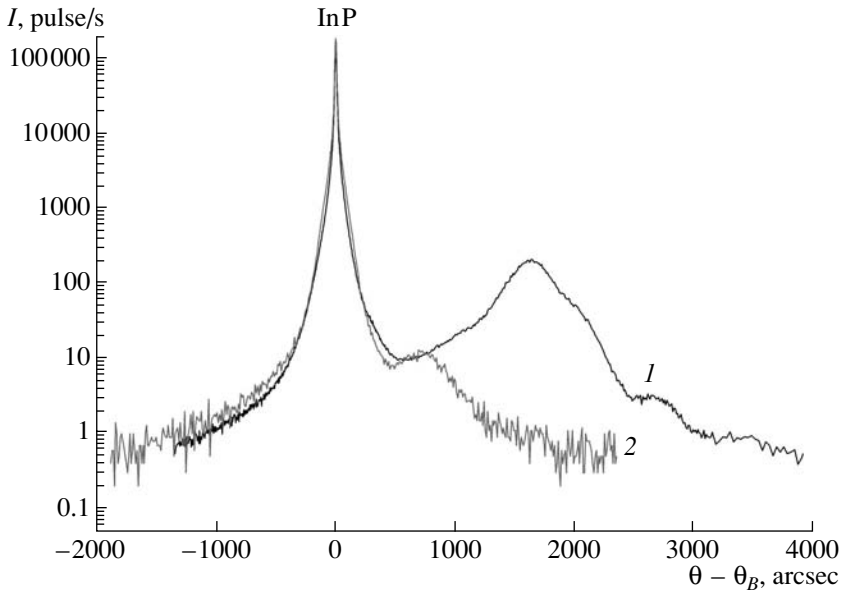

Fig. 5. Rocking curves of the sample *A*. (*1*) 400; (*2*) 200 reflection.

ent periods, which indicates a high quality of the layers with relatively sharp interfaces. The rocking curve of sample *B* has two pronounced maxima corresponding to the reflection from the $In_xGa_{1-x}As$ and $In_yAl_{1-y}As$ solid solutions. In addition to the well developed maximum due to the InP substrate, the rocking curve of the sample *A* has only one weak diffraction maximum with a large half-width *W* in the region of positive angles. Practically no thickness oscillations of the heterostructure as a whole were observed.

To identify the diffraction maxima on the patterns from samples *A* and *B*, we performed some additional measurements. We obtained rocking curves for 200 reflections of samples *A* and *B* (Figs. 5, 7). The heterostructures studied consist of the layers in which some In atoms in the InAs crystal lattice are replaced by Ga or Al atoms. The characteristic feature of the sphalerite structure is a weak intensity of the 200 reflection in comparison with the 400 reflection. This is associated with the fact that the structure factor of the 200 reflection is determined by the difference of scattering powers of the elements located in different structurally equivalent positions in the crystal lattice. The smaller this difference (in substitutional solid solutions,

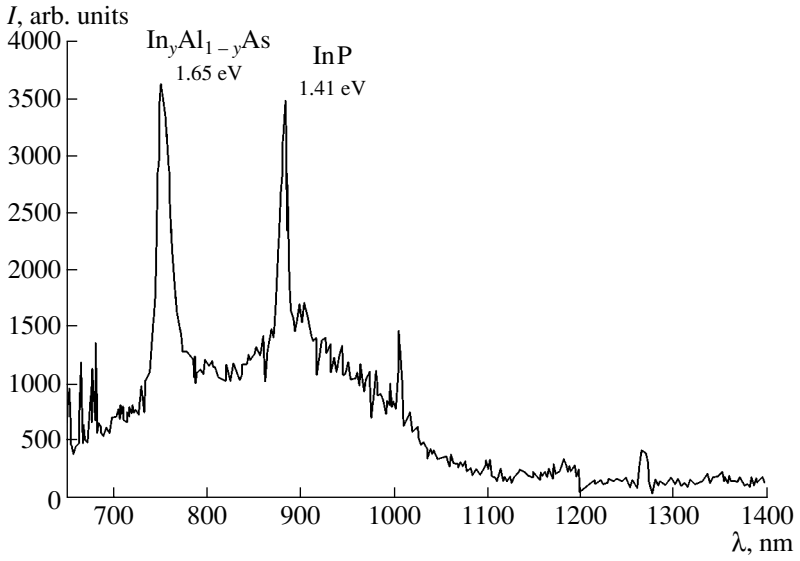

Fig. 6. Photoluminescence spectrum of the intermediate HEM structure *A* at one of the points at the surface (no photoluminescence peak due to the $In_xGa_{1-x}As$ quantum well was observed at $\lambda \cong 1540$ nm).

the scattering power of the metal sublattice of the structure is replaced by the scattering factor averaged over the given composition), the more pronounced the decreases in the structure factor of the 200 reflection.

As shown in our calculations and the simulated rocking curves for the structures under study, in the case of the 200 reflection only the diffraction maxima from ~500-nm-thick epitaxial layers are seen, whereas 40-nm-thick layers give no noticeable diffraction peaks. This allows us to state that the additional diffraction maximum in Fig. 5 should be attributed to a buffer layer. In this case, the In content in the layer is considerably lower that the value set by the growth technology ($y = 0.432$ instead of 0.52). The calculated intensities of the rocking-curve indicate a low quality of this buffer layer (the intensity of the respective maximum is lower by an order of magnitude than the calculated intensity). It should be indicated that the curves in Fig. 5 practically do not show the maximum due to the $In_xGa_{1-x}As$ channel. This allows us to conclude that the $In_xGa_{1-x}As$ layer seems to consist of a number of sublayers with diffuse boundaries. The weak oscillations seen in Fig. 5 indicate the existence in the heterostructure of a 265-Å-thick epitaxial layer corresponding to the sum of the thicknesses of the barrier and spacer $In_yAl_{1-y}As$ layers (230 and 40 Å, respectively) (Fig. 2).

The X-ray diffraction data obtained are consistent with the photoluminescence data. The photoluminescence spectra of sample *A* have low intensities because of the poor quality of the layers grown (Fig. 6); no maximum due to the quantum $In_xGa_{1-x}As$ dot was observed at all. The position of the maximum due to the buffer $In_yAl_{1-y}As$ layer on the photoluminescence spectrum was different at different points of sample *A* and its value ranged within 1.57–1.65 eV. This indicates a low *y* value in the buffer layer. In this case, the In content in different regions of the sample was different. The calculations show that the *y* value in the buffer layer ranges within 0.45–0.47, which may result from the reevaporation of In atoms because of insufficiently dense As flow, which also affects the electrophysical properties of these structures.

The situation is completely different for diffraction curves of sample *B* (Fig. 7). The measurements on this crystal were performed for the symmetric 400 and 200 reflections and also on the 311 reflection. To exclude the influence of inhomogeneity over the sample surface, all three rocking curves were obtained practically for the same illuminated area (the error did not exceed 5%). Preliminary analysis of all the three rocking curves allows us to state that sample *B* corresponds to the technological growth parameters. The rocking curve of the 400 reflection clearly shows the maxima due to the buffer $In_yAl_{1-y}As$ layer and $In_xGa_{1-x}As$ channel. The In content in the buffer $In_yAl_{1-y}As$ layer is evaluated as $y = 0.54 \pm 0.02$ (instead of 0.52 given by the growth technology). In the range of positive angles for the 400 reflection, there is maximum due to $In_xGa_{1-x}As$ (as was indicated above, it is essentially weakened in the case of 200 reflection, but is clearly seen for the 311 reflection). According to the results of all three measurements, the In content in $In_xGa_{1-x}As$ is evaluated as $x = 0.516 \pm 0.025$ (instead of 0.53 given by the growth technology). A large number of oscillations with different periods observed on these rocking curves (Fig. 7) allowed us not only to reliably determine the thicknesses of the layers grown but also to evaluate the sharpness of the interfaces between these layers. The angular distances between various oscillations of the rocking curves of the 400, 200, and

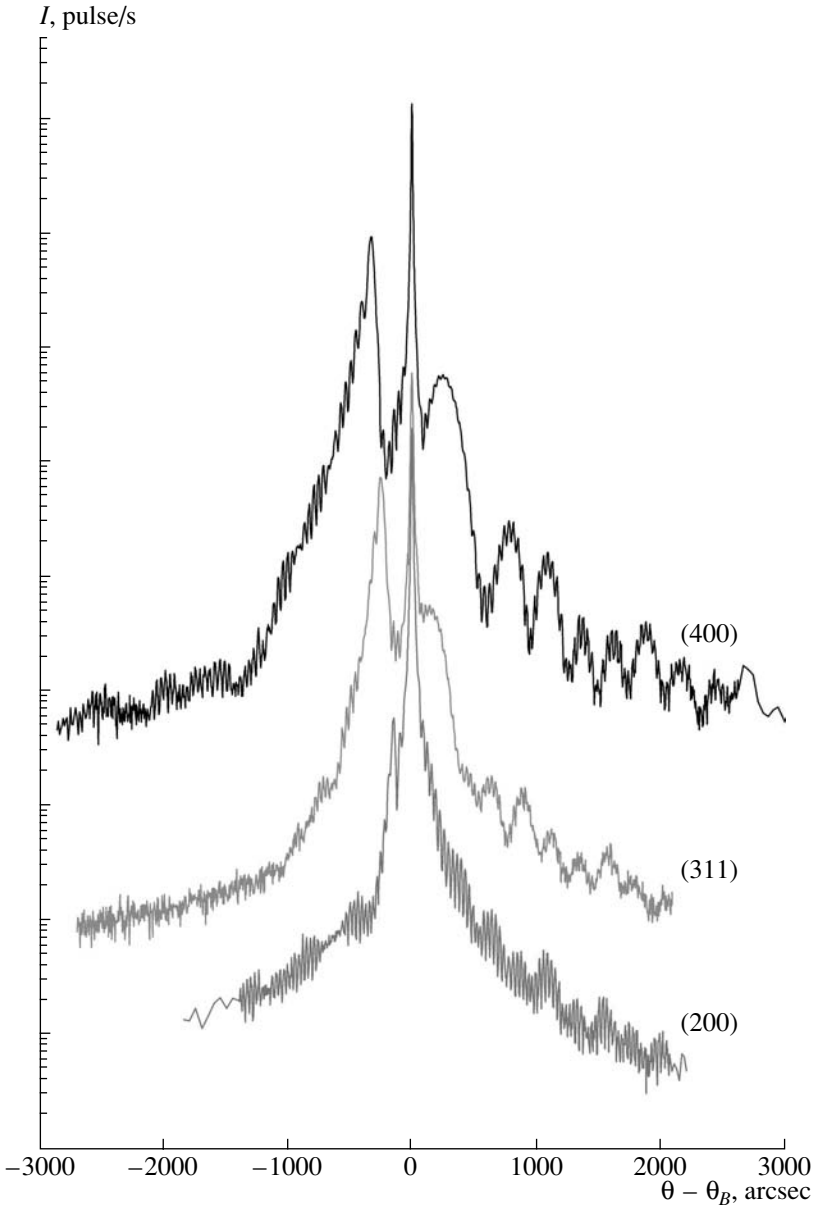

Fig. 7. Rocking curves from the sample *B* for the 400, 200, and 311 reflections.

311 reflections allowed us to evaluate the average thicknesses of individual layers of the heterostructure *B*. The total thickness of the whole heterostructure on an InP substrate equals 5500 ± 270 Å, the thickness of the layer of the $In_xGa_{1-x}As$ channel is 350 ± 17 Å, and the total thickness of the spacer and barrier $In_yAl_{1-y}As$ layers is 265 ± 13 Å. The heterolayer parameters obtained are in good accordance with the values given by the growth technology (Fig. 1).

In turn, the photoluminescence spectra of sample *B* with high electrophysical characteristics also noticeably differ from the spectra of sample *A* by high intensities of the peaks and the signal due to the $In_{0.53}Ga_{0.47}As$ channel (Fig. 8). This indicates a rather high structural quality of the corresponding layers, which is confirmed by analysis of the respective rocking curves.

The calculations based on the position of the maximum due to the buffer $In_yAl_{1-y}As$ layer on the photoluminescence spectrum show that the average *y* value equals 0.535. Such a deviation of the composition (*y* value) of the $In_yAl_{1-y}As$ layers from +3% to –1% set by the growth technology seems to be quite admissible and produces no considerable effect on the change in the mobility in the two-dimensional electron gas. According to the photoluminescence spectra of this sample, we have for the $In_xGa_{1-x}As$ channel $x = 0.515$ at the admissible deviation of the In content without

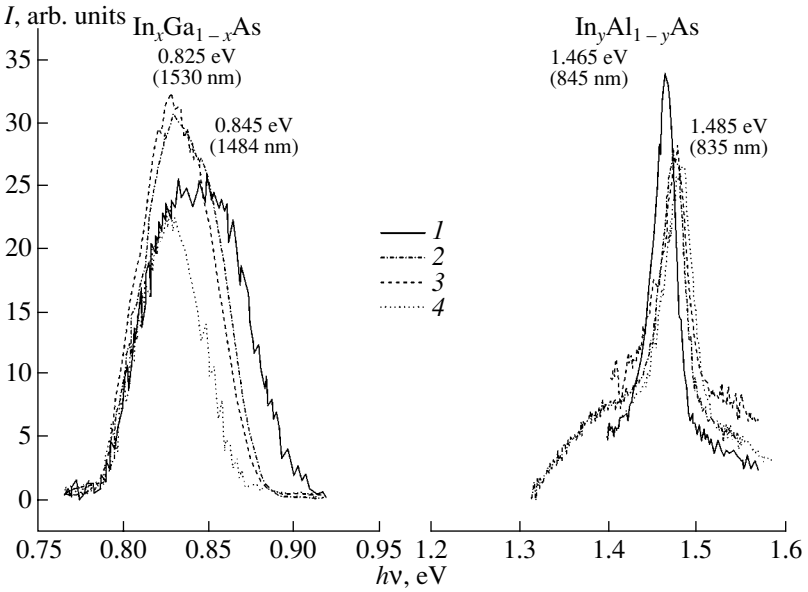

Fig. 8. Photoluminescence spectra at different points (*1–4*) of the surface of the test HEM structure *B*.

deterioration of the properties of the two-dimensional gas (±3%).

CONCLUSIONS

Thus, one may state that the above technological experiments and the diffraction and photoluminescence measurements allowed us to refine the Russian technology for growth of high-quality $In_{0.53}Ga_{0.47}As/In_{0.52}Al_{0.48}As$ heterostructures on InP substrates.

The use of the combined X-ray diffractometric data and photoluminescence spectroscopy data allowed us to obtain reliable information on the parameters and quality of heterostructures grown. The rocking curves allowed us to follow the influence of the growth conditions on the quality of a multilayer structure. The composition and layer parameters in high-quality samples *B* correspond to those set by the growth technology. The characteristics of a two-dimensional electron gas in these samples are at the level of the best characteristics achieved in the world; therefore, these heterostructures may be used to prepare fast transistors and integral amplifiers at the frequencies of 40 GHz and higher.

We had no aim to perform detailed layer-by-layer analysis of the structural perfection of individual layers and interfaces between them. Such analysis will be considered in following publications.

ACKNOWLEDGMENTS

The study was supported by the Federal Agency on Science and Innovations (State Contract no. 37.029.1.1.034), the Presidium of the Russian Academy of Sciences (Complex Program *Nanodimensional Quantum Structures*), Russian Foundation for Basic Research, project no. 03-02-17-382, and the Program of the Leading Scientific Schools (project no. NSh-14.04.2003.2).

REFERENCES

1. D. Theron, Y. Cordier, X. Wallart, *et al.*, in *Proceedings of GAAS 2001 Conference* (London, 2001), p. 53.
2. K. Y. Hur, R. A. McTaggart, M. P. Ventresca, *et al.*, IEEE Electron Device Lett. **16** (9), 390 (1995).
3. L. D. Nguyen, A. S. Brown, M. A. Thompson, *et al.*, IEEE Trans. Electron Devices **39** (9), 2007 (1992).
4. R. M. Imamov, A. A. Lomov, É. M. Pashaev, *et al.*, Poverkhnost, No. 12, 11 (1999).
5. A. M. Afanas'ev and R. M. Imamov, Kristallografiya **48** (5), 786 (2003) [Crystallogr. Rep. **48**, 728 (2003)].

Translated by L. Man

Crystallography Reports, Vol. 50, No. 2, 2005, pp. 327–334. Translated from Kristallografiya, Vol. 50, No. 2, 2005, pp. 363–371.

CRYSTAL GROWTH

Physical and Physicochemical Processes Accompanying Powder Synthesis, Growth of $PbMoO_4$ Crystals, and Their Annealing in Various Media: I. Solid-State Mechanism of the Formation of the Pb_2MoO_5 Microheterogeneous Phase in $PbMoO_4$ Crystals

V. T. Gabrielyan[1, 2], O. S. Grunskiĭ[1], A. A. Gukasov[2], A. V. Denisov[1], N. S. Nikogosyan[2], and L. M. Fedorova[3]

[1] *Russian Center of Laser Physics of St. Petersburg State University, St. Petersburg, 198504 Russia*
e-mail: tigran@home.rclph.spbu.ru
[2] *Institute for Physical Research, Academy of Sciences of Armenia, Ashtarak, 138410 Armenia*
[3] *Russian State Professional Pedagogical University, Yekaterinburg, 620012 Russia*

Received November 20, 2003

Abstract—In this study, the first of the proposed cycle, the conditions and the mechanism of nucleation and formation of particles of the Pb_2MoO_5 phase in $PbMoO_4$ crystals, which are due to the physicochemical features of the heating, melting, and solidification of $PbMoO_4$, are considered. It is shown that preferred evaporation of one of the composite components of this compound, MoO_3, leads to the violation of the initial stoichiometry and formation of excess PbO in a charge at the synthesis stage and in a melt during the crystal growth. The formation of the Pb_2MoO_5 phase in crystals with excess PbO occurs during their postgrowth cooling at temperatures below 930°C (eutectics between $PbMoO_4$ and Pb_2MoO_5). The results of the differential thermal analysis, X-ray diffraction analysis, high-temperature powder diffraction study, and annealing of crystals in specific media confirm the solid-state mechanism of the formation of the Pb_2MoO_5 phase in $PbMoO_4$ crystals.

INTRODUCTION

The problems inherent in the growth of compounds with high volatility are complicated by the fact that, along with the evaporation of the grown compound from a melt, its components, which also have a high vapor pressure, evaporate as well. Under the conditions considered, at a relatively high evaporation of one of the components, its content in the melt decreases and an excess of the other component (or components, depending on the number of components in the system) is formed. The crystal growth from such systems is accompanied by the violation of their composition with respect to the main components and, finally, the formation of other phases existing in the phase diagrams at both sides of the compound grown.

The above physicochemical considerations seem to be especially important as applied to $PbMoO_4$ crystals, since a characteristic feature of their growth is that it is accompanied by intensive melt evaporation.

In this study, we consider the conditions and the mechanism of the nucleation and formation of micronucleation particles of the Pb_2MoO_5 phase in $PbMoO_4$ crystals caused by the physicochemical features of heating, melting, and solidification of $PbMoO_4$.

EXPERIMENTAL METHODS

Solid-phase synthesis of $PbMoO_4$ and Pb_2MoO_5 was performed by multistage annealing of mixtures of initial binary oxides (PbO and MoO_3) of specified composition with a stepwise increase in temperature and intermediate grinding using ethyl alcohol as a dispersive homogenizing medium.

X-ray phase analysis (XPA) of polycrystalline and single-crystal samples was carried out on a TUR-M-62 diffractometer in filtered CoK_α radiation. Identification of the nature of the phases formed was carried out in the range of Bragg angles $\theta = 26°–60°$ using the most characteristic lines. The concentration of Pb_2MoO_5 was quantitatively estimated by the disappearing-phase method. For comparison, we used the X-ray diffraction patterns of artificial mixtures of $PbMoO_4$ with specified concentrations of the Pb_2MoO_5 phase (0.3, 0.5, 1.0, 1.5, and 2.0 wt %). The diffraction patterns were compared with references obtained for single-phase synthesized charges of $PbMoO_4$ and Pb_2MoO_5.

High-temperature powder diffraction study of phase transformations was performed on a DRON-3 diffractometer equipped with a KRV-1100 high-temperature attachment [1].

1063-7745/05/5002-0327$26.00 © 2005 Pleiades Publishing, Inc.

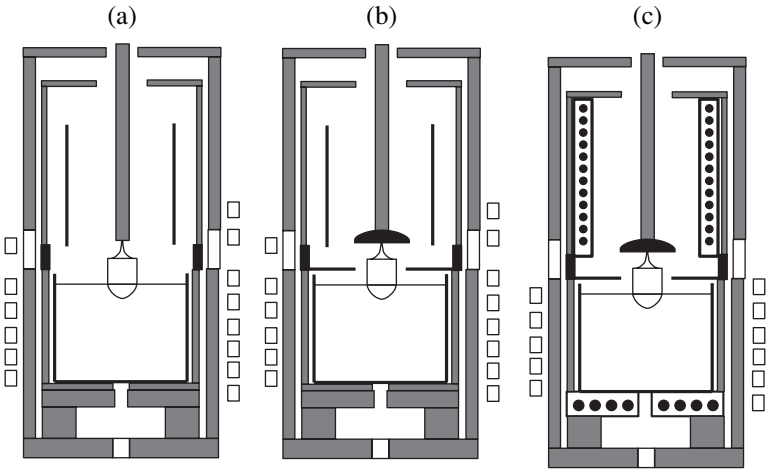

Fig. 1. Designs of heating units for crystal growth: (a) a high-frequency heating system; (b) system *a* supplemented with a diaphragm and a screen; and (c) a system with high-frequency heating of the crucible, an upper resistive afterheater, and bottom heating of the crucible.

For indexing and determining the initial ratio of the peak intensities, conventional (at room temperature) XPA of the samples was performed before the high-temperature powder diffraction study. The samples were ground in an agate mortar using ethyl alcohol as a dispersive medium, deposited on a glass disk 25 mm in diameter, and dried.

The conditions of the X-ray phase analysis, beginning with room temperature and, then, at 100, 200, 300, 350, 400, 450, 500, 550, and 600°C with exposure no less than 1 h at each of the listed temperatures, were as follows: CuK_α radiation; the voltage and current in the tube were 35 kV and 20 mA, respectively; the range of diffraction angles was $2\theta = 10°–70°$ with marks spaced at intervals of 0.1°; the velocity of chart tape was 2400 mm/h; the counter speed was 2–4 deg/min; the range of count rates was 200–1000 count/s; and the time constant was 5 s.

The phase transformations occurring in the reaction mixture with a successive increase in temperature were fixed by changes in the diffraction pattern on the chart tape: disappearance of old peaks, appearance of new ones, and redistribution of diffraction maxima due to changes in the composition.

The diffraction patterns were processed using the programs DEBAI (indexing), PARAM (calculation of the unit-cell parameters), and Powder cell 1.8 (simulation of powder diffraction patterns based on structural data). The X-ray diffraction patterns obtained were compared with the PDF file data (card nos. 8–475 ($PbMoO_4$), 38–1477 (PbO), 5–508 (MoO_3), and 24–579 (Pb_2MoO_5)).

Differential thermal analysis (DTA) was used for qualitative and quantitative determination of the phase composition of synthesized charges and melts solidified after long-term exposure and subsequent cooling. This analysis was performed on an OD-102 derivatograph under the following conditions: temperature *t* up to 1200°C, a linear heating rate of 5–10 K/min, and sensitivities of 1/5 and 1/2. The characteristic peaks of thermal effects were fixed using the heating curves, and the melting temperatures of eutectic mixtures were determined from the positions of the maxima.

Crystal growth was performed by the Czochralski method on Donets-1 and RUMO-1P systems with high-frequency (450 and 8 kHz, respectively) heating. The control system in RUMO-1P provided the possibility of programmed control of the growth process using a precise weight sensor to monitor the crystal weight. Different variants of crystallization units (see Fig. 1) were used, depending on the problem stated in each specific experiment. The constructions of the crystallization units made it possible to change in a wide range the axial and radial temperature gradients in the crystal–melt system by changing the position of the crucible in the high-frequency inductor; combine induction heating of the crucible with a melt and resistive heating using an upper afterheater; or, if necessary, introduce bottom heating of the crucible. The crucible with a melt was installed on an alumina ceramic support and a seed with a crystal to be grown was fixed by a holder on a water-cooled pulling rod, which was rotated and moved in the vertical direction by a pulling mechanism. The latter made it possible to change the pulling and rotation rates of a crystal in the ranges 0.19–10 mm/h and 0–50 rpm, respectively.

Annealing of crystals. The grown crystals were previously annealed in a muffle furnace at 900–950°C in air to remove residual stresses. Then, plates $20 \times 25 \times (3–5)$ mm^3 in size, oriented perpendicular to the growth direction, were cut from the crystals and polished. After careful scanning in a He–Ne laser beam, the samples containing second-phase inclusions were chosen. A platinum box, into which fine powder of either PbO or

MoO_3 (depending on the problem stated) was poured, was placed in a zero-gradient zone of a horizontal tube furnace. The furnace design made it possible to perform annealing in a specified medium in the filling or flow modes. The plates were uniformly placed on a platinum grid, which, in turn, was installed above the platinum box. The annealing temperature was chosen taking into account the melting temperature of the oxide, depending on the problem stated. Disappearance or appearance of a phase in a transmitted laser beam after annealing allowed us to indirectly estimate and confirm the occurrence of one of the solid-phase reactions described here.

Vapor pressures of PbO, MoO_3, and $PbMoO_4$. The results of the investigations aimed at determining the vapor pressures of PbO and MoO_3 by the Knudsen, Langmuir, flux, boiling point, and mass-spectroscopy methods performed by different researchers were analyzed in detail in [2]. From all data reported in [2], we chose the values of the vapor pressures P_{PbO} and P_{MoO_3}, which are most consistent with each other and whose temperature ranges correspond to the conditions of solid-phase synthesis of the $PbMoO_4$ charge and the crystal growth performed here: P_{PbO} = 0.13 Pa and P_{MoO_3} = 13 Pa.

RESULTS AND DISCUSSION. PHASE FORMATION AT DIFFERENT STAGES

Stage of charge synthesis. It is known [2] that $PbMoO_4$ is characterized by high vapor pressure of both binary oxides, PbO and MoO_3, even at temperatures close to 700°C. Therefore, it is rather difficult to obtain crystals of an exact stoichiometric composition. When an equimolar mechanical mixture of the noted oxides is melted into the crucible, provided that $P_{MoO_3} \gg P_{PbO}$, the solid-phase reaction between the oxides and further melting of the mixture will occur with pronounced preferred evaporation of MoO_3. This process may finally lead to uncontrolled violation of the required melt stoichiometry and, furthermore, the composition of the grown crystal. Hence, it is necessary to carefully analyze the conditions of the solid-phase charge synthesis at which the combined oxides, interacting at knowingly low temperatures, would provide in the next stages completeness of the reaction without significant and, what is especially important, nonuniform evaporation of the reacting components. The above considerations put the problem of determining the initial interaction temperature and the temperature range of strong interaction between the reacting components. This problem lies in the basis of establishing conditions of solid-phase charge synthesis.

The data in the literature on the solid-phase reaction between PbO and MoO_3 deal mainly with the conditions of preparing $PbMoO_4$ and disregard the probability of forming the Pb_2MoO_5 phase [3] and, moreover, the conditions and kinetics of its synthesis [4–6]. As was shown in [7], in the PbO : MoO_3 mixture in the temperature range 400–450°C, along with $PbMoO_4$, the Pb_2MoO_5 phase is also formed and exists as an intermediate product. Hence, the character and the kinetic parameters of the solid-phase interactions should be assigned, most likely, to the formation of the total product, $PbMoO_4$ + Pb_2MoO_5, rather than to the synthesis of an individual molybdate. Finally, using XPA, DTA, electrical resistivity measurements, and high-temperature powder diffraction study, the initial interaction temperature and the temperature range of strong interaction were determined and refined in [8–11] for the reaction mixtures PbO : MoO_3 and 2PbO : MoO_3 (XPA, DTA, and high-temperature powder diffraction study were used for powder samples and measurements of electrical resistivity were performed with pelleted samples). The results obtained made it possible to formulate the main regularities of the solid-phase reactions in the mixtures under consideration and optimize the conditions of multistage charge synthesis for the growth of $PbMoO_4$ crystals.

The set of experimental data obtained by the abovementioned methods makes it possible to represent the processes occurring during the solid-phase synthesis in mixtures of PbO and MoO_3 oxides as the following sequence:

(i) Independent of the initial composition of the reaction mixture (1 : 1 or 2 : 1), the primary product of the interaction is $PbMoO_4$, which is formed at 300°C by the reaction:

$$PbO + MoO_3 = PbMoO_4. \quad (1)$$

(ii) In the next stage, with a further increase in temperature, the Pb_2MoO_5 phase is formed starting from 350°C:

$$PbMoO_4 + PbO = Pb_2MoO_5. \quad (2)$$

(iii) As temperature increases more, the formation of the final reaction product is enhanced. It should be noted that in an equimolar (stoichiometric, 1 : 1) mixture, gradual disappearance of the Pb_2MoO_5 phase was observed beginning from 450°C and the single-phase final product ($PbMoO_4$) was completely formed at 650°C:

$$Pb_2MoO_5 + MoO_3 = PbMoO_4. \quad (3)$$

At the same time, in a mixture with the 2 : 1 composition, a decrease in the intensity of diffraction lines of the intermediate reaction product ($PbMoO_4$) was observed in the X-ray diffraction patterns beginning from 600°C and the final product (Pb_2MoO_5) was completely formed at 750°C by reaction (2).

As can be seen from the table, the data on the initial interaction temperature and the temperature range of strong interaction, obtained by three independent methods, are in good agreement with each other. Some dif-

Initial interaction temperatures and the temperature ranges of strong interaction for different PbO : MoO_3 mixtures

Initial mixture	Temperature range of the formation of an intermediate phase, °C (XPA)	Temperature of the final product formation, °C (XPA)	Initial interaction temperature, °C, according to the data of			Temperature range of strong interaction, °C (XPA)	References
			resistivity measurements	DTA	XPA		
PbO : MoO_3	Pb_2MoO_5	$PbMoO_4$	210	300	300	350–500	[9, 10]
	350–600	650					
	400–450	600			300	350–500	[8]
	450–550	600			350	350–500	[12]
2PbO : MoO_3	$PbMoO_4$	Pb_2MoO_5	240	350	300	400–650	[9, 10]
	300–750	800					

ferences in the data are related to the methods of investigation and the modes of isothermal (XPA) and nonisothermal (DTA and electrical resistivity measurements) heating of the mixtures.

Analysis of reactions (1) and (2) and the sequence of disappearance of the initial and intermediate phases in different mixtures indicate that the interaction between oxides has a complex and multistage character. Taking into account the multiregion character of interaction and on the basis of the results of more detailed study of the kinetics and the mechanism of formation of lead molybdates by the method of contact diffusion annealing treatments of pelleted samples [8], the sequence of all crystallochemical transformations can be represented more exactly by the following schemes:

$$PbO + MoO_3 \longrightarrow PbMoO_4 + PbO + MoO_3$$
$$\longrightarrow Pb_2MoO_5 + PbMoO_4 + PbO + MoO_3$$
$$\longrightarrow PbMoO_4 + Pb_2MoO_5 + MoO_3$$
$$\longrightarrow PbMoO_4 + PbMoO_4 \longrightarrow PbMoO_4$$

in the synthesis of $PbMoO_4$ and

$$PbO + MoO_3 + PbO$$
$$\longrightarrow PbMoO_4 + PbO + MoO_3 + PbO$$
$$\longrightarrow PbMoO_4 + PbO + Pb_2MoO_5$$
$$\longrightarrow Pb_2MoO_5 + Pb_2MoO_5 \longrightarrow Pb_2MoO_5$$

in the synthesis of Pb_2MoO_5.

The diagram in Fig. 2 gives a pictorial representation of the relations between the initial, intermediate, and final products in the mixtures of the noted compositions in different stages of solid-phase synthesis.

Thus, independent of the relations between the initial components, the primary product of the solid-phase synthesis is the $PbMoO_4$ lead molybdate, which is more thermally stable as compared with Pb_2MoO_5: their melting temperatures are 1065 and 952°C, respectively. The latter circumstance is in good agreement with the Baikov principle [12], according to which the primary product of the interaction is the compound differing from other possible compounds in the system by the highest melting temperature. The above-described features of the phase formation confirm the Baikov principle for another related oxide system of the scheelite group: PbO–WO_3 ($PbWO_4$ and Pb_2WO_5 have t_{melt} = 1123 and 900°C, respectively).

Stage of crystal growth. Study of the grown $PbMoO_4$ crystals in a transmitted He–Ne laser beam (Fig. 3a) and on a JEOL X-ray microanalyzer (Figs. 3b, 3c) showed that the dominant internal defects in these crystals are gas bubbles and microscopic second-phase particles. Both these defects cause strong scattering of laser radiation in crystals, which leads to a significant decrease in the efficiency of light transformation and, in fact, make such crystals unfit for use in acoustooptic devices. At the same time, the crystals containing only second-phase inclusions, after specific annealing in dosed media leading to their disappearance, turn out to be quite appropriate for acoustooptic applications. The factors responsible for the formation of gas bubbles in a melt and their capture by a grown crystal, as well as the ways of their elimination, will be considered in another study of this cycle. Here, we will consider the nature of the phase microheterogeneity in the crystals, which is due to the physicochemical features of heating a charge; its subsequent melting; crystallization; and, finally, cooling of the grown crystal.

Even when an absolutely single-phase charge is used, its melting in a crucible and a rather long-term process of crystal growth occur with intense melt evaporation. Note that, despite the congruent character of melting of $PbMoO_4$, along with the molybdate, PbO and MoO_3 combined oxides also evaporate from the melt. At the preferential evaporation of MoO_3, long-term crystal growth should lead to uncontrolled violation of the initial stoichiometry with the formation of excess PbO in the melt and, furthermore, in the crystal. Taking into account that $PbMoO_4$ has a relatively narrow and two-sided (daltonide) homogeneity region limited by the compositions with 49.85–50.50 mol % of MoO_3 [13], a crystal can grow within the noted solubil-

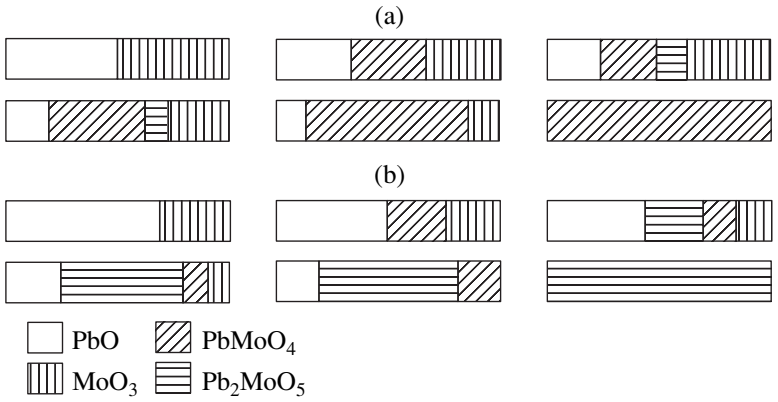

Fig. 2. Schematic diagram of the phase relations in the mixtures PbO : MoO_3 = (a) 1 : 1 and (b) 2 : 1 in different stages of the solid-phase synthesis.

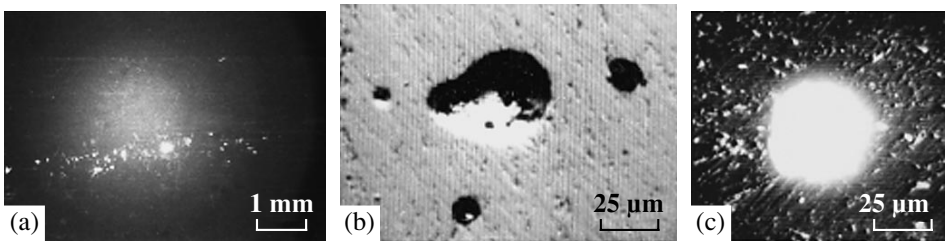

Fig. 3. Inclusions in $PbMoO_4$ crystals: (a) gas bubbles in a transmitted He–Ne laser beam, (b) gas bubbles with the Pb_2MoO_5 phase; and (c) a gas bubble in the absence of the Pb_2MoO_5 phase.

ity range of the components with an excess of one of them and, respectively, with a deficit of the other component. The latter circumstance, in accordance with the results of studying the kinetics and mechanism of solid-phase transformations in the $PbMoO_4$–PbO system, may lead to solid-phase reaction (2) in the grown crystal with the formation of the micronucleus phase Pb_2MoO_5. Fine dispersed particles of this phase, formed in a $PbMoO_4$ crystal during its postgrowth cooling below 930°C (the temperature of the eutectics between $PbMoO_4$ and Pb_2MoO_5), are one of the two above-mentioned types of scattering centers.

The physicochemical justification of the most probable mechanism of the formation of the microheterogeneous phase Pb_2MoO_5 in the $PbMoO_4$ matrix is beyond doubt, since it is even more difficult to suggest the possibility of precipitation of MoO_3,[1] which is also (as Pb_2MoO_5) adjacent to the $PbMoO_4$ phase in the PbO–MoO_3 phase diagram but at the other side. With preferential evaporation of this component in the stages of charge synthesis or crystal growth (as repeatedly noted above), there must be a deficit rather than an excess of MoO_3. However, without an excess of this component, both phases ($PbMoO_4$ and MoO_3) cannot coexist below the eutectic temperature (670°C). Therefore, to maintain the composition of the melt close to equimolar throughout the growth process, an excess amount (up to 1.0 mol %) of MoO_3 must be introduced to compensate for its loss by evaporation.

The formation of phase inclusions and their distribution in the volume of grown crystals is determined, primarily, by the growth duration. Figure 4 shows the photographs of the crystals grown with different exposures of a melt before growth.

The crystals grown from a fresh charging (i.e., without exposure, immediately after the charge melting) do not contain any inclusions (Fig. 4a, scattering centers are absent). With additional charging and corresponding growth cycles (the duration of one growth cycle, including melting, growth, annealing, and cooling of the crystal, is ~50 h), the total exposure of the melt increases, due to which aging of the melt and its enrichment with one of the components occur. As a result, the subsequent crystals may contain phase inclusions formed in different growth stages. Depending on the growth stage, these inclusions will be located in the end region, in the middle (Fig. 4b), or throughout the entire

[1] The presence of the two-sided homogeneity region, provided there were no preferential evaporation of MoO_3, would formally allow for the coexistence of the noted phases and, accordingly, the possibility of precipitation of the MoO_3 phase when, vice versa, preferential evaporation of the other oxide (PbO) would occur.

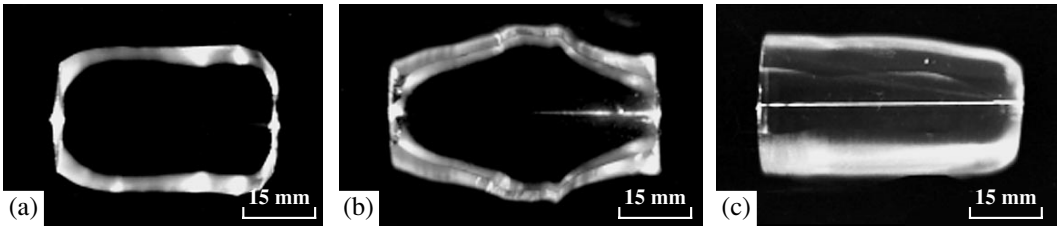

Fig. 4. $PbMoO_4$ crystals grown with different melt exposures: (a) from a fresh charging directly after the melting (scattering centers are absent); (b) after four growth cycles with additional chargings (scattering centers arise beginning with the middle of the crystal); (c) after six growth cycles with additional chargings (scattering centers throughout the crystal volume).

volume (Fig. 4c). In this context, in order to obtain crystals with reproducible properties, it is more expedient to use a single charging to grow large (≥70% of the melt volume in a crucible) crystals rather than multiple processes with additional chargings to grow several crystals in a cycle.

The arguments in favor of the probable reasons and the mechanism of formation of the Pb_2MoO_5 phase are quite convincing. Nevertheless, we should note that, while the identification of Pb_2MoO_5 in a synthesized charge containing this phase by XPA was fairly easy, this method showed only traces of Pb_2MoO_5 in the grown crystal containing many scattering particles, which could be observed visually. However, one or two highly weak reflections cannot serve as a convincing indication of the presence of the Pb_2MoO_5 phase. In this context, a need arises for carrying out experiments whose results would make it possible to reliably confirm the above-described solid-state mechanism of formation of phase inclusions in $PbMoO_4$ crystals grown by the Czochralski method.

As was noted above, nonuniform (with respect to composition) evaporation of a melt leads to the formation of excess PbO in it. Hence, it is quite obvious that, owing to the known repulsion mechanism, which acts during the entire growth process, the PbO content in the melt will always exceed that in the grown crystal. Therefore, the solid-phase reaction (2) can and should occur also in the melt solidified after growth, in which the amount of the tentative phase (Pb_2MoO_5) will be sufficient for its unambiguous identification by XPA and DTA. Within this problem, identical weights of synthesized single-phase $PbMoO_4$ charge were melted in a platinum crucible and kept isothermally in the growth system for 0, 50, 100, 200, and 300 h at a temperature close to the growth temperature. Then, after a short-term growth of crystals of the same size (10–12 mm in diameter and 15–20 mm in length), the melts were cooled and the presence of the Pb_2MoO_5 phase was analyzed.

The crystals grown after isothermal exposures of the corresponding melts were qualitatively analyzed in a transmitted laser beam. A pronounced tendency toward an increase in the relative number of scattering particles in these crystals was revealed. XPA and DTA unambiguously showed the presence of the Pb_2MoO_5 phase in these crystals.

XPA. The characteristic lines of Pb_2MoO_5, absent for the reference (τ = 0 h), arise in the pattern of the sample exposed for τ = 200 h and their intensity significantly increases for the sample with τ = 300 h.

DTA. According to the phase diagram [7], $PbMoO_4$ forms two eutectic mixtures in the $PbO–MoO_3$ system:

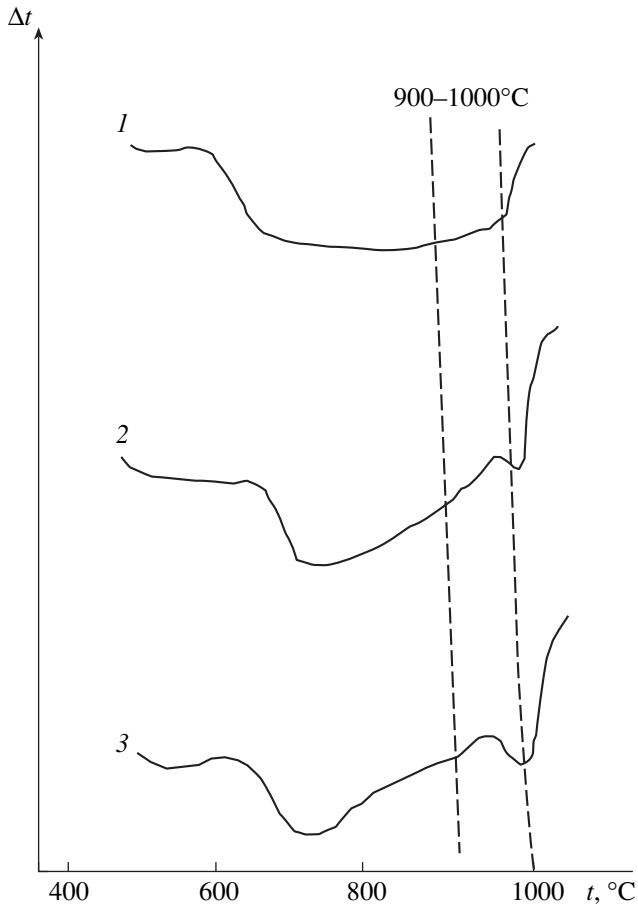

Fig. 5. DTA curves (linear heating rate 0.13 K/s) for melts with different exposures before the growth: τ = (*1*) 0, (*2*) 200, and (*3*) 300 h. Endothermic peaks (930°C) are between the reference points 900 and 1000°C (beginning of the melting of $PbMoO_4$).

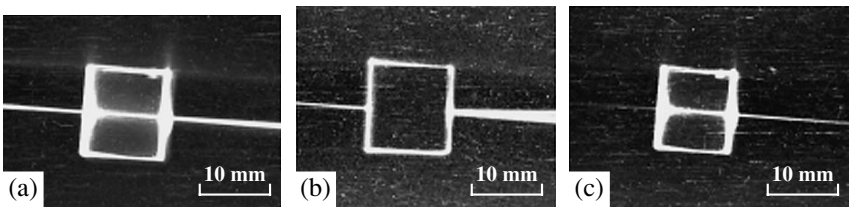

Fig. 6. $PbMoO_4$ plates (a) before annealing and after annealing in (b) MoO_3 and (c) PbO powders.

$PbMoO_4 + MoO_3$ and $PbMoO_4 + Pb_2MoO_5$ with solidus temperatures of 670 and 930°C, respectively. Melting of these mixtures, in contrast to single-phase $PbMoO_4$, should be accompanied by the endothermic effect at the noted temperatures. If we take into account the above considerations concerning the solid-state genesis of the phase formation in different stages of $PbMoO_4$ growth, the detection of the endothermic effect at 930°C is of the most interest.

Figure 5 shows the DTA curves for the melts with different exposures: $\tau = 0$, 200, and 300 h; the derivatograms for the melts exposed for $\tau = 50$ and 100 h are not shown due to the very low concentration of the Pb_2MoO_5 phase in the solidified melts. For $\tau = 50$ h, the endothermic effect was completely absent and the derivatogram, in fact, was the same as that for the sample with $\tau = 0$ h. For $\tau = 100$ h, a weak peak was observed. The endothermic effects observed for the melts exposed for $\tau = 200$ and 300 h show rather large peaks, whose distinctive feature is the increase in the area with increasing exposure of the melt. This is indicative of the corresponding increase in the Pb_2MoO_5 content in the $PbMoO_4$ melt solidified after the long-term exposure. Quantitative comparison of the XPA and DTA data for the melts subjected to long-term evaporation and reference artificial mixtures of $PbMoO_4$ with specified Pb_2MoO_5 contents showed that the concentration of the impurity phase in the melt exposed for $\tau = 200$ h is in the range 1–2 wt %.

The results of the investigation performed confirm, although indirectly, the solid-state mechanism of formation of the phase microheterogeneity in a $PbMoO_4$ matrix in the form of micronucleation particles of the Pb_2MoO_5 phase, whose presence significantly deteriorates the optical homogeneity of crystals used in acoustooptics.

Stage of crystal annealing. Recalling the nature and the solid-state mechanism of formation of the micronucleus phase in $PbMoO_4$ crystals, we should note that, however justified this assumption is physicochemically, the convincing argument in its favor is, nevertheless, the identification of second-phase inclusions as the Pb_2MoO_5 phase by other (along with XPA and DTA) methods.

For the crystal containing a significant amount of fine-dispersed particles of the tentative Pb_2MoO_5 phase (which could be visually observed), the detection of this phase by XPA was almost impossible in view of the fact that its content in the crystal (<2.5%) was below the lower limit of XPA sensitivity. In this context, taking into account the data on the kinetics and mechanism of solid-phase reactions, we performed a series of experiments with annealing the grown crystals in specific media. The results obtained confirmed (indirectly but with a high degree of confidence) the solid-state mechanism of the formation of phase inclusions in $PbMoO_4$ in different growth stages.

Series 1. Plates cut from $PbMoO_4$ crystals with a high concentration of scattering microinclusions were annealed in MoO_3 powder. If these inclusions are indeed micronucleation particles of the Pb_2MoO_5 phase, under the conditions of diffusion mass transfer due to the solid-phase reaction (3), this phase should disappear and the $PbMoO_4$ phase should be formed. Taking into account the melting temperature of MoO_3 (795°C), the samples were annealed at 500°C for several hours. Figures 6a and 6b show the photographs of the samples analyzed in a transmitted laser beam before and after the annealing. These photographs give an idea of how reaction (3) occurs under the conditions considered.

Series 2. The nature of the phase inclusions was established indirectly. Hence, to reliably verify our suggestion, the samples annealed in MoO_3 powder and containing no phase inclusions were annealed anew in PbO powder in the temperature range 650–700°C (below the melting temperature of PbO: 886°C). The appearance of scattering particles in the samples (Fig. 6c) is a convincing argument in favor of the solid-phase reaction (2).

CONCLUSIONS

Analysis of the data reported shows that, independent of the experimental conditions—either solid-phase charge synthesis or direct crystal growth—the initial oxides, PbO and MoO_3, have the highest vapor pressure in the reaction mixture $PbO : MoO_3$ and in the melt of the final compound $PbMoO_4$. At all temperatures, $P_{PbO} \gg P_{MoO_3}$ and significant evaporation of $PbMoO_4$ begins only near its melting temperature

(1065°C). On the basis of these facts, we can conclude the following:

(i) The preferential evaporation of MoO_3, one of the components of $PbMoO_4$, leads to uncontrolled violation of the initial stoichiometry and the formation of excess PbO in the charge in the stage of its synthesis and, then, in the melt during the crystal growth.

(ii) The formation of the micronucleus Pb_2MoO_5 phase in $PbMoO_4$ crystals grown from a melt containing excess PbO, as a typical result of spontaneous decomposition of the solid solution, occurs via a solid-state mechanism, similar to reaction (2), during their cooling below 930°C (the temperature of the eutectics between $PbMoO_4$ and Pb_2MoO_5).

(iii) To decrease the probability of formation of the Pb_2MoO_5 phase in $PbMoO_4$ crystals, by taking into account the preferential evaporation of MoO_3, it is expedient to introduce an excess of MoO_3 into the initial $PbMoO_4$ charge to compensate for the loss of this component by evaporation.

(iv) The reproducibility of the physical characteristics of crystals depends to a large extent on the number of crystals grown using one charging of the crucible with subsequent meltings for each crystal. Under the conditions considered here, even for the fifth or sixth crystal grown in such a process cycle, the total exposure of the melt approaches 200–300 h. Such exposures, according to the results of this study, are favorable for the formation of the impurity phase Pb_2MoO_5.

REFERENCES

1. S. K. Filatov, *High-Temperature Crystal Chemistry* (Nedra, St. Petersburg, 1990) [in Russian].
2. E. K. Kazenas and D. M. Chizhikov, *Pressure and Composition of Vapor over Oxides of Chemical Elements* (Nauka, Moscow, 1976), p. 108 [in Russian].
3. I. F. Kononyuk, V. A. Shnyp, and M. I. Borisyuk, Izv. Akad. Nauk SSSR, Neorg. Mater. **5** (8), 1422 (1969).
4. A. N. Zobnina and I. P. Kislyakov, Izv. Akad. Nauk SSSR, Neorg. Mater. **2** (12), 2199 (1966).
5. A. N. Zobnina, S. I. Kopeĭkin, and I. P. Kislyakov, Izv. Akad. Nauk SSSR, Neorg. Mater. **8** (12), 2149 (1972).
6. Zh. G. Bazarova, M. V. Mokhosoev, É. A. Kirillov, and K. N. Fedorov, Izv. Akad. Nauk SSSR, Neorg. Mater. **14** (8), 1504 (1979).
7. T. M. Yanushkevich, Candidate's Dissertation in Chemistry (Ural State Univ., Sverdlovsk, 1973).
8. Ye. V. Tkachenko, L. M. Fedorova, V. T. Gabrielyan, *et al.*, *Main Regularities of Three-Phase Interaction of PbO and MoO_3*, Available from ONIITÉKhIM, No. 3278/79 (Cherkassy, 1980).
9. Ye. V. Tkachenko, L. M. Fedorova, V. T. Gabrielyan, *et al.*, Zh. Neorg. Khim. **25** (6), 1443 (1980).
10. L. M. Fedorova, Candidate's Dissertation in Chemistry (Ural State Univ., Sverdlovsk, 1983).
11. A. V. Denisov, V. T. Gabrielyan, O. S. Grunskiĭ, and E. N. Kotel'nikova, in *Proceedings of International Conference on Crystallogenesis and Mineralogy* (St. Petersburg, 2001), p. 88.
12. P. P. Budnikov and A. M. Ginstling, *Reactions in Solid Mixtures* (Stroĭizdat, Moscow, 1971) [in Russian].
13. V. T. Gabrielyan, L. M. Feodorova, Ye. V. Tkachenko, *et al.*, Cryst. Res. Technol. **21** (4), 439 (1986).

Translated by Yu. Sin'kov

Crystallography Reports, Vol. 50, No. 2, 2005, pp. 335–337. Translated from Kristallografiya, Vol. 50, No. 2, 2005, pp. 372–374.

CRYSTALLOGRAPHIC SOFTWARE

New Force Field for Molecular Simulation and Crystal Design Developed Based on the "Data Mining" Method

D. W. M. Hofmann* and L. N. Kuleshova**

** University of Frankfurt on Main, Marie Curie Str., Frankfurt on Main, D-60439 Germany*
e-mail: detlef.hofmann@chemie.uni-frankfurt.de
*** Nesmeyanov Institute of Organoelement Compounds, Russian Academy of Sciences, ul. Vavilova 28, Moscow, 119991 Russia*
e-mail: lukul@xrlab.ineos.ac.ru

Received October 6, 2004

Abstract—The Data Mining algorithm is used to analyze the information of the Cambridge Structural Database (CSD) with the aim to develop a force field which describes intermolecular interactions. The force-field parameters obtained are successfully tested in calculations of sublimation energy; in construction of polar crystals; in prediction of crystal packings, including predictions based on X-ray powder diffraction data; and in prognosis of protein–ligand interactions and stability of polymorphs. The parametrization developed may also be used in other programs. The parameters are given for all the atomic species encountered in the CSD together with the instructions for their use. © *2005 Pleiades Publishing, Inc.*

INTRODUCTION

Data mining is a powerful technique for extracting predictive information from large databases [1]. The automated analysis offered by data mining goes beyond the retrospective analysis of data. Data mining tools can answer questions that are too time consuming to resolve with methods based on the first principles. In data mining, databases are searched for hidden patterns to reveal predictive information in patterns that are too complicated for experts to identify. This Data Mining method is widely used, e.g., for prognosis of price formation and marketing, quality control of various products, etc. D.W.M. Hofmann suggested the use of the Data Mining algorithm for analysis of the information stored in the Cambridge Structural Database (CSD) in order to develop a force field which would describe intermolecular interactions [2]. In this approach, a force field is described by pair atom–atom potential functions whose shape is not postulated a priori but is established in the process of their optimization (Trained Potentials). The force-field parameters thus obtained are successfully tested in calculations of sublimation energy and design of polar crystals [3], prediction of crystal packings [4] (including predictions based on X-ray powder diffraction data [5]) and protein structures, and prognosis of protein–ligand interactions [6] and polymorph stability [7]. All the necessary computations were performed using the programs ScorCryst and FlexCryst written by D. Hofmann [8]. The parametrization used in these programs may also be useful in other programs. The potential function and the parameters of the force field developed by Hofmann for a pair of H···H atoms are indicated in the table and are represented graphically in the figure. The complete parametrization set for all the atomic species encountered in the CSD is deposited in VINITI (no. 1596-B2004, October 13, 2004).[1] The description of the potential functions and the instructions for their use in computations are given below.

DESCRIPTION OF A FORCE FIELD

The energy of intermolecular interaction between the two molecules I and J in Hofmann's force field is described by a sum of pair atom–atom interactions. If a pair of molecules consists of n_I and n_J atoms, respectively, the energy of their interaction is calculated as

$$E_{IJ} = \sum_{i=1}^{n_I} \sum_{j=1}^{n_J} \varepsilon_{ij r_{ij}}.$$

In the table, the atomic species are indicated by the corresponding atomic numbers. The only exception is made for hydrogen atoms which are divided into four subtypes depending on the atomic species linked to the given hydrogen atom: C–H (type 2), O–H (type 18), N–H (type 10), and the *X*–H (type 1) for all the remaining atoms. The use of various types of hydrogen atoms is very important for correct modeling of hydrogen bonds. In this case, the m and n values in the table represent

$m = \min(type(i), type(j))$ (minimum atomic number in this pair of i and j atoms);

[1] To obtain the set of parametrization, one should contact VINITI at dep@viniti.ru.

Potential function of a pair of (C)H···H(C) atoms

ε	*m*	*n*	*k*	ε	*m*	*n*	*k*
0.0104	2	2	3	2.8963	2	2	31
0.0273	2	2	4	2.8418	2	2	32
0.0162	2	2	5	2.5323	2	2	33
0.0289	2	2	6	3.9187	2	2	34
−0.0100	2	2	7	3.1392	2	2	35
−0.0772	2	2	8	2.1169	2	2	36
−0.0856	2	2	9	2.4206	2	2	37
−0.1075	2	2	10	1.7225	2	2	38
−0.1100	2	2	11	1.7119	2	2	39
−0.0690	2	2	12	2.3694	2	2	40
−0.0087	2	2	13	2.5355	2	2	41
0.0589	2	2	14	0.7463	2	2	42
0.1571	2	2	15	0.6021	2	2	43
0.2919	2	2	16	2.5862	2	2	44
0.4282	2	2	17	3.5320	2	2	45
0.5835	2	2	18	4.2421	2	2	46
0.8825	2	2	19	1.5933	2	2	47
1.1640	2	2	20	1.1476	2	2	48
1.4178	2	2	21	1.2376	2	2	49
1.6440	2	2	22	2.0973	2	2	50
1.9108	2	2	23	2.6430	2	2	51
2.3182	2	2	24	3.1096	2	2	52
2.3050	2	2	25	3.2295	2	2	53
2.5221	2	2	26	2.8449	2	2	54
2.6600	2	2	27	4.4408	2	2	55
2.9927	2	2	28	5.8357	2	2	56
3.8019	2	2	29	7.6392	2	2	58
4.3982	2	2	30	9.2890	2	2	59

$n = \max(type(i), type(j))$ (maximum atomic number in this pair of i and j atoms).

The energy potential $\varepsilon_{ijr_{ij}}$ for a pair of i and j atoms is a function of the distance and atomic species. The form of the energy potential f_{ij} for each pair of i and j atoms is determined with the aid of the reference points (k). When choosing the number of the reference points for the given pair of atoms, one has to maintain the compromise between the necessary accuracy of the energy function and the number of the experimental data which increases with an increase of the number of atomic species according to a quadratic law. If one assumes the reciprocal quadratic dependence of the energy potential f (and, correspondingly, of the reference point $k = \lfloor f \rfloor$) on the distance r_{ij},

$$f = 100/r_{ij}^2 \ [\text{Å}]^2,$$

it becomes possible to take into account many more reference points in the region of short interatomic distances and considerably less points in the region of large interatomic distances. The selected reference-point distribution describes the potential in the region of short distances more accurately than in the region of large distances. Since in the region of large distances the potential is smooth, the limited number of reference points in this case does not lead to loss of the accuracy. Moreover, the energy ε_{ij} is calculated for a pair of atoms the distance r_{ij} between which is lower than a certain threshold value $r_{threshold} = 5.77$ Å.[2]

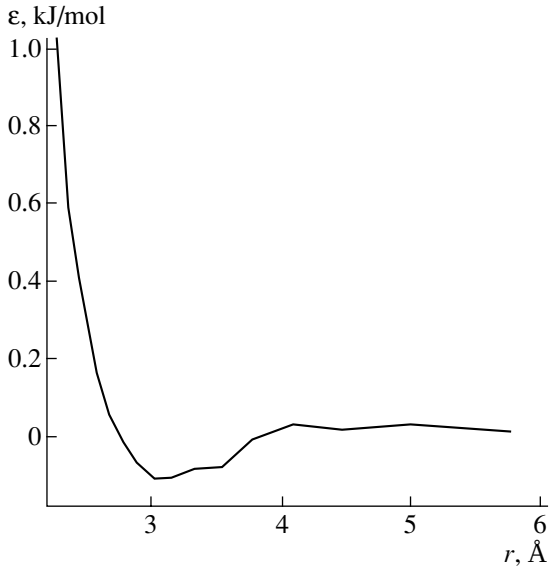

Potential function for a pair of (C)H···H(C) atoms.

Now replace the pair potential in the initial formula for energy to obtain

$$E_{IJ}\ [\text{kJ/mol}] = \sum_{i=1}^{n_I}\sum_{j=1}^{n_J} \varepsilon_{m_{ij}n_{ij}r_{ij}}.$$

Interpolating the energy potential between the neighboring reference points linearly, we obtain the continuous potential (figure)

$$\varepsilon_{mnr_{ij}}\ [\text{kJ/mol}] = (f-k)\varepsilon_{mnk+1} + (k+1-f)\varepsilon_{mnk}.$$

[2] Since the table gives the value $k_{\min} = 3$,

$$r_{threshold} = \sqrt{100/k_{\min}} = 5.77.$$

Since the accuracy of the potential parametrization directly depends on the number of the crystal structures determined and their quality (which are constantly increasing), we hope that Hofmann's parametrization will become a useful tool for the direct solution of many crystallographic problems and molecular designing.

REFERENCES

1. R. O. Duda and P. E. Hart, *Pattern Classification and Scene Analysis* (Wiley, New York, 1973; Mir, Moscow, 1976).
2. D. W. M. Hofmann and T. Lengauer, J. Mol. Model. **4**, 132 (1998).
3. D. W. M. Hofmann, L. N. Kuleshova, and M. Yu. Antipin, Cryst. Growth Design **4** (6), 1395 (2004).
4. G. M. Day, W. Motherwell, H. Ammon, *et al.*, Acta Crystallogr. (in preparation).
5. M. U. Schmidt, D. W. M. Hofmann, C. Buchsbaum, and H. J. Metz (in preparation).
6. J. Apostolakis, D. W. M. Hofmann, and T. Lengauer, *Using Simple Learning Machines to Derive a New Potential for Molecular Modelling* (Prous Science, Barselona, 2001), p. 125.
7. L. N. Kuleshova, D. V. M. Hofmann, and M. Yu. Antipin, Kristallografiya (2005) (in press).
8. D. W. M. Hofmann and T. Lengauer, Acta Crystallogr., Sect. A: Found. Crystallogr. **53**, 225 (1997).

Translated by L. Man

Crystallography Reports, Vol. 50, No. 2, 2005, pp. 338–342. Translated from Kristallografiya, Vol. 50, No. 2, 2005, pp. 375–380.

MEMORIAL DATA

To the 80th Anniversary of the Birth of Boris Nikolaevich Grechushnikov (1925–1993)

T. F. Veremeĭchik

Shubnikov Institute of Crystallography, Russian Academy of Sciences, Leninskiĭ pr. 59, Moscow, 119333 Russia
e-mail: tomver@online.ru

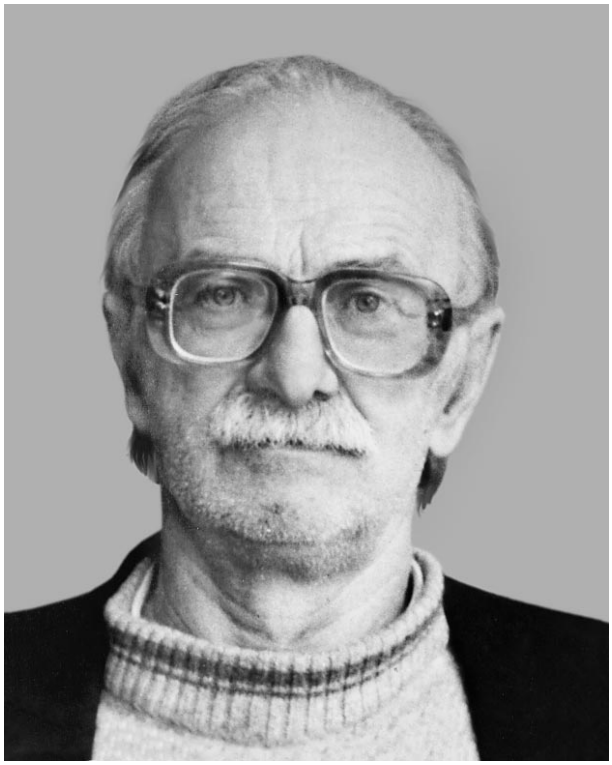

"Wenn du als Jüngling deinen Vater ehrst,
So wirst du gern von ihm empfangen;
Wenn du als Mann die Wissenschaft vermehrst,
So kann dein Sohn zu höhrem Ziel gelangen."[1]

J.W. Goethe, Faust, Insel-Verlag, 1958, p. 160

Professor Boris Nikolaevich Grechushnikov, honorary Scientist of the Russian Federation and Doctor of Physics and Mathematics, was an outstanding scientist of bright and original talent. His works on Fourier spectroscopy, optical and resonance spectroscopy, and crystal optics had a strong influence on modern physical and applied optics, spectroscopy, and laser physics. Grechushnikov was the author of 6 monographs and approximately 250 other publications. He also wrote the chapter "Optical Properties of Crystals" for the four-volume crystallographic encyclopedia Modern Crystallography. Grechushnikov prepared more than twenty candidates of science. He guided or participated in the fulfillment of a number of important governmental orders on the creation of new technologies for the defense industry. For his scientific achievements, he

[1] *"Dost thou thy father honor, as a youth?*
Then may his teaching cheerfully impel thee:
Dost thou, as man, increase the stores of truth?
Then may thine own son afterwards excel thee."

"Faust," Translated by Bayard Taylor, Houghton, Muffin and Co., Boston and New York, 1898

1063-7745/05/5002-0338$26.00

was decorated with the Order of the October Revolution and numerous other medals.

In 2005, we will celebrate the 60th anniversary of the victory in the Great Patriotic War of 1941–1945. Grechushnikov was a defender of his native country; he participated in the arduous Battle of Kursk, where he was badly wounded. He rendered great services to his country and was awarded the military orders of the Red Star and the Patriotic War of the First Degree and several medals.

Grechushnikov's attitude to life was remarkable. In fact, he eschewed materialistic tendencies and cherished the spirit of ethical standards. The essence of his life comprised constant learning, acquisition of new knowledge, and thought.

All past events have broadened our knowledge about human nature. Technological, informational, democratic, and other kinds of revolutions have changed our ideas of what is and is not allowed. The eternal question "to possess or to exist" has received a global answer: to possess. It seems that all deep human instincts and especially the individualistic elements have been awoken. Grechushnikov symbolized the opposite attitude to life: self-sacrifice and human solidarity. His fate fully reflects the fate of his people. His deeds have made him a hero of Russian history.

ABRIDGED BIOGRAPHICAL DATA

Grechushnikov was born on February 18, 1925, in the city of Kazan. His father, Nikola@i Grechushnikov, a senior lecturer at the Department of Mathematics, Bashkirian Pedagogical Institute, was the author of several publications on the theory of nomography. His mother was a pharmacist. During the Civil War, his father was an officer in the White Army. Later, in Soviet times, this fact influenced the life of his family: they had to move from city to city, so Grechushnikov's school years were spent in Kazan, Makhachkala, and Ufa.

In 1942, Grechushnikov entered the Physical–Mathematical Faculty, Kazan State University, but, on January 1, 1943, he was called up to the Red Army. After a short training at the infantry school in the city of Zhitomir, an 18-year-old Grechushnikov arrived at the beginning of summer 1943 to the front. As a soldier, he participated in the famous Battle of Kursk. He was wounded at Belgorod, lost a leg, and long recuperated in military hospitals. In June 1944, he was discharged from the army.

Grechushnikov returned to Kazan University in 1945 and graduated with distinction from the Department of Theoretical Physics in 1949. In those years, student groups at the universities consisted of one to two people. His professors were well known mathematicians and physicists such as E.K. Zavoĭskiĭ, A.P. Norden, F.D. Gakhov, and others. From his family, Grechushnikov inherited high spirituality, an interest in science, and the love to work. In university he developed his rare talents and excellent memory and added a brilliant education to these qualities.

In 1950 Grechushnikov started writing entrance exams to enter a postgraduate course in Moscow. He passed the exams on dialectic and historical materialism with the mark "good" and on quantum mechanics and crystallography with the mark "excellent." The exams on quantum mechanics and crystallography were administered by A.V. Shubnikov, N.V. Belov, M.A. Markov, and Z.G. Pinsker; exams on crystallography, by Shubnikov, Belov, G.G. Lemmlein, and E.E. Flint. It is easy to imagine the excitement and confusion of a young student standing before such distinguished commissions. He passed the first exam in quantum mechanics in May 1950, and he passed all the other exams later in April 1951. This long interval is explained by the refusal to accept him into the postgraduate course at the Lebedev Physical Institute, USSR Academy of Sciences, because his father participated in the Civil War on the side of the White Army.

In 1951 Grechushnikov became a postgraduate student at the Laboratory of Crystal Optics of the Institute of Crystallography, USSR Academy of Sciences, headed then by N.E. Vedeneeva. His scientific supervisor was Shubnikov. In 1953 Grechushnikov defended his candidate's dissertation. One of his opponents was Professor V.L. Ginzburg, a future Nobel Prize winner.

Also in 1951 Grechushnikov started working at the Institute of Crystallography and continued working there up to his last days. In 1966, he became head of the Laboratory of Crystal Optics, which was later reorganized into the Laboratory of Crystal Spectroscopy. In 1980, Grechushnikov defended his doctoral dissertation and, this time, one of his opponents was another Nobel Prize winner: Academician A.M. Prokhorov.

BASIC SCIENTIFIC ACHIEVEMENTS AND ORGANIZING ACTIVITY

One of Grechushnikov's distinctive qualities was his brilliant erudition in the theoretical and experimental general physics, computational methods, and programming. A physicist–theoretician with a broad scope, he was also an outstanding experimentalist. He was a laborious person and enlivened these around him. It is possibly these qualities that allowed him to obtain a number of new results in some fields of theoretical and applied spectroscopy.

The 1950s–1960s seem to be the period where his creative scientific activity blossomed. Professor V.L. Indenbom, an opponent of Grechushnikov's doctoral dissertation wrote, "Looking back, one may only admire Grechushnikov's gift for choosing the appropriate directions of research."

One of his first publications [1] entitled *Absorption Spectra of Ruby Crystals at Various Temperatures*, a constituent part of his candidate's dissertation, was

dedicated to the first experimental evidence of the interaction between a photoinduced transition in an impurity center and crystal-lattice vibrations. It became clear that this interaction determines crystal colors. Relaxation of perturbations in the electronic subsystem is one of the main processes determining possible generation. This study formed the basis for the development of laser physics now widely used in numerous modern technologies and in medicine.

One of the most impressive achievements of the Institute of Crystallography during its existence was the discovery of Fourier spectroscopy by Grechushnikov in coauthorship with G.I. Distler and I.P. Petrov. Grechushnikov performed his studies independently and simultaneously with foreign scientists, but these studies were associated with classified subjects and, therefore, could not be published at that time. This explains the fact that foreign publications on this effect, first and foremost those by Prof. P. Jaquinot and P. J. Fellgett, appeared somewhat earlier than Grechushnikov's. Grechushnikov was given a tribute, and his contribution to Fourier spectroscopy was recognized in Lovenstain's review *History and State of Fourier Spectroscopy* [2] and in the review *Boris Nikolaevich Grechushnikov, an Outstanding Scientist in Modern Physical and Applied Optics* written by Prokhorov *et al.* [3]. This new method of recording spectra of sources allowed one to increase the threshold sensitivity of the classical methods by a factor of several hundred. Today Fourier spectroscopy is widely used to record weakly luminous astronomical and biological objects, as well as objects whose identification is important for military and other purposes.

In the classical methods, the spatial resolution of a radiation into monochromatic fluxes is done with the aid of various prisms, diffraction gratings, etc. The gain in the signal-to-noise ratio in Fourier spectroscopy is obtained because of the simultaneous action on a detector of all the spectral elements of the radiation and two-stage processing of the signal. Grechushnikov and his colleagues developed the optimum models of Fourier spectrometers based on interference-polarization filters and a polarization interferometer. The working models of these devices were used to obtain the unique well-resolved individual luminosity spectra of Saturn and its rings and also weak luminescence in laser destruction. Grechushnikov showed that spectroscopy should be developed by designing new devices that change the program of measurements depending on the input information. It is this principle that underlies the operation of modern recording units.

At that time Grechushnikov used polarization optics to solve a number of problems of civil defense, including the development of an effective defense for the advanced naval harbor. Grechushnikov and Distler suggested a solution based on the use of large-scale infrared polarization devices supplied having night-vision devices with special attachments that would allow the analysis of false and reference sources around advanced navy harbors. The method allowed periodical (at short periods) recording of the fairway in mine fields around the harbor. Fourier spectrometry of sea noise was used to reveal unknown underwater objects, and polarization optics was used to determine the current submarine coordinates without surfacing.

Grechushnikov became a coauthor of the method of infrared flaw detection for solving an important problem of material quality. The new methods, developed mainly in cooperation with V.S. Chudakov, allowed visualization of internal stresses, nonstoichiometry, inhomogeneity in the impurity distribution, and other defects by following the changes of their optical characteristics. The devices designed for studying crystal defects were manufactured and used in industry and in research and industrial institutions. Grechushnikov's capacity for work also allowed him to participate in the studies on growth of quality crystals for science and industry performed by the Institute of Crystallography. Various optical and spectral methods were used in Grechushnikov's works on quartz piezoelectric plates performed in cooperation with L.G. Chentsova; on sapphire with various activators performed in cooperation with A.A. Popova; and on ruby crystals for enhancement of radiation in the microwave and optical ranges performed in cooperation with Kh.S. Bagdasarov and V.Ya. Khaimov-Mal'kov, respectively.

At the same time, Grechushnikov also delivered lectures at Moscow State University and the Institute of Steel and Alloys. He later lectured at the Institute of Crystallography.

In 1966, Grechushnikov became head of the Laboratory of Spectroscopy. His erudition allowed him to perform many-sided complex studies of the optical and spectral properties of various crystals. Development of diverse experimental methods was accompanied by development of the theory of light interaction with a crystal. New highly educated physicists came to the laboratory. These were graduates of the Institute of Physical Problems (G.I. Kosourov, B.K. Sevast'yanov, I.N. Kalinkina, O.V. Kachalov, and A.Ya. Parshin) and students from the Faculty of Physics of Moscow State University and Moscow Physical–Technical Institute.

Fourier spectroscopy was further developed in cooperation with Parshin (now a corresponding member of the Russian Academy of Sciences), Petrov, and S.V. Koryshev. They designed and constructed new Fourier spectrometers and described mathematically and optimized their operation. Grechushnikov, together with A.F. Konstantinova and V.A. Shamburov, further developed classical crystal optics and worked out in detail the modern theory of light propagation and its transformation in crystals and suggested new experimental methods for measuring parameters of light. Grechushnikov, D.T. Sviridov, and T.F. Veremeĭchik studied promising new crystals. The accuracy of the theory of the crystal field was increased by taking into account some fine effects. Impurity-free and activated crystals

were studied experimentally by the methods of optical (with Petrov) and EPR spectroscopy (together with Petrov and V.F. Karyagin, respectively), by NMR spectroscopy (together with V.Yu. Galitskiĭ, Yu.A. Sokolov, and V.A. Detinich), and by circular dichroism (together with Z.B. Perekalina). The spectral methods were also used for study and quality control of yttrium–aluminum garnet (YAG) activated by transition elements (in cooperation with Bagdasarov) and study of optical characteristics of cuprous oxide (in cooperation with L.S. Starostina).

The development of new methods required the development of an adequate theory and methods for data processing. The unique results in this field were obtained by Grechushnikov together with V.V. Volkov, Kalinkina, and Parshin. By appropriately processing their experimental data, this group to managed considerably increase the efficiency of the experimental results. Similar data processing was also performed in structural crystallography during the development of new approaches to the Patterson function (in cooperation with Belov and V. V. Ilyukhin).

It should be mentioned that Grechushnikov was one of the first scientists who widely used computers for solving scientific problems. He himself wrote many programs and often performed the computations.

At different times Grechushnikov worked with independent groups organized in his laboratory: Kosourov's group for nonlinear optics, holography, and amplification of radiation frequency (Kalinkina, Kachalov, and M.P. Goloveĭ); Sevast'yanov's group for spectroscopy of activated crystals under pumping conditions (V.P. Orekhova, L.B. Pasternak, S.V. Volkov, *et al.*); Sviridov's group (development of mathematical apparatus of the theory of crystal field which related the structure and spectra of impurity centers and applied it to the study of laser crystals (Veremeĭchik); and Shamburov's group for transformation of light waves by crystals and the use of fine effects of this transformation in various devices (E.A. Evdishchenko and A.I. Vislobokov).

For about twenty-five years, Grechushnikov headed the joint seminar of the Department of Crystal Properties at the Institute of Crystallography. Grechushnikov's unselfish activity demonstrated the measure of his devotedness to science and his encyclopedic knowledge. At this seminar hundreds of doctoral and candidate's dissertations, as well as other works performed at the Institute of Crystallography and other institutions, were discussed. Deeply penetrating into the essence of these studies and showing deep interest in these studies, Grechushnikov often helped the authors better understand discussed problems, see them as a whole, and reveal fine theoretical and experimental details.

Grechushnikov also guided the Moscow Seminar on Electron Paramagnetic Resonance and for many years participated in the Scientific Council on Radiospectroscopy of Condensed Media at the Presidium of the USSR Academy of Sciences. Together with Konstantinova, he organized annual seminars and conferences on optics of anisotropic media.

The many-sided nature of Grechushnikov is also seen from the topics considered at the so-called First-of-April Seminar, having no analogues at the institutions of the Academy of Sciences. The seminar had the aim of improving scientific and personal contacts and broad education. In addition to the members of the Institute of Crystallography and Grechushnikov himself, this seminar was attended by many. The topics discussed ranged from Dali's painting, then almost unknown in the Soviet Union, to prognosis of the periods of magnetic-field perturbation. A.P. Levanyuk drank distilled water and stated at the food table the complete theory of sanitary starvation. Parshin demonstrated that the 13th day of each month is most often Friday. Sviridov delivered a lecture on insects. Grechushnikov considered Durer's magic squares, spoke about the life of Euler and other scientists, considered Hippocrates' Lunar, etc.

SOME MEMOIRS ABOUT GRECHUSNIKOV

Grechushnikov was a man of high inherent culture. He happily combined composure, thoughtfulness in communication with other people, self-control and tolerance, and respect for his opponents' opinions no matter their age or rank. All these features attracted people as if they had joined in something bright and joyous. He was full of energy and liked to work. Grechushnikov, being a gifted leader full of energy, was able to stimulate people's curiosity and interest to participate in his work.

Religious people believe that a man may distinguish in another person only those sins he himself possesses. A highly moral person, Grechushnikov did not like to criticize his colleagues as many creative and competitive people do. If he had to criticize someone, he did it very gently and only in private. He liked people and had a sense of community. Grechushnikov did not only advise numerous colleagues and visitors: someone always stayed at his apartment. Sometimes, these were people he had never met before: they were brought home by his wife, who recognized them somewhere downtown from their Arkhangel'sk accents.

Grechushnikov's personal qualities attracted special attraction. V.I. Alshits said at the seminar dedicated to the 70th anniversary of Grechushnikov's birth, "Boris Nikolaevich was the most beloved person at the institute." This is also confirmed by many well-known facts. A Nobel Prize winner offered himself as an opponent of Grechushnikov's doctoral dissertation. Grechushnikov's colleagues made a film dedicated to his fiftieth birthday which was full of love and humor and verses written by L. Pasternak, a son of a Nobel Prize winner. The first deed of Sevast'yanov after his appointment to the directory of the Institute of Crystallography, was to help Grechushnikov get a new comfortable apartment as an invalid of the Great Patriotic War. When Grechushnikov became seriously ill, his colleagues Bag-

dasarov and A.A. Chernov managed to get a very rare remedy and invite for him the best doctor; they also helped in the solution of many other problems. Indenbom was a friend of our laboratory and, after Grechushnikov's death, a seriously ill Indenbom once again showed his devotion to Grechushnikov. He suggested writing a detailed review of Grechushnikov's publications, managed to invite Academician Prokhorov and Director of the Institute of Crystallography Academician Vainshtein to write such a review, and himself participated in this work. Kachalov, who, in fact, participated in writing of the review article [3], refused to write his name as a coauthor because the number of potential coauthors seemed to be too large. Konstantinova for 25 years was a scientific secretary of all the seminars headed by Grechushnikov.

Grechushnikov was a man of diverse talents and interests. He was highly sensitive to words and enjoyed reading unique and elegant books written by Newton and Euler. He knew Lermontov's poems by heart and liked to read Tsvetaeva's verses. He wrote his articles in one sitting and practically never introduced any corrections. He spoke plainly, directly, and without affectation. His language was clear and reserved and, at the same time, was harmonic and had clear sense.

Grechushnikov had several hobbies. He liked to repair clocks and watches and did so for everybody. He especially liked striking clocks. In his apartment he had several such clocks. He also liked astronomy and had a small observatory at home. Therefore, nobody ever could hear from him that the most important thing is health: how fleeting is that which we deem most important.

Grechushnikov played chess and loved fishing. He developed his own attitude to nature and never loudly admired its beauty. It seemed that he tried to penetrate the essence of natural phenomena. "How can such powerful trees be formed from water and soil?" he used to ask. He named a beautiful large blue fish in his home aquarium "Elizaveta Petrovna" after the Russian empress who liked the color blue.

Grechushnikov's civic stand was definite and invariable. It is impossible to say that he loved Russia because he simply was one of its inherent parts. Once he told us about the luckiest moment in his life. He was badly wounded and lied without a leg on the ground near a medical train; it was then that he realized himself to be involved in Russian history for the benefit of the people. Therefore, everything which happened to his country happened to him as well. He highly regarded perestroika. The situation was grave for him because, being an invalid, he could not get to the institute: he did not have enough money for taking a taxi. He overcame his depression; he was courageous. No matter when we visited him, he was always working at the writing table and joked "I am like a rusty nail in a fence." The texts and formulas were always prepared and written on library cards.

The time and place of his death also to seem be symbolic. He died at 2:30 p.m. on October 3, 1993, in the hospital of the Academy of Sciences located behind the Moscow department store. At that very moment, thousands of people on the nearby October Square rose to defend the legitimate parliament.

CONCLUDING REMARKS

We would like to say a few words about some peculiar facts related to Grechushnikov.

It seems that Grechushnikov was the only scientist who had as opponents of his candidate's and doctoral dissertations future Nobel Prize winners. The opponent of his candidate's dissertation was future Academician and Nobel Prize winner V.L. Ginzburg. The opponent of his doctoral dissertation, A.M. Prokhorov, was also an Academician and a Nobel Prize winner. This fact shows the commensurate scientific and moral scale of the competitor and his opponents. We should also mention another person who worked at Grechushnikov's laboratory, L.B. Pasternak, a son of Leonid Pasternak, a Nobel Prize winner in literature. The second peculiar fact is that of 50 scientists who worked with Grechushnikov during his life, 7 people were related to different pairs of twins. Among the older generation, Chentsova, Grechushnikov himself, and Volkov had twin siblings; from the next generation, Kalinkina, Evdishchenko, and Volkov were parents of twins. In 2004 twin grandsons were born in Kachalov's family. According to the causality principle, this fact may be interpreted as "Grechushnikov's rule": a human being is close to a human being. Probably it is the way of nature to grant Grechushnikov's qualities to future generations. This allows us to believe that the self-sacrifice, love, and talent inherent in Grechushnikov will be inherited by new generations.

The inherent right of an individual in modern society is to acquire, possess, and obtain income. Grechushnikov was an extremely modest person in life and modestly estimated his work. In fact, he belonged to minority, but it is this the minority that forms the basis of a reasonable life of humanity.

ACKNOWLEDGMENTS

I am grateful to A.F. Konstantinova and E.A. Evdishchenko for their help and valuable remarks, as well as to O.V. Kachalov, V.V. Volkov, V.I. Simonov, and T.A. Karpeeva.

REFERENCES

1. J. Lovenstain, Appl. Opt. **5** (5), 845 (1966).
2. A. M. Prokhorov, B. K. Vaĭnshteĭn, V. L. Indenbom, *et al.*, Kristallografiya **40** (6), 1113 (1995) [Crystallogr. Rep. **40**, 1036 (1995)].
3. B. N. Grechushnikov, Dokl. Akad. Nauk SSSR **99** (5), 707 (1954).

Translated by L. Man